TA 8.

Finite element analysis in geotechnical engineering

Theory

David M. Potts and Lidija Zdravković

Imperial College of Science, Technology and Medicine

Thomas Telford

Published by Thomas Telford Publishing, Thomas Telford Ltd, 1 Heron Quay, London E14 4JD.
URL: http://www.t-telford.co.uk

Distributors for Thomas Telford books are
USA: ASCE Press, 1801 Alexander Bell Drive, Reston, VA 20191-4400, USA
Japan: Maruzen Co. Ltd, Book Department, 3–10 Nihonbashi 2-chome, Chuo-ku, Tokyo 103
Australia: DA Books and Journals, 648 Whitehorse Road, Mitcham 3132, Victoria

First published 1999

Also available from Thomas Telford Books
Finite element analysis in geotechnical engineering: application. ISBN 0 7277 2783 4

A catalogue record for this book is available from the British Library

ISBN: 0 7277 2753 2

Printed and bound in Great Britain by Bookcraft (Bath) Limited

Contents

Preface

While the finite element method has been used in many fields of engineering practice for over thirty years, it is only relatively recently that it has begun to be widely used for analysing geotechnical problems. This is probably because there are many complex issues which are specific to geotechnical engineering and which have only been resolved relatively recently. Perhaps this explains why there are few books which cover the application of the finite element method to geotechnical engineering.

For over twenty years we, at Imperial College, have been working at the leading edge of the application of the finite element method to the analysis of practical geotechnical problems. Consequently, we have gained enormous experience of this type of work and have shown that, when properly used, this method can produce realistic results which are of value to practical engineering problems. Because we have written all our own computer code, we also have an in-depth understanding of the relevant theory.

Based on this experience we believe that, to perform useful geotechnical finite element analysis, an engineer requires specialist knowledge in a range of subjects. Firstly, a sound understanding of soil mechanics and finite element theory is required. Secondly, an in-depth understanding and appreciation of the limitations of the various constitutive models that are currently available is needed. Lastly, users must be fully conversant with the manner in which the software they are using works. Unfortunately, it is not easy for a geotechnical engineer to gain all these skills, as it is vary rare for all of them to be part of a single undergraduate or postgraduate degree course. It is perhaps, therefore, not surprising that many engineers, who carry out such analyses and/or use the results from such analyses, are not aware of the potential restrictions and pitfalls involved.

This problem was highlighted when we recently gave a four day course on numerical analysis in geotechnical engineering. Although the course was a great success, attracting many participants from both industry and academia, it did highlight the difficulty that engineers have in obtaining the necessary skills required to perform good numerical analysis. In fact, it was the delegates on this course who urged us, and provided the inspiration, to write this book.

The overall objective of the book is to provide the reader with an insight into the use of the finite element method in geotechnical engineering. More specific aims are:

- To present the theory, assumptions and approximations involved in finite element analysis;
- To describe some of the more popular constitutive models currently available and explore their strengths and weaknesses;
- To provide sufficient information so that readers can assess and compare the capabilities of available commercial software;
- To provide sufficient information so that readers can make judgements as to the credibility of numerical results that they may obtain, or review, in the future;
- To show, by means of practical examples, the restrictions, pitfalls, advantages and disadvantages of numerical analysis.

The book is primarily aimed at users of commercial finite element software both in industry and in academia. However, it will also be of use to students in their final years of an undergraduate course, or those on a postgraduate course in geotechnical engineering. A prime objective has been to present the material in the simplest possible way and in manner understandable to most engineers. Consequently, we have refrained from using tensor notation and presented all theory in terms of conventional matrix algebra.

When we first considered writing this book, it became clear that we could not cover all aspects of numerical analysis relevant to geotechnical engineering. We reached this conclusion for two reasons. Firstly, the subject area is so vast that to adequately cover it would take many volumes and, secondly, we did not have experience with all the different aspects. Consequently, we decided only to include material which we felt we had adequate experience of and that was useful to a practising engineer. As a result we have concentrated on static behaviour and have not considered dynamic effects. Even so, we soon found that the material we wished to include would not sensibly fit into a single volume. The material has therefore been divided into theory and application, each presented in a separate volume.

Volume 1 concentrates on the theory behind the finite element method and on the various constitutive models currently available. This is essential reading for any user of a finite element package as it clearly outlines the assumptions and limitations involved. Volume 2 concentrates on the application of the method to real geotechnical problems, highlighting how the method can be applied, its advantages and disadvantages, and some of the pitfalls. This is also essential reading for a user of a software package and for any engineer who is commissioning and/or reviewing the results of finite element analyses.

This volume of the book (i.e. Volume 1) consists of twelve chapters. Chapter 1 considers the general requirements of any form of geotechnical analysis and provides a framework for assessing the relevant merits of the different methods of analysis currently used in geotechnical design. This enables the reader to gain an insight into the potential advantage of numerical analysis over the more

'conventional' approaches currently in use. The basic finite element theory for linear material behaviour is described in Chapter 2. Emphasis is placed on highlighting the assumptions and limitations. Chapter 3 then presents the modifications and additions that are required to enable geotechnical analysis to be performed.

The main limitation of the basic finite element theory is that it is based on the assumption of linear material behaviour. Soils do not behave in such a manner and Chapter 4 highlights the important facets of soil behaviour that ideally should be accounted for by a constitutive model. Unfortunately, a constitutive model which can account for all these facets of behaviour, and at the same time be defined by a realistic number of input parameters which can readily be determined from simple laboratory tests, does not exist. Nonlinear elastic constitutive models are presented in Chapter 5 and although these are an improvement over the linear elastic models that were used in the early days of finite element analyses, they suffer severe limitations. The majority of constitutive models currently in use are based on the framework of elasto-plasticity and this is described in Chapter 6. Simple elasto-plastic models are then presented in Chapter 7 and more complex models in Chapter 8.

To use these nonlinear constitutive models in finite element analysis requires an extension of the theory presented in Chapter 2. This is described in Chapter 9 where some of the most popular nonlinear solution strategies are considered. It is shown that some of these can result in large errors unless extreme care is exercised by the user. The procedures required to obtain accurate solutions are discussed.

Chapter 10 presents the finite element theory for analysing coupled problems involving both deformation and pore fluid flow. This enables time dependent consolidation problems to be analysed.

Three dimensional problems are considered in Chapter 11. Such problems require large amounts of computer resources and methods for reducing these are discussed. In particular the use of iterative equation solvers is considered. While these have been used successfully in other branches of engineering, it is shown that, with present computer hardware, they are unlikely to be economical for the majority of geotechnical problems.

The theory behind Fourier Series Aided Finite Element Analysis is described in Chapter 12. Such analysis can be applied to three dimensional problems which possess an axi-symmetric geometry but a non axi-symmetric distribution of material properties and/or loading. It is shown that analyses based on this approach can give accurate results with up to an order of magnitude saving in computer resources compared to equivalent analyses performed with a conventional three dimensional finite element formulation.

Volume 2 of this book builds on the material given in this volume. However, the emphasis is less on theory and more on the application of the finite element method in engineering practice. Topics such as obtaining geotechnical parameters

from standard laboratory and field tests and the analysis of tunnels, earth retaining structures, cut slopes, embankments and foundations are covered. A chapter on benchmarking is also included. Emphasis is placed on explaining how the finite element method should be applied and what are the restrictions and pitfalls. In particular, the choice of suitable constitutive models for the various geotechnical boundary value problems is discussed at some length. To illustrate the material presented, examples from the authors experiences with practical geotechnical problems are used. Although we have edited this volume, and written much of the content, several of the chapters involve contributions from our colleagues at Imperial College.

All the numerical examples presented in both this volume and Volume 2 of this book have been obtained using the Authors' own computer code. This software is not available commercially and therefore the results presented are unbiased. As commercial software has not been used, the reader must consider what implications the results may have on the use of such software.

London
November 1998

David M. Potts
Lidija Zdravković

1. Geotechnical analysis

1.1 Synopsis

This chapter considers the analysis of geotechnical structures. Design requirements are presented, fundamental theoretical considerations are discussed and the various methods of analysis categorised. The main objective of the chapter is to provide a framework in which different methods of analysis may be compared. This will provide an insight into the potential advantages of numerical analysis over the more 'conventional' approaches currently in use.

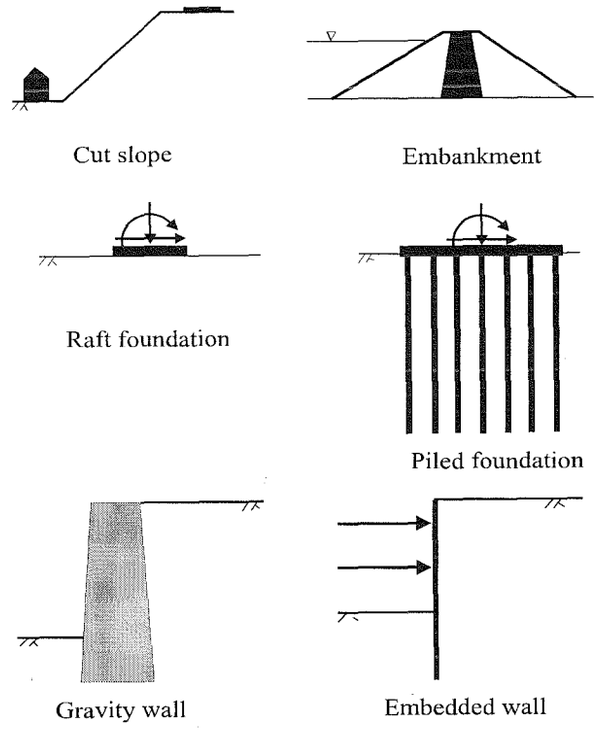

Figure 1.1: Examples of geotechnical structures

1.2 Introduction

Nearly all civil engineering structures involve the ground in some way. Cut slopes, earth and rockfill embankments, see Figure 1.1, are made from geological materials. The soil (or rock) provides both the destabilising and stabilising forces which maintain equilibrium of the structure. Raft and piled foundations transfer loads from buildings, bridges and offshore structures to be resisted by the ground. Retaining walls enable vertical excavations to be made. In most situations the soil provides both the activating and resisting forces, with the wall and its structural support providing a transfer mechanism. Geotechnical engineering, therefore, plays a major role in the design of civil engineering structures.

The design engineer must assess the forces imposed in the soil and structural members, and the potential movements of both the structure and the surrounding soil. Usually these have to be determined under both working and ultimate load conditions.

Traditionally geotechnical design has been carried out using simplified analyses or empirical approaches. Most design codes or advice manuals are based on such approaches. The introduction of inexpensive, but sophisticated, computer hardware and software has resulted in considerable advances in the analysis and design of geotechnical structures. Much progress has been made in attempting to model the behaviour of geotechnical structures in service and to investigate the mechanisms of soil-structure interaction.

At present, there are many different methods of calculation available for analysing geotechnical structures. This can be very confusing to an inexperienced geotechnical engineer. This chapter introduces *geotechnical analysis*. The basic theoretical considerations are discussed and the various methods of analysis categorised. The main objectives are to describe the analysis procedures that are in current use and to provide a framework in which the different methods of analysis may be compared. Having established the place of numerical analysis in this overall framework, it is then possible to identify its potential advantages.

1.3 Design objectives

When designing any geotechnical structure, the engineer must ensure that it is stable. Stability can take several forms.

Firstly, the structure and support system must be stable as a whole. There must be no danger of rotational, vertical or translational failure, see Figure 1.2.

Secondly, overall stability must be established. For example, if a retaining structure supports sloping ground, the possibility of the construction promoting an overall slope failure should be investigated, see Figure 1.3.

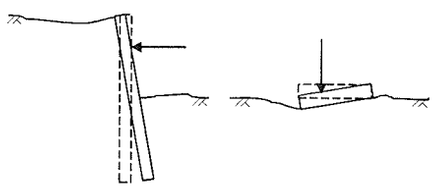

Figure 1.2: Local stability

The loads on any structural elements involved in the construction must also be calculated, so that these may be designed to carry them safely.

Movements must be estimated, both of the structure and of the ground. This is particularly important if there are adjacent buildings and/or sensitive services. For example, if an excavation is to be made in an urban area close to existing services and buildings, see Figure 1.4, one of the key design constraints is the effect that the excavation has on the adjacent structures and services. It may be necessary to predict any structural forces induced in these existing structures and/or services.

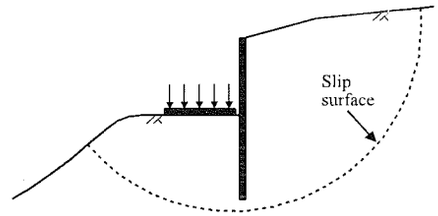

Figure 1.3: Overall stability

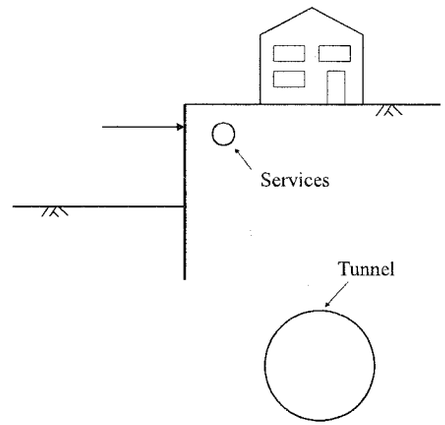

Figure 1.4: Interaction of structures

As part of the design process, it is necessary for an engineer to perform calculations to provide estimates of the above quantities. *Analysis* provides the mathematical framework for such calculations. A good analysis, which simulates real behaviour, allows the engineer to understand problems better. While an important part of the design process, analysis only provides the engineer with a tool to quantify effects once material properties and loading conditions have been set. The design process involves considerably more than *analysis*.

1.4 Design requirements

Before the design process can begin, a considerable amount of information must be assembled. The basic geometry and loading conditions must be established. These are usually defined by the nature of the engineering project.

A geotechnical site investigation is then required to establish the ground conditions. Both the soil stratigraphy and soil properties should be determined. In this respect it will be necessary to determine the strength of the soil and, if ground movements are important, to evaluate its stiffness too. The position of the ground water table and whether or not there is underdrainage or artesian conditions must also be established. The possibility of any changes to these water conditions should be investigated. For example, in many major cities around the world the ground water level is rising.

The site investigation should also establish the location of any services (gas, water, electricity, telecommunications, sewers and/or tunnels) that are in the vicinity of the proposed construction. The type (strip, raft and/or piled) and depth of the foundations of any adjacent buildings should also be determined. The allowable movements of these services and foundations should then be established.

Any restrictions on the performance of the new geotechnical structure must be identified. Such restrictions can take many different forms. For example, due to the close proximity of adjacent services and structures there may be restrictions imposed on ground movements.

Once the above information has been collected, the design constraints on the geotechnical structure can be established. These should cover the construction period and the design life of the structure. This process also implicitly identifies which types of structure are and are not appropriate. For example, when designing an excavation, if there is a restriction on the movement of the retained ground, propped or anchored embedded retaining walls are likely to be more appropriate than gravity or reinforced earth walls. The design constraints also determine the type of design analysis that needs to be undertaken.

1.5 Theoretical considerations

1.5.1 Requirements for a general solution

In general, a theoretical solution must satisfy *Equilibrium, Compatibility,* the material *Constitutive behaviour* and *Boundary conditions* (both *force* and *displacement*). Each of these conditions is considered separately below.

1.5.2 Equilibrium

To quantify how forces are transmitted through a continuum engineers use the concept of stress (force/unit area). The magnitude and direction of a stress and the manner in which it varies spatially indicates how the forces are transferred. However, these stresses cannot vary randomly but must obey certain rules.

Before considering the concept of stresses, an analogous example of the problem of water flowing through a tank full of sand is presented in Figure 1.5. The tank full of sand has one inlet and two outlets. This figure indicates vectors of water velocity at discrete points within the tank. The size of the arrows represents the magnitude of the flow velocity, while their orientation shows the direction of flow. Due to the closer proximity of the left hand outlet to the inlet, more water flows in this direction than to the right hand outlet. As would be expected, the flows are very small in regions A, B and C. Such a result could be observed by using a transparent tank and injecting dye into the flow.

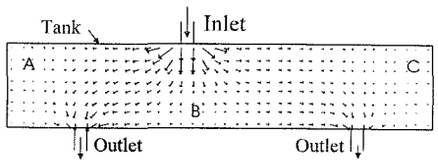

Figure 1.5: Flow trajectories

Similarly, a concrete beam, supported by two reactions on its lower surface and loaded by a load L on its upper surface, is presented in Figure 1.6. Clearly, for overall equilibrium the reactions must be $2L/3$ and $L/3$. What is not so clear, however, is how the load is transferred through the beam. It is not possible to see how the load is transmitted in this case. As noted above, engineers use the concept of stress to investigate the load transfer. Stresses are essentially fictitious quantities. For example, the manner in which the major principal stress varies through the beam is given in Figure 1.6. The length of the trajectories represents the magnitude of the stress and their orientation its direction.

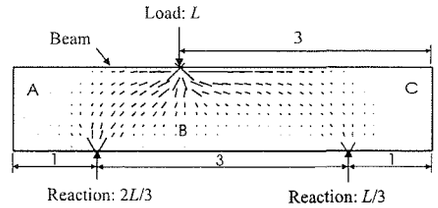

Figure 1.6: Stress trajectories

Whereas the velocity of flow is a vector with essentially three components, one in each of the Cartesian coordinate directions, stress is a tensor consisting of six components. In the same way as there are rules which govern the flow of water through the tank, there are also rules which control the manner in which the stress components vary throughout the concrete beam. Neglecting inertia effects and all body forces, except self weight, stresses *in* a soil mass must satisfy the following three equations (Timoshenko and Goodier (1951)):

$$\begin{aligned} \frac{\partial \sigma_x}{\partial x} + \frac{\partial \tau_{yx}}{\partial y} + \frac{\partial \tau_{zx}}{\partial z} + \gamma &= 0 \\ \frac{\partial \tau_{xy}}{\partial x} + \frac{\partial \sigma_y}{\partial y} + \frac{\partial \tau_{zy}}{\partial z} &= 0 \\ \frac{\partial \tau_{xz}}{\partial x} + \frac{\partial \tau_{yz}}{\partial y} + \frac{\partial \sigma_z}{\partial z} &= 0 \end{aligned} \qquad (1.1)$$

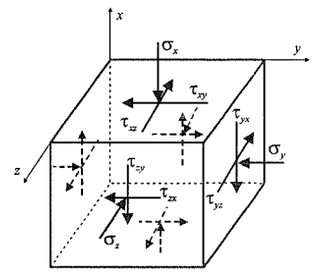

Figure 1.7: Stresses on a typical element

The following should be noted:

- self weight, γ, acts in the x direction;
- compressive stresses are assumed positive;
- the equilibrium Equations (1.1) are in terms of total stresses;
- stresses must satisfy the boundary conditions (i.e. at the boundaries the stresses must be in equilibrium with the applied surface traction forces).

1.5.3 Compatibility

Physical compatibility

Compatible deformation involves no overlapping of material and no generation of holes. The physical meaning of compatibility can be explained by considering a

plate composed of smaller plate elements, as shown in Figure 1.8a. After straining, the plate elements may be so distorted that they form the array shown in Figure 1.8b. This condition might represent failure by rupture. Alternatively, deformation might be such that the various plate elements fit together (i.e. no holes created or overlapping) as shown in Figure 1.8c. This condition represents a compatible deformation.

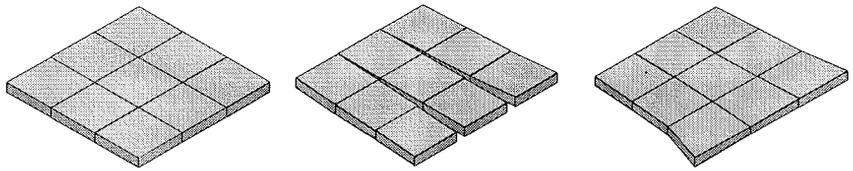

a) Original b) Non-compatible c) Compatible

Figure 1.8: Modes of deformation

Mathematical compatibility

The above physical interpretation of compatibility can be expressed mathematically, by considering the definition of strains. If deformations are defined by continuous functions u, v and w in the x, y and z directions respectively, the strains (assuming small strain theory and a compression positive sign convention) are defined as (Timoshenko and Goodier (1951)):

$$\varepsilon_x = -\frac{\partial u}{\partial x} \; ; \; \varepsilon_y = -\frac{\partial v}{\partial y} \; ; \; \varepsilon_z = -\frac{\partial w}{\partial z}$$
$$\gamma_{xy} = -\frac{\partial v}{\partial x} - \frac{\partial u}{\partial y} \; ; \; \gamma_{yz} = -\frac{\partial w}{\partial y} - \frac{\partial v}{\partial z} \; ; \; \gamma_{xz} = -\frac{\partial w}{\partial x} - \frac{\partial u}{\partial z} \qquad (1.2)$$

As the six strains are a function of only three displacements, they are not independent. It can be shown mathematically that for a compatible displacement field to exist, all the above components of strain and their derivatives must exist (are bounded) and be continuous to at least the second order. The displacement field must satisfy any specified displacements or restraints imposed on the boundary.

1.5.4 Equilibrium and compatibility conditions

Combining the Equilibrium (Equations (1.1)) and Compatibility conditions (Equations (1.2)), gives:

Unknowns:	6 stresses + 6 strains + 3 displacements	= 15
Equations:	3 equilibrium + 6 compatibility	= 9

To obtain a solution therefore requires 6 more equations. These come from the constitutive relationships.

1.5.5 Constitutive behaviour

This is a description of material behaviour. In simple terms it is the stress - strain behaviour of the soil. It usually takes the form of a relationship between stresses and strains and therefore provides a link between equilibrium and compatibility.

For calculation purposes the constitutive behaviour has to be expressed mathematically:

$$\begin{Bmatrix} \Delta\sigma_x \\ \Delta\sigma_y \\ \Delta\sigma_z \\ \Delta\tau_{xy} \\ \Delta\tau_{xz} \\ \Delta\tau_{zy} \end{Bmatrix} = \begin{bmatrix} D_{11} & D_{12} & D_{13} & D_{14} & D_{15} & D_{16} \\ D_{21} & D_{22} & D_{23} & D_{24} & D_{25} & D_{26} \\ D_{31} & D_{32} & D_{33} & D_{34} & D_{35} & D_{36} \\ D_{41} & D_{42} & D_{43} & D_{44} & D_{45} & D_{46} \\ D_{51} & D_{52} & D_{53} & D_{54} & D_{55} & D_{56} \\ D_{61} & D_{62} & D_{63} & D_{64} & D_{65} & D_{66} \end{bmatrix} \begin{Bmatrix} \Delta\varepsilon_x \\ \Delta\varepsilon_y \\ \Delta\varepsilon_z \\ \Delta\gamma_{xy} \\ \Delta\gamma_{xz} \\ \Delta\gamma_{zy} \end{Bmatrix} \qquad (1.3)$$

or

$$\Delta\boldsymbol{\sigma} = [\boldsymbol{D}]\ \Delta\boldsymbol{\varepsilon}$$

For a linear elastic material the $[\boldsymbol{D}]$ matrix takes the following form:

$$\frac{E}{(1+\mu)} \begin{bmatrix} (1-\mu) & \mu & \mu & 0 & 0 & 0 \\ \mu & (1-\mu) & \mu & 0 & 0 & 0 \\ \mu & \mu & (1-\mu) & 0 & 0 & 0 \\ 0 & 0 & 0 & (1/2-\mu) & 0 & 0 \\ 0 & 0 & 0 & 0 & (1/2-\mu) & 0 \\ 0 & 0 & 0 & 0 & 0 & (1/2-\mu) \end{bmatrix} \qquad (1.4)$$

where E and μ are the Young's Modulus and Poisson's ratio respectively.

However, because soil usually behaves in a nonlinear manner, it is more realistic for the constitutive equations to relate increments of stress and strain, as indicated in Equation (1.3), and for the $[\boldsymbol{D}]$ matrix to depend on the current and past stress history.

The constitutive behaviour can either be expressed in terms of total or effective stresses. If specified in terms of effective stresses, the principle of effective stress ($\sigma = \sigma' + \sigma_f$) may be invoked to obtain total stresses required for use with the equilibrium equations:

$$\Delta\boldsymbol{\sigma}' = [\boldsymbol{D}']\ \Delta\boldsymbol{\varepsilon}; \quad \Delta\boldsymbol{\sigma}_f = [\boldsymbol{D}_f]\ \Delta\boldsymbol{\varepsilon}; \quad \text{therefore } \Delta\boldsymbol{\sigma} = ([\boldsymbol{D}'] + [\boldsymbol{D}_f])\ \Delta\boldsymbol{\varepsilon} \qquad (1.5)$$

where $[\boldsymbol{D}_f]$ is a constitutive relationship relating the change in pore fluid pressure to the change in strain. For undrained behaviour, the change in pore fluid pressure is related to the volumetric strain (which is small) via the bulk compressibility of the pore fluid (which is large), see Chapter 3.

1.6 Geometric idealisation

In order to apply the above concepts to a real geotechnical problem, certain assumptions and idealisations must be made. In particular, it is necessary to specify soil behaviour in the form of a mathematical constitutive relationship. It may also be necessary to simplify and/or idealise the geometry and/or boundary conditions of the problem.

1.6.1 Plane strain

Due to the special geometric characteristics of many of the physical problems treated in soil mechanics, additional simplifications of considerable magnitude can be applied. Problems, such as the analysis of retaining walls, continuous footings, and the stability of slopes, generally have one dimension very large in comparison with the other two, see Figure 1.9. Hence, if the force and/or applied displacement boundary conditions are perpendicular to, and independent of, this dimension, all cross sections will be the same. If the z dimension of the problem is large, and it can be assumed that the state existing in the x-y plane holds for all planes parallel to it, the displacement of any x-y cross section, relative to any parallel x-y cross section, is zero. This means that w=0, and the displacements u and v are independent of the z coordinate. The conditions consistent with these approximations are said to define the very important case of *plane strain*:

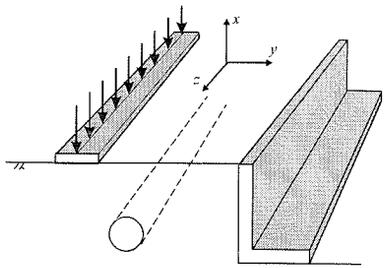

Figure 1.9: Examples of plane strain

$$\varepsilon_z = -\frac{\partial w}{\partial z} = 0 \; ; \; \gamma_{yz} = -\frac{\partial w}{\partial y} - \frac{\partial v}{\partial z} = 0 \; ; \; \gamma_{xz} = -\frac{\partial w}{\partial x} - \frac{\partial u}{\partial z} = 0 \qquad (1.6)$$

The constitutive relationship then reduces to:

$$\begin{Bmatrix} \Delta\sigma_x \\ \Delta\sigma_y \\ \Delta\sigma_z \\ \Delta\tau_{xy} \\ \Delta\tau_{xz} \\ \Delta\tau_{zy} \end{Bmatrix} = \begin{bmatrix} D_{11} & D_{12} & D_{14} \\ D_{21} & D_{22} & D_{24} \\ D_{31} & D_{32} & D_{34} \\ D_{41} & D_{42} & D_{44} \\ D_{51} & D_{52} & D_{54} \\ D_{61} & D_{62} & D_{64} \end{bmatrix} \begin{Bmatrix} \Delta\varepsilon_x \\ \Delta\varepsilon_y \\ \Delta\gamma_{xy} \end{Bmatrix} \qquad (1.7)$$

However, for elastic and the majority of material idealisations currently used to represent soil behaviour D_{52}=D_{51}=D_{54}=D_{61}=D_{62}=D_{64}=0, and consequently $\Delta\tau_{xz}$=$\Delta\tau_{zy}$=0. This results in four non-zero stress changes, $\Delta\sigma_x$, $\Delta\sigma_y$, $\Delta\sigma_z$ and $\Delta\tau_{xy}$.

It is common to consider only the stresses σ_x, σ_y and τ_{xy} when performing analysis for plane strain problems. This is acceptable if D_{11}, D_{12}, D_{14}, D_{21}, D_{22}, D_{24}, D_{41}, D_{42} and D_{44} are not dependent on σ_z. This condition is satisfied if the soil is assumed to be elastic. It is also true if the Tresca or Mohr-Coulomb failure condition is adopted (see Chapter 7) and it is assumed that the intermediate stress σ_2=σ_z. *Such an assumption is usually adopted for the simple analysis of geotechnical problems*. It should be noted, however, that these are special cases.

1.6.2 Axi-symmetry

Some problems possess rotational symmetry. For example, a uniform or centrally loaded circular footing, acting on a homogeneous or horizontally layered foundation, has rotational symmetry about a vertical axis through the centre of the foundation. Cylindrical triaxial samples, single piles and caissons are other examples where such symmetry may exist, see Figure 1.10.

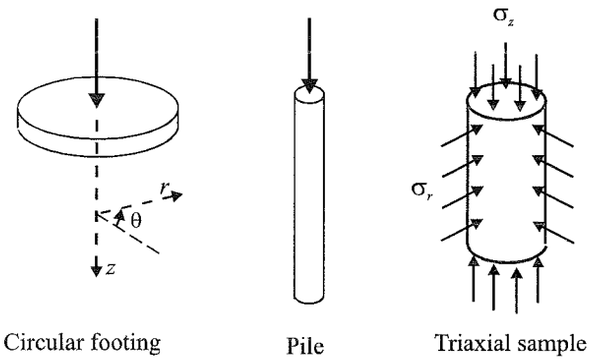

Figure 1.10: Examples of axi-symmetry

In this type of problem it is usual to carry out analyses using cylindrical coordinates r (radial direction), z (vertical direction) and θ (circumferential direction). Due to the symmetry, there is no displacement in the θ direction and the displacements in the r and z directions are independent of θ and therefore the strains reduce to (Timoshenko and Goodier (1951)):

$$\varepsilon_r = -\frac{\partial u}{\partial r} \; ; \; \varepsilon_z = -\frac{\partial v}{\partial z} \; ; \; \varepsilon_\theta = -\frac{u}{r} \; ; \; \gamma_{rz} = -\frac{\partial v}{\partial r} - \frac{\partial u}{\partial z} \; ; \; \gamma_{r\theta} = \gamma_{z\theta} = 0 \qquad (1.8)$$

where u and v are the displacements in the r and z directions respectively.

This is similar to the plane strain situation discussed above and, consequently, the same arguments concerning the $[\boldsymbol{D}]$ matrix apply here too. As for plane strain, there are four non-zero stress changes, $\Delta\sigma_r$, $\Delta\sigma_z$, $\Delta\sigma_\theta$ and $\Delta\tau_{rz}$.

1.7 Methods of analysis

As noted above, fundamental considerations assert that for an exact theoretical solution the requirements of *equilibrium, compatibility, material behaviour* and *boundary conditions*, both force and displacement, must all be satisfied. It is therefore useful to review the broad categories of analysis currently in use against these theoretical requirements.

Current methods of analysis can be conveniently grouped into the following categories: closed form, simple and numerical analysis. Each of these categories is considered separately. The ability of each method to satisfy the fundamental theoretical requirements and provide design information are summarised in Tables 1.1 and 1.2 respectively.

Table 1.1: Basic solution requirements satisfied by the various methods of analysis

METHOD OF ANALYSIS		SOLUTION REQUIREMENTS				
		Equilibrium	Compatibility	Constitutive behaviour	Boundary conditions: Force	Boundary conditions: Disp
Closed form		S	S	Linear elastic	S	S
Limit equilibrium		S	NS	Rigid with a failure criterion	S	NS
Stress field		S	NS	Rigid with a failure criterion	S	NS
Limit analysis	Lower bound	S	NS	Ideal plasticity with associated flow rule	S	NS
	Upper bound	NS	S		NS	S
Beam-Spring approaches		S	S	Soil modelled by springs or elastic interaction factors	S	S
Full Numerical analysis		S	S	Any	S	S

S - Satisfied; NS - Not Satisfied

Table 1.2: Design requirements satisfied by the various methods of analysis

METHOD OF ANALYSIS		DESIGN REQUIREMENTS						
		Stability			Wall & supports		Adjacent structures	
		Wall & support	Base heave	Overall	Structural force	Displacement	Structural force	Displacement
Closed form (Linear elastic)		No	No	No	Yes	Yes	Yes	Yes
Limit equilibrium		Yes	Separate calcul.	Separate calcul.	Yes	No	No	No
Stress field		Yes	Separate calcul.	Separate calcul.	Yes	No	No	No
Limit analysis	Lower bound	Yes	Separate calcul.	Separate calcul.	Crude estimate	No	No	No
	Upper bound	Yes	Separate calcul.	Separate calcul.	Crude estimate	Crude estimate	No	No
Beam-Spring approaches		Yes	No	No	Yes	Yes	No	No
Full Numerical analysis		Yes	Yes	Yes	Yes	Yes	Yes	Yes

1.8 Closed form solutions

For a particular geotechnical structure, if it is possible to establish a realistic constitutive model for material behaviour, identify the boundary conditions, and combine these with the equations of equilibrium and compatibility, an exact theoretical solution can be obtained. The solution is exact in the theoretical sense, but is still approximate for the real problem, as assumptions about geometry, the applied boundary conditions and the constitutive behaviour have been made in idealising the real physical problem into an equivalent mathematical form. In principle, it is possible to obtain a solution that predicts the behaviour of a problem

from first loading (construction/excavation) through to the long term and to provide information on movements and stability from a single analysis.

A closed form solution is, therefore, the ultimate method of analysis. In this approach all solution requirements are satisfied and the theories of mathematics are used to obtain complete analytical expressions defining the full behaviour of the problem. However, as soil is a highly complex multi-phase material which behaves nonlinearly when loaded, complete *analytical* solutions to realistic geotechnical problems are not usually possible. Solutions can only be obtained for two very simple classes of problem.

Firstly, there are solutions in which the soil is assumed to behave in an isotropic linear elastic manner. While these can be useful for providing a first estimate of movements and structural forces, they are of little use for investigating stability. Comparison with observed behaviour indicates that such solutions do not provide realistic predictions.

Secondly, there are some solutions for problems which contain sufficient geometric symmetries that the problem reduces to being essentially one dimensional. Expansion of spherical and infinitely long cylindrical cavities in an infinite elasto-plastic continuum are examples.

1.9 Simple methods

To enable more realistic solutions to be obtained, approximations must be introduced. This can be done in one of two ways. Firstly, the constraints on satisfying the basic solution requirements may be relaxed, but mathematics is still used to obtain an approximate analytical solution. This is the approach used by the pioneers of geotechnical engineering. Such approaches are considered as 'simple methods' in what follows. The second way, by which more realistic solutions can be obtained, is to introduce numerical approximations. All requirements of a theoretical solution are considered, but may only be satisfied in an approximate manner. This latter approach is considered in more detail in the next section.

Limit equilibrium, *Stress field* and *Limit analysis* fall into the category of 'simple methods'. All methods essentially assume the soil is at failure, but differ in the manner in which they arrive at a solution.

1.9.1 Limit equilibrium

In this method of analysis an 'arbitrary' failure surface is adopted (assumed) and *equilibrium* conditions are considered for the failing soil mass, assuming that the failure criterion holds everywhere along the failure surface. The failure surface may be planar, curved or some combination of these. Only the global equilibrium of the 'blocks' of soil between the failure surfaces and the boundaries of the problem are considered. The internal stress distribution within the blocks of soil is not considered. Coulomb's wedge analysis and the method of slices are examples of limit equilibrium calculations.

Example: Critical height of a vertical cut

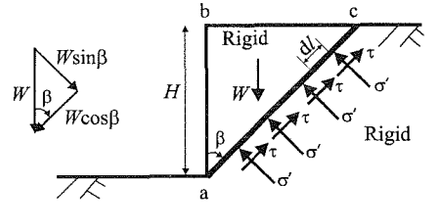

Failure criterion: $\tau = c' + \sigma' \tan\varphi'$

Figure 1.11: Failure mechanism for limit equilibrium solution

The actual distributions of σ and τ along the failure surface 'ac', presented in Figure 1.11, are unknown. However, if l is the length of the failure surface 'ac', then:

$$\int_0^l \tau \, dl = \int_0^l c' \, dl + \int_0^l \sigma' \tan\varphi' \, dl = c'l + \tan\varphi' \int_0^l \sigma' \, dl \qquad (1.9)$$

where c' and φ' are the soil's cohesion and angle of shearing resistance respectively.

Applying equilibrium to the wedge 'abc', i.e. resolving forces normal and tangential to failure surface 'ac', gives:

$$\begin{aligned} \int_0^l \sigma' dl &= W\sin\beta \\ \int_0^l \tau \, dl &= W\cos\beta \end{aligned} \qquad (1.10)$$

Noting that $W=\frac{1}{2}\gamma H^2\tan\beta$ and $l=H/\cos\beta$, Equations (1.9) and (1.10) can be combined to give:

$$H = \frac{2\,c'\cos\varphi'}{\gamma\cos(\beta+\varphi')\sin\beta} \qquad (1.11)$$

The value of the angle β which produces the most conservative (lowest) value of H is obtained from $\partial H/\partial\beta=0$:

$$\frac{\partial H}{\partial \beta} = \frac{-2\,c'\cos\varphi'\cos(2\beta+\varphi')}{\gamma(\sin\beta\cos(\beta+\varphi'))^2} \qquad (1.12)$$

Equation (1.12) equals zero if $\cos(2\beta+\varphi')=0$. Therefore $\beta = \pi/4-\varphi'/2$.

Substituting this angle into Equation (1.11) yields the *Limit equilibrium* value of H_{LE}:

$$H_{LE} = \frac{2\,c'\cos\varphi'}{\gamma\cos(\pi/4+\varphi'/2)\sin(\pi/4-\varphi'/2)} = \frac{4c'}{\gamma}\tan(\pi/4+\varphi'/2) \qquad (1.13)$$

In terms of *total stress*, the equation reduces to:

$$H_{LE} = \frac{4\,S_u}{\gamma} \tag{1.14}$$

where S_u is the undrained strength.
Note: This solution is identical to the upper bound solution obtained assuming a planar sliding surface (see Section 1.9.3). The lower bound solution gives half the above value.

1.9.2 Stress field solution

In this approach the soil is assumed to be at the point of failure everywhere and a solution is obtained by combining the failure criterion with the equilibrium equations. For plane strain conditions and the Mohr-Coulomb failure criterion this gives the following:

Equilibrium equations:

$$\begin{aligned} \frac{\partial \sigma_x}{\partial x} + \frac{\partial \tau_{xy}}{\partial y} &= 0 \\ \frac{\partial \tau_{xy}}{\partial x} + \frac{\partial \sigma_y}{\partial y} &= \gamma \end{aligned} \tag{1.15}$$

Mohr-Coulomb failure criterion (from Figure 1.12):

$$\sigma_1' - \sigma_3' = 2c'\cos\varphi' + (\sigma_1' + \sigma_3')\sin\varphi' \tag{1.16}$$

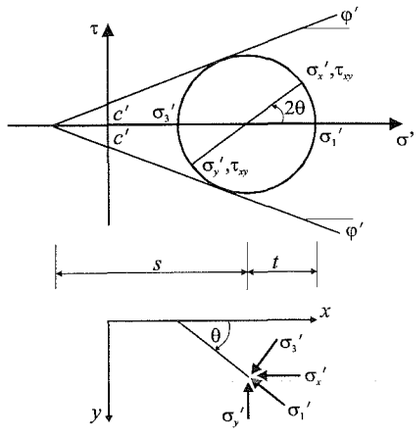

Figure 1.12: Mohr's circle of stress

Noting that:

$$\begin{aligned} s &= c'\cot\varphi' + \tfrac{1}{2}(\sigma_1' + \sigma_3') \\ &= c'\cot\varphi' + \tfrac{1}{2}(\sigma_x' + \sigma_y') \end{aligned}$$

$$t = \tfrac{1}{2}(\sigma_1' - \sigma_3') = [\tfrac{1}{4}(\sigma_x' - \sigma_y')^2 + \tau_{xy}^2]^{0.5}$$

and substituting in Equation (1.16), gives the following alternative equations for the Mohr-Coulomb criterion:

$$t = s\sin\varphi' \tag{1.17}$$

$$[\tfrac{1}{4}(\sigma_x' - \sigma_y')^2 + \tau_{xy}^2]^{0.5} = [c'\cot\varphi' + \tfrac{1}{2}(\sigma_x' + \sigma_y')]\sin\varphi' \tag{1.18}$$

The equilibrium Equations (1.15) and the failure criterion (1.18) provide three equations in terms of three unknowns. It is therefore theoretically possible to obtain a solution. Combining the above equations gives:

$$\begin{aligned} (1+\sin\varphi'\cos2\theta)\frac{\partial s}{\partial x} + \sin\varphi'\sin2\theta\frac{\partial s}{\partial y} + 2s\sin\varphi'(\cos2\theta\frac{\partial \theta}{\partial y} - \sin2\theta\frac{\partial \theta}{\partial x}) &= 0 \\ \sin\varphi'\sin2\theta\frac{\partial s}{\partial x} + (1-\sin\varphi'\cos2\theta)\frac{\partial s}{\partial y} + 2s\sin\varphi'(\sin2\theta\frac{\partial \theta}{\partial y} + \cos2\theta\frac{\partial \theta}{\partial x}) &= \gamma \end{aligned} \tag{1.19}$$

These two partial differential equations can be shown to be of the hyperbolic type. A solution is obtained by considering the characteristic directions and obtaining equations for the stress variation along these characteristics (Atkinson and Potts (1975)). The differential equations of the stress characteristics are:

$$\begin{aligned} \frac{dy}{dx} &= \tan[\theta - (\pi/4 - \varphi'/2)] \\ \frac{dy}{dx} &= \tan[\theta + (\pi/4 - \varphi'/2)] \end{aligned} \tag{1.20}$$

Along these characteristics the following equations hold:

$$\begin{aligned} ds - 2s\tan\varphi'\,d\theta &= \gamma(dy - \tan\varphi'\,dx) \\ ds + 2s\tan\varphi'\,d\theta &= \gamma(dy + \tan\varphi'\,dx) \end{aligned} \tag{1.21}$$

Equations (1.20) and (1.21) provide four differential equations with four unknowns x, y, s, and θ which, in principle, can be solved mathematically. However, to date, it has only been possible to obtain analytical solutions for very simple problems and/or if the soil is assumed to be weightless, γ=0. Generally, they are solved numerically by adopting a finite difference approximation.

Solutions based on the above equations usually only provide a partial stress field which does not cover the whole soil mass, but is restricted to the zone of interest. In general, they are therefore not Lower bound solutions (see Section 1.9.3).

The above equations provide what appears to be, and some times is, static determinacy, in the sense that there are the same number of equations as unknown stress components. In most practical problems, however, the boundary conditions involve both forces and displacements and the static determinacy is misleading. Compatibility is not considered in this approach.

Rankine active and passive stress fields and the earth pressure tables obtained by Sokolovski (1960, 1965) and used in some codes of practice are examples of stress field solutions. Stress fields also form the basis of analytical solutions to the bearing capacity problem.

1.9.3 Limit analysis

The theorems of limit analysis (Chen (1975)) are based on the following assumptions:

- Soil behaviour exhibits perfect or ideal plasticity, work hardening/softening does not occur. This implies that there is a single yield surface separating elastic and elasto-plastic behaviour.

- The yield surface is convex in shape and the plastic strains can be derived from the yield surface through the normality condition.
- Changes in geometry of the soil mass that occur at failure are insignificant. This allows the equations of virtual work to be applied.

With these assumptions it can be shown that a unique failure condition will exist. The bound theorems enable estimates of the collapse loads, which occur at failure, to be obtained. Solutions based on the 'safe' theorem are safe estimates of these loads, while those obtained using the 'unsafe' theorem are unsafe estimates. Use of both theorems enable bounds to the true collapse loads to be obtained.

Unsafe theorem

An unsafe solution to the true collapse loads (for the ideal plastic material) can be found by selecting any kinematically possible failure mechanism and performing an appropriate work rate calculation. The loads so determined are either on the unsafe side or equal to the true collapse loads.

This theorem is often referred to as the 'Upper bound' theorem. As equilibrium is not considered, there is an infinite number of solutions which can be found. The accuracy of the solution depends on how close the assumed failure mechanism is to the real one.

Safe theorem

If a statically admissible stress field covering the whole soil mass can be found, which nowhere violates the yield condition, then the loads in equilibrium with the stress field are on the safe side or equal to the true collapse loads.

This theorem is often referred to as the 'Lower bound' theorem. A statically admissible stress field consists of an equilibrium distribution of stress which balances the applied loads and body forces. As compatibility is not considered, there is an infinite number of solutions. The accuracy of the solution depends on how close the assumed stress field is to the real one.

If safe and unsafe solutions can be found which give the same estimates of collapse loads, then this is the correct solution for the ideal plastic material. It should be noted that in such a case all the fundamental solution requirements are satisfied. This can rarely be achieved in practice. However, two such cases in which it has been achieved are (i) the solution of the undrained bearing capacity of a strip footing, on a soil with a constant undrained shear strength, S_u (Chen (1975)), and (ii) the solution for the undrained lateral load capacity of an infinitely long rigid pile embedded in an infinite continuum of soil, with a constant undrained shear strength (Randolph and Houlsby (1984)).

Example: Critical height of a vertical cut in undrained clay

Unsafe solution (Upper bound)

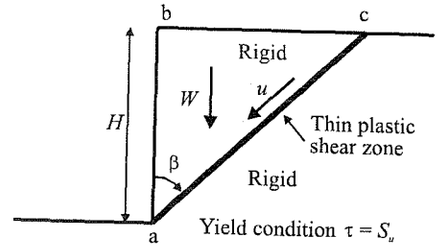

Figure 1.13: Failure mechanism for unsafe analysis

Rigid block 'abc' moves with respect to the rigid base along the thin plastic shear zone 'ac', Figure 1.13. The relative displacement between the two rigid blocks is u. Internal rate of energy dissipation is:

$$= u\, S_u\, H / \cos\beta \tag{1.22}$$

Rate of work done by external forces is:

$$= \tfrac{1}{2} H^2\, u\, \gamma \sin\beta \tag{1.23}$$

Equating equations (1.22) and (1.23) gives:

$$H = 4S_u/(\gamma \sin 2\beta) \tag{1.24}$$

Because this is an unsafe estimate, the value of β which produces the smallest value of H is required. Therefore:

$$\frac{\partial H}{\partial \beta} = -\frac{8S_u \cos 2\beta}{\gamma \sin^2 2\beta} \tag{1.25}$$

Equation (1.25) equals zero if $\cos 2\beta = 0$. Therefore $\beta = \pi/4$ which, when substituted in Equation (1.24), gives:

$$H_{UB} = 4S_u / \gamma \tag{1.26}$$

Safe solution (Lower bound)

Stress discontinuities are assumed along lines *ab* and *ac* in Figure 1.14. From the Mohr's circles, see Figure 1.14, the stresses in regions 1 and 2 approach yield simultaneously as H is increased. As this is a safe solution, the maximum value of H is required. This occurs when the Mohr's circles for zones 1 and 2 just reach the yield condition. Therefore:

$$H_{LB} = 2S_u / \gamma \tag{1.27}$$

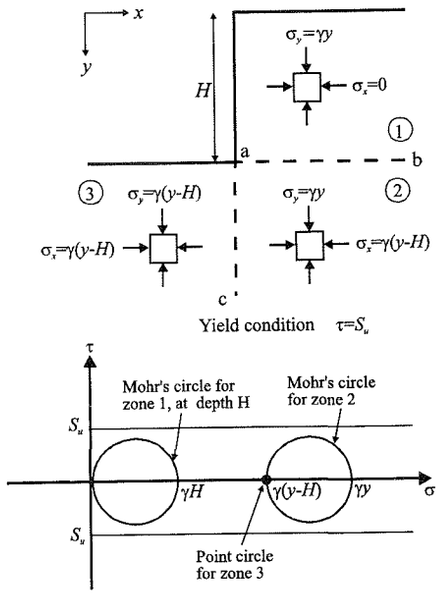

Figure 1.14: Stress field for safe solution

1.9.4 Comments

The ability of these simple methods to satisfy the basic solution requirements is shown in Table 1.1. Inspection of this table clearly shows that none of the methods satisfy all the basic requirements and therefore do not necessarily produce an exact theoretical solution. All methods are therefore approximate and it is, perhaps, not surprising that there are many different solutions to the same problem.

As these approaches assume the soil to be everywhere at failure, they are not strictly appropriate for investigating behaviour under working load conditions. When applied to geotechnical problems, they do not distinguish between different methods of construction (e.g. excavation versus backfilling), nor account for in situ stress conditions. Information is provided on local stability, but no information on soil or structural movements is given and separate calculations are required to investigate overall stability.

Notwithstanding the above limitations, simple methods form the main stay of most design approaches. Where they have been calibrated against field observation their use may be appropriate. However, it is for cases with more complex soil-structure interaction, where calibration is more difficult, that these simple methods are perhaps less reliable. Because of their simplicity and ease of use it is likely that they will always play an important role in the design of geotechnical structures. In particular, they are appropriate at the early stages of the design process to obtain first estimates of both stability and structural forces.

1.10 Numerical analysis

1.10.1 Beam-spring approach

This approach is used to investigate soil-structure interaction. For example, it can be used to study the behaviour of axially and laterally loaded piles, raft foundations, embedded retaining walls and tunnel linings. The major approximation is the assumed soil behaviour and two approaches are commonly used. The soil behaviour is either approximated by a set of unconnected vertical and horizontal springs (Borin (1989)), or by a set of linear elastic interaction factors (Papin *et al.* (1985)). Only a single structure can be accommodated in the analysis. Consequently, only a single pile or retaining wall can be analyzed. Further approximations must be introduced if more than one pile, retaining wall or foundation interact. Any structural support, such as props or anchors (retaining wall problems), are represented by simple springs (see Figure 1.15).

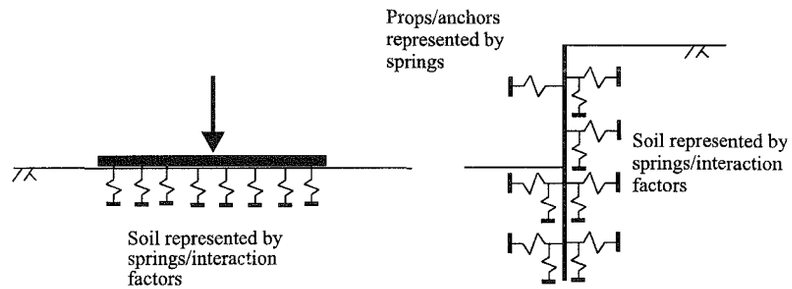

Figure 1.15: Examples of beam-spring problems

To enable limiting pressures to be obtained, for example on each side of a retaining wall, 'cut offs' are usually applied to the spring forces and interaction factors representing soil behaviour. These cut off pressures are usually obtained from one of the simple analysis procedures discussed above (e.g. Limit equilibrium, Stress fields or Limit analysis). It is important to appreciate that these limiting pressures are not a direct result of the beam-spring calculation, but are obtained from separate approximate solutions and then imposed on the beam-spring calculation process.

Having reduced the boundary value problem to studying the behaviour of a single isolated structure (e.g. a pile, a footing or a retaining wall) and made gross assumptions about soil behaviour, a complete theoretical solution to the problem is sought. Due to the complexities involved, this is usually achieved using a computer. The structural member (e.g. pile, footing or retaining wall) is represented using either finite differences or finite elements and a solution that satisfies all the fundamental solution requirements is obtained by iteration.

Sometimes computer programs which perform such calculations are identified as finite difference or finite element programs. However, it must be noted that it

is only the structural member that is represented in this manner and these programs should not be confused with those that involve full discretisation of both the soil and structural members by finite differences or finite elements, see Section 1.10.2.

As solutions obtained in this way include limits to the earth pressures that can develop adjacent to the structure, they can provide information on local stability. This is often indicated by a failure of the program to converge. However, numerical instability may occur for other reasons and therefore a false impression of instability may be given. Solutions from these calculations include forces and movements of the structure. They do not provide information about global stability or movements in the adjacent soil. They do not consider adjacent structures.

It is difficult to select appropriate spring stiffnesses and to simulate some support features. For example, when analysing a retaining wall it is difficult to account realistically for the effects of soil berms. Retaining wall programs using interaction factors to represent the soil have problems in dealing with wall friction and often neglect shear stresses on the wall, or make further assumptions to deal with them. For the analysis of retaining walls a single wall is considered in isolation and structural supports are represented by simple springs fixed at one end (grounded). It is therefore difficult to account for realistic interaction between structural components such as floor slabs and other retaining walls. This is particularly so if 'pin-jointed' or 'full moment' connections are appropriate. As only the soil acting on the wall is considered in the analysis, it is difficult to model realistically the behaviour of raking props and ground anchors which rely on resistance from soil remote from the wall.

1.10.2 Full numerical analysis

This category of analysis includes methods which attempt to satisfy all theoretical requirements, include realistic soil constitutive models and incorporate boundary conditions that realistically simulate field conditions. Because of the complexities involved and the nonlinearities in soil behaviour, all methods are numerical in nature. Approaches based on finite difference and finite element methods are those most widely used. These methods essentially involve a computer simulation of the history of the boundary value problem from green field conditions, through construction and in the long term.

Their ability to accurately reflect field conditions essentially depends on (i) the ability of the constitutive model to represent real soil behaviour and (ii) correctness of the boundary conditions imposed. The user has only to define the appropriate geometry, construction procedure, soil parameters and boundary conditions. Structural members may be added and withdrawn during the numerical simulation to model field conditions. Retaining structures composed of several retaining walls, interconnected by structural components, can be considered and, because the soil mass is modelled in the analysis, the complex interaction between raking struts or ground anchors and the soil can be accounted for. The effect of time on the development of pore water pressures can also be simulated by including coupled

consolidation. No postulated failure mechanism or mode of behaviour of the problem is required, as these are predicted by the analysis. The analysis allows the complete history of the boundary value problem to be predicted and a single analysis can provide information on all design requirements.

Potentially, the methods can solve full three dimensional problems and suffer none of the limitations discussed previously for the other methods. At present, the speed of computer hardware restricts analysis of most practical problems to two dimensional plane strain or axi-symmetric sections. However, with the rapid development in computer hardware and its reduction in cost, the possibilities of full three dimensional simulations are imminent.

It is often claimed that these approaches have limitations. Usually these relate to the fact that detailed soils information or a knowledge of the construction procedure are needed. In the Authors' opinion, neither of these are limitations. If a numerical analysis is anticipated during the design stages of a project, it is then not difficult to ensure that the appropriate soil information is obtained from the site investigation. It is only if a numerical analysis is an after thought, once the soil data has been obtained, that this may present difficulties. If the behaviour of the boundary value problem is not sensitive to the construction procedure, then any reasonable assumed procedure is adequate for the analysis. However, if the analysis is sensitive to the construction procedure then, clearly, this is important and it will be necessary to simulate the field conditions as closely as possible. So, far from being a limitation, numerical analysis can indicate to the design engineer where, and by how much, the boundary value problem is likely to be influenced by the construction procedure. This will enable adequate provision to be made within the design.

Full numerical analyses are complex and should be performed by qualified and experienced staff. The operator must understand soil mechanics and, in particular, the constitutive models that the software uses, and be familiar with the software package to be employed for the analysis. Nonlinear numerical analysis is not straight forward and at present there are several algorithms available for solving the nonlinear system of governing equations. Some of these are more accurate than others and some are increment size dependent. There are approximations within these algorithms and errors associated with discretization. However, these can be controlled by the experienced user so that accurate predictions can be obtained.

Full numerical analysis can be used to predict the behaviour of complex field situations. It can also be used to investigate the fundamentals of soil/structure interaction and to calibrate some of the simple methods discussed above.

The finite element method and its use in analysing geotechnical structures is the subject of the remaining chapters of this book.

1.11. Summary

1. Geotechnical engineering plays a major role in the design of nearly all civil engineering structures.

2. Design of geotechnical structures should consider:
   - Stability: local and overall;
   - Structural forces: bending moments, axial and shear forces in structural members;
   - Movements of the geotechnical structure and adjacent ground;
   - Movements and structural forces induced in adjacent structures and/or services.
3. For a complete theoretical solution the following four conditions should be satisfied:
   - Equilibrium;
   - Compatibility;
   - Material constitutive behaviour;
   - Boundary conditions.
4. It is not possible to obtain closed form analytical solutions incorporating realistic constitutive models of soil behaviour which satisfy all four fundamental requirements.
5. The analytical solutions available (e.g. Limit equilibrium, Stress fields and Limit analysis) fail to satisfy at least one of the fundamental requirements. This explains why there is an abundance of different solutions in the literature for the same problem. These simple approaches also only give information on stability. They do not provide information on movements or structural forces under working load conditions.
6. Simple numerical methods, such as the beam-spring approach, can provide information on local stability and on wall movements and structural forces under working load conditions. They are therefore an improvement over the simpler analytical methods. However, they do not provide information on overall stability or on movements in the adjacent soil and the effects on adjacent structures or services.
7. Full numerical analysis can provide information on all design requirements. A single analysis can be used to simulate the complete construction history of the retaining structure. In many respects they provide the ultimate method of analysis, satisfying all the fundamental requirements. However, they require large amounts of computing resources and an experienced operator. They are becoming widely used for the analysis of geotechnical structures and this trend is likely to increase as the cost of computing continues to decrease.

2. Finite element theory for linear materials

2.1 Synopsis

This chapter introduces the finite element method for linear problems. The basic theory is described and the finite element terminology is introduced. For simplicity, discussion is restricted to two dimensional plane strain situations. However, the concepts described have a much wider applicability. Sufficient information is given to enable linear elastic analysis to be understood.

2.2 Introduction

The finite element method has a wide range of engineering applications. Consequently, there are many text books on the subject. Unfortunately, there are few books that consider specifically the application of the finite element method in geotechnical engineering. This chapter presents a basic outline of the method, with particular attention to the areas involving approximation. The discussion is restricted to linear elastic two dimensional plane strain conditions. Only continuum elements are considered and attention is focussed on the 'displacement based' finite element approach. The chapter begins with a brief overview of the main stages of the method and follows with a detailed discussion of each stage.

2.3 Overview

The finite element method involves the following steps.

Element discretisation

This is the process of modelling the geometry of the problem under investigation by an assemblage of small regions, termed *finite elements*. These elements have *nodes* defined on the element boundaries, or within the element.

Primary variable approximation

A primary variable must be selected (e.g. displacements, stresses etc.) and rules as to how it should vary over a finite element established. This variation is expressed in terms of nodal values. In geotechnical engineering it is usual to adopt displacements as the primary variable.

Element equations

Use of an appropriate variational principle (e.g. Minimum potential energy) to derive element equations:

$$[\boldsymbol{K}_E]\{\Delta \boldsymbol{d}_E\} = \{\Delta \boldsymbol{R}_E\} \tag{2.1}$$

where $[\boldsymbol{K}_E]$ is the element stiffness matrix, $\{\Delta \boldsymbol{d}_E\}$, is the vector of incremental element nodal displacements and $\{\Delta \boldsymbol{R}_E\}$ is the vector of incremental element nodal forces.

Global equations

Combine element equations to form global equations

$$[\boldsymbol{K}_G]\{\Delta \boldsymbol{d}_G\} = \{\Delta \boldsymbol{R}_G\} \tag{2.2}$$

where $[\boldsymbol{K}_G]$ is the global stiffness matrix, $\{\Delta \boldsymbol{d}_G\}$ is the vector of all incremental nodal displacements and $\{\Delta \boldsymbol{R}_G\}$ is the vector of all incremental nodal forces.

Boundary conditions

Formulate boundary conditions and modify global equations. Loadings (e.g. line and point loads, pressures and body forces) affect $\{\Delta \boldsymbol{R}_G\}$, while the displacements affect $\{\Delta \boldsymbol{d}_G\}$.

Solve the global equations

The global Equations (2.2) are in the form of a large number of simultaneous equations. These are solved to obtain the displacements $\{\Delta \boldsymbol{d}_G\}$ at all the nodes. From these nodal displacements secondary quantities, such as stresses and strains, are evaluated.

2.4 Element discretisation

The geometry of the boundary value problem under investigation must be defined and quantified. Simplifications and approximations may be necessary during this process. This geometry is then replaced by an equivalent *finite element mesh* which is composed of small regions called finite elements. For two dimensional problems, the finite elements are usually triangular or quadrilateral in shape, see Figure 2.1. Their geometry is specified in terms of the coordinates of key points on the element called *nodes*. For elements with straight sides these nodes are usually located at the element corners. If the elements have curved sides then additional nodes, usually at the midpoint of each side, must be introduced. The set of elements in the complete mesh are connected together by the element sides and a number of *nodes*.

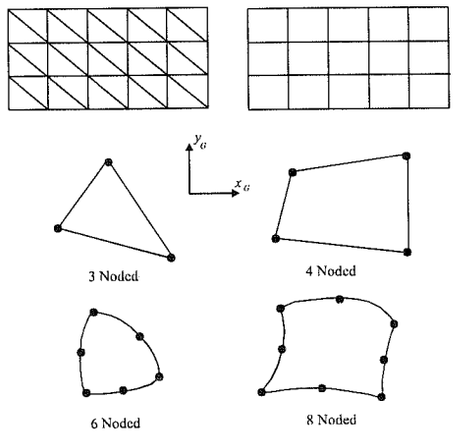

Figure 2.1: Typical 2D finite elements

In order to refer to the complete finite element mesh, the elements and nodes must be numbered in systematic manner. An example of a numbering scheme for a mesh of 4 noded quadrilateral elements is shown in Figure 2.2. The nodes are numbered sequentially from left to right and from bottom to top; the elements are numbered separately in a similar fashion. To describe the location of an element in the mesh, an *element connectivity list* is used. This list contains the node numbers in the element, usually in an anticlockwise order. For example, the connectivity list of element 2 is 2, 3, 7, 6.

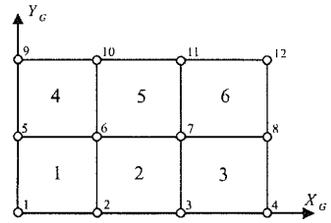

Figure 2.2: Element and node numbering

When constructing the finite element mesh the following should be considered.

- The geometry of the boundary value problem must be approximated as accurately as possible.
- If there are curved boundaries or curved material interfaces, the higher order elements, with mid-side nodes should be used, see Figure 2.3.
- In many cases geometric discontinuities suggest a natural form of subdivision. For example, discontinuities in boundary gradient, such as re-entrant corners or cracks, can be modelled by placing nodes at the discontinuity points. Interfaces between materials with different properties can be introduced by element sides, see Figure 2.4.
- Mesh design may also be influenced by the applied boundary conditions. If there are discontinuities in loading, or point loads, these can again be introduced by placing nodes at the discontinuity points, see Figure 2.5.

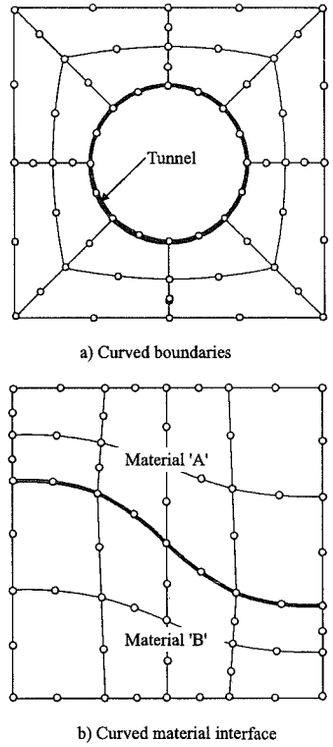

Figure 2.3: Use of higher order elements

In combination with the above factors, the size and the number of elements depend largely on the material behaviour, since this influences the final solution. For linear material behaviour the procedure is relatively straightforward and only the zones where unknowns vary rapidly need special attention. In order to obtain accurate

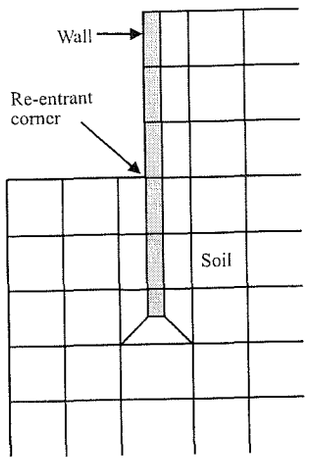

Figure 2.4: Geometric discontinuities

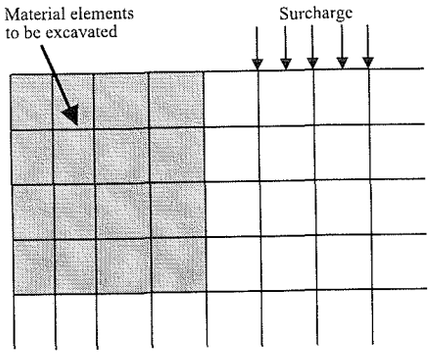

Figure 2.5: Effect of boundary conditions

solutions, these zones require a *refined mesh* of smaller elements. The situation is more complex for general nonlinear material behaviour, since the final solution may depend, for example, on the previous loading history. For such problems the mesh design must take into account the boundary conditions, the material properties and, in some cases, the geometry, which all vary throughout the solution process. In all cases a mesh of regular shaped elements will give the best results. Elements with widely distorted geometries or long thin elements should be avoided (see Figure 2.6 for example).

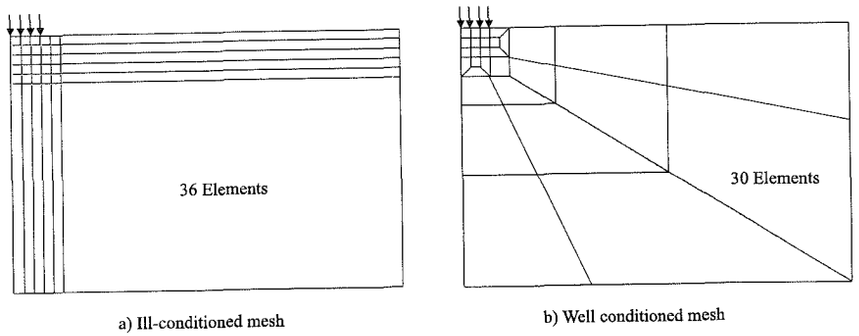

Figure 2.6: Examples of good and bad meshes

2.5 Displacement approximation

In the displacement based finite element method the primary unknown quantity is the displacement field which varies over the problem domain. Stresses and strains are treated as secondary quantities which can be found from the displacement field once it has been determined. In two dimensional plane strain situations the displacement field is characterised by the two global displacements u and v, in the x and y coordinate directions respectively.

The main approximation in the finite element method is to *assume* a particular form for the way these displacement components vary over the domain under investigation. Clearly, this assumed variation must satisfy the conditions of compatibility. Over each element the displacement components are assumed to have a simple polynomial form, where the order of the polynomial depends on the number of nodes in the element. The displacement components are then expressed in terms of their values at the nodes. For example, consider the displacement equations for the three noded triangular element shown in Figure 2.7:

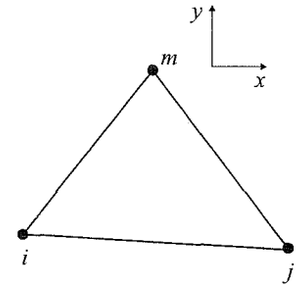

Figure 2.7: Three noded element

$$u = a_1 + a_2 x + a_3 y$$
$$v = b_1 + b_2 x + b_3 y \qquad (2.3)$$

The six constants a_1 - b_3 can be expressed in terms of the nodal displacements by substituting the nodal coordinates into the above equations, and then solving the two sets of three simultaneous equations which arise:

$$\begin{aligned} u_i &= a_1 + a_2 x_i + a_3 y_i \\ u_j &= a_1 + a_2 x_j + a_3 y_j \\ u_m &= a_1 + a_2 x_m + a_3 y_m \end{aligned} \qquad (2.4)$$

$$\begin{aligned} v_i &= b_1 + b_2 x_i + b_3 y_i \\ v_j &= b_1 + b_2 x_j + b_3 y_j \\ v_m &= b_1 + b_2 x_m + b_3 y_m \end{aligned} \qquad (2.5)$$

The above simultaneous equations are solved for a_1 - b_3 in terms of the nodal displacements u_i , u_j , u_m , v_i , v_j and v_m, to give:

$$\begin{Bmatrix} u \\ v \end{Bmatrix} = [N]\{u_i \; u_j \; u_m \; v_i \; v_j \; v_m\}^{\mathrm{T}} = [N]\begin{Bmatrix} u \\ v \end{Bmatrix}_{nodes} \qquad (2.6)$$

where the matrix [*N*] is known as the matrix of *shape functions*. The displacement components u and v are now expressed in terms of their values at the nodes. For three and four noded elements there is, therefore, a linear variation of displacement across the element, see Figure 2.8. For the higher order six and eight noded

elements the displacement field varies quadratically across the element.

The accuracy of a finite element analysis depends on the size of the elements and the nature of the displacement approximation. For the accuracy to increase as the elements become smaller, the displacement approximation must satisfy the following *compatibility* conditions.

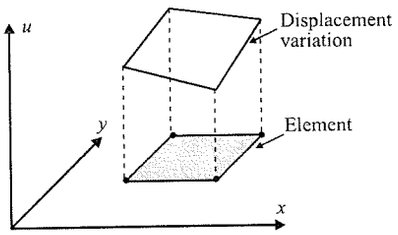

Figure 2.8: Linear variation of displacements across a 4 noded element

- Continuity of the displacement field. In order to avoid gaps or overlaps occurring when the domain is loaded, the displacement components must vary continuously within each element and across each element side. This can be achieved by ensuring that the displacements on an element side depend only on the displacements of the nodes situated on that side, see Figure 2.9.
- The displacement approximation should be able to represent rigid body movement. Examples of such movements are translations and rotations. Such displacements do not induce strains in an element.
- The displacement approximation should be able to represent constant strain rates.

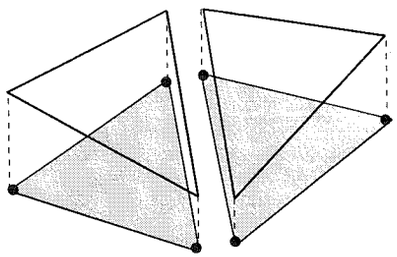

Figure 2.9: Continuity of displacement field

The simple polynomial approximation presented above satisfies these compatibility conditions.

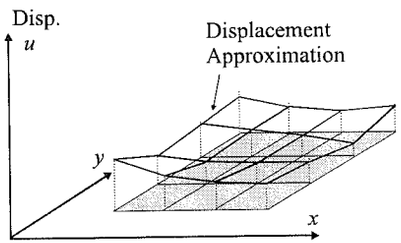

Figure 2.10: Variation of displacement across a mesh of 4 noded elements

The essential feature of the element-wise approximation is that the variation of the unknown displacements within an element is expressed as a simple function of the displacements at the nodes. The problem of determining the displacement field throughout the finite element mesh is, therefore, reduced to determining the displacement components at a finite number of nodes. These nodal displacements are referred to as the unknown *degrees of freedom*. For two dimensional plane strain problems there are two degrees of freedom at each node: the u and v displacements.

2.5.1 Isoparametric finite elements

The choice of the finite elements to be used for two dimensional problems depends largely on the geometry being modelled and the type of analysis required. For geotechnical problems, the main requirement is that the element types should be useful for all the geometric situations that may arise, including cases where structures have curved boundaries or curved material interfaces. Both triangular and quadrilateral types of elements could equally well be used, since both of these types are easily modified, by the addition of mid-side nodes, to accurately represent curved edges. As the finite element equations are slightly easier to formulate for the quadrilateral family of isoparametric elements, these will be used for any of the derivations presented in this book. This does not imply that quadrilateral elements are in any way superior to triangular elements. In fact, some experts are of the opinion that triangular elements are superior. For completeness, the derivation of the interpolation and shape functions for triangular elements is presented in Appendix II.1 of this chapter.

An 8 noded quadrilateral isoparametric element is shown in Figure 2.11. This element is widely used in geotechnical finite element software. It can be used as a general shaped quadrilateral element with curved sides. The *global* element is derived from a *parent* element which has the same number of nodes, but is defined with respect to a *natural* coordinate system. Figure 2.11 shows the configuration of the parent element. The natural coordinates S, T for this element satisfy the conditions $-1 \le S \le 1$, $-1 \le T \le 1$.

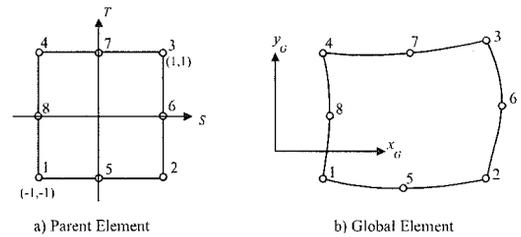

Figure 2.11: 8 noded isoparametric element

The basic procedure in the isoparametric finite element formulation is to express the element displacements and element geometry in terms of interpolation functions using the natural coordinate system. The term isoparametric arises from the fact that the parametric description used to describe the variation of the unknown displacements within an element is exactly the same as that used to map the geometry of the element from the *global axes* to the *natural axes*.

For the element shown in Figure 2.11 the global coordinates of a point in the element can be expressed by coordinate interpolations of the form:

$$x = \sum_{i=1}^{8} N_i x_i \quad ; \quad y = \sum_{i=1}^{8} N_i y_i \tag{2.7}$$

where x_i and y_i are the global coordinates of the eight nodes in the element, and N_i, i=1,..,8, are called *interpolation functions*. For isoparametric elements the interpolation functions are expressed in terms of the natural coordinates S and T which vary from -1 to +1. To construct the interpolation functions for the eight

noded isoparametric element, the following properties are used. Firstly, there is one interpolation function corresponding to each node in the element and each function is quadratic in the natural coordinates S and T. Secondly, the interpolation function N_1 is equal to 1 at node 1 ($S = -1$, $T = -1$) and is equal to zero at the other seven nodes; a similar relation holds for the interpolation functions N_2, N_3, ..., N_8. Using these properties it can be shown that the interpolation functions take the form:

Mid - side nodes:	Corner nodes:
$N_5 = \frac{1}{2}(1-S^2)(1-T)$	$N_1 = \frac{1}{4}(1-S)(1-T) - \frac{1}{2}N_5 - \frac{1}{2}N_8$
$N_6 = \frac{1}{2}(1+S)(1-T^2)$	$N_2 = \frac{1}{4}(1+S)(1-T) - \frac{1}{2}N_5 - \frac{1}{2}N_6$
$N_7 = \frac{1}{2}(1-S^2)(1+T)$	$N_3 = \frac{1}{4}(1+S)(1+T) - \frac{1}{2}N_6 - \frac{1}{2}N_7$
$N_8 = \frac{1}{2}(1-S)(1-T^2)$	$N_4 = \frac{1}{4}(1-S)(1+T) - \frac{1}{2}N_7 - \frac{1}{2}N_8$

(2.8)

Since the element is isoparametric, the displacements within the element are interpolated in the same way as the geometry. Therefore, the above interpolation functions N_1, N_2, ..., N_8 are used as the shape functions in Equation (2.6). Consequently, the displacements within the 8 noded isoparametric element are also assumed to be quadratic in S and T.

The main advantage of the isoparametric formulation is that the element equations need only be evaluated in the parent element coordinate system. Thus, for each element in the mesh the stiffness matrix integrals can be evaluated by a standard procedure. The integrations need only be performed over a square, with S and T varying between −1 and +1. The boundary conditions can be determined in a similar fashion. If gravity loads are applied, the nodal forces are determined from element integrals, which can again be reduced to integrals over the parent element. If stress boundary conditions are applied, the nodal forces are determined from integrals over the boundary of the mesh. In this case, the integrals can be reduced to line integrals over the sides of the parent element.

For all types of finite elements the best results are obtained if the elements have reasonable shapes. Wildly distorted elements may lead to different forms of inaccuracy. For example, in the case of isoparametric elements difficulties may be encountered if the distortions lead to a non-unique mapping between the global and parent elements. For the quadrilateral isoparametric element described above, the following points should be observed.

- To avoid a non-unique global to parent element mapping, all the interior angles, at the element corners, should be smaller than 180°. In particular, the best results are obtained if these angles lie between 30° and 150°.
- If an element becomes thin, the stiffness coefficients corresponding to the transverse degrees of freedom are considerably larger than those corresponding to the longitudinal displacements. This results in numerical ill-conditioning of the system equations which can lead to large errors in the solution. To avoid this the ratio between the longest and shortest sides of an element should be smaller than 5:1. For anisotropic materials, if the longitudinal direction of the element is parallel to the stiffest material direction, this ratio may be exceeded.

- The location of mid-side nodes greatly affects the uniqueness of the global to parent element mapping. For elements with curved sides, experience has shown that the best results are obtained if the radius of curvature of each side is larger than the length of the longest side.

2.6 Element equations

Element equations are those that govern the deformational behaviour of each element. They essentially combine the compatibility, equilibrium and constitutive conditions.

Displacements: As noted above, the chosen displacements are assumed to be given by:

$$\{\Delta \boldsymbol{d}\} = \begin{Bmatrix} \Delta \boldsymbol{u} \\ \Delta \boldsymbol{v} \end{Bmatrix} = [\boldsymbol{N}] \begin{Bmatrix} \Delta u \\ \Delta v \end{Bmatrix}_n = [\boldsymbol{N}] \{\Delta \boldsymbol{d}\}_n \tag{2.9}$$

Strains: The strains corresponding to these displacements follow from Equation (1.2):

$$\Delta\varepsilon_x = -\frac{\partial(\Delta u)}{\partial x} \;;\; \Delta\varepsilon_y = -\frac{\partial(\Delta v)}{\partial y} \;;\; \Delta\gamma_{xy} = -\frac{\partial(\Delta u)}{\partial y} - \frac{\partial(\Delta v)}{\partial x}$$
$$\Delta\varepsilon_z = \Delta\gamma_{xz} = \Delta\gamma_{zy} = 0 \;;\; \{\Delta\varepsilon\}^{\mathrm{T}} = \{\Delta\varepsilon_x \; \Delta\varepsilon_y \; \Delta\gamma_{xy} \; \Delta\varepsilon_z\}^{\mathrm{T}} \tag{2.10}$$

Combining Equations (2.9) and (2.10) for an element with n nodes leads to:

$$\begin{Bmatrix} \Delta\varepsilon_x \\ \Delta\varepsilon_y \\ \Delta\gamma_{xy} \\ \Delta\varepsilon_z \end{Bmatrix} = -\begin{bmatrix} \frac{\partial N_1}{\partial x} & 0 & \frac{\partial N_2}{\partial x} & 0 & \cdots & \cdots & \frac{\partial N_n}{\partial x} & 0 \\ 0 & \frac{\partial N_1}{\partial y} & 0 & \frac{\partial N_2}{\partial y} & \cdots & \cdots & 0 & \frac{\partial N_n}{\partial y} \\ \frac{\partial N_1}{\partial y} & \frac{\partial N_1}{\partial x} & \frac{\partial N_2}{\partial y} & \frac{\partial N_2}{\partial x} & \cdots & \cdots & \frac{\partial N_n}{\partial y} & \frac{\partial N_n}{\partial x} \\ 0 & 0 & 0 & 0 & \cdots & \cdots & 0 & 0 \end{bmatrix} \begin{Bmatrix} \Delta u_1 \\ \Delta v_1 \\ \Delta u_2 \\ \Delta v_2 \\ \cdots\cdots \\ \cdots\cdots \\ \Delta u_n \\ \Delta v_n \end{Bmatrix} \tag{2.11}$$

or more conveniently:

$$\{\Delta\,\varepsilon\} = [\boldsymbol{B}] \{\Delta \boldsymbol{d}\}_n \tag{2.12}$$

where the matrix $[\boldsymbol{B}]$ contains only derivatives of the shape functions N_i, while $\{\Delta \boldsymbol{d}\}_n$ contains the list of nodal displacements for a single element.

If isoparametric elements are being used, the shape functions are identical to the interpolation functions, see Section 2.5.1, and N_i depend only on the natural coordinates S and T. Consequently, the global derivatives $\partial N_i / \partial x$, $\partial N_i / \partial y$ in Equation (2.11) cannot be determined directly. However, using the chain rule which relates the x, y derivatives to the S, T derivatives gives:

$$\begin{Bmatrix} \frac{\partial N_i}{\partial S} & \frac{\partial N_i}{\partial T} \end{Bmatrix}^{\mathrm{T}} = [\boldsymbol{J}] \begin{Bmatrix} \frac{\partial N_i}{\partial x} & \frac{\partial N_i}{\partial y} \end{Bmatrix}^{\mathrm{T}} \tag{2.13}$$

where $[\boldsymbol{J}]$ is the Jacobian matrix:

$$[\boldsymbol{J}] = \begin{bmatrix} \dfrac{\partial x}{\partial S} & \dfrac{\partial y}{\partial S} \\ \dfrac{\partial x}{\partial T} & \dfrac{\partial y}{\partial T} \end{bmatrix} \tag{2.14}$$

Hence, on inverting Equation (2.13), the global derivatives of the interpolation functions are given by:

$$\begin{Bmatrix} \dfrac{\partial N_i}{\partial x} \\ \dfrac{\partial N_i}{\partial y} \end{Bmatrix} = \frac{1}{|\boldsymbol{J}|} \begin{bmatrix} \dfrac{\partial y}{\partial T} & -\dfrac{\partial y}{\partial S} \\ -\dfrac{\partial x}{\partial T} & \dfrac{\partial x}{\partial S} \end{bmatrix} \begin{Bmatrix} \dfrac{\partial N_i}{\partial S} \\ \dfrac{\partial N_i}{\partial T} \end{Bmatrix} \tag{2.15}$$

where $|\boldsymbol{J}|$ is the Jacobian determinant:

$$|\boldsymbol{J}| = \frac{\partial x}{\partial S}\frac{\partial y}{\partial T} - \frac{\partial y}{\partial S}\frac{\partial x}{\partial T} \tag{2.16}$$

The coordinate derivatives in Equations (2.15) and (2.16), which arise from the Jacobian transformation, can be found by differentiating the isoparametric relations given by Equation (2.7).

Constitutive model: The constitutive behaviour can be written as in Equation (1.3):

$$\{\Delta\sigma\} = [\boldsymbol{D}]\{\Delta\varepsilon\} \tag{2.17}$$

where $\{\Delta\boldsymbol{\sigma}\}^{\mathrm{T}} = [\Delta\sigma_x \;\; \Delta\sigma_y \;\; \Delta\tau_{xy} \;\; \Delta\sigma_z]$

For isotropic linear elastic materials the constitutive matrix $[\boldsymbol{D}]$ takes the form given in Section 1.5.5 of Chapter 1. The form of the matrix for transversely isotropic materials is presented in Chapter 5.

To determine the element equations for linear material behaviour, the principle of minimum potential energy is invoked. This principle states that the static equilibrium position of a loaded linear elastic body is the one which minimises the total potential energy. The total potential energy of a body is defined as:

Total potential energy (E) = Strain energy (W) - Work done by the applied loads (L)

The principle of minimum potential energy states that for equilibrium:

$$\delta\Delta E = \delta\Delta W - \delta\Delta L = 0 \tag{2.18}$$

The strain energy, ΔW, is defined as:

$$\Delta W = \tfrac{1}{2}\int_{Vol}\{\Delta\varepsilon\}^{\mathrm{T}}\{\Delta\sigma\}\,\mathrm{d}Vol = \tfrac{1}{2}\int_{Vol}\{\Delta\varepsilon\}^{\mathrm{T}}[\boldsymbol{D}]\{\Delta\varepsilon\}\,\mathrm{d}Vol \tag{2.19}$$

where the integrations are over the volume of the body.

The work done by applied loads, ΔL, can be divided into contributions from body forces and surface tractions and can, therefore, be expressed as:

$$\Delta L = \int_{Vol}\{\Delta\boldsymbol{d}\}^{\mathrm{T}}\{\Delta\boldsymbol{F}\}\,\mathrm{d}Vol + \int_{Srf}\{\Delta\boldsymbol{d}\}^{\mathrm{T}}\{\Delta\boldsymbol{T}\}\,\mathrm{d}Srf \tag{2.20}$$

where:

$\{\Delta\boldsymbol{d}\}^{\mathrm{T}} = \{\Delta\boldsymbol{u}\,,\,\Delta\boldsymbol{v}\}$ = displacements;
$\{\Delta\boldsymbol{F}\}^{\mathrm{T}} = \{\Delta\boldsymbol{F}_x\,,\,\Delta\boldsymbol{F}_y\}$ = body forces;
$\{\Delta\boldsymbol{T}\}^{\mathrm{T}} = \{\Delta\boldsymbol{T}_x\,,\,\Delta\boldsymbol{T}_y\}$ = surface tractions (line loads, surcharge pressures);
Srf is that part of the boundary of the domain over which the surface tractions are applied.

Combining Equations (2.19) and (2.20) the total potential energy of the body becomes:

$$\Delta E = \tfrac{1}{2}\int_{Vol}\{\Delta\varepsilon\}^{\mathrm{T}}[\boldsymbol{D}]\{\Delta\varepsilon\}\,\mathrm{d}Vol - \int_{Vol}\{\Delta\boldsymbol{d}\}^{\mathrm{T}}\{\Delta\boldsymbol{F}\}\,\mathrm{d}Vol - \int_{Srf}\{\Delta\boldsymbol{d}\}^{\mathrm{T}}\{\Delta\boldsymbol{T}\}\,\mathrm{d}Srf \tag{2.21}$$

The essence of the finite element method is now to discretise the problem into elements. This has two effects. Firstly, the potential energy is replaced by the sum of the potential energies of the separate elements:

$$\Delta E = \sum_{i=1}^{N}\Delta E_i \tag{2.22}$$

where N = number of elements. Secondly, the variation of the displacements can be expressed in terms of nodal values using Equation (2.9). Equation (2.21) therefore becomes:

$$\Delta E = \sum_{i=1}^{N}\left[\tfrac{1}{2}\int_{Vol}\left(\{\Delta\boldsymbol{d}\}_n^{\mathrm{T}}[\boldsymbol{B}]^{\mathrm{T}}[\boldsymbol{D}][\boldsymbol{B}]\{\Delta\boldsymbol{d}\}_n - 2\{\Delta\boldsymbol{d}\}_n^{\mathrm{T}}[\boldsymbol{N}]^{\mathrm{T}}\{\Delta\boldsymbol{F}\}\right)\mathrm{d}Vol - \int_{Srf}\{\Delta\boldsymbol{d}\}_n^{\mathrm{T}}[\boldsymbol{N}]\{\Delta\boldsymbol{T}\}\,\mathrm{d}Srf\right]_i \tag{2.23}$$

where the volume integral is now over the volume of an element and the surface integral is over that portion of the element boundary over which surface tractions are specified. The principal unknowns are the incremental nodal displacements over the whole mesh, $\{\Delta\boldsymbol{d}\}_n$. Minimising the potential energy with respect to these incremental nodal displacements gives:

$$\delta\Delta E = \sum_{i=1}^{N}(\{\delta\Delta\boldsymbol{d}\}_n^{\mathrm{T}})_i\Big[\int_{Vol}[\boldsymbol{B}]^{\mathrm{T}}[\boldsymbol{D}][\boldsymbol{B}]\,\mathrm{d}Vol\,\{\Delta\boldsymbol{d}\}_n - \int_{Vol}[\boldsymbol{N}]^{\mathrm{T}}\{\Delta\boldsymbol{F}\}\,\mathrm{d}Vol - \int_{Srf}[\boldsymbol{N}]^{\mathrm{T}}\{\Delta\boldsymbol{T}\}\,\mathrm{d}Srf\Big]_i = 0 \tag{2.24}$$

which is equivalent to a set of equations of the form:

$$\sum_{i=1}^{N}[\boldsymbol{K}_E]_i\left(\{\Delta\boldsymbol{d}\}_n\right)_i = \sum_{i=1}^{N}\{\Delta\boldsymbol{R}_E\} \tag{2.25}$$

where: $[\boldsymbol{K}_E] = \int_{Vol}[\boldsymbol{B}]^{\mathrm{T}}[\boldsymbol{D}][\boldsymbol{B}]\,\mathrm{d}Vol$ = *Element stiffness matrix*;
$\{\Delta\boldsymbol{R}_E\} = \int_{Vol}[\boldsymbol{N}]^{\mathrm{T}}\{\Delta\boldsymbol{F}\}\,\mathrm{d}Vol + \int_{Srf}[\boldsymbol{N}]^{\mathrm{T}}\{\Delta\boldsymbol{T}\}\,\mathrm{d}Srf$ = *Right hand side load vector.*

Thus the problem is reduced to determining and summing the separate *element equilibrium equations*:

$$\left[\boldsymbol{K}_E\right]\left\{\Delta \boldsymbol{d}\right\}_n = \left\{\Delta \boldsymbol{R}_E\right\} \tag{2.26}$$

The element stiffness matrix for isoparametric elements is evaluated using the natural coordinate system. The isoparametric coordinate transformation gives:

$$\mathrm{d}Vol = t\,\mathrm{d}x\,\mathrm{d}y = t\left|\boldsymbol{J}\right|\mathrm{d}S\,\mathrm{d}T \tag{2.27}$$

where for plane strain problems the thickness t is unity and the element stiffness matrix, $[\boldsymbol{K}_E]$, becomes:

$$\left[\boldsymbol{K}_E\right] = \int_{-1}^{1}\int_{-1}^{1} t\left[\boldsymbol{B}\right]^{\mathrm{T}}\left[\boldsymbol{D}\right]\left[\boldsymbol{B}\right]\left|\boldsymbol{J}\right|\mathrm{d}S\,\mathrm{d}T \tag{2.28}$$

In Equation (2.28) $|\boldsymbol{J}|$ is given by Equation (2.16) and represents the determinant of the Jacobian matrix arising from the mapping between global and parent elements. The explicit evaluation of Equation (2.28) cannot usually be performed, except for very special element shapes. It is therefore convenient to use a numerical integration procedure.

2.6.1 Numerical integration

To evaluate the element stiffness matrix and right hand side vector, integrations must be performed. The explicit evaluation of these element integrals cannot usually be performed, except for special cases, and therefore a numerical integration scheme is employed. For example, consider the one dimensional integral, $\int_{-1}^{1} f(x)\mathrm{d}x$, shown graphically in Figure 2.12a. The simplest way to perform numerical integration is to split the x range of the integral (i.e. $-1<x<1$) into a number of equal steps of size a and assume that the area under the curve is equal to the sum of the trapezoidal areas $a(f(x_i)+f(x_{i-1}))/2$. Such a procedure is often referred to as the *Trapezoidal rule*. This procedure can be refined to obtain the greatest accuracy for the minimum number of function evaluations, $f(x_i)$, and several different procedures are available. Essentially, the integral of a function is replaced by a weighted sum of the function evaluated at a number of *integration points* (sampling points). For example, consider a one dimensional integral with three integration points, Figure 2.12b:

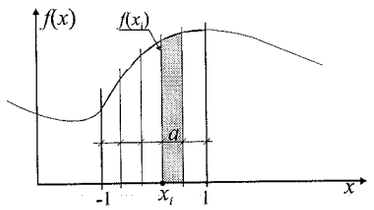

a) Integration using Trapezoidal rule

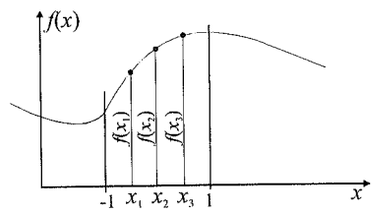

b) Gaussian integration

Figure 2.12: Examples of numerical integration

$$\int_{-1}^{1} f(x)\,dx = \sum_{i=1}^{3} W_i f(x_i) = W_1 f(x_1) + W_2 f(x_2) + W_3 f(x_3) \tag{2.29}$$

where: W_i are weights;

$f(x_i)$ are the values of the function at the three integration points $x_{i=1,2,3}$.

The values of the weights, W_i, and the location of the integration points, x_i, depend on the nature of the integration scheme being used. The number of integration points determines the *integration order*. The higher order of integration gives the more accurate integration process. Unfortunately, the number of function evaluations also depends on the integration order, so the cost of an analysis will increase when a higher order integration is employed. This becomes particularly important for two and three dimensional integrals where an array of integration points is required. For example, for a two dimensional generalisation of the integral discussed above, an array of 3x3 integration points would be required. For three dimensional element this increases to a 3x3x3 array.

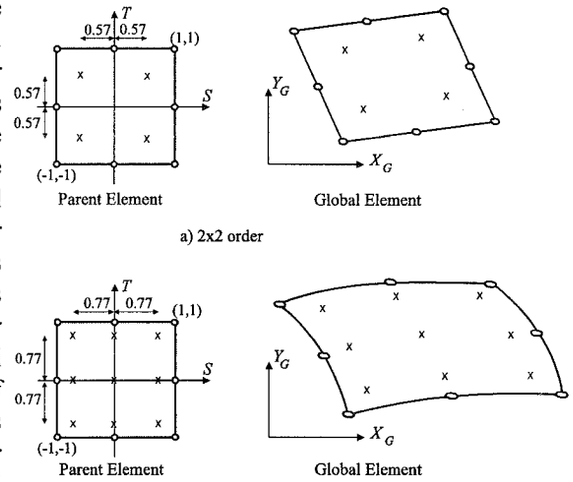

Figure 2.13: Location of Gauss points

The most common numerical integration scheme is *Gaussian integration* and the integration points are often referred to as *Gauss points*. For Gaussian integration the optimum integration order depends on the type of element being used and on its shape. Experience has shown that for the 8 noded isoparametric element either a 2x2 or a 3x3 order should be used. Figure 2.13 illustrates the locations of the Gauss points in the parent element and an example of their positions in a global element for the 2x2 and 3x3 integration orders. 2x2 and 3x3 integration orders are often referred to as *reduced* and *full* integration, respectively.

For nonlinear problems (see Chapter 9), the element stiffness matrix at a particular increment may, in general, depend on the stresses and strains determined at the previous increment. Since the stiffness matrix is determined by numerical integration and the element equations are referred to the integration points, it is also convenient to restrict evaluation of the stresses and strains to these points. Hence, in many programs the output listings provide values of stresses and strains at integration points.

2.7 Global equations

The next stage in the formulation of the finite element equations is the assembly of the separate element equilibrium equations into a set of global equations:

$$\left[\boldsymbol{K}_G\right]\left\{\Delta \boldsymbol{d}\right\}_{nG} = \left\{\Delta \boldsymbol{R}_G\right\} \tag{2.30}$$

where: $[\boldsymbol{K}_G]$ = the global stiffness matrix;
$\{\Delta \boldsymbol{d}\}_{nG}$ = a vector containing the unknown degrees of freedom (nodal displacements) for the entire finite element mesh;
$\{\Delta \boldsymbol{R}_G\}$ = the global right hand side load vector.

As each element stiffness matrix is formed according to the procedure described in Section 2.6, it is then assembled into the overall global stiffness matrix. This assembly process is called the *direct stiffness method.* The terms of the global stiffness matrix are obtained by summing the individual element contributions whilst taking into account the degrees of freedom which are common between elements. This process is described in more detail in Section 2.7.1. The terms of the right hand side load vector are obtained in a similar manner by summing the individual loads acting at each node. Further details of the load vector are given in Section 2.8 and in Chapter 3.

It is clear from Equation (2.28) that, if the constitutive matrix $[\boldsymbol{D}]$ is symmetric, the element stiffness matrices and hence the global stiffness matrix will also be symmetric. This situation occurs for a wide range of material behaviour, including linear elastic material behaviour. The non-zero terms of the global stiffness matrix arise from the connections between the degrees of freedom through the elements. From the geometry of the mesh, each degree of freedom is only connected to a small number of other degrees of freedom; hence, the global stiffness matrix will contain many zero terms. In addition, most of the zero terms will be outside a diagonal band, see Section 2.7.1. The assembly, storage and solution schemes used for the global stiffness matrix take into account its symmetric and banded structure.

2.7.1 The direct stiffness assembly method

The essence of the direct stiffness method is to assemble the individual terms of the element stiffness matrix, $[\boldsymbol{K}_E]$, into the overall global stiffness matrix, $[\boldsymbol{K}_G]$, according to the global degree of freedom numbering scheme. At the element level, the stiffness matrix terms correspond to the relative stiffness between the degrees of freedom contained in the element. At the mesh level, the stiffness matrix terms correspond to the relative stiffness between the degrees of freedom over the whole mesh. For this reason the size of the global stiffness matrix will depend on the total number of degrees of freedom and the non-zero terms will occur from the connections between the degrees of freedom through the elements.

To illustrate the stages of the assembly process it is convenient to consider a mesh of 4 noded elements with only one degree of freedom at each node (note: for two dimensional analyses there are usually two degrees of freedom at each node). With only one degree of freedom at each node the stiffness matrices are much

simpler and the assembly process is easier to describe. In such a situation 'degree of freedom' may be associated with 'node number'.

The numbering of the degrees of freedom and the form of the stiffness matrix for a single 4 noded element is illustrated in Figure 2.14. It is assumed that all the stiffness matrices are symmetric and therefore only the diagonal and upper triangle of terms are indicated.

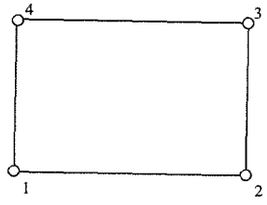

$$\left[\boldsymbol{K}_E\right] = \begin{bmatrix} K_{11} & K_{12} & K_{13} & K_{14} \\ & K_{22} & K_{23} & K_{24} \\ SYM & & K_{33} & K_{34} \\ & & & K_{44} \end{bmatrix}$$

Figure 2.14: Stiffness matrix for a single element

If this single element becomes part of a mesh of elements then, with respect to the global degree of freedom numbering, the stiffness matrix will take the form shown in Figure 2.15. The numerical values of the stiffness terms remain the same, but the quantities they represent in global terms become different. For example, in Figure 2.14 the stiffness term K_{11} refers to element degree of freedom 1, whereas in Figure 2.15 the same degree of freedom becomes global degree of freedom 2; hence the contribution of the element to the global value of K_{22} is equal to K_{11}. The important thing to note here is that each row and column of the element stiffness matrix corresponds to each degree of freedom of the element.

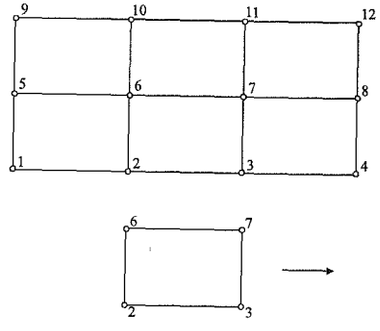

$$\left[\boldsymbol{K}_E\right] = \begin{bmatrix} K_{22} & K_{23} & K_{27} & K_{26} \\ & K_{33} & K_{37} & K_{36} \\ SYM & & K_{77} & K_{76} \\ & & & K_{66} \end{bmatrix}$$

Figure 2.15: Element stiffness matrix in terms of global degrees of freedom

The assembly process can now be demonstrated using the stiffness matrices expressed in terms of the global degrees of freedom. Figure 2.16 shows a simple mesh containing two elements and the degree of freedom numbers. The stages of Figure 2.16 show the complete assembly of the global stiffness matrix for this simple mesh. It should be noted that there is some re-ordering of the terms due to

differences between the standard element numbering and the degree of freedom numbering. In addition, the terms in the global stiffness matrix corresponding to the degrees of freedom which are common to more than one element arise from summing the contributions from the respective elements. For degrees of freedom occurring in only one element there is only one term assembled into the global stiffness matrix.

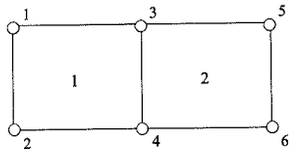

a) Two element mesh

$$\begin{bmatrix} K^1_{11} & K^1_{12} & K^1_{14} & K^1_{13} \\ & K^1_{22} & K^1_{24} & K^1_{23} \\ & & K^1_{44} & K^1_{43} \\ & & & K^1_{33} \end{bmatrix} \rightarrow \left[\begin{array}{c|c|c|c|c|c} K^1_{11} & K^1_{12} & K^1_{13} & K^1_{14} & & \\ & K^1_{22} & K^1_{23} & K^1_{24} & & \\ & & K^1_{33} & K^1_{34} & & \\ & & & K^1_{44} & & \\ & SYM & & & & \\ & & & & & \end{array}\right]$$

Stiffness matrix for element 1

Global stiffness matrix

b) Assembly of element 1

$$\begin{bmatrix} K^2_{33} & K^2_{34} & K^2_{36} & K^2_{35} \\ & K^2_{44} & K^2_{46} & K^2_{45} \\ & & K^2_{66} & K^2_{65} \\ & & & K^2_{55} \end{bmatrix} \rightarrow \left[\begin{array}{c|c|c|c|c|c} K^1_{11} & K^1_{12} & K^1_{13} & K^1_{14} & & \\ & K^1_{22} & K^1_{23} & K^1_{24} & & \\ & & K^1_{33}+K^2_{33} & K^1_{34}+K^2_{34} & K^2_{35} & K^2_{36} \\ & & & K^1_{44}+K^2_{44} & K^2_{45} & K^2_{46} \\ & SYM & & & K^2_{55} & K^2_{56} \\ & & & & & K^2_{66} \end{array}\right]$$

Stiffness matrix for element 2

Global stiffness matrix

c) Assembly of element 2

$$[K_G] = \begin{bmatrix} K_{11} & K_{12} & K_{13} & K_{14} & & \\ & K_{22} & K_{23} & K_{24} & & \\ & & K_{33} & K_{34} & K_{35} & K_{36} \\ & & & K_{44} & K_{45} & K_{46} \\ & SYM & & & K_{55} & K_{56} \\ & & & & & K_{66} \end{bmatrix}$$

d) Final assembled structure of the global stiffness matrix

Figure 2.16: Assembly procedure for a simple mesh with two elements

The structure of the global stiffness matrix becomes particularly important if efficient use is to be made of the computer storage, as is discussed in Section 2.9. At this stage, a few points can be made concerning the structure of the assembled stiffness matrix shown in Figure 2.16d. The non-zero terms in the global stiffness matrix arise only from the connection between degrees of freedom through the elements. Thus for each row in the global stiffness matrix, the last non-zero term corresponds to the highest degree of freedom to which a particular degree of freedom is connected. This property leads to a global stiffness matrix which is generally sparse (i.e. the matrix has many zero terms) and banded (i.e. the non-zero terms are concentrated along the main diagonal).

2.8 Boundary conditions

The final stage in setting up the global system of equations is the application of the boundary conditions. These are the load and displacement conditions which fully define the boundary value problem being analysed.

Loading conditions, line loads and surcharge pressures, affect the right hand side of the global system of equations. If line or point forces are prescribed, these can be assembled directly into the right hand side vector $\{\Delta \boldsymbol{R}_G\}$. If pressure boundary conditions are defined, these must first be expressed as equivalent nodal forces before being added to $\{\Delta \boldsymbol{R}_G\}$. As with the assembly process for the stiffness matrix, the assembly of the right hand side vector is performed with respect to the global degree of freedom numbering system. Body forces also contribute to $\{\Delta \boldsymbol{R}_G\}$, as do the forces from *excavated* and *constructed* elements. These boundary conditions are discussed in greater detail in Chapter 3.

Displacement boundary conditions affect $\{\Delta \boldsymbol{d}\}_{nG}$. The equation corresponding to the prescribed degree of freedom (displacement component) must be effectively eliminated during the solution process, see Section 2.9. In all cases sufficient displacement conditions must be prescribed in order to retain any rigid body modes of deformation, such as rotations or translations of the whole finite element mesh. If these conditions are not satisfied, the global stiffness matrix will be singular and the equations cannot be solved. For two dimensional plane strain problems at least two nodes must have a prescribed displacement in the x direction and one node a prescribed displacement in the y direction, or, alternatively, two nodes must have a prescribed displacement in the y direction and one node a prescribed displacement in the x direction.

2.9 Solution of global equations

Once the global stiffness matrix has been established and the boundary conditions added, it mathematically forms a large system of simultaneous equations. These have to be solved to give values for the nodal displacements $\{\Delta \boldsymbol{d}\}_{nG}$. There are several different mathematical techniques for solving large systems of equations. Most finite element programs adopt a technique based on Gaussian elimination.

However, for three dimensional problems iterative techniques may be more cost effective, see Chapter 11.

To illustrate the Gaussian elimination technique, one particular method of solution is described. In this approach the stiffness matrix is stored as a 'sky line profile' and inversion of the stiffness matrix follows a triangular decomposition. It should be noted, however, that other procedures are available (Crisfield (1986)).

2.9.1 Storage of the global stiffness matrix

Because of the sparse and banded nature of the stiffness matrix it is not necessary to store the complete stiffness matrix. Reductions in storage can be obtained by taking into account the symmetry of the matrix and only storing the diagonal and upper triangle of terms. This reduces the storage space by almost a half. As an example, Figure 2.17 shows the structure of the global stiffness matrix and the terms which need to be stored for a simple finite element mesh composed of four 4 noded elements. Again, for simplicity, it is assumed that there is only one degree of freedom at each node.

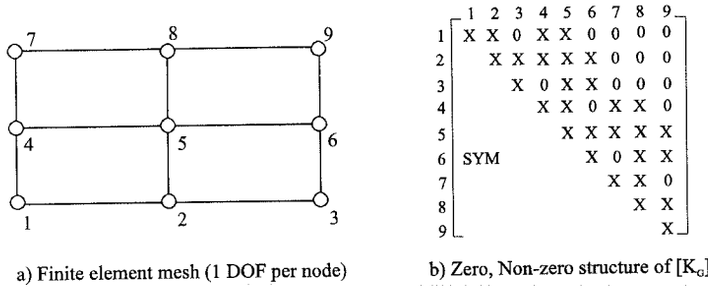

a) Finite element mesh (1 DOF per node)

b) Zero, Non-zero structure of $[K_G]$

Figure 2.17: Structure of the global stiffness matrix

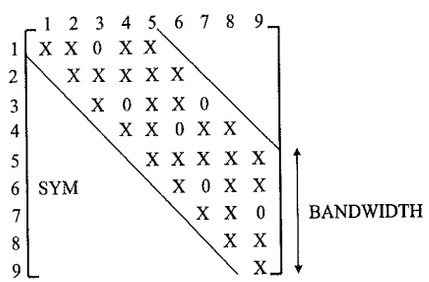

Figure 2.18: Diagonal band structure of $[K_G]$

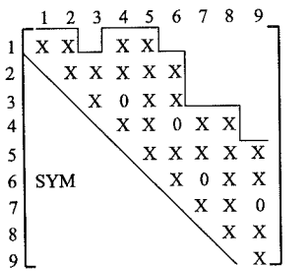

Figure 2.19: Column-profile structure of $[K_G]$

As pointed out in Section 2.7.1, the global stiffness matrix has a diagonal band structure, see Figure 2.18. The last non-zero term in any row corresponds to the highest degree of freedom number to which a particular degree of freedom is

connected through an element. For example, the last non-zero term in row 4 corresponds to degree of freedom 8 and it is seen in Figure 2.17 that degree of freedom 8 is the highest degree of freedom to which 4 is connected. Counting for each column the number of terms above the diagonal term up to the last non-zero term (column height) and taking the maximum value of this quantity over all the columns, gives the *bandwidth* of the matrix. It is clear from Figure 2.18 that the bandwidth measured column-wise is the same as measured row-wise and in this example equals 5. An efficient compact storage scheme based on the band structure is shown in Figure 2.18. In this case the stiffness matrix is stored row-wise as a two dimensional array and the number of columns in the array is equal to the bandwidth. Alternatively, the stiffness matrix could be stored column-wise, but this has no effect on the storage requirements or the equation algorithm.

The band storage shown in Figure 2.18 requires space for a number of zero terms which are contained within the band. Many of these terms are not required by the solution algorithm and remain zero throughout the solution process; hence they need not be stored. The most efficient storage scheme is based on the column-profile shown in Figure 2.19. The column-profile contains the terms in each column from the diagonal up to the last non-zero term and may contain zero terms within the profile. Comparing Figures 2.18 and 2.19, it can be seen that the column-profile scheme is essentially a variable bandwidth storage and the zero terms between the profile and diagonal band are omitted. The zero terms within the profile are essential in the solution algorithm and the storage locations normally contain non-zero terms at the end of the solution process, see Section 2.9.2.

As noted above, the bandwidth for any degree of freedom is the difference between the highest degree of freedom connected through an element to that degree of freedom, and the degree of freedom itself. This difference therefore depends on the way the degrees of freedom are numbered. There are several algorithms available for renumbering the degrees of freedom to minimise the bandwidth (Cuthill and McKee (1969), Gibbs *et al.* (1976), Everstine (1979)).

2.9.2 Triangular decomposition of the global stiffness matrix

The solution technique associated with the column-profile storage scheme is based on a triangular decomposition of the global stiffness matrix. Formally, this decomposition reduces the stiffness matrix to the following matrix product:

$$\left[\boldsymbol{K}_G\right] = \left[\boldsymbol{L}\right]\left[\boldsymbol{DM}\right]\left[\boldsymbol{L}\right]^{\mathrm{T}} \tag{2.31}$$

where $[\boldsymbol{L}]$ is a lower triangular matrix of the form:

$$\left[\boldsymbol{L}\right] = \begin{bmatrix} 1 & & & & \\ L_{21} & 1 & & 0 & \\ L_{31} & L_{32} & 1 & & \\ \cdot\cdot & \cdot\cdot & \cdot\cdot & \cdot\cdot & \cdot\cdot \\ L_{n1} & L_{n2} & L_{n3} & \cdot\cdot & 1 \end{bmatrix} \tag{2.32}$$

and $[\boldsymbol{DM}]$ is a diagonal matrix:

$$[\boldsymbol{DM}] = \begin{bmatrix} D_1 & & & & \\ & D_2 & & 0 & \\ & & D_3 & & \\ & 0 & & .. & \\ & & & & D_n \end{bmatrix} \tag{2.33}$$

In this section explanation is given of how the terms of $[\boldsymbol{L}]$ and $[\boldsymbol{DM}]$ are derived from the terms of $[\boldsymbol{K}_G]$, and how $[\boldsymbol{DM}]$ and $[\boldsymbol{L}]^T$ overwrite the diagonal and off-diagonal terms of $[\boldsymbol{K}_G]$, respectively, within the column-profile storage scheme. To illustrate the process, a full n x n symmetric matrix will be considered:

$$[\boldsymbol{K}] = \begin{bmatrix} K_{11} & K_{12} & K_{13} & \ldots & K_{1n} \\ & K_{22} & K_{23} & \ldots & K_{2n} \\ & & K_{33} & \ldots & K_{3n} \\ & & & \ldots & \ldots \\ & & & & K_{nn} \end{bmatrix} \tag{2.34}$$

Using the triangular factors defined by Equations (2.32) and (2.33) and forming the matrix product given by Equation (2.31), transforms the $[\boldsymbol{K}]$ matrix into the following form:

$$[\boldsymbol{K}] = \begin{bmatrix} D_1 & L_{12}D_1 & L_{13}D_1 & \ldots & L_{1n}D_1 \\ & L_{12}^2D_1 + D_2 & L_{13}L_{12}D_1 + L_{23}D_2 & \ldots & L_{1n}L_{12}D_1 + L_{2n}D_2 \\ & & L_{13}^2D_1 + L_{23}^2D_2 + D_3 & \ldots & L_{1n}L_{13}D_1 + L_{2n}L_{23}D_2 + L_{3n}D_3 \\ & & & \ldots & \ldots \\ & & & & L_{1n}^2D_1 + L_{2n}^2D_2 + L_{3n}^2D_3 + \ldots + D_n \end{bmatrix} \tag{2.35}$$

In order to determine the terms of the triangular factors $[\boldsymbol{DM}]$ and $[\boldsymbol{L}]$, the terms of the matrix $[\boldsymbol{K}]$ given in Equations (2.34) and (2.35) need to be equated. The order in which these equations are then solved characterises a number of different solution algorithms. Some algorithms solve the equations by following the terms in the rows of $[\boldsymbol{K}]$, some follow the columns of $[\boldsymbol{K}]$ and others modify all the terms of $[\boldsymbol{K}]$ successively. Essentially, all these algorithms are equivalent and require the same number of arithmetic operations. However, the column-wise technique has certain advantages in that a smaller number of intermediate terms need to be evaluated, consequently reducing the time of the calculation. The set of equations to be solved is listed below:

$$\begin{aligned} D_1 &= K_{11} \\ \\ L_{12} &= K_{12}/D_1 \\ D_2 &= K_{22} - L_{12}^2 D_1 \\ \\ L_{13} &= K_{13}/D_1 \\ L_{23} &= [K_{23} - L_{13}L_{12}D_1]/D_2 \end{aligned}$$

$$\begin{aligned} D_3 &= K_{33} - L_{13}^2 D_1 - L_{23}^2 D_2 \\ \\ L_{1n} &= K_{1n}/D_1 \\ L_{2n} &= [K_{2n} - L_{1n}L_{12}]/D_2 \\ L_{3n} &= [K_{3n} - L_{1n}L_{13}D_1 - L_{2n}L_{23}D_2]/D_3 \\ \ldots &\quad \ldots \\ D_n &= K_{nn} - L_{1n}^2 D_1 - L_{2n}^2 D_2 - L_{3n}^2 D_3 - \ldots - L_{n-1,n}^2 D_{n-1} \end{aligned} \tag{2.36}$$

Each term of $[\boldsymbol{DM}]$ and $[\boldsymbol{L}]$ is obtained in sequence, using values of $[\boldsymbol{K}]$ and values of $[\boldsymbol{DM}]$ and $[\boldsymbol{L}]$ which are previously determined. Hence, it is easy to see how the values of $[\boldsymbol{K}]$ can be overwritten by $[\boldsymbol{DM}]$ and $[\boldsymbol{L}]$. Finally, the upper triangle of the stiffness matrix will contain the terms:

$$[\boldsymbol{K}] = \begin{bmatrix} D_1 & L_{12} & L_{13} & \ldots & L_{1n} \\ & D_2 & L_{23} & \ldots & L_{2n} \\ & & D_3 & \ldots & L_{3n} \\ & & & \ldots & \ldots \\ & & & & D_n \end{bmatrix} \tag{2.37}$$

For the maximum efficiency there is some advantage in carefully ordering the computations in each column. These are performed in three stages: firstly, the off-diagonal terms are modified by an inner product accumulation; secondly, the off-diagonal terms are divided by a corresponding diagonal term and, thirdly, a new diagonal term is found. This is shown in the set of Equations (2.36).

2.9.3 Solution of the finite element equations

Having determined the triangular factors $[\boldsymbol{DM}]$ and $[\boldsymbol{L}]$ of the global stiffness matrix $[\boldsymbol{K}_G]$, the solution of the finite element equations can be performed in three stages. The process solves Equation (2.30), now written in the form:

$$[\boldsymbol{L}][\boldsymbol{DM}][\boldsymbol{L}]^T\{\Delta \boldsymbol{d}\} = \{\Delta \boldsymbol{R}\} \tag{2.38}$$

where $\{\Delta \boldsymbol{d}\}$ is the vector of unknown degrees of freedom and $\{\Delta \boldsymbol{R}\}$ is the right hand side vector of prescribed nodal forces. Setting

$$\{\Delta \boldsymbol{d}''\} = [\boldsymbol{DM}][\boldsymbol{L}]^T\{\Delta \boldsymbol{d}\} \tag{2.39}$$

the first stage of the solution process finds $\{\Delta \boldsymbol{d}''\}$ as:

$$\{\Delta \boldsymbol{d}''\} = [\boldsymbol{L}]^{-1}\{\Delta \boldsymbol{R}\} \tag{2.40}$$

by forward substitution. Then, setting

$$\{\Delta \boldsymbol{d}'\} = [\boldsymbol{L}]^T\{\Delta \boldsymbol{R}\} \tag{2.41}$$

gives:

$$\{\Delta \boldsymbol{d}'\} = [\boldsymbol{DM}]^{-1}\{\Delta \boldsymbol{d}''\} \tag{2.42}$$

The final stage of the solution process then determines

$$\{\Delta \boldsymbol{d}\} = [\boldsymbol{L}]^{-\mathrm{T}}\{\Delta \boldsymbol{d}'\} \tag{2.43}$$

by backward substitution. The three stages of the solution technique are performed with the triangular factors $[\boldsymbol{DM}]$ and $[\boldsymbol{L}]$, which are stored in column-profile form in a one-dimensional array. The decomposed stiffness matrix remains unchanged throughout the solution process and all the calculations are performed on the right hand side vector. Hence, the same solution process could be repeated with many different load vectors, without having to re-decompose the stiffness matrix. To illustrate this solution process, each of the three stages is considered in detail below.

STAGE 1: Forward substitution

This stage solves a set of equations of the form:

$$\begin{bmatrix} 1 & & & & \\ L_{12} & 1 & & 0 & \\ L_{13} & L_{23} & 1 & & \\ .. & .. & .. & .. & .. \\ L_{1n} & L_{2n} & L_{3n} & .. & 1 \end{bmatrix} \begin{Bmatrix} \Delta d_1'' \\ \Delta d_2'' \\ \Delta d_3'' \\ \dots \\ \Delta d_n'' \end{Bmatrix} = \begin{Bmatrix} f_1 \\ f_2 \\ f_3 \\ \dots \\ f_n \end{Bmatrix} \tag{2.44}$$

which lead, simply by forward substitution, to:

$$\begin{aligned} \Delta d_1'' &= f_1 \\ \Delta d_2'' &= f_2 - L_{12}\Delta d_2'' \\ \Delta d_3'' &= f_3 - L_{13}\Delta d_1'' - L_{23}\Delta d_2'' \\ \dots \quad & \dots \qquad\qquad \dots\dots \\ \Delta d_n'' &= f_n - \sum_{k=1}^{n-1} L_{kn}\Delta d_k'' \end{aligned} \tag{2.45}$$

Since the terms of $[\boldsymbol{L}]$ are stored in column-profile form, some of the terms indicated in Equations (2.44) and (2.45) may be outside the column-profile and are therefore zero. In practice, the forward substitution sums indicated in Equation (2.45) are only evaluated over the number of terms of $[\boldsymbol{L}]$ within the column-profile.

STAGE 2: Invert diagonal matrix

In this stage the simple equation is solved:

$$\begin{bmatrix} D_1 & & & & \\ & D_2 & & 0 & \\ & & D_3 & & \\ & 0 & & .. & \\ & & & & D_n \end{bmatrix} \begin{Bmatrix} \Delta d_1' \\ \Delta d_2' \\ \Delta d_3' \\ \dots \\ \Delta d_n' \end{Bmatrix} = \begin{Bmatrix} \Delta d_1'' \\ \Delta d_2'' \\ \Delta d_3'' \\ \dots \\ \Delta d_n'' \end{Bmatrix} \tag{2.46}$$

which gives:

$$\begin{aligned} \Delta d_1' &= \Delta d_1''/D_1 \\ \Delta d_2' &= \Delta d_2''/D_2 \\ \Delta d_3' &= \Delta d_3''/D_3 \\ \dots \quad &= \qquad \dots \\ \Delta d_n' &= \Delta d_n''/D_n \end{aligned} \tag{2.47}$$

STAGE 3: Backward substitution

Finally, a set of equations is solved, of the form:

$$\begin{bmatrix} 1 & L_{12} & L_{13} & \dots & L_{1n} \\ & 1 & L_{23} & \dots & L_{2n} \\ & & 1 & \dots & L_{3n} \\ & 0 & & \dots & \dots \\ & & & & 1 \end{bmatrix} \begin{Bmatrix} \Delta d_1 \\ \Delta d_2 \\ \Delta d_3 \\ \dots \\ \Delta d_n \end{Bmatrix} = \begin{Bmatrix} \Delta d_1' \\ \Delta d_2' \\ \Delta d_3' \\ \dots \\ \Delta d_n' \end{Bmatrix} \tag{2.48}$$

which lead, by backward substitution, to the solution:

$$\begin{aligned} \Delta d_n &= \Delta d_n' \\ \Delta d_{n-1} &= \Delta d_{n-1}' - L_{n-1,n}\Delta d_n \\ \Delta d_{n-2} &= \Delta d_{n-2}' - L_{n-2,n-1}\Delta d_{n-1} - L_{n-2,n}\Delta d_n \\ \dots \quad & \dots \qquad\qquad \dots \\ \Delta d_1 &= \Delta \mathrm{d}_1' - \sum_{k=2}^{n} L_{1k}\Delta d_k \end{aligned} \tag{2.49}$$

The backward substitution sums indicated in Equation (2.49) are only evaluated over the number of terms of $[\boldsymbol{L}]$ which lie within the column profile.

The solution process described above is extremely efficient and has the advantage that the decomposed stiffness matrix remains unchanged. This fact is particularly important for nonlinear problems which are solved by iteration. In this case successive solution estimates can be obtained by modifying the right hand side load vector, using a stiffness matrix which needs to be decomposed into triangular factors only once.

2.9.4 Modification due to displacement boundary conditions

In most finite element calculations displacement boundary conditions are defined in order to restrict rigid body movements, or to restrain part of the structure. These conditions imply that certain degrees of freedom are prescribed and the system of equations:

$$[\boldsymbol{K}_G]\{\Delta \boldsymbol{d}\}_{nG} = \{\Delta \boldsymbol{R}_G\} \tag{2.50}$$

needs to be modified in order to enforce these conditions. To see the effect on the system of equations when a particular degree of freedom, for example Δd_j, is prescribed, Equation (2.50) is written in the full form (Equation (2.51)). In this case, the force term ΔR_j becomes unknown and is usually required in the solution as a reaction term:

$$\begin{bmatrix} K_{11} & .. & K_{1j} & .. & K_{1n} \\ .. & .. & .. & .. & .. \\ K_{j1} & .. & K_{jj} & .. & K_{jn} \\ .. & .. & .. & .. & .. \\ K_{n1} & .. & K_{nj} & .. & K_{nn} \end{bmatrix} \begin{Bmatrix} \Delta d_1 \\ .. \\ \Delta d_j \\ .. \\ \Delta d_n \end{Bmatrix} = \begin{Bmatrix} \Delta R_1 \\ .. \\ \Delta R_j \\ .. \\ \Delta R_n \end{Bmatrix} \tag{2.51}$$

Since Δd_j is prescribed, the j^{th} equation in system (2.51) is not required and can be replaced by the simpler equation:

$$\Delta d_j = a_j \tag{2.52}$$

where a_j is the prescribed value. In addition, each other equation contains a term $K_{ij}\Delta d_j$, which is also known and can therefore be transferred to the right hand side. Performing these two operations, Equation (2.51) reduces to :

$$\begin{bmatrix} K_{11} & .. & 0 & .. & K_{1n} \\ .. & .. & .. & .. & .. \\ 0 & .. & 1 & .. & 0 \\ .. & .. & .. & .. & .. \\ K_{n1} & .. & 0 & .. & K_{nn} \end{bmatrix} \begin{Bmatrix} \Delta d_1 \\ .. \\ \Delta d_j \\ .. \\ \Delta d_n \end{Bmatrix} = \begin{Bmatrix} \Delta R_1 - K_{1j}a_j \\ .. \\ \Delta a_j \\ .. \\ \Delta R_n - K_{nj}a_j \end{Bmatrix} \tag{2.53}$$

Thus the prescribed degree of freedom is taken into account by replacing the j^{th} row and column in $[\boldsymbol{K}_G]$ by zeros, the diagonal term by 1 and updating the right hand side vector by simple correction terms. This method has the advantage that the symmetry of the stiffness matrix is not destroyed and, hence, the modifications can easily be made within the compact column-profile storage scheme before the solution process. However, this method, as it stands, has two important disadvantages. The first is that the terms of $[\boldsymbol{K}_G]$ are overwritten by 0's and 1's and hence the value of the reaction force ΔR_j cannot be found later by back substitution. The second disadvantage occurs for incremental or iterative techniques where the values of the prescribed degrees of freedom change. In such cases, the modifications to the right-hand side vector cannot be performed, because the required terms of $[\boldsymbol{K}_G]$ are not saved, and a complete new global stiffness matrix must be formed at each stage.

The above disadvantages are avoided by a simple modification of the standard decomposition and solution procedures. First, it is assumed that the stiffness matrix is effectively replaced by the matrix shown in Equation (2.53). However, the terms in the j^{th} row and column of $[\boldsymbol{K}_G]$ are not actually changed. During the decomposition of $[\boldsymbol{K}_G]$ the terms associated with the j^{th} row and column of $[\boldsymbol{K}_G]$ are skipped over during the calculations (since they are assumed to be zero), and the remaining columns are decomposed as before. Prior to the solution process, the right-hand side vector is modified using the prescribed values and the correct terms from $[\boldsymbol{K}_G]$. Then finally, during the solution process, the j^{th} row and column of $[\boldsymbol{K}_G]$ are again effectively ignored. This technique clearly allows the reaction forces to be calculated by simply back-substituting the solution into the appropriate equations stored within the decomposed $[\boldsymbol{K}_G]$.

2.10 Calculation of stresses and strains

Once the global equations have been solved and values of the nodal displacements obtained, secondary quantities, such as stresses and strains, can be evaluated. Strains can be found using Equation (2.11) and these can then be combined with the constitutive matrix, $[\boldsymbol{D}]$, to obtain stresses, see Equation (2.17).

2.11 Example

To illustrate the application of the finite element method, the boundary value problem of a strip footing on an isotropic linear elastic soil, as shown in Figure 2.20, is considered. The footing has a width of 12m and the soil has a Young's modulus $E = 10000$ kN/m^2, and a Poisson's ratio $\mu = 0.4$. As there is a vertical plane of symmetry through the centre of the footing, the finite element analysis needs to consider only half of the problem.

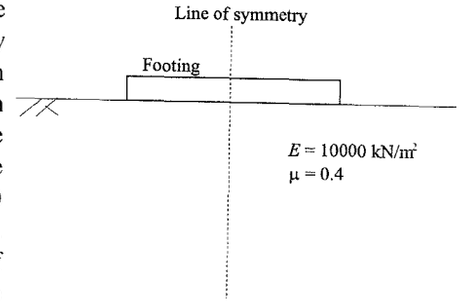

Figure 2.20: Footing problem

The finite element mesh used to analyse this problem is shown in Figure 2.21. It consists of 42 eight noded isoparametric elements. Only the soil is discretised into finite elements. The foundation is represented by appropriate boundary conditions. As it is necessary to analyse a finite domain, the mesh extends 20m horizontally and 20m vertically.

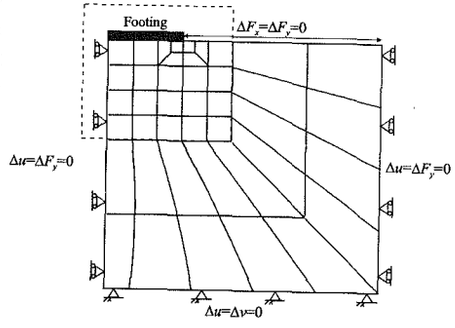

Figure 2.21: Finite element mesh for strip footing problem

With finite element analyses, it is necessary to specify an x (horizontal) and y (vertical) boundary condition at each node on the boundary of the mesh. This boundary condition can be either a prescribed nodal displacement or a nodal force. For the strip footing problem, it is assumed that both the displacements Δu and Δv, in the horizontal and vertical directions, are zero for all nodes along the bottom boundary of the mesh, see Figure 2.21. Consequently, nodal reactions (forces) will be generated in both the horizontal and vertical directions as a result of the analysis. On the vertical side boundaries, the horizontal displacement, Δu, and the vertical force, ΔF_y, have been assumed to be zero. The $\Delta F_y = 0$ condition implies that there can be no vertical shear stress on these

boundaries and the nodes are, therefore, free to move in the vertical direction. Horizontal reactions will, however, be generated at the nodes as a result of the analysis. Along the top boundary of the mesh, from the edge of the strip footing to the right hand side boundary, both the vertical, ΔF_y, and horizontal, ΔF_x, nodal forces are assumed to be zero. This implies a stress free surface which is free to move both vertically and horizontally.

The boundary condition applied to the mesh boundary immediately below the position of the strip footing depends on whether the footing is *rigid* or *flexible* and/or *smooth* or *rough*. Three different alternatives for this boundary condition are shown in Figure 2.22.

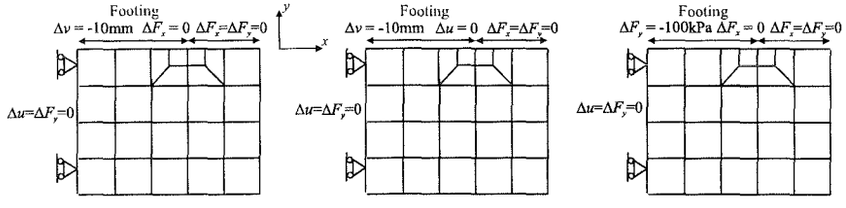

a) Smooth rigid footing b) Rough rigid footing c) Smooth flexible footing

Figure 2.22: Footing boundary conditions

In Figure 2.22a the footing is assumed to be rigid and smooth. Consequently, a vertical displacement of 10mm (downward) and ΔF_x=0 is prescribed at each node beneath the position of the footing. In Figure 2.22b the same vertical displacement boundary condition is applied, but instead of the horizontal force being zero, the horizontal displacement $\Delta u = 0$. This models a rough rigid footing. In both the above cases a rigid footing is simulated by applying a uniform vertical displacement to the footing. In Figure 2.22c a uniform surcharge pressure is applied via the vertical nodal forces, ΔF_y, to the nodes beneath the position of the footing. In addition, the horizontal nodal forces, ΔF_x, are assumed to be zero. These boundary conditions therefore model a smooth flexible footing.

It should be noted that many finite element programs do not require that the user specifies an x (horizontal) and y (vertical) boundary condition at each node on the boundary of the mesh. In such a situation, the program will make an implicit assumption. Usually, if a boundary condition is not prescribed, the program will assume that the appropriate nodal force is zero. For example, if only a vertical displacement is specified at a particular node, the program will assume the horizontal force $\Delta F_x = 0$.

Analyses with all three of the footing boundary conditions given in Figure 2.22 have been performed. The surface settlement profiles predicted by these analyses are compared in Figure 2.23. To aid comparison, the vertical settlement, Δv, has been normalised by the settlement under the centre of the footing, Δv_{max}. The settlement profiles for both the smooth and the rough rigid footings are very similar.

The analytical solution for a smooth flexible footing on an isotropic elastic half-space predicts that the vertical displacements are infinite. However, finite values are predicted by elastic theory if the elastic material has a finite depth. For the situation analysed above, the analytical prediction of the vertical settlement at the edge of the footing is 0.057m. This compares favourably with the finite element prediction of 0.054m. Finite element predictions closer to the analytical solution can be obtained if a more refined mesh is used.

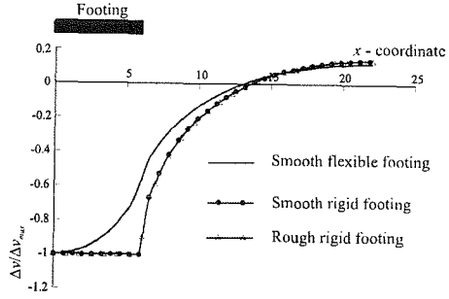

Figure 2.23: Ground surface settlements

Vectors of ground movement predicted by the finite element analysis of the rough rigid footing are shown in Figure 2.24. These vectors indicate the distribution of movements within the elastic soil. The contours of the major principal stress, $\Delta\sigma_1$, are shown in Figure 2.25.

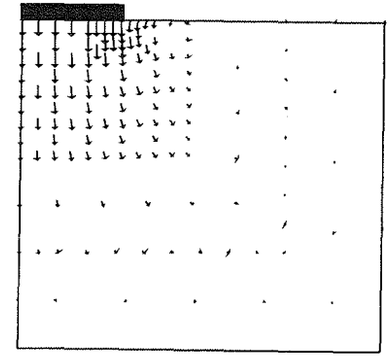

Figure 2.24: Vectors of ground movement

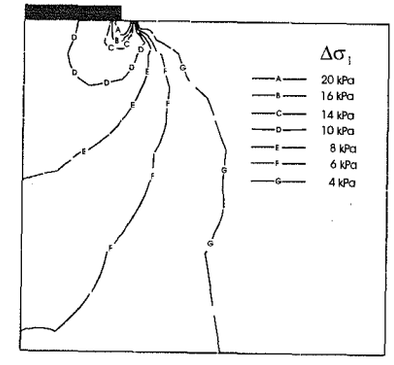

Figure 2.25: Contours of principal stress

2.12 Axi-symmetric finite element analysis

In the preceding discussion a plane strain situation has been assumed when developing the finite element equations. The basic procedures are, however, similar for plane stress, axi-symmetric and full three dimensional situations.

As discussed in Chapter 1, several geotechnical problems can be idealised as axi-symmetric, e.g. axially loaded piles and circular foundations. In this type of problem it is usual to adopt cylindrical coordinates r (radial direction), z (vertical direction) and θ (circumferential direction), Figure 2.26, as opposed to the

Cartesian coordinates used for plane strain analysis. There are four non-zero stresses (σ_r, σ_z, σ_θ and τ_{rz}), four non-zero strains (ε_r, ε_z, ε_θ and γ_{rz}), and two displacements (u and v) in the r and z direction, respectively. The development of the finite element equations is very similar to that presented for plane strain situations.

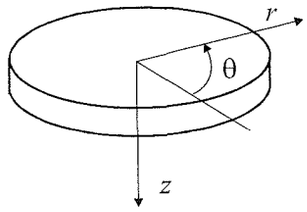

Figure 2.26: Cylindrical coordinates

The problem is discretised into finite elements in the r-z plane. If isoparametric elements are used, the geometry of the elements is expressed using Equation (2.7), with r and z replacing x and y respectively. As with plane strain problems, the nodal degrees of freedom are the displacements u and v. The formulation of the element equations follows the procedure outlined in Section 2.6, but with Equation (2.10) replaced by:

$$\Delta\varepsilon_r = -\frac{\partial(\Delta u)}{\partial r}\ ;\ \Delta\varepsilon_z = -\frac{\partial(\Delta v)}{\partial z}\ ;\ \Delta\varepsilon_\theta = -\frac{\Delta u}{r}$$
$$\Delta\gamma_{rz} = -\frac{\partial(\Delta v)}{\partial r} - \frac{\partial(\Delta u)}{\partial z}\ ;\ \Delta\gamma_{r\theta} = \Delta\gamma_{z\theta} = 0 \qquad (2.54)$$

Equation (2.11) replaced by:

$$\begin{Bmatrix}\Delta\varepsilon_r\\ \Delta\varepsilon_z\\ \Delta\gamma_{rz}\\ \Delta\varepsilon_\theta\end{Bmatrix} = -\begin{bmatrix} \frac{\partial N_1}{\partial r} & 0 & \frac{\partial N_2}{\partial r} & 0 & \cdots & \cdots & \frac{\partial N_n}{\partial r} & 0\\ 0 & \frac{\partial N_1}{\partial z} & 0 & \frac{\partial N_2}{\partial z} & \cdots & \cdots & 0 & \frac{\partial N_n}{\partial z}\\ \frac{\partial N_1}{\partial z} & \frac{\partial N_1}{\partial r} & \frac{\partial N_2}{\partial z} & \frac{\partial N_2}{\partial r} & \cdots & \cdots & \frac{\partial N_n}{\partial z} & \frac{\partial N_n}{\partial r}\\ \frac{N_1}{r} & 0 & \frac{N_2}{r} & 0 & \cdots & \cdots & \frac{N_2}{r} & 0 \end{bmatrix}\begin{Bmatrix}\Delta u_1\\ \Delta v_1\\ \Delta u_2\\ \Delta v_2\\ \cdots\\ \cdots\\ \Delta u_n\\ \Delta v_n\end{Bmatrix} \qquad (2.55)$$

all references to x and y replaced by r and z, respectively, and the thickness t in Equations (2.27) and (2.28) replaced by $2\pi r$. The assembly and solution of the global equations follow the procedures described in Sections 2.7 to 2.9.

The application of the finite element method to three dimensional problems is discussed in Chapter 11.

2.13 Summary

1. The finite element method involves the following steps:
   - Element discretisation;
   - Selection of nodal displacements as primary variables;
   - Derivation of element equations using minimum potential energy;
   - Assembly of element equations to form global equations;
   - Formulation of boundary conditions (nodal displacements and forces);
   - Solution of global equations.

2. For geotechnical analyses triangular or quadrilateral elements with curved sides are usually employed.
3. Isoparametric elements are popular. In this formulation, both the element displacements and element geometry are expressed using the same interpolation functions which are expressed in terms of natural coordinates.
4. Numerical integration is used to establish the element stiffness matrix. Consequently, stresses and strains are usually output at integration points.
5. The global stiffness matrix is symmetric if the constitutive matrix is symmetric. The global stiffness matrix is also sparse and banded. These properties are used to develop efficient storage algorithms.
6. Gaussian elimination is usually adopted to solve (invert) the global stiffness matrix. This can involve triangulation of the matrix.
7. Care must be taken when dealing with prescribed displacements.
8. Stresses and strains are secondary quantities which are calculated from the nodal displacements.

Appendix II.1: Triangular finite elements

II.1.1 Derivation of area coordinates

Derivation of shape and interpolation functions for triangular elements is shown using the example of the three noded element, presented in Figure II.1. The position of an interior point P, in global coordinates x and y, is determined by the vector $\vec{r}$:

$$\vec{r} = x\,\vec{i} + y\vec{j} = x_3\vec{i} + y_3\vec{j} + \xi\,\vec{e}_1 + \eta\,\vec{e}_2 \qquad (II.1)$$

where: $\vec{i}, \vec{j}$ = unit vectors in global coordinate system x, y
$\vec{e}_1, \vec{e}_2$ = unit vectors in local coordinate system ξ, η
ξ, η = system of local coordinates coinciding with two sides of a triangle.

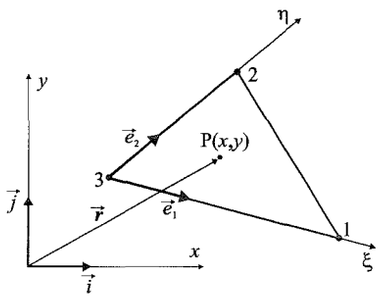

Figure II.1: Three noded triangular element

If, instead of ξ, η coordinates, normalized coordinates are introduced, such as:

$$L_1 = \frac{\xi}{l_{31}}\ ;\ L_2 = \frac{\eta}{l_{32}}$$

where l_{31} and l_{32} are the lengths of sides 3,1 and 3,2 of the triangle in Figure II.1, then new coordinates L_1 and L_2 vary only between 0 and 1. Equation (II.1) can now be written as:

$$\vec{r} = x_3\vec{i} + y_3\vec{j} + l_{31}L_1\vec{e}_1 + l_{32}L_2\vec{e}_2 \qquad (II.2)$$

When $l_{31}\vec{e}_1$ and $l_{32}\vec{e}_2$ are expressed in terms of global coordinates, i.e:

$$l_{31}\vec{e}_1 = (x_1 - x_3)\,\vec{i} + (y_1 - y_3)\,\vec{j}$$

$$l_{32}\vec{e}_2 = (x_2 - x_3)\,\vec{i} + (y_2 - y_3)\,\vec{j}$$

then vector $\vec{r}$ becomes:

$$\vec{r} = [L_1 x_1 + L_2 x_2 + (1 - L_1 - L_2)x_3]\,\vec{i} + [L_1 y_1 + L_2 y_2 + (1 - L_1 - L_2)y_3]\,\vec{j} \qquad \text{(II.3)}$$

The link between coordinates x and y and L_i, i=1,2,3, is therefore:

$$x = L_1 x_1 + L_2 x_2 + L_3 x_3$$
$$y = L_1 y_1 + L_2 y_2 + L_3 y_3 \qquad \text{(II.4)}$$

where L_3=1−L_1−L_2.

All three coordinates L_i, i=1,2,3, vary between 0 and 1 and represent interpolation functions, N_i, of a three noded triangle:

$$x = \sum_{i=1}^{3} N_i x_i$$
$$y = \sum_{i=1}^{3} N_i y_i \quad , \quad N_i = L_i \qquad \text{(II.5)}$$

The geometric meaning of these coordinates can be obtained by manipulating Equation (II.4), which can be written in the form:

$$\begin{Bmatrix} x \\ y \\ 1 \end{Bmatrix} = \begin{bmatrix} x_1 & x_2 & x_3 \\ y_1 & y_2 & y_3 \\ 1 & 1 & 1 \end{bmatrix} \begin{Bmatrix} L_1 \\ L_2 \\ L_3 \end{Bmatrix} \qquad \text{(II.6)}$$

Inverting Equation (II.6) gives expressions for coordinates L_i, i=1,2,3, in terms of global coordinates:

$$\begin{Bmatrix} L_1 \\ L_2 \\ L_3 \end{Bmatrix} = \frac{1}{2\Delta} \begin{bmatrix} a_1 & b_1 & c_1 \\ a_2 & b_2 & c_2 \\ a_3 & b_3 & c_3 \end{bmatrix} \begin{Bmatrix} 1 \\ x \\ y \end{Bmatrix} \qquad \text{(II.7)}$$

or

$$L_i = \frac{1}{2\Delta}(a_i + b_i x + c_i y) \quad , \quad i = 1,2,3 \qquad \text{(II.8)}$$

In Equation (II.7), Δ is the determinant of the system of Equations (II.6) and it can be shown to represent the area of a triangle in Figure II.1. Parameters a_i, b_i and c_i are:

$$\begin{array}{lll} a_1 = x_2 y_3 - x_3 y_2 & a_2 = x_3 y_1 - x_1 y_3 & a_3 = x_1 y_2 - x_2 y_1 \\ b_1 = y_2 - y_3 & b_2 = y_3 - y_1 & b_3 = y_1 - y_2 \\ c_1 = x_3 - x_2 & c_2 = x_1 - x_3 & c_3 = x_2 - x_1 \end{array} \qquad \text{(II.9)}$$

It can also be shown that the nominator in Equation (II.8) represents areas of the three triangles, marked as 1, 2 and 3, in Figure II.2.

Therefore the geometric interpretation of the coordinates L_i, i=1,2,3, is that they represent the ratio of the area, A_i, of the appropriate triangle, 1, 2 or 3, and the total area of the element, A:

$$L_i = \frac{A_i}{A} \quad , \qquad i = 1,2,3 \qquad \text{(II.10)}$$

Consequently, they are named 'area coordinates'.

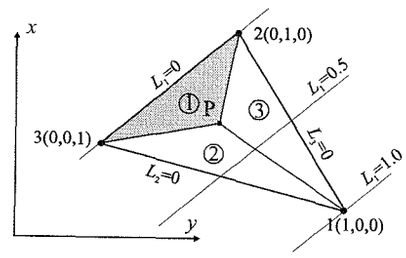

Figure II.2: Area coordinates of a triangular element

II.1.2 Isoparametric formulation

In the same way as for quadrilateral elements, the isoparametric formulation is also used for triangular elements. Figure II.3 shows a three noded isoparametric parent triangular element and its global derivative. The parent element is a right angled triangle, in natural coordinates T and S, where $0 \le T \le 1$ and $0 \le S \le 1$.

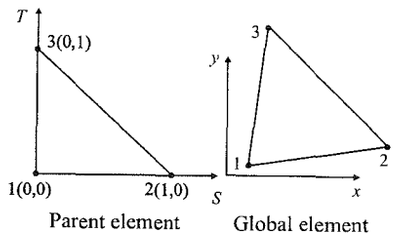

Figure II.3: Isoparametric triangular element

Interpolation functions N_i , i=1,2,3, can now be expressed in terms of natural coordinates S and T as:

$$N_1 = 1 - S - T$$
$$N_2 = S \qquad \text{(II.11)}$$
$$N_3 = T$$

For higher order 6 noded triangular elements, Figure II.4, it can be shown that the interpolation functions become:

Mid - side nodes:

$$N_4 = 4S(1 - S - T)$$
$$N_5 = 4S\,T$$
$$N_6 = 4T(1 - S - T) \qquad \text{(II.12)}$$

Corner nodes:

$$N_1 = 1 - S - T$$
$$N_2 = S$$
$$N_3 = T$$

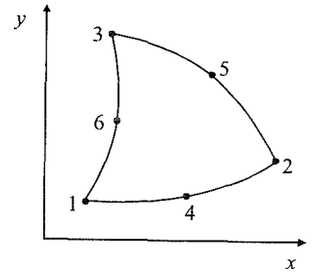

Figure II.4: Six noded triangular element

Figure II.5 shows the location of Gauss integration points for a triangular element for 3 and 7-point integration.

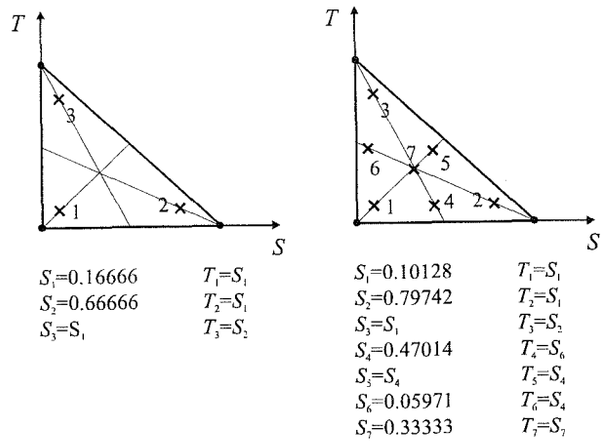

Figure II.5: Gauss integration points for triangular element

3. Geotechnical considerations

3.1 Synopsis

This chapter discusses the enhancements that must be made to the standard finite element theory, to enable realistic analysis of geotechnical problems to be made. The modifications required to enable pore fluid pressures to be calculated in undrained analysis are described. Special finite elements that can be used to model structures and their interface with the ground are presented. Finally, a whole array of boundary conditions that are relevant to geotechnical analysis are described. By the end of this chapter the reader should have sufficient information to be able to formulate linear finite element analysis of a wide range of geotechnical problems.

3.2 Introduction

In the preceding chapter the finite element theory for linear materials was described. As presented, the theory is applicable to the analysis of any linear elastic continuum. However, as it stands, there are severe limitations to its application in geotechnical engineering, and without additional refinements only a very small range of problems can be tackled. In particular, the constitutive behaviour is formulated as a relationship between changes in total stress and strain, whereas in geotechnical engineering it is usual to split the total stress tensor into effective stresses and pore fluid pressures. It is also common practice to express the constitutive behaviour in terms of effective stress parameters. Clearly, some modifications to the standard theory are necessary for this to be accommodated.

Many geotechnical problems involve the interaction between structures and soil. Consequently, in finite element analyses of these problems it is necessary to model both the structure, the ground and the interface between them, see Figure 3.1. For example, when analysing tunnelling problems it is important to realistically model the tunnel lining and its interface with the soil. If the lining is of the segmental type, it will also be necessary to realistically model the interfaces between the segments. In many cases this involves the use of special finite elements in addition to the continuum elements described in Chapter 2.

In Chapter 2 only displacement, line loads and surface surcharge boundary conditions were discussed. For structural engineering applications these boundary conditions are sufficient to analyse a wide range of problems. However, for geotechnical engineering a much wider range of boundary conditions is required

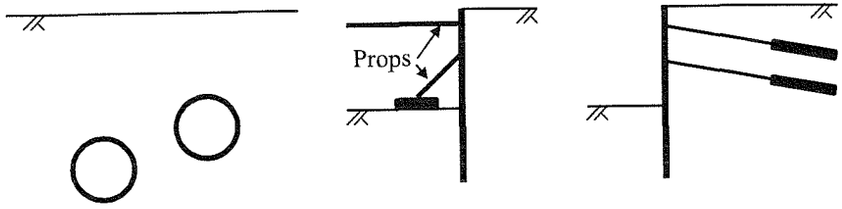

a) Tunnels b) Propped wall c) Anchored wall

Figure 3.1: Examples of soil-structure interaction

if realistic analyses are to be performed. For example, many geotechnical problems involve excavation and construction, see Figure 3.2. Many also involve changes in pore water pressure. Special boundary conditions are often required to model soil structure interaction.

This chapter describes how the above conditions can be accommodated in finite element analyses. Their application in specific geotechnical problems is discussed in Volume 2 of this book.

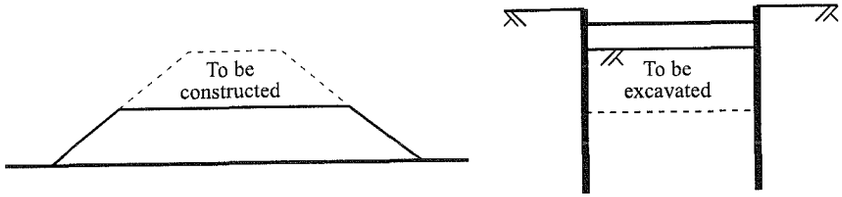

a) Embankment construction b) Basement excavation

Figure 3.2: Examples of construction and excavation

3.3 Total stress analysis

In Chapter 2 the soil constitutive behaviour was expressed in the simple form:

$$\{\Delta\sigma\} = [\boldsymbol{D}]\{\Delta\varepsilon\} \tag{3.1}$$

where $\{\Delta\sigma\}=[\Delta\sigma_x, \Delta\sigma_y, \Delta\sigma_z, \Delta\tau_{xy}, \Delta\tau_{xz}, \Delta\tau_{yz}]^T$ and $\{\Delta\varepsilon\}=[\Delta\varepsilon_x, \Delta\varepsilon_y, \Delta\varepsilon_z, \Delta\gamma_{xy}, \Delta\gamma_{xz}, \Delta\gamma_{yz}]^T$ are the incremental total stress and strain vectors and $[\boldsymbol{D}]$ is the assumed relationship between these vectors. For the present considerations, $[\boldsymbol{D}]$ is assumed to be the isotropic linear elastic matrix, given in Section 1.5.5 of Chapter 1. Alternative constitutive matrices will be discussed in Chapters 5, 6, 7 and 8. As noted in Chapter 1, it is necessary for Equation (3.1) to provide a relationship between increments of total stress and strain, because the equilibrium equations are

expressed in terms of total stress. The finite element formulation presented so far can therefore be used to analyse the following two classes of problems:

- Fully drained problems in which there is no change in pore fluid pressure, $\Delta p_f = 0$. This implies that changes in effective and total stress are the same, i.e. $\{\Delta\sigma'\}=\{\Delta\sigma\}$, and that the $[\boldsymbol{D}]$ matrix contains the effective constitutive behaviour. For example, for isotropic linear elastic behaviour $[\boldsymbol{D}]$ will be based on a drained Young's modulus, E', and drained Poisson's ratio, μ'.
- Fully undrained behaviour in which the $[\boldsymbol{D}]$ matrix is expressed in terms of total stress parameters. For isotropic linear elastic behaviour $[\boldsymbol{D}]$ is based on an undrained Young's modulus, E_u, and an undrained Poisson's ratio, μ_u.

In the second class of problems, if the soil is saturated there would be no volume change. For an isotropic elastic soil this would be modelled by, ideally, setting the undrained Poisson's ratio, μ_u, equal to 0.5. However, as can be seen by inspection of the isotropic linear elastic $[\boldsymbol{D}]$ matrix given in Section 1.5.5, this results in severe numerical problems as all terms of the $[\boldsymbol{D}]$ matrix become infinite. To avoid such indeterminate behaviour it is usual to set the undrained Poisson's ratio to be less than 0.5, but greater than 0.49.

To illustrate the effect of a high Poisson's ratio, a smooth flexible strip footing resting on an isotropic elastic layer of soil of finite depth has been analysed, using the finite element mesh shown in Figure 3.3a, for a range of Poisson's ratios. The analyses are similar to those discussed in Section 2.11, except that the mesh contains more elements and has a greater lateral extent. This enables more accurate solutions to be obtained. The boundary conditions are the same as in Section 2.11. The surcharge loading on the footing was 100kPa and the Young's modulus of the soil E'=10000 kPa. Analyses were performed with Poisson's ratio, μ, ranging from 0 to 0.4999999. Two sets of analyses were performed, in one set *single*, and in the other *double* precision arithmetic was used. For single precision arithmetic seven significant figures are used to represent real numbers, while in double precision fourteen significant figures are used. Clearly, double precision arithmetic is more accurate than single precision. The vertical settlement of the ground surface at the edge of the strip footing is plotted against the value of Poisson's ratio in Figure 3.3b.

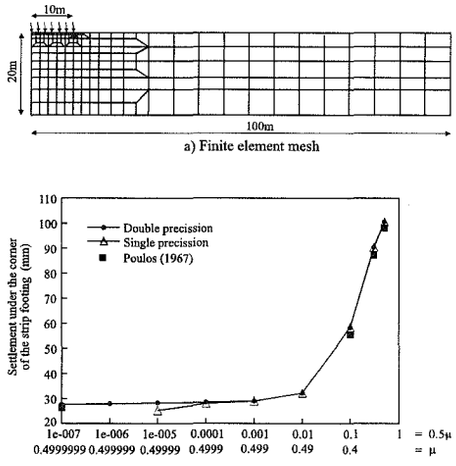

a) Finite element mesh

b) Settlement under the corner of strip footing vs. Poisson's ratio

Figure 3.3: Effect of Poisson's ratio on the behaviour of a smooth flexible strip footing

Also shown in Figure 3.3b, for comparison, are results from Poulos (1967) for $\mu = 0$, 0.2, 0.4 and 0.5. These have been obtained using the graphs given in the paper, which are based on numerical integration of the basic elastic solution for a point load. The results are, therefore, approximate. Overall, the predictions from the finite element analyses agree well with those of Poulos.

Results from the finite element analyses using double precision arithmetic indicate that once Poisson's ratio exceeds 0.499, the value has little effect on the prediction, which itself is in good agreement with that given by Poulos for $\mu = 0.5$. For the analyses with single precision arithmetic it was not possible to invert the stiffness matrix for Poisson's ratios greater than 0.49999, due to numerical instability (i.e. a negative pivot occurred during the inversion process). In addition, although a solution was obtained for $\mu = 0.49999$, it is in error, see Figure 3.3b.

These results show that, for this problem, if a value of Poisson's ratio $\mu = 0.499$ is used, the results would be very similar to that for $\mu = 0.5$ The results also show that the maximum value of μ that can be tolerated without numerical instability depends on the precision of the arithmetic. In this respect it should be noted that most finite element software use double precision arithmetic. The maximum value of μ that can be used also depends on the algorithm used for inversion of the global stiffness matrix and is also problem dependent. Consequently, there are no hard and fast rules available as to the exact value of μ that should be used to represent undrained conditions. Some texts suggest using a value of $\mu = 0.49$ to represent undrained conditions. As can be seen from Figure 3.3b this would result in a modest error for the smooth flexible strip footing under investigation.

Another difficulty that arises with the analysis of nearly incompressible materials ($\mu \rightarrow 0.5$) is that, for many problems, predictions of changes in mean stress ($= (\Delta\sigma_x + \Delta\sigma_y + \Delta\sigma_z)/3$) can have large errors. This problem is discussed in detail by Naylor (1974), who shows that accurate results can be obtained by using reduced Gaussian integration (see Section 2.6.1) and by using stress values sampled at the integration points.

3.4 Pore pressure calculation

The results from the undrained analysis considered above are in terms of changes in total stress. No information is provided on changes in pore fluid pressure. However, in many situations the changes in pore fluid pressure are required. It is also more convenient to express the constitutive behaviour in terms of effective stress parameters. This is particularly valid for the more advanced constitutive models, see Chapter 8. It would therefore be advantageous if undrained analyses could be performed considering both the changes in effective stress and pore fluid pressure and using a $[\boldsymbol{D}]$ matrix which is expressed in terms of effective stress parameters. This can be done by invoking the principle of effective stress.

Consider the application of a load which causes a local change in total stress, $\{\Delta\sigma\}$, and change in strain, $\{\Delta\varepsilon\}$, in an element of soil. If there is no drainage, an excess pore fluid pressure, Δp_f, is established. The principle of effective stress requires that:

where:

$$\{\Delta\sigma\} = \{\Delta\sigma'\} + \{\Delta\sigma_f\} \tag{3.2}$$

$$\{\Delta\sigma_f\} = \{\Delta p_f \;\; \Delta p_f \;\; \Delta p_f \;\; 0 \;\; 0 \;\; 0\}^T \tag{3.3}$$

Since the solid and fluid phases of the soil deform together in the undrained condition (i.e there is negligible relative movement between the two phases), the strains, in the macroscopic sense, are the same in each phase. Relating the stress components of Equation (3.2) to strain gives, in addition to Equation (3.1):

$$\{\Delta\sigma'\} = [\boldsymbol{D}']\{\Delta\varepsilon\} \tag{3.4}$$

$$\{\Delta\sigma_f\} = [\boldsymbol{D}_f]\{\Delta\varepsilon\} \tag{3.5}$$

Substituting Equations (3.1), (3.4) and (3.5) into Equation (3.2) gives:

$$[\boldsymbol{D}] = [\boldsymbol{D}'] + [\boldsymbol{D}_f] \tag{3.6}$$

Equation (3.6) provides a relationship between the stiffness in terms of total stress, $[\boldsymbol{D}]$, the stiffness in terms of effective stress, $[\boldsymbol{D}']$, and the pore fluid stiffness, $[\boldsymbol{D}_f]$. This last matrix, $[\boldsymbol{D}_f]$, is related to the bulk modulus of the pore fluid, K_f, which is treated as a single phase. Two phase pore fluids, as occur in partially saturated soils, can be included by a suitable choice of K_f. Since a fluid cannot transmit shear, it is apparent from Equation (3.5) that $[\boldsymbol{D}_f]$ has the form (for the general three dimensional stress situation):

$$[\boldsymbol{D}_f] = K_e \begin{bmatrix} 1_3 & 0_3 \\ 0_3 & 0_3 \end{bmatrix} \tag{3.7}$$

in which K_e is a constant, 1_3 is a 3 x 3 matrix all elements of which are 1, and 0_3 is a 3x3 null matrix. It is shown below how the equivalent bulk modulus of the pore fluid, K_e, is related to K_f. This follows from Naylor (1974).

If n is the soil porosity then, in a unit volume of soil, the pore fluid occupies a volume n and the solid soil particles a volume $1-n$. Let K_s be the bulk modulus of the solid soil particles. An increment in pore fluid pressure, Δp_f, causes compression in both the pore fluid and the solid soil particles. The associated increment in effective stress, $\{\Delta\sigma'\}$, also causes, in general, a volume change in the solid soil particles. However, as this stress must act through the particle contacts, which have a small area, this volume change is likely to be small. If it is assumed that this volume change is negligible, the total volume change per unit volume of soil, $\Delta\varepsilon_v$, is given by:

$$\Delta\varepsilon_v = \frac{n}{K_f}\Delta p_f + \frac{(1-n)}{K_s}\Delta p_f \tag{3.8}$$

Substituting Equation (3.7) into (3.5) gives three identical equations:

$$\Delta p_f = K_e(\Delta\varepsilon_x + \Delta\varepsilon_y + \Delta\varepsilon_z) = K_e\Delta\varepsilon_v$$

or:

$$\Delta\varepsilon_v = \frac{\Delta p_f}{K_e} \tag{3.9}$$

Equating Equations (3.8) and (3.9) and re-arranging gives:

$$K_e = \frac{1}{\frac{n}{K_f} + \frac{(1-n)}{K_s}} \tag{3.10}$$

Equation (3.10) can usually be simplified. K_s is nearly always very much greater then the bulk modulus of the soil skeleton (i.e. the bulk modulus of the soil in the absence of pore fluid). If the pore fluid has a significant compressibility so that K_s is also much greater than K_f, Equation (3.10) then simplifies to:

$$K_e = \frac{K_f}{n} \tag{3.11}$$

For saturated soils both K_f and K_s are much larger than the soil skeleton stiffness. Their exact value may then be unimportant, and it is convenient to assume $K_f = K_s$. Consequently, Equation (3.10) reduces to:

$$K_e = K_f \tag{3.12}$$

The above theory is valid for any porous material for which the principle of effective stress applies and for which incremental $[\boldsymbol{D}]$ matrices (i.e. incremental stress-strain laws) exist. Consequently, while it is valid for a simple isotropic linear elastic soil, it is also applicable to the more advanced soil constitutive models described in Chapters 7 and 8.

It is a straightforward process to combine the above theory with the finite element method. Instead of specifying the components of the total stress constitutive matrix, $[\boldsymbol{D}]$, the components of the effective stress constitutive matrix, $[\boldsymbol{D}']$, and the pore fluid equivalent bulk modulus, K_e, are specified. The two are then combined using Equation (3.6) to give $[\boldsymbol{D}]$. The calculation of element stiffness, global stiffness assembly and solution of system equations follow the standard procedure described in Chapter 2. The only other difference occurs when calculating stresses. Here K_e is used to calculate the change in pore fluid pressure, Δp_f, from the predicted volumetric strain, using Equation (3.9), and $[\boldsymbol{D}']$ is used to calculate the changes in effective stress, using Equation (3.4). The changes in total stress can then be found by either summing the effective stress and pore fluid pressure changes, or by using Equation (3.1). If K_e is zero, as in a drained analysis, the division into pore fluid pressure and effective stress components still occurs, but the pore fluid pressures do not change during loading.

When performing an undrained analysis, a value for K_e must be set. In the Authors' experience, analysis involving saturated soil is unlikely to be sensitive to the actual magnitude selected, as long as it is large. However, the use of too high a value can lead to numerical instability. This occurs as the equivalent undrained total stress Poisson's ratio, μ_u, approaches 0.5. The Authors recommend setting K_e

to equal βK_{skel}, where β has a value between 100 and 1000, and K_{skel} is the bulk modulus of the soil skeleton, which can be calculated from the effective stress parameters forming the $[\boldsymbol{D}']$ matrix. For an isotropic linear elastic soil it can be shown that the equivalent undrained total stress Poisson's ratio, μ_u, is related to the drained (effective) Poisson's ratio, μ', and β by the following equation:

$$\mu_u = \frac{A}{(1+2A)}, \text{ where } A = \frac{(1+\mu')}{(1-2\mu')}\left[\frac{\mu'}{(1+\mu')} + \frac{\beta}{3}\right] \tag{3.13}$$

Table 3.1 indicates how μ_u varies with β for $\mu' = 0.1$ and $\mu' = 0.3$.

Table 3.1: Equivalent values of μ_u

β	μ_u	
	μ'=0.1	μ'=0.3
10	0.4520	0.4793
100	0.4946	0.4977
1000	0.4994	0.4998

For analysis involving the time dependent dissipation of excess pore water pressures, coupled finite element analysis must be performed. Such analyses are discussed in detail in Chapter 10.

3.5 Finite elements to model structural components

3.5.1 Introduction

Many geotechnical problems involve soil structure interaction, see Figure 3.1. Therefore, when applying finite element analysis to such problems it is necessary to include the structural components, e.g. retaining walls, props, anchors, tunnel linings, foundations etc., in the finite element mesh. In theory, it is possible to use the 2D continuum elements discussed in Chapter 2 to model these structural components, but in practice this can have drawbacks. For example, in many situations the dimensions of the structural elements are small compared to the overall geometry and therefore, to model them with 2D continuum elements would result in either a very large number of elements, or elements with unacceptable aspect ratios.

In many instances the interest is not in the detailed distribution of stresses within the structural members, but in the distribution of averaged quantities such as bending moments, axial and shear forces. These can be obtained from the stresses within the 2D continuum elements, but additional calculations are required.

To overcome these shortcomings, special finite elements have been developed. These elements are formulated by essentially collapsing one, or more, dimensions

of the structural component to zero. For example a retaining wall can be modelled using a beam element which has no width. The element is formulated directly in terms of bending moments, axial and shear forces and their associated strains. Consequently, the quantities of engineering interest come directly from the finite element analysis.

There are several different formulations available in the literature for these special structural elements. This chapter describes a 3 noded isoparametric curved Mindlin beam element which was developed by the numerical geotechnical research group at Imperial College, Day (1990), Day and Potts (1990). This element was developed to be compatible with the 2D elements described in Chapter 2. It is therefore isoparametric and uses the same quadratic interpolation functions as the 2D elements. It can accommodate axial stresses, bending moments and shear stresses and their associated strains. If used in a plane strain or an axi-symmetric analysis this element effectively becomes a shell element.

The impetus for developing a new element arose because those that exist in the literature contain severe deficiencies. In particular, some cannot account for rigid body movements. These deficiencies and the advantages of the new element are discussed in detail by Day and Potts (1990).

3.5.2 Strain definitions

The strains for this particular beam element, shown in Figure 3.4, are defined as follows (Day (1990)):

Axial strain:

$$\varepsilon_l = -\frac{\mathrm{d}u_l}{\mathrm{d}l} - \frac{w_l}{R} \qquad (3.14)$$

Bending strain:

$$\chi_l = \frac{\mathrm{d}\theta}{\mathrm{d}l} \qquad (3.15)$$

Shear strain:

$$\gamma = \frac{u_l}{R} - \frac{\mathrm{d}w_l}{\mathrm{d}l} + \theta \qquad (3.16)$$

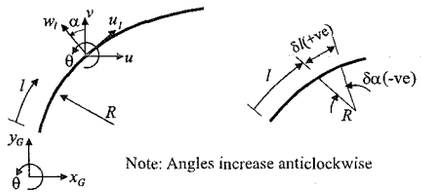

Figure 3.4: Definition of terms and axes

where l is the distance along the beam, u_l and w_l are the displacements tangential and normal to the beam, R is the radius of curvature, and θ is the cross section rotation. The definitions (3.14) to (3.16) are for a compression positive sign convention.

It is useful to rewrite Equations (3.14) to (3.16) in terms of the displacements u and v in the global x_G and y_G coordinate directions. The transformation of displacements from global to local components is given by:

$$\begin{aligned} u_l &= v\sin\alpha + u\cos\alpha \\ w_l &= v\cos\alpha - u\sin\alpha \end{aligned} \qquad (3.17)$$

and noting that (Figure 3.4):

$$\frac{\mathrm{d}\alpha}{\mathrm{d}l} = -\frac{1}{R} \qquad (3.18)$$

gives the following expressions for Equations (3.14) to (3.16) in terms of the global displacements:

Axial strain:
$$\varepsilon_l = -\frac{\mathrm{d}u}{\mathrm{d}l}\cos\alpha - \frac{\mathrm{d}v}{\mathrm{d}l}\sin\alpha \qquad (3.19)$$

Bending strain:
$$\chi_l = \frac{\mathrm{d}\theta}{\mathrm{d}l} \qquad (3.20)$$

Shear strain:
$$\gamma = \frac{\mathrm{d}u}{\mathrm{d}l}\sin\alpha - \frac{\mathrm{d}v}{\mathrm{d}l}\cos\alpha + \theta \qquad (3.21)$$

While the above strain terms are sufficient for plane strain analysis, additional terms are required for axi-symmetric analysis, (Day (1990)):

Circumferential membrane strain:
$$\varepsilon_\psi = \frac{w_l\sin\alpha - u_l\cos\alpha}{r_o} = -\frac{u}{r_o} \qquad (3.22)$$

Circumferential bending strain:
$$\chi_\psi = \frac{\theta\cos\alpha}{r_o} \qquad (3.23)$$

where r_o is the circumferential radius, see Figure 3.5, and u and v are re-defined as the displacements in the directions normal and parallel to the axis of revolution.

3.5.3 Constitutive equation

The strain terms presented above are related to the element forces and bending moments by the expression:

$$\{\Delta\sigma\} = [\boldsymbol{D}]\{\Delta\varepsilon\} \qquad (3.24)$$

where $\{\Delta\varepsilon\}=[\Delta\varepsilon_l, \Delta\chi_l, \Delta\gamma, \Delta\varepsilon_\psi, \Delta\chi_\psi]^T$, $\{\Delta\boldsymbol{\sigma}\}=[\Delta F, \Delta M, \Delta S, \Delta F_\psi, \Delta M_\psi]^T$, with the incremental components being: ΔF - the meridional force, ΔM - the bending moment, ΔS - the shear force, ΔF_ψ - the circumferential force and ΔM_ψ - the circumferential bending moment. For plane strain analysis ΔF is the incremental in-plane axial force, ΔF_ψ is the incremental out of plane force and $\Delta\varepsilon_\psi = \Delta\chi_\psi = 0$.

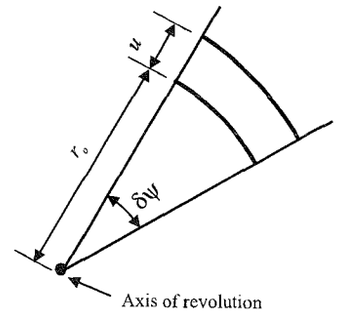

Figure 3.5: Definition of r_o

For isotropic linear elastic behaviour, the $[\boldsymbol{D}]$ matrix takes the form:

$$[\boldsymbol{D}]=\begin{bmatrix} \frac{EA}{(1-\mu^2)} & 0 & 0 & \frac{EA\mu}{(1-\mu^2)} & 0 \\ 0 & \frac{EI}{(1-\mu^2)} & 0 & 0 & \frac{EI\mu}{(1-\mu^2)} \\ 0 & 0 & kGA & 0 & 0 \\ \frac{EA\mu}{(1-\mu^2)} & 0 & 0 & \frac{EA}{(1-\mu^2)} & 0 \\ 0 & \frac{EI\mu}{(1-\mu^2)} & 0 & 0 & \frac{EI}{(1-\mu^2)} \end{bmatrix} \tag{3.25}$$

The beam (or shell) properties are the moment of inertia, I, and cross sectional area, A. In plane strain and axi-symmetric analysis these are specified for a unit width of the shell. E and μ are the Young's modulus and Poisson's ratio and k is a shear correction factor.

The distribution of shear stress across the cross sectional area of a beam (or shell) in bending is nonlinear. The beam element formulation, however, uses a single value to represent the shear strain. The correction factor, k, is a factor applied to the cross sectional area so that the strain energy in the finite element model, calculated over the area kA, is equal to the actual strain energy over the area A. The shear correction factor is dependent on the shape of the cross section. For a rectangular section, k=5/6. Bending deflections of slender beams dominate their behaviour and the solution is very insensitive to the value of k.

3.5.4 Finite element formulation

For finite element analysis the global displacements u and v, and the cross section rotation, θ, are taken as nodal degrees of freedom. This means that for plane strain and axi-symmetric analyses there are three degrees of freedom at each node, compared to the two degrees of freedom for the continuum elements described in Chapter 2.

The $\boldsymbol{B}$ matrix is defined as:

$$\begin{Bmatrix} \varepsilon_l \\ \chi_l \\ \gamma \\ \varepsilon_\psi \\ \chi_\psi \end{Bmatrix} = \begin{bmatrix} B_1 \\ B_2 \\ B_3 \\ B_4 \\ B_5 \end{bmatrix} \{\delta\} \tag{3.26}$$

where B_i represents row i of the $\boldsymbol{B}$ matrix, and $\boldsymbol{\delta}$ is the vector of nodal displacements and rotations (i.e. degrees of freedom) defined, for a 3 noded element in Figure 3.6, as:

$$\delta = \{\, u_1 \;\; v_1 \;\; \theta_1 \;\; u_2 \;\; v_2 \;\; \theta_2 \;\; u_3 \;\; v_3 \;\; \theta_3 \,\}^{\mathrm{T}} \tag{3.27}$$

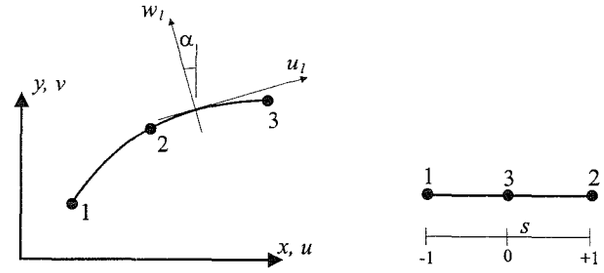

a) Gobal coordinates b) Natural ordinate

Figure 3.6: Three noded beam (or shell) element

The coordinates and global degrees of freedom at any point on the element are related to the nodal values using the shape functions, N_i. Hence:

$$\begin{aligned} x &= \sum_{i=1}^{3} N_i x_i & \frac{\mathrm{d}x}{\mathrm{d}s} &= \sum_{i=1}^{3} N_i' x_i \\ y &= \sum_{i=1}^{3} N_i y_i & \frac{\mathrm{d}y}{\mathrm{d}s} &= \sum_{i=1}^{3} N_i' y_i \\ u &= \sum_{i=1}^{3} N_i u_i & \frac{\mathrm{d}u}{\mathrm{d}s} &= \sum_{i=1}^{3} N_i' u_i \\ v &= \sum_{i=1}^{3} N_i v_i & \frac{\mathrm{d}v}{\mathrm{d}s} &= \sum_{i=1}^{3} N_i' v_i \\ \theta &= \sum_{i=1}^{3} N_i \theta_i & \frac{\mathrm{d}\theta}{\mathrm{d}s} &= \sum_{i=1}^{3} N_i' \theta_i \end{aligned} \tag{3.28}$$

where the prime denotes the derivative with respect to s. The isoparametric shape functions are defined by Equation (3.29):

$$\begin{aligned} N_1 &= \tfrac{1}{2} s\,(s-1) \\ N_2 &= \tfrac{1}{2} s\,(s+1) \\ N_3 &= (1-s^2) \end{aligned} \tag{3.29}$$

where s is the natural ordinate that varies from −1 to +1 over the element length (Figure 3.6). For brevity, it is written that $S = \sin\alpha$ and $C = \cos\alpha$, where $\sin\alpha$ and $\cos\alpha$ are calculated from Figure 3.7 as:

$$\begin{aligned} \sin\alpha &= \frac{1}{|\boldsymbol{J}|}\frac{\mathrm{d}y}{\mathrm{d}s} \\ \cos\alpha &= \frac{1}{|\boldsymbol{J}|}\frac{\mathrm{d}x}{\mathrm{d}s} \end{aligned} \tag{3.30}$$

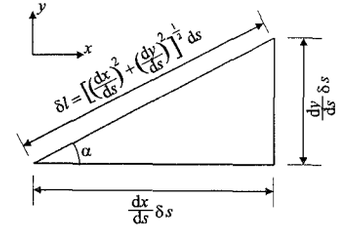

Figure 3.7: Transformation of coordinates

The determinant of $\boldsymbol{J}$ is calculated as:

$$|\boldsymbol{J}| = \left[\left(\frac{dx}{ds}\right)^2 + \left(\frac{dy}{ds}\right)^2\right]^{\frac{1}{2}} \tag{3.31}$$

Noting also that $dl = |\boldsymbol{J}|\,ds$ (see Figure 3.7), the rows of the $\boldsymbol{B}$ matrix are:

$$B_1 = -\frac{1}{|\boldsymbol{J}|}\left\{CN_1' \;\; SN_1' \;\; 0 \;\; CN_2' SN_2' \;\; 0 \;\; CN_3' SN_3' \;\; 0\right\} \tag{3.32}$$

$$B_2 = \frac{1}{|\boldsymbol{J}|}\left\{0 \;\; 0 \;\; N_1' \;\; 0 \;\; 0 \;\; N_2' \;\; 0 \;\; 0 \;\; N_3'\right\} \tag{3.33}$$

B_3, B_4 and B_5 can also be defined in terms of N_i and N_i'. However, when such a formulation is used with full (3x3) integration, membrane and shear force locking occurs. This is indicated by widely fluctuating axial and shear forces and is a common problem with beam and shell elements. To overcome this problem a field consistent approach is used. This is achieved by using substitute shape functions for some of the terms in the strain equations (Day (1990)). These substitute shape functions take the form:

$$\begin{aligned} \overline{N}_1 &= \frac{1}{2}\left(\frac{1}{3} - s\right) \\ \overline{N}_2 &= \frac{1}{2}\left(\frac{1}{3} + s\right) \\ \overline{N}_3 &= \frac{2}{3} \end{aligned} \tag{3.34}$$

They are derived from a least squares smoothed approximation to the usual isoparametric shape functions given by Equations (3.29). The substitute shape functions coincide with the usual isoparametric shape functions at the reduced Gaussian integration points, see Figure 3.8.

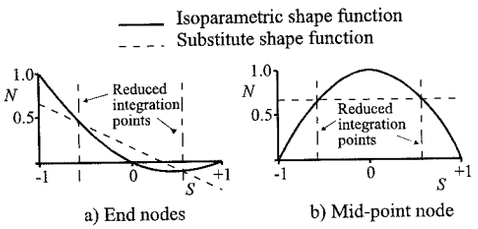

Figure 3.8: Substitute shape functions for 3 noded element

These shape functions are used for the interpolation of θ in Equations (3.21) and (3.23), of u in Equation (3.22) and for the calculation of r_o in Equations (3.22) and (3.23). The derivatives of the substitute shape functions are not used. The use of substitute shape functions for only some of the terms in the strain equations is therefore equivalent to selective reduced integration of these terms. Additionally, if reduced (2 point) Gaussian integration is used to evaluate the stiffness matrix, the result is independent of which shape functions have been used.

Using the substitute shape functions, $\overline{N}_i$, to define the variation of θ over the element in the definition of γ, gives:

$$B_3 = \left\{-\frac{CN_1'}{|\boldsymbol{J}|} \;\; -\frac{SN_1'}{|\boldsymbol{J}|} \;\; \overline{N}_1 \;\; -\frac{CN_2'}{|\boldsymbol{J}|} \;\; -\frac{SN_2'}{|\boldsymbol{J}|} \;\; \overline{N}_2 \;\; -\frac{CN_3'}{|\boldsymbol{J}|} \;\; -\frac{SN_3'}{|\boldsymbol{J}|} \;\; \overline{N}_3\right\} \tag{3.35}$$

For the circumferential (out of plane) strain terms the current radius, r_o, becomes:

$$r_o = \sum_{i=1}^{3} \overline{N}_i x_i \tag{3.36}$$

In the definition of ε_ψ, B_4 becomes:

$$B_4 = -\frac{1}{r_o}\left\{\overline{N}_1 \;\; 0 \;\; 0 \;\; \overline{N}_2 \;\; 0 \;\; 0 \;\; \overline{N}_3 \;\; 0 \;\; 0\right\} \tag{3.37}$$

and in the definition of χ_ψ, B_5 becomes:

$$B_5 = \frac{C}{r_o}\left\{0 \;\; 0 \;\; \overline{N}_1 \;\; 0 \;\; 0 \;\; \overline{N}_2 \;\; 0 \;\; 0 \;\; \overline{N}_3\right\} \tag{3.38}$$

The element stiffness matrix, $[\boldsymbol{K}_E]$, is given by (see Section 2.6):

$$\left[\boldsymbol{K}_E\right] = \int_0^{length} \left[\boldsymbol{B}\right]^{\mathrm{T}} \left[\boldsymbol{D}\right]\left[\boldsymbol{B}\right] dl \tag{3.39}$$

where l is the length of the element and the constitutive matrix $[\boldsymbol{D}]$ is given by Equation (3.25). The integral is evaluated in the natural ordinate system, see Figure 3.6, giving:

$$\left[\boldsymbol{K}_E\right] = \int_{-1}^{1} \left[\boldsymbol{B}\right]^{\mathrm{T}} \left[\boldsymbol{D}\right]\left[\boldsymbol{B}\right]|\boldsymbol{J}|\, ds \tag{3.40}$$

while the use of substitute shape functions, as described above, prevents locking of the solution for straight beam (shell) elements. Locking can still occur with curved beam elements. The problem can be overcome by using reduced integration for all strain terms.

3.5.5 Membrane elements

The beam element described above can be degenerated to form another element which cannot transmit bending moments or shear forces. In plane strain and axi-symmetric analyses it is a pin-ended membrane element, capable of transmitting forces tangential to the surface only (membrane forces). It is essentially a spring, but differs from a spring in that it can be curved and it is treated in the same way as all other elements in the analysis.

This element has two degrees of freedom per node: the displacements u and v in the global x_G and y_G directions respectively. In plane strain analysis the element has only one strain term, the longitudinal strain, ε_l, given by:

$$\varepsilon_l = -\frac{\mathrm{d}u_l}{\mathrm{d}l} - \frac{w_l}{R} \tag{3.41}$$

In axi-symmetric analysis the additional circumferential strain is given by:

$$\varepsilon_\psi = -\frac{u}{r_o} \tag{3.42}$$

These definitions are the same as for beam elements (Equations (3.14) and (3.22)).

The terms in the constitutive matrix, $[\boldsymbol{D}]$, are equal to the corresponding terms in the beam element constitutive matrix and are as follows:

$$[\boldsymbol{D}] = \begin{bmatrix} \dfrac{EA}{(1-\mu^2)} & \dfrac{EA\mu}{(1-\mu^2)} \\ \dfrac{EA\mu}{(1-\mu^2)} & \dfrac{EA}{(1-\mu^2)} \end{bmatrix} \tag{3.43}$$

The finite element formulation is similar to the formulation of these terms for the beam element, Section 3.5.4. The usual isoparametric shape functions are, however, used for the interpolation of u and r_o in Equation (3.42) (i.e. the substitute shape functions are not used).

The advantages of using an element of this type as opposed to the use of spring boundary conditions (which are discussed subsequently in this chapter) are:

- Different behaviour can easily be specified through a constitutive law and an elasto-plastic formulation. For example, a maximum axial force may be specified by a yield function, F, of the form: F = axial force ± constant.
- In axi-symmetric analysis, hoop forces can provide significant restraint. These are included in an analysis by using membrane elements. Spring boundary conditions do not account for the effect of hoop forces.

Membrane elements are useful for the analysis of soil-structure interaction problems. A constitutive law that does not allow tension can be used to model pin-ended retaining wall props that fall out if the wall moves away from the prop after installation. An element which can only resist tensile forces (i.e. not compression) can be used to model flexible reinforcing strips, such as geofabrics, embedded in the soil.

3.6 Finite elements to model interfaces

3.6.1 Introduction

In any soil-structure interaction situation, relative movement of the structure with respect to the soil can occur. The use of continuum elements, with compatibility of displacements, in a finite element analysis of these situations prohibits relative movement at the soil-structure interface, Figure 3.9. Nodal compatibility of the finite element method constrains the adjacent structural and soil elements to move together. Interface, or joint elements as they are sometimes called, can be used to

model the soil-structure boundary such as the sides of a wall or pile, or the underside of a footing. Particular advantages are the ability to vary the constitutive behaviour of the soil-structure interface (i.e. the maximum wall friction angle) and to allow differential movement of the soil and the structure, i.e. slip and separation. Many methods have been proposed to model discontinuous behaviour at the soil-structure interface, as listed below.

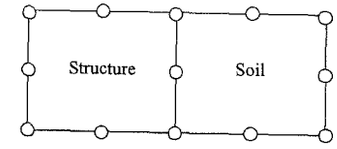

Figure 3.9: Soil-structure interface using continuum elements

- Use of thin continuum elements with standard constitutive laws (Pande and Sharma (1979), Griffiths (1985)), Figure 3.10.
- Linkage elements in which only the connections between opposite nodes are considered (Hermann (1978), Frank *et al.* (1982)). Usually opposite nodes are connected by discrete springs, Figure 3.11.
- Special interface or joint elements of either zero or finite thickness (Goodman *et al.* (1968), Ghaboussi *et al.* (1973), Carol and Alonso (1983), Wilson (1977), Desai *et al.* (1984), Beer (1985)), Figure 3.12.
- Hybrid methods where the soil and structure are modelled separately and linked through constraint equations to maintain compatibility of force and displacement at the interface (Francavilla and Zienkiewicz (1975), Sachdeva and Ramakrishnan (1981), Katona (1983), Lai and Booker (1989)).

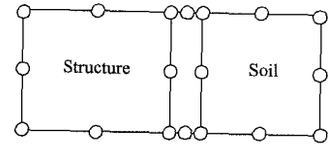

Figure 3.10: Use of continuum elements to model interface

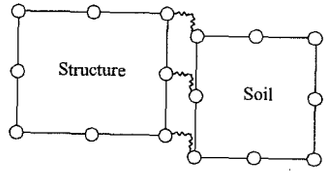

Figure 3.11: Use of springs to model interface

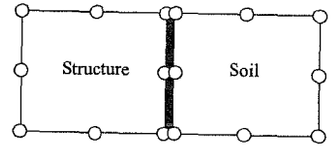

Figure 3.12: Use of special interface elements

Among these alternatives, the use of zero thickness interface elements is probably the most popular. Such an element has been developed by the numerical geotechnical research group at Imperial College, Day (1990). A brief description of this element for 2D plane strain and axi-symmetric conditions is presented in the following sections.

3.6.2 Basic theory

The isoparametric interface element is described by Beer (1985) and Carol and Alonso (1983). The element (see Figure 3.13) with four or six nodes is fully

compatible with four and eight noded quadrilateral, and three and six noded triangular, isoparametric 2D elements.

The interface stress consists of the normal and shear components. The normal stress, σ, and the shear stress, τ, are related by the constitutive equation to the normal and tangential element strains, ε and γ:

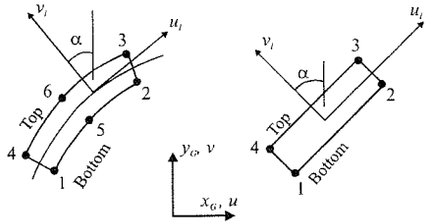

a) 6-noded element b) 4-noded element

Figure 3.13: Isoparametric interface elements

$$\begin{Bmatrix} \Delta\tau \\ \Delta\sigma \end{Bmatrix} = [\boldsymbol{D}] \begin{Bmatrix} \Delta\gamma \\ \Delta\varepsilon \end{Bmatrix} \qquad (3.44)$$

For isotropic linear elastic behaviour the $[\boldsymbol{D}]$ matrix takes the form:

$$[\boldsymbol{D}] = \begin{bmatrix} K_s & 0 \\ 0 & K_n \end{bmatrix} \qquad (3.45)$$

where K_s and K_n are the elastic shear stiffness and normal stiffness respectively.

The interface element strain is defined as the relative displacement of the top and bottom of the interface element:

$$\gamma = \Delta u_l = u_l^{\text{bot}} - u_l^{\text{top}} \qquad (3.46)$$

$$\varepsilon = \Delta v_l = v_l^{\text{bot}} - v_l^{\text{top}} \qquad (3.47)$$

where:

$$\begin{aligned} u_l &= v\sin\alpha + u\cos\alpha \\ v_l &= v\cos\alpha - u\sin\alpha \end{aligned} \qquad (3.48)$$

and u and v are the global displacements in the x_G and y_G directions respectively. Hence:

$$\begin{aligned} \gamma &= (v^{\text{bot}} - v^{\text{top}})\sin\alpha + (u^{\text{bot}} - u^{\text{top}})\cos\alpha \\ \varepsilon &= (v^{\text{bot}} - v^{\text{top}})\cos\alpha - (u^{\text{bot}} - u^{\text{top}})\sin\alpha \end{aligned} \qquad (3.49)$$

3.6.3 Finite element formulation

Figure 3.14 shows a six noded interface element. The strains are defined as:

$$\begin{Bmatrix} \gamma \\ \varepsilon \end{Bmatrix} = \begin{Bmatrix} u_l^{\text{bot}} - u_l^{\text{top}} \\ v_l^{\text{bot}} - v_l^{\text{top}} \end{Bmatrix} \qquad (3.50)$$

The transformation of local to global displacements is written in matrix form as (Figure 3.14):

$$\begin{Bmatrix} u_l \\ v_l \end{Bmatrix} = \begin{bmatrix} \cos\alpha & \sin\alpha \\ -\sin\alpha & \cos\alpha \end{bmatrix} \begin{Bmatrix} u \\ v \end{Bmatrix} \qquad (3.51)$$

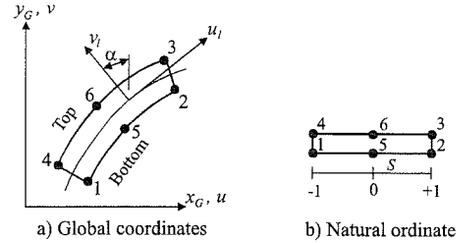

a) Global coordinates b) Natural ordinate

Figure 3.14: 6 noded interface element

Substitution into Equation (3.50) gives:

$$\begin{Bmatrix} \gamma \\ \varepsilon \end{Bmatrix} = \begin{bmatrix} \cos\alpha & \sin\alpha \\ -\sin\alpha & \cos\alpha \end{bmatrix} \begin{Bmatrix} u^{\text{bot}} - u^{\text{top}} \\ v^{\text{bot}} - v^{\text{top}} \end{Bmatrix} \qquad (3.52)$$

The global displacements (u, v) at any point in the element are expressed in terms of the nodal displacements, using the isoparametric shape functions, N_i:

$$\begin{aligned} u^{\text{top}} &= N_3u_3 + N_4u_4 + N_6u_6 \\ u^{\text{bot}} &= N_1u_1 + N_2u_2 + N_5u_5 \end{aligned} \qquad (3.53)$$

and

$$\begin{aligned} v^{\text{top}} &= N_3v_3 + N_4v_4 + N_6v_6 \\ v^{\text{bot}} &= N_1v_1 + N_2v_2 + N_5v_5 \end{aligned} \qquad (3.54)$$

where the subscript refers to the node number.

The isoparametric shape functions, N_i, are defined as:

$$\begin{aligned} N_1 &= N_4 = \tfrac{1}{2}s(s-1) \\ N_2 &= N_5 = \tfrac{1}{2}s(s+1) \\ N_3 &= N_6 = (1-s^2) \end{aligned} \qquad (3.55)$$

where s is the natural ordinate that varies from -1 to +1 over the element length (Figure 3.14). Substitution of Equations (3.53) and (3.54) into (3.52) gives:

$$\begin{Bmatrix} \gamma \\ \varepsilon \end{Bmatrix} = [\boldsymbol{B}] \{\delta\} \qquad (3.56)$$

where $\boldsymbol{\delta}$ is the vector of nodal displacements (degrees of freedom) defined as:

$$\{\delta\} = \{ u_1\ v_1\ u_2\ v_2\ u_3\ v_3\ u_4\ v_4\ u_5\ v_5\ u_6\ v_6 \}^{\mathrm{T}} \qquad (3.57)$$

and

$$[\boldsymbol{B}] = \begin{bmatrix} \cos\alpha & \sin\alpha \\ -\sin\alpha & \cos\alpha \end{bmatrix} \begin{bmatrix} N_1 & 0 & N_2 & 0 & -N_3 & 0 & -N_4 & 0 & N_5 & 0 & -N_6 & 0 \\ 0 & N_1 & 0 & N_2 & 0 & -N_3 & 0 & -N_4 & 0 & N_5 & 0 & -N_6 \end{bmatrix} \qquad (3.58)$$

The element stiffness matrix, $[\boldsymbol{K}_E]$, is given by (see Section 2.6):

$$\left[\boldsymbol{K}_E\right] = \int_0^l \left[\boldsymbol{B}\right]^{\mathrm{T}} \left[\boldsymbol{D}\right] \left[\boldsymbol{B}\right] \mathrm{d}l \tag{3.59}$$

where l is the length of the element and the constitutive matrix $[\boldsymbol{D}]$ is given by Equation (3.44) or (3.45). The integral is evaluated in the natural ordinate system, see Figure 3.14, giving:

$$\left[\boldsymbol{K}_E\right] = \int_{-1}^{1} \left[\boldsymbol{B}\right]^{\mathrm{T}} \left[\boldsymbol{D}\right] \left[\boldsymbol{B}\right] |\boldsymbol{J}| \, \mathrm{d}s \tag{3.60}$$

where $|\boldsymbol{J}|$ is given by Equation (3.31).

The coordinates of the top and bottom of the interface are defined in terms of the nodal coordinates, using the shape functions (Equation (3.55)). For small displacement analysis, in which the calculations are based on the original geometry, coordinates x and y are:

$$\begin{aligned} x^{\mathrm{top}} &= x^{\mathrm{bot}} = N_1 x_1 + N_2 x_2 + N_5 x_5 \\ y^{\mathrm{top}} &= y^{\mathrm{bot}} = N_1 y_1 + N_2 y_2 + N_5 y_5 \end{aligned} \tag{3.61}$$

and

$$\begin{aligned} \frac{\mathrm{d}x}{\mathrm{d}s} &= N_1' x_1 + N_2' x_2 + N_5' x_5 \\ \frac{\mathrm{d}y}{\mathrm{d}s} &= N_1' y_1 + N_2' y_2 + N_5' y_5 \end{aligned} \tag{3.62}$$

where the prime denotes the derivative with respect to s. The trigonometric functions, $\sin\alpha$ and $\cos\alpha$, are given by Equation (3.30).

3.6.4 Comments

It has been found that zero thickness interface elements can suffer from numerical instabilities if they have widely different stiffnesses from the adjacent continuum and/or structural beam elements. This problem has been addressed by Day and Potts (1994).

Zero thickness interface elements also present problems during mesh generation, because adjacent nodes on each side of the element have identical coordinates. Problems can also arise where interface elements intersect. An elegant way of overcoming these problems is presented by Potts and Day (1991).

3.7 Boundary conditions

3.7.1 Introduction

The term *Boundary conditions* is used to cover all possible additional conditions that may be necessary to fully describe a particular problem. The types of boundary conditions can be classified according to their influence on the global system of equations given by Equation (2.30):

$$\left[\boldsymbol{K}_G\right]\left\{\Delta \boldsymbol{d}\right\}_{nG} = \left\{\Delta \boldsymbol{R}_G\right\}$$

The first group of boundary conditions affects only the right hand side (i.e. $\{\Delta \boldsymbol{R}_G\}$) of the system equations. These boundary conditions are loading conditions such as *Point loads*, *Boundary stresses*, *Body forces*, *Construction* and *Excavation*.

The second group of boundary conditions affects only the left hand side (i.e. $\{\Delta \boldsymbol{d}\}_{nG}$) of the system equations. These are kinematic conditions such as *Prescribed displacements*.

The final group of boundary conditions are more complex, since they affect the whole structure of the system equations. These conditions include: *Local axes*, which require a transformation of the stiffness matrix and the right hand side load vector; *Tied freedoms*, which affect the numbering of the degrees of freedom and the stiffness matrix assembly procedure; and *Springs*, which again affect the stiffness matrix assembly procedure.

The following sections of this chapter describe in detail the boundary condition options necessary for performing geotechnical finite element analysis. As noted in Section 2.11, for plane strain (and axi-symmetric) problems it is necessary to specify an x (r) and y (z) boundary condition at each node on the boundary of the finite element mesh. This boundary condition can either be a prescribed nodal displacement or a nodal force. It should be noted that many finite element programs do not insist that the user specifies all these conditions. In such a situation the program makes an implicit assumption for the unspecified nodal conditions. Usually, if a boundary condition is not prescribed, the program assumes that the appropriate nodal force is zero.

3.7.2 Local axes

In most applications, the degrees of freedom at each node (e.g. the two nodal displacements for plane strain or axi-symmetric problems) are referred to the global system of axes. Thus, for compatibility, the stiffness matrices and load conditions are also determined with respect to the global axes. However, in order to apply boundary conditions at an angle to the global directions, it is sometimes necessary to define a set of *Local axes* at certain nodes. In such cases the stiffness matrices and load conditions, for the elements containing the nodes with local axes, need to be transformed.

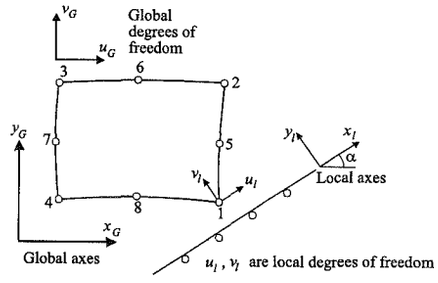

Figure 3.15: Sliding boundary condition

As an example, Figure 3.15 shows a problem with a sliding boundary condition. In this case, node 1 is required to move only parallel to the x_l direction,

where x_l makes an angle α with the global x_G axis. This is most easily achieved by defining local axes x_l, y_l for node 1 and setting the second degree of freedom at node 1 to zero ($v_l = 0$).

If local axes are defined, it is necessary to transform the element stiffness matrices and the load boundary conditions prior to assembling the global system of equations. For 2D plane strain and axi-symmetric analyses the element stiffness matrix $[\boldsymbol{K}_E]$ is transformed from global axes to local axes by:

$$\left[\boldsymbol{K}_E\right]_{local} = \left[\boldsymbol{Q}\right]^{\mathrm{T}}\left[\boldsymbol{K}_E\right]_{global}\left[\boldsymbol{Q}\right] \tag{3.63}$$

where $[\boldsymbol{Q}]$ is a rotation matrix of direction cosines defined by the expression:

$$\left\{\Delta \boldsymbol{d}\right\}_{global} = \left[\boldsymbol{Q}\right]\left\{\Delta \boldsymbol{d}\right\}_{local} \tag{3.64}$$

which relates the local displacements to the global displacements. For example, for a 4 noded isoparametric element, the rotation matrix $[\boldsymbol{Q}]$ takes the form:

$$\left[\boldsymbol{Q}\right] = \begin{bmatrix} \cos\alpha_1 & -\sin\alpha_1 & 0 & 0 & 0 & 0 & 0 & 0 \\ \sin\alpha_1 & \cos\alpha_1 & 0 & 0 & 0 & 0 & 0 & 0 \\ 0 & 0 & \cos\alpha_2 & -\sin\alpha_2 & 0 & 0 & 0 & 0 \\ 0 & 0 & \sin\alpha_2 & \cos\alpha_2 & 0 & 0 & 0 & 0 \\ 0 & 0 & 0 & 0 & \cos\alpha_3 & -\sin\alpha_3 & 0 & 0 \\ 0 & 0 & 0 & 0 & \sin\alpha_3 & \cos\alpha_3 & 0 & 0 \\ 0 & 0 & 0 & 0 & 0 & 0 & \cos\alpha_4 & -\sin\alpha_4 \\ 0 & 0 & 0 & 0 & 0 & 0 & \sin\alpha_4 & \cos\alpha_4 \end{bmatrix} \tag{3.65}$$

where angles α_1, α_2, α_3, α_4 define the orientation of the local axes with respect to the global axes at each of the four nodes. In practice, the number of multiplications performed in evaluating Equation (3.63) is greatly reduced by only processing the non-zero sub-matrices of the matrix (3.65).

The transformation of the right hand side load vector can be performed in a similar manner. Using the definition of $\{\Delta \boldsymbol{R}_E\}$ given in Section 2.6, the transformed load vector becomes:

$$\left\{\Delta \boldsymbol{R}_E\right\}_{local} = \left[\boldsymbol{Q}\right]^{\mathrm{T}}\left\{\Delta \boldsymbol{R}_E\right\}_{global} \tag{3.66}$$

where $[\boldsymbol{Q}]$ is again of the form of Equation (3.65) (note: $[\boldsymbol{Q}]^{-1} = [\boldsymbol{Q}]^{\mathrm{T}}$). The transformation Equation (3.66) is indicated at the element level, however, in practice it is more convenient to take account of the local axes in the assembled right hand side vector, $\{\Delta \boldsymbol{R}_G\}$.

3.7.3 Prescribed displacements

In addition to the application of prescribed displacement conditions to represent structural boundaries, a sufficient number of displacement components must be specified to restrict any rigid body translations or rotations. If these conditions are not prescribed, the global stiffness matrix becomes singular and the system equations cannot be solved.

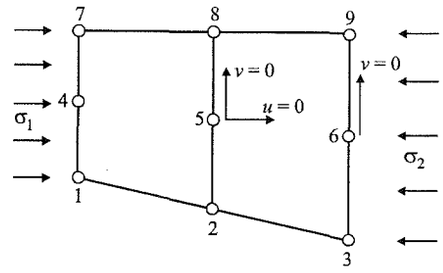

Figure 3.16: Removal of rigid body modes

To remove the rigid body modes, which for two dimensions consist of two translations and one rotation, the user should effectively prescribe the values of at least three degrees of freedom. Care should be taken, particularly with the rotational mode, that the prescribed displacements do restrain *all* the rigid body modes. Figure 3.16 shows an example of a plane strain body deformed by stress boundary conditions. The choice of prescribed displacements, which restrain the rigid body modes, is not unique and depends on the displacement solution required. Figure 3.16 shows the case where the rigid body modes are removed by specifying three degrees of freedom: these are $u = 0$, $v = 0$ at node 5 and $v = 0$ at node 6.

Problems involving symmetrical bodies and symmetrical boundary conditions can be solved by analysing only half of the total body, see Section 2.11. For such cases displacement boundary conditions can be applied to ensure that the line of symmetry remains undeformed. These displacement conditions may also be useful in removing certain rigid body modes.

The definition of a prescribed displacement component is equivalent to specifying the value of a degree of freedom. Thus, if local axes are also specified at certain nodes, the prescribed displacements refer to the displacement components with respect to the new local system of axes. The application of the prescribed displacements is performed simultaneously with the solution of the global system of equations. For a detailed description of this process see Section 2.9.4. Only an outline of the technique is given here.

The global equilibrium Equations (2.30), can be partitioned in the form:

$$\begin{bmatrix} \boldsymbol{K}_u & \boldsymbol{K}_{up} \\ \boldsymbol{K}_{up}^{\mathrm{T}} & \boldsymbol{K}_p \end{bmatrix}\begin{Bmatrix} \Delta \boldsymbol{d}_u \\ \Delta \boldsymbol{d}_p \end{Bmatrix} = \begin{Bmatrix} \Delta \boldsymbol{R}_u \\ \Delta \boldsymbol{R}_p \end{Bmatrix} \tag{3.67}$$

where $\Delta \boldsymbol{d}_u$ are the unknown degrees of freedom and $\Delta \boldsymbol{d}_p$ corresponds to the prescribed displacements. The first matrix equation from Equation (3.67) gives:

$$\left[\boldsymbol{K}_u\right]\left\{\Delta \boldsymbol{d}_u\right\} = \left\{\overline{\Delta \boldsymbol{R}_u}\right\} \tag{3.68}$$

where

$$\left\{\overline{\Delta \boldsymbol{R}_u}\right\} = \left\{\Delta \boldsymbol{R}_u\right\} - \left[\boldsymbol{K}_{up}\right]\left\{\Delta \boldsymbol{d}_p\right\} \tag{3.69}$$

Thus the unknown displacements $\{\Delta \boldsymbol{d}_u\}$ can be calculated from a modified system of global equilibrium Equations (3.68).

Having determined $\{\Delta \boldsymbol{d}_u\}$ from Equation (3.68), the second matrix Equation (3.67) gives:

$$\{\Delta \boldsymbol{R}_p\} = [\boldsymbol{K}_{up}]^T \{\Delta \boldsymbol{d}_u\} + [\boldsymbol{K}_p]\{\Delta \boldsymbol{d}_p\} \tag{3.70}$$

Hence, the *Reaction forces* corresponding to each prescribed displacement can also be calculated.

In the solution scheme presented in Section 2.9 the application of prescribed displacements is performed without re-arranging the global system of equations as implied by Equation (3.67). The equations corresponding to $\{\Delta \boldsymbol{R}_p\}$ are skipped over whilst the Equations (3.68) are solved, and the coefficients of $[\boldsymbol{K}_{up}]^T$ and $[\boldsymbol{K}_p]$ are then used to determine the reaction forces.

If beam (shell) elements are being used to model structural components, these elements have a rotational degree of freedom, θ, in addition to the two displacements, see Section 3.5.2. To realistically model the behaviour of the structural components it may be necessary to prescribe values of some of the nodal rotations.

3.7.4 Tied degrees of freedom

This boundary condition option allows a condition of equal displacement components to be imposed at one or more nodes, whilst the magnitude of the components remain unknown.

To explain where this concept might be useful, the problem of a smooth rigid strip footing is considered. Such a situation is shown in Figure 3.17, where symmetry has been assumed and half the footing is between nodes A and B. The footing is subject to a vertical load, P, and it is required to calculate the magnitude of the resulting footing settlement. The geometry and finite element mesh are assumed to be the same as that used for the example discussed in Section 2.11. Because the behaviour of the footing under a given load is required, this load has to form part of the boundary conditions. As the footing is rigid, it is also required that it displaces vertically by the same amount across its width. Unfortunately, the magnitude of this vertical displacement is not known, in fact the reason for doing the analysis is to determine just this quantity. One solution to this problem is to use the tied freedoms concept. The boundary

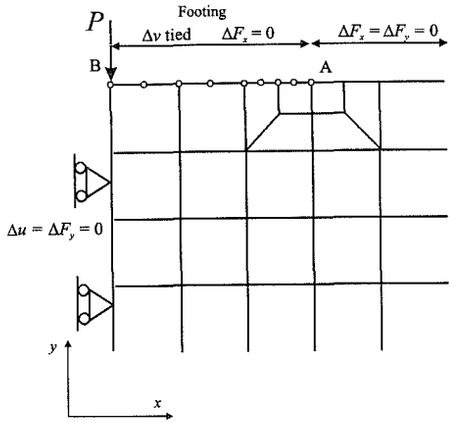

Figure 3.17: Boundary conditions for a smooth strip footing subject to a vertical load P

conditions to be applied to the mesh boundary immediately below the position of the strip footing are shown in Figure 3.17. A vertical nodal force, $\Delta F_y = P$, is applied to node B, on the line of symmetry, and zero horizontal nodal forces, $\Delta F_x = 0$, are applied to nodes on the boundary between A and B. In addition, the nodes between A and B are constrained to move vertically by the same amount by using tied freedoms. This is achieved in the finite element analysis by assigning a single degree of freedom number to the vertical degree of freedom at each of the nodes along the boundary between A and B.

In general, the set of tied displacement components are given a single degree of freedom number, which appears only once in the assembled global equilibrium equations. Thus, tying degrees of freedom alters the structure of the global stiffness matrix and in some cases may increase the total profile (i.e. the number of terms of $[\boldsymbol{K}_G]$ which need to be stored).

As an example, Figure 3.18 shows a problem of frictionless contact between two bodies. The nodes 25, 26, 27, 28 in the upper body are defined to be coincident with the nodes 19, 20, 21, 22 respectively, of the lower body. The problem is to find the indentation stresses induced from the weight of the upper body. Since the two bodies are in contact, a condition of no-penetration must be specified for the contact zone. This condition is most easily imposed by tying the degrees of freedom with a set of constraint equations:

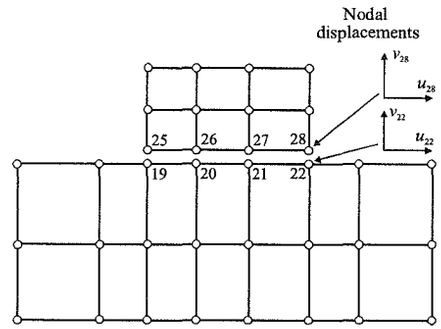

Figure 3.18: Frictionless contact problem

$$v_{19} = v_{25} \;;\; v_{20} = v_{26} \;;\; v_{21} = v_{27} \;;\; v_{22} = v_{28} \tag{3.71}$$

The incorporation of the Equations (3.71) in the solution procedure is achieved by simply numbering the displacement components at the tied nodes with the same degree of freedom numbers. Thus, for example, v_{19} and v_{25} will be given the same degree of freedom number.

Since the degrees of freedom (or displacements) are measured positive with respect to the local system of axes at each node, the flexibility of this feature is greatly increased if combined with the *Local axes* feature described in Section 3.7.2. Figure 3.19 shows the effective global constraints which can be achieved by tying the two degrees of freedom at a single node and by adjusting the orientation of the local axes x_l, y_l which make an angle α with the global axes x_G, y_G. The global displacements (measured positive in the x_G, y_G directions) are indicated by u and v.

If the degrees of freedom are tied between two nodes, the effective global constraints depend on the orientation of the local axes at both of the nodes. As an

example, Figure 3.20 shows the case where the degrees of freedom are tied between two nodes labelled A and B. The local axes at node A are, for simplicity, chosen to be coincident with the global axes, and the local axes at node B are varied. The orientation of the local axes, and hence the degrees of freedom, are again indicated by notation x_l, y_l; the global displacements are given by u and v.

A further option for defining tying constraints is to tie the degrees of freedom over a range of boundary nodes as indicated in the strip footing problem shown in Figure 3.17.

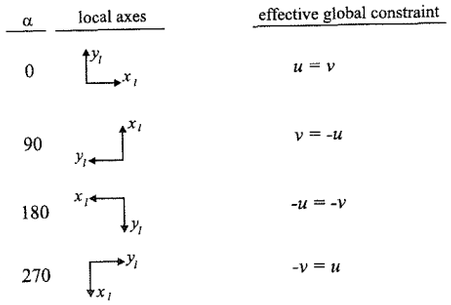

Figure 3.19: Effective global constraints for tying at a single node

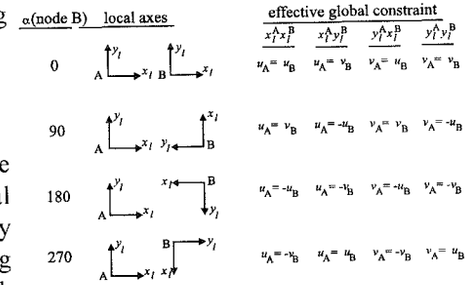

Figure 3.20: Effective global constraints for tying between two nodes

3.7.5 Springs

As an alternative to using membrane elements to model structural components which can sustain only membrane (i.e. axial) forces, spring boundary conditions can be used. Springs are usually assumed to be linear, with a constant stiffness, k_s, and can be applied in finite element analysis in three different ways.

Firstly, they can be placed between two nodes in the mesh. Figure 3.21 shows a very crude excavation problem in which two such springs are used. The first spring spans between nodes i and j and represents a prop. The second spring spans between nodes m and n and represents an end bearing pile. These springs essentially act as linear two noded membrane elements. They therefore contribute to the global stiffness matrix. The equilibrium equation for the spring between nodes i and j is:

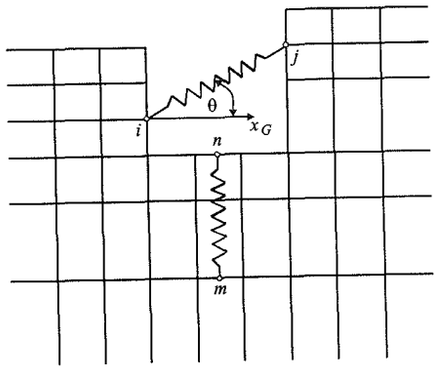

Figure 3.21: Spring between 2 nodes

$$k_s\begin{bmatrix} \cos^2\theta & \sin\theta\cos\theta & -\cos^2\theta & -\sin\theta\cos\theta \\ \sin\theta\cos\theta & \sin^2\theta & -\sin\theta\cos\theta & -\sin^2\theta \\ -\cos^2\theta & -\sin\theta\cos\theta & \cos^2\theta & \sin\theta\cos\theta \\ -\sin\theta\cos\theta & -\sin^2\theta & \sin\theta\cos\theta & \sin^2\theta \end{bmatrix}\begin{Bmatrix} \Delta u_i \\ \Delta v_i \\ \Delta u_j \\ \Delta v_j \end{Bmatrix} = \begin{Bmatrix} \Delta R_{xi} \\ \Delta R_{yi} \\ \Delta R_{xj} \\ \Delta R_{yj} \end{Bmatrix} \quad (3.72)$$

where θ is the inclination of the spring to the global x_G axis, see Figure 3.21. The spring stiffness, k_s, multiplied by the trigonometric matrix above must be added to the global stiffness matrix during the assemble process. It affects the terms relating to the displacement degrees of freedom of nodes i and j.

Secondly, springs can be applied at a single node. Such an example is shown in Figure 3.22 which shows a symmetric excavation, with a spring applied at node i to represent a prop. In this situation it is implicitly assumed that the end of the spring not attached to the node is 'grounded' and restrained from moving in any direction. Such springs also contribute to the global stiffness matrix. The equilibrium equation for this spring is:

$$k_s\begin{bmatrix} \cos^2\theta & \sin\theta\cos\theta \\ \sin\theta\cos\theta & \sin^2\theta \end{bmatrix}\begin{Bmatrix} \Delta u_i \\ \Delta v_i \end{Bmatrix} = \begin{Bmatrix} \Delta R_{xi} \\ \Delta R_{yi} \end{Bmatrix} \quad (3.73)$$

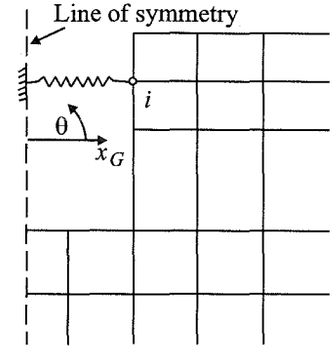

Figure 3.22: Spring at a single node

where, in general, θ is the inclination of the spring to the global x_G direction. In the above example $\theta = 0°$. Again, the spring stiffness, k_s, multiplied by the trigonometric matrix must be added to the global stiffness matrix during the assembly process.

The third option is to apply a continuous spring along a part of the boundary of the mesh. An example is shown in Figure 3.23 where such a spring is placed along the bottom boundary of the mesh. It is important to note that these are not discrete springs positioned at nodes, but are continuous along the mesh boundary. They must therefore be converted into equivalent nodal springs before they can be assembled into the global stiffness matrix. It can be shown that, for a single element side, the contribution to the global stiffness matrix takes the form:

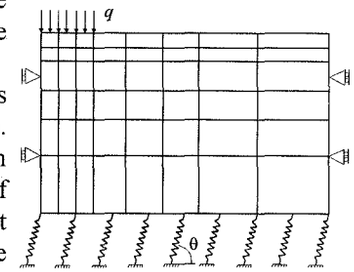

Figure 3.23: Continuous spring along mesh boundary

$$\int_{Srf} [N]^T [K_s][N]\, dSrf \quad (3.74)$$

where:

$$\left[K_s\right] = k_s \begin{bmatrix} \cos^2\theta & \sin\theta\cos\theta \\ \sin\theta\cos\theta & \sin^2\theta \end{bmatrix}$$

and *Srf* is the element side over which the spring acts. Clearly, the above equation only contributes to the global stiffness terms of the nodes along the element side. If the spring spans across more than one element, then the contribution from each element must be added into the global stiffness matrix. The integral in Equation (3.74) can be evaluated numerically for each element side, in a similar fashion to that described for boundary stress in Section 3.7.6.

3.7.6 Boundary stresses

Stress boundary conditions have to be converted into equivalent nodal forces. In many finite element programs the calculation of the equivalent nodal forces is performed automatically for generally distributed boundary stresses and for arbitrarily shaped boundaries.

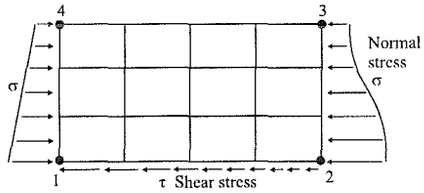

Figure 3.24: Example of stress boundary conditions

To illustrate this, Figure 3.24 shows an example of the type of boundary stresses which may be defined. Between the points 1 and 2 a linearly decreasing shear stress is applied; between points 2 and 3 a generally varying normal stress is applied; the side 3 to 4 is stress-free; and between points 4 and 1 a linearly increasing normal stress is applied. To determine the nodal forces, which are equivalent to the stress boundary conditions, the expression for the surface traction contribution to the element right hand side load vector is utilised, see Section 2.6:

$$\left\{\Delta \boldsymbol{R}_E\right\} = \int_{Srf} \left[\boldsymbol{N}\right]^{\mathrm{T}} \left\{\Delta \boldsymbol{T}\right\} \mathrm{d}Srf \tag{3.75}$$

where $[N]$ is given by Equation (2.8), $\{\Delta T\}$ is the incremental global surface traction vector (i.e. boundary stresses) and '*Srf*' (i.e. Surface) is the element side over which tractions are prescribed. The integral (3.75) can be evaluated numerically for each element side over which the tractions act. The first stage of this process is to transform the surface integral (3.75) into an one dimensional form in the natural coordinate system:

$$\left\{\Delta \boldsymbol{R}_E\right\} = \int_{-1}^{1} t \left[\boldsymbol{N}'\right]^{\mathrm{T}} \left\{\Delta \boldsymbol{T}\right\} \left|\boldsymbol{J}'\right| \mathrm{d}s \tag{3.76}$$

where t is unity for plane strain problems and equals $2\pi r$ for axi-symmetric problems, $[N']$ contains the interpolation functions on the element side, and $|J'|$ is the Jacobian determinant obtained from mapping the element side from the

global element to the parent element. For example, for a 4 noded isoparametric element, $[N']$ takes the form:

$$\left[\boldsymbol{N}'\right] = \begin{bmatrix} N_1' & 0 & N_2' & 0 \\ 0 & N_1' & 0 & N_2' \end{bmatrix} \tag{3.77}$$

where

$$\begin{aligned} N_1' &= \tfrac{1}{2}(1-S) \\ N_2' &= \tfrac{1}{2}(1+S) \end{aligned} \tag{3.78}$$

are interpolation functions for the element side. The Jacobian determinant for each point on the element side is given by:

$$\left|\boldsymbol{J}'\right| = \left(\left(\frac{\mathrm{d}x}{\mathrm{d}S}\right)^2 + \left(\frac{\mathrm{d}y}{\mathrm{d}S}\right)^2\right)^{\frac{1}{2}} \tag{3.79}$$

where the coordinate derivatives are obtained by differentiating the simplified isoparametric relations:

$$x = \sum_{i=1}^{2} N_i' x_i \quad ; \quad y = \sum_{i=1}^{2} N_i' y_i \tag{3.80}$$

and x_i, y_i are the global coordinates of the two nodes on the element side.

The final stage in the calculation of the nodal forces is to evaluate Equation (3.76) using an one dimensional Gaussian integration procedure, as described in Section 2.6.1. In this procedure, the integral (3.76) is replaced by a weighted sum of the integrand evaluated at a number of Gaussian integration points.

To determine the integration point value of the surface traction vector $\{\Delta T\}$, the applied stress must be transformed according to the orientation of the surface element at the integration point and the defined sign convention for stresses. One such sign convention is that normal stresses (σ) are positive if oriented outwards from the boundary of the body, while shear stresses (τ) are positive if oriented in a tangentially anticlockwise sense with respect to the boundary of the body. Using this convention gives:

$$\left\{\Delta \boldsymbol{T}_I\right\} = \sigma_I \begin{Bmatrix} \cos\theta_I \\ \sin\theta_I \end{Bmatrix} \tag{3.81}$$

if normal stresses are prescribed, or

$$\left\{\Delta \boldsymbol{T}_I\right\} = \tau_I \begin{Bmatrix} -\sin\theta_I \\ \cos\theta_I \end{Bmatrix} \tag{3.82}$$

if shear stresses are prescribed, where θ_I is the angle between the boundary normal and the global x_G axis, and the subscript I denotes the integration point value. The angle θ_I is determined by inverting the expression:

$$\tan(\theta_l + 90) = \frac{dy}{dx} = \left[\frac{\sum_{i=1}^{2} \frac{\partial N_i'}{\partial S} y_i}{\sum_{i=1}^{2} \frac{\partial N_i'}{\partial S} x_i} \right]_{at\ S_l} \tag{3.83}$$

which is obtained by differentiating Equation (3.80).

In all cases the equivalent nodal forces, which are calculated from Equation (3.76), are initially referred to the global system of axes. If local axes are defined, the nodal forces are transformed accordingly, as described in Section 3.7.2.

3.7.7 Point loads

A further option for applying traction boundary conditions is to apply discrete nodal point loads. For plane strain and axi-symmetric analyses they are line loads, with their length perpendicular to the plane of the mesh. This allows the user to manually define stress boundary conditions over a range of the boundary, or to define a point load at a single node. Point loads can be defined with respect to a set of *Point loading axes*.

As an example, Figure 3.25 shows the case where a single point load is applied at an angle to the boundary of the body. If point loads are defined over a part of the mesh boundary and are required to represent a continuous stress distribution, the values of the point loads must be calculated in a manner consistent with minimising the potential energy of the body, as described in Chapter 2. This requires that the work done by the point loads, in displacing the nodal points, is equal to the work done by the continuous stress distribution in deforming the boundary. The point loads must therefore be calculated from an integral of the form given in Equation (3.75).

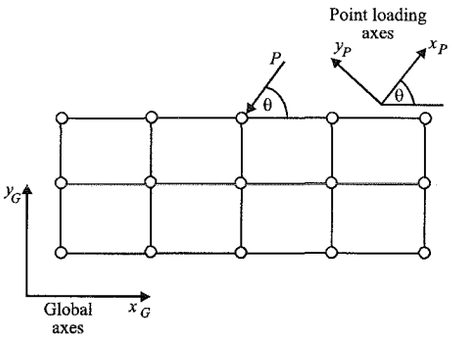

Figure 3.25: Orientation of point loading axes

For simple element shapes and simple stress distributions the equivalent nodal forces can be evaluated exactly. Some examples are illustrated in Figure 3.26 for element sides with 2 and 3 nodes.

In all cases the point loads, which are initially defined with respect to the x_p, y_p point loading axes, or with respect to the boundary normal, are transformed to the global system of axes. If local axes are defined, the nodal forces are transformed again as described in Section 3.7.2.

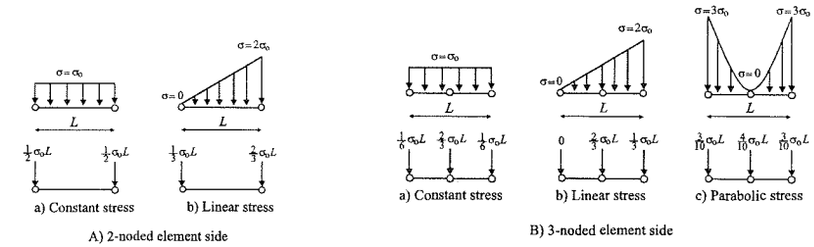

Figure 3.26: Equivalent nodal forces for element side with A) 2 nodes and B) 3 nodes

3.7.8 Body forces

Gravity loading, or body forces, play an important role in most geotechnical problems. In a similar fashion to the other loading conditions discussed above, the application of body forces as a boundary condition requires the calculation of equivalent nodal forces. In most finite element programs the calculation of nodal forces corresponding to body forces is performed automatically. The body force can act in any direction and its magnitude over the mesh can be varied.

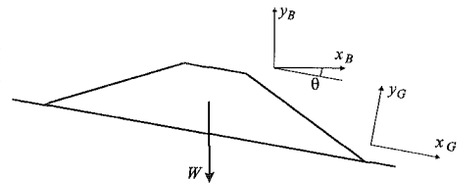

Figure 3.27: Body force loading axes for sediment layer on a slope

To illustrate the application of body forces and the definition of the body force axes, consider the example shown in Figure 3.27. This example shows a cross-section of an embankment which lies on a slope and which is deforming under its own weight. For convenience, the global axes are chosen to be parallel to the slope. Thus in order to apply the gravitational field, a set of body force loading axes x_B, y_B must be defined, where x_B makes an angle θ with the global x_G axis. The gravitational field is then defined with respect to the y_B axis.

The nodal forces equivalent to the body force are calculated element-wise, using the body force contribution to the right hand side vector, see Section 2.6:

$$\{\Delta \boldsymbol{R}_E\} = \int_{Vol} [N]^T \{\Delta \boldsymbol{F}_G\}\, dVol \tag{3.84}$$

where $[N]$ is given by Equation (2.8), $\{\Delta \boldsymbol{F}_G\}$ is the global body force vector and Vol is the volume of the element. The body force vector $\{\Delta \boldsymbol{F}_G\}$ is determined with respect to the global axes by using:

$$\begin{Bmatrix} \Delta F_{xG} \\ \Delta F_{yG} \end{Bmatrix} = \Delta\gamma \begin{Bmatrix} \cos\beta \\ \sin\beta \end{Bmatrix} \tag{3.85}$$

where $\Delta\gamma$ is the increment of bulk unit weight; $\beta = \theta$ or $\theta+90°$ depending on whether $\Delta\gamma$ refers to the x_B or y_B component of body force, respectively; and θ is the angle between the x_B and x_G axes.

The integral (3.84) is evaluated numerically over each element, by using the procedure described in Section 2.6.1 for the element stiffness matrix. First, the body force integral is transformed to the natural coordinate system:

$$\left\{\Delta \boldsymbol{R}_E\right\} = \int_{-1}^{1}\int_{-1}^{1} t\left[\boldsymbol{N}\right]^T\left|\boldsymbol{J}\right| \,\mathrm{d}S\,\mathrm{d}T\left\{\Delta \boldsymbol{F}_G\right\} \tag{3.86}$$

where t equals unity for plane strain problems and $t=2\pi r$ for axi-symmetric problems; and $|\boldsymbol{J}|$ is the determinant of the Jacobian, given by Equation (2.16), arising from the mapping between the global and parent elements. The global force vector $\{\Delta \boldsymbol{F}_G\}$ can be removed from the integral, since it is constant over the element. The integral in Equation (3.86) is determined using a two dimensional Gaussian integration procedure, as described in Section 2.6.1.

The above process is repeated for each element in the mesh and the individual element nodal force vectors are combined to form an overall equivalent nodal force vector. This overall force vector is initially referred to the global axes, so that if local axes are also defined, the nodal forces are transformed accordingly, as described in Section 3.7.2. Clearly, the units of body force, $\Delta\gamma$, must be consistent with the length units used to define the mesh geometry and the stress units used to define the material properties (e.g. Young's modulus).

3.7.9 Construction

Many geotechnical problems involve the placing of new material, such as embankment construction and backfilling behind a retaining wall. Simulation of such activities in a finite element analysis is not straightforward. The software must be able to accommodate the following:

- Elements representing the material to be constructed must be present in the original finite element mesh, but must be *deactivated*, either by prior excavation, or at the outset of the analysis. On construction the elements are reactivated.
- Construction of material must be performed incrementally since, even for a linear elastic material, superposition does not hold. When constructing an embankment the layered construction procedure must be followed, with each increment of the analysis simulating the construction of a layer of fill.
- During construction, the elements representing the new material must have a constitutive model which is consistent with its behaviour during construction. Once constructed, the constitutive model should change to represent the behaviour of the material once placed.
- When an element is constructed, the addition of its weight to the finite element mesh must be simulated by applying self weight body forces to the constructed element.

When constructing material, the following procedure is recommended:

- Divide the analysis into a set of increments and make sure that all elements to be constructed are deactivated prior to the increment at which construction starts.
- For a particular increment the elements to be constructed are reactivated and given a constitutive model appropriate to the material behaviour during placing. This often means that the material has a low stiffness.
- Nodal forces due to the self weight body forces of the constructed material are calculated in a similar fashion to that explained for body forces in Section 3.7.8, and added to the right hand side load vector.
- The global stiffness matrix and all other boundary conditions are assembled for the increment. The equations are solved to obtain the incremental changes in displacements, strains and stresses.
- Before application of the next increment, the constitutive model for the elements just constructed is changed to represent the behaviour of the fill material once placed. Displacements of any nodes which are only connected to the constructed elements (i.e. not connected to elements that were active at the previous increment) are zeroed. Depending on the constitutive models used to represent the constructed material, it may be necessary to establish state parameters (e.g. hardening parameters for elasto-plastic models) and/or adjust the stresses in the constructed elements. If the stresses are adjusted, then care must be taken that equivalent changes are made to the accumulated right hand side vector to ensure equilibrium is maintained.
- Apply the next increment of analysis.

As an example, consider the problem of constructing the embankment shown in Figure 3.28. The embankment has been split into four horizontal layers of material and therefore is constructed in four increments. At the outset of the analysis all elements in the embankment are deactivated. In increment 1, layer 1 is to be constructed and therefore, at the beginning of the increment, all the elements in this layer are reactivated (i.e. added to the active mesh) and assigned a constitutive model appropriate to the material behaviour during placing. Self weight body forces are then assumed for these elements and the equivalent nodal forces calculated and added to the incremental right hand side vector. The global stiffness matrix and other boundary conditions are assembled and a solution found. The incremental displacements calculated for the nodes connected to the

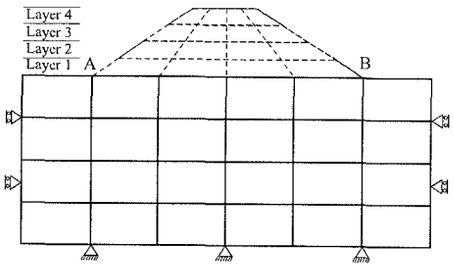

Figure 3.28: Embankment construction

constructed elements, but not connected to those elements forming the original ground (i.e. all active nodes above line AB), are zeroed. A new constitutive model appropriate to the behaviour of the fill once placed is then assigned to the elements just constructed. Any material state parameters are then calculated and any stress adjustments made (applicable to the more complex constitutive models discussed in Chapter 8).

The procedure for construction of layers 2, 3 and 4 follows similar steps. The final result is obtained by accumulating the results from each increment of the analysis. Clearly, the results of the analysis will depend on the number and therefore thickness of the construction layers. This is discussed in detail in Volume 2 of this book.

Deactivation of elements can be accounted for in one of two ways. The best way is not to include the deactivated elements in the formulation of the finite element equations. This means that no account is taken of their element stiffness matrices or of the nodal degrees of freedom, which are only connected to deactivated elements, during assembly of the global stiffness matrix and right hand side vector. As far as the finite element formulation is concerned, it is as if the deactivated elements do not exist. Although this is the recommended way of dealing with deactivated elements, it implies that the finite element software must have sophisticated book keeping arrangements for keeping track of data, as the active mesh will change throughout an analysis. An alternative procedure, which simplifies the book keeping, is to leave the deactivated elements in the active mesh, but assume that they have a very low stiffness. The deactivated elements are often called 'ghost elements'. In this procedure the elements do contribute to the element equations and all degrees of freedom remain active. Their effect on the solution depends on the stiffnesses that they assume. Most software that use this approach automatically set low stiffness values for the ghost elements, or encourage the user to set low values. However, care must be taken that the resulting Poisson's ratio does not approach 0.5. If it does, the ghost elements become incompressible, which can have a serious effect on the predictions.

Because of the complexities involved in simulating construction, many finite element programs orientated towards structural engineering are unsuitable for performing such analyses.

3.7.10 Excavation

Excavation of soil is involved in many geotechnical problems. Its simulation in a finite element analysis can be summarised as follows. Figure 3.29a shows a body of soil from which the shaded portion A is to be excavated, leaving the unshaded portion B. No displacements or changes in stress occur if material is removed, but replaced by tractions (T) which are equal to the internal stresses in the soil mass that act on the excavated surface before A is removed, see Figure 3.29b. The behaviour of B due to the excavation of A will be identical to the behaviour of B when the tractions (T) are removed, for example by applying equal and opposite tractions as indicated in Figure 3.29c.

Simulation of a stage of excavation therefore involves determination of the tractions, T, at the new soil boundary, determination of the stiffness of the soil mass B, and application of tractions, $-T$, to that new soil boundary. Finite element implementation of this process involves determination of the nodal forces which are equivalent to the tractions shown in Figure 3.29c. These forces can be calculated from the excavated elements adjacent to the excavation boundary using:

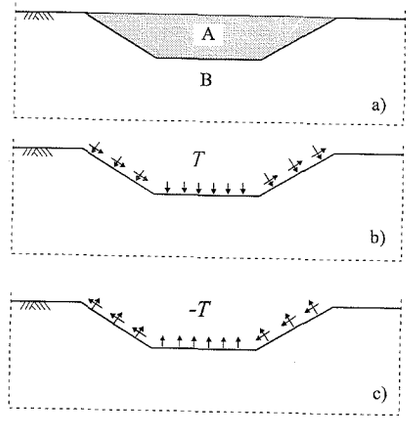

Figure 3.29: Simulation of excavation

$$\{\boldsymbol{R}_E\} = \int_{Vol} [\boldsymbol{B}]^T \{\sigma\} \, dVol - \int_{Vol} [\boldsymbol{N}]^T \gamma \, dVol \qquad (3.87)$$

where $\{\sigma\}$ is the stress vector in the element, γ is the bulk unit weight and Vol is the volume of the excavated element. Only the forces appropriate to the nodes on the excavated surface are placed in $\{\boldsymbol{R}_E\}$. This calculation is repeated for all excavated elements adjacent to the excavation boundary. This procedure is based on Brown and Booker (1985).

When simulating excavation in a geotechnical problem it is usual that structural elements or supports are added as excavation proceeds. It is therefore necessary to split the analysis into a sequence of increments. This is also necessary if nonlinear constitutive models are used. The procedure followed in the analysis is therefore as follows:

- Specify the elements to be excavated for a particular increment.
- Using Equation (3.87) determine the equivalent nodal forces to be applied to the excavation boundary to simulate removal of the elements. Tag the elements to be excavated as *deactivated* and remove them from the active mesh.
- Assemble the remaining boundary conditions and the global stiffness matrix using the active mesh. Solve the finite element equations to give the incremental changes in displacements, stresses and strains.
- Add the incremental changes of displacements, stresses and strains to the accumulated values existing before the increment to give the updated accumulated values.
- Perform the next increment of the analysis.

3.7.11 Pore pressures

When performing analyses in which the total stresses are expressed in terms of effective stresses and pore water pressures, see Section 3.4, it may be appropriate to specify changes in pore water pressure.

In the finite element analysis it is necessary to specify changes in pore fluid pressure in terms of equivalent nodal forces. It can be shown that for an element with a specified change in pore fluid pressure, Δp_f, the equivalent nodal forces are given by:

$$\left\{\boldsymbol{R}_E\right\} = -\int_{Vol}\left[\boldsymbol{B}\right]^{\mathrm{T}}\left\{\Delta\sigma_f\right\}\,\mathrm{d}Vol \tag{3.88}$$

where $\{\Delta\sigma_f\}$ is given by Equation (3.3). Two scenarios often occur:

Firstly, a set change in the pore water pressure in part of a finite element mesh may be required. For example, during excavation in layered soils it may be necessary to de-water granular layers to prevent bottom heave, see Figure 3.30.

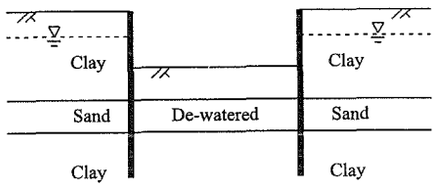

Figure 3.30: Excavation de-watering

Secondly, dissipation of excess pore water pressures may be needed. For example, consider a strip footing which has initially been loaded under undrained conditions. The original part of the analysis could be performed with the equivalent bulk modulus of the pore water, K_e, set to a high value, see Section 3.4. Excess pore water pressures would then be calculated, see Figure 3.31. Once the footing is loaded, K_e could be set to zero and the excess pore water pressures dissipated by specifying changes equal and opposite to those calculated during loading. An estimate of the effects of full consolidation could therefore be calculated. However, no information would be available about intermediate states during the consolidation process. Such an approach is appropriate if the soil behaviour is linear elastic. An approximation is involved if the constitutive behaviour is nonlinear. This arises because there is an implicit assumption that stress changes are proportional throughout the consolidation period. In practice, stress changes may be far from proportional. Under the loaded footing pore water pressures will dissipate first at the edge, causing a relatively rapid effective stress change in this region. The effective stresses at the centre will change more slowly. The extent of the error involved depends on the constitutive model. To model the consolidation process accurately, coupled analyses should be performed, see Chapter 10.

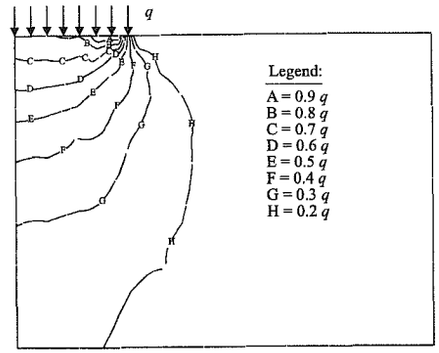

Figure 3.31: Excess pore water pressures under smooth flexible strip footing

3.8 Summary

1. Drained analysis in which pore water pressures are ignored can be performed by using effective stress material properties.
2. Undrained analysis can be performed in terms of total stress using total stress material properties. Care must be taken when Poisson's ratio approaches 0.5.
3. Analysis can also be performed in which the total stress tensor is split into effective stresses and pore fluid pressures. This enables undrained analysis to be carried out using effective stress material properties in which the change in effective stresses and pore water pressures are calculated. It also allows drained analyses to be carried out, in which changes in the pore water pressures can be prescribed.
4. It is often difficult to model structural elements using continuum finite elements. Alternative structural elements are available. Beam/shell elements can be used when the structural member can sustain bending moments and axial and shear forces. Alternatively, if the structural element can only sustain axial forces, membrane elements may be used. A detailed description of both elements has been given.
5. The interface between structural elements and soil can be modelled in a variety of ways. A special interface element which has zero thickness has been described in this chapter. The use of this element in practical boundary value problems is discussed in Volume 2 of this book.
6. There are three classes of boundary conditions that arise in finite element analysis. The first class affects only the right hand side of the governing equations. These conditions are loading conditions such as boundary stresses, body forces, etc... The second class affects the left hand side of the governing equations. These are kinematic conditions such as prescribed displacements. The third class is more complex, since they affect the whole structure of the system equations. These conditions include local axes, tied freedoms and springs.
7. The following boundary conditions have been described in detail:
   - Local axes;
   - Prescribed displacements;
   - Tied degrees of freedom;
   - Springs;
   - Boundary stresses;
   - Point loads;
   - Body forces;
   - Construction;
   - Excavation;
   - Pore pressures.

4. Real soil behaviour

4.1 Synopsis

This chapter reviews real soil behaviour. It considers clay and sand soils and then soils containing a range of particle sizes. The main facets of soil behaviour are identified by considering results from laboratory tests. Data are presented without prejudice from any theoretical framework, and can therefore be used to verify and compare with the theoretical constitutive models described in subsequent chapters.

4.2 Introduction

The finite element theory presented in Chapter 2 assumed material behaviour to be linear elastic. Unfortunately, real soils do not behave in such an ideal and simple manner. If they did, failure would never occur and geotechnical engineers would probably not be needed. Real soil behaviour is highly nonlinear, with both strength and stiffness depending on stress and strain levels. For realistic predictions to be made of practical geotechnical problems, a more complex constitutive model is therefore required. As this involves nonlinear behaviour, further developments are required to the finite element theory. These developments are presented and discussed in Chapter 9.

Due to the complexity of real soil behaviour, a single constitutive model that can describe all facets of behaviour, with a reasonable number of input parameters, does not yet exist. Consequently, there are many models available, each of which has strengths and weaknesses. In Chapters 5, 7 and 8 a variety of constitutive models that have been, and still are, used to represent soil behaviour are described. However, before delving into the complex theory behind these mathematical models, it is useful to consider real soils and identify the important aspects of their behaviour. Such information provides a framework which can then be used to assess and compare the various different constitutive models.

Soil behaviour is a complex subject and it is not possible to cover every aspect in a single chapter. Consequently, only the most important issues are discussed here. It is assumed that the reader is familiar with soil mechanics and in particular with conventional laboratory testing of soil samples and the manner in which the results from such tests are presented. The aim is to summarise the more important characteristics of soil behaviour as observed in laboratory tests, rather than to introduce new concepts to the reader. The chapter begins by considering the

behaviour of clay soils. Behaviour under one dimensional compression and when subjected to shear under triaxial stress and strain conditions is presented. The effects of the magnitude of the intermediate principal stress, the orientation of the principal stresses and shearing to large strains on clay behaviour are then discussed. Sand soils are considered in the same way and the differences in behaviour noted. Although pure clay and sand soils do exist, many soils contain a range of particle sizes from clay to sand, with their behaviour reflecting their composition. In the last part of this chapter the behaviour of several of these soils is compared. The chapter ends by summarising the more important facets of soil behaviour which, ideally, should be reproduced by constitutive models.

4.3 Behaviour of clay soils

4.3.1 Behaviour under one dimensional compression

The behaviour of clays under one dimensional compression is usually investigated in an *oedometer*. Typically a cylindrical sample of soil 60mm in diameter and 20mm high is subjected to vertical compression, while movement in the radial direction is prevented. Results from a test on reconstituted Pappadai clay (Cotecchia (1996)) are shown Figure 4.1, where the vertical effective stress, σ_v', is plotted against the void ratio, e. As is the custom, the vertical effective stress is plotted on a logarithmic scale. The soil sample has been subjected to compression with two cycles of unloading/reloading.

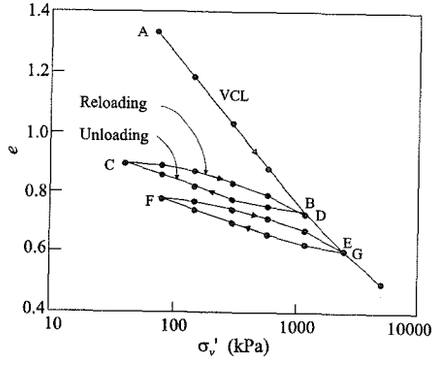

Figure 4.1: One dimensional consolidation of Pappadai clay (Cotecchia (1996))

In its initial condition, when placed in the oedometer, the reconstituted clay is in a normally consolidated state represented by point A in Figure 4.1. On loading (increasing σ_v') the sample compresses and its void ratio reduces travelling down the virgin consolidation line (VCL) (i.e. A to B). At B the sample is unloaded and swells travelling along the swelling line BC. On reloading the sample moves along the line CDE. At point D it rejoins the VCL and remains on this line with any further increase in vertical stress. If unloaded again the soil will move along another swelling curve. For example, when unloaded from point E the soil follows the line EF. It is generally assumed that swelling loops, such as BCD and EFG ,are parallel.

Soil which is on the VCL is said to be normally consolidated because it has never been subjected to a higher vertical stress. Soil on a swelling loop is defined as overconsolidated, with an overconsolidation ratio (OCR) defined as $\sigma_{v'\,max}/\sigma_v'$,

where $\sigma_v'_{max}$ and σ_v' are the maximum vertical effective stress the sample has ever experienced and the current vertical effective stress, respectively. For an increment of vertical stress normally consolidated soil suffers a much larger change in void ratio than an overconsolidated soil. This implies that overconsolidated soils are much stiffer than normally consolidated soils. Overconsolidated soils subjected to reloading experience a rapid reduction in stiffness as their stress state approaches the VCL.

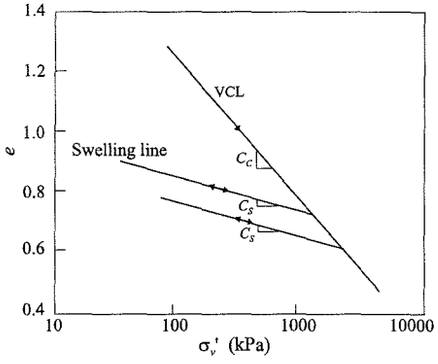

Figure 4.2: Idealised behaviour of clays in one dimensional consolidation

To use results like those shown in Figure 4.1 for design purposes simplifications are often introduced. For example, it is often assumed that the VCL is a straight line in e-$\log_{10}\sigma_v'$ space, with a gradient C_c, and that the swelling loop can be replaced with a single line of gradient C_s, see Figure 4.2. However, such an approach is not universally accepted. For example, some geotechnical engineers advocate plotting the results in $\log_{10}e$-$\log_{10}\sigma_v'$ space before making the idealisations for the VCL and swelling loops, while others prefer to plot results in terms of mean effective stress instead of vertical effective stress and/or to use natural logarithms. Some of these idealisation are discussed in greater depth in subsequent chapters.

4.3.2 Behaviour when sheared

The behaviour of soil when subjected to shear can be investigated in a range of apparatuses (e.g. triaxial, true triaxial, direct shear, simple shear, torsional shear, hollow cylinder etc.). However, the most common test performed on soils is the conventional triaxial test, in which a cylindrical sample is subjected to a constant radial stress, σ_r, and then sheared by either increasing (triaxial compression), or reducing (triaxial extension) the axial stress, σ_a. Most tests are performed on samples with a diameter of 38mm and a height of 76mm, although tests on larger samples with diameters of 50mm or 100mm and heights of 100m or 200mm are sometimes performed (especially when the effects of macrofabric are of interest). However, the latter tests are not popular for clay soils as pore pressure equalisation within the sample takes more time and therefore the tests take much longer to perform. Although there are loading platens at the top and bottom of the samples which can affect the stress distribution within the sample, uniform stress and strain conditions are assumed when interpreting the results.

Typical results from a series of tests performed on K_o consolidated samples of clay from Pentre in Shropshire are shown in Figure 4.3 (Connolly (1999)). All samples were K_o (i.e. no radial strain) normally consolidated from A to B, see Figure 4.3. The samples were then K_o unloaded to a particular value of

overconsolidation ratio, with each sample having a different OCR. At this point all drainage valves were closed and the samples were sheared undrained to failure, by either increasing or decreasing the axial stress. The resulting effective stress paths are shown in Figure 4.3. Several important facets of soil behaviour are evident in this plot. Firstly, the effective stress paths for samples with an OCR<3 bend to the left, having a smaller mean effective stress at the end of the test than they had at the beginning. This implies that, when sheared, the samples tried to contract, however, as undrained conditions were enforced this resulted in the generation of compressive (positive) pore water pressures. In contrast, the stress paths for the heavily overconsolidated samples (OCR≥3) bend to the right. This implies dilatant behaviour and the generation of tensile (negative) pore water pressures.

The stress states of all samples at failure tend to plot on a straight line which passes through the origin. This line is often referred to as the critical state line and is defined by an angle of shearing resistance, φ_{cs}'. The relevant φ_{cs}' angles for the stress paths shown in Figure 4.3 are 32° and 28° for compression and extension respectively. Although not evident in Figure 4.3, sometimes for heavily overconsolidated clay the stress paths pass above the critical state line before they reach failure. This implies a peak effective strength, in terms of a cohesion, c', and an angle of shearing resistance, φ', greater than that at ultimate failure.

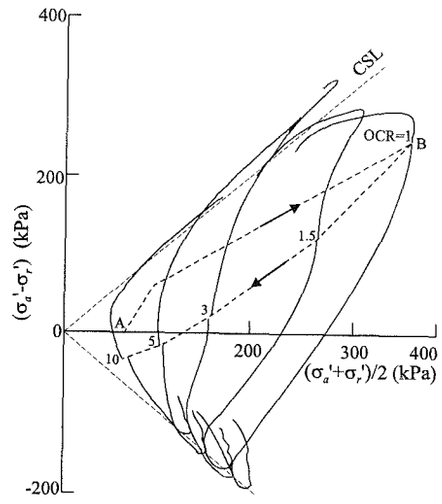

Figure 4.3: Effective triaxial stress paths for laminated Pentre clay (Connolly (1999))

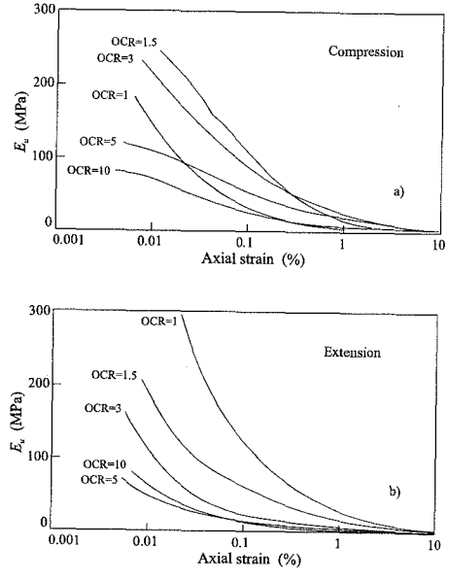

Figure 4.4: Undrained Young's moduli for Pentre clay (Connolly (1999))

For lightly overconsolidated samples the deviator stress ($=(\sigma_a'-\sigma_r')$) reaches a peak value and then reduces as ultimate failure is approached. This implies that the undrained strength, S_u, which is defined as half the maximum deviator stress, occurs before the full angle of shearing resistance has been mobilised. In contrast, for the heavily overconsolidated samples the deviator stress obtains its highest value at ultimate failure.

The variation of secant Young's modulus E_u ($=(\sigma_a-\sigma_{ao})/(\varepsilon_a-\varepsilon_{ao})$, (where σ_{ao} and ε_{ao} are the axial total stress and the axial strain just prior to undrained shearing respectively) with change in axial strain, $\varepsilon_a-\varepsilon_{ao}$, are shown in Figures 4.4a and 4.4b, for the compression and extension tests respectively. These plots clearly show that the soil becomes progressively less stiff as it is sheared. This occurs for all samples, but is particularly marked for the lightly overconsolidated samples where the stiffness drops by more than an order of magnitude.

It is also evident from Figure 4.4 that the stiffness magnitude depends on *OCR*. However, it should be noted that both *OCR* and the mean effective stress, p' ($=(\sigma_1'+\sigma_2'+\sigma_3')/3$), vary for each test. It is therefore not possible to identify the influence of each of these parameters from the data presented. The effect on stiffness of stress level alone is shown in Figure 4.5 (Soga *et al.* (1995)), where the results from four torsional tests on isotropically normally consolidated kaolin are presented. The tests differ only in that the magnitude of the consolidation stress changes. The results indicate the typical decay of stiffness with strain as shown in Figures 4.4a and 4.4b, but more importantly they indicate a nonlinear relationship between stiffness and mean effective stress, p'.

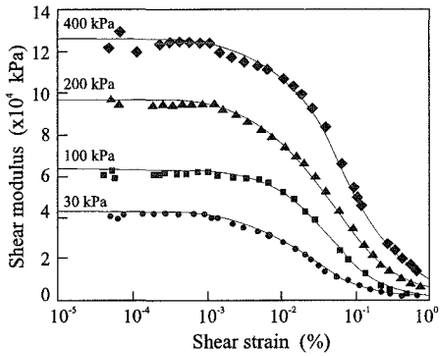

Figure 4.5: Dependence of kaolin stiffness on stress level (Soga et al. (1995))

From the above observations it is clear that the overconsolidation ratio and the magnitude of the mean effective stress have a large influence on soil behaviour.

4.3.3 Effect of stress path direction

The direction of the stress path also affects the stiffness characteristics of the soil. This has been investigated by Smith (1992) who performed a set of triaxial probing tests on Bothkennar clay, see Figure 4.6. All samples were first consolidated along path ABC and then swelled to D. K_o conditions were applied over portions BC and CD of this stress path. At point D the samples were allowed to age before being sheared drained along a variety of stress path directions. The variation of stiffness with strain for the probing stages of these tests is shown in Figures 4.7 and 4.8. In

Figure 4.7 the equivalent tangent bulk modulus, K_{tan}' ($=\Delta p'/\Delta\varepsilon_v$), normalised by the mean effective stress, p', is plotted against accumulated volumetric strain from the start of the probing stage, ε_v. The equivalent tangent shear modulus, G_{tan} ($=\Delta(\sigma_a'-\sigma_r')/3\Delta\varepsilon_s$), normalised by p' is plotted against accumulated triaxial deviatoric strain from the start of the probing stage, ε_s ($=2/3(\varepsilon_a-\varepsilon_r)$), in Figure 4.8. Both of these plots indicate that the soil stiffness decreases as the sample is strained and in this respect agree with the data given in Figure 4.4 for Pentre clay. However, they also show that the magnitude of the stiffness and the manner in which it decays with strain depend on the direction of the probing stress path. Also shown on Figure 4.8 is the value of the shear modulus, $G_{seismic}$, obtained from seismic tests performed at Bothkennar.

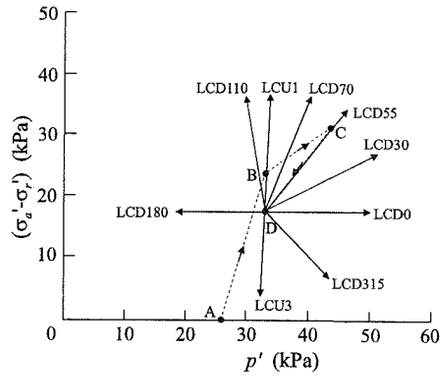

Figure 4.6: Probing stress paths for Bothkennar clay (Smith (1992))

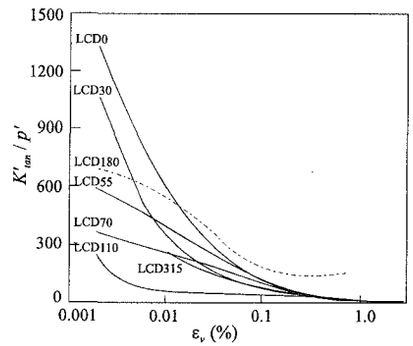

Figure 4.7: Bulk stiffness for Bothkennar clay (Smith (1992))

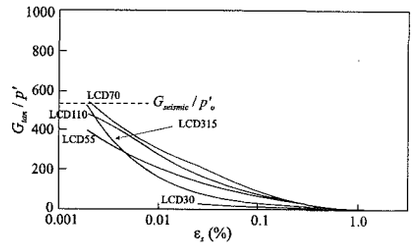

Figure 4.8: Shear stiffness for Bothkennar clay (Smith (1992))

4.3.4 Effect of the magnitude of the intermediate principal stress

As noted above, the drained strength parameters of Pentre clay vary depending on whether the clay is subjected to triaxial compression or extension. The differences between these two types of test are that in the compression tests the intermediate principal stress, σ_2, is equal to the minor principal stress, σ_3, and the major principal stress, σ_1, is vertical (i.e. $\alpha = 0°$, where α is the angle between the direction of the

major principal stress and the direction of deposition of the soil). In contrast, in the extension tests the intermediate principal stress, σ_2, equals the major principal stress, σ_1, and the latter stress now acts radially (i.e. $\alpha = 90°$). Consequently, the strength difference could result from the magnitude of the intermediate principal stress, σ_2, or the orientation, α, of σ_1, or a combination of both. To separate the effects of each of these differences, special tests must be performed. Results from tests to quantify the effect of the orientation of the major principal stress are discussed in the next section. The influence of the magnitude of the intermediate principal stress, σ_2, is considered below.

In order to isolate the effect of the intermediate principal stress, a series of tests should be performed in which only this quantity is varied, with all other parameters remaining the same. However, it is not possible to satisfy this requirement in conventional testing equipment and therefore tests must be performed in specialist equipment (i.e. true triaxial, directional shear cell or hollow cylinder apparatuses). To date, a comprehensive set of tests on a clay soil have yet to be performed, however data exist for sands and for clay-sand mixtures and these are discussed subsequently.

For clays, data exist from conventional triaxial and plane strain tests on the same soil and it is of interest to compare such results. As noted above, for triaxial compression $\sigma_2 = \sigma_3$ and $\alpha = 0°$, while for plane strain compression $\alpha = 0°$ and the intermediate stress σ_2 is somewhere between σ_1 and σ_3. Its exact value is difficult to measure in plane strain tests, but the test data that are available suggest that $0.15 \leq [(\sigma_2 - \sigma_3)/(\sigma_1 - \sigma_3)] \leq 0.35$. Vaid and Campanella (1974) tested similar samples of K_o normally consolidated undisturbed Haney clay in both triaxial and plane strain compression. In terms of undrained strength, S_u, these tests indicated that in plane strain the strength was some 10% higher than in triaxial compression (i.e. S_u/σ_{vc}' values of 0.296 and 0.268 were obtained in plane strain and triaxial compression respectively, where σ_{vc}' is the vertical effective consolidation stress). In terms of the peak angle of shearing resistance, φ', little difference was observed, with plane strain and triaxial compression giving values of 31.6° and 29.8°.

Vaid and Campanella also performed plane strain and triaxial extension tests on the same Haney clay. In triaxial extension $\sigma_2 = \sigma_1$ and $\alpha = 90°$, while for plane strain extension $\alpha = 90°$ and the intermediate stress σ_2 is again somewhere between σ_1 and σ_3. These results indicated that in plane strain S_u was about 25% higher than in triaxial extension (i.e. S_u/σ_{vc}' values of 0.211 and 0.168 were obtained in plane strain and triaxial extension respectively). Again, there were only small differences in the peak angle of shearing resistance, with the plane strain and triaxial tests giving 34.3° and 33.8° respectively.

A tentative conclusion from the above results from tests on clay is that the value of the intermediate principal stress has a modest effect on S_u, but little effect on φ'. For sands and sand-clay mixtures the effects on φ' appear to be greater, as is discussed in later sections of this chapter. The above results also indicate that the mode of shearing, compression or extension, and therefore the value of α has a much larger effect on both S_u and φ'.

4.3.5 Anisotropy

For convenience, laboratory test data are usually interpreted assuming that the clay behaves in an isotropic manner. This is evident in the data presented above, where equivalent isotropic measures of stiffness have been used. In general, soil is unlikely to be completely isotropic, because of the way in which it was originally deposited. In fact, it is only likely to be isotropic in the plane normal to its direction of deposition. Such a material is usually called 'cross anisotropic' or 'transversely isotropic'. In such a material both strength and stiffness depend on both the magnitude and orientation of the applied stresses. However, it is not easy to investigate the anisotropic behaviour of clays in conventional laboratory triaxial and shear box tests. This is one of the reasons why anisotropic effects have been neglected in the past. However, in recent years special testing devices (e.g. directional shear cell and hollow cylinder apparatus) have been developed to investigate anisotropic effects and, consequently, limited data exist.

Data on the undrained shear strength of K_o consolidated reconstituted Boston Blue clay are given in Figure 4.9. These data come from a series of tests performed in a directional shear cell by Seah (1990), in which similar samples were sheared with different orientations of the major principal stress to the direction of deposition, α (see insert in Figure 4.9). In Figure 4.9 the undrained shear strength, S_u, normalised by the vertical consolidation stress, σ_p' (i.e. vertical stress after K_o consolidation/ swelling), is plotted against α, for normally consolidated clay and clay with an OCR=4. It can be seen that the undrained strength drops significantly, by up to 50%, as α increases, indicating a strong anisotropic effect. If the clay was isotropic, the undrained strength would be unaffected by the value of α.

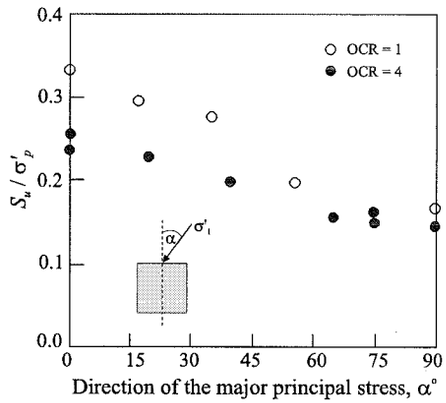

Figure 4.9: Undrained strength anisotropy of Boston Blue clay (Seah (1990))

There is also limited evidence that clay has an anisotropic stiffness. For example, the ratios of horizontal to vertical Young's modulus, E_h'/E_v', for a range of clay soils are tabulated in Table 4.1. The data suggest that this ratio depends on the clay type and its OCR, and varies with strain level during shearing.

4.3.6 Behaviour at large strains

Most laboratory testing devices cannot provide reliable data at large strains (>20%) due to the existence of non-uniformities occurring in the sample. For example,

Table 4.1: Review of stiffness ratio for natural and reconstituted clays

Reference	Soil	Strain level (%)	E_h'/E_v'
Ward *et al.* (1959)	London clay	0.2 0.6	1.4 2.4
Kirkpatric and Rennie (1972)	Reconstituted kaolin	very large	0.6 - 0.84
Franklin and Mattson (1972)	Reconstituted kaolin	very small	1.8 - 4.0
Atkinson (1975)	London clay	~ 1	2
Lo *et al.* (1977)	Leda clay	0.4 - 0.6	0.55
Saada *et al.* (1978)	Reconstituted Edgar kaolin	0.0001 0.007	1.25 1.35
Yong and Silvestri (1979)	Champlain clay	0.5 - 1.0	0.62
Graham and Houlsby (1983)	Winnipeg clay	~ 3	1.78
Kirkgard and Lade (1991)	S.Francisco bay mud	large	1.2 - 1.8

samples tend to develop localised failure zones at large strains, within which the stresses and strains cannot be reliably determined from the instrumentation.

The ring shear device was developed to overcome these shortcomings. In the version of this apparatus developed by Bishop *et al.* (1971), a ring of soil with an outer diameter of 152.4mm, an inner diameter of 101.6mm, and an initial thickness of 19mm, is sheared torsionally by rotating the top of the sample, while keeping the bottom fixed. During this process the vertical stress is usually maintained constant. The results from such tests indicate that, for many clays, strength decreases with large strains, dropping well below the peak strength observed at small strains in triaxial tests, until a residual value is reached. A typical result from such a test is shown in Figure 4.10 for London clay (Parathiras (1994)). It can be seen that at large strains the residual shear stress that the soil can sustain is approximately 50% of the peak value mobilised at much smaller strains. In terms of drained strength this residual condition corresponds to a cohesion, c_r'=2 kPa, and an angle of shearing resistance, φ_r'=12°. Typically, peak strength parameters

of c_p'=7 kPa and φ_p'=20° are quoted for London clay (Potts *et al.* (1997)). The reduction from peak to residual conditions is usually associated with the clay particles in the shear zone re-aligning themselves in the direction of shearing.

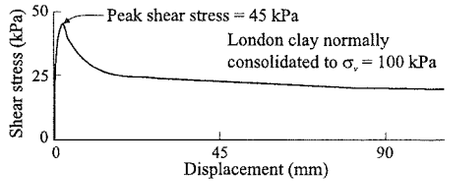

Figure 4.10: Residual strength of London clay (Parathiras (1994))

Clearly, residual strength and the rate of loss of strength from peak to residual can be very important in problems involving progressive failure and in situations where established failure surfaces already exist (e.g due to geological processes), see Potts *et al.* (1990).

4.4 Behaviour of sands

Many of the features described above for clays also apply to sands. However, sands possess additional complexities in their behaviour due their particulate nature and mode of deposition. Sands are more permeable than clays and therefore require shorter testing times. Consequently, more extensive testing of sands has been performed. The results from these tests enable the effects of the magnitude of the intermediate principal stress and of the anisotropic properties to be investigated in detail.

4.4.1 Behaviour under one dimensional compression

When considering the behaviour of a deposit of sedimentary clay, it is recognised that the clay begins its existence in the form of a slurry and that its current state results from a combination of consolidation and swelling stages. It may therefore be considered that all parts of the deposit have a unique starting point, namely, the clay slurry. However, such an assumption is not valid for sands, as sands can be deposited at different rates, resulting in a range of initial densities which influence subsequent behaviour.

Figure 4.11 shows the compression characteristics of two samples of Ticino sand (Pestana (1994)): one initially in a dense state with e_o = 0.6, the other in a loose state with e_o = 0.8. It should be noted that when attempting to set up identical sand samples, it is difficult to achieve exactly the same initial void ratio every time, either for a loose or a dense state. There is, therefore, a multiplicity of initial void ratios of sand for the same stress point. When the two samples are compressed one dimensionally, they follow normal compression lines (NCLs) which, at high values of effective stress, approach a unique virgin compression line (VCL). As the samples have different initial void ratios, the NCLs are not coincident. The VCL is approached when the sand particles start to crush. The magnitude of the vertical stress at which this occurs is dependent on the strength of the soil particles (Coop (1990)). For example, for the loose Ticino sand, shown in Figure 4.11, the VCL is reached only when the vertical effective stress exceeds 10 MPa. For the dense

sample an even higher vertical stress is required, due to the greater number of contact points compared to the loose sample. Consequently, the stress levels and behaviour associated with most geotechnical structures usually relate to the early parts of the normal compression curves (NCLs). Unloading/reloading results in hysteresis loops as discussed above for clay, and, although not shown in Figure 4.11, it is commonly observed that unload/reload loops are parallel when the data is plotted in e-$\log_{10}\sigma_v'$ space.

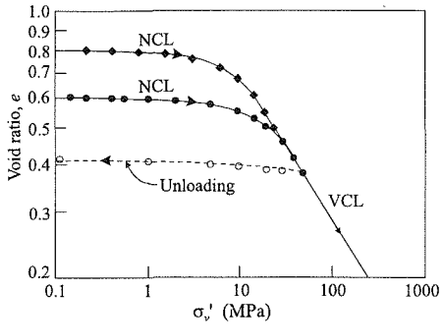

Figure 4.11: One dimensional behaviour of Ticino sand (Pestana (1994))

4.4.2 Behaviour when sheared

As with the behaviour under one dimensional compression, the behaviour of sand subjected to shearing is also affected by its initial density. Stress paths from triaxial compression and extension tests performed on loose Ham River sand (Kuwano (1998)) and dense Dunkirk sand (Kuwano (1998)) are shown in Figures 4.12 and 4.13 respectively. Both of these plots show results from a series of tests in which the sand was one dimensionally compressed and then unloaded from its initial state to a series of *OCR* values, before being sheared undrained in either triaxial compression or extension. The two figures, although for different sands, indicate typical trends observed in sand soils.

Considering the results from the loose Ham River sand shown in Figure 4.12, the following trends are noted. For all *OCR*s the stress paths for both the compression and extension tests initially bend to the left, indicating a contractant tendency, which manifests itself in positive (compressive) pore water pressures. However, with further loading this compressive tendency reduces and becomes dilative, imposing negative pore water pressures which bend the

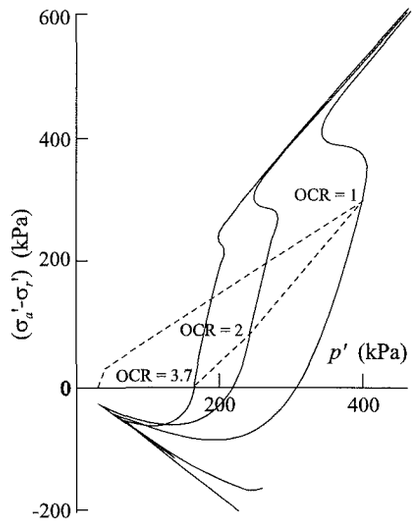

Figure 4.12: Effective triaxial stress paths for loose Ham River sand (Kuwano (1998))

stress path to the right. The kink in the stress path at which soil behaviour changes from a compressive to a dilative tendency is often referred to as the 'phase transformation point'. As the *OCR* increases the initial contractive tendency reduces and the dilative tendency increases.

For the dense Dunkirk sand, shown in Figure 4.13, a similar contractive followed by dilative tendency is only observed in the extension tests on samples with *OCR*s of 1 and 2. For extension tests on samples with a higher *OCR* and for all compressive tests only a dilative tendency is observed.

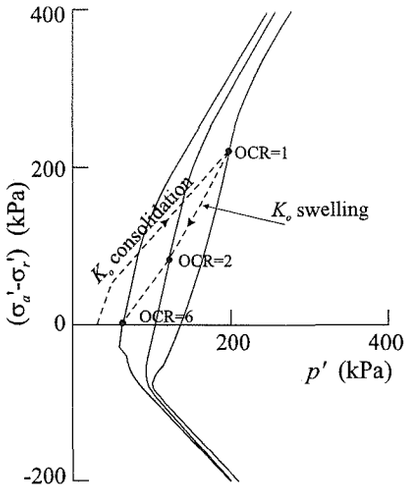

Figure 4.13: Effective triaxial stress paths for dense Dunkirk sand (Kuwano (1998))

For both the loose and dense sands the compression and extension tests approach a respective common failure line at large strains. Once this line is reached both the loose and dense sands have a tendency to dilate and therefore generate negative pore water pressures, which push the stress state further up the failure line. Consequently, the samples keep on taking higher and higher deviator stress and do not indicate a critical state condition as is usually observed for clays. The tests are usually stopped when either the pore water cavitates, the test apparatus reaches its load capacity, or when the samples become so non-uniform that measurements of stress and strain are unreliable. It is conceivable that a critical state does exist at higher stress levels, but that this can only be reached in special high pressure test apparatus. Such a hypothesis has been put forward by Coop (1990) and is consistent with the existence of a unique VCL at high stresses.

For both the loose and dense sands the failure lines are well defined in both triaxial compression and extension. These can be represented by straight lines in Figure 4.12 and 4.13 which pass through the origin of stress space (i.e. $c' = 0.0$), giving compression and extension strengths of $\varphi_c' = 33°$ and $\varphi_e' = 22°$ for loose Ham River sand, and $\varphi_c' = 37°$ and $\varphi_e' = 25°$ for dense Dunkirk sand. At low stress levels there is some experimental evidence to indicate that the failure lines are curved rather than straight giving angles of shearing resistance φ_c' and φ_e' that vary with mean effective stress (Stroud (1971)).

It can be concluded from Figures 4.12 and 4.13 that the looser the sand and the lower the *OCR*, the greater the initial contractive tendency on shearing. However, at large strains this tendency reduces and is replaced by a dilatant one which pushes the stress path along the failure line.

If the above tests had been performed drained, instead of undrained, the stress paths would have been straight and failure would have occurred when they

intersected the Mohr-Coulomb failure line. The stress state would then remain at this intersection point, regardless of any further straining. During further straining dilation would continue to occur with the rate of dilation being dependent on the initial void ratio and *OCR* of the sample. Such dilation appears to continue until large strains, when the sample becomes non-uniform and the measurements become unreliable.

The existence and location of a critical state for sand, while of academic interest, is only relevant in practice to undrained problems, or where the sand is kinematically constrained. As sands are usually highly permeable, undrained conditions only occur when the loading is extremely fast, such as under seismic loading. Kinematically constrained conditions might occur at the base of deep foundations, such as piles, and for penetration problems such as interpreting the results from cone penetrometers. For many geotechnical structures, such as shallow foundations and retaining walls, sand behaves in a drained manner and the volume changes at failure do not have a large influence on collapse loads and it is only the inclination of the failure line (i.e. φ') that is important. This problem is discussed further in Volume 2 of this book, when the analyses of boundary value problems are considered.

The variation of secant Young's modulus, E_u, with axial strain, $\varepsilon_a - \varepsilon_{ao}$, for the triaxial compression and extension tests on loose Ham River sand are shown in Figure 4.14a and 4.14b respectively. Similar plots for the dense Dunkirk sand are shown in Figures 4.15a and 4.15b. These plots show similar trends to those for Pentre clay given in Figure 4.4.

The effect on stiffness of stress level alone is shown in Figure 4.16, where results from three torsional shear tests on K_o normally compressed loose Ham River sand are presented. The tests differ only in that the compression stress changes. The results indicate a nonlinear relationship between stiffness and stress level. For further interpretation of these tests the reader is referred to Porović and Jardine (1994).

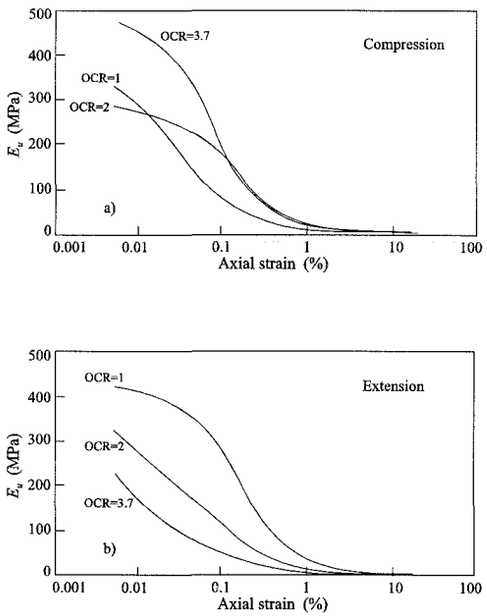

Figure 4.14: Undrained Young's moduli for loose Ham River sand (Kuwano (1998))

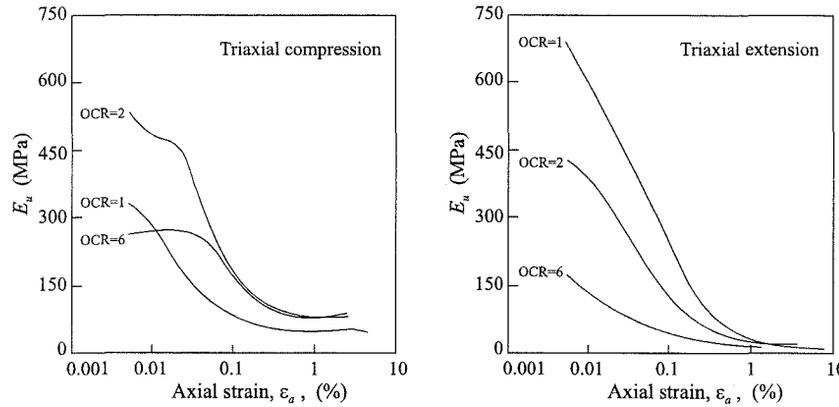

Figure 4.15: Undrained Young's moduli for dense Dunkirk sand (Kuwano (1998))

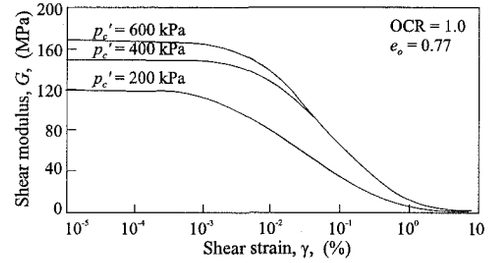

Figure 4.16: Dependence of sand stiffness on stress level (Porović and Jardine (1994))

4.4.3 Effect of the magnitude of the intermediate principal stress

As noted above, the drained strength parameters of sand differ depending on whether the sand is subjected to triaxial compression or extension. As stated in Section 4.3.4, in compression tests the intermediate principal stress, σ_2, is equal to the minor principal stress, σ_3, and the major principal stress, σ_1, is vertical (i.e. $\alpha = 0°$). In contrast, in extension tests the intermediate principal stress, σ_2, equals the major principal stress, σ_1, and the latter stress now acts horizontally (i.e. $\alpha = 90°$). Consequently, the strength difference could result from the magnitude of the intermediate principal stress, σ_2, or the orientation, α, of σ_1, or a combination of both. In order to investigate the influence of the magnitude of the intermediate principal stress, σ_2, results from isotropically compressed drained true triaxial tests

on dense Cumbria sand are considered in Figure 4.17 (Ochiai and Lade (1983)). In these tests the orientation of the sample was maintained the same and the major principal stress always acted in the vertical direction (i.e. $\alpha = 0°$). The samples were all sheared in a similar manner, with the exception that the relative magnitude of the intermediate principal stress differed from test to test. In Figure 4.17 the relative magnitude of the intermediate stress is expressed by the value of b $(=(\sigma_2-\sigma_3)/(\sigma_1-\sigma_3))$ and is plotted against the effective angle of shearing resistance, φ'. It can be seen that there is an increase of up to 9° in φ' as the intermediate principal stress increases from being equal to σ_3 ($b = 0$) towards σ_1 ($b = 1$).

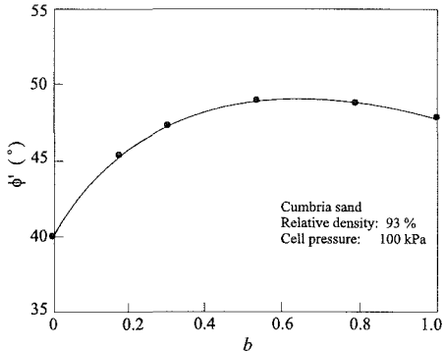

Figure 4.17: Effect of 'b' on ϕ' for sand (Ochiai and Lade (1983))

4.4.4 Anisotropy

As noted for clays, the behaviour of isotropic soils is independent of the orientation of the major principal stress, all other things being equal. Conversely, differences in behaviour observed in tests performed with different values of α (i.e. orientation of the direction of σ_1 with respect to the direction of deposition) provide an indication of the degree of anisotropy. Several sands have been tested in this way.

Results from a series of hollow cylinder tests performed on K_o normally compressed Ham River sand are presented in Figure 4.18, in the form of the peak angle of shearing resistance, φ_p', against α (Hight (1998)). All the tests had $b = 0.3$ and were similar except for the value of α. The results indicate a marked variation of φ_p' with α. The effect of changing α is large, indicating a high degree of anisotropy in the sand, much larger than that observed for clay soils.

Sands also exhibit anisotropic stiffness behaviour. This can be seen in Figure 4.19 which shows results from Kohata *et al.* (1997), who tested

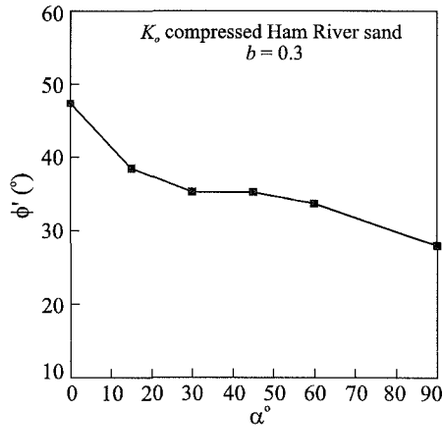

Figure 4.18: Effect of 'α' on ϕ' for sand (Hight (1998))

prismatic samples of a range of sands and gravels. For each soil type a series of samples were normally compressed with different ratios of the vertical and horizontal effective stress, σ_v'/σ_h'. The samples were then subjected to small cycles of both vertical and horizontal loading from which small strain values of E_v' and E_h' could be calculated. The results from three sands, Toyoura, SLB and Ticino, are shown in Figure 4.19 where the ratio E_v'/E_h' is plotted against the ratio σ_v'/σ_h'. If the samples were isotropic $E_v'/E_h'=1$, the greater the departure from this value the larger the anisotropy.

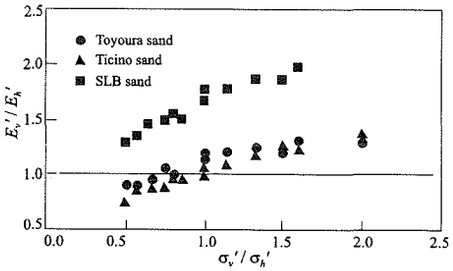

Figure 4.19: Stiffness anisotropy of sands (Kohata et al. (1997))

The results show that for all three sands the degree of anisotropy changes with σ_v'/σ_h'. The results also show that the amount of anisotropy is much larger for SLB sand than for both Toyoura and Ticino sand.

4.4.5 Behaviour at large strains

Sands do not appear to suffer large reductions in their strength properties when subjected to large strains. In this respect they differ from the behaviour of many clay soils.

4.5 Behaviour of soils containing both clay and sand

While clays and sands have many facets of behaviour in common, there are several important areas where they differ. In reality, soils seldom contain either all clay or all sand sized particles. In fact, many soils contain a range of particle sizes and their behaviour varies depending on their constitution. In this section the behaviour of some of these soils will be compared and some of the controlling factors identified.

4.5.1 Comparison of sedimentary soils

In this section the behaviour of the following nine sedimentary soils is compared:

1. Ham River sand (HRS) (Kuwano (1998)). This is a quartz based sand that was prepared in a loose state with an initial void ratio $e_o = 0.8$.
2. Dunkirk sand (DKS) (Kuwano (1998)). This is a quartz based sand with approximately 10% calcareous shell fragments, prepared in a dense state with an initial void ratio, $e_o = 0.65$.
3. HRS + 10% (by weight) kaolin (HK) (Georgiannou (1988)). This was prepared in a loose state with an initial void ratio $e_o = 0.8$.

4. Silica silt (HPF4) (Ovando-Shelley (1986)). This is an angular silt, obtained from pure quartz, which was prepared in a loose state with an initial void ratio $e_o = 0.95$.
5. Silica silt (HPF4) (Zdravković (1996)). This is the same silt as above, but prepared in a dense state, with an initial void ratio $e_0 = 0.65$.
6. Artificial clay (KSS) (Rossato (1992)). This material was prepared by mixing 50% kaolin with 25% fine sand and 25% silt and consolidating it from a slurry. The percentages quoted refer to proportion by weight.
7. Lower Cromer till (LCT) (Gens (1982)). This is reconstituted low plasticity till which was consolidated from a slurry.
8. Pentre clay (PEN) (Connolly (1999)). This is a natural silty clay.
9. Bothkennar clay (BC) (Smith (1992)). This is a natural high plasticity clay.

The grading curves for these materials are compared in Figure 4.20. All soils have been tested in the laboratory in a standard triaxial apparatus (Bishop and Wesley (1975)). The samples were sheared undrained in either compression or extension after K_o consolidation, followed by K_o swelling to a range of *OCR*s. In all cases, tests were performed covering a typical range of stresses encountered in engineering practice.

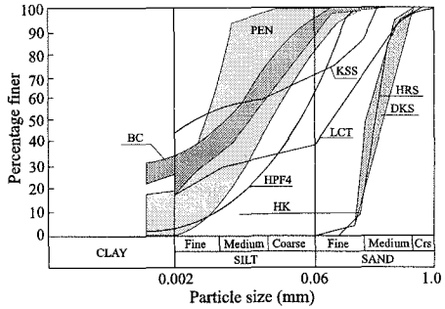

Figure 4.20: Grading curves for different soils

Figure 4.21 compares the compressibility of some of the above soils under K_o conditions. It is evident from this figure that the sands have the lowest compressibility and that compressibility increases with clay content. The Pentre clay, which consists of both clay and silt sized particles, shows a spread of volume change behaviour, depending on whether the samples were relatively silty or clayey, or had laminated or marbled macro-structures. To emphasize the effect of clay content on compressibility the results for HRS (0% kaolin), HK (10% kaolin), KSS (50% kaolin) and kaolin (100% kaolin) are compared in Figure 4.22.

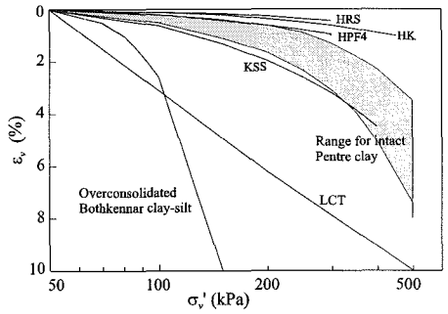

Figure 4.21: Compressibility of different soils

The effective stress paths observed in undrained triaxial compression and extension, following K_o consolidation to a range of *OCR*s, are presented in Figure 4.23 for eight of the soils listed above. The results for LCT, KSS and Pentre clays

show the typical behaviour associated with clay soils. The stress paths for normally consolidated samples all indicate a contractive tendency giving rise to positive, shear induced, pore water pressures. This contractive tendency diminishes with increase in *OCR* and after a critical *OCR* of about 3 is exceeded, the samples show a tendency to try to dilate producing negative, shear induced, pore water pressures. All stress paths indicate a well defined final state which corresponds to critical state conditions.

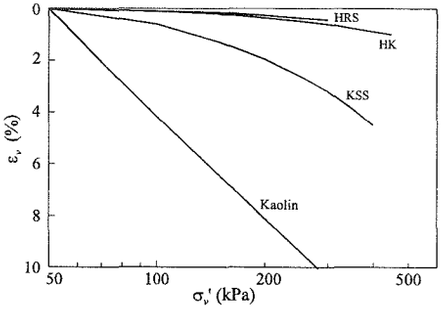

Figure 4.22: Effect of clay content on compressibility of soil

The behaviour of sand is illustrated by the results from HRS and DKS. With dense DKS the shearing in compression leads to the mean effective stress increasing for all *OCR*s, indicating a tendency to try to dilate and therefore the generation of negative shear induced pore water pressures. The same behaviour is observed at high *OCR*s when the sand is sheared in extension. However at low *OCR*s the extension tests indicate an initial contractive tendency (positive shear induced pore water pressures) followed by a tendency to try to dilate, and therefore the generation of negative shear induced pore water pressures. For both the compression and extension tests the effective stress paths travel along an inclined failure line to high values of mean effective stress. Within a range of stresses typically associated with geotechnical structures, they show no sign of reaching a well defined final stress state. The large strain behaviour of loose HRS is similar to that of the dense DKS. However, all the loose samples sheared in compression show a tendency to try to contract with the generation of positive shear induced pore water pressures on first shearing. On further shearing these samples revert to a tendency to dilate, resulting in the generation of negative shear induced pore water pressures.

It is interesting to compare the results from the tests on HRS and HK in more detail. HK consists of 90% HRS mixed with 10% kaolin. Both soils had an initial void ratio of 0.8. It is evident that the addition of the small quantity of kaolin has a marked effect on the shape of the stress paths. For the HK compression tests, the onset of a tendency to try to compress and therefore generate positive excess pore water pressures is abrupt and so intense that it results in a drop in deviatoric stress. Quite large positive shear induced pore water pressures are generated before the material undergoes phase transformation and begins to try to dilate. The effective stress paths then travel up the failure line to large values of mean effective stress in a similar manner to loose sands. Further tests were performed by Georgiannou (1988) with different amounts of kaolin. Some of the results for K_o normally consolidated samples are shown in Figure 4.24. Both triaxial compression and

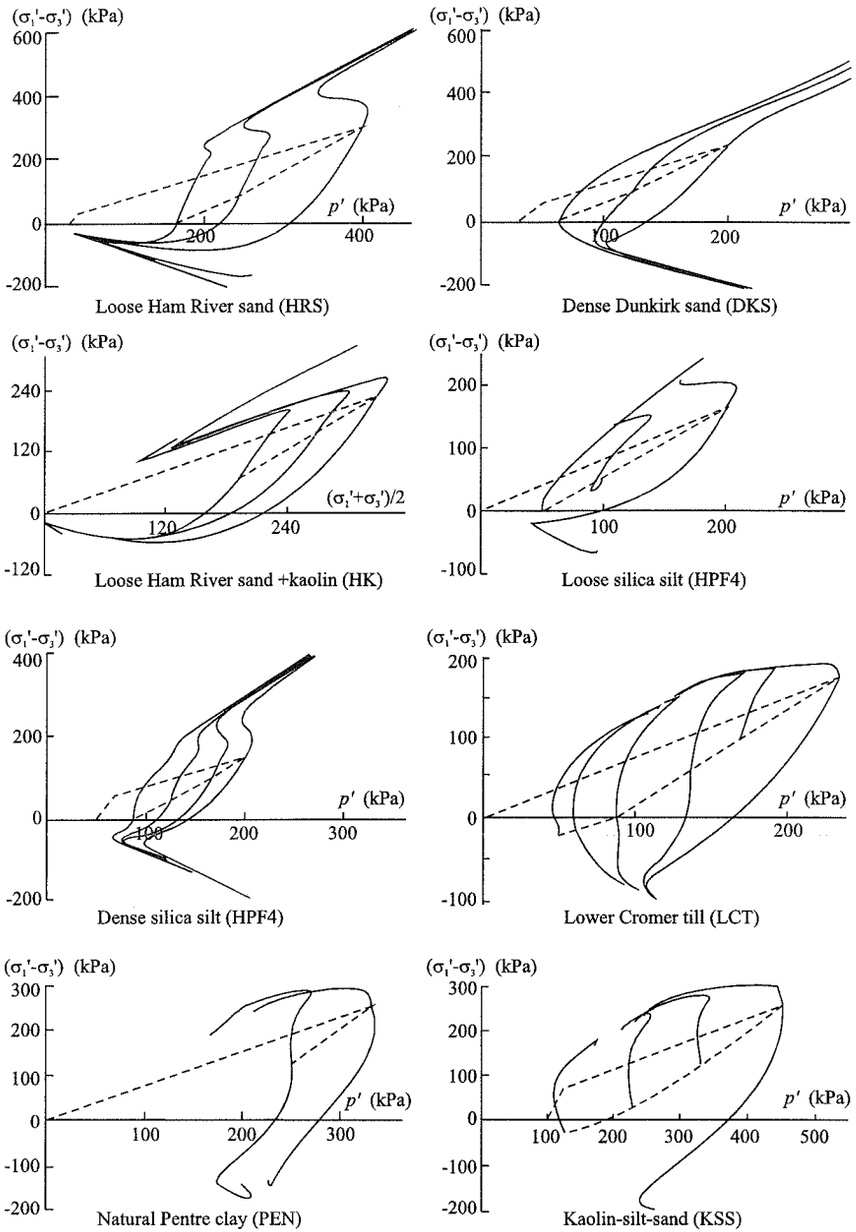

Figure 4.23: Effective stress paths in undrained triaxial compression and extension for different soil types

extension tests on HRS/kaolin mixtures, with 7.5% and 3.5% (by weight) kaolin, are shown. For comparison, results from tests on pure HRS are also shown. Clearly the addition of only a small quantity of clay can have a major effect on soil behaviour.

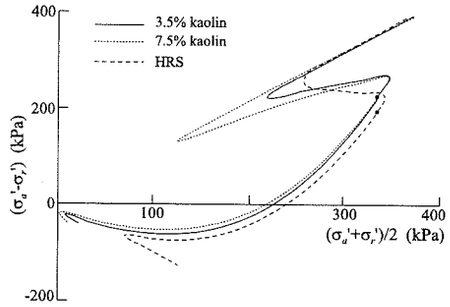

Figure 4.24: Effect of clay content on effective stress paths (Georgiannou (1988))

Comparing the behaviour of the silt HPF4 with the other materials it is evident that it follows the general pattern established for sands. Loose samples of HPF4 behave similarly to loose HRS, and dense HPF4 responds in the same way as dense DKS. The dense HPF4 shows a strongly dilative tendency in compression and does not reach a clear peak resistance or critical state in either compression or extension. A far more contractive tendency is observed in extension, with the mean effective stress falling by up to 50% before reaching the phase transformation point. In a similar fashion to that observed for dense sands, the dense HPF4 exhibits a weaker 'memory' of its past stress history than do most clay soils. Consequently, when tested in an overconsolidated state, its yielding characteristics appear to be less clearly associated with those shown by normally consolidated samples.

Zdravković (1996) also performed complex hollow cylinder tests on dense HPF4 silt. From some of these tests it was possible to determine the anisotropic stiffness properties. Results for K_o consolidated silt with an OCR=1.3 are shown in Figure 4.25 in the form of the variation of vertical and horizontal Young's moduli, E_v' and E_h', and shear modulus, G_{vh}, with increase in deviatoric strain, E_d. The large differences between E_v' and E_h' clearly indicate a strong anisotropic behaviour. The decrease in stiffness with increase in strain is typical of most soils as discussed in the previous sections of this chapter.

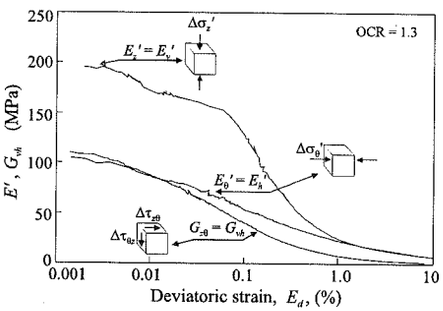

Figure 4.25: Anisotropic stiffness properties of silt (Zdravković (1996))

Hollow cylinder tests have also been performed on KSS and HK (Menkiti (1995)) and HRS (Hight (1998)). One objective of these tests was to investigate strength anisotropy. The variation of the angle of shearing resistance, φ', with α for all these materials and the dense HPF4 are given in Figure 4.26. All tests were

performed with the intermediate stress, σ_2, having a value between σ_1 and σ_3. The results show that φ' is affected by the value of α and therefore that the soils are anisotropic. They also indicate that the degree of anisotropy reduces as the clay content increases. For example, there is a much larger variation in φ' for HRS than there is for KSS.

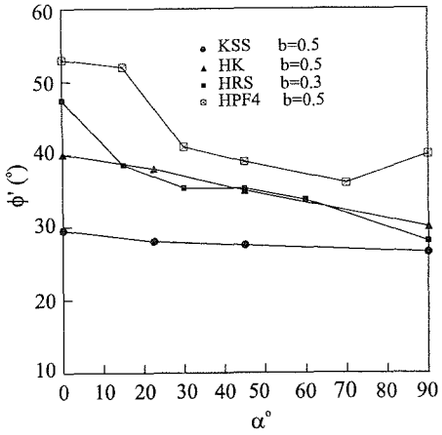

Figure 4.26: Variation of ϕ' with α for some soils

4.5.2 Residual soils

So far the discussion and data presented in this chapter have been concerned with sedimentary soils. Such soils are essentially eroded from parent rock, transported by either water or wind and then deposited in a new location. In contrast, residual soils are formed in-situ by weathering of parent rock. The initial parent rock is often quite strong, having a bonded structure and therefore possessing considerable cohesion. The weathering process reduces the number and the strength of the bonds. As weathering is not a uniform process, residual soils have a wide variation in cohesive strength. Clearly, the bonded structure of these soils affects their behaviour. Due to the highly variable nature of many residual soils it is often difficult to obtain an accurate picture of the effects of bonding. This has led some researchers to manufacture artificial bonded soils (Maccarini (1987), Bressani (1990).

As an example of the behaviour of a residual soil, results from two triaxial compression tests on Gravina di Puglia calcarenite are shown in Figure 4.27 (Lagioia (1994) and

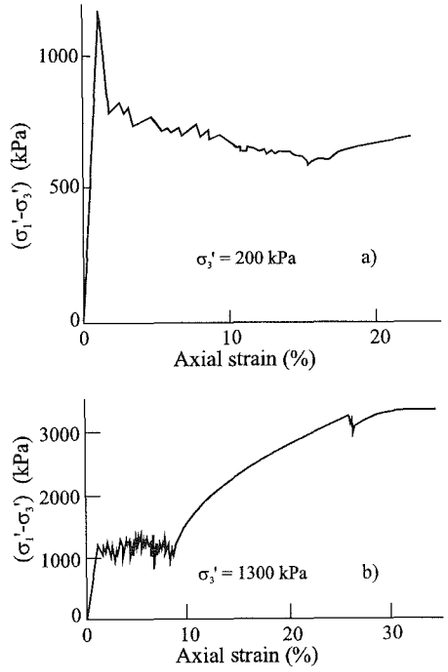

Figure 4.27: Stress-strain behaviour of calcarenite (Lagioia (1994))

Lagioia and Nova (1995)). Both samples were isotropically consolidated and then sheared drained. The results shown in Figure 4.27a are for a sample consolidated to a mean effective stress of 200kPa. When sheared the soil is initially very stiff, but when the deviatoric stress reaches 1200 kPa the bonds begin to break and the sample is unable to sustain further deviatoric stress and therefore the stress strain curve shows a softening effect. At first, this softening is quite steep but with further straining it becomes more moderate. After approximately 15% axial strain the devaitoric stress increases and the material begins to harden. The behaviour from then on resembles that of an unbonded sample of the same material. Different behaviour can be observed in Figure 4.27b which shows the results for a similar sample but this time isotropically consolidated to 1300 kPa before being sheared. Again, the sample is initially very stiff. However, when the deviatoric stress reaches nearly 1200 kPa and bond degradation begins, the deviator stress does not reduce but remains constant. This behaviour continues until the axial strain reaches approximately 10% at which point the material begins to harden again and behave like an unbonded sample. The spiky nature of the stress strain curve up to an axial strain of 10% is believed to reflect the erratic process involved in bond degradation. The behaviour during this process is clearly dependent on the level of the mean effective stress.

In both samples the stress-strain behaviour is approximately linear until bond degradation begins in earnest when the deviator stress reaches 1200 kPa. Closer inspection of this part of the loading curve indicates that the samples are behaving in an approximately isotropic linear elastic manner.

4.5.3 Residual strength

It was noted in Section 4.3.6 that when clays are sheared to very large strains their strength decreases from a peak value to a residual value. In terms of an angle of shearing resistance, φ, it is not unusual for the residual value to be half of the peak value for clays. Such a drop in strength at large strains is not observed for sands. For soils containing both sand and clay sized particles the behaviour depends on their clay content. This is illustrated in Figure 4.28a, which shows how the residual angle of shearing resistance, φ_r', varies with clay fraction (% of clay in terms of volume) for several real soils. For low clay fractions (< 20%) φ_r' is high, having a value similar to the peak angle of shearing resistance. However, at clay fractions greater than 40%, φ_r' is relatively small and much lower than the peak value. For clay fractions between 20% and 40%, φ_r' is sensitive to the clay content.

Further data on residual strength is given in Figure 4.28b, where φ_r' are plotted against plasticity index, I_p. As the value of the plasticity index reflects the clay fraction this data indicate a similar trend to the data observed in Figure 4.28a.

The effect of clay fraction on residual strength has been considered in detail by Lupini *et al.* (1981). They show that at low clay fractions turbulent shearing involves rolling and translation of soil particles, rather than direct sliding. In contrast, for high clay fractions shearing can involve sliding between clay particles

and that with straining the clay particles become aligned. It is this sliding and realignment that explains the low residual strengths.

4.6 Concluding remarks

Ideally any constitutive model should be able to simulate all the above facets of soil behaviour. However, only very advanced models are able to do this. Some of these are discussed in Chapter 8 where it is shown that, although they have the ability to accurately reproduce soil behaviour, they require many input parameters, some of which are not easily obtained from conventional site investigation or laboratory test data. Consequently, in practice a compromise has to be made between using an advanced model, which requires the results from special laboratory tests to define its parameters, and simple models, which may not reproduce all facets of soil behaviour, but can be readily defined from the available data. If the compromise is towards using the simpler models, which is often the case, it is important that the model can at least reproduce the soil behaviour that is dominant in the problem under investigation. For example, if the problem is likely to involve soil instability, then clearly it is important to model correctly the soil strength, for example in slope stability and retaining wall design. However, if the concern is over soil movements, it is more important to model accurately the stiffness behaviour of the soil, for example when assessing movements adjacent to a multi-strutted excavation.

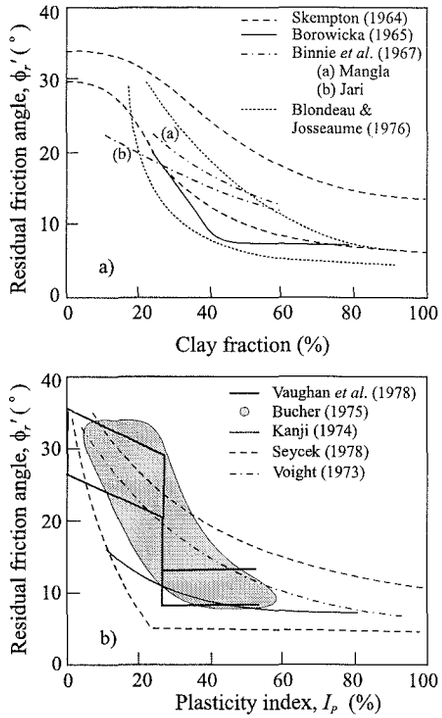

Figure 4.28: Effect of clay fraction and plasticity index on residual angle of shearing resistance (Lupini et al. (1981))

4.7 Summary

From the preceding discussions the following important facets of soil behaviour can be identified:

1. The stiffness, both bulk and shear, of a soil element increases as the soil particles are pressed closer together, i.e. as the mean effective stress, p', increases and/or the void ratio reduces.

2. Overconsolidated soils experience a rapid reduction in stiffness when a stress state associated with the pre-consolidation stress is reached.
3. On a change in the stress path direction the stiffness of the soil is likely to increase. This increase depends on the amount that the stress path changes direction. It is particularly noticeable if there is a complete reversal in direction and the soil is unloaded.
4. Generally, heavily overconsolidated clays and dense sands attempt to dilate (expand) on shearing, whereas lightly overconsolidated clays and loose sands attempt to compress. However, loose sands may revert to a tendency to dilate as failure is approached. The tendency to dilate also depends on mean effective stress. At low stress levels there is a greater tendency to dilate, whereas at very high stress levels even dense sands compress. If a fully saturated soil is sheared undrained, volume changes are suppressed. However, the volume change tendencies are still there and therefore negative shear induced pore water pressures are generated in dilatant phases of soil behaviour and positive shear induced pore water pressures occur during the compressive phases.
5. The shear stiffness reduces as the soil is sheared, i.e. due to an increase in deviator stress and strain. This change in stiffness is particularly marked at the beginning of shearing when the deviatoric strains are quite small.
6. A soil element fails when a certain stress state is reached. Such a stress state forms part of a failure criterion. In conventional soil mechanics a Mohr-Coulomb failure criterion is usually adopted. Undrained failure is not as well defined for sands as for clays. Some soils show brittle behaviour, where their capacity to sustain deviatoric stress reduces with further straining, after reaching the failure criterion.
7. Many real soils contain a range of particle sizes and their behaviour depends on their composition. A small amount of clay particles can have a large influence on the behaviour of sands.
8. Most soils show some tendency to behave in an anisotropic manner.

5. Elastic constitutive models

5.1 Synopsis

When presenting the finite element theory in Chapter 2 the soil was assumed to behave as an isotropic linear elastic material. This chapter and Chapters 6, 7 and 8 describe alternative constitutive models for soil behaviour. This chapter begins with a short introduction to stress invariants. The remainder of the chapter is devoted to elastic constitutive models. For completeness, both isotropic and anisotropic linear elastic models are presented. Nonlinear elastic models in which the material parameters vary with stress and/or strain levels are then described.

5.2 Introduction

The finite element theory presented in Chapter 2 assumed material behaviour to be linear elastic. The review of real soil behaviour presented in Chapter 4 indicates that such an assumption is unrealistic for soils. For realistic predictions to be made of practical geotechnical problems a more complex constitutive model is required.

In this chapter and Chapters 6, 7 and 8 a variety of constitutive models that have been, and still are, used to represent soil behaviour are described. This chapter begins by introducing the concept of invariant measures of stress and strain, which are particularly useful when considering the behaviour of isotropic soils. The remainder of the chapter is then devoted to elastic constitutive models which, although of limited use, form a useful introduction to constitutive models. For completeness, both isotropic and anisotropic linear elastic constitutive matrices are given. Nonlinear elastic models in which the material parameters vary with stress and/or strain levels are then described.

More advanced constitutive models, based on elasto-plasticity, are presented in Chapters 6, 7 and 8. The extension of the finite element theory to deal with nonlinear constitutive models forms the topic of Chapter 9. The usefulness and applicability of the various constitutive models to real geotechnical problems is discussed in Volume 2 of this book.

5.3 Invariants

The magnitudes of the components of the stress vector (i.e. σ_x, σ_y, σ_z, τ_{xy}, τ_{xz}, τ_{yz}) depend on the chosen direction of the coordinate axes, see Figure 5.1. The

principal stresses (σ_1, σ_2 and σ_3) however, always act on the same planes and have the same magnitude, no matter which direction is chosen for the coordinate axes. They are therefore *invariant* to the choice of axes. Consequently, the state of stress can be fully defined by either specifying the six component values for a fixed direction of the coordinate axis, or by specifying the magnitude of the principal stresses and the directions of the three planes on which these principal stresses act. In either case six independent pieces of information are required.

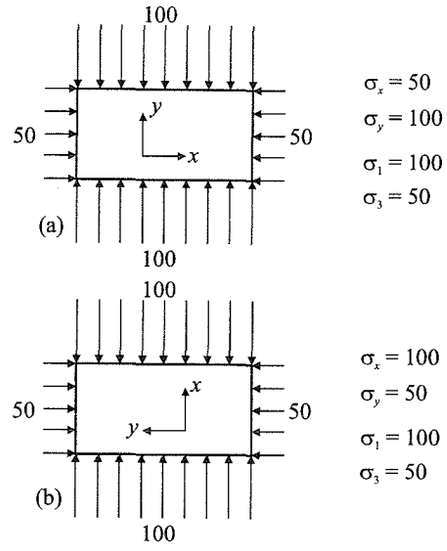

Figure 5.1: Effect of change of axes on magnitude of stress components

For materials which are isotropic, i.e. whose properties are the same in all directions, it is often convenient to consider only certain aspects of the stress tensor, rather than to have to specify all six quantities. For example, if one is only interested in the magnitude of maximum and minimum direct stresses in the material, then only the principal values σ_1 and σ_3 are required. On the other hand, if one is interested in the overall magnitude of the stress, all three principal stresses would be needed, but not the directions of the planes on which they act. In geotechnical engineering it is often convenient to work with alternative invariant quantities which are combinations of the principal effective stresses. A convenient choice of these invariants is:

Mean effective stress:
$$p' = \tfrac{1}{3}\left(\sigma_1' + \sigma_2' + \sigma_3'\right) \qquad (5.1)$$

Deviatoric stress:
$$J = \tfrac{1}{\sqrt{6}}\sqrt{\left(\sigma_1' - \sigma_2'\right)^2 + \left(\sigma_2' - \sigma_3'\right)^2 + \left(\sigma_3' - \sigma_1'\right)^2} \qquad (5.2)$$

Lode's angle:
$$\theta = \tan^{-1}\left[\tfrac{1}{\sqrt{3}}\left(2\frac{(\sigma_2' - \sigma_3')}{(\sigma_1' - \sigma_3')} - 1\right)\right] \qquad (5.3)$$

This choice of invariants is not arbitrary because the above quantities have geometric significance in principal effective stress space. The value of p' is a measure of the distance along the space diagonal ($\sigma_1'=\sigma_2'=\sigma_3'$), of the current deviatoric plane from the origin, in principal effective stress space (a deviatoric plane is any plane perpendicular to the space diagonal). The value of J provides a measure of the distance of the current stress state from the space diagonal in the deviatoric plane, and the magnitude of θ defines the orientation of the stress state

within this plane. For example, consider the stress state represented by point P ($\sigma_1'^P$, $\sigma_2'^P$, $\sigma_3'^P$) which has invariants p'^P, J^P and θ^P in Figure 5.2. The distance of the deviatoric plane in which point P lies, from the origin, is $p'^P\sqrt{3}$, see Figure 5.2a. The distance of P from the space diagonal in the deviatoric plane is given by $J^P\sqrt{2}$, and the orientation of P within this plane by the value of θ^P, see Figure 5.2b. On this figure, $(\sigma_1')^{pr}$, $(\sigma_2')^{pr}$ and $(\sigma_3')^{pr}$ refer to the projections of the principal stress axes onto the deviatoric plane. As $\sigma_1'^P \geq \sigma_2'^P \geq \sigma_3'^P$, P is constrained to lie between the lines marked $\theta = -30°$ and $\theta = +30°$. These limiting values of θ correspond to triaxial compression ($\sigma_1'^P \geq \sigma_2'^P = \sigma_3'^P$) and triaxial extension ($\sigma_1'^P = \sigma_2'^P \geq \sigma_3'^P$) respectively.

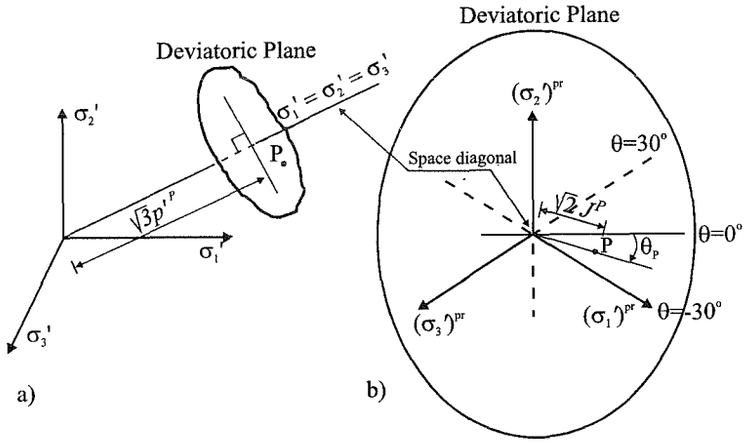

Figure 5.2: Invariants in principal stress space

The principal stresses can be expressed in terms of these alternative invariants using the following equations:

$$\begin{Bmatrix}\sigma_1'\\ \sigma_2'\\ \sigma_3'\end{Bmatrix} = p'\begin{Bmatrix}1\\1\\1\end{Bmatrix} + \frac{2}{\sqrt{3}}J\begin{Bmatrix}\sin\left(\theta+\frac{2\pi}{3}\right)\\ \sin\theta\\ \sin\left(\theta-\frac{2\pi}{3}\right)\end{Bmatrix} \tag{5.4}$$

The above discussion is also applicable to the accumulated strain vector (ε_x, ε_y, ε_z, γ_{xy}, γ_{xz}, γ_{yz}) and its principal values (ε_1, ε_2 and ε_3). It is also applicable to the incremental strain vector ($\Delta\varepsilon_x$, $\Delta\varepsilon_y$, $\Delta\varepsilon_z$, $\Delta\gamma_{xy}$, $\Delta\gamma_{xz}$, $\Delta\gamma_{yz}$). However, for geotechnical engineering only two alternative invariants are usually defined. A suitable choice for these invariants is:

Incremental volumetric strain:

$$\Delta\varepsilon_v = \Delta\varepsilon_1 + \Delta\varepsilon_2 + \Delta\varepsilon_3 \tag{5.5}$$

Incremental deviatoric strain:

$$\Delta E_d = \frac{2}{\sqrt{6}}\sqrt{\left(\Delta\varepsilon_1 - \Delta\varepsilon_2\right)^2 + \left(\Delta\varepsilon_2 - \Delta\varepsilon_3\right)^2 + \left(\Delta\varepsilon_3 - \Delta\varepsilon_1\right)^2} \tag{5.6}$$

The basis for selecting the above quantities is that the incremental work $\Delta W = \{\sigma'\}^T\{\Delta\varepsilon\} = p'\Delta\varepsilon_v + J\Delta E_d$. The accumulated strain invariants are then given by $\varepsilon_v = \int\Delta\varepsilon_v$ and $E_d = \int\Delta E_d$. The accumulated volumetric strain, ε_v, can also be obtained from Equation (5.5), but with the incremental principal strains replaced by the accumulated values. At first sight it might also seem that, by substituting the accumulated principal strains for the incremental values in Equation (5.6), the value of E_d can be obtained. However, in general, this is not so. The reason why such an approach is incorrect is shown diagrammatically in Figure 5.3a, which shows part of a deviatoric plane in principal strain space. At position 'a' an element of soil has been subjected to no deviatoric strain, $E_d^a = 0$. Some loading is applied and the strain state moves to position 'b'. The incremental deviatoric strain is ΔE_d^b and the accumulated deviatoric strain is $E_d^b = \Delta E_d^b$. A further increment of load is applied which causes a change in the direction of the strain path. This causes the strain state to move to position 'c', with an incremental deviatoric strain ΔE_d^c. The accumulated deviatoric strain is now given by $E_d^c = \Delta E_d^b + \Delta E_d^c$, and is represented by the length of the path 'abc' on Figure 5.3a. If an equation similar to Equation (5.6) is evaluated with the principal accumulated strains corresponding to position 'c', it represents the length of the path 'ac'. This clearly does not reflect the accumulated value of the incremental deviatoric strain as defined by Equation (5.6). The paths 'abc' and 'ac' are identical only if the directions of ΔE_d^b and ΔE_d^c are the same in the deviatoric plane, see Figure 5.3b. Clearly, such a situation only occurs if the strain path remains straight during loading. In general, such a condition does not apply. It might, however, occur in some laboratory tests for determining soil properties.

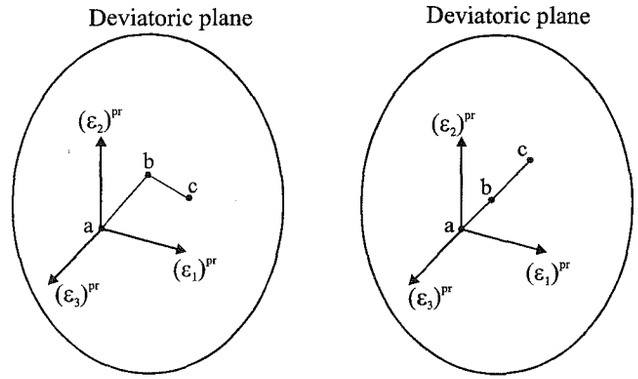

a) Change in the strain path direction b) Monotonic strain path direction

Figure 5.3: Strain path directions in the deviatoric plane

Following similar logic, it can also be shown that $J \neq \int \Delta J$ if ΔJ is calculated from an equation similar to Equation (5.2), but with the accumulated principal stresses replaced by the incremental values.

Alternative definitions for stress and strain invariants can be, and are, used. Some of these are discussed subsequently in Chapter 8.

5.4 Elastic behaviour

The basic assumption of elastic behaviour, that is common to all the elastic models discussed here, is that the directions of principal incremental stress and incremental strain coincide. The general constitutive matrix relates increments of total stress to increments of strain:

$$\begin{Bmatrix} \Delta\sigma_x \\ \Delta\sigma_y \\ \Delta\sigma_z \\ \Delta\tau_{xz} \\ \Delta\tau_{yz} \\ \Delta\tau_{xy} \end{Bmatrix} = \begin{bmatrix} D_{11} & D_{12} & D_{13} & D_{14} & D_{15} & D_{16} \\ D_{21} & D_{22} & D_{23} & D_{24} & D_{25} & D_{26} \\ D_{31} & D_{32} & D_{33} & D_{34} & D_{35} & D_{36} \\ D_{41} & D_{42} & D_{43} & D_{44} & D_{45} & D_{46} \\ D_{51} & D_{52} & D_{53} & D_{54} & D_{55} & D_{56} \\ D_{61} & D_{62} & D_{63} & D_{64} & D_{65} & D_{66} \end{bmatrix} \begin{Bmatrix} \Delta\varepsilon_x \\ \Delta\varepsilon_y \\ \Delta\varepsilon_z \\ \Delta\gamma_{xz} \\ \Delta\gamma_{yz} \\ \Delta\gamma_{xy} \end{Bmatrix} \tag{5.7}$$

As noted in Section 3.4, it is possible to divide the total stress constitutive matrix $[\boldsymbol{D}]$, given above, into the sum of the effective stress matrix $[\boldsymbol{D}']$ and the pore fluid matrix $[\boldsymbol{D}_f]$. Consequently, the constitutive behaviour can be defined either by $[\boldsymbol{D}]$ or $[\boldsymbol{D}']$.

Elastic constitutive models can take many forms: some assume the soil to be isotropic, others assume that it is anisotropic; some assume the soil to be linear, others that it is nonlinear, with parameters dependent on stress and/or strain level. Several of the models that have been used for geotechnical analysis are presented below.

5.5 Linear isotropic elasticity

An isotropic material is one that has point symmetry, i.e. every plane in the body is a plane of symmetry for material behaviour. In such a situation it can be shown that only two independent elastic constants are necessary to represent the behaviour and that the constitutive matrix becomes symmetrical. In structural engineering it is common to use Young's modulus, E', and Poisson's ratio, μ', for these parameters. Equation (5.7) then takes the form shown in Equation (5.8).

If the material behaviour is linear then E' and μ' are constants and the constitutive matrix expressed as a relationship between accumulated effective stresseses $\{\sigma'\}$ and strains $\{\varepsilon\}$ is the same as that given in Equation (5.8). It is also possible to express the constitutive matrix as a relationship between total stress and strain, either on an incremental or accumulated basis. In this case the appropriate parameters are the undrained Young's modulus, E_u, and Poisson's ratio, μ_u.

$$\begin{Bmatrix} \Delta\sigma'_x \\ \Delta\sigma'_y \\ \Delta\sigma'_z \\ \Delta\tau_{xz} \\ \Delta\tau_{yz} \\ \Delta\tau_{xy} \end{Bmatrix} = \frac{E'}{(1+\mu')(1-2\mu')} \begin{bmatrix} 1-\mu' & \mu' & \mu' & 0 & 0 & 0 \\ & 1-\mu' & \mu' & 0 & 0 & 0 \\ & & 1-\mu' & 0 & 0 & 0 \\ & & & \frac{1-2\mu'}{2} & 0 & 0 \\ & sym & & & \frac{1-2\mu'}{2} & 0 \\ & & & & & \frac{1-2\mu'}{2} \end{bmatrix} \begin{Bmatrix} \Delta\varepsilon_x \\ \Delta\varepsilon_y \\ \Delta\varepsilon_z \\ \Delta\gamma_{xz} \\ \Delta\gamma_{yz} \\ \Delta\gamma_{xy} \end{Bmatrix} \tag{5.8}$$

For geotechnical purposes, it is often more convenient to characterize soil behaviour in terms of the elastic shear modulus, G, and effective bulk modulus, K'. Equation (5.7) then becomes:

$$\begin{Bmatrix} \Delta\sigma'_x \\ \Delta\sigma'_y \\ \Delta\sigma'_z \\ \Delta\tau_{xz} \\ \Delta\tau_{yz} \\ \Delta\tau_{xy} \end{Bmatrix} = \begin{bmatrix} K'+\frac{4}{3}G & K'-\frac{2}{3}G & K'-\frac{2}{3}G & 0 & 0 & 0 \\ & K'+\frac{4}{3}G & K'-\frac{2}{3}G & 0 & 0 & 0 \\ & & K'+\frac{4}{3}G & 0 & 0 & 0 \\ & & & G & 0 & 0 \\ & sym & & & G & 0 \\ & & & & & G \end{bmatrix} \begin{Bmatrix} \Delta\varepsilon_x \\ \Delta\varepsilon_y \\ \Delta\varepsilon_z \\ \Delta\gamma_{xz} \\ \Delta\gamma_{yz} \\ \Delta\gamma_{xy} \end{Bmatrix} \tag{5.9}$$

where

$$G = \frac{E'}{2(1+\mu')} \quad ; \quad K' = \frac{E'}{3(1-2\mu')} \tag{5.10}$$

Again, it is also possible to express the constitutive matrix in terms of undrained stress parameters. As water cannot sustain shear stresses, the undrained and effective shear modulus are the same, hence the use of G without a prime in Equations (5.9) and (5.10). Consequently, only K' has to be replaced by K_u in Equation (5.9) to obtain the total stress constitutive matrix, $[\boldsymbol{D}]$.

These linear isotropic elastic models do not simulate any of the important facets of soil behaviour highlighted in Chapter 4. They therefore have limited use for analysing geotechnical problems. Their inability to reproduce even basic soil behaviour is evident from the linear deviatoric stress - strain and deviatoric strain - volume strain curves that they predict for an ideal drained triaxial compression test, see Figure 5.4. However, these models are often used to represent structural elements (e.g. retaining walls, floor slabs etc.)

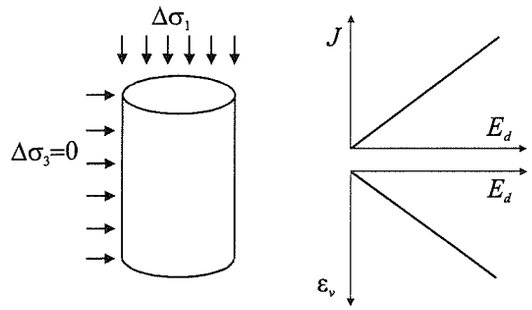

Figure 5.4: Elastic prediction of a drained triaxial compression test

5.6 Linear anisotropic elasticity

As shown in Chapter 4 soil behaviour is rarely truly isotropic, often exhibiting anisotropy. Mathematically, if a material is fully anisotropic, the [***D***] matrix in Equation (5.7) becomes fully populated. This implies that 36 independent parameters are required to define the values of D_{ij}. However, thermodynamic strain energy considerations (Love (1927)) imply that the [***D***] matrix must be symmetrical, i.e. $D_{ij} = D_{ji}$, for $i \neq j$. The total number of independent anisotropic parameters therefore reduces to 21.

Many materials, however, show limited forms of anisotropy. For soil deposits it is often assumed that their anisotropic characteristics depend on the mode of deposition and stress history. Soils that are deposited normally onto a plane are likely to exhibit an axis of symmetry in the depositional direction, i.e. their characteristics do not vary in the plane of deposition. In Figure 5.5 Cartesian coordinates are allocated to a sediment such that the z-axis is in the direction of sediment deposition, S, while x and y axes are in the plane of deposition, P.

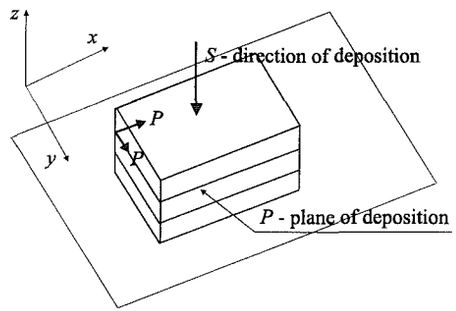

Figure 5.5: Axes orientations for considering transverse isotropy

The above type of anisotropy is known as 'transverse isotropy', or 'cross-anisotropy' or 'orthotropy' and reduces the number of unknown material parameters to seven. The relationship between incremental stress and strain components is given by matrix [***D***] in Equation (5.11):

$$\begin{bmatrix} A(1-\mu'_{SP}\mu'_{PS})E'_P & A(\mu'_{PP}+\mu'_{SP}\mu'_{PS})E'_P & A\mu'_{SP}(1+\mu'_{PP})E'_P & 0 & 0 & 0 \\ A(\mu'_{PP}+\mu'_{SP}\mu'_{PS})E'_P & A(1-\mu'_{SP}\mu'_{PS})E'_P & A\mu'_{SP}(1+\mu'_{PP})E'_P & 0 & 0 & 0 \\ A\mu'_{PS}(1+\mu'_{PP})E'_S & A\mu'_{PS}(1+\mu'_{PP})E'_S & A(1-\mu'_{PP}\mu'_{PP})E'_S & 0 & 0 & 0 \\ 0 & 0 & 0 & G_{PS} & 0 & 0 \\ 0 & 0 & 0 & 0 & G_{PS} & 0 \\ 0 & 0 & 0 & 0 & 0 & G_{PP} \end{bmatrix} \tag{5.11}$$

where

$$A = \frac{1}{1-2\mu'_{SP}\mu'_{PS}-2\mu'_{SP}\mu'_{PS}\mu'_{PP}-\mu'^2_{PP}} \tag{5.12}$$

E_S' - Young's modulus in the depositional direction;
E_P' - Young's modulus in the plane of deposition ;
μ_{SP}' - Poisson's ratio for straining in the plane of deposition due to the stress acting in the direction of deposition;
μ_{PS}' - Poisson's ratio for straining in the direction of deposition due to the stress acting in the plane of deposition;
μ_{PP}' - Poisson's ratio for straining in the plane of deposition due to the stress acting in the same plane;
G_{PS} - Shear modulus in the plane of the direction of deposition;
G_{PP} - Shear modulus in the plane of deposition.

However, due to symmetry requirements it can be shown that:

$$\frac{\mu'_{SP}}{E'_S} = \frac{\mu'_{PS}}{E'_P} \tag{5.13}$$

and

$$G_{PP} = \frac{E'_P}{2(1+\mu'_{PP})} \tag{5.14}$$

This reduces the number of parameters required to define transversely isotropic behaviour from seven to five. Matrix [***D***] in Equation (5.11) then reduces to the symmetrical form of Equation (5.15).

Again, it is possible to express the constitutive matrix given by Equations (5.15) in terms of undrained stress parameters. As the material parameters are constant, the [***D***] matrices given in Equations (5.11) and (5.15) also relate accumulated stresses and strains. While the model enables anisotropic stiffness to be modelled, it does not satisfy any of the other important facets of soil behaviour discussed in Chapter 4.

$$\begin{bmatrix} A(1-\mu_{SP}'^2\frac{E_P'}{E_S'})E_S' & A(\mu_{PP}'+\mu_{SP}'^2\frac{E_P'}{E_S'})E_S' & A\mu_{SP}'(1+\mu_{PP}')E_S' & 0 & 0 & 0 \\ & A(1-\mu_{SP}'^2\frac{E_P'}{E_S'})E_S' & A\mu_{SP}'(1+\mu_{PP}')E_S' & 0 & 0 & 0 \\ & & A(1-\mu_{PP}'^2\frac{E_S'^2}{E_P'})E_S' & 0 & 0 & 0 \\ & & & G_{PS} & 0 & 0 \\ & & & & G_{PS} & 0 \\ & & & & & \frac{E_P'}{2(1+2\mu_{PP}')} \end{bmatrix} \quad (5.15)$$

where

$$A = \frac{1}{\left(1+\mu_{PP}'\right)\left[\frac{E_S'}{E_P'}\left(1-\mu_{PP}'\right)-2\mu_{SP}'^2\right]} \quad (5.16)$$

5.7 Nonlinear elasticity

5.7.1 Introduction

A logical first step to improving the linear elastic models described above is to make the material parameters depend on stress and/or strain level. By doing this it is possible to satisfy several of the requirements discussed in Chapter 4. As there are only two parameters required to define isotropic elastic behaviour, this is relatively straightforward. However, it is much more difficult for anisotropic behaviour as there are five material constants. Consequently, most of the nonlinear elastic models that are currently in use assume isotropic behaviour.

When dealing with isotropic elasticity, the two material properties can be chosen arbitrarily from E, μ, K or G. For geotechnical engineering it is often convenient to use bulk modulus, K, and shear modulus, G. The reason for this is that the behaviour of soil under changing mean (bulk) stress is very different to that under changing deviatoric (shear) stress. For instance, under increasing mean stress the bulk stiffness of the soil will usually increase, whereas under increasing deviatoric stress the shear stiffness will reduce. Furthermore, inspection of Equation (5.9) indicates that, for isotropic elasticity, the two modes of deformation are decoupled, i.e. changes in mean stress, $\Delta p'$, do not cause distortion (no shear strains) and changes in deviatoric stress do not cause volume change. While this is clearly helpful when formulating a constitutive model, it must be noted that real soils do not usually behave in this decoupled manner. For example, the application of a pure deviatoric stress in a direct or simple shear test does inflict volumetric straining.

Five particular nonlinear models are now presented. These are the bi-linear, K-G, hyperbolic and two small strain stiffness models.

5.7.2 Bi-linear model

This model assumes that the bulk and shear stiffness are constant until the stress state reaches the failure condition. Once this occurs, the tangential shear modulus, G, is set to a very small value. Ideally, it should be set to zero, but if this is done there would not be a one to one relationship between incremental deviatoric stresses and strains. This would lead to ill conditioning of the finite element equations and numerical instability. Therefore, in practice G is set to a small, but finite value. The resulting stress-strain curves for this model are shown in Figure 5.6. Clearly, if on reaching failure the stress state is unloaded, the shear modulus would revert to its initial pre-failure value.

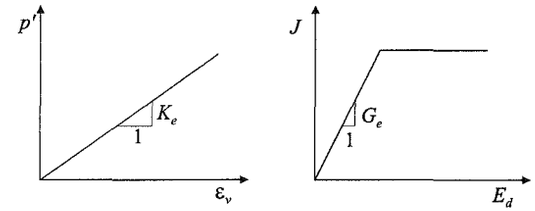

Figure 5.6: Bi-linear model

This model requires two elastic parameters, K_e and G_e (or the equivalent E_e and μ_e), to define the pre-failure elastic behaviour. In addition, it requires parameters to define the failure surface. For example, if a Mohr-Coulomb failure surface is used, a further two parameters, cohesion c' and angle of shearing resistance φ', are needed.

5.7.3 K - G model

In many respects this model is a logical extension of the bi-linear model. The tangential (i.e. incremental) bulk, K_t, and shear, G_t, moduli are explicitly defined in terms of stress invariants:

$$K_t = K_{to} + \alpha_K p' \quad (5.17)$$

$$G_t = G_{to} + \alpha_G p' + \beta_G J \quad (5.18)$$

The model therefore needs five parameters, K_{to}, α_K, G_{to}, α_G and β_G, to describe material behaviour. These can be chosen to fit available soil data. As with the bi-linear model, the parameters can be selected such that the tangential (incremental) shear stiffness becomes very small when failure is approached. This is achieved by setting β_G negative. Values of cohesion, c', and angle of shearing resistance, φ', are therefore used when determining the values of the five input parameters. The model can also be used for unloading in much the same way as the bi-linear model. A simple way of implementing this is to set β_G to zero on unloading. The bulk modulus, K_t, therefore remains unaffected, but the shear modulus, G_t, changes

abruptly to a higher value. If subsequent reloading brings the stress state near to failure again, β_G is reset to its former value. The resulting stress-strain curves for this model are shown in Figure 5.7. This model is described in detail by Naylor *et al.* (1981).

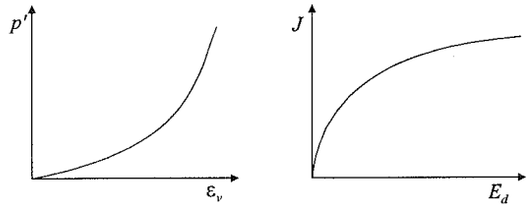

Figure 5.7: K-G model

5.7.4 Hyperbolic model

While the two models described above are essentially incremental in that they directly define the change in tangential moduli, the hyperbolic model relates accumulated stress to accumulated strain. Differentiation is then required to obtain the equivalent incremental form for use in finite element analysis.

The original model is attributed to Kondner (1963), however, it has been extensively developed by Duncan and his co-workers and is commonly known as the 'Duncan and Chang' model (after Duncan and Chang (1970)). In its initial form it was originally formulated to fit undrained triaxial test results and was based on two parameters and the implicit assumption that Poisson's ratio was 0.5. With use, further refinements were added and the model was applied to both drained and undrained boundary value problems. The number of parameters needed to define the model also increased to nine (Seed *et al.* (1975)).

The original model was based on the following hyperbolic equation:

$$(\sigma_1 - \sigma_3) = \frac{\varepsilon}{a + b\varepsilon} \tag{5.19}$$

where σ_1 and σ_3 are the major and minor principal stresses, ε the axial strain and a and b are material constants. It can be shown that if $\sigma_1 = \sigma_3$ the reciprocal of a is the initial tangential Young's modulus, E_i, see Figure 5.8a. The reciprocal of b is the failure value of $\sigma_1 - \sigma_3$, approached asymptotically by the stress-strain curve, see Figure 5.8a.

Kondner and his coworkers showed that the values of the material properties may be determined most readily if the stress-strain data from laboratory tests are plotted on transformed axes, as shown in Figure 5.8b. Rewriting Equation (5.19) in the same form gives:

$$\frac{\varepsilon}{(\sigma_1 - \sigma_3)} = a + b\varepsilon \tag{5.20}$$

It may be noted that a and b are the intercept and the slope of the resulting straight line, see Figure 5.8b. By plotting laboratory stress-strain data in the form shown in Figure 5.8b it is easy to determine the values of the parameters a and b corresponding to the best fit between a hyperbola (a straight line in Figure 5.8b) and the test data.

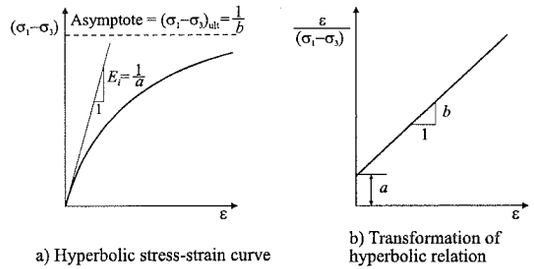

Figure 5.8: Hyperbolic model

For finite element use it is common to differentiate Equation (5.19) to obtain the variation of the tangent Young's modulus, E_t, with stress level, $(\sigma_1-\sigma_3)$:

$$E_t = \frac{\partial(\sigma_1 - \sigma_3)}{\partial\varepsilon} = \frac{a}{(a + b\varepsilon)^2} \tag{5.21}$$

As noted above, various further developments have been made to the original formulation. In particular it has been extended to deal with drained behaviour. While an improvement over linear elasticity, the model is incapable of representing many of the important facets of soil behaviour discussed in Chapter 4.

A potential problem can arise with this model due to the assumption of a constant Poisson's ratio. When shear failure is approached, the tangent Young's modulus reduces to zero. Combining this with the constant Poisson's ratio results in both the tangent shear and bulk moduli also reducing. While this is reasonable for the shear modulus, it is not realistic for the bulk modulus. The only situation where this does not occur is when Poisson's ratio is exactly 0.5. However, as discussed in Chapter 3, it is not usually possible to use such a value in a finite element analysis. Even for a value of Poisson's ratio close to 0.5 the bulk modulus reduces to a zero.

5.7.5 Small strain stiffness model

The three models described above have been in existence for many years and were developed to cover the complete stress-strain range from first loading all the way to failure. In recent years, however, due to advances in electronic instrumentation, it has been possible to measure the behaviour of soils more accurately. In particular it has been found that soils undergo a large and rapid change in stiffness when initially subjected to relatively small changes in strain. Such behaviour has been

described in Chapter 4. Many of the constitutive models in existence could not account for such behaviour and this, consequently, led to further developments. One of the earliest models developed specifically to deal with the concept of small strain behaviour was that described by Jardine *et al.* (1986). Because this model is based on nonlinear isotropic elasticity, it is appropriate to briefly describe it here.

The secant expressions that describe the variation of shear and bulk moduli are:

$$\frac{G_{sec}}{p'} = A + B\cos\left[\alpha\left(\log_{10}\left(\frac{E_d}{\sqrt{3}C}\right)\right)^{\gamma}\right] \tag{5.22}$$

$$\frac{K_{sec}}{p'} = R + S\cos\left[\delta\left(\log_{10}\left(\frac{|\varepsilon_v|}{T}\right)\right)^{\eta}\right] \tag{5.23}$$

where, G_{sec} is the secant shear modulus, K_{sec} the secant bulk modulus, p' the mean effective stress, and the strain invariants E_d and ε_v are given by:

$$E_d = \frac{2}{\sqrt{6}}\sqrt{(\varepsilon_1-\varepsilon_2)^2+(\varepsilon_2-\varepsilon_3)^2+(\varepsilon_1-\varepsilon_3)^2} \tag{5.24}$$

$$\varepsilon_v = \varepsilon_1 + \varepsilon_2 + \varepsilon_3 \tag{5.25}$$

and A, B, C, R, S, T, α, γ, δ and η are all material constants. Due to the cyclic trigonometric nature of Equations (5.22) and (5.23) it is common to set minimum ($E_{d,\min}$, $\varepsilon_{v,\min}$) and maximum($E_{d,\max}$, $\varepsilon_{v,\max}$) strain limits below which and above which the moduli vary with p' alone, and not with strain. Typical variations of secant shear and bulk moduli for London clay are shown in Figure 5.9.

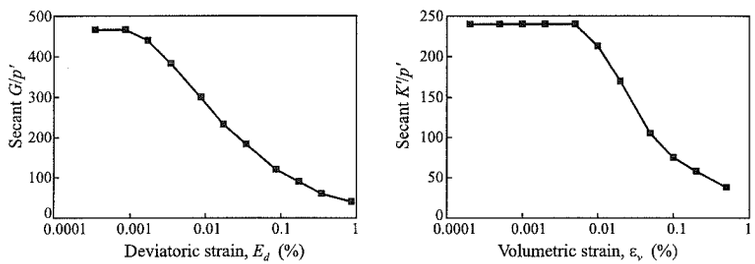

Figure 5.9: Variation of shear and bulk moduli with strain level

To use this model in a finite element analysis, the secant expressions given by Equations (5.22) and (5.23) are differentiated to give the following tangent values:

$$\frac{3G}{z} = A + B(\cos\alpha)X^{\gamma} - \frac{B\alpha\gamma X^{\gamma-1}}{2.303}(\sin\alpha)X^{\gamma} \tag{5.26}$$

$$\frac{K}{z} = R + S(\cos\delta)Y^{\eta} - \frac{S\delta\mu Y^{\eta-1}}{2.303}(\sin\delta)Y^{\eta} \tag{5.27}$$

where

$$X = \log_{10}\left(\frac{E_d}{\sqrt{3}C}\right) \quad ; \quad Y = \log_{10}\left(\frac{|\varepsilon_v|}{T}\right) \tag{5.28}$$

As noted above, this model was developed to simulate soil behaviour in the small strain range. It was not intended to be used to deal with behaviour at large strains when the soil approaches failure. Consequently, the model is usually used in conjunction with a plastic model which deals with the large strain behaviour. Elasto-plastic models are discussed in Chapter 6, 7 and 8. The use of this model to analyse real engineering structures is described in Volume 2 of this book.

5.7.6 Puzrin and Burland model

While the small strain stiffness model described above is capable of modelling soil behaviour under small stress and strain perturbations, it is lacking in theoretical rigour and fails to account for several important facets of real soil behaviour. In particular, it does not account for the change in stiffness observed when the direction of the stress path changes. However, its use by Jardine *et al.* (1986) to investigate the behaviour of a range of geotechnical problems highlighted the importance of modelling the small strain behaviour of soils. As a result, considerable effort has, and still is, being directed at improving our understanding of the mechanical processes controlling stress-strain behaviour of soils at small strains.

Based on limited experimental evidence, it has been postulated that, in stress space, the stress state is surrounded by a small-strain region (SSR), where the stress-strain behaviour is nonlinear but very stiff and fully recoverable, so that cycles of stress form closed hysteretic loops. Inside this region the stress state is surrounded by a smaller region where the soil response is linear elastic (the LER). When the stresses change, both these regions move with the stress state as illustrated by the dotted lines in Figure 5.10. This concept of kinematic regions of high stiffness was put forward by Skinner (1975) and developed by Jardine (1985, 1992).

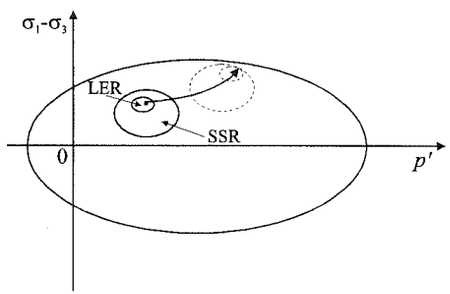

Figure 5.10: Kinematic regions of high stiffness

Puzrin and Burland (1998) adopted the above framework and developed a constitutive model to describe the behaviour of soil within the SSR. They assumed behaviour within the LER to be linear elastic and that once the stress state was

outside the SSR behaviour could be explained by conventional elasto-plasticity. Their work therefore concentrated only on the behaviour within the SSR. As published, the model is restricted to conventional triaxial stress space and therefore must be extended to general stress space before it can be used in finite element analyses. Addenbrooke *et al.* (1997) used such an extended version of this model to investigate the influence of pre-failure soil stiffness on the numerical analysis of tunnel construction. Although they used a simple Mohr-Coulomb elasto-plastic model to represent soil behaviour beyond the SSR, their extension of the Puzrin and Burland model is independent of how behaviour beyond the SSR is modelled. This model is now presented.

Since the model is assumed to be isotropic, it is formulated in terms of stress invariants, see Section 5.3. The stress space surrounding a stress point, or local origin, is divided into three regions, see Figure 5.11. The first region is the linear elastic region (LER). In the second region, the small strain region (SSR), the deviatoric and volumetric stress-strain behaviour is defined by a logarithmic curve (Puzrin and Burland (1996)). Each of these regions is bounded by an elliptical boundary surface. Because the deviatoric stress invariant, J, is always positive, these surfaces plot as half ellipses in Figure 5.11. In the final region, between the SSR boundary and the plastic yield surface (which is defined independent of the pre-failure model), the soil behaviour is again elastic, with the shear, G, and bulk, K, moduli being associated with the SSR boundary. To be consistent with experimental data, see Chapter 4, the stiffnesses in both the LER and SSR are mean stress dependent.

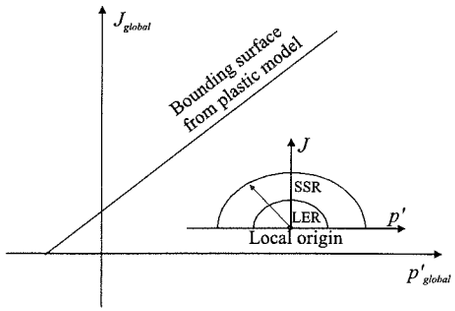

Figure 5.11: The stress regions surrounding a local origin in J-p′ space

The equations defining soil behaviour are now presented. Note that p', J (the mean and deviatoric stress invariants), ε_v and E_d (the volumetric and deviatoric strain invariants) are calculated from the local origin (see Figure 5.11).

Behaviour within the LER

The elliptical boundary to the LER is given by:

$$F_{LER}(p',J) = 1 + n^2\left(\frac{J}{p'}\right)^2 - \left(\frac{a_{LER}}{p'}\right)^2 = 0 \qquad (5.29)$$

where a_{LER} is a parameter defining the size of the LER. Within this boundary, the shear and bulk moduli are defined by:

$$K_{LER} = \frac{K_{LER}^{ref}}{(p'^{ref})^{\beta}}(p')^{\beta} \quad ; \quad G_{LER} = \frac{G_{LER}^{ref}}{(p'^{ref})^{\gamma}}(p')^{\gamma} \qquad (5.30)$$

where K_{LER}^{ref} and G_{LER}^{ref} are values of the bulk and shear elastic moduli, respectively in the LER, at the mean effective stress p'^{ref}.

The value of the parameter a_{LER} can be determined from an undrained triaxial test as $a_{LER} = n\,J_{LER}^{u}$, where J_{LER}^{u} is the value of the deviatoric stress at the LER boundary and $n = \sqrt{(K_{LER} / G_{LER})}$. The parameters β and γ control the manner in which the moduli depend on mean effective stress.

Behaviour within the SSR

The boundary to the SSR is also given by an ellipse:

$$F_{SSR}(p',J) = 1 + n^2\left(\frac{J}{p'}\right)^2 - \left(\frac{a_{SSR}}{p'}\right)^2 = 0 \qquad (5.31)$$

where a_{SSR} is a parameter defining the size of the SSR. It can be determined from an undrained triaxial test as $a_{SSR}=nJ_{SSR}^{u}$, where J_{SSR}^{u} is the value of the deviatoric stress at the SSR boundary, and n is defined above.

Between the LER and the SSR the elastic moduli depend both on mean effective stress and on strain and obey the following logarithmic reductions:

$$K = K_{LER}\left[1 - \alpha\left(\frac{(x_v - x_e)R\left[\ln(1 + x_v - x_e)\right]^{R-1}}{(1 + x_v - x_e)} + \left[\ln(1 + x_v - x_e)\right]^{R}\right)\right] \qquad (5.32)$$

$$G = G_{LER}\left[1 - \alpha\left(\frac{(x_D - x_e)R\left[\ln(1 + x_D - x_e)\right]^{R-1}}{(1 + x_D - x_e)} + \left[\ln(1 + x_D - x_e)\right]^{R}\right)\right] \qquad (5.33)$$

where

$$\alpha = \frac{x_u - 1}{(x_u - x_e)\left[\ln(1 + x_u - x_e)\right]^{R}} \qquad (5.34)$$

$$R = \left[\left(\frac{1 - x_e}{x_u - x_e} - b\right)\left(\frac{(1 + x_u - x_e)[\ln(1 + x_u - x_e)]}{x_u - 1}\right)\right] \qquad (5.35)$$

$$x_u = \frac{2K_{LER}u}{a_{SSR}a_{SSR}} \quad ; \quad x_v = \frac{|\varepsilon_v|K_{LER}}{p'_{SSR}}$$
$$x_D = \frac{E_d G_{LER}}{J_{SSR}} \quad ; \quad x_e = \frac{a_{LER}}{a_{SSR}} \qquad (5.36)$$

in which x_u is the normalised strain at the SSR boundary, x_e the normalised strain at the LER boundary, and b is the ratio of tangent modulus on the SSR boundary to the value within the LER:

$$b = \frac{G_{SSR}}{G_{LER}} = \frac{K_{SSR}}{K_{LER}} \qquad (5.37)$$

and u is the incremental strain energy, which can be determined from an undrained trixial test, being equal to $0.5E_{SSR}{}^{u}J_{SSR}{}^{u}$, where $E_{SSR}{}^{u}$ and $J_{SSR}{}^{u}$ are the deviatoric strain and deviaoric stress on the SSR boundary, respectively.

Behaviour outside the SSR

Outside the SSR the moduli are the bulk modulus, $K = bK_{LER}$, and the shear modulus, $G=bG_{LER}$. In future developments of the model it may be possible to use a hardening/softening plastic model and associate the SSR boundary with initial yielding. The elastic parameters G and K at the SSR boundary could then be related to the elasto-plastic shear and bulk stiffness. Such an approach would essentially define the parameter b which would then no longer be required as an input parameter to the model. The principles behind such an approach are outlined by Puzrin and Burland (1998).

Within this model, a stress path reversal results in the relocation of the local stress origin at the reversal point, so reinvoking the small-strain high-stiffness behaviour and enabling the model to simulate closed hysteretic loops. In this respect, a stress path reversal is defined if the increment of normalised mean or deviatoric stress is less than zero:

$$\mathrm{d}\left(\frac{p'}{p'_{SSR}}\right) = \frac{p'_{SSR}\,\mathrm{d}p' - p'\,\mathrm{d}p'_{SSR}}{p'^{2}_{SSR}} \geq 0$$

and (5.38)

$$\mathrm{d}\left(\frac{J}{J_{SSR}}\right) = \frac{J_{SSR}\,\mathrm{d}J - J\,\mathrm{d}J_{SSR}}{J^{2}_{SSR}} \geq 0$$

where J_{SSR} and p'_{SSR} are the linear projections of the current stress state J and p' on the SSR, see Figure 5.12. According to this criterion the loading reversal can occur at any stress state within the SSR and not only on its boundary.

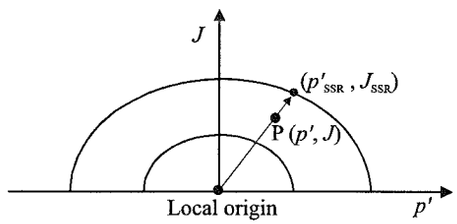

Figure 5.12: Projection of the current stress state on SSR

A total of eight parameters are required to define the model. These are, u/p', b, a_{LER}/p', a_{SSR}/p', K_{LER}/p', G_{LER}/p', β and γ. However, as the bulk and shear moduli depend on p', they can become very small as p' reduces. Addenbrooke *et al.* (1997) therefore introduced minimum values G_{min} and K_{min} which act as cut off values calculated from the above equations.

A major difference between this model and the small strain stiffness model described in the previous section is that in this model both the shear and bulk stiffness decay simultaneously as the stress state moves through the SSR. In contrast, in the previous model the decay of shear and bulk stiffness depends only on deviatoric and volumetric strains respectively. Consequently, the small strain stiffness model allows only shear stiffness reduction on deviatoric straining with no volumetric straining, and bulk stiffness reduction on volumetric straining with no deviatoric strain, while the Puzrin and Burland model forces shear and bulk moduli reduction together, independent of straining.

5.8 Summary

1. In general, six independent pieces of information are required to define the state of stress. If the material is isotropic the magnitude of the stress can be quantified using three independent stress invariants. These invariants can be the three principal stresses or some combination of these. However, if the material is anisotropic all six pieces of information are required. The above statements also apply to strains.
2. Linear isotropic elastic models, which require only two material parameters, do not reproduce any of the important facets of real soil behaviour identified in Chapter 4. Linear cross-anisotropic elastic models, which require five material parameters, do not really improve the situation, although they can reproduce anisotropic stiffness behaviour.
3. Nonlinear elastic models, in which the material parameters vary with stress and/or strain level, are a substantial improvement over their linear counterparts. Due to the number of parameters involved, most nonlinear elastic models assume isotropic behaviour. However, they still fail to model some of the important facets of real soil behaviour. In particular, they cannot reproduce the tendency to change volume when sheared. Also, because of the inherent assumption of coincidence of principal incremental stress and strain directions, they cannot accurately reproduce failure mechanisms.

6. Elasto-plastic behaviour

6.1 Synopsis

This chapter introduces the framework and assumptions of elasto-plastic material behaviour. Elastic perfectly plastic and elastic strain hardening/softening plastic behaviour is defined. The concepts of yield and plastic potential surfaces and of hardening and softening rules are introduced. It is shown that the framework can simulate many of the facets of behaviour exhibited by real soils. The chapter finishes by deriving the theoretical equations necessary for construction of the elasto-plastic constitutive matrix.

6.2 Introduction

In the previous chapter some elastic constitutive models were presented. While such models are relatively simple, they cannot simulate many of the important characteristics of real soil behaviour. Improvements can be made by extending these models using the theory of plasticity. The objective of this chapter is to describe the concepts of elasto-plastic behaviour and how it may be formulated for use in finite element analysis.

The chapter begins by considering the uniaxial behaviour of a linear elastic-plastic material. By using this simple problem as an example, the ideas of plastic yield, hardening and softening are introduced. It is then shown that many of the facets of real soil behaviour are consistent with such concepts and, therefore, that the framework has considerable potential. While the uniaxial problem provides an ideal introduction, the concepts of plasticity must be expressed in general stress and strain space, if they are to be used to describe soil behaviour under multi-stress conditions. The basic ingredients for a general elasto-plastic model are therefore presented. These are then used to examine the behaviour of an elasto-plastic material subjected to a biaxial stress state. The chapter finishes by deriving the theoretical equations necessary for construction of the elasto-plastic constitutive matrix for use in finite element analysis. Examples of specific elasto-plastic models are given in Chapters 7 and 8.

6.3 Uniaxial behaviour of a linear elastic perfectly plastic material

Figure 6.1 shows a uniaxially loaded bar of an ideal linear elasto-plastic material, which is loaded by applying a compressive axial strain, ε. This figure also shows the stress-strain curve for this bar. On first straining the bar behaves elastically and its stress-strain response travels along the line AB. As the material is linear elastic, the gradient of the line AB is given by the Young's modulus, E. If the straining process is stopped before the stress in the bar reaches point B and the bar is unstrained (i.e. unloaded), the stress-strain response moves back down the line BA. Consequently, as long as the straining does not cause the stress to reach point B, the bar behaves in a linear elastic manner and, when unloaded, returns to its original undeformed state, with no permanent strains. If the bar is strained beyond ε_B, to point C, the stress strain curve passes through point B. At B the yield stress, σ_Y, is reached and the bar becomes plastic. There is no longer a linear relationship between stress and strain and the stress in the bar remains constant and equal to σ_Y. If the bar is now unloaded it becomes elastic and the stress strain curve follows the path CD, which is parallel to the path BA. When unloaded such that the axial stress is zero, i.e. point D, there is still a strain in the bar. This strain is equivalent to the plastic strain experienced when straining along the path BC and is given by $\varepsilon_C^p = \varepsilon_C - \varepsilon_B$. Thus the bar does not return to its original shape, but suffers a permanent shortening. If the bar is now reloaded, the stress strain curve re-traces the path DC until point C is reached, at which point the axial stress equals the yield stress and the bar becomes plastic again. It then moves along path CF. Clearly, if the straining is not sufficient to take the stress to point C, the bar behaves linear elastically.

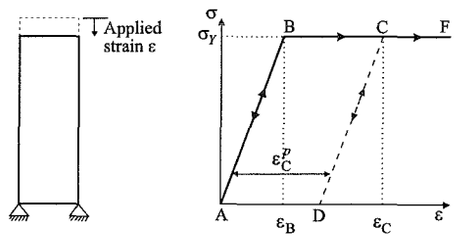

Figure 6.1: Uniaxial loading of linear elastic perfectly plastic material

Behaviour is reversible, and therefore elastic, on the inclined paths AB and DC, whereas on the path BCF behaviour is not reversible. For example, it is impossible to retrace the path CB. If, instead of subjecting the bar to strain controlled loading, the bar is loaded by an increasing stress, it is impossible to apply a stress greater than the yield stress σ_Y. Any attempt to do so would result in infinite strains. A material conforming to the idealised behaviour shown in Figure 6.1 is called *linear elastic perfectly* (or *ideal*) *plastic*.

6.4 Uniaxial behaviour of a linear elastic strain hardening plastic material

Figure 6.2 shows another idealised uniaxial stress-strain curve. Behaviour of the bar when strained is similar to that described above, but with one subtle difference. Initially, if the bar is strained it behaves elastically along path AB. If it is strained beyond point B to point C the initial yield stress σ_{YB} is exceeded, but instead of the stress remaining constant and equal to σ_{YB}, as in Figure 6.1, it increases to σ_{YC}. On unloading from point C the bar becomes elastic again and follows the linear path CD which is parallel to BA. As before, there is a permanent (plastic) strain left in the bar when it is fully unloaded to point D, i.e. $\sigma = 0$. On reloading the bar initially behaves elastically, path DC, until point C is reached, where it becomes plastic. The yield stress at point C, σ_{YC}, is greater than that at B and has increased as a result of the plastic straining from B to C. Eventually, if the bar is strained to point F the stress strain curve becomes horizontal and the stress in the bar remains constant. A material which behaves in this manner is called a *linear elastic strain* (or *work*) *hardening plastic*.

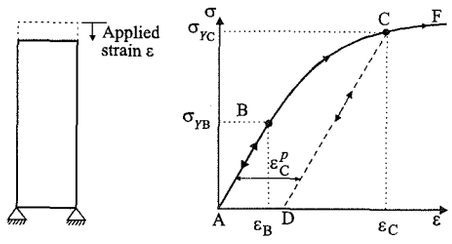

Figure 6.2: Uniaxial loading of linear elastic strain hardening plastic material

6.5 Uniaxial behaviour of a linear elastic strain softening plastic material

A third class of plastic material can now be identified where the yield stress, instead of increasing during plastic straining, decreases. The behaviour of such a material when subjected to uniaxial straining is shown in Figure 6.3. Behaviour is again linear elastic on first loading and during any unload - reload loops. However, during plastic straining, along path BCF, the yield stress reduces. Such a material is called a *linear elastic strain* (or *work*) *softening material*.

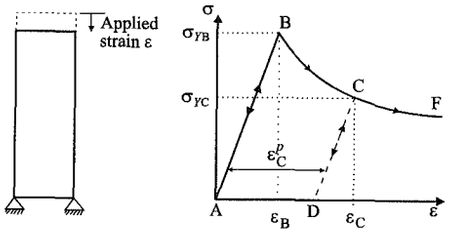

Figure 6.3: Uniaxial loading of linear elastic strain softening plastic material

From an engineering point of view, material that behaves in this brittle manner is of particular concern because, if strained beyond its initial yield point (i.e. point B in Figure 6.3), its yield stress reduces and its capacity to resist load diminishes.

6.6 Relevance to geotechnical engineering

Although the above examples are for simple uniaxial conditions, they highlight the difference between the three main forms of elasto-plastic behaviour. It is interesting to compare the behaviour described above, with some of the more common features of soil behaviour. For example, if the stress-strain curve given in Figure 6.2 is re-plotted with the stress axis horizontal and the strain axis vertical, see Figure 6.4a, it bares some resemblance to the behaviour observed in an oedometer test, see Figure 6.4b. Soil behaviour on a swelling line is often assumed to be reversible and therefore is akin to behaviour on an elastic unload-reload loop (i.e. path CDC in Figure 6.4a). Behaviour on the virgin consolidation line is irreversible (i.e. it is only possible to travel down the line, not up it) and results in permanent strains. It is therefore similar to behaviour along the strain hardening path BCF of Figure 6.4a.

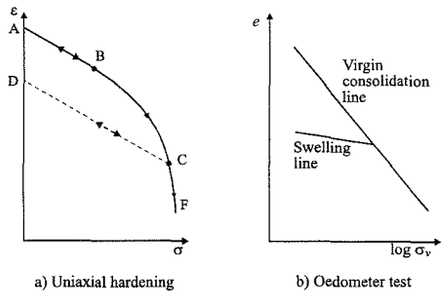

Figure 6.4: Similarity between uniaxial hardening and an oedometer test

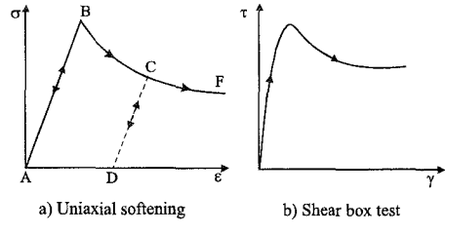

Figure 6.5: Similarity between uniaxial softening and direct simple shear test

Similarity also exists between the strain softening behaviour given in Figure 6.3 and reproduced in Figure 6.5a, and the shear stress - shear strain behaviour observed in a direct or simple shear test on dense sand, shown in Figure 6.5b.

6.7 Extension to general stress and strain space

For the above concepts of elasto-plastic materials to be of general use, behaviour must be formulated in general multi-axial stress and strain space. Because there are six independent components of stress and six of strain, this presents a formidable task. However, if the material can be assumed to be isotropic (i.e. properties independent of orientation) and as yield is essentially dependent on stress magnitude, simplifications can be achieved by working with invariants of stress and strain. As noted in Chapter 5, three stress invariants are required to determine the magnitude of stress. These invariants can be the principal stresses, or some combination of these values. For plasticity it is usual to express behaviour in an incremental form and to use *accumulated* stress and *incremental* strain invariants.

Clearly, working in terms of invariants considerably reduces the complexity of the task of formulating elasto-plastic behaviour, because the number of stress and strain parameters reduces from six to three. However, it comes at the cost of assuming the material to be isotropic. To model anisotropic behaviour the formulation must be in terms of six independent stresses and six strains.

6.8 Basic concepts

To formulate an elasto-plastic constitutive model requires the following four essential ingredients.

6.8.1 Coincidence of axes

The principal directions of accumulated stress and incremental plastic strain are assumed to coincide. This differs from elastic behaviour where the principal directions of incremental stress and incremental strain coincide.

6.8.2 A yield function

In the uniaxial situations described in Sections 6.3 to 6.5 the yield stress, σ_Y, indicates the onset of plastic straining. In the multi-axial situation it is not sensible to talk about a yield stress, as there are now several non- zero components of stress. Instead, a yield function, F, is defined, which is a scalar function of stress (expressed in terms of either the stress components or stress invariants) and state parameters, $\{\boldsymbol{k}\}$:

$$F\left(\{\sigma\}\ ,\ \{\boldsymbol{k}\}\right)=0 \tag{6.1}$$

This function separates purely elastic from elasto-plastic behaviour. In general, the surface is a function of the stress state $\{\boldsymbol{\sigma}\}$ and its size also changes as a function of the state parameters $\{\boldsymbol{k}\}$, which can be related to hardening/softening parameters. For perfect plasticity $\{\boldsymbol{k}\}$ is constant and represents the magnitude of the stresses at yield. It is analogous to σ_Y in Figure 6.1. For hardening and softening plasticity $\{\boldsymbol{k}\}$ varies with plastic straining to represent how the magnitude of the stress state at yield changes. It is analogous to the curves BCF in Figures 6.2 (hardening) and 6.3 (softening). If the hardening or softening is related to the magnitude of the plastic strains, the model is known as *strain hardening/softening*. Alternatively, if it is related to the magnitude of plastic work, the model is known as *work hardening/softening*.

The value of the yield function F is used to identify the type of material behaviour. Purely elastic behaviour occurs if $F(\{\boldsymbol{\sigma}\},\{\boldsymbol{k}\})<0$, and plastic (or elasto-plastic) behaviour occurs if $F(\{\boldsymbol{\sigma}\},\{\boldsymbol{k}\})=0$. $F(\{\boldsymbol{\sigma}\},\{\boldsymbol{k}\})>0$ signifies an impossible situation. Equation (6.1) plots as a surface in a stress space. For example, if Equation (6.1) is expressed in terms of the principal stresses and $\sigma_2 = 0$, the yield function can be plotted as shown in Figure 6.6a. Such a plot of the yield function is called a *yield curve*. If σ_2 is not set to zero but is allowed to vary, the yield function has to be plotted in three dimensional σ_1-σ_2-σ_3 space where it forms a *yield surface*, see Figure 6.6b. The space enclosed by this surface is called the *elastic domain*. The advantage of assuming isotropic behaviour and therefore expressing the yield function in terms of stress invariants should now be apparent. If such an assumption is not made, the yield function has to be expressed in terms of six stress components and it therefore forms a surface in six dimensional space. Clearly, it is not possible to draw such a space and therefore visualisation of such a surface is difficult!

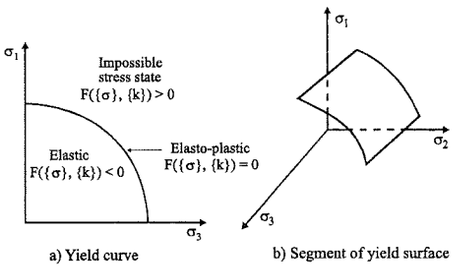

Figure 6.6: Yield function presentation

6.8.3 A plastic potential function

In the uniaxial examples considered in Sections 6.3 to 6.5 it is implicitly assumed that the plastic strains take place in the same direction as the imposed stress. For the uniaxial case this is self evident. However, in the multi-axial case the situation is more complex as there are potentially six components of both stress and strain. It is therefore necessary to have some means of specifying the direction of plastic straining at every stress state. This is done by means of a *flow rule* which can be expressed as follows:

$$\Delta\varepsilon_i^p = \Lambda\frac{\partial P(\{\sigma\},\{\boldsymbol{m}\})}{\partial\sigma_i} \tag{6.2}$$

where $d\varepsilon_i^p$ represents the six components of incremental plastic strain, P is the *plastic potential* function and Λ is a scalar multiplier. The plastic potential function is of the form:

$$P\left(\{\sigma\},\{\boldsymbol{m}\}\right)=0 \tag{6.3}$$

where $\{\boldsymbol{m}\}$ is essentially a vector of state parameters the values of which are immaterial, because only the differentials of P with respect to the stress components are needed in the flow rule, see Equation (6.2).

Equation (6.2) is shown graphically in Figure 6.7. Here a segment of a plastic potential surface is plotted in principal stress space. Because of the assumption of coincidence of principal directions of accumulated stress and incremental plastic strain, it is possible to plot incremental principal strains and accumulated principal stresses on the same axes. The outward vector normal to the plastic potential surface at the current stress state has components which provide the relative magnitudes of the plastic strain increment components. This is more easily shown in Figure 6.7b, where it is assumed that $\sigma_2 = 0$ and the plastic potential function is plotted in two dimensional σ_1 - σ_3 space. It should be noted that the normal vector

only provides an indication of the relative sizes of the strain components. The value of the scalar parameter Λ in Equation (6.2) controls their magnitude. Λ is dependent on the hardening/softening rule which is discussed later. In general, the plastic potential can be a function of the six independent stress components and has a corresponding surface in six dimensional stress space, to which the components of a vector normal to the surface at the current stress state represent the relative magnitudes of the incremental strain components.

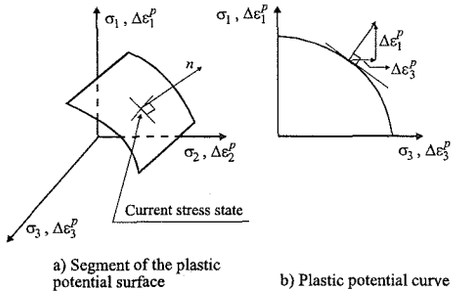

Figure 6.7: Plastic potential presentation

Sometimes a further simplification is introduced by assuming the plastic potential function to be the same as the yield function (i.e. $P(\{\boldsymbol{\sigma}\},\{\boldsymbol{m}\}) = F(\{\boldsymbol{\sigma}\},\{\boldsymbol{k}\})$). In this case the flow rule is said to be *associated*. The incremental plastic strain vector is then normal to the yield surface and the *normality condition* is said to apply. In the general case in which the yield and plastic potential functions differ (i.e. $P(\{\boldsymbol{\sigma}\},\{\boldsymbol{m}\}) \neq F(\{\boldsymbol{\sigma}\},\{\boldsymbol{k}\})$), the flow rule is said to be *non-associated.*

Flow rules are of great importance in constitutive modelling because they govern dilatancy effects which in turn have a significant influence on volume changes and on strength, see Chapter 4. Whether or not the flow rule is associated or non-associated also has a cost implication in finite element analysis. As shown subsequently in this chapter, if the flow rule is associated, the constitutive matrix is symmetric and so is the global stiffness matrix. On the other hand, if the flow rule is non-associated both the constitutive matrix and the global stiffness matrix become non-symmetric. The inversion of non-symmetric matrices is much more costly, both in terms of storage and computer time.

6.8.4 The hardening/softening rules

The hardening/softening rules prescribe how the state parameters $\{\boldsymbol{k}\}$ vary with plastic straining. This enables the scalar parameter, Λ, in Equation (6.2) to be quantified. If the material is perfectly plastic, no hardening or softening occurs and the state parameters $\{\boldsymbol{k}\}$ are constant. Consequently, no hardening or softening rules are required. In such materials Λ is undefined. This follows from the fact that once the stress state reaches, and is maintained at, yield the material strains indefinitely. However, for materials which harden and/or soften during plastic straining, rules are required to specify how the yield function changes.

For example, in the uniaxial compression of a strain hardening material discussed in Section 6.4 and shown on Figure 6.2, the yield stress, σ_Y, increases

with plastic straining along the path BCF. At any point along this path the strains can be separated into elastic and plastic components. It is then possible to plot how the yield stress, σ_Y, varies with plastic strain, ε^p, as shown in Figure 6.8. A relationship of this type is called a *hardening rule.* For the strain softening uniaxial example discussed in Section 6.5 and shown in Figure 6.3, the yield stress reduces and again it is possible to plot how σ_Y varies with plastic strain ε^p. This is also shown in Figure 6.8 and such a relationship is called a *softening rule.*

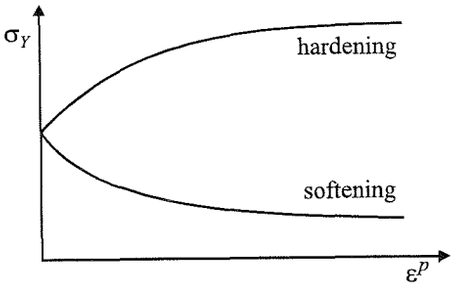

Figure 6.8: Examples of hardening/softening rules

In multi-axial situations it is common to relate changes in size of the yield surface to the components (or invariants) of the accumulated plastic strain. Such hardening/softening rules are then called *strain hardening/softening.* Alternatively, but less commonly, the change in size of the yield surface can be related to the increase in plastic work, $W^p = \int \{\boldsymbol{\sigma}\}^T \{\Delta\boldsymbol{\varepsilon}^p\}$. Such hardening/softening rules are called *work hardening/softening.*

So in general, having accepted coincidence of principal directions of accumulated stress and incremental plastic strain, three further pieces of information are required to formulate an elasto-plastic model. A yield function which signals when the material becomes plastic, and a plastic potential function which determines the direction of plastic straining, are compulsory ingredients. If the material hardens or softens, a hardening/softening rule is required. Specific examples of such models are given in Chapters 7 and 8.

To indicate how the above concepts work in multi-axis stress conditions, a two dimensional stress situation is now considered. For simplicity, associated conditions are assumed, with the yield and plastic potential surfaces being given by the same function.

6.9 Two dimensional behaviour of a linear elastic perfectly plastic material

For this material the yield surface is fixed in stress space and does not change position when loading takes place. If the stress state remains below the yield surface behaviour is entirely elastic. If the stress state reaches the yield surface plastic straining occurs. It is not possible for the stress state to extend beyond the yield surface.

Consider an element of soil acted upon by a two dimensional system of stresses σ_x, σ_y, as shown in Figure 6.9. Initially the sample is stress free at point 'o'. The stress component σ_x is then increased while keeping σ_y=0 until point 'a' is reached. Because the stress state remains below (inside) the yield surface (curve), behaviour

is entirely elastic. Although σ_y does not change, there is a strain ε_y due to the Poisson's ratio effect (ε_y is likely to be negative if $0 < \mu < ½$). The strain ε_y can only be zero if Poisson's ratio, μ, is zero. The stress σ_x is then kept constant and σ_y increased until it reaches the yield surface at point 'b'. While the stress remains below the yield surface, behaviour is again elastic and the strain ε_y is controlled by the elastic moduli. Once the yield surface is reached (point 'b'), it is not possible to increase σ_y any further. Plastic straining occurs. If the stress state is maintained at point 'b', the plastic strains will keep increasing indefinitely. However, the ratio between plastic strain components $d\varepsilon_x^p$ and $d\varepsilon_y^p$ is fixed by the gradient of the yield surface (equal to the plastic potential in this case) at point 'b'. The element of soil has failed.

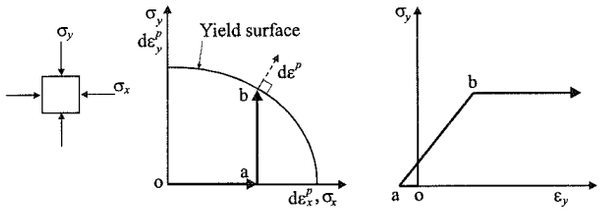

Figure 6.9: Two dimensional behaviour of a linear elastic perfectly plastic material

If the element of soil considered above is part of the soil mass in a boundary value problem, for example under the edge of a footing, it may be surrounded by soil that is behaving elastically, with stresses below yield. In such a condition the plastic straining of the element is restricted. Only when sufficient elements of soil are failing so that a collapse mechanism develops, can the strains increase indefinitely.

6.10 Two dimensional behaviour of a linear elastic hardening plastic material

In this case the position and/or size of the yield surface changes as plastic straining occurs. If the yield surface changes size, but is always centred about the same position, hardening is often called *isotropic hardening*, see Figure 6.10. If, on the other hand, the yield surface does not change in size, but changes position in stress space, it is called *kinematic hardening*. In general, hardening can include components of both isotropic and kinematic hardening.

Following the same loading sequence on an element of soil as described in the previous section, results in the same behaviour until the initial yield surface is encountered at 'b', see Figure 6.11. With further increase in σ_y plastic straining occurs and the yield surface expands (isotropic hardening) according to the hardening law. As it is now possible to increase σ_y , elastic strains develop

simultaneously with the plastic strains (i.e. soil behaviour is elasto-plastic). With further loading the gradient of the yield surface, and therefore the ratio of the plastic strain components $d\varepsilon_x^p$ and $d\varepsilon_y^p$, is likely to change. Eventually, the yield surface stops hardening and failure occurs, similar to the perfect plasticity case discussed above.

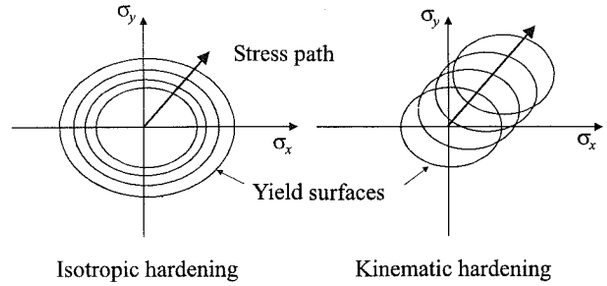

Figure 6.10: Types of hardening

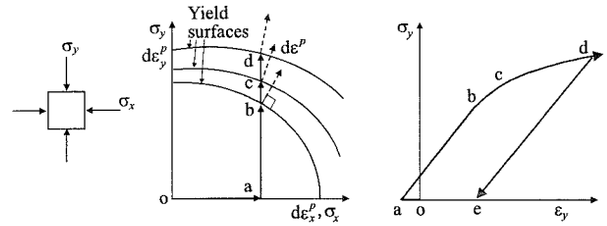

Figure 6.11: Two dimensional behaviour of a linear elastic hardening plastic material

If at stage 'd' stress σ_y is removed such that the stress path 'd-a' is followed, the stress strain curve follows the path 'd-e'. Behaviour is elastic on initial unloading and remains so if the model is of the isotropic hardening type. If the model is of the kinematic hardening type unloading may be sufficient to invoke plastic behaviour again, but such complications are not considered here. After complete unloading there is a permanent strain, ε_y , which is equal to the plastic strain ε_y^p generated during loading from 'b' to 'd'. If σ_y is then increased again, behaviour remains elastic until the stress state reaches point 'd', when elasto-plastic behaviour is re-initiated.

6.11 Two dimensional behaviour of a linear elastic softening plastic material

In this case behaviour is similar to that for strain hardening, except that the size of the yield surface reduces with increase in plastic straining.

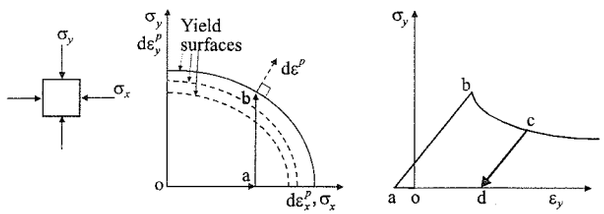

Figure 6.12: Two dimensional behaviour of a linear elastic softening plastic material

Following the same loading sequence as described in Sections 6.9 and 6.10 for perfect and strain or work hardening plasticity, results in the same behaviour until the initial yield surface is encountered at 'b', see Figure 6.12. Once the initial yield surface is encountered, plastic straining occurs and the size of the yield surface reduces (isotropic softening). It is therefore not possible for σ_y to remain at the value associated with point 'b'. Any attempt to do so results in indefinite plastic strains. If, instead of controlling σ_y attention is switched to controlling ε_y (i.e. switch from stress to strain boundary conditions), the strain softening stress-strain curve shown above can be followed. If at some stage during plastic straining ε_y is reduced, the soil behaves elastically (i.e. path 'c-d'). If ε_y is then increased again, the unloading path ('c-d') is retraced until the soil yields again (at point 'c'). The yield stress is now lower than it was initially.

6.12 Comparison with real soil behaviour

To simulate the behaviour of real soil it is necessary to have a model that involves both strain hardening and softening, see Figure 6.13.

It should be noted that one of the fundamental differences between elastic and elasto-plastic behaviour is that in the former strain increments are proportional to stress increments, whereas in the latter strain increments are a function of the current stress state and therefore the strain increments are not likely to be in the same directions as the applied stress increments.

In the above discussion it is implicitly assumed that elastic behaviour is linear. However, this is not realistic and it is possible to combine nonlinear elasticity with the elasto-plastic framework. Due to the complex nature of soil it has not been

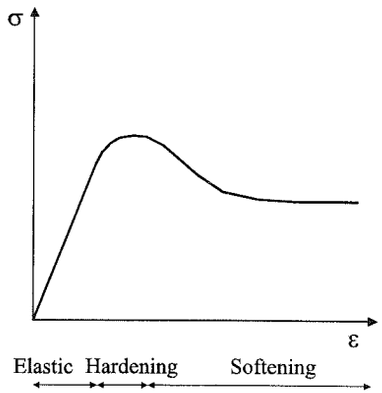

Figure 6.13: Real soil behaviour involving hardening and softening

possible, to date, to develop an elasto-plastic model that can capture all the facets of real soil behaviour and be defined by a limited set of input parameters that can be readily obtained from simple laboratory tests. There are therefore many such models currently in the literature. These range from simple to extremely complicated models. Some are formulated in terms of total and others in terms of effective stress. Some simple models will be discussed in Chapter 7, while more complicated ones are the subject of Chapter 8.

6.13 Formulation of the elasto-plastic constitutive matrix

Having defined the basic ingredients of an elasto-plastic constitutive model, it is now necessary to obtain a relationship between incremental stresses and incremental strains in the form of Equation (2.17):

$$\{\Delta\sigma\} = [\boldsymbol{D}^{ep}]\{\Delta\varepsilon\} \tag{6.4}$$

where $[\boldsymbol{D}^{ep}]$ is used to distinguish that the constitutive matrix is elasto-plastic, as opposed to purely elastic. The matrix $[\boldsymbol{D}]$ is retained to represent the purely elastic matrix.

The incremental total strains, $\{\Delta\varepsilon\}$, can be split into elastic, $\{\Delta\varepsilon^e\}$, and plastic, $\{\Delta\varepsilon^p\}$, components to give:

$$\{\Delta\varepsilon\} = \{\Delta\varepsilon^e\} + \{\Delta\varepsilon^p\} \tag{6.5}$$

The incremental stresses, $\{\Delta\sigma\}$, are related to the incremental elastic strains, $\{\Delta\varepsilon^e\}$, by the elastic constitutive matrix, $[\boldsymbol{D}]$, in the form:

$$\{\Delta\sigma\} = [\boldsymbol{D}]\{\Delta\varepsilon^e\} \tag{6.6}$$

or alternatively:

$$\{\Delta\varepsilon^e\} = [\boldsymbol{D}]^{-1}\{\Delta\sigma\} \tag{6.7}$$

Combining Equations (6.5) and (6.6) gives:

$$\{\Delta\sigma\} = [\boldsymbol{D}](\{\Delta\varepsilon\} - \{\Delta\varepsilon^p\}) \tag{6.8}$$

The incremental plastic strains, $\{\Delta\varepsilon^p\}$, are related to the plastic potential function, $P(\{\sigma\},\{\boldsymbol{m}\}) = 0$, via the flow rule given by Equation (6.2). This can be written as:

$$\{\Delta\varepsilon^p\} = \Lambda\left\{\frac{\partial P(\{\sigma\},\{\boldsymbol{m}\})}{\partial\sigma}\right\} \tag{6.9}$$

where Λ is a scalar. Substituting Equation (6.9) into Equation (6.8) gives:

$$\{\Delta\sigma\} = [\boldsymbol{D}]\{\Delta\varepsilon\} - \Lambda[\boldsymbol{D}]\left\{\frac{\partial P(\{\sigma\},\{\boldsymbol{m}\})}{\partial\sigma}\right\} \tag{6.10}$$

When the material is plastic the stress state must satisfy the yield function $F(\{\sigma\},\{\boldsymbol{k}\}) = 0$. Consequently, $dF(\{\sigma\},\{\boldsymbol{k}\}) = 0$ which, on using the chain rule of differentiation, gives:

$$dF(\{\sigma\},\{k\}) = \left\{\frac{\partial F(\{\sigma\},\{k\})}{\partial \sigma}\right\}^T \{\Delta\sigma\} + \left\{\frac{\partial F(\{\sigma\},\{k\})}{\partial k}\right\}^T \{\Delta k\} = 0 \quad (6.11)$$

This equation is known as the *consistency equation* (or condition). It can be rearranged to give:

$$\{\Delta\sigma\} = -\frac{\left\{\frac{\partial F(\{\sigma\},\{k\})}{\partial k}\right\}^T \{\Delta k\}}{\left\{\frac{\partial F(\{\sigma\},\{k\})}{\partial \sigma}\right\}^T} \quad (6.12)$$

Combining Equations (6.10) and (6.12) gives:

$$\Lambda = \frac{\left\{\frac{\partial F(\{\sigma\},\{k\})}{\partial \sigma}\right\}^T [D]\{\Delta\varepsilon\}}{\left\{\frac{\partial F(\{\sigma\},\{k\})}{\partial \sigma}\right\}^T [D]\left\{\frac{\partial P(\{\sigma\},\{m\})}{\partial \sigma}\right\} + A} \quad (6.13)$$

where

$$A = -\frac{1}{\Lambda}\left\{\frac{\partial F(\{\sigma\},\{k\})}{\partial k}\right\}^T \{\Delta k\} \quad (6.14)$$

Substituting Equation (6.13) into (6.10) gives:

$$\{\Delta\sigma\} = [D]\{\Delta\varepsilon\} - \frac{[D]\left\{\frac{\partial P(\{\sigma\},\{m\})}{\partial \sigma}\right\}\left\{\frac{\partial F(\{\sigma\},\{k\})}{\partial \sigma}\right\}^T [D]\{\Delta\varepsilon\}}{\left\{\frac{\partial F(\{\sigma\},\{k\})}{\partial \sigma}\right\}^T [D]\left\{\frac{\partial P(\{\sigma\},\{m\})}{\partial \sigma}\right\} + A} \quad (6.15)$$

Comparison of Equations (6.4) and (6.15) gives the elasto-plastic constitutive matrix $[D^{ep}]$ as:

$$[D^{ep}] = [D] - \frac{[D]\left\{\frac{\partial P(\{\sigma\},\{m\})}{\partial \sigma}\right\}\left\{\frac{\partial F(\{\sigma\},\{k\})}{\partial \sigma}\right\}^T [D]}{\left\{\frac{\partial F(\{\sigma\},\{k\})}{\partial \sigma}\right\}^T [D]\left\{\frac{\partial P(\{\sigma\},\{m\})}{\partial \sigma}\right\} + A} \quad (6.16)$$

The form of the parameter A given by Equation (6.14) depends on the type of plasticity (e.g. perfect plasticity, strain hardening/softening plasticity or work hardening/softening plasticity).

Perfect plasticity

In this case the state parameters, $\{k\}$, are constants and consequently

$$\left\{\frac{\partial F(\{\sigma\},\{k\})}{\partial k}\right\}^T = 0 \quad (6.17)$$

which in turn gives $A = 0$.

Strain hardening/softening plasticity

In this case the state parameters, $\{k\}$, are related to the accumulated plastic strains, $\{\varepsilon^p\}$. Consequently, Equation (6.14) can be written as:

$$A = -\frac{1}{\Lambda}\left\{\frac{\partial F(\{\sigma\},\{k\})}{\partial k}\right\}^T \frac{\partial\{k\}}{\partial\{\varepsilon^p\}}\{\Delta\varepsilon^p\} \quad (6.18)$$

If there is a linear relationship between $\{k\}$ and $\{\varepsilon^p\}$ so that

$$\frac{\partial\{k\}}{\partial\{\varepsilon^p\}} = \text{a constant (i.e. independent of } \{\varepsilon^p\}) \quad (6.19)$$

then on substitution into Equation (6.18), along with the flow rule given by Equation (6.9), the unknown scalar, Λ, cancels and A becomes determinant.

If there is not a linear relationship between $\{k\}$ and $\{\varepsilon^p\}$, the differential ratio on the left hand side of Equation (6.19) is a function of the plastic strains and therefore a function of Λ. When substituted into Equation (6.18), along with the flow rule given by Equation (6.9), the Λ's do not cancel and A becomes indeterminant. It is then not possible to evaluate the constitutive matrix $[D^{ep}]$.

In practice all strain hardening/softening models assume a linear relationship between the state parameters $\{k\}$ and the plastic strains $\{\varepsilon^p\}$.

Work hardening/softening plasticity

In this type of plasticity the state parameters, $\{k\}$, are related to the accumulated plastic work, W^p, which is dependent on the plastic strains. It can be shown, following a similar argument to that presented above for strain hardening/softening plasticity, that as long as there is a linear relationship between the state parameters $\{k\}$ and the plastic work, W^p, the parameter A defined by Equation (6.14) becomes independent of the unknown scalar, Λ, and therefore is determinant. If the relationship between $\{k\}$ and W^p is not linear, A becomes a function of Λ and it is not possible to evaluate the constitutive matrix $[D^{ep}]$.

If the elastic constitutive matrix, $[D]$, is symmetric, which it is for isotropic and cross anisotropic elasticity, then the elasto-plastic constitutive matrix, $[D^{ep}]$, given by Equation (6.16), is also symmetric if its numerator, given by:

$$[D]\left\{\frac{\partial P(\{\sigma\},\{m\})}{\partial \sigma}\right\}\left\{\frac{\partial F(\{\sigma\},\{k\})}{\partial \sigma}\right\}^T [D] \quad (6.20)$$

is symmetric. It is a simple matter to show that this only occurs if:

$$\left\{\frac{\partial P(\{\sigma\},\{m\})}{\partial \sigma}\right\} = \left\{\frac{\partial F(\{\sigma\},\{k\})}{\partial \sigma}\right\} \quad (6.21)$$

which implies that the yield and plastic potential functions must be identical. As noted earlier, this occurs in a special class of plasticity in which the flow rule is said to be associated. Substitution of a symmetric $[D^{ep}]$ for all elements in a finite element mesh, into the assembly process, results in a symmetric global stiffness matrix.

For the general case in which the flow rule is non-associated and the yield and plastic potential functions differ, the constitutive matrix $[D^{ep}]$ is non-symmetric. When assembled into the finite element equations this results in a non-symmetric global stiffness matrix. The inversion of such a matrix is more complex and requires more computing resources, both memory and time, than a symmetric matrix.

Some commercial programs are unable to deal with non-symmetric global stiffness matrices and, consequently, restrict the type of plastic models that can be accommodated to those which have an associated flow rule.

6.14 Summary

1. Elasto-plastic theory provides probably the best framework available in which to formulate constitutive models that can realistically simulate real soil behaviour. Three types of plastic behaviour are identified: perfect plasticity and strain (or work) hardening and softening plasticity. These models assume elastic behaviour prior to yield and can therefore utilise the benefits of both elastic and plastic behaviour.
2. The elasto-plastic framework can incorporate both linear and nonlinear elastic behaviour. Consequently, all the models described in Chapter 5 can be incorporated.
3. Elasto-plastic models are based on the assumption that the principal directions of accumulated stress and incremental plastic strain coincide. They require two essential pieces and one optional piece of information for their definition. The essential ingredients are a yield function, which separates purely elastic from elasto-plastic behaviour, and a plastic potential (or flow rule) which prescribes the direction of plastic straining. The optional ingredient is a set of hardening/softening rules which describe how the state parameters (e.g. strength) vary with plastic strain (or plastic work).
4. If the yield and plastic potential surfaces coincide, the model is said to be associated (or to satisfy the normality condition). This results in a symmetric constitutive matrix and consequently a symmetric global finite element stiffness matrix. If such a condition does not hold, both matrices are non-symmetric. This results in the use of greater computer resources, both time and memory, for finite element analyses.

7. Simple elasto-plastic constitutive models

7.1 Synopsis

This chapter presents the basic equations for some simple elasto-plastic constitutive models. Initially the Tresca and von Mises elastic perfectly plastic models are described. These are expressed in terms of total stresses and apply to undrained soil behaviour. Soil behaviour in terms of effective stresses is then considered and it is shown how the well known Coulomb failure condition can be extended to give the Mohr-Coulomb and Drucker-Prager models. The Mohr-Coulomb model is then extended by introducing strain hardening/softening plasticity. The chapter continues by introducing the critical state framework for soil behaviour and the basic assumptions of the popular Cam clay and modified Cam clay models. Some useful modifications to this basic formulation are then discussed. The chapter ends with a discussion on the importance of the shape of the plastic potential, in the deviatoric plane, on plane strain behaviour.

7.2 Introduction

In this chapter the elasto-plastic framework presented in Chapter 6 is used to construct some simple constitutive models. Initially the Tresca and von Mises elastic perfectly plastic models are described. These models are expressed in terms of total stress and apply to undrained soil behaviour. To describe general soil behaviour, it is necessary to express the constitutive model in terms of effective stresses. Using such an approach it is shown how the well known Coulomb failure criterion can be extended to give the Mohr-Coulomb and Drucker-Prager models. Although the above models are restricted in their ability to reproduce real soil behaviour, as described in Chapter 4, they form the basis of classical soil mechanics theory.

Further improvements to the simple constitutive models can be made by introducing hardening and/or softening plasticity. As an example, an extended version of the Mohr-Coulomb model is described.

The development of critical state constitutive models has provided a major advance in the use of plasticity theory in geomechanics. A relatively simple model, using an associated flow rule, is able to predict, at least qualitatively, a great number of the fundamental aspects of soil behaviour described in Chapter 4. This has led to the development of many different critical state type constitutive models,

each trying to improve the fit to real soil behaviour. The use of these models in numerical analyses of geotechnical problems has become one of the most characteristic features of computational geomechanics. After a brief introduction to the basic assumptions behind critical state soil mechanics, the popular Cam clay and modified Cam clay models are described. Both these models were initially developed for triaxial stress space and further assumptions are needed before they can be used to analyse boundary value problems, consequently their extension to general stress conditions is explored. Some of the more popular modifications to these models are also presented.

This chapter ends with a discussion on the importance of the shape of the plastic potential in the deviatoric plane on the behaviour in plane strain boundary value problems. It is shown that this shape governs the relative magnitude of the intermediate principal stress (e.g. expressed by the value of b or θ) at failure, which in turn controls the mobilised strength.

7.3 Tresca model

It is usual practice to plot soil test results in terms of a two dimensional stress state, using a Mohr's circle of stress. For example, if a conventional triaxial test is performed, it is common to plot the results in terms of the vertical and horizontal total stresses, σ_v and σ_h, or the vertical and horizontal effective stresses, σ_v' and σ_h'. If testing a saturated clay, the Mohr's circle of stress at failure is often plotted in terms of total stress and may look like that given in Figure 7.1. If two similar samples are tested at different cell pressures, without allowing any consolidation, conventional soil mechanics theory suggests that the Mohr's circles of stress at failure for the two samples have the same diameter, but plot at different positions on the σ axis, see Figure 7.1. A failure criterion is then adopted which relates the undrained strength, S_u, to the diameter of the Mohr's circle at failure. Noting that in a conventional triaxial test $\sigma_1 = \sigma_v$ and $\sigma_3 = \sigma_h$, this can be expressed as:

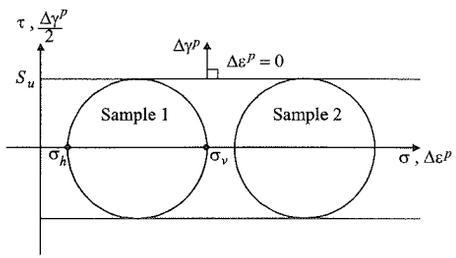

Figure 7.1: Mohr's circles of total stress

$$\sigma_1 - \sigma_3 = 2S_u \tag{7.1}$$

In the Tresca model this failure criterion is adopted as a yield surface and the yield function becomes:

$$F\left(\{\sigma\},\{k\}\right) = \sigma_1 - \sigma_3 - 2S_u = 0 \tag{7.2}$$

For general stress states it is necessary to calculate all three principal stresses (σ_a, σ_b and σ_c) and determine the major, σ_1, and minor, σ_3, values before this

equation can be evaluated. Consequently, for finite element analysis, it is more convenient to rewrite Equation (7.2) in terms of the stress invariants, p, J and θ (see Equations 5.1 to 5.3), using Equations 5.4, to give:

$$F\left(\{\sigma\},\{k\}\right) = J\cos\theta - S_u = 0 \tag{7.3}$$

In principal total stress space this yield function plots as a regular hexagonal cylinder, which has the space diagonal as its line of symmetry, see Figure 7.2. The hexagonal shape, which has six-fold symmetry in the deviatoric plane, arises due to the six permutations of the major and minor principal stress (e.g. $\sigma_a > \sigma_b > \sigma_c$; $\sigma_b > \sigma_a > \sigma_c$; ... etc). As this model is perfectly plastic there is no hardening/softening law required. The state parameter $\{k\}=S_u$ is assumed constant (i.e. independent of plastic strain and/or plastic work).

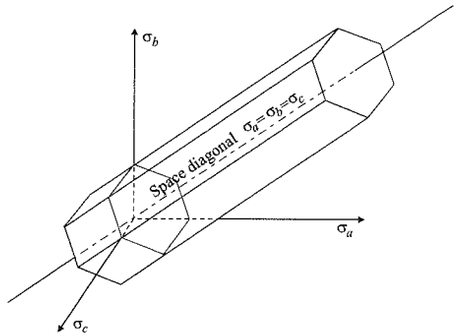

Figure 7.2: Tresca yield surface in principal stress space

The only remaining piece of information required to complete the plastic part of the model is the plastic potential function, $P(\{\sigma\},\{m\})$. As the model is intended to simulate the undrained behaviour of saturated clay, it should predict zero volumetric strains. Since the soil can be purely elastic (i.e. below the yield surface), or purely plastic (i.e. on the yield surface), both the elastic and plastic components of the volumetric strain must be zero. This clearly constrains the choice of the plastic potential. A convenient choice is to assume associated plastic flow and adopt the yield function given by Equation (7.3) as the plastic potential. Remembering that incremental plastic strains can be plotted on the same axes as accumulated stresses, see Section 6.8, then on Figure 7.1 the vector of incremental plastic strain is vertical (i.e. normal to the yield surface). This implies no incremental plastic direct strains and therefore no incremental plastic volumetric strain. A more direct way of showing this is to differentiate the plastic potential function with respect to p. This gives:

$$\Delta\varepsilon_v^p = \Lambda\frac{\partial P(\{\sigma\},\{m\})}{\partial p} = \Lambda\frac{\partial F(\{\sigma\},\{k\})}{\partial p} = 0 \tag{7.4}$$

The choice of associated plastic flow with $P(\{\sigma\},\{m\}) = F(\{\sigma\},\{k\})$ therefore satisfies the no plastic volumetric strain condition.

To complete the model it is only necessary to define the elastic parameters. As there should be no elastic volumetric strains, $\mu_u \approx 0.5$. The model can therefore be defined by specifying the undrained strength, S_u, and the undrained Young's modulus, E_u.

Construction of the elasto-plastic constitutive matrix $[\boldsymbol{D}^{ep}]$ (Equation (6.16)), requires the elastic constitutive matrix $[\boldsymbol{D}]$, which depends on E_u and μ_u (see Equation (5.8)), the partial derivatives of the yield and plastic potential functions, $\partial F(\{\sigma\},\{k\})/\partial\sigma$ and $\partial P(\{\sigma\},\{m\})/\partial\sigma$, and the hardening and softening parameter A, which is zero for perfect plasticity. To evaluate the partial derivatives of $F(\{\sigma\},\{k\})$ and $P(\{\sigma\},\{m\})$ use is made of the chain rule:

$$\frac{\partial F(\{\sigma\},\{k\})}{\partial\sigma}=\frac{\partial F(\{\sigma\},\{k\})}{\partial p}\frac{\partial p}{\partial\sigma}+\frac{\partial F(\{\sigma\},\{k\})}{\partial J}\frac{\partial J}{\partial\sigma}+\frac{\partial F(\{\sigma\},\{k\})}{\partial\theta}\frac{\partial\theta}{\partial\sigma}$$
$$\frac{\partial P(\{\sigma\},\{m\})}{\partial\sigma}=\frac{\partial P(\{\sigma\},\{m\})}{\partial p}\frac{\partial p}{\partial\sigma}+\frac{\partial P(\{\sigma\},\{m\})}{\partial J}\frac{\partial J}{\partial\sigma}+\frac{\partial P(\{\sigma\},\{m\})}{\partial\theta}\frac{\partial\theta}{\partial\sigma} \qquad (7.5)$$

The values of $\partial p/\partial\sigma$, $\partial J/\partial\sigma$ and $\partial\theta/\partial\sigma$ are model independent and are evaluated in Appendix VII.1. For the Tresca model $F(\{\sigma\},\{k\}) = P(\{\sigma\},\{m\})$ and:

$$\frac{\partial F}{\partial p}=\frac{\partial P}{\partial p}=0\ ;\ \frac{\partial F}{\partial J}=\frac{\partial P}{\partial J}=\cos\theta\ ;\ \frac{\partial F}{\partial\theta}=\frac{\partial P}{\partial\theta}=-J\sin\theta \qquad (7.6)$$

7.4 Von Mises model

It is evident from Figure 7.2 that, when plotted in three dimensional principal total stress space, the Tresca yield surface has corners. In particular, the intersection of the surface with a deviatoric plane (i.e. a plane normal to the space diagonal) produces a regular hexagon which has its corners at triaxial compression and extension points. These corners imply singularities in the yield function which have in the past caused havoc when attempting to use the yield function to obtain analytical (i.e. closed form) solutions to simple boundary value problems. These corners can also cause difficulties in numerical analysis. For example, the partial differentials of the yield and plastic potential functions required to define $[\boldsymbol{D}^{ep}]$, see Equation (6.16), are not uniquely defined at the corners. However, there are ways that such difficulties can be overcome.

Due to the analytical difficulties involved in using the Tresca criterion, applied mathematicians have often simplified the yield function expression so that it plots as a circular cylinder in principal stress space, instead of a hexagonal cylinder, see Figure 7.3. This can easily be achieved by rewriting Equation (7.3) in the following form:

$$F(\{\sigma\},\{k\}) = J-\alpha = 0 \qquad (7.7)$$

where α is a material parameter representing the shear strength of the

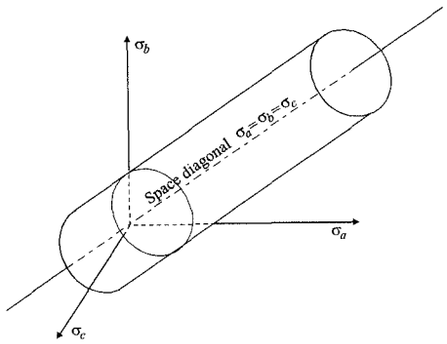

Figure 7.3: Von Mises yield surface in principal stress space

soil. This form of the yield function is often attributed to von Mises. In a deviatoric plane this yield function plots as a circle.

The problem now is to relate the value of α to the undrained shear strength of the soil. The problem is shown schematically in Figure 7.4, which shows the regular Tresca hexagon plotted in a deviatoric plane. Also shown are two von Mises circles, one which circumscribes, and the other which inscribes, the Tresca hexagon. If it is accepted that the von Mises yield function is an approximation to the Tresca function, then a circle that provides the best fit to the hexagon in Figure 7.4 is required. By comparing Equations (7.3) and (7.7) the following relationship is obtained:

$$\alpha=\frac{S_u}{\cos\theta} \qquad (7.8)$$

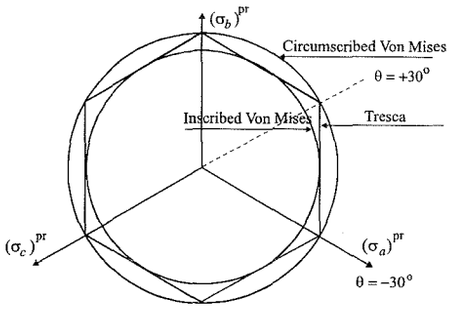

Figure 7.4: Comparison of Tresca and von Mises failure criteria in a deviatoric plane

This equation enables the two yield functions to be matched at a particular value of Lode's angle, θ. For example, the circumscribed circle shown in Figure 7.4 touches the Tresca hexagon at $\theta = \pm 30°$. This gives $\alpha = 1.155S_u$. The inscribed circle touches at $\theta = 0°$ and therefore $\alpha = S_u$. A better 'fit' circle may be that associated with $\theta = \pm 15°$, giving $\alpha = 1.035S_u$.

The model is completed by assuming associated flow conditions, with $P(\{\sigma\},\{m\})=F(\{\sigma\},\{k\})$, and therefore the plastic potential function is also given by Equation (7.7). The elastic behaviour is controlled by assuming Poisson's ratio $\mu_u \approx 0.5$ and prescribing a Young's modulus E_u. The partial derivatives of the yield and plastic potential functions required to evaluate the elasto-plastic constitutive matrix $[\boldsymbol{D}^{ep}]$ (Equation (6.16)), can be found from equation 7.5, with:

$$\frac{\partial F}{\partial p}=\frac{\partial P}{\partial p}=0\ ;\ \frac{\partial F}{\partial J}=\frac{\partial P}{\partial J}=1\ ;\ \frac{\partial F}{\partial\theta}=\frac{\partial P}{\partial\theta}=0 \qquad (7.9)$$

7.5 Mohr-Coulomb model

If the results of laboratory tests are plotted in terms of effective stresses, the Mohr's circles of stress at failure are often idealised as shown in Figure 7.5. It is usual to assume that the tangent to the failure circles from several tests, performed with different initial effective stresses, is straight. This line is called the Coulomb failure criterion and can be expressed as:

$$\tau_f = c' + \sigma'_{nf}\tan\varphi' \qquad (7.10)$$

where τ_f and σ_{nf}' are the shear and normal effective stresses on the failure plane,

and the cohesion, c', and angle of shearing resistance, φ', are material parameters. Using the Mohr's circle of stress, shown in Figure 7.5, and noting that $\sigma_1'=\sigma_v'$ and $\sigma_3'=\sigma_h'$, Equation (7.10) can be rewritten as:

$$\sigma_1' - \sigma_3' = 2c'\cos\varphi' + (\sigma_1' + \sigma_3')\sin\varphi' \tag{7.11}$$

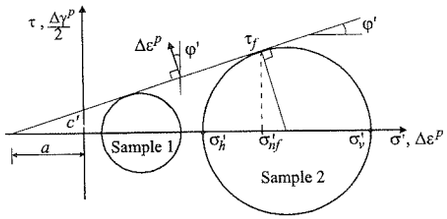

Figure 7.5: Mohr's circles of effective stress

This is often called the Mohr-Coulomb failure criterion and in the present model is adopted as the yield function:

$$F(\{\sigma'\},\{\boldsymbol{k}\}) = \sigma_1' - \sigma_3' - 2c'\cos\varphi' - (\sigma_1' + \sigma_3')\sin\varphi' \tag{7.12}$$

Following similar arguments to that put forward for the Tresca model, it is more convenient to rewrite this equation in terms of stress invariants p', J and θ. Therefore, substituting Equation (5.4) into Equation (7.12) and rearranging gives:

$$F(\{\sigma'\},\{\boldsymbol{k}\}) = J - \left(\frac{c'}{\tan\varphi'} + p'\right) g(\theta) = 0 \tag{7.13}$$

where:

$$g(\theta) = \frac{\sin\varphi'}{\cos\theta + \dfrac{\sin\theta\sin\varphi'}{\sqrt{3}}} \tag{7.14}$$

In principal effective stress space the yield function (7.13) plots as an irregular hexagonal cone as shown in Figure 7.6. The six-fold symmetry again arises from the possible permutations of principal stresses.

It is of interest to note that if S_u is substituted for c' and φ' is set to zero in Equation (7.13), the Tresca yield function given earlier by Equation (7.3) is obtained.

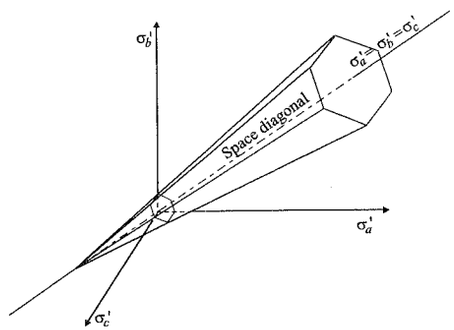

Figure 7.6: Mohr-Coulomb yield surface in principal stress space

As the Mohr-Coulomb model is assumed to be perfectly plastic, there is no hardening/softening law required. The state parameter $\{\boldsymbol{k}\}=\{c',\varphi'\}^T$ is assumed constant, independent of plastic strain or plastic work.

To complete the plastic part of the model a plastic potential function, $P(\{\sigma'\},\{\boldsymbol{m}\})$, is required. Similar to the Tresca model, an associated flow rule, with $P(\{\sigma'\},\{\boldsymbol{m}\})=F(\{\sigma'\},\{\boldsymbol{k}\})$, could be adopted. As shown on Figure 7.5, the plastic strain increment vector is then inclined at an angle φ' to the vertical and indicates negative (i.e. tensile) direct plastic strains. This in turn results in a dilatant plastic volumetric strain. For this situation the angle of dilation, ν, defined by Equation (7.15) and shown graphically in Figure 7.7, is equal to the angle of shearing resistance, φ':

$$\nu = \sin^{-1}\left(-\frac{\Delta\varepsilon_1^p + \Delta\varepsilon_3^p}{\Delta\varepsilon_1^p - \Delta\varepsilon_3^p}\right) \tag{7.15}$$

This can be verified by substituting values for $\Delta\varepsilon_1^p = \Lambda\partial P(\{\sigma'\},\{\boldsymbol{m}\})/\partial\sigma_1'$ and $\Delta\varepsilon_3^p = \Lambda\partial P(\{\sigma'\},\{\boldsymbol{m}\})/\partial\sigma_3'$, with $P(\{\sigma'\},\{\boldsymbol{m}\})$ given by Equation (7.12), into Equation (7.15).

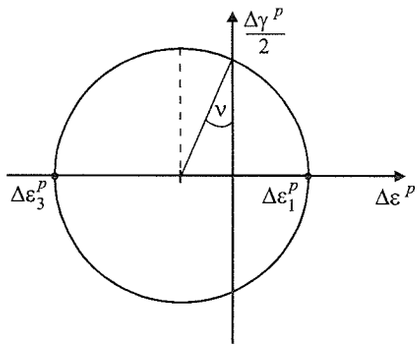

Figure 7.7: Mohr's circle of plastic strains

There are two drawbacks to this approach. Firstly, the magnitude of the plastic volumetric strains (i.e. the dilation) is much larger than that observed in real soils, and secondly, once the soil yields it will dilate for ever. Real soil, which may dilate initially on meeting the failure surface, will often reach a constant volume condition (i.e. zero incremental plastic volumetric strains) at large strains.

The first drawback can be partly rectified by adopting a non-associated flow rule, where the plastic potential function is assumed to take a similar form to that of the yield surface, Equation (7.13), but with φ' replaced by ν. This gives:

$$P(\{\sigma'\},\{\boldsymbol{m}\}) = J - (a_{pp} + p')g_{pp}(\theta) = 0 \tag{7.16}$$

where

$$g_{pp}(\theta) = \frac{\sin\nu}{\cos\theta + \dfrac{\sin\theta\sin\nu}{\sqrt{3}}} \tag{7.17}$$

and a_{pp} is the distance of the apex of the plastic potential cone from the origin of principal effective stress space. It is akin to $c'/\tan\varphi'$ in the yield function, see Equation (7.13).

Noting that the plastic potential must also pass through the current stress state which, because the soil is plastic, must be on the yield surface, the situation shown in Figure 7.8 is obtained. In this figure, p_c', J_c and θ_c (not shown) are the stress invariants at the current state of stress which is assumed to be on the yield surface. As both the yield and plastic potential surface must pass through this stress state, p_c', J_c and θ_c can be substituted into Equations (7.13) and (7.16) to obtain the following equations:

$$\begin{aligned} J_c - \left(\frac{c'}{\tan\varphi'} + p_c'\right) g(\theta_c) &= 0 \\ J_c - \left(a_{pp} + p_c'\right) g_{pp}(\theta_c) &= 0 \end{aligned} \tag{7.18}$$

Solving for a_{pp} gives:

$$a_{pp} = \left(\frac{c'}{\tan\varphi'} + p'_c\right)\frac{g(\theta_c)}{g_{pp}(\theta_c)} - p'_c \qquad (7.19)$$

which, on substitution into Equation (7.16), gives the required plastic potential function:

$$P(\{\sigma'\},\{\boldsymbol{m}\}) = J - \left[\left(\frac{c'}{\tan\varphi'} + p'_c\right)\frac{g(\theta_c)}{g_{pp}(\theta_c)} - p'_c + p'\right]g_{pp}(\theta) = 0 \qquad (7.20)$$

While the yield surface is fixed in p'-J-θ space, the plastic potential surface moves so as to pass through the current stress state. This is acceptable as only the derivatives of the plastic potential with respect to the stress components are needed to form the elasto-plastic constitutive matrix $[\boldsymbol{D}^{ep}]$, see Equation (6.16). If $v = \varphi'$, Equation (7.20) becomes the same as Equation (7.13) and associated conditions arise. However, $v < \varphi'$ results in non-associated conditions, and as v reduces less dilation is generated. If $v = 0°$, zero plastic dilation (i.e. no plastic volume strain) occurs. Consequently, by prescribing the angle of dilation, v, the predicted plastic volumetric strains can be controlled.

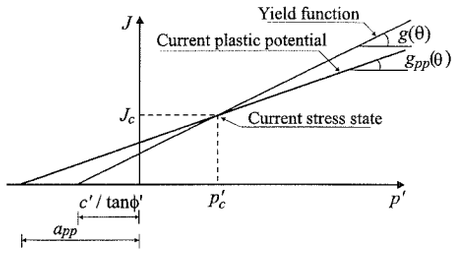

Figure 7.8: Relationship between the yield and plastic potential functions

Although the use of a non-associated flow rule enables the magnitude of the incremental plastic volumetric strains to be restricted, the model still predicts increasing volumetric strains, no matter how far the soil is sheared. This is unrealistic and can give unreasonable predictions in some boundary value problems. This is discussed in more detail in Volume 2 of this book. One way around this problem is to allow the angle of dilation to vary with plastic strain. Such a model is presented later in this chapter.

To summarise, the Mohr-Coulomb model requires 5 parameters. Three of these, c', φ' and v, control the plastic behaviour, and the remaining two, E' and μ', control the elastic behaviour. If associated conditions are assumed, the number of parameters reduces to 4, as $v = \varphi'$.

The partial derivatives of the yield and plastic potential functions required to evaluate the elasto-plastic constitutive matrix can be found using the chain rule:

$$\frac{\partial F(\{\sigma'\},\{\boldsymbol{k}\})}{\partial \sigma'} = \frac{\partial F(\{\sigma'\},\{\boldsymbol{k}\})}{\partial p'}\frac{\partial p'}{\partial \sigma'} + \frac{\partial F(\{\sigma'\},\{\boldsymbol{k}\})}{\partial J}\frac{\partial J}{\partial \sigma'} + \frac{\partial F(\{\sigma'\},\{\boldsymbol{k}\})}{\partial \theta}\frac{\partial \theta}{\partial \sigma'}$$

$$\frac{\partial P(\{\sigma'\},\{\boldsymbol{m}\})}{\partial \sigma'} = \frac{\partial P(\{\sigma'\},\{\boldsymbol{m}\})}{\partial p'}\frac{\partial p'}{\partial \sigma'} + \frac{\partial P(\{\sigma'\},\{\boldsymbol{m}\})}{\partial J}\frac{\partial J}{\partial \sigma'} + \frac{\partial P(\{\sigma'\},\{\boldsymbol{m}\})}{\partial \theta}\frac{\partial \theta}{\partial \sigma'} \qquad (7.21)$$

where the values of $\partial p'/\partial \boldsymbol{\sigma}'$, $\partial J/\partial \boldsymbol{\sigma}'$ and $\partial \theta/\partial \boldsymbol{\sigma}'$ are model independent and are evaluated in Appendix VII.1, and:

$$\frac{\partial F(\{\sigma'\},\{\boldsymbol{k}\})}{\partial p'} = -g(\theta)\ ;\quad \frac{\partial F(\{\sigma'\},\{\boldsymbol{k}\})}{\partial J} = 1$$

$$\frac{\partial F(\{\sigma'\},\{\boldsymbol{k}\})}{\partial \theta} = \left(\frac{c'}{\tan\varphi'} + p'\right)\frac{\sin\varphi'}{\left(\cos\theta + \frac{\sin\theta\sin\varphi'}{\sqrt{3}}\right)^2}\left(\sin\theta - \frac{\cos\theta\sin\varphi'}{\sqrt{3}}\right) \qquad (7.22)$$

$$\frac{\partial P(\{\sigma'\},\{\boldsymbol{m}\})}{\partial p'} = -g_{pp}(\theta)\ ;\quad \frac{\partial P(\{\sigma'\},\{\boldsymbol{m}\})}{\partial J} = 1$$

$$\frac{\partial P(\{\sigma'\},\{\boldsymbol{m}\})}{\partial \theta} = \left(a_{pp} + p'\right)\frac{\sin\nu}{\left(\cos\theta + \frac{\sin\theta\sin\nu}{\sqrt{3}}\right)^2}\left(\sin\theta - \frac{\cos\theta\sin\nu}{\sqrt{3}}\right) \qquad (7.23)$$

7.6 Drucker-Prager model

As with the Tresca model described earlier, the Mohr-Coulomb yield function has corners when plotted in principal effective stress space, see Figure 7.6. These corners imply singularities in the yield function. In particular, the partial derivatives with respect to the stress components, which are needed to define the elasto plastic constitutive matrix $[\boldsymbol{D}^{ep}]$, see Equation 6.16, are not unique at the corners. Although these corners can be dealt with in finite element analysis, this involves the use of some elaborate computer code which inevitably results in the use of more computer resources. Consequently, earlier pioneers of the subject sought simplifications. The most common, but not the only, way to overcome the corner problem is to modify the yield function so that it plots as a cylindrical cone, see Figure 7.9. This can simply be achieved by replacing $g(\theta)$ in Equation (7.13) by a constant, M_{JP}, (i.e. independent of θ). The yield function then becomes:

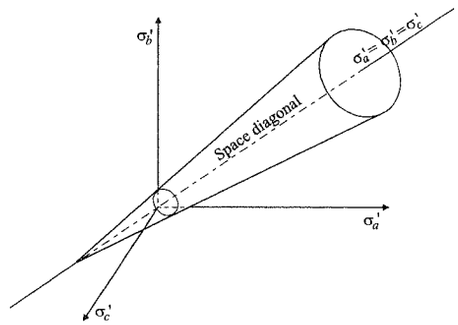

Figure 7.9: Drucker-Prager yield surface in principal stress space

$$F(\{\sigma'\},\{\boldsymbol{k}\}) = J - \left(\frac{c'}{\tan\varphi'} + p'\right)M_{JP} = 0 \qquad (7.24)$$

where M_{JP} is a material constant. This form of the yield function is often called the Drucker-Prager or 'extended von Mises' yield function. In the deviatoric plane it plots as a circle.

To use this model in geotechnical engineering M_{JP} must be related to the angle of shearing resistance, φ'. The problem is shown schematically in Figure 7.10 where the irregular hexagon of the Mohr-Coulomb surface is compared with the circular shape of the Drucker-Prager surface in the deviatoric plane. Two alternative Drucker-Prager circles are shown, one circumscribes, while the other inscribes, the irregular Mohr-Coulomb hexagon. Assuming that the Mohr-Coulomb surface is correct, then the Drucker-Prager circle that provides the best fit to the hexagon is required. Comparing Equations (7.13) and (7.24) gives:

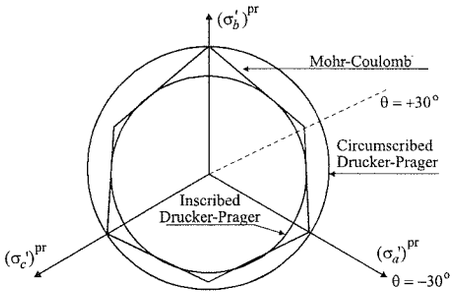

Figure 7.10: Drucker-Prager and Mohr-Coulomb yield surfaces in the deviatoric plane

$$M_{JP} = g(\theta) = \frac{\sin\varphi'}{\cos\theta + \dfrac{\sin\theta\sin\varphi'}{\sqrt{3}}} \qquad (7.25)$$

This equation allows the two yield surfaces to be matched at a particular value of the Lode's angle, θ. For example, the circumscribed surface shown in Figure 7.10 touches the Mohr-Coulomb hexagon at $\theta = -30°$ (triaxial compression). Substitution of $\theta = -30°$ into Equation (7.25) gives:

$$M_{JP}^{\theta=-30°} = \frac{2\sqrt{3}\sin\varphi'}{3-\sin\varphi'} \qquad (7.26)$$

Likewise, the Drucker-Prager circle which touches the Mohr-Coulomb hexagon at $\theta = +30°$ (triaxial extension) can be found by substituting $\theta = +30°$ into Equation (7.25) to give:

$$M_{JP}^{\theta=+30°} = \frac{2\sqrt{3}\sin\varphi'}{3+\sin\varphi'} \qquad (7.27)$$

To find the value of M_{JP} for the inscribed circle, the value of θ at which this circle is tangential to the Mohr-Coulomb hexagon must first be determined. This can be done by finding the value of θ which produces a minimum value of M_{JP} in Equation (7.25). Differentiating Equation (7.25) with respect to θ and setting the resulting expression to zero gives:

$$\theta^{ins} = \tan^{-1}\left(\frac{\sin\varphi'}{\sqrt{3}}\right) \qquad (7.28)$$

Substituting this value of θ into Equation (7.25) provides the value of M_{JP}^{ins}.

The model is completed by adopting a non-associated plastic potential function of the form:

$$P(\{\sigma'\},\{\boldsymbol{m}\}) = J - \left[\left(\frac{c'}{\tan\varphi'} + p_c'\right)\frac{M_{JP}}{M_{JP}^{pp}} - p_c' + p'\right]M_{JP}^{pp} = 0 \qquad (7.29)$$

where M_{JP}^{pp} is the gradient of the plastic potential function in J-p' space, see Figure 7.11. If $M_{JP}^{pp} = M_{JP}$ the yield and plastic potential functions are the same and the model becomes associated. M_{JP}^{pp} can be related to the angle of dilation, ν, by equating $M_{JP}^{pp} = g_{pp}(\theta)$, where $g_{pp}(\theta)$ is given by Equation (7.17).

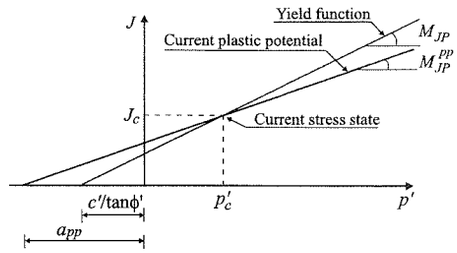

Figure 7.11: Relationship between the yield and plastic potential functions

As with the Mohr-Coulomb model, the elastic behaviour is controlled by assuming a Young's modulus, E', and Poisson's ratio, μ'. The model therefore requires 5 parameters. The partial derivatives of the yield and plastic potential functions, required to evaluate the elasto-plastic constitutive matrix $[\boldsymbol{D}^{ep}]$, are again determined from Equation (7.21), with:

$$\frac{\partial F(\{\sigma'\},\{\boldsymbol{k}\})}{\partial p'} = -M_{JP} \;;\; \frac{\partial F(\{\sigma'\},\{\boldsymbol{k}\})}{\partial J} = 1 \;;\; \frac{\partial F(\{\sigma'\},\{\boldsymbol{k}\})}{\partial \theta} = 0 \qquad (7.30)$$

$$\frac{\partial P(\{\sigma'\},\{\boldsymbol{m}\})}{\partial p'} = -M_{JP}^{pp} \;;\; \frac{\partial P(\{\sigma'\},\{\boldsymbol{m}\})}{\partial J} = 1 \;;\; \frac{\partial P(\{\sigma'\},\{\boldsymbol{m}\})}{\partial \theta} = 0 \qquad (7.31)$$

7.7 Comments on simple elastic perfectly plastic models

In the previous sections four simple linear elastic perfectly plastic models have been considered. The difference between the Tresca and von Mises, and the Mohr-Coulomb and Drucker-Prager models, is essentially their shape in the deviatoric plane. Working from the conventional assumption that the strength is related to the difference between major and minor principal stresses results in the Tresca model (for total stress) and the Mohr-Coulomb model (for effective stress). The implicit assumption in these models is therefore that yield and strength are independent of the intermediate principal stress, σ_2. This, in turn, leads to the yield and plastic potential functions plotting as a hexagonal cylinder (Tresca) and a hexagonal cone (Mohr-Coulomb) in principal stress space.

The von Mises and the Drucker-Prager models give a circular cylinder and a circular cone respectively, when the yield and plastic potential surfaces are plotted in principal stress space. This means that both yield and strength are dependent on the intermediate principal stress, σ_2. Although this subtle difference might, at this stage, seem to be academic, it can have some serious effects in the analysis of boundary value problems. This is discussed further in Volume 2 of this book.

Unfortunately, there is little experimental data available to accurately quantify the effect of the intermediate principal stress on soil behaviour. To investigate such behaviour in the laboratory requires the use of complex test equipment, such as hollow cylinder or true triaxial devices. The limited data that does exist suggests that both yield and failure functions plot as smoothed surfaces (i.e. no corners) in the deviatoric plane, with a shape somewhere between that of the hexagons and circles shown in Figures 7.4 and 7.10. Alternative shapes could be used in the above models. For example, in the Mohr-Coulomb model a simple way of changing the shape in the deviatoric plane is to redefine the function $g(\theta)$ given by Equation (7.14). Examples of this are given in Section 7.9.2.

As conventional soil mechanics is based on the Tresca and Mohr-Coulomb models, it seems sensible to use these models in preference to the von Mises and Drucker-Prager models. This has the advantage that the finite element analysis is then compatible with conventional soil mechanics, but has the disadvantage that the software has to deal with the corners of the yield and plastic potential surfaces.

To increase the flexibility of the models, it is also possible to replace the linear elastic with nonlinear elastic behaviour, by allowing the elastic constants to vary with stress and/or stain level.

7.8 An elastic strain hardening/softening Mohr-Coulomb model

To improve the Mohr-Coulomb model described in Section 7.5, the strength parameters, c' and φ', and the angle of dilation, v, can all be allowed to vary with the accumulated plastic strains. For example, a model could be developed which assumes the variation of c' and φ' with accumulated deviatoric plastic strain, E_d^p, as shown in Figure 7.12. There are three zones: in zone 1, c' and φ' are assumed to increase linearly from initial values (c_i' and φ_i') to peak values (c_p' and φ_p'); in zone 2, c' and φ' remain constant and equal to the peak values; in zone 3, c' and φ' reduce from the peak values to residual values (c_r' and φ_r'), either in a linear or exponential manner. Consequently, stain hardening occurs in zone 1, behaviour is perfectly plastic in zone 2, and strain softening occurs in zone 3. The angle of dilation, v, is assumed to be proportional to the angle of shearing resistance, φ', in zones 1 and 2 (i.e. $v=\psi\varphi'$, were ψ is a constant), whereas in zone 3 it is assumed to reduce from the peak value assumed in zone 2 to a residual value, v_r, in the same manner as φ' reduces (i.e. either linearly or

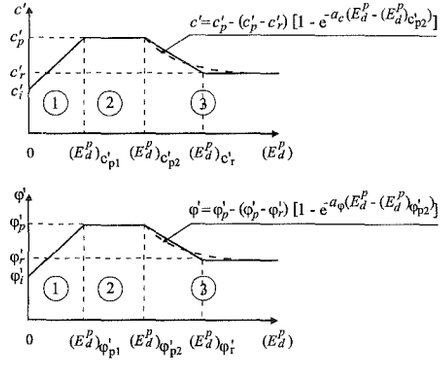

Figure 7.12: Hardening rules

exponentially). In general, the model requires the following input parameters:

Plastic parameters: c_i', c_p', c_r', φ_i', φ_p', φ_r, $(E_d^p)_{cp1}$, $(E_d^p)_{cp2}$, $(E_d^p)_{\varphi p1}$, $(E_d^p)_{\varphi p2}$, ψ, v_r and either $(E_d^p)_{cr}$, $(E_d^p)_{\varphi r}$ (linear softening), or a_c, a_φ (exponential softening)

Elastic parameters: E' and μ' or the parameters for a nonlinear elastic model.

While this represents a substantial amount of input data, it does give the model maximum flexibility. By suitable choice of parameters it is possible to simplify the model and only use some of its components. For example, if $c_i'=c_p'=c_r'$ and $\varphi_i'=\varphi_p'=\varphi_r'$ the model reduces to the conventional perfectly plastic Mohr-Coulomb model described in Section 7.5. Likewise, if $c_i'=c_p'$ and $\varphi_i'=\varphi_p'$ and $(E_d^p)_{cp1} = (E_d^p)_{\varphi p1} = (E_d^p)_{cp2} = (E_d^p)_{\varphi p2} = 0$, then only the softening part of the model (i.e. zone 3) is active.

In each of the three zones mathematical expressions can be assigned to the variation of c' and φ' with E_d^p and therefore the hardening/softening rules can be expressed in a piece-wise manner. This enables the parameter A, defined by Equation (6.14), to be calculated, and this, with the partial differentials of the yield and plastic potential functions, leads to the constitutive matrix $[\boldsymbol{D}^{ep}]$.

In this context the yield and plastic potential derivatives are given by Equation (7.21), together with Equations (7.22) and (7.23). The parameter A, for strain hardening/softening, is derived from Equation (6.14) as:

$$A = -\left(\frac{\partial F(\{\sigma'\},\{k\})}{\partial \varphi'}\frac{\partial \varphi'}{\partial E_d^p} + \frac{\partial F(\{\sigma'\},\{k\})}{\partial c'}\frac{\partial c'}{\partial E_d^p}\right)\frac{\partial P(\{\sigma'\},\{m\})}{\partial J} \qquad (7.32)$$

The yield and plastic potential derivatives in Equation (7.32) are independent of the three zones and, from Equations (7.13) and (7.16), these are:

$$\begin{aligned}
\frac{\partial P(\{\sigma'\},\{m\})}{\partial J} &= 1 \\
\frac{\partial F(\{\sigma'\},\{k\})}{\partial c'} &= -\frac{g(\theta)}{\tan\varphi'} \\
\frac{\partial F(\{\sigma'\},\{k\})}{\partial \varphi'} &= \frac{g(\theta)}{\sin^2\varphi'}\left[c' - \left(\frac{c'}{\tan\varphi'} + p'\right) g(\theta)\cos\theta\cos\varphi'\right]
\end{aligned} \qquad (7.33)$$

The derivatives of φ' and c' depend on the distribution of these parameters in each of the three zones:

Zone 1: Linear

$$\frac{\partial \varphi'}{\partial E_d^p} = \frac{\varphi_p' - \varphi_i'}{(E_d^p)_{\varphi' p1}} \quad ; \quad \frac{\partial c'}{\partial E_d^p} = \frac{c_p' - c_i'}{(E_d^p)_{c' p1}}$$

Zone 2: Constant

$$\frac{\partial \varphi'}{\partial E_d^p} = 0 \;\; ; \;\; \frac{\partial c'}{\partial E_d^p} = 0$$

Zone 3: Exponential

$$\frac{\partial \varphi'}{\partial E_d^p} = a_\varphi (\varphi_r' - \varphi_p') \, e^{-a_\varphi [E_d^p - (E_d^p)_{\varphi_{p2}'}]}$$

$$\frac{\partial c'}{\partial E_d^p} = a_c (c_r' - c_p') \, e^{-a_c [E_d^p - (E_d^p)_{c_{p2}'}]}$$

Zone 3: Linear

$$\frac{\partial \varphi'}{\partial E_d^p} = \frac{\varphi_r' - \varphi_p'}{(E_d^p)_{\varphi_r'} - (E_d^p)_{\varphi_{p2}'}}$$

$$\frac{\partial c'}{\partial E_d^p} = \frac{c_r' - c_p'}{(E_d^p)_{c_r'} - (E_d^p)_{c_{p2}'}}$$

(7.34)

A model similar to that described above was used, with nonlinear elastic behaviour below the yield surface, to analyse the progressive failure of Carsington dam (Potts *et al.* (1990)) and to investigate the delayed collapse of cut slopes in stiff clay (Potts *et al.* (1997)).

7.9 Development of the critical state models

Since the work of Coulomb (1776) and Rankine (1857), there has been a long history of applications of the theory of plasticity to geomechanics. Slip line theory and the theorems of limit analysis are in frequent use. However, the development of realistic constitutive models for soils has lagged significantly behind the corresponding formulations for metals, in spite of the fact that the features of soil behaviour mentioned previously, see Chapter 4, are clearly consistent with the elasto-plastic framework. Early attempts of taking into account the frictional character of geo-materials by extending the von Mises failure criterion (Drucker and Prager, (1952)), or by generalising the Mohr-Coulomb failure envelope, see Figures 7.6 and 7.9, failed to model adequately many basic features of soil behaviour (see Chapter 4). Also, adoption of associated flow rules implied the prediction of excessive dilatancy during yield.

In the 1950's, several developments occurred which led towards the formulation of the first critical state models. Drucker *et al.* (1957) suggested the existence of a cap yield surface controlled by volume change, Roscoe *et al.* (1958) postulated a behavioural framework based on the concepts of critical state and the existence of a state boundary surface, and Calladine (1963) suggested the theory of hardening plasticity as a basis for a consistent formulation of the models.

The first critical state models were the series of Cam clay formulations, developed at the University of Cambridge, by Roscoe and his co-workers. The formulation of the original Cam clay model as an elasto-plastic constitutive law is presented by Roscoe and Schofield (1963) and Schofield and Wroth (1968). Afterwards, Roscoe and Burland (1968) proposed the modified Cam clay model. The first numerical implementations date back to the early 1970's (Smith (1970), Simpson (1973) and Naylor (1975)).

7.9.1 Basic formulation in triaxial stress space

Both the Cam clay and modified Cam clay models were originally developed for triaxial loading conditions. These models are essentially based on the following assumptions:

- A piece of clay, which is subjected to slow, perfectly drained isotropic ($\sigma_1'=\sigma_2'=\sigma'_3$) compression, moves along a trajectory in the v-lnp' plane (v = specific volume = 1+e), which consists of a virgin consolidation line and a set of swelling lines, see Figure 7.13. Initially, on first loading, the soil moves down the virgin consolidation line. If subsequently unloaded from point 'b', it moves up the swelling line 'bc'. If re-loaded, it moves back down this same swelling line until point 'b' is reached, at which point it begins to move down the virgin consolidation line again. If unloaded from point 'd', it moves up the swelling line 'de'. The virgin consolidation line and the swelling lines are assumed to be straight in v-lnp' space and are given by the following equations:

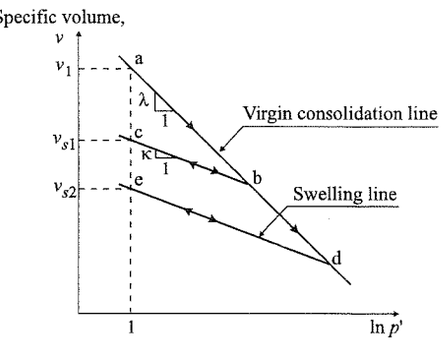

Figure 7.13: Behaviour under isotropic compression

$$\begin{aligned} v + \lambda (\ln p') &= v_1 \quad \text{(virgin consolidation line)} \\ v + \kappa (\ln p') &= v_s \quad \text{(swelling line)} \end{aligned} \tag{7.35}$$

The values of κ, λ and v_1 are characteristics of the particular type of clay, whereas the value of v_s is different for each swelling line. Volume change along the virgin consolidation line is mainly irreversible or *plastic*, while volume change along a swelling line is reversible or *elastic*.

- The behaviour under increasing triaxial shear stress, $q = \sigma_v'-\sigma_h' = \sqrt{3}J$, is assumed to be elastic until a yield value of q is reached, which can be obtained from the yield function $F(\{\boldsymbol{\sigma}'\},\{\boldsymbol{k}\}) = 0$. As noted above, behaviour is elastic along swelling lines and therefore the yield function plots above each swelling line as shown in Figure 7.14. For Cam clay and modified Cam clay the yield surface is assumed to take the form:

$$F(\{\sigma'\},\{k\}) = \frac{J}{p' M_J} + \ln\left(\frac{p'}{p_o'}\right) = 0 \quad \text{(Cam clay)} \tag{7.36}$$

$$F(\{\sigma'\},\{k\}) = \left(\frac{J}{p' M_J}\right)^2 - \left(\frac{p_o'}{p'} - 1\right) = 0 \quad \text{(modified Cam clay)} \tag{7.37}$$

where p' is the mean effective stress (see Equation (5.1)), J is the deviatoric stress (see Equation (5.2)), M_J is another clay parameter, and p_o' is the value of

p' at the intersection of the current swelling line with the virgin consolidation line, see Figure 7.14. The projections of these curves onto the J-p' plane are shown in Figures 7.15a and 7.15b. The Cam clay yield surface plots as a logarithmic curve, whereas the modified Cam clay yield surface plots as an ellipse. The parameter p_o' essentially controls the size of the yield surface and has a particular value for each swelling line. As there is a yield surface for each swelling line, the yield function, given by either Equation (7.36) or (7.37), defines a surface in v-J-p' space, called the *Stable State Boundary Surface*, see Figure 7.16. If the v-J-p' state of the clay plots inside this surface, its behaviour is elastic, whereas if its state lies on the surface it is elasto-plastic. It is not possible for the clay to have a v-J-p' state that lies outside this surface.

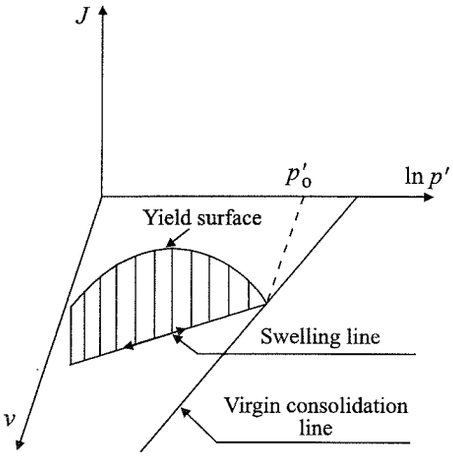

Figure 7.14: Yield surface

- Hardening/softening is isotropic and is controlled by the parameter p_o' which is related to the plastic volumetric strain, ε_v^p, by:

$$\frac{dp_o'}{p_o'} = d\varepsilon_v^p \frac{v}{\lambda - \kappa} \qquad (7.38)$$

Equation (7.38) therefore provides the hardening rule.

- When the soil is plastic (i.e. on the Stable State Boundary Surface), the plastic strain increment vector is taken normal to the yield curve. Consequently, the model is associated, with the plastic potential $P(\{\sigma'\},\{m\})$ being given either by Equation (7.36) (Cam clay) or Equation (7.37) (modified Cam clay).

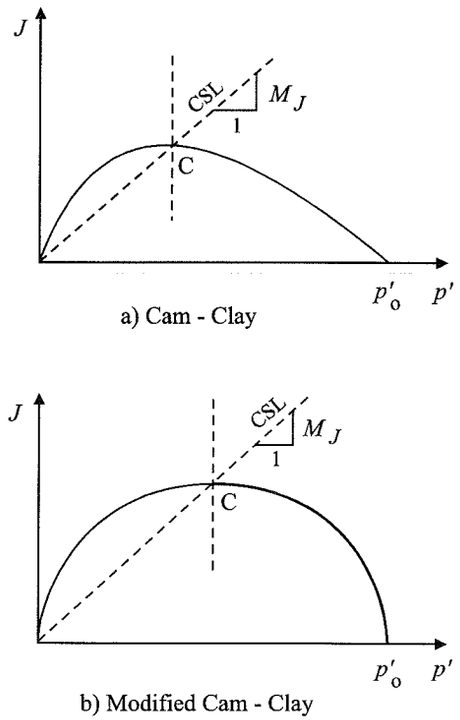

Figure 7.15: Projection of yield surface onto J-p′ plane

- As noted above, behaviour along a swelling line is elastic. This means that the elastic volumetric strain, ε_v^e, can be determined from Equation (7.35):

$$d\varepsilon_v^e = \frac{dv}{v} = \frac{\kappa}{v}\frac{dp'}{p'} \qquad (7.39)$$

This gives the elastic bulk modulus, K, as:

$$K = \frac{dp'}{d\varepsilon_v^e} = \frac{vp'}{\kappa} \qquad (7.40)$$

In the original formulation, no elastic shear strains are considered. To avoid numerical problems and to achieve a better modelling inside the state boundary surface, elastic shear strains are usually computed from an elastic shear modulus, G, which is an additional model parameter.

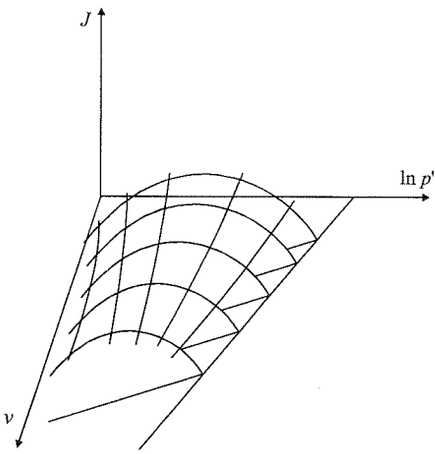

Figure 7.16: State boundary surface

In the above form, both the Cam clay and modified Cam clay models require five material parameters: v_1, κ, λ, M_J and G. Sometimes an elastic Poisson's ratio, μ, is specified instead of G.

The discontinuity of the yield surface of the original Cam clay model at J=0, see Figure 7.15a, implies difficulties both theoretical and practical. As the flow rule is associated, isotropic stress changes at that point cause non-zero shear strains, see Figure 7.17a. Although this can be avoided by assuming that at this location there is a corner to the yield surface and therefore that the incremental strain vector is parallel to the p' axis, there is still a sudden jump in the plastic strain vector as the deviatoric stress increases, see Figure 7.17b. This model may also have problems in predicting a reasonable stress response for some applied incremental strain ratios. It was because of these problems that the modified Cam clay model was

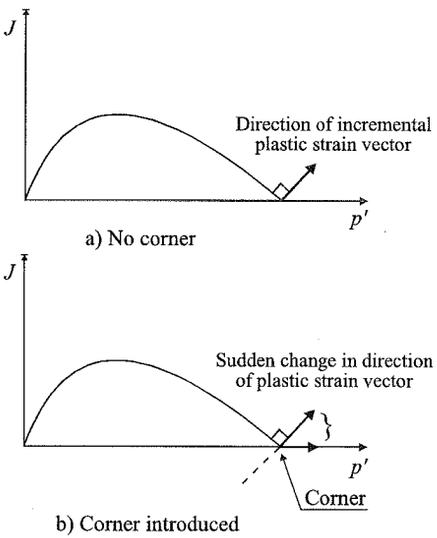

Figure 7.17: Discontinuous nature of the original Cam clay yield surface

developed. By adopting an ellipse for the shape of the yield surface, see Equation (7.37), the above problems are eliminated. As both the Cam clay and modified Cam clay models share most of their features (except the yield surface shape), they are considered here as the basic formulation of the critical state models. Some of the consequences of the models are now examined.

In Figure 7.15, point C represents the point on the yield (and plastic potential) curve with a horizontal slope. At that point, incremental plastic volumetric strains are zero and the yield curve becomes stationary (no hardening/softening, see Equation (7.38)). A point like C is the final state for a soil taken to failure, independently of initial conditions. Such a state is called the *critical state* and has long been identified as a basic feature of soil behaviour. The succession of critical state points for different yield surfaces lies, due to the assumption of isotropic hardening, on the straight line CSL, of slope M_J, in Figure 7.15. The model makes compatible, in a natural way, associated plasticity with a frictional envelope and zero dilation for ultimate conditions.

Another feature of soil behaviour successfully predicted by both Cam clay models is the different volumetric response of soil, depending on its stress history. If a soil element yields at a point to the right of C, incremental plastic volumetric strains are positive (compressive), see Figure 7.18, and hardening behaviour ensues (i.e. Equation (7.38) predicts an increase in p_o'). This side of the yield surface is called *wet* or *subcritical*. If yielding takes place to the left of C (*dry* or *supercritical* side) the incremental plastic volumetric strains are negative (dilatant), see Figure 7.18, and softening behaviour results (i.e. Equation (7.38) predicts a decrease in p_o'). Therefore, the yield surface to the left of the critical state point acts also as a failure surface.

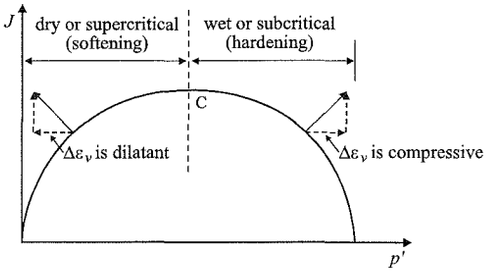

Figure 7.18: Volumetric behaviour of Cam clay models

These models also predict a unique state boundary surface, see Figure 7.16, outside which no state of the soil is permissible and a unique specific volume - critical state stress relationship. This is in accordance with observations reported in the literature (Rendulic (1936), Hvorslev (1937) and Henkel (1960)). The consolidation/swelling behaviour and the yielding of soils at the pre-consolidation pressure, Figure 7.13, is also well predicted.

To illustrate the ability of these models to simulate soil behaviour, predictions for ideal drained and undrained triaxial compression tests on normally and overconsolidated modified Cam clay are presented in Figures 7.19 and 7.20. These predictions were obtained using the analytical expressions given in Appendix VII.2. The soil samples are initially isotropically normally consolidated to

p'=200kPa and the material properties are based on Bothkennar clay, Allman and Atkinson (1992). The model parameters are: v_1=2.67, λ=0.181, κ=0.025, M_f=0.797, G=20000 MPa).

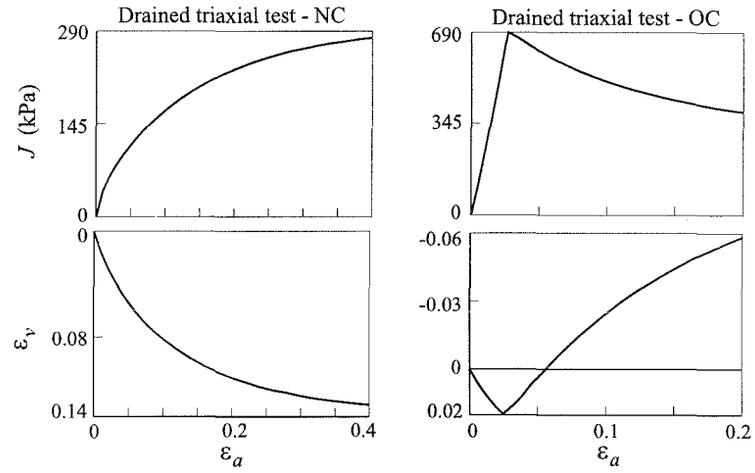

Figure 7.19: Drained triaxial compression tests with modified Cam clay model

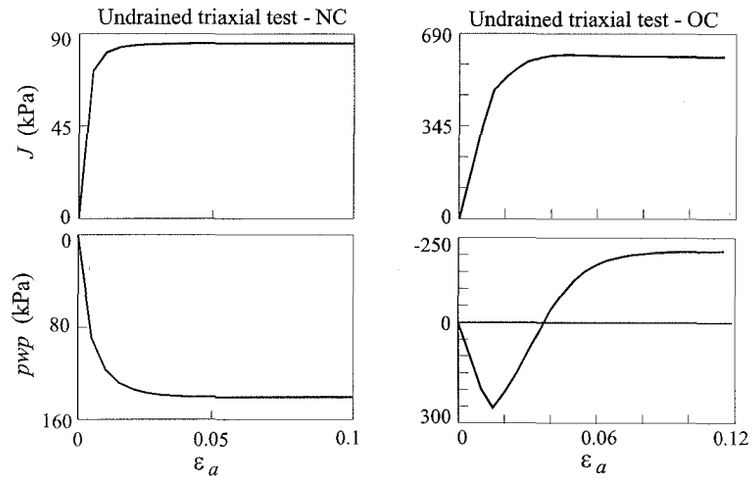

Figure 7.20: Undrained triaxial compression tests with modified Cam clay model

7.9.2 Extension to general stress space

The original critical state formulation is based, almost exclusively, on laboratory results from conventional triaxial tests. The portions of stress space in which these tests operate are severely restricted as the intermediate principal stress must be equal to either the major or the minor principal stress. Because of this, the basic formulation is developed in terms of q ($=\sigma_1'-\sigma_3'$) and p'. For numerical analysis, the models have to be generalised to full stress space by making some assumption on the shape of the yield surface and plastic potential in the deviatoric plane. The first generalisation (Roscoe and Burland (1968)) is achieved by effectively replacing q by J. This substitution is made in Equations (7.36) and (7.37). In general stress space this is equivalent to assuming that the yield and plastic potential surfaces (and hence the failure surface) are circles in the deviatoric plane, see Figure 7.21. However, it is well known that a circle does not represent well the failure conditions for soils, where a Mohr-Coulomb type failure criterion is more appropriate. Roscoe and Burland (1968) suggest that circular (in the deviatoric plane) yield surfaces should be used combined with a Mohr-Coulomb failure criterion. This implies, however, that critical state conditions can only be reached under triaxial compression conditions ($\sigma_2'=\sigma_3'$).

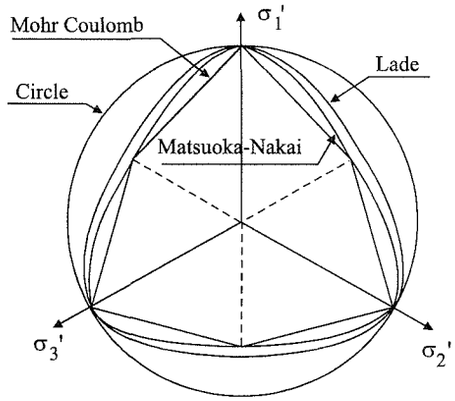

Figure 7.21: Failure surfaces in the deviatoric plane

In order to obtain a Mohr-Coulomb hexagon for the yield surface in the deviatoric plane, M_J in Equations (7.36) and (7.37) must be replaced by $g(\theta)$:

$$g(\theta)=\frac{\sin\varphi'_{cs}}{\cos\theta+\frac{\sin\theta\sin\varphi'_{cs}}{\sqrt{3}}} \tag{7.41}$$

where φ_{cs}' is the critical state angle of shearing resistance which replaces M_J as an input parameter. This expression gives the hexagon shown in Figure 7.21. Equations (7.36) and (7.37) then become:

$$F(\{\sigma'\},\{k\})=\frac{J}{p'g(\theta)}+\ln\left(\frac{p'}{p'_o}\right)=0 \quad \text{(Cam clay)} \tag{7.42}$$

$$F(\{\sigma'\},\{k\})=\left(\frac{J}{p'g(\theta)}\right)^2-\left(\frac{p'_o}{p'}-1\right)=0 \quad \text{(modified Cam clay)} \tag{7.43}$$

Critical state conditions then occur with a constant φ_{cs}'. The discontinuity of the Mohr-Coulomb expression at $\theta=-30°$ and $\theta=+30°$ requires, usually, some ad hoc rounding of the corners. Although sufficient as a first approximation, and certainly superior to a circle, the Mohr-Coulomb criterion does not achieve a perfect agreement with observed soil failure conditions.

Other failure surfaces have been suggested which are continuous and agree better with experimental results in the deviatoric plane. Matsuoka and Nakai's (1974) and Lade's (Lade and Duncan (1975)) are the best known, see Figure 7.21. In terms of $g(\theta)$ Matsuoka and Nakai's surface can be expressed as:

$$g(\theta)=\sqrt{J_{2\eta}^f} \tag{7.44}$$

where $J_{2\eta}^f$ can be obtained for a specific value of Lode's angle, θ, by solving the following cubic equation:

$$(C_{\mathrm{MN}}-3)J_{2\eta}^f+\frac{2}{\sqrt{27}}C_{\mathrm{MN}}\sin3\theta(J_{2\eta}^f)^{3/2}-(C_{\mathrm{MN}}-9)=0 \tag{7.45}$$

in which:

$$C_{\mathrm{MN}}=\frac{9-3M_J^2}{\frac{2\sqrt{3}}{9}M_J^3-M_J^2+1}$$

where M_J is the gradient of the critical state line in J-p' space, corresponding to triaxial compression, $\theta=-30°$. In terms of the critical state angle of shearing resistance in triaxial compression, $(\varphi_{cs}')^{\theta=-30}$, M_J in Equation (7.45) can be expressed as:

$$M_J=\frac{2\sqrt{3}\sin\varphi_{cs}'^{\theta=-30^\circ}}{3-\sin\varphi_{cs}'^{\theta=-30^\circ}} \tag{7.46}$$

The Lade's surface can also be expressed by Equation (7.44), with $J_{2\eta}^f$ obtained for a specific value of Lode's angle, θ, and mean effective stress, p', from the following equation:

$$J_{2\eta}^f+\frac{2}{\sqrt{27}}\sin3\theta(J_{2\eta}^f)^{3/2}-C_{\mathrm{L}}=0 \tag{7.47}$$

in which:

$$C_{\mathrm{L}}=\frac{\frac{\eta_1}{27}\left(\frac{p_a}{3p'}\right)^m}{1+\frac{\eta_1}{27}\left(\frac{p_a}{3p'}\right)^m}$$

where η_1 and m are material properties, and p_a is atmospheric pressure.

As an alternative, Van Eekelen (1980) proposes a family of continuous deviatoric plane yield surfaces (or plastic potentials). They are expressed as:

$$g(\theta)=X(1+Y\sin3\theta)^{-Z} \tag{7.48}$$

where X, Y and Z are constants. There are restrictions on Y and Z if convex surfaces

are required. The substitution of $g(\theta)$ into Equations (7.42) and (7.43) provides a flexible way to incorporate a desired shape for yield surfaces or plastic potentials in the deviatoric plane. Circular, Lade and Matsuoka and Nakai surface shapes can also be well approximated by Equation (7.48).

The importance of the model formulation in the deviatoric plane is highlighted by Potts and Gens (1984). They demonstrate that the adoption of a plastic potential shape, $g_{pp}(\theta)$, in the deviatoric plane and a dilation angle, ν, determines the value of the Lode's angle at failure, θ_f, in problems involving plane strain deformation. They show that some of the plastic potential expressions proposed in the literature do not guarantee realistic values of θ_f. They also indicate that it is often necessary to have different shapes of the yield and plastic potential surfaces in the deviatoric plane. For example, if the yield surface uses Equation (7.41), which gives a Mohr-Coulomb hexagon in the deviatoric plane, then a different shape must be adopted for the plastic potential, otherwise plane strain failure occurs with either $\theta_f = -30°$ (i.e. triaxial compression) or $\theta_f = 30°$ (i.e. triaxial extension). The use of different shapes of the yield and plastic potential surfaces in the deviatoric plane results in a non-associated constitutive model. This problem is discussed in Section 7.12 of this chapter.

The satisfactory modelling of many of the most important features of soil behaviour, by very economical means in terms of hypotheses and parameters, explains the success of the Cam clay models. Of course, when predictions are compared quantitatively with experimental results, it is found that simple models like these are not able to reproduce exactly the real behaviour of soils. It should be pointed out, however, that this basic formulation often gives sufficiently accurate predictions, particularly in absence of stress reversals or stress rotations. Successful results are reported in the prediction symposia of Montreal and Grenoble (Wroth and Houlsby (1980) and Houlsby *et al.* (1982)). A lucid discussion of the capabilities and shortcomings of the basic formulation and its relationship with observed behaviour is presented in Wroth and Houlsby (1985). Even at present, modified Cam clay remains the most widely used critical state model in computational applications.

For completeness, the equations necessary to establish the constitutive matrix $[\boldsymbol{D}^{ep}]$ are given in Appendix VII.3, for a modified Cam clay model with a Mohr-Coulomb hexagon and a circle for the shapes of the yield and plastic potential surfaces in the deviatoric plane, respectively.

7.9.3 Undrained strength

As noted previously, the material parameters used to define both Cam clay and modified Cam clay models include the consolidation parameters (v_1, κ and λ), the drained strength parameter (φ_{cs}' or M_J) and its variation in the deviatoric plane, and the elastic parameter (μ or G). They do not involve the undrained shear strength, S_u. As these models are often used to represent the undrained behaviour of soft clays, whose strength is conventionally expressed in terms of S_u, this can be

inconvenient. The undrained shear strength, S_u, can be derived from the input parameters and the initial state of stress as shown in Appendix VII.4. The resulting equations are:

Cam clay:

$$\frac{S_u}{\sigma_{vi}'} = g(\theta)\cos\theta\,\frac{OCR}{3}\,(1+2K_o^{NC})\left[\frac{(1+2K_o^{OC})}{(1+2K_o^{NC})OCR}\right]^{\frac{\kappa}{\lambda}} e^{\left(1-\frac{\kappa}{\lambda}\right)(B-1)} \tag{7.49}$$

Modified Cam clay:

$$\frac{S_u}{\sigma_{vi}'} = g(\theta)\cos\theta\,\frac{OCR}{6}\,(1+2K_o^{NC})[1+B^2]\left[\frac{2(1+2K_o^{OC})}{(1+2K_o^{NC})\,OCR\,[1+B^2]}\right]^{\frac{\kappa}{\lambda}} \tag{7.50}$$

By using these equations it is possible to select input parameters (κ, λ, and φ_{cs}' or M_J) and initial stress conditions (OCR, K_o), so that the desired undrained strength distribution can be obtained. In this respect care must be exercised because the undrained strength is always zero when the initial vertical effective stress is zero. A full discussion on this topic can be found in Volume 2 of this book.

7.10 Modifications to the basic formulation of critical state models

A great number of modifications have been proposed to the basic formulation of the critical state models described in Section 7.9. The motivation has been to try to achieve a better agreement between predicted and observed soil behaviour and to model new types of phenomena like, for instance, cyclic loading effects. The ISSMFE (1985) reference is an excellent review of elasto-plastic constitutive laws available for soils, where the most important critical state modifications are presented. Here, only those modifications actually used in numerical analyses are discussed. As the critical state formulation is so pervasive in constitutive modelling of soils, it is not easy to set the limits separating critical state models from other types. A rather non-restrictive criterion is used here.

The following specific topics are considered: yield surface on the dry or supercritical side, modifications due to K_o consolidation, and modelling behaviour inside the main yield surface.

7.10.1 Yield surface on the supercritical side

A drawback of the basic Cam clay formulation that became apparent very soon is that the yield curves adopted, Figure 7.15, overestimate significantly failure stresses on the supercritical (dry) side. Moreover, Hvorslev (1937) had found that a straight line approximates satisfactorily the failure envelope for overconsolidated soils. Figure 7.22 shows some experimental results indicating these points. It is not surprising, therefore, that a straight line was adopted as the yield surface on the supercritical side, see Figure 7.23, in one of the earliest computational applications

of Cam clay models (Zienkiewicz and Naylor (1973)). This new yield curve is often termed the Hvorslev surface. If associated plasticity is adopted, an excessive dilatancy rate results, like in the classical Mohr-Coulomb or Drucker-Prager models discussed in Sections 7.5 and 7.6. Also, an associated flow implies a discontinuity at the critical state point. Because of this, Zienkiewicz and Naylor (1973) use a non-associated flow rule, with dilatancy increasing linearly form zero, at the critical state point, to some fixed value at $p' = 0$. Similar formulations have been used by Tanaka *et al.* (1986). This approach has also been used at Imperial College. In addition, the numerical group at Imperial College has also had success using the Cam clay yield surface as the plastic potential associated with the Hvorslev surface.

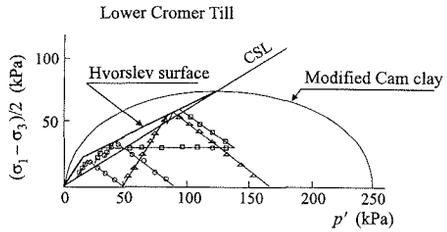

Figure 7.22: Experimental results on supercritical side (after Gens (1982))

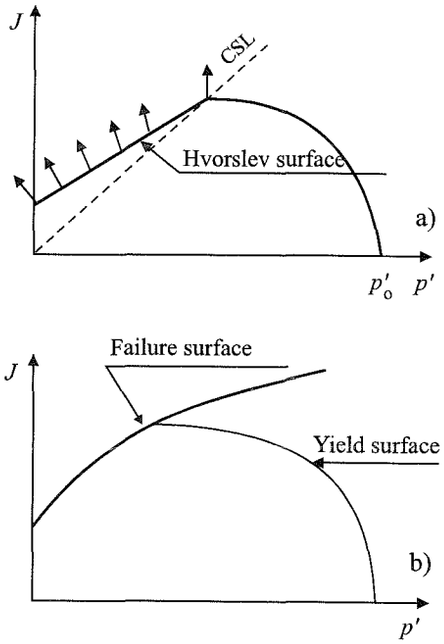

Figure 7.23: Modifications to the supercritical surface a) Hvorslev surface; b) Cap model

The 'Cap models' (Di Maggio and Sandler (1971) and Sandler *et al.* (1976)) can be considered basically as critical state models, with modified supercritical yield surfaces. The Cap yield surface, see Figure 7.23b, moves according to the changes in plastic volumetric strain, but the *failure* surface is fixed. No softening behaviour is, therefore, predicted. The simplicity and flexibility of the model means that it has been used in a number of numerical analyses (e.g. Sandler and Rubin (1979), Chen and Baladi (1985) and Daddazio *et al.* (1987)).

Although modifications to the supercritical yield surfaces are necessary to predict realistic failure stresses in that region, they are not generally implemented in most software. This is probably all right if the computational application refers to materials in the subcritical region (i.e. lightly overconsolidated clays). A general model, however, should include a modification of the type described above, to obtain realistic predictions in all cases.

7.10.2 Yield surface for K_o consolidated soils

The basic Cam clay formulation is based on results of tests performed on isotropically consolidated samples. However, experimental evidence strongly suggests (Parry and Nadarajah (1973), Tavenas and Leroueil (1977)) that for K_o normally consolidated clays (i.e. consolidation under conditions of zero lateral strain) yield surfaces are not centred on the $J = 0$ axis, but are rotated towards the K_o consolidation line in stress space. Accordingly, various proposals have been made for changing the classical yield surface to other shapes, more or less centred on the K_o line (Ohta and Wroth (1976), Kavvadas and Baligh (1982), Sekiguchi and Ohta (1977), Mouratidis and Magnan (1983)).

In Sekiguchi and Ohta's models, the parameter $\eta = J/p'$ is replaced by $\eta' = J/p' - J_a/p_a'$, where J_a and p_a' are the values of J and p' at the end of anisotropic consolidation. This causes a rotation of the yield surface around the stress origin resulting in a yield surface like that depicted in Figure 7.24a. Computational applications using models of this type have been reported (Matsui and Abe (1981, 1982), Hata *et al.* (1985), Ohta *et al.* (1985)).

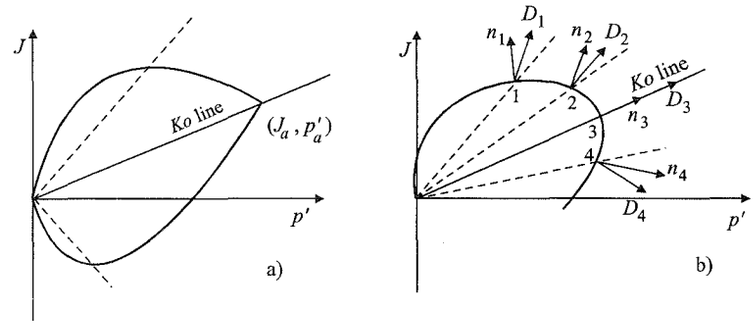

Figure 7.24: Yield surfaces for K_o consolidated soils a) Sekiguchi and Ohta model; b) MELANIE model

Mouratidis and Magnan (1983) developed the constitutive model MELANIE, based on the conceptual framework YLIGHT (Tavenas (1981)), which is based on extensive experimental work carried out at the University of Laval on soft sensitive Canadian clays. The main differences with the basic critical state formulation are:

- A new yield locus centred on the K_o line, see Figure 7.24b;
- A non-associated flow rule. The plastic strain increment vector, D_i, bisects the angle between the normal to the yield surface, n_i, and the η = constant line.

The model has been applied to analysis of geotechnical field problems usually associated with construction of embankments on soft ground (Magnan *et al.* (1982a, 1982b), Magnan and Babchia (1985)).

The new shape of the yield surface is obviously caused by the anisotropy developed during K_o consolidation. For these models to be fully consistent, they should incorporate the development of anisotropy with plastic strain, which results

in a progressive change of the shape of the yield surface. Although some models of this type have been proposed (Hashigushi (1977), Banerjee *et al.* (1985)), they do not appear to have been used in numerical analyses. A model which does satisfy this requirement, and which has been used in numerical analysis, is the MIT model. This model is described in Chapter 8.

In absence of sufficient comparisons between these K_o formulations and the basic one, it is not easy to evaluate the importance of incorporating the new type of yield surfaces in the critical state models. On the one hand, they appear to represent better the real behaviour of K_o consolidated clays, but on the other hand the classical Cam clay models have been often successful in modelling the field behaviour of natural clays (presumably K_o consolidated). A reported comparison between the two types of formulation (Magnan *et al.* (1982)) involved the analysis of an embankment on soft clay, using the modified Cam clay and MELANIE models. The results of the comparison are inconclusive. Modified Cam clay appears to predict better the displacements. Pore water pressures are well predicted by either model. Without other comparisons and without identifying more closely the causes for the prediction differences, it is not possible to reach definite conclusions about the advantages of adopting the models described in this section.

7.10.3 Elastic component of the model

One of the assumptions of the basic critical state formulation is that the elastic volumetric strain increment is given by Equation (7.39). Assuming isotropy, this assumption results in a nonlinear elastic model in which the bulk stiffness, K, varies according to Equation (7.40). K is, therefore, proportional to p' and v (=1+e), although the change in the latter variable is usually small and is sometimes neglected.

The original critical state formulation does not impose any conditions on the shear component of the elastic model. The first computational applications adopt a constant Poisson's ratio, μ, which results in a variable shear modulus, G, also proportional to p':

$$G = \frac{3(1-2\mu)}{2(1+\mu)}\frac{vp'}{\kappa} \tag{7.51}$$

However, Zytinski *et al.* (1978) demonstrate that this model is not conservative and that energy may, therefore, be extracted from certain loading cycles. In practice, this fact may not be too important if monotonic loading is considered, but may become significant if the loading involves many stress reversals. Consequently, a constant value of G is often adopted to ensure a conservative elastic model. However, a constant G does not agree well with experimental observations and may imply negative values of Poisson's ratio at low stresses, which is physically unreasonable.

Houlsby (1985) studied the conditions for conservative elastic behaviour when:

- G is proportional to mean effective stress, p', or

- G is proportional to the hardening parameter, p_o', (i.e. the isotropic pre-consolidation pressure).

Both these hypotheses are consistent with available experimental evidence. In the first case, a conservative model is possible if the bulk modulus, K, is made slightly dependent on deviatoric stress. Constant stress ratio lines, $\eta = J/p'$, become contours of constant elastic deviatoric strain. The second case involves elastic/plastic coupling. Formulating the problem within the framework of a thermomechanical approach to plasticity theory (Houlsby (1982)), it is found that the assumption of proportionality between G and p_o' leads to a slight change in the shape of the yield surface.

In any case, the above elastic models are, in general, too simple to represent adequately the real behaviour of soil for stress states inside the yield surface. Jardine *et al.* (1986) demonstrate the importance of adopting a realistic stiffness variation to obtain proper patterns of displacement distributions in typical boundary value problems. For problems involving monotonic loading, it may be convenient to adopt a more complex nonlinear elastic model to represent the behaviour of the soil inside the yield locus. At Imperial College the empirical expressions given by Jardine *et al.* (1986), which are based on experimental evidence, have been used with some success (Jardine and Potts (1988)). These expressions are described in Chapter 5.

It is important to note that the unique relationship between critical state stresses and specific volume (and therefore void ratio) does not hold, if the elastic model departs from Equation (7.39), for the computation of elastic volumetric strains.

7.10.4 Plastic behaviour inside the main yield surface

As pointed out above, a simple elastic model is not sufficient to model satisfactorily the behaviour of soil inside the yield surface. This is particularly important when cyclic loading is considered, since irrecoverable, cumulative behaviour should be accurately modelled if realistic predictions are to be made. To achieve this, many different models have been proposed that use various forms of plasticity: multi-surface, two-surface (Mroz *et al.* (1978)), bounding surface (Dafalias and Herrmann (1982)), generalised plasticity (Pande and Pietruszczak (1982), Nova and Hueckel (1981)). Now, the basic critical state formulation has a secondary role, merely providing an overall framework into which the different models are inserted. Therefore, only a brief summary of the topic is presented in this chapter.

The formulations used in numerical analyses can be divided into two groups:

- Models in which cyclic loading effects are described by means of a separate formulation which is added to a suitable static model (Van Eekelen and Potts (1978), Zienkiewicz *et al.* (1978)).
- Complete models in which cyclic loading effects are the consequence of the overall formulation of the full model (Dafalias and Herrmann (1982), Prevost (1978), Carter *et al.* (1982), Zienkiewicz *et al.* (1985), Pastor *et al.* (1985)).

This distinction is important for computational applications. The second category of models can describe more accurately the real behaviour of the soil, including hysteresis effects, but they become costly if a large number of cycles (as in design storms for offshore structures) must be considered.

Van Eekelen and Potts (1978) use the pore water pressure generated by cyclic loading as the *fatigue* parameter of a separate formulation. Its increase per cycle depends on the normalised stress amplitude of the cycle. The static part of the model is a form of the critical state formulation called Drammen clay with internal yielding. An application to the problem of a gravity structure subjected to a storm loading of more than 3500 cycles is presented by Potts (1985). Zienkiewicz *et al.* (1978) use the volumetric strain as the *fatigue* variable, the increase of which depends on the total length of the deviatoric strain path. This *densification* model coupled to a critical state formulation is used for the analysis of a layer of saturated sand subjected to a horizontal earthquake shock (Zienkiewicz *et al.* (1981)).

The same problem is used (Zienkiewicz *et al.* (1982)) to compare the results of the *densification* model with two other constitutive models from the second group (Dafalias and Herrmann (1982), Carter *et al.* (1982)). The pore water pressure build-up predictions of the three models show significant differences, the faster increase corresponding to the *densification* model.

A further development has been the introduction of a generalised plasticity-bounding surface model in the basic critical state formulation (Zienkiewicz *et al.* (1985), Pastor *et al.* (1985)). It leads to a model with relatively few parameters and with a good predictive capacity. This model has been recently applied to the analysis of 1D and 2D dynamic centrifuge models, resulting in good agreement between computed and observed results (Tanaka *et al.* (1987), Zienkiewicz *et al.* (1987)). The availability of simpler realistic models and increased computing power have now made possible the use of complete critical state models in analysis of dynamic problems.

Although the main motivation behind these developments has been the proper modelling of the dynamic behaviour of soils, there is scope for applications to static problems. An example is the use of Prevost's (1978) model in the analysis of shield tunnelling in soft soils (Clough *et al.* (1983, 1985)). An interesting comparison is performed between the predictions of this model and those obtained using modified Cam clay. Both models yield basically similar results, with marginally better predictions in the case of Prevost's model. This is perhaps due to the loading/unloading process involved in the operation of advanced shield tunnelling.

Sometimes, formulations assuming plastic yield inside the main yield surface have been prompted by a desire to increase the robustness of nonlinear computational applications. Naylor (1985) proposed a modification to the basic critical state formulation which combines the mapping of bounding surface plasticity with a *parallel* composite material model. As a result, the elasto-plastic transition is smoother, improving numerical robustness and achieving a better modelling of soil behaviour. The formulation has the interesting consequence that,

on the supercritical side, failure is achieved before the main yield locus is reached. The Hvorslev surface modifications become, therefore, less necessary.

7.11 Alternative shapes for the yield and plastic potential surfaces for critical state models

7.11.1 Introduction

In the original Cam clay model the shape of the plastic potential surface was obtained by assuming a simple frictional form for the plastic work. Based on this assumption and considering a triaxial state of stress, the dilatancy, D, varies linearly with the stress ratio $\eta = J/p'$ (see Figure 7.25), where:

$$\begin{aligned} D &= \Delta\varepsilon_v^p / \Delta\varepsilon_d^p \\ \Delta\varepsilon_v^p &= \Delta\varepsilon_1^p + 2\Delta\varepsilon_3^p \quad \text{- plastic volumetric strain rate} \\ \Delta\varepsilon_d^p &= \tfrac{2}{\sqrt{3}}(\Delta\varepsilon_1^p - \Delta\varepsilon_3^p) \quad \text{- plastic deviatoric strain rate} \end{aligned} \tag{7.52}$$

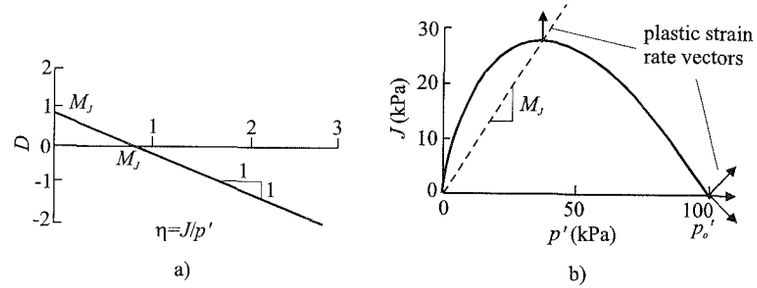

Figure 7.25: Cam clay model: a) dilatancy versus stress ratio relation; b) plastic potential curve

This relationship is then integrated to give the following expression for the plastic potential:

$$P(\{\sigma'\},\{\boldsymbol{m}\}) = \frac{J}{p'M_J} + \ln\left(\frac{p'}{p_o'}\right) = 0 \tag{7.53}$$

where p_o' is a hardening/softening parameter defining the current size of the surface, and M_J is a material parameter defining the value of η where there is no plastic volumetric strain increment, see Figure 7.25 and Section 7.9.1. Associated flow conditions are assumed and Equation (7.53) is therefore used as the yield surface, see Equation (7.36).

There are two main limitations with the mathematical expression given by Equation (7.53). Firstly, as noted in Section 7.9.1, the curve has a singularity on the mean effective stress axis for $J = 0$ and $p' = p_o'$, see Figure 7.25b. When the stress state and loading history of a soil element are such that it is located at this

point, there is a range of possible directions for the plastic strain rate vector. On the contrary, for an isotropic material this vector is expected to be parallel to the p' axis, giving infinite dilatancy. The second limitation is that the D-η relation has a slope of unity. While many real soils exhibit such a linear relationship, the gradient is often not unity.

To overcome these limitations alternative mathematical expressions have been postulated. For example, an ellipse, Equation (7.37), was used by Roscoe and Burland (1968) and more recently a 'tear' shaped surface has been proposed by Nova (1991). Desai (1980) proposed a generalised expression for the yield function using a polynomial equation in terms of the three invariants of the stress tensor. It can be shown that some of the well established yield functions can be obtained with an appropriate choice of the non-zero coefficients of this polynomial. The shapes of the yield and plastic potential surfaces vary significantly from model to model. Unfortunately, the mathematical expressions adopted in most models do not allow for a wide selection of shapes for the yield and plastic potential surfaces. As these have a major influence on model predictions, it is important that they accurately represent real soil behaviour. Real soils appear to exhibit a variety of shapes and it is therefore desirable to adopt an expression which has flexibility.

In attempt to develop a plastic potential surface similar to that of the original Cam clay model, but without the limitations described above, Lagioia *et al.* (1996) have obtained a mathematical expression which is extremely versatile. Not only are the limitations of the original Cam clay model eliminated, but the new expression can produce a wide range of shapes, varying from the original 'bullet' shape to the 'tear' shape, which is finding favour in more recent models. The majority of the shapes currently in use in the literature can be modelled by means of an appropriate choice of parameters. Because of the flexibility the new expression provides, it can be used to define both the yield and plastic potential surfaces in a non-associated model by simply using two sets of shape parameters. A brief description of this new expression is now presented, for a more detailed description the reader is referred to the original paper by Lagioia *et al.* (1996).

7.11.2 Development of a new expression in triaxial stress space

To begin with the development of the mathematical expression, triaxial compression stress conditions are considered. As noted for Cam clay and modified Cam clay in Section 7.9.2, several options are available to extend such an expression to general stress conditions, and how these may be implemented in the new expression is discussed subsequently.

As noted above for the Cam clay model, it is useful to examine the plastic deformation by considering the variation of dilatancy, D, with stress ratio, η ($=J/p'$). According to the classical theory of plasticity, the derivatives of the plastic potential surface provide the relative magnitudes of the plastic strain rates:

$$\Delta\varepsilon_i^p = \Lambda \frac{\partial P(\{\sigma'\},\{\boldsymbol{m}\})}{\partial \sigma_i'} \tag{7.54}$$

in which Λ is a scalar multiplier and $\Delta\varepsilon_i^p$ is the plastic strain increment vector, see Sections 6.8.3 and 6.13. The dilatancy D can therefore be written as:

$$D = \frac{\Delta\varepsilon_v^p}{\Delta\varepsilon_d^p} = \frac{\Lambda \dfrac{\partial P(\{\sigma'\},\{\boldsymbol{m}\})}{\partial p'}}{\Lambda \dfrac{\partial P(\{\sigma'\},\{\boldsymbol{m}\})}{\partial J}} = -\frac{\mathrm{d}J}{\mathrm{d}p'} \tag{7.55}$$

Rewriting this expression in terms of η and p' gives:

$$\frac{\mathrm{d}p'}{p'} = -\frac{\mathrm{d}\eta}{D+\eta} \tag{7.56}$$

The objective is to establish an expression for the plastic potential, $P(\{\sigma'\},\{\boldsymbol{m}\})$, such that the plastic strain rates give a plot in the D-η plane of a line of general slope μ_p. Moreover, the following constraints should be satisfied:

$$\begin{aligned} \eta = 0 \quad &\Rightarrow \quad D \to \infty \\ \eta = M_{PJ} &\Rightarrow \quad D = 0 \end{aligned} \tag{7.57}$$

which imply that an isotropic material exhibits only plastic volumetric strains when tested isotropically (η=0), and the critical state condition must apply when the stress ratio attains the value of M_{PJ} in triaxial compression.

The differences between these conditions and those of the original Cam clay model are in the free choice of the value of μ_P and that the line tends continuously to $D = \infty$ when the stress ratio η tends to zero.

One possible expression for the relation between the dilatancy and the stress ratio, which satisfies the required conditions, is:

$$D = \mu_p (M_{PJ} - \eta)\left(\frac{\alpha_P M_{PJ}}{\eta} + 1\right) \tag{7.58}$$

in which α_P is a parameter which defines how close to the $\eta = 0$ axis the curve must start to bend towards $D = \infty$. The mathematical expression of the plastic potential curve in triaxial compression can then be obtained by substitution of Equation (7.58) into Equation (7.56) and by integration. It is worth noting that two different integral expressions can be obtained, depending on the value of the slope μ_P. One is valid for any value of μ_P, except $\mu_P = 1$, for which it is not defined, and the other is valid for $\mu_P = 1$. In practice, the first option can be considered to be the general expression as the $\mu_P = 1$ option can be closely reproduced by imposing μ_P to be approximately equal to unity (e.g. 0.99999 or 1.00001). Consequently, only details of this expression are given below.

The equation resulting from the integration of Equation (7.58) is:

$$P(\{\sigma'\},\{\boldsymbol{m}\}) = \frac{p'}{p_p'} - \frac{\left(1+\dfrac{\eta_p}{K_{P2}}\right)^{\frac{K_{P2}}{\beta_P}}}{\left(1+\dfrac{\eta_p}{K_{P1}}\right)^{\frac{K_{P1}}{\beta_P}}} = 0 \tag{7.59}$$

where:

$$\beta_P = (1-\mu_P)(K_{P1}-K_{P2}) \tag{7.60}$$

$$K_{P1} = \frac{\mu_P(1-\alpha_P)}{2(1-\mu_P)}\left[1+\sqrt{1-\frac{4\alpha_P(1-\mu_P)}{\mu_P(1-\alpha_P)^2}}\right] \tag{7.61}$$

$$K_{P2} = \frac{\mu_P(1-\alpha_P)}{2(1-\mu_P)}\left[1-\sqrt{1-\frac{4\alpha_P(1-\mu_P)}{\mu_P(1-\alpha_P)^2}}\right] \tag{7.62}$$

and η_P is the normalised value of the stress ratio η:

$$\eta_P = \frac{\eta}{M_{PJ}} \tag{7.63}$$

The Equation (7.59) is defined for positive values of η_P and for:

$$\begin{aligned} 1+\frac{\eta_P}{K_{P1}} &\geq 0 \\ 1+\frac{\eta_P}{K_{P2}} &\geq 0 \end{aligned} \tag{7.64}$$

Four parameters are required to define the surface: M_{PJ}, p_P', μ_P and α_P. The geometrical meaning of these four parameters is shown in Figure 7.26.

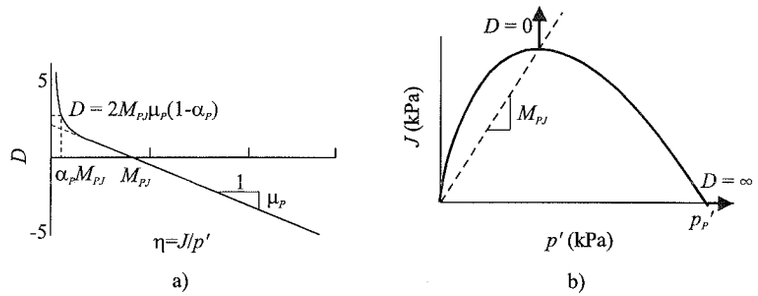

Figure 7.26: Geometrical identification of curve parameters

If normality is assumed, Equation (7.59) also becomes the yield surface and p_P' becomes the hardening/softening parameter p_o', see Section 7.9.1. However, if non-associated conditions are assumed, the yield surface may take a similar form to Equation (7.59), but with different values for the parameters M_J, μ and α:

$$F(\{\sigma'\},\{k\}) = \frac{p'}{p_o'} - \frac{\left(1+\frac{\eta_F}{K_{F2}}\right)^{\frac{K_{F2}}{\beta_F}}}{\left(1+\frac{\eta_F}{K_{F1}}\right)^{\frac{K_{F1}}{\beta_F}}} = 0 \tag{7.65}$$

where:

$$\beta_F = (1-\mu_F)(K_{F1}-K_{F2}) \tag{7.66}$$

$$K_{F1} = \frac{\mu_F(1-\alpha_F)}{2(1-\mu_F)}\left[1+\sqrt{1-\frac{4\alpha_F(1-\mu_F)}{\mu_F(1-\alpha_F)^2}}\right] \tag{7.67}$$

$$K_{P2} = \frac{\mu_F(1-\alpha_F)}{2(1-\mu_F)}\left[1-\sqrt{1-\frac{4\alpha_F(1-\mu_F)}{\mu_F(1-\alpha_F)^2}}\right] \tag{7.68}$$

$$\eta_F = \frac{\eta}{M_{FJ}} \tag{7.69}$$

The parameters M_{PJ} and M_{FJ} are the values of the stress ratio corresponding to a horizontal tangent to the curves in the J-p' plane. If the expression is used to describe a plastic potential, i.e. Equation (7.59), M_{PJ} is related to the effective angle of shearing resistance via the expression:

$$M_{PJ} = \frac{2\sqrt{3}\,\sin\varphi_{cs}'}{3-\sin\varphi_{cs}'} \tag{7.70}$$

whilst if it is used for a yield surface, Equation (7.65), M_{FJ} has to be chosen geometrically. The parameters p_P' and p_o' fix the size of the curves on the mean effective stress axis. For a plastic potential, p_P' becomes a dummy parameter because only the derivations of the equation are used. For a yield curve, p_o' has the usual conceptual meaning of a state parameter (i.e. hardening/softening parameter, see Section 7.9.1). The parameters μ_P, μ_F and α_P, α_F have already been described. If the equation is used for defining a plastic potential, then α_P fixes the proportion of M_{PJ} that the stress ratio must attain for the dilatancy to be equal to:

$$D = 2\mu_P M_{PJ}(1-\alpha_P) \tag{7.71}$$

If the expression is used to represent a yield surface, then the values of the two parameters, μ_F and α_F, are determined by fitting the experimental yield surface. It is apparent that if a Cam clay type of surface is required, then α_P (or α_F) is chosen to be a very small number. The smaller α the sharper the bullet shape for $p'=p_P'$ (or p_o').

From the above equations it appears that there is no restriction on the choice of the value of parameter M_{PJ} (or M_{FJ}), whilst for μ_P (or μ_F) and α_P (or α_F) the following restrictions apply:

$$\begin{aligned} \alpha_P &\neq 1 \quad ; \quad \alpha_F \neq 1 \\ \mu_P &\neq 1 \quad ; \quad \mu_F \neq 1 \end{aligned} \tag{7.72}$$

Moreover, if $\mu_P < 1$ or $\mu_F < 1$ then μ_P or μ_F must satisfy the following conditions:

$$\mu_P > \frac{4\alpha_P}{(1-\alpha_P)^2+4\alpha_P} \quad ; \quad \mu_F > \frac{4\alpha_F}{(1-\alpha_F)^2+4\alpha_F} \tag{7.73}$$

If $\alpha_P < 1$ (or $\alpha_F < 1$) and $\mu_P < 1$ (or $\mu_F < 1$) then the surface is rounded not only for $p'=p_P'$ (or $p'=p_o'$), but also for $p'=0$ and therefor the normalised stress ratio at the origin is:

$$\eta_P^{p'=0} = \infty \quad ; \quad \eta_F^{p'=0} = \infty \tag{7.74}$$

A finite value of the normalised stress ratio η_P (or η_F) at the origin is obtained in all other situations. If $\alpha_P < 1$ (or $\alpha_F < 1$) and $\mu_P > 1$ (or $\mu_F > 1$), the normalised stress ratio η_P (or η_F) at the origin is:

$$\eta_P^{p'=0} = -K_{P1} \quad ; \quad \eta_F^{p'=0} = -K_{F1} \tag{7.75}$$

and if $\alpha_P > 1$ (or $\alpha_F > 1$) then, no matter the value of μ,

$$\eta_P^{p'=0} = -K_{P2} \quad ; \quad \eta_F^{p'=0} = -K_{F2} \tag{7.76}$$

In these conditions the yield curve or the plastic potential curve has a finite value of stress ratio for $p' = 0$. This property could be used to represent some form of a cut off at high values of the stress ratio. It is apparent that if non-associated conditions are assumed, care should be taken to ensure that the stress ratio values, attained by the soil when satisfying the yield surface, are still valid for the plastic potential.

By varying the parameters α_P (α_F) and μ_P (μ_F) it is possible to obtain curves with very different shapes. Figure 7.27 shows the effect of the variation of the parameter α_P for fixed values of the parameters μ_P, M_{PJ} and p_P'. It is apparent that the variation of the parameter α_P controls the rounding of the 'bullet' corner at $p' = p_P'$. This parameter also governs the relative proportions of the curve on either side of the line with slope M_{PJ} and therefore whether the curve has a 'bullet' or a 'tear' shape.

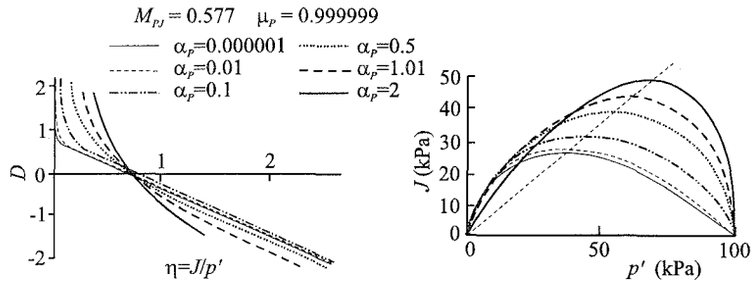

Figure 7.27: Effect of the parameter α_P on the shape of the curve

Figure 7.28 shows the effect of the variation of the parameter μ_P for fixed values of the parameters α_P, M_{PJ} and p_P'. As μ_P becomes larger than unity, the curve is characterised by a finite value of the stress ratio at the origin of stress space.

Lagioia *et al.* (1996) show how, by suitable choice of parameters, the new expressions can fit many of the well established curves given in the literature. They also show how the new expressions can accurately fit experimental data.

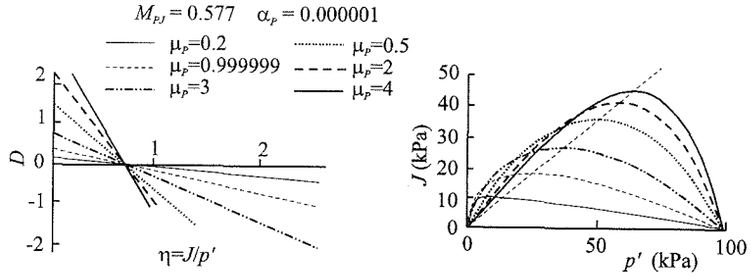

Figure 7.28: Effect of the parameter μ_P on the shape of the curve

7.11.3 Generalisation of the expression

So far only triaxial compression stress states have been considered. The simplest way to generalise the expressions given by Equations (7.59) and (7.65) to three dimensional stress space is to replace η_P and η_F with:

$$\eta_P = \frac{\eta}{g_{pp}(\theta)} \quad \text{and} \quad \eta_F = \frac{\eta}{g(\theta)} \tag{7.77}$$

where $g_{pp}(\theta)$ and $g(\theta)$ can take any of the forms given in Section 7.9.2.

This model has been used in analysing the behaviour of structured soils under triaxial conditions, Lagioia and Potts (1997).

7.12 The effect of the plastic potential in plane strain deformation

As noted in Section 7.9.2, the shape of the plastic potential, $g_{pp}(\theta)$, in the deviatoric plane can have a significant influence in problems involving plane strain deformation. This can be understood as follows.

For plane strain deformation, the out of plane strain increment $\Delta\varepsilon_2$ is, by definition, zero. If the soil is assumed to be elasto-plastic, then:

$$\Delta\varepsilon_2 = \Delta\varepsilon_2^e + \Delta\varepsilon_2^p = 0 \tag{7.78}$$

At failure, the elastic component $\Delta\varepsilon_2^e$ reduces to zero as there is no change in stress. Consequently,

$$\Delta\varepsilon_2^p = 0 \tag{7.79}$$

Defining the angle of dilation at failure by Equation (7.15) and using the result given in Equation (7.79), leads to the following expression for the Lode's angle of the plastic strain increments at failure:

$$\theta_{\Delta\varepsilon^p} = \tan^{-1}\left(\frac{\sin\nu}{\sqrt{3}}\right) \tag{7.80}$$

The plastic strain increment direction is also normal to the projection of the plastic potential curve on the deviatoric plane, expressed as $g_{pp}(\theta)$. Such a curve is shown schematically in Figure 7.29, for one sixth of the deviatoric plane. From this figure:

$$x = g_{pp}(\theta)\ \sin\theta$$
$$y = g_{pp}(\theta)\ \cos\theta$$

and therefore:

$$\frac{dy}{dx} = \frac{\frac{\partial g_{pp}(\theta)}{\partial\theta}\cos\theta - g_{pp}(\theta)\sin\theta}{\frac{\partial g_{pp}(\theta)}{\partial\theta}\sin\theta + g_{pp}(\theta)\cos\theta} \qquad (7.81)$$

As the plastic strain increment vector is normal to the plastic potential,

$$\theta_{\Delta\varepsilon^p} = \tan^{-1}(-dy/dx) \qquad (7.82)$$

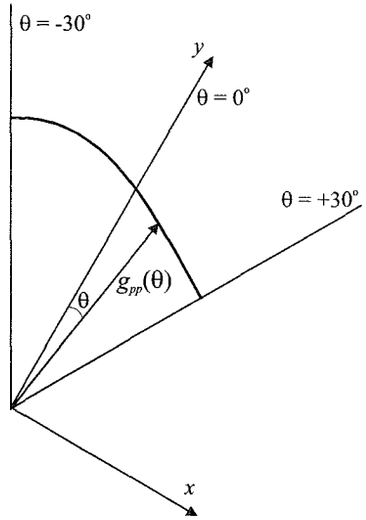

Figure 7.29: Plastic potential surface

Combining Equations (7.80) and (7.82) gives:

$$-\frac{\sin\nu}{\sqrt{3}} = \frac{\frac{\partial g_{pp}(\theta)}{\partial\theta}\cos\theta - g_{pp}(\theta)\sin\theta}{\frac{\partial g_{pp}(\theta)}{\partial\theta}\sin\theta + g_{pp}(\theta)\cos\theta} \qquad (7.83)$$

Substitution of the expression for $g_{pp}(\theta)$ and the angle of dilation, ν, at failure into the Equation (7.83) results in the value of the Lode's angle, θ_f, of the stresses at failure. For example, if Equation (7.48) is adopted for the plastic potential and it is assumed that there is no volume change at failure, $\nu = 0°$ (i.e. at critical state conditions), Equation (7.83) reduces to:

$$\tan\theta = -\frac{3\ ZY\cos 3\theta}{(1 + Y\sin 3\theta)} \qquad (7.84)$$

The solution of the above equation for θ gives the Lode's angle of the stress state at failure, θ_f, for plane strain conditions with no dilation. Alternatively, Equation (7.84) allows the selection of values of Z and Y to give a desired value of θ_f.

From the above considerations it may be concluded that the expression assumed for $g_{pp}(\theta)$, along with the required dilation angle, determines the value of the Lode's angle θ_f for plane strain deformation. This holds no matter what expression is assumed for the yield function. However, the expression for the yield function determines the strength, J_f, mobilised at this θ_f value.

It is now of interest to examine the consequences of the above equations for several of the models presented in this chapter.

(i) Drucker-Prager model

For this model the shapes of both the plastic potential and yield surfaces are assumed to be circular in the deviatoric plane, see Equations (7.24) and (7.29), giving:

$$g_{pp}(\theta) = M_{JP}^{pp} \qquad (7.85)$$

where M_{JP}^{pp} is independent of θ. Substitution of Equation (7.85) into Equation (7.83) gives:

$$\tan\theta_f = \frac{\sin\nu}{\sqrt{3}} \qquad (7.86)$$

The Lode's angle of the stress state at failure is therefore directly dependent on the angle of dilation ν. If $\nu = 0°$, then θ at failure equals 0°. A similar result is obtained for the von Mises model in which the dilation is zero and therefore θ at failure is also zero.

(ii) Mohr-Coulomb model

The shape of the plastic potential in the deviatoric plane, $g_{pp}(\theta)$, is given by Equation (7.17). Substituting this expression for $g_{pp}(\theta)$ into Equation (7.81) gives:

$$\frac{dy}{dx} = -\frac{\sin\nu}{\sqrt{3}} \qquad (7.87)$$

which, from Equation (7.82), results in:

$$\theta_{\Delta\varepsilon^p} = \tan^{-1}\left(\frac{\sin\nu}{\sqrt{3}}\right) \qquad (7.88)$$

As this expression is independent of θ, the plastic strain increment direction is constant in the deviatoric plane. Comparison of Equations (7.80) and (7.88) indicates that the above value of $\theta_{\Delta\varepsilon^p}$ is consistent with the plane strain condition. Consequently, in this particular situation where the shape of the plastic potential in the deviatoric plane is a straight line, the Lode's angle of the stress state at failure is not uniquely determined, but may take any value between −30° and +30°. This is true no matter what value of the angle of shearing resistance, φ', is adopted. A similar situation can be shown to occur for the Tresca model.

(iii) Critical state model

As noted in Section 7.9.2, various options are available for specifying the shape of the yield and plastic potential surfaces in the deviatoric plane. If a circular shape is assumed by specifying M_J as a constant, then at failure, when critical state conditions occur, the dilation is zero and consequently Equation (7.86) with $\nu = 0°$ is valid. Therefore failure occurs with a stress state corresponding to $\theta = 0°$.

Alternatively, if Equation (7.48) is used to define $g_{pp}(\theta)$, the Lode's angle of the stress state at failure can be obtained from Equation (7.84).

Problems occur if a Mohr-Coulomb hexagon is used. In this case $g_{pp}(\theta)$ is given by Equation (7.41). Substituting this expression into Equation (7.82) gives:

$$\theta_{\Delta\varepsilon^p} = \tan^{-1}\left(\frac{\sin\varphi'_{cs}}{\sqrt{3}}\right) \tag{7.89}$$

As for the Mohr-Coulomb model, this expression is independent of θ and the plastic strain increment direction is constant in the deviatoric plane. However, comparison of Equation (7.89) with Equation (7.80), with $\nu = 0°$, indicates that the above value of $\theta_{\Delta\varepsilon^p}$ is not consistent with the plane strain condition which gives $\theta_{\Delta\varepsilon^p} = 0$. The state of stress is therefore forced to either triaxial compression ($\theta = -30°$), or extension ($\theta = +30°$), where there is a corner in the plastic potential. Here, the plastic strain increment direction is not uniquely defined and may accommodate the condition stipulated by Equation (7.80). Clearly, this is unrealistic as most soils fail with θ between $-10°$ and $-25°$. To overcome this problem an alternative expression must be used for $g_{pp}(\theta)$, such as one of those given in Section 7.9.2. It is, however, still possible to use the Mohr-Coulomb hexagon given by Equation (7.41) to define the shape of the yield function in the deviatoric plane. In such a situation the yield and plastic potential functions differ, leading to non-associated conditions. The model outlined in Appendix VII.3 has the option for using a Mohr-Coulomb hexagon and a circle for the shapes of the yield and plastic potential functions in the deviatoric plane, respectively.

Finite element analyses have been performed by Potts and Gens (1984) to quantify the above effects in boundary value problems involving plane strain deformation. They used a form of the modified Cam clay model for their predictions, and concluded:

- The value of θ_f, which is determined from the shape assumed for the plastic potential, has a major influence on both pre-failure and failure predictions for problems involving plane strain deformation.
- It is the value of θ_f at failure, as opposed to the actual shape of the plastic potential, that has the dominating influence on soil behaviour. This implies that two plastic potential functions, which have different shapes in the deviatoric plane, but which produce the same θ_f value, give similar predictions. The shape of plastic potential is therefore important in the sense that it defines θ_f.
- The shape of the yield surface in the deviatoric plane appears to have a much smaller effect on drained behaviour, as long as the correct value of the angle of shearing resistance, φ_{cs}', is obtained at θ_f. This applies to both the behaviour before and at failure. Consequently, if normality is assumed, with the shape of the yield function in the deviatoric plane being identical to that of the plastic potential and giving the correct angle of shearing resistance, the same overall behaviour can be obtained.
- For undrained loading situations the plastic potential has little effect on both the predicted pre-failure and failure behaviour, as long as the same undrained shear strength at failure is obtained at θ_f. It should be remembered however, that θ_f is directly dependent on the plastic potential.

It may be concluded that great care must be exercised when developing general constitutive models of soil behaviour, especially in the development of the plastic potential and its shape in the deviatoric plane. Unfortunately, there are limited experimental data available from which the plastic potential may be derived. However, as noted above, it is the value of θ_f which dominates the behaviour and not the finer details of the actual shape of the plastic potential. Experimental data (Green (1971), Hambly and Roscoe (1969), Henkel and Wade (1966), Cornforth (1961), Menkiti (1995) and Zdravković (1996)) suggest that the value of θ_f lies approximately between $0°$ and $-25°$. It would therefore appear appropriate to ensure that any assumed plastic potential defines a value of θ_f in this range.

7.13 Summary

1. Of the simple elastic perfectly plastic models described, the Tresca and Mohr-Coulomb models are thought to be more appropriate than von Mises and Drucker-Prager, because they are based on the same assumptions as conventional soil mechanics.
2. It is important that the Mohr-Coulomb model has a non-associated flow rule. If it assumes an associated flow rule, it is likely to overpredict the tendency for the soil to dilate.
3. The Mohr-Coulomb model can be improved by allowing the strength parameters, c' and φ', and the angle of dilation, ν, to vary with deviatoric plastic strain, E_d^p.
4. Critical state models (CSMs) are based on isotropic elastic strain hardening/softening plasticity theory.
5. Conventionally, the consolidation and shearing behaviour of soils are considered separately. CSMs are able to simulate both aspects of soil behaviour and as such provide a significant advance in soil modelling over the simpler Tresca and Mohr-Coulomb models.
6. The original CSMs (e.g. Cam clay and modified Cam clay) are formulated for triaxial stress space. Additional assumptions are therefore required to generalise the models for use in numerical analysis. This can, and has in the literature, been done in several different ways. Because the manner in which the model is generalised can have a major impact on predictions, it is important that the procedure adopted is well understood.
7. Many modifications to the basic formulation have been made in the literature. These include the provision of a Hvorslev surface on the supercritical side, improved shapes for the yield and plastic potential surfaces, re-alignment of the yield surface about the K_o consolidation line, modification of the nonlinear elastic behaviour within the yield surface and the introduction of secondary plasticity within the yield surface.
8. The basic CSMs require five input parameters. These include the consolidation

parameters (v_1, κ and λ), the drained strength parameter (φ' or M_J), and the elastic parameter (μ or G). They do not involve the undrained strength, S_u, however, this can be derived from the input parameters and the initial state of stress.

9. The shape of the plastic potential surface in the deviatoric plane and the dilation angle, v, determine the value of the Lode's angle at failure, θ_f, in problems involving plane strain deformation.

Appendix VII.1: Derivatives of stress invariants

- Mean total stress:

$$p = \frac{\sigma_1 + \sigma_2 + \sigma_3}{3} = \frac{\sigma_x + \sigma_y + \sigma_z}{3} \tag{VII.1}$$

$$\left\{\frac{\partial p}{\partial \boldsymbol{\sigma}}\right\} = \frac{1}{3}\{1\ 1\ 1\ 0\ 0\ 0\}^{\mathrm{T}} \tag{VII.2}$$

- Mean effective stress:

$$p' = \frac{\sigma_1' + \sigma_2' + \sigma_3'}{3} = \frac{\sigma_x' + \sigma_y' + \sigma_z'}{3} \tag{VII.3}$$

$$\left\{\frac{\partial p'}{\partial \boldsymbol{\sigma}'}\right\} = \frac{1}{3}\{1\ 1\ 1\ 0\ 0\ 0\}^{\mathrm{T}} \tag{VII.4}$$

- Deviatoric stress:

$$\begin{aligned} J &= \left\{\frac{1}{6}\left[\left(\sigma_1' - \sigma_2'\right)^2 + \left(\sigma_2' - \sigma_3'\right)^2 + \left(\sigma_3' - \sigma_1'\right)^2\right]\right\}^{\frac{1}{2}} \\ &= \left\{\frac{1}{6}\left[\left(\sigma_x' - \sigma_y'\right)^2 + \left(\sigma_x' - \sigma_z'\right)^2 + \left(\sigma_y' - \sigma_z'\right)^2 + \tau_{xy}^2 + \tau_{zx}^2 + \tau_{yz}^2\right]\right\}^{\frac{1}{2}} \end{aligned} \tag{VII.5}$$

$$\left\{\frac{\partial J}{\partial \boldsymbol{\sigma}'}\right\} = \frac{1}{2J}\left\{\sigma_x' - p' \quad \sigma_y' - p' \quad \sigma_z' - p' \quad 2\tau_{xy} \quad 2\tau_{xz} \quad 2\tau_{yz}\right\}^{\mathrm{T}} \tag{VII.6}$$

- Lode's angle:

$$\theta = \tan^{-1}\left[\frac{1}{\sqrt{3}}\left(2\frac{\sigma_2' - \sigma_3'}{\sigma_1' - \sigma_3'} - 1\right)\right] = -\frac{1}{3}\sin^{-1}\left(\frac{3\sqrt{3}}{2}\frac{\det \boldsymbol{s}}{J^3}\right) \tag{VII.7}$$

where:

$$\det \boldsymbol{s} = \begin{vmatrix} \sigma_x' - p' & \tau_{xy} & \tau_{zx} \\ \tau_{xy} & \sigma_y' - p' & \tau_{yz} \\ \tau_{zx} & \tau_{yz} & \sigma_z' - p' \end{vmatrix}$$

or:

$$\begin{aligned} \det \boldsymbol{s} = {} & (\sigma_x' - p')(\sigma_y' - p')(\sigma_z' - p') - (\sigma_x' - p')\tau_{yz}^2 - (\sigma_y' - p')\tau_{zx}^2 \\ & - (\sigma_z' - p')\tau_{xy}^2 + 2\tau_{xy}\tau_{yz}\tau_{zx} \end{aligned}$$

$$\left\{\frac{\partial \theta}{\partial \boldsymbol{\sigma}'}\right\} = \frac{\sqrt{3}}{2\cos 3\theta J^3}\left[\frac{\det \boldsymbol{s}}{J}\left\{\frac{\partial J}{\partial \boldsymbol{\sigma}'}\right\} - \left\{\frac{\partial (\det \boldsymbol{s})}{\partial \boldsymbol{\sigma}'}\right\}\right] \tag{VII.8}$$

Note: The values of J and θ above are expressed in terms of effective stress, however, if total stresses are substituted for effective stresses in these expressions, the same numerical values of J and θ are obtained and $\{\partial J/\partial \boldsymbol{\sigma}\} = \{\partial J/\partial \boldsymbol{\sigma}'\}$ and $\{\partial \theta/\partial \boldsymbol{\sigma}\} = \{\partial \theta/\partial \boldsymbol{\sigma}'\}$.

Appendix VII.2: Analytical solutions for triaxial test on modified Cam clay

Modified Cam clay is a popular constitutive model for representing normally to moderately overconsolidated soils and is widely used in finite element analysis of geotechnical problems. Due to the complexity of the model, there are few closed form analytical solutions against which finite element programs can be calibrated. This appendix presents solutions for ideal (i.e. no end effects) drained and undrained triaxial tests. The model is fully defined with five parameters, κ, λ, v_1, M_J, and G, which are defined in Chapter 7.

Flow rule and plastic potential

Associated plasticity is assumed, with the yield function, $F(\{\boldsymbol{\sigma}'\},\{\boldsymbol{k}\})$, and plastic potential function, $P(\{\boldsymbol{\sigma}'\},\{\boldsymbol{m}\})$, given by:

$$F(\{\sigma'\},\{k\}) = P(\{\sigma'\},\{m\}) = \frac{J^2}{p'^2 M_J^2} - \frac{p_o'}{p'} + 1 = 0 \tag{VII.9}$$

where: p_o' = the hardening parameter, see Figure VII.1;
p' = the mean effective stress;
J = the deviatoric stress.

The plastic flow directions and yield function gradients are obtained by differentiating Equation (VII.9):

$$\begin{aligned} \frac{\partial F(\{\sigma'\},\{k\})}{\partial J} &= \frac{\partial P(\{\sigma'\},\{m\})}{\partial J} = \frac{2J}{p'^2 M_J^2} \\ \frac{\partial F(\{\sigma'\},\{k\})}{\partial p'} &= \frac{\partial P(\{\sigma'\},\{m\})}{\partial p'} = -\frac{2J^2}{p'^3 M_J^2} + \frac{p_o'}{p'^2} \end{aligned} \tag{VII.10}$$

If the stress state remains plastic, the consistency condition ($\mathrm{d}F(\{\boldsymbol{\sigma}'\},\{\boldsymbol{k}\}) = 0$) must be satisfied. Differentiating Equation (VII.9) gives:

$$\frac{\mathrm{d}p_o'}{p_o'} = \frac{2J}{p'p_o' M_J^2}\mathrm{d}J - \frac{\mathrm{d}p'}{p'} + 2\frac{\mathrm{d}p'}{p_o'} \tag{VII.11}$$

Hardening law

Hardening is assumed to be isotropic and dependent on the plastic volumetric strain, ε_v^p, as:

$$\frac{dp_o'}{p_o'} = \frac{v}{\lambda - \kappa} d\varepsilon_v^p \qquad \text{(VII.12)}$$

Elastic behaviour

Elastic volumetric strains are given by:

$$d\varepsilon_v^e = \frac{dp'}{K} = \frac{\kappa}{vp'} dp' \qquad \text{(VII.13)}$$

where K is the elastic bulk modulus. In the original formulation of modified Cam clay no elastic deviatiorc strains are considered, implying an infinite value of G. To avoid numerical difficulties and to achieve a better modelling inside the yield surface, elastic deviatoric strains are usually calculated from a finite value of G. Various alternatives have been proposed in the literature and three of these are considered here:

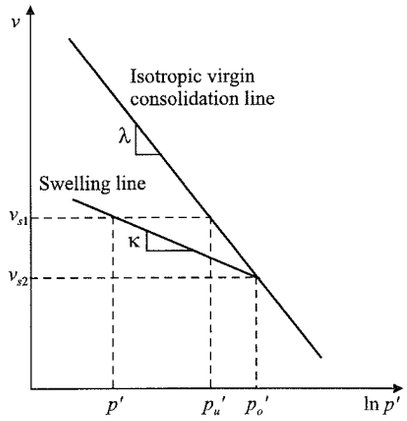

Figure VII.1: Virgin consolidation and swelling line

1. G is a multiple of the hardening parameter, p_o' ($G = g\, p_o'$).
2. G is specified using a constant Poisson's ratio, μ.
3. G is constant.

VII.2.1 Drained triaxial test

In this test a cylindrical sample of soil, representing modified Cam clay, is subjected to axial compression, while the radial total stress is maintained constant and no excess pore water pressures are allowed to develop. The initial stresses in the sample are given by $p' = p_i'$ and $J = J_i$. These boundary conditions result in the following stress path (see Figure VII.2):

$$p' = \frac{J}{\sqrt{3}} + p_h' \qquad \text{(VII.14)}$$

and

$$dp' = \frac{dJ}{\sqrt{3}}$$

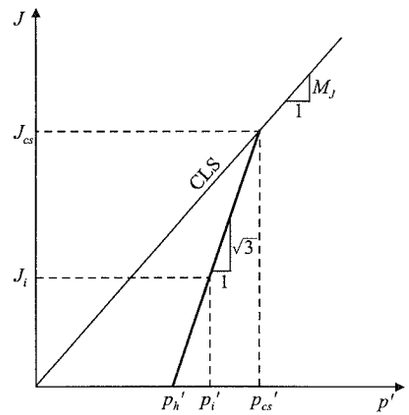

Figure VII.2: Drained triaxial compression stress path

where p_h' ($= p_i' - J_i/\sqrt{3}$) is the intercept of the stress path with the p' axis. The analytical solutions presented below give the values of volumetric strain, ε_v, deviatoric strain, E_d, and mean effective stress, p_c', associated with any current value of deviatoric stress, J_c. The critical state condition imposes limits to the values of p_c' and J_c. These values are p_{cs}' and J_{cs}, given by the intersection of the critical state line and the drained stress path, and can be expressed as:

$$J_{cs} = \frac{M_J p_h'}{1 - \frac{M_J}{\sqrt{3}}} \quad ; \quad p_{cs}' = \frac{p_h'}{1 - \frac{M_J}{\sqrt{3}}} \qquad \text{(VII.15)}$$

The value of E_d is divided into its plastic and elastic components, E_d^p and E_d^e respectively, and similarly ε_v is divided into ε_v^p and ε_v^e. The following solutions assume that over the limits of the integrals the specific volume is constant.

Elastic strains

Elastic volumetric strain

The elastic volumetric strains are given by integrating Equation (VII.13):

$$\varepsilon_v^e = \int_{p_i'}^{p_c'} \frac{\kappa}{v} \frac{dp'}{p'} = \frac{\kappa}{v} \ln\left(1 + \frac{J_c - J_i}{p_i'\sqrt{3}}\right) \qquad \text{(VII.16)}$$

Elastic deviatoric strain

CASE 1: $G = g\, p_o'$

From Equation (VII.9):

$$p_o' = \frac{J^2}{M_J^2 p'} + p' \qquad \text{(VII.17)}$$

Combining this equation with Equation (VII.14) and substituting in the expression for G, enables the elastic deviatoric strain to be expressed as:

$$E_d^e = \int_{J_i}^{J_c} \frac{dJ}{\sqrt{3}G} = \int_{J_i}^{J_c} \frac{dJ}{\sqrt{3}gp_o'} = \int_{J_i}^{J_c} \frac{M_J^2}{g} \frac{\sqrt{3}p_h' + J}{3J^2 + M_J^2(3p_h'^2 + 2\sqrt{3}p_h'J + J^2)} dJ \qquad \text{(VII.18)}$$

Applying integration of partial fractions to Equation (VII.18) gives:

$$E_d^e = \frac{\sqrt{3}M_J}{g(3+M_J^2)} \left\{ \tan^{-1}\left[\frac{J(3+M_J^2)}{3M_J p_h'} + \frac{M_J}{\sqrt{3}}\right] + \frac{3\sqrt{3}}{2} M_J \ln\left[J^2(3+M_J^2) + 2\sqrt{3}M_J^2 p_h' J + 3M_J^2 p_h'^2\right] \right\}_{J_i}^{J_c} \qquad \text{(VII.19)}$$

CASE 2: Constant Poisson's ratio, μ

The shear modulus, G, can be expressed using μ and the expression for K given in Equation (VII.13):

$$G = \frac{3vp'(1-2\mu)}{2(1+\mu)\kappa} \tag{VII.20}$$

The elastic deviatoric strain can therefore be evaluated by combining this Equation with Equation (VII.14):

$$\begin{aligned} E_d^e &= \int_{J_i}^{J_c} \frac{\mathrm{d}J}{\sqrt{3}G} = \int_{J_i}^{J_c} \frac{2(1+\mu)\kappa}{3\sqrt{3}v\left(p'_h + \frac{J}{\sqrt{3}}\right)(1-2\mu)}\mathrm{d}J \\ &= \frac{2(1+\mu)\kappa}{3v(1-2\mu)} \ln\left(\frac{\sqrt{3}p'_h + J_c}{\sqrt{3}p'_h + J_i}\right) \end{aligned} \tag{VII.21}$$

CASE 3: Constant shear modulus

The elastic deviatoric strain is given by:

$$E_d^e = \int_{J_i}^{J_c} \frac{\mathrm{d}J}{\sqrt{3}G} = \left[\frac{J}{\sqrt{3}G}\right]_{J_i}^{J_c} = \frac{J_c - J_i}{\sqrt{3}G} \tag{VII.22}$$

Plastic strains

Plastic straining only begins when the stress path intersects the initial yield surface. The position of the initial yield surface relative to the initial stress state depends on the overconsolidation ratio, which defines the initial value of p_o' (i.e. p_{oi}'). Using Equations (VII.9) and (VII.14) the intersect point, defined by p_y' and J_y, is given by the following expressions:

$$\begin{aligned} J_y &= \text{positive root of} \\ &= \frac{\frac{2p'_h - p'_{oi}}{\sqrt{3}} \pm \sqrt{4p'_h(p'_h - p'_{oi})\frac{3+M_J^2}{3M_J^2} - \left(\frac{2p'_h - p'_{oi}}{\sqrt{3}}\right)^2}}{2\frac{3+M_J^2}{3M_J^2}} \end{aligned} \tag{VII.23}$$

$$p'_y = \frac{J_y}{\sqrt{3}} + p'_h$$

Plastic volumetric strain

The plastic volumetric strain can be obtained by substituting Equations (VII.11) and (VII.14) into Equation (VII.12):

$$\begin{aligned} \varepsilon_v^p &= \frac{\lambda-\kappa}{v}\int_{J_y}^{J_c}\left[-\frac{1}{\sqrt{3}p'_h + J} + \frac{2(3+M_J^2)J + 2\sqrt{3}M_J^2 p'_h}{(3+M_J^2)J^2 + 2\sqrt{3}M_J^2 p'_h J + 3M_J^2 p_h'^2}\right]\mathrm{d}J \\ &= \frac{\lambda-\kappa}{v}\left[-\ln(\sqrt{3}p'_h + J) + \ln[(3+M_J^2)J^2 + 2\sqrt{3}M_J^2 p'_h J + 3M_J^2 p_h'^2]\right]_{J_y}^{J_c} \end{aligned} \tag{VII.24}$$

Plastic deviatoric strains

The incremental plastic deviatoric and volumetric strains are related by:

$$\mathrm{d}E_d^p = \Lambda\frac{\partial P(\{\sigma'\},\{m\})}{\partial J} = \Lambda\frac{2J}{p'^2M_J^2};\mathrm{d}\varepsilon_v^p = \Lambda\frac{\partial P(\{\sigma'\},\{m\})}{\partial p'} = -\Lambda\left(\frac{2J^2}{p'^3M_J^2} - \frac{p'_o}{p'^2}\right) \tag{VII.25}$$

Combining the second of these equations with Equations (VII.9), (VII.11) and (VII.12) gives the following expression for the plastic scalar multiplier, Λ:

$$\Lambda = \frac{\lambda-\kappa}{v}M_J^2 p'^2\frac{2Jp'\mathrm{d}J + M_J^2 p'^2\mathrm{d}p' - J^2\mathrm{d}p'}{(M_J^2p'^2 + J^2)(M_J^2p'^2 - J^2)} \tag{VII.26}$$

Substituting Equation (VII.26) into the first part of Equation (VII.25) and then removing the p' terms using Equations (VII.14), gives the following expression for the plastic deviatoric strain:

$$\begin{aligned} \mathrm{d}E_d^p = \frac{\lambda-\kappa}{v}\int_{J_y}^{J_c}\Bigg[&\frac{-2\sqrt{3}p'_h}{J^2(3+M_J^2) + 2\sqrt{3}M_J^2p'_hJ + 3M_J^2p_h'^2} + \\ &\frac{\frac{1}{M_J}}{\sqrt{3}M_Jp'_h + J(M_J - \sqrt{3})} + \frac{\frac{1}{M_J}}{\sqrt{3}M_Jp'_h + J(M_J + \sqrt{3})}\Bigg]\mathrm{d}J \end{aligned} \tag{VII.27}$$

Carrying out the integration gives the following expression for the deviatoric plastic strain:

$$\begin{aligned} E_d^p = \Bigg\{&-\frac{2}{\sqrt{3}}\frac{\lambda-\kappa}{vM_J}\tan^{-1}\left[\frac{J(3+M_J^2)}{3M_Jp'_h} + \frac{M_J}{\sqrt{3}}\right] + \\ &\frac{\lambda-\kappa}{v}\Bigg[\frac{1}{M_J(M_J-\sqrt{3})}\ln\left(\sqrt{3}M_Jp'_h + J(M_J-\sqrt{3})\right) + \\ &\frac{1}{M_J(M_J+\sqrt{3})}\ln\left(\sqrt{3}M_Jp'_h + J(M_J+\sqrt{3})\right)\Bigg]\Bigg\}_{J_y}^{J_c} \end{aligned} \tag{VII.28}$$

VII.2.2 Undrained triaxial test

In this test a cylindrical sample of modified Cam clay is subjected to axial compression, while the radial total stress is maintained constant and no volume change is allowed. The initial stresses in the sample are given by p_i' and J_i. In the derivations that follow use is made of p_u', which is the mean effective stress on the isotropic virgin consolidation line at the void ratio at which the undrained test is being carried out, see Figure VII.1. The relationship between p_u' and the current values of p' and p_o' can be obtained from the equations of the swelling and virgin consolidation lines and is:

$$\frac{p_o'}{p'} = \left(\frac{p_u'}{p'}\right)^{\frac{1}{\xi}} \qquad \text{where} \quad \xi = 1 - \frac{\kappa}{\lambda} \tag{VII.29}$$

Using the above equation to eliminate p_o' from the yield function (Equation (VII.9)) gives:

$$J = p' M_J \sqrt{\left(\frac{p_u'}{p'}\right)^{\frac{1}{\xi}} - 1} \tag{VII.30}$$

As p_u' remains constant in an undrained test, Equation (VII.30) provides the stress path in J - p' space once yielding occurs. Prior to yielding the stress path is vertical, i.e. $\Delta p' = 0$.

The analytical solutions given below provide values of E_d and J_c associated with any current value of p_c'. The critical state condition imposes a limit to the value of p_c', such that for initial stress states 'wet' of critical $p_{cs}' \le p_c' \le p_i'$, and for initial states 'dry' of critical $p_{cs}' \ge p_c' \ge p_i'$, where p_{cs}' is the critical state value of p'. Values of J_{cs} and p_{cs}' can be found from the intersection of the critical state line and the undrained stress path given by Equation (VII.30):

$$p_{cs}' = \frac{p_u'}{2^{\xi}} \quad ; \quad J_{cs} = M_J \frac{p_u'}{2^{\xi}} \tag{VII.31}$$

At any stage during the test the pore water pressure can be determined from the difference between the total and effective mean stress, using Equations (VII.14) and (VII.30).

For convenience, E_d is divided into its plastic and elastic components, E_d^p and E_d^e, respectively. Although there is no total volumetric strain, there are equal and opposite elastic and plastic components, ε_v^e and ε_v^p.

Elastic deviatoric strains

CASE 1: $G = g\, p_o'$

Using Equation (VII.29) to express p_o' as a function of p' and p_u' and differentiating the undrained stress path given by Equation (VII.30) to obtain an expression for dJ, the elastic deviatoric strain is given by:

$$E_d^e = \int_{J_i}^{J_c} \frac{\mathrm{d}J}{\sqrt{3}G} = \frac{M_J}{\sqrt{3}g} \int_{p_i}^{p_c} \frac{1 - \frac{1}{2\xi} - \left(\frac{p_u'}{p'}\right)^{-\frac{1}{\xi}}}{p' \sqrt{\left(\frac{p_u'}{p'}\right)^{\frac{1}{\xi}} - 1}} \mathrm{d}p' \tag{VII.32}$$

Integration of Equation (VII.32) then results in the following:

$$E_d^e = \xi \frac{M_J}{\sqrt{3}g} \left[\frac{\sqrt{\left(\frac{p_u'}{p'}\right)^{\frac{1}{\xi}} - 1}}{\left(\frac{p_u'}{p'}\right)^{\frac{1}{\xi}}} - \left(1 - \frac{1}{\xi}\right) \tan^{-1} \sqrt{\left(\frac{p_u'}{p'}\right)^{\frac{1}{\xi}} - 1} \right]_{p_i'}^{p_c'} \tag{VII.33}$$

CASE 2: Constant Poisson's ratio, μ

Differentiating the undrained stress path given by Equation (VII.30) to obtain an expression for dJ, and using Equation (VII.20), the elastic deviatoric strain is given by:

$$E_d^e = \int_{J_i}^{J_c} \frac{\mathrm{d}J}{\sqrt{3}G} = \frac{2(1+\mu)\,\kappa M_J}{3\sqrt{3}\,v\,(1-2\mu)} \int_{p_i'}^{p_c'} \frac{\left(\frac{p_u'}{p'}\right)^{\frac{1}{\xi}} \left(1 - \frac{1}{2\xi}\right) - 1}{p' \sqrt{\left(\frac{p_u'}{p'}\right)^{\frac{1}{\xi}} - 1}} \mathrm{d}p' \tag{VII.34}$$

Integrating this equation gives:

$$E_d^e = \frac{2(1+\mu)\,M_J\,\xi\,\kappa}{3\sqrt{3}\,v\,(1-2\mu)} \left[2 \tan^{-1} \sqrt{\left(\frac{p_u'}{p'}\right)^{\frac{1}{\xi}} - 1} - \left(2 - \frac{1}{\xi}\right) \sqrt{\left(\frac{p_u'}{p'}\right)^{\frac{1}{\xi}} - 1} \right]_{p_i'}^{p_c'} \tag{VII.35}$$

CASE 3: Constant shear modulus

The elastic deviatoric strain is given by the following equation:

$$E_d^e = \int_{J_i}^{J_c} \frac{\mathrm{d}J}{\sqrt{3}G} = \left[\frac{J}{\sqrt{3}G} \right]_{J_i}^{J_c} = \left[p' \frac{M_J}{\sqrt{3}G} \sqrt{\left(\frac{p_u'}{p'}\right)^{\frac{1}{\xi}} - 1} \right]_{p_i'}^{p_c'} \tag{VII.36}$$

Plastic deviatoric strains

The incremental plastic volumetric and deviatoric strains are expressed in Equation (VII.25). Noting that in an undrained test $\varepsilon_v^e = -\varepsilon_v^p$, Equation (VII.13), which gives $d\varepsilon_v^e$, can be combined with Equation (VII.25) to give the expression for Λ:

$$\Lambda = \frac{\kappa}{v}\frac{dp'}{\dfrac{2J^2}{p'^2 M_J^2} - \dfrac{p'_o}{p'}} \qquad \text{(VII.37)}$$

Substituting this into the first part of Equation (VII.25) and using Equation (VII.29) gives:

$$E_d^p = \int_{p_i'}^{p_e'} 2\frac{\kappa}{vp'M_J}\frac{\sqrt{\left(\dfrac{p'_u}{p'}\right)^{\frac{1}{\xi}} - 1}}{\left(\dfrac{p'_u}{p'}\right)^{\frac{1}{\xi}} - 2}\,dp' \qquad \text{(VII.38)}$$

Note: Due to the undrained condition, purely elastic behaviour occurs with no change in p'. Consequently, at first yield $p_y' = p_i'$. Integrating Equation (VII.38) gives:

$$E_d^p = -\frac{2\kappa\xi}{vM_J}\left[\tan^{-1}\sqrt{\left(\frac{p'_u}{p'}\right)^{\frac{1}{\xi}} - 1} - \frac{1}{2}\ln\left(\frac{1+\sqrt{\left(\dfrac{p'_u}{p'}\right)^{\frac{1}{\xi}} - 1}}{1-\sqrt{\left(\dfrac{p'_u}{p'}\right)^{\frac{1}{\xi}} - 1}}\right)\right]_{p_i'}^{p_e'} \qquad \text{(VII.39)}$$

Peak strength

In an undrained triaxial test the stress path follows Equation (VII.30). It is of interest to identify the magnitude of the peak deviatoric stress, J_p, and the mean effective stress at which it occurs, p_p', and to compare J_p with J_{cs}. Differentiating Equation (VII.30) with respect to p' and equating to zero, gives the expression for p_p'. Then J_p can be found by substituting this value of p_p' into Equation (VII.30):

$$p'_p = p'_u\left(\frac{2\xi-1}{2\xi}\right)^{\xi} \quad ; \quad J_p = M_J p'_u\left(\frac{2\xi-1}{2\xi}\right)^{\xi}\sqrt{\frac{1}{2\xi-1}} \qquad \text{(VII.40)}$$

Comparing the above expression for p_p' with the expression for p_{cs}' indicates that J_p occurs on the 'dry' side of the critical state. The ratio of J_p to J_{cs} can be found by dividing Equation (VII.40) by Equation (VII.31), which gives:

$$\frac{J_p}{J_{cs}} = \left(\frac{1-\dfrac{2\kappa}{\lambda}}{1-\dfrac{\kappa}{\lambda}}\right)^{1-\frac{\kappa}{\lambda}}\sqrt{\frac{1}{1-\dfrac{2\kappa}{\lambda}}} \qquad \text{(VII.41)}$$

The variation of J_p/J_{cs} with κ/λ is given in Figure VII.3. This shows that for values of $\kappa/\lambda > 0$ the peak deviator stress J_p exceeds J_{cs}. These results imply that strain softening behaviour occurs for stress states 'dry' of critical.

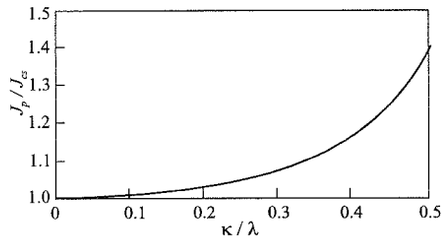

Figure VII.3: J_p/J_{cs} in undrained triaxial test

Appendix VII.3: Derivatives for modified Cam clay model

Yield function

The shape of the yield surface in the deviatoric plane is assumed to be a Mohr-Colulomb hexagon given by:

$$g(\theta) = \frac{\sin\varphi'_{cs}}{\cos\theta + \frac{1}{\sqrt{3}}\sin\theta\sin\varphi'_{cs}} \qquad \text{(VII.42)}$$

The yield surface is given by:

$$F(\{\sigma'\},\{k\}) = \left(\frac{J}{p'g(\theta)}\right)^2 - \left(\frac{p'_o}{p'} - 1\right) = 0 \qquad \text{(VII.43)}$$

The differentials required to evaluate the elasto-plastic constitutive matrix $[\boldsymbol{D}^{ep}]$ (see Equation (6.16)) can be obtained from Equations (7.21), together with:

$$\begin{aligned}
\frac{\partial F(\{\sigma'\},\{k\})}{\partial p'} &= \frac{1}{p'}\left[1 - \left(\frac{J}{p'g(\theta)}\right)^2\right] \\
\frac{\partial F(\{\sigma'\},\{k\})}{\partial J} &= \frac{2J}{\left(p'g(\theta)\right)^2} \\
\frac{\partial F(\{\sigma'\},\{k\})}{\partial \theta} &= \frac{2J^2}{p'^2 g(\theta)}\,\frac{\frac{1}{\sqrt{3}}\cos\theta\sin\varphi'_{cs} - \sin\theta}{\sin\varphi'_{cs}}
\end{aligned} \qquad \text{(VII.44)}$$

Plastic potential

To avoid the problems outlined in Section 7.12, Equation (VII.43) is used for the plastic potential, but the shape in the deviatoric plane is assumed to be circular. This is achieved by replacing the variable θ by the parameter $\theta(\sigma')$, which represents the Lode's angle at the point in stress space at which the gradients of the plastic potential are required. The plastic potential therefore has rotational symmetry and $P(\{\boldsymbol{\sigma}'\},\{\boldsymbol{m}\})$ is the surface of revolution generated by the intersection of $F(\{\boldsymbol{\sigma}'\},\{\boldsymbol{k}\})$ with the plane $\theta = \theta(\sigma')$. Therefore:

$$P(\{\sigma'\},\{\boldsymbol{m}\}) = \left(\frac{J}{p'g(\theta(\sigma'))}\right)^2 - \left(\frac{p'_o}{p'} - 1\right) = 0 \qquad \text{(VII.45)}$$

The differentials required to evaluate $[\boldsymbol{D}^{ep}]$ in Equation (6.16) can be obtained from Equation (7.21), with:

$$\begin{aligned}
\frac{\partial P(\{\sigma'\},\{\boldsymbol{m}\})}{\partial p'} &= \frac{1}{p'}\left[1 - \left(\frac{J}{p'g(\theta(\sigma'))}\right)^2\right] \\
\frac{\partial P(\{\sigma'\},\{\boldsymbol{m}\})}{\partial J} &= \frac{2J}{\left(p'g(\theta(\sigma'))\right)^2} \\
\frac{\partial P(\{\sigma'\},\{\boldsymbol{m}\})}{\partial \theta} &= 0
\end{aligned} \qquad \text{(VII.46)}$$

Hardening parameter

The hardening parameter A required to evaluate the elasto-plastic constitutive matrix is given by:

$$A = -\frac{1}{\Lambda}\frac{\partial F(\{\sigma'\},\{\boldsymbol{k}\})}{\partial k}\,\mathrm{d}k = -\frac{1}{\Lambda}\frac{\partial F(\{\sigma'\},\{\boldsymbol{k}\})}{\partial p'_o}\,\mathrm{d}p'_o \qquad \text{(VII.47)}$$

Noting that:

$$\mathrm{d}p'_o = p'_o\,\mathrm{d}\varepsilon_v^p\,\frac{v}{\lambda-\kappa} = p'_o\frac{v}{\lambda-\kappa}\Lambda\frac{\partial P(\{\sigma'\},\{\boldsymbol{m}\})}{\partial p'} \qquad \text{(VII.48)}$$

and:

$$\frac{\partial F(\{\sigma'\},\{\boldsymbol{k}\})}{\partial p'_o} = -\frac{1}{p'}$$

gives:

$$A = \frac{v}{\lambda-\kappa}\frac{p'_o}{p'^2}\left[1 - \left(\frac{J}{p'g(\theta(\sigma'))}\right)^2\right] \qquad \text{(VII.49)}$$

Appendix VII.4: Undrained strength for critical state models

In this appendix expressions are given for undrained strength, S_u, for both Cam clay and modified Cam clay models. For both models the expressions are derived following a similar procedure. Consequently, a detailed explanation is only provided for the modified Cam clay model.

Modified Cam clay

The yield surface for this model is given by Equation (VII.43). The undrained strength, S_u, is related to the deviatoric stress at failure, J_f, by (see Equation (7.8)):

$$S_u = J_f\cos\theta \qquad \text{(VII.50)}$$

For triaxial compression conditions, where $\theta = -30°$, the following relationship exists:

$$J = \frac{(\sigma'_1 - \sigma'_3)}{\sqrt{3}} \qquad \text{(VII.51)}$$

and from Figure VII.1:

$$\frac{p'_o}{p'} = \left(\frac{p'_o}{p'_u}\right)^{\frac{\lambda}{\kappa}} \qquad \text{(VII.52)}$$

where p' is the current value of the mean effective stress.

For an element of soil in the ground which has an initial vertical effective stress σ_{vi}' and overconsolidation ratio OCR (= $\sigma_{vm}'/\sigma_{vi}'$, where σ_{vm}' is the maximum vertical effective stress that the element of soil has been subjected to), the horizontal effective stress is given by:

$$\sigma'_{hi} = K_o^{OC}\sigma'_{vi} \qquad \text{(VII.53)}$$

where K_o^{OC} is the current value of the coefficient of earth pressure at rest. As noted above, the maximum vertical and horizontal effective stress that the soil element has ever experienced are given by:

$$\sigma'_{vm} = OCR\sigma'_{vi} \quad ; \quad \sigma'_{hm} = K_o^{NC}\sigma'_{vm} \qquad \text{(VII.54)}$$

where K_o^{NC} is the value of the coefficient of earth pressure at rest, associated with normal consolidation.

Equations (VII.54) can now be used to define the stress invariants J_m and p_m':

$$J_m = \frac{\sigma'_{vm} - \sigma'_{hm}}{\sqrt{3}} = \frac{1 - K_o^{NC}}{\sqrt{3}}\,OCR\,\sigma'_{vi} \qquad \text{(VII.55)}$$

$$p'_m = \frac{\sigma'_{vm} + 2\sigma'_{hm}}{3} = \frac{1 + 2K_o^{NC}}{3}\,OCR\,\sigma'_{vi} \qquad \text{(VII.56)}$$

Because the stress state associated with σ_{vm}', σ_{hm}', J_m and p_m' is normally consolidated, it must lie on the yield surface. Consequently, using Equation (VII.43) we can write:

$$\left(\frac{J_m}{p_m' g(-30°)}\right)^2 = \frac{p_o'}{p_m'} - 1 \qquad \text{(VII.57)}$$

Substituting Equations (VII.55) and (VII.56) into (VII.57) and rearranging provides the following expression for the current hardening parameter p_o':

$$p_o' = \sigma_{vi}' \, OCR \, \frac{(1+2K_o^{NC})}{3}(1+B^2) \qquad \text{(VII.58)}$$

where:

$$B = \frac{\sqrt{3}(1-K_o^{NC})}{g(-30^o)\,(1+2K_o^{NC})} \qquad \text{(VII.59)}$$

Using Equation (VII.52) gives the following value for p_u':

$$p_u' = p_o'\left(\frac{p_i'}{p_o'}\right)^{\frac{\kappa}{\lambda}} = \sigma_{vi}' \, OCR \, \frac{(1+2K_o^{NC})}{3}(1+B^2)\left[\frac{(1+2K_o^{OC})}{(1+2K_o^{NC})\,OCR\,(1+B^2)}\right]^{\frac{\kappa}{\lambda}} \qquad \text{(VII.60)}$$

When the undrained strength is mobilised, the soil element is at the critical state, with stresses J_{cs} and p_{cs}'. These stresses are related by the equation:

$$J_{cs} = p_{cs}' \, g(\theta) \qquad \text{(VII.61)}$$

which, on substitution in Equation (VII.43), gives:

$$p_{cs}' = p_{o,cs}'/2 \qquad \text{(VII.62)}$$

Combining Equations (VII.52) and (VII.62) gives:

$$\frac{p_{o,cs}'}{p_{cs}'} = \left(\frac{p_{o,cs}'}{p_u'}\right)^{\frac{\lambda}{\kappa}} = 2 \qquad \text{(VII.63)}$$

Consequently,

$$p_{o,cs}' = p_u'(2)^{\frac{\kappa}{\lambda}} \qquad \text{(VII.64)}$$

Combining Equations (VII.50), (VII.60), (VII.61), (VII.62) and (VII.64) gives the desired expression for S_u:

$$S_u = J_{cs}\cos\theta$$
$$= OCR \, \sigma_{vi}' \, g(\theta)\cos\theta\frac{(1+2K_o^{NC})}{6}(1+B^2)\left[\frac{2(1+2K_o^{OC})}{(1+2K_o^{NC})\,OCR\,(1+B^2)}\right]^{\frac{\kappa}{\lambda}} \qquad \text{(VII.65)}$$

If the soil element is normally consolidated, $K_o^{OC} = K_o^{NC}$ and $OCR = 1$. Therefore, Equation (VII.65) reduces to:

$$S_u = \sigma_{vi}' \, g(\theta)\cos\theta\frac{(1+2K_o^{NC})}{3}\left(\frac{1+B^2}{2}\right)^{1-\frac{\kappa}{\lambda}} \qquad \text{(VII.66)}$$

Note

If the shape of the yield surface in the deviatoric plane is given by a circle, then $g(\theta) = M_J$. Alternatively, $g(\theta)$ can be given by one of the expressions discussed in Section 7.9.2.

The value of K_o^{NC} is often assumed to be given by Jaky's (1948) formula:

$$K_o^{NC} = 1 - \sin\varphi_{cs}' \qquad \text{(VII.67)}$$

and K_o^{OC} by the Mayne and Kulhawy (1982) expression:

$$K_o^{OC} = K_o^{NC} \, OCR^{\sin\varphi_{cs}'} \qquad \text{(VII.68)}$$

Cam clay

The yield surface for this model is given by Equation (7.43):

$$F(\{\sigma'\},\{k\}) = \frac{J}{p' g(\theta)} + \ln\left(\frac{p'}{p_o'}\right) = 0 \qquad \text{(VII.69)}$$

Using the same procedure as outlined above for the modified Cam clay model, gives the following expression for the undrained strength:

$$S_u = OCR \, \sigma_{vi}' \, g(\theta)\cos\theta\frac{(1+2K_o^{NC})}{3}\left[\frac{(1+2K_o^{OC})}{(1+2K_o^{NC})\,OCR}\right]^{\frac{\kappa}{\lambda}} e^{(1-\frac{\kappa}{\lambda})(B-1)} \qquad \text{(VII.70)}$$

For normally consolidated conditions Equation (VII.70) reduces to:

$$S_u = \sigma_{vi}' \, g(\theta)\cos\theta\frac{(1+2K_o^{NC})}{3} e^{(1-\frac{\kappa}{\lambda})(B-1)} \qquad \text{(VII.71)}$$

8. Advanced constitutive models

8.1. Synopsis

In Chapter 7 simple elasto-plastic constitutive models of soil behaviour were considered. Although these models are restricted in their ability to reproduce real soil behaviour, they form the basis of classical soil mechanics theory. For example, most foundation and earth pressure calculations rely on either the Tresca or Mohr-Coulomb failure criteria. In this chapter a few of the more advanced soil models that are currently available are considered. These models are so complex that they must be combined with numerical analysis if they are to be used to investigate boundary value problems. Modelling the limited tensile capacity of soils is considered first and a constitutive model based on the framework of elasto-plasticity is presented. Extension of the elasto-plasticity theory presented in Chapter 6, to enable this model to be combined with other elasto-plastic constitutive models and incorporated into finite element analysis, is then presented. As an example of a model with multiple yield and plastic potential surfaces Lade's double yield surface model is described. The chapter concludes by describing the basic concepts of multi-surface kinematic 'bubble' models and bounding surface plasticity models. The anisotropic MIT-E3 model is briefly described as an example of the bounding surface plasticity model. The objective of the chapter is to present an overview of these more complex models, rather than an in depth description. This should give the reader an insight into the current state of the art concerning constitutive modelling and of the direction of possible future developments.

8.2 Introduction

As noted in Chapter 4, geotechnical materials exhibit irreversible behaviour, yield phenomena and shear induced dilatancy. These features strongly suggest that plasticity theory should be an appropriate framework for the description of the behaviour of soil. This framework was presented in Chapter 6 and some simple elasto-plastic models were presented in Chapter 7. While these simple models are an improvement over linear and nonlinear elastic models, they cannot reproduce all the important facets of real soil behaviour. To improve matters, more complex elasto-plastic constitutive models are needed. Some of these advanced models are reviewed in this chapter.

As most geotechnical materials cannot sustain large tensile stresses, the problem of modelling them as a material with limited tensile capacity often arises in practice. For example, if a Tresca or a modified Cam clay model is adopted to represent soil behaviour, unrealistic tensile stresses can occur. Several options are available to correct for this deficiency. In this chapter some of these are described and a model based on elasto-plasticity is presented, which can be combined with any other constitutive model to ensure the soil can only sustain a predetermined amount of tension. This introduces the problem of dealing with two yield and plastic potential surfaces which are simultaneously active. Consequently, the theory presented in Chapter 6 is extended to accommodate such behaviour for use in finite element analysis.

Having developed a theory for multiple yield surface models, Lade's double yield surface model is described. As noted in Volume 2 of this book, this model is useful for representing the behaviour of fill material. The chapter concludes by describing the basic framework for multi-surface kinematic 'bubble' models and bounding surface plasticity models. As an example of the latter, a brief description of the versatile MIT-E3 model is given. This model is highly complex, being able to simulate both inherent and induced anisotropy. Currently this model is used for research, but it does indicate what the future may hold.

All the models described in this chapter and in Chapter 7 are implemented in the computer code ICFEP (Imperial College Finite Element Program) and are used in examples presented subsequently in this volume and in Volume 2 of this book.

8.3 Modelling of soil as a limited tension material

8.3.1 Introduction

The structural nature of soil material is such that it can only sustain very little or no tensile stresses, when compared to its capacity to sustain compressive stresses. The same phenomena can also be observed with a fissured or jointed rock mass at its various degrees of weathering. An appropriate constitutive model for such a material should therefore not permit the soils tensile strength to be exceeded. It should also control the way tensile cracks initiate and then develop.

To date, various approaches for dealing with a limited tension material in numerical analysis exist. These include use of an anisotropic stiffness (Zienkiewicz and Cheng (1967)) and the stress transfer method (Zienkiewicz *et al.* (1968)). Both these approaches have shortcomings (Nyaoro (1989)).

Three basic approaches can also be identified for dealing with the rotation of the stress state upon tensile crack formation: (i) changing the anisotropic material axes (Cope *et al.* (1980)); (ii) allowing additional cracks to form (De Borst and Nauta (1984), (1985)) when rotation of the principal axis of tensile stress has exceeded a certain threshold angle, say 30° to 45°; (iii) assuming that upon formation of a second crack all stiffness at the respective point is lost (Nilson (1982)). All three methods can be shown to have serious drawbacks when applied to soil behaviour (Nyaoro (1989)).

It therefore appears that there is scope for improvement in the modelling of tensile failure. In this respect a realistic model of tensile fracturing should:

- Allow for free rotation of the crack orientation;
- Differentiate between the behaviour of closed pre-cracked surfaces and open cracks;
- Differentiate between the modes of straining associated with tensile cracking and that of the intact material;
- Accommodate elements within the material which simultaneously undergo tensile and shear failure.

To the Authors' knowledge a constitutive model which satisfies all of the above facets does not currently exist. However, a model developed at Imperial College by Nyaoro (1989) satisfies all but the second item above and provides considerable improvement over the alternative approaches. This constitutive model, which is based on elasto-plastic theory, allows for crack formation and subsequent rotation in a systematic manner. It can be used in conjunction with any other material model which describes the shear behaviour of the soil. For example, it can be used with simple elastic, elasto-plastic (e.g. Mohr-Coulomb), or critical state (e.g. modified Cam clay) models. The main features of this limited tension model are presented below.

8.3.2 Model formulation

As noted in Chapter 6, if soil behaviour is elasto-plastic, the incremental constitutive behaviour takes the form $\{\Delta\sigma\} = [\boldsymbol{D}^{ep}]\{\Delta\varepsilon\}$. The elasto-plastic constitutive matrix, $[\boldsymbol{D}^{ep}]$, is evaluated from the elastic matrix, $[\boldsymbol{D}]$, the stress derivatives of the yield and plastic potential functions and the hardening/softening laws, see Equation (6.16).

The constitutive behaviour for tensile fracturing has been developed within this framework. The model, in its current form, is assumed to be perfectly plastic and therefore does not have a hardening/softening law. However, there is no reason why such a law could not be included. In fact, such a law would be desirable when modelling soils with a finite tensile strength, because this strength must drop rapidly (instantaneously) to zero when a crack opens. In subsequent sections the yield and plastic potential functions are first presented, followed by a discussion on how the model should be implemented.

8.3.2.1 Yield surface

Tensile cracking occurs if the minor principal stress, σ_3', equals the tensile strength, T_o, (a negative quantity) of the soil, see Equation (5.4):

$$\sigma_3' = p' + \frac{2J}{\sqrt{3}}\sin(\theta - \frac{2\pi}{3}) = T_o \qquad (8.1)$$

The yield function can then be written as:

$$F(\{\sigma'\},\{\boldsymbol{k}\}) = T_o - p' - \frac{2J}{\sqrt{3}}\sin(\theta - \frac{2\pi}{3}) = 0 \qquad (8.2)$$

In the above equations effective stresses are used and therefore it is effective principal stresses that are being checked against the tensile strength. The model could equally well be formulated in terms of total stresses.

Equation (8.2) defines a yield surface along which the stress state can flow during tensile fracture. Such an approach enables the tensile crack to continuously rotate if it so wishes, and therefore overcomes the problem of setting threshold values of crack rotation. This yield surface plots as a triangular cone in principal effective stress space, see Figure 8.1a.

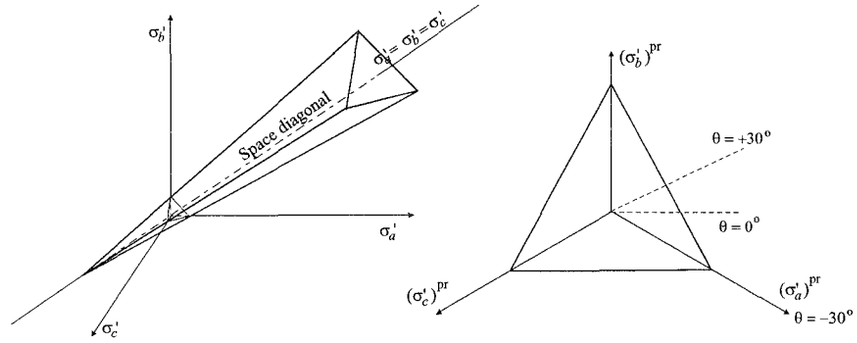

a) Tensile yield surface in principal stress space b) Shape of tensile yield surface in deviatoric plane

Figure 8.1: Tensile yield surface

The intersection of this cone with a deviatoric plane produces the triangle shown in Figure 8.1b. As with the Tresca or Mohr-Coulomb yield surfaces, care has to be taken at the corners of this yield surface because these correspond to singularities, see Nyaoro (1989).

The stress derivatives of the yield function required to construct the elasto-plastic constitutive matrix can be obtained from Equation (7.21), together with:

$$\frac{\partial F}{\partial p'} = -1 \;\; ; \;\; \frac{\partial F}{\partial J} = -\frac{2}{\sqrt{3}}\sin(\theta - \frac{2\pi}{3}) \;\; ; \;\; \frac{\partial F}{\partial \theta} = -\frac{2}{\sqrt{3}}\cos(\theta - \frac{2\pi}{3}) \qquad (8.3)$$

8.3.2.2 Plastic potential

In this model crack strains are simulated by assuming that they are plastic and therefore given by (see Equation (6.9)):

$$\{\Delta\varepsilon^{\text{crack}}\} = \{\Delta\varepsilon^{p}\} = \Lambda\left\{\frac{\partial P(\{\sigma'\},\{\boldsymbol{m}\})}{\partial\sigma'}\right\} \qquad (8.4)$$

where Λ is a scalar multiplier and $P(\{\sigma'\},\{m\})$ is the plastic potential function associated with tensile yielding. Evaluation of the plastic strains from Equation (8.4) requires the stress derivatives of the plastic potential function. These can be written as:

$$\left\{\frac{\partial P(\{\sigma'\},\{m\})}{\partial \sigma'}\right\} = \frac{\partial P(\{\sigma'\},\{m\})}{\partial p'}\left\{\frac{\partial p'}{\partial \sigma'}\right\} + \frac{\partial P(\{\sigma'\},\{m\})}{\partial J}\left\{\frac{\partial J}{\partial \sigma'}\right\} + \frac{\partial P(\{\sigma'\},\{m\})}{\partial \theta}\left\{\frac{\partial \theta}{\partial \sigma'}\right\} \tag{8.5}$$

The above derivatives can be determined if either an expression for $P(\{\sigma'\},\{m\})$ is given, or, alternatively, if its differentials with respect to p', J and θ are specified directly. The latter alternative was adopted by Nyaoro (1989) who determined the differentials for the situations where one or two cracks were operational, see Figure 8.2. These correspond to the situations where either one or two principal stresses reach the tensile strength.

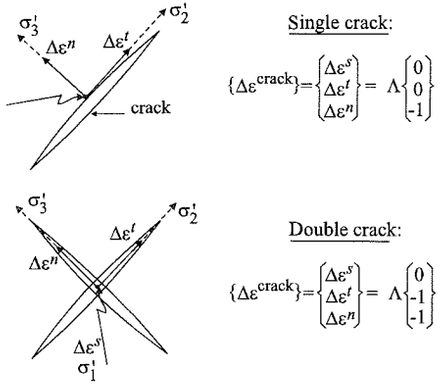

Figure 8.2: Tensile crack orientation

Although elegant, the approach adopted by Nyaoro (1989) is unnecessary. A much simpler approach, which results in exactly the same crack strains, is to assume associated flow conditions and adopt the yield function given by Equation (8.2) as the plastic potential. Equations (8.3), (8.4) and (8.5), along with stress derivatives given in Appendix VII.1, can then be used to calculate crack strains.

8.3.2.3 Finite element implementation

The above limited tension model can be combined with any other constitutive model. For example, it could be used with the Mohr-Coulomb or Cam clay models. In such cases the limited tension yield surface forms only part of a bounding surface of elastic stress states. An example is given in Figure 8.3 where both a plastic shear yield curve and a limited tension yield curve are shown. If an element of soil has a stress state represented by point 'a' it is elastic, because it is beneath both yield curves. If a stress increment is applied such that the stress state moves in the direction 'ab', the shear yield surface is met and elasto-plastic behaviour is controlled by this surface and its associated plastic potential and hardening law. Alternatively, if the direction of the stress path is 'ac', then the limited tension yield surface is met and behaviour is controlled by this model. During further straining the stress path may follow the limited tension curve to the intersection of the two yield curves (i.e. along path 'cd'). Once it reaches the intersection, two possibilities arise. Firstly, the stress path may move onto the shear yield surface in the direction 'db', in which case behaviour is controlled by the shear model. Alternatively, the boundary conditions and material behaviour might constrain the stress state to remain at the intersection of the two yield surfaces, in which case both shear and limited tension models are active simultaneously. In the latter case, the theory given in Section 6.13 must be extended to accommodate two yield and plastic potential surfaces which are simultaneously active. Such an extension is presented in the next section of this chapter. A similar choice is available for a stress path that first reaches the shear yield surface. It can either remain on this surface, or it can move towards the intersection and then onto the limited tension yield surface, or it can reach the intersection and stay there. The nature of the two yield models and the boundary conditions of the problem determine which option is taken.

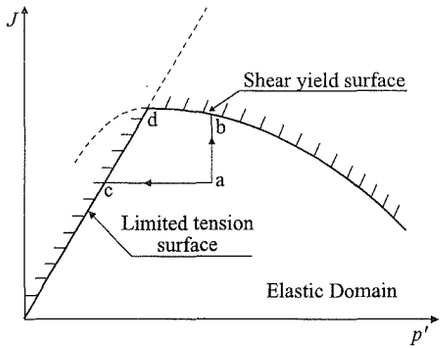

Figure 8.3: Combination of limited tension and plastic shear models of soil behaviour

8.4 Formulation of the elasto-plastic constitutive matrix when two yield surfaces are simultaneously active

In Section 6.13 the relationship between incremental stresses and incremental strains, when soil behaviour is governed by an elasto-plastic constitutive model with a single yield surface, was derived. It was shown that such a relationship could be written as:

$$\{\Delta\sigma\} = [\boldsymbol{D}^{ep}]\{\Delta\varepsilon\} \tag{8.6}$$

where $[\boldsymbol{D}^{ep}]$ is the elasto-plastic constitutive matrix which is a function of the elastic matrix $[\boldsymbol{D}]$, the stress differentials of the yield and plastic potential functions and the hardening law, see Equation (6.16). In this section this theory is extended to obtain an expression for the $[\boldsymbol{D}^{ep}]$ matrix for elasto-plastic behaviour involving two yield surfaces which are acting simultaneously.

As before, the incremental total strains, $\{\Delta\varepsilon\}$, are split into elastic, $\{\Delta\varepsilon^e\}$, and plastic, $\{\Delta\varepsilon^p\}$, components. In addition, the plastic component is subdivided into plastic strains associated with each of the two yield surfaces, $\{\Delta\varepsilon^{p1}\}$ and $\{\Delta\varepsilon^{p2}\}$. This gives:

$$\{\Delta\varepsilon\} = \{\Delta\varepsilon^e\} + \{\Delta\varepsilon^{p1}\} + \{\Delta\varepsilon^{p2}\} \tag{8.7}$$

The incremental stresses $\{\Delta\sigma\}$ are related to the incremental elastic strains $\{\Delta\varepsilon^e\}$ by the elastic constitutive matrix, $[\boldsymbol{D}]$, in the form:

$$\{\Delta\sigma\} = [\boldsymbol{D}]\{\Delta\varepsilon^e\} \tag{8.8}$$

or alternatively:

$$\{\Delta\varepsilon^e\} = [\boldsymbol{D}]^{-1}\{\Delta\sigma\} \tag{8.9}$$

Combining Equations (8.7) and (8.8) gives:

$$\{\Delta\sigma\} = [\boldsymbol{D}]\left(\{\Delta\varepsilon\} - \{\Delta\varepsilon^{p1}\} - \{\Delta\varepsilon^{p2}\}\right) \tag{8.10}$$

The incremental plastic strains, $\{\Delta\varepsilon^{p1}\}$ and $\{\Delta\varepsilon^{p2}\}$, are related to the plastic potential functions, $P_1(\{\sigma\},\{\boldsymbol{m}_1\})$ and $P_2(\{\sigma\},\{\boldsymbol{m}_2\})$, associated with each of the yield surfaces via the respective flow rules. Consequently, they may be written as:

$$\{\Delta\varepsilon^{p1}\} = \Lambda_1\left\{\frac{\partial P_1(\{\sigma\},\{\boldsymbol{m}_1\})}{\partial\sigma}\right\} \tag{8.11}$$

$$\{\Delta\varepsilon^{p2}\} = \Lambda_2\left\{\frac{\partial P_2(\{\sigma\},\{\boldsymbol{m}_2\})}{\partial\sigma}\right\} \tag{8.12}$$

where Λ_1 and Λ_2 are scalars. For presentation purposes, the plastic potential functions are written simply as P_1 and P_2 in the following equations. Substituting Equations (8.11) and (8.12) into (8.10) gives:

$$\{\Delta\sigma\} = [\boldsymbol{D}]\{\Delta\varepsilon\} - \Lambda_1[\boldsymbol{D}]\left\{\frac{\partial P_1}{\partial\sigma}\right\} - \Lambda_2[\boldsymbol{D}]\left\{\frac{\partial P_2}{\partial\sigma}\right\} \tag{8.13}$$

When the soil is plastic and both yield surfaces are active, the stress state must satisfy both yield functions, i.e. $F_1(\{\sigma\},\{\boldsymbol{k}_1\})=0$ and $F_2(\{\sigma\},\{\boldsymbol{k}_2\})=0$. This consistency condition gives $\Delta F_1(\{\sigma\},\{\boldsymbol{k}_1\}) = \Delta F_2(\{\sigma\},\{\boldsymbol{k}_2\}) = 0$, which, on using the chain rule of differentiation, gives (note: the yield functions are simply written as F_1 and F_2 in the subsequent text):

$$\Delta F_1 = \left\{\frac{\partial F_1}{\partial\sigma}\right\}^{\mathrm{T}}\{\Delta\sigma\} + \left\{\frac{\partial F_1}{\partial\boldsymbol{k}_1}\right\}^{\mathrm{T}}\{\Delta\boldsymbol{k}_1\} \tag{8.14}$$

$$\Delta F_2 = \left\{\frac{\partial F_2}{\partial\sigma}\right\}^{\mathrm{T}}\{\Delta\sigma\} + \left\{\frac{\partial F_2}{\partial\boldsymbol{k}_2}\right\}^{\mathrm{T}}\{\Delta\boldsymbol{k}_2\} \tag{8.15}$$

Substituting Equation (8.13) into Equations (8.14) and (8.15) yields:

$$\Delta F_1 = \left\{\frac{\partial F_1}{\partial\sigma}\right\}^{\mathrm{T}}[\boldsymbol{D}]\{\Delta\varepsilon\} - \Lambda_1\left\{\frac{\partial F_1}{\partial\sigma}\right\}^{\mathrm{T}}[\boldsymbol{D}]\left\{\frac{\partial P_1}{\partial\sigma}\right\} - \Lambda_2\left\{\frac{\partial F_1}{\partial\sigma}\right\}^{\mathrm{T}}[\boldsymbol{D}]\left\{\frac{\partial P_2}{\partial\sigma}\right\} - \Lambda_1 A_1 = 0 \tag{8.16}$$

$$\Delta F_2 = \left\{\frac{\partial F_2}{\partial\sigma}\right\}^{\mathrm{T}}[\boldsymbol{D}]\{\Delta\varepsilon\} - \Lambda_1\left\{\frac{\partial F_2}{\partial\sigma}\right\}^{\mathrm{T}}[\boldsymbol{D}]\left\{\frac{\partial P_1}{\partial\sigma}\right\} - \Lambda_2\left\{\frac{\partial F_2}{\partial\sigma}\right\}^{\mathrm{T}}[\boldsymbol{D}]\left\{\frac{\partial P_2}{\partial\sigma}\right\} - \Lambda_2 A_2 = 0 \tag{8.17}$$

where:

$$\begin{aligned} A_1 &= -\frac{1}{\Lambda_1}\left\{\frac{\partial F_1}{\partial\boldsymbol{k}_1}\right\}\{\Delta\boldsymbol{k}_1\} \\ A_2 &= -\frac{1}{\Lambda_2}\left\{\frac{\partial F_2}{\partial\boldsymbol{k}_2}\right\}\{\Delta\boldsymbol{k}_2\} \end{aligned} \tag{8.18}$$

Equations (8.16) and (8.17) can be written as:

$$\Lambda_1 L_{11} + \Lambda_2 L_{12} = T_1 \tag{8.19}$$

$$\Lambda_1 L_{21} + \Lambda_2 L_{22} = T_2 \tag{8.20}$$

where:

$$L_{11} = \left\{\frac{\partial F_1}{\partial\sigma}\right\}^{\mathrm{T}}[\boldsymbol{D}]\left\{\frac{\partial P_1}{\partial\sigma}\right\} + A_1 \tag{8.21}$$

$$L_{22} = \left\{\frac{\partial F_2}{\partial\sigma}\right\}^{\mathrm{T}}[\boldsymbol{D}]\left\{\frac{\partial P_2}{\partial\sigma}\right\} + A_2 \tag{8.22}$$

$$L_{12} = \left\{\frac{\partial F_1}{\partial\sigma}\right\}^{\mathrm{T}}[\boldsymbol{D}]\left\{\frac{\partial P_2}{\partial\sigma}\right\} \tag{8.23}$$

$$L_{21} = \left\{\frac{\partial F_2}{\partial\sigma}\right\}^{\mathrm{T}}[\boldsymbol{D}]\left\{\frac{\partial P_1}{\partial\sigma}\right\} \tag{8.24}$$

$$T_1 = \left\{\frac{\partial F_1}{\partial\sigma}\right\}^{\mathrm{T}}[\boldsymbol{D}]\{\Delta\varepsilon\} \tag{8.25}$$

$$T_2 = \left\{\frac{\partial F_2}{\partial\sigma}\right\}^{\mathrm{T}}[\boldsymbol{D}]\{\Delta\varepsilon\} \tag{8.26}$$

Equations (8.19) and (8.20) are two simultaneous equations with the two unknowns Λ_1 and Λ_2. Solution of these equations gives Λ_1 and Λ_2 as:

$$\Lambda_1 = (L_{22}T_1 - L_{12}T_2)/(L_{11}L_{22} - L_{12}L_{21}) \tag{8.27}$$

$$\Lambda_2 = (L_{11}T_2 - L_{21}T_1)/(L_{11}L_{22} - L_{12}L_{21}) \tag{8.28}$$

Substituting these two equations into Equation (8.13) gives $[\boldsymbol{D}^{ep}]$ as:

$$[\boldsymbol{D}^{ep}] = [\boldsymbol{D}] - \frac{[\boldsymbol{D}]}{\Omega}\left[\left\{\frac{\partial P_1}{\partial\sigma}\right\}\{\boldsymbol{b}_1\}^{\mathrm{T}} + \left\{\frac{\partial P_2}{\partial\sigma}\right\}\{\boldsymbol{b}_2\}^{\mathrm{T}}\right][\boldsymbol{D}] \tag{8.29}$$

where:

$$\Omega = L_{11}L_{22} - L_{12}L_{21}$$

$$\{b_1\} = L_{22}\left\{\frac{\partial F_1}{\partial \sigma}\right\} - L_{12}\left\{\frac{\partial F_2}{\partial \sigma}\right\}$$
$$\{b_2\} = L_{11}\left\{\frac{\partial F_2}{\partial \sigma}\right\} - L_{21}\left\{\frac{\partial F_1}{\partial \sigma}\right\}$$

As before, the values of A_1 and A_2 depend on the type of plasticity, e.g. perfect, strain hardening/softening, or work hardening/softening plasticity, see Section 6.13. Equation (8.29) results in a non-symmetric constitutive matrix if either of the yield surfaces involves non-associated flow. Following a similar approach to that presented above, it is a simple matter to extend the theory to deal with elasto-plastic behaviour involving more than two yield surfaces which are active simultaneously.

8.5 Lade's double hardening model

8.5.1 Introduction

As an example of a constitutive model that involves two yield surfaces, Lade's double hardening model (Lade (1977)) is briefly described. This model is based on concepts from nonlinear elasticity and isotropic work hardening/softening plasticity theories. Although the model is applicable to general three dimensional stress conditions, the input parameters can all be derived entirely from the results of standard laboratory tests. This model is appropriate for simulating the behaviour of granular soils.

Lade's double hardening model has been used extensively at Imperial College for modelling the behaviour of fill materials used in embankment construction. The model's implementation into finite element analysis is not straight forward and is described in detail by Kovačević (1994). Only a brief overview of the model is given in this chapter. Examples of the use of the model are given in Volume 2 of this book.

8.5.2 Overview of model

The model involves two work hardening/softening yield surfaces, called the *conical* and *cap* yield surfaces, see Figure 8.4. These surfaces enclose the elastic domain. If a soil is normally consolidated, it is plastic and its state of stress is on both yield surfaces, for example point 'a' in Figure 8.4a. If it is then sheared, its behaviour depends on the direction of the stress path. If the stress path is directed below both yield surfaces

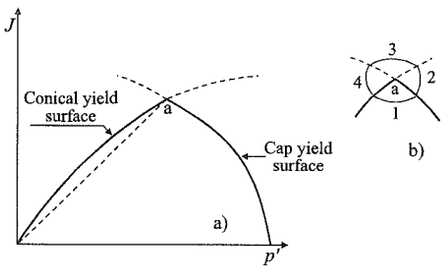

Figure 8.4: Yield surfaces for Lade's double hardening model

(i.e. into zone 1 in Figure 8.4b), behaviour is nonlinear elastic. If directed into zone 2, behaviour is elasto-plastic, with the cap yield surface active. As this surface is work hardening, it expands. The conical yield surface is dormant and therefore does not move. If the stress path is directed into zone 3, both yield surfaces are activated simultaneously. They both expand. If the stress path is directed into zone 4, then the conical yield surface is activated and it expands/contracts. The cap surface is dormant and remains fixed in space.

8.5.3 Elastic behaviour

The purely elastic response (i.e. zone 1) is described by isotropic elasticity and therefore requires two independent elastic parameters. A stress dependent Young's modulus, E, and a constant Poisson's ratio, μ, are adopted. In some of the earlier versions of this model the choice of expression for E was non-conservative, with the result that energy could be extracted from certain loading cycles (Zytinski *et al.* (1978)). Although in practice this may not be important, Lade and Nelson (1987) derived an alternative expression for Young's modulus from theoretical considerations based on the principle of conservation of energy. The resulting expression is:

$$E = Np_a\left[\left(\frac{3p'}{p_a}\right)^2 + \frac{6(1+\mu)}{(1-2\mu)}\left(\frac{J}{p_a}\right)^2\right]^{\omega} \qquad (8.30)$$

where μ is Poisson's ratio, p_a is atmospheric pressure and N and ω are material constants.

8.5.4 Failure criterion

The failure criterion has a curved shape in J-p' space, see Figure 8.5a, and a rounded triangular shape in the deviatoric plane, see Figure 8.5b. It is expressed by the following equation:

$$27\left(\frac{p'^3}{I_3} - 1\right)\left(\frac{3p'}{p_a}\right)^m = \eta_1 \qquad (8.31)$$

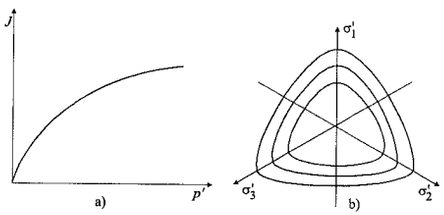

Figure 8.5: Failure criterion

where m and η_1 are material constants.

The apex angle and the curvature of the failure surface increase with values of η_1 and m respectively. For $m = 0$ the failure surface is straight in J-p' space. The stress invariant I_3 is given as:

$$\begin{aligned} I_3 &= \sigma'_1\sigma'_2\sigma'_3 \\ &= \sigma'_x\sigma'_y\sigma'_z + 2\tau_{xy}\tau_{yz}\tau_{zx} - (\sigma'_x\tau_{yz}^2 + \sigma'_y\tau_{zx}^2 + \sigma'_z\tau_{xy}^2) \\ &= p'^3 - p'^2J^2 - \frac{4}{3\sqrt{3}}J^3\left(\frac{1}{2} + \cos 2\theta\right)\sin\theta \end{aligned}$$

8.5.5 Conical yield function

As noted above, the plastic *expansive* strains, $\{\Delta\varepsilon^{p1}\}$, are governed by a conical yield surface. Like the failure surface, it has curved meridians in J-p' space and a smoothly rounded triangular cross-section in the deviatoric plane, see Figure 8.5. It takes a very similar form to Equation (8.31):

$$F_1(\{\sigma'\},\{\boldsymbol{k}_1\}) = 27\left(\frac{p'^3}{I_3}-1\right)\left(\frac{3p'}{p_a}\right)^m - H_1 = 0 \qquad (8.32)$$

where H_1 is work hardening/softening parameter which defines the size of the surface. At failure $H_1 = \eta_1$.

8.5.6 Conical plastic potential function

The plastic potential associated with the conical yield surface (see Figure 8.6) takes the form:

$$P_1(\{\sigma'\},\{\boldsymbol{m}_1\}) = 27p' - \left[27+\eta_2\left(\frac{p_a}{3p'}\right)^m\right]I_3 \qquad (8.33)$$

where:

$$\eta_2 = \rho H_1 + R\left(\frac{\sigma_3'}{p_a}\right)^{\frac{1}{2}} + t$$

and ρ, R and t are dimensionless parameters. The flow rule for this part of the model is therefore non-associated.

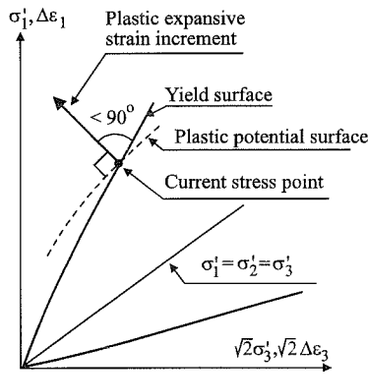

Figure 8.6: Yield and plastic potential surfaces for plastic 'expansive' strains

8.5.7 Conical hardening law

The work hardening parameter, H_1, in Equation (8.32) is given by:

$$H_1 = \eta_1\left[\xi\, e^{(1-\xi)}\right]^{\frac{1}{q}} \quad ; \quad q \geq 1 \qquad (8.34)$$

where:

$$\begin{aligned}\xi &= \Sigma(\Delta W_{p1}/W_{p1p})\\ \Delta W_{p1} &= \{\sigma\}^T\{\Delta\varepsilon^{p1}\}\\ W_{p1p} &= C\,p_a\,(\sigma_3'/p_a)^l\\ q &= \alpha+\beta(\sigma_3'/p_a),\ q\geq 1\end{aligned}$$

α, β, C and l are material parameters and $\{\Delta\varepsilon^{p1}\}$ are the incremental plastic strains associated with the conical yield surface. ΔW_{p1} is the incremental plastic *expansive* work, while W_{p1p} is the accumulated plastic work associated with the conical yield surface at peak strength.

8.5.8 Cap yield function

The yield surface corresponding to the plastic *collapse* strains, $\{\Delta\varepsilon^{p2}\}$, forms a cap on the open end of the conical yield surface, as shown in Figure 8.4. This cap yield surface is shaped as a sphere, with its centre at the origin of principal stress space. It is defined by the following equation:

$$F_2(\{\sigma'\},\{\boldsymbol{k}_2\}) = 9p'^2 + 2I_2 - H_2 = 0 \qquad (8.35)$$

where:

$$\begin{aligned}I_2 &= -(\sigma_1'\sigma_2' + \sigma_2'\sigma_3' + \sigma_3'\sigma_1')\\ &= J^2 - 3p'^2\end{aligned}$$

and H_2 is a work hardening parameter which defines the size of the surface.

8.5.9 Cap plastic potential function

The plastic potential function is obtained by assuming associated flow conditions, therefore $P_2(\{\sigma'\},\{\boldsymbol{m}_2\}) = F_2(\{\sigma'\},\{\boldsymbol{k}_2\})$, where $F_2(\{\sigma'\},\{\boldsymbol{k}_2\})$ is given by Equation (8.35).

8.5.10 Cap hardening law

The work hardening parameter H_2 in Equation (8.35) is given by:

$$H_2 = p_a^2\left[\frac{W_{p2}}{Cp_a}\right]^{\frac{1}{p}} \qquad (8.36)$$

where C and p are dimensionless material parameters, and W_{p2} is the accumulated plastic work associated with the cap yield surface and is given by:

$$W_{p2} = \Sigma(\Delta W_{p2}) = \Sigma(\{\sigma'\}^T\{\Delta\varepsilon^{p2}\})$$

8.5.11 Comments

A schematic diagram of the yielding process with both yield surfaces active is shown for the triaxial plane in Figure 8.7, where the plastic strain increment vectors are superimposed on the stress space. The total plastic strain increment is calculated as the vector sum of the two components (=$\{\Delta\varepsilon^{p1}\}$+$\{\Delta\varepsilon^{p2}\}$). In order to obtain the total strain increment for the stress change from point A to point B, the elastic strain component should be added (see Equation (8.7)). It is worth noting that yielding resulting from outward movement of the cap does not result in eventual failure. Failure is controlled entirely by the conical yield surface.

A total of fourteen parameters are required to characterise the behaviour of the model. Three of these parameters are associated with the elastic response (N, ω and μ); two are required for the plastic *collapse* strain component (C and p); and nine are required for the plastic *expansive* strain component (η_1, m, ρ, R, t, α, β, P and l). Derivatives of the yield and plastic potential functions, necessary for the construction of the elasto-plastic constitutive matrix in Equation (8.29), are given in Appendix VIII.1.

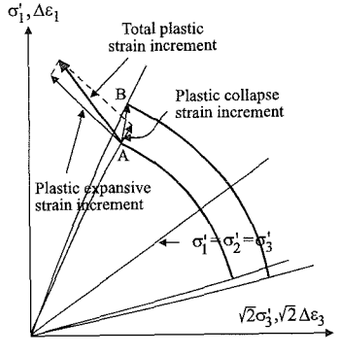

Figure 8.7: Yielding process with both yield surfaces activated

8.6 Bounding surface formulation of soil plasticity

8.6.1 Introduction

As discussed in Chapter 6 and used in Chapter 7, a conventional yield surface separates elastic behaviour (i.e. stress states within the yield surface) from elasto-plastic behaviour (i.e. stress states on the yield surface). Consequently, for stress paths remaining within the yield surface only recoverable elastic straining occurs. In reality, soils often exhibit non-recoverable behaviour on unloading and reloading. For example, volumetric strains and pore water pressures accumulate during drained and undrained cyclic deviatoric loading respectively. As such loading moves the stress path below the yield surface, most conventional elasto-plastic models are unable to recover the observed soil behaviour. In order to overcome such deficiencies further development of the elasto-plastic framework is necessary.

One such development is the introduction of the concept of bounding surface plasticity (Dafalias (1975), Krieg (1975), Dafalias and Popov (1976)). In this approach a bounding surface is defined. In many respects this surface resembles a conventional yield surface, however, plastic straining is allowed for stress states within the surface if loading occurs. The magnitude of this plastic straining is a function of behaviour defined for stress states on the bounding surface and of the proximity of the current stress state to the bounding surface.

8.6.2 Bounding surface plasticity

A bounding surface (see Figure 8.8) is defined in a similar way to that of a conventional yield surface:

$$F(\{\sigma'\},\{k\}) = 0 \tag{8.37}$$

A plastic potential and a hardening/softening rule are associated with this surface. For a soil element with a stress state on the bounding surface (i.e. $\bar{\sigma}'$ in Figure 8.8), the bounding surface acts in the same manner as a conventional yield surface. For example, if the soil element is unloaded such that the stress state moves inside the bounding surface, purely elastic behaviour occurs. Alternatively, if the element is loaded, it remains on the bounding surface and its elasto-plastic behaviour is controlled by the bounding surface (acting as a conventional yield surface), the plastic potential, the hardening/softening rule and the elastic parameters.

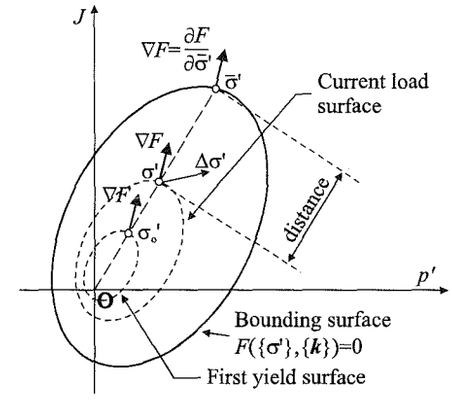

Figure 8.8: Schematic illustration of the bounding surface

If, on the other hand, the stress state of the soil element lies inside the bounding surface, i.e. point σ_o' in Figure 8.8, due to, for example, some previous history of loading followed by unloading, the behaviour on subsequent straining departs from that associated with classical elasto-plasticity, which would predict purely elastic behaviour both for loading and unloading. In the bounding surface framework, while elastic behaviour occurs if the soil element is unloaded, elasto-plastic behaviour occurs on loading. To quantify the elasto-plastic behaviour on loading requires the gradients of the yield function ($\partial F(\{\boldsymbol{\sigma}'\},\{\boldsymbol{k}\})/\partial\boldsymbol{\sigma}'$) and the plastic potential function ($\partial P(\{\boldsymbol{\sigma}'\},\{\boldsymbol{m}\})/\partial\boldsymbol{\sigma}'$) and a hardening modulus A (see Equation (6.16)). In general, these quantities are related to those associated with the bounding surface using *mapping* rules, which are dependent on the proximity of the current stress state to the bounding surface.

Consider the situation in which a soil sample is subjected to loading and unloading such that its current stress state corresponds to point σ_o' in Figure 8.8. If the soil element is now loaded, it behaves elasto-plastically. Point σ_o' is therefore associated with a change from elastic to elasto-plastic behaviour and is defined as the most recent 'first yield point'. A 'first yield surface', which has a similar shape to the bounding surface, but scaled down to pass through the current stress state σ_o', is also established. In fact, this surface is used in the same way as a conventional yield surface, to distinguish between loading and unloading when the

soil element is strained from point σ_o'. As the first yield surface is homeothetic to the bounding surface, with respect to the origin of stress space, the gradient of the surface at point σ_o' is the same as the gradient of the bounding surface at the image point $\bar{\sigma}'$, see Figure 8.8. If the image point $\bar{\sigma}'$ is located at the intersection of the bounding surface with the straight line which passes though the stress state σ_o' and the origin of stress space O, as illustrated in Figure 8.8, it satisfies the simple radial rule. The corollary is that this rule enables the image point, associated with any stress state within the bounding surface, to be obtained by constructing a radial line which passes through the stress point and the origin. Where this line intersects the bounding surface defines the position of the image point. Other rules have been used in the literature, but the simple radial rule has been shown to be appropriate in many cases. A plastic potential, or more conveniently the gradients of a plastic potential, $\partial P_o(\{\boldsymbol{\sigma}_o'\},\{\boldsymbol{m}_o\})/\partial\boldsymbol{\sigma}'$, and a plastic hardening modulus, A_o, are defined for the first yield point σ_o' and provide sufficient information to enable the elasto-plastic behaviour to be evaluated on first loading from point σ_o'. If loading persists, for example towards the image point $\bar{\sigma}'$, as indicated in Figure 8.8, elasto-plastic behaviour continues. To evaluate this behaviour again requires values of the yield and plastic potential function gradients and the plastic hardening modulus A. For the situation shown in Figure 8.8, where the stress state moves from σ_o' to σ', a current load surface is defined, which passes through σ'. This surface is again homeothetic to the bounding surface with respect to the origin. It is used in the same way as a conventional yield surface to establish whether subsequent stress changes cause loading or unloading. If loading occurs, it is also used as a yield surface to evaluate $\partial F(\{\boldsymbol{\sigma}'\},\{\boldsymbol{k}\})/\partial\boldsymbol{\sigma}'$. It should, however, be noted that these gradients are the same as those on the bounding surface at the image point $\bar{\sigma}'$. The gradients of the plastic potential, $\partial P(\{\boldsymbol{\sigma}'\},\{\boldsymbol{m}\})/\partial\boldsymbol{\sigma}'$, and the plastic hardening modulus, A, are obtained by interpolation between the equivalent values on the first yield surface (i.e. associated with point σ_o') and the bounding surface (i.e. at the image point $\bar{\sigma}'$), using scalar mapping functions which depend on the relative position of the current load surface with respect to the first yield and bounding surfaces. If loading continues, the above procedure is repeated until the stress state reaches the bounding surface. If unloading occurs, behaviour becomes elastic. If subsequently reloading occurs, a new first yield point and first yield surface are established at the new reversal point.

During elasto-plastic behaviour with the stress state below the bounding surface, the size and orientation of the bounding surface can change. This arises if the hardening/softening parameters $\{\boldsymbol{k}\}$, associated with the bounding surface (8.37), are dependent on plastic strains.

In summary, the essential ingredients of a bounding surface model are the definition of the bounding surface itself, the gradients of the plastic potential both on the bounding and first yield surfaces, the plastic hardening modulus on the bounding and first yield surfaces and the mapping functions which define how the plastic potential gradients and the hardening modulus change as loading continues from the first yield surface towards the bounding surface.

8.7 MIT soil models

8.7.1 Introduction

As an example of a model based on the bounding surface plasticity concept, a model developed at the Massachusetts Institute of Technology (MIT) is presented. The model, named as MIT-E3, was developed by Whittle (1987) to describe the behaviour of overconsolidated clays. This model evolved from MIT-E1, a model developed by Kavvadas (1982) for normally consolidated clays. Both models are based on modified Cam clay (Roscoe and Burland (1968)). However, several extension have been made to the basic critical state framework to enable the representation of certain features of soil behaviour not realised by modified Cam clay. The key features of MIT-E1 are an anisotropic yield surface, kinematic plasticity and significant strain softening behaviour under undrained conditions. The two additional features incorporated into MIT-E3 are small strain nonlinear elasticity using a closed loop hysteretic stress-strain formulation, and bounding surface plasticity, wherein plastic straining occurs within the conventionally defined yield locus. Whittle (1993) demonstrated the ability of MIT-E3 to accurately represent the behaviour of three different clays when subjected to a variety of loading paths.

The constitutive laws for MIT-E3 were first published in Whittle (1987) and were subsequently presented in Whittle (1991, 1993) and Hashash (1992). There are differences between the equations shown in these publications. These differences are described in Ganendra (1993) and Ganendra and Potts (1995) and the correct form of each equation is disclosed. There are also certain ambiguities and inaccuracies in the description of MIT-E3 in all four publications. These are also highlighted by Ganendra (1993) and Ganendra and Potts (1995) and either corrected or explained in a clear, well defined manner.

8.7.2 Transformed variables

For a constitutive model to be able to reproduce anisotropic soil behaviour (i.e. a different response when loaded in different directions), formulation in terms of stress and strain invariants has to be abandoned. The use of invariants inevitably leads to an isotropic formulation, which is what most of the currently existing models assume. To deal with anisotropy, one has to use all six components of the stress tensor and six components of the strain tensor, or some meaningful combination of these components.

The constitutive laws for the MIT-E3 model are expressed in terms of transformed variables, see Table 8.1. The transformed variables for any quantity (e.g. stresses, strains) comprise a linear combination of the tensorial measures of the quantity. They are analogous to their tensorial counterparts, since there is a complete interchangeability between these two forms of representing any quantity.

Table 8.1: Transformed variables for MIT-E3 model

Effective stress	Strain	Yield surface gradient	Plastic flow direction	Anisotropy
$(p', \boldsymbol{s})$	$(\varepsilon, \boldsymbol{E})$	$(Q, \boldsymbol{Q})$	$(P, \boldsymbol{P})$	$(1, \boldsymbol{b})$
$p' = \frac{\sigma'_x + \sigma'_y + \sigma'_z}{3}$	$\varepsilon = \varepsilon_x + \varepsilon_y + \varepsilon_z$	$Q = Q_x + Q_y + Q_z$	$P = P_x + P_y + P_z$	1
$s_1 = \frac{2\sigma'_y - \sigma'_x - \sigma'_z}{\sqrt{6}}$	$E_1 = \frac{2\varepsilon_y - \varepsilon_x - \varepsilon_z}{\sqrt{6}}$	$Q_1 = \frac{2Q_y - Q_x - Q_z}{\sqrt{6}}$	$P_1 = \frac{2P_y - P_x - P_z}{\sqrt{6}}$	$b_1 = \frac{2b_y - b_x - b_z}{\sqrt{6}}$
$s_2 = \frac{2\sigma'_z - \sigma'_x}{\sqrt{2}}$	$E_2 = \frac{2\varepsilon_z - \varepsilon_x}{\sqrt{2}}$	$Q_2 = \frac{2Q_z - Q_x}{\sqrt{2}}$	$P_2 = \frac{2P_z - P_x}{\sqrt{2}}$	$b_2 = \frac{2b_z - b_x}{\sqrt{2}}$
$s_3 = \sqrt{2}\sigma_{xy}$	$E_3 = \sqrt{2}\varepsilon_{xy}$	$Q_3 = \sqrt{2}Q_{xy}$	$P_3 = \sqrt{2}P_{xy}$	$b_3 = \sqrt{2}\, b_{xy}$
$s_4 = \sqrt{2}\sigma_{yz}$	$E_4 = \sqrt{2}\varepsilon_{yz}$	$Q_4 = \sqrt{2}Q_{yz}$	$P_4 = \sqrt{2}P_{yz}$	$b_4 = \sqrt{2}\, b_{yz}$
$s_5 = \sqrt{2}\sigma_{zx}$	$E_5 = \sqrt{2}\varepsilon_{zx}$	$Q_5 = \sqrt{2}Q_{zx}$	$P_5 = \sqrt{2}P_{zx}$	$b_5 = \sqrt{2}\, b_{zx}$

8.7.3 Hysteretic elasticity

The hysteretic elasticity formulation simulates the strongly nonlinear nature of overconsolidated clays in an unload-reload cycle. Figure 8.9 illustrates the closed symmetric hysteresis loop response of a sample which undergoes isotropic unloading (point A to B) from the virgin consolidation line, VCL, followed by reloading back to the VCL (B to A). Important characteristics of this response are:

- The large initial stiffness and the subsequent drop in stiffness;
- The continuous variation of stiffness both from A to B and from B to A;
- The abrupt change in stiffness at B, notionally termed a load reversal point;
- The absence of irrecoverable strains within a cycle.

The hysteretic formulation of elasticity used to realise these characteristics is based on Hueckel and Nova (1979) and consists of (i) a criterion for identifying the load reversal point and (ii) an expression for the tangential bulk stiffness, which is a function of the current stress state and the load reversal point.

The MIT-E3 expression for elastic bulk modulus, K, is obtained by modifying Equation (7.40):

$$K = \frac{vp'}{\kappa_0(1+\delta)} \tag{8.38}$$

where κ_0 is the initial slope of the swelling line in v-lnp' space after a load reversal and is a material property; δ is a state variable which is a measure of the difference between the current stress state $(p', \boldsymbol{s})$ and the stresses at the load reversal point $(p'^{\text{rev}}, \boldsymbol{s}^{\text{rev}})$, and is given by:

$$\delta = Cn(\ln X + \omega X_s)^{n-1} \tag{8.39}$$

with C, n and ω being material properties. Vector $\boldsymbol{s} = \{s_i\}$, $i = 1, \ldots, 5$, is the deviatoric stress vector expressed using transformed variables, see Table 8.1. X and X_s are state variables defined as:

$$X = \begin{cases} \dfrac{p'}{p'^{\text{rev}}} & \text{if } p' > p'^{\text{rev}} \\ \dfrac{p'^{\text{rev}}}{p'} & \text{if } p' < p'^{\text{rev}} \end{cases} \tag{8.40a}$$

$$X_s = \sqrt{\sum_{i=1}^{5}\left(\eta_i - \eta_i^{\text{rev}}\right)^2} \tag{8.40b}$$

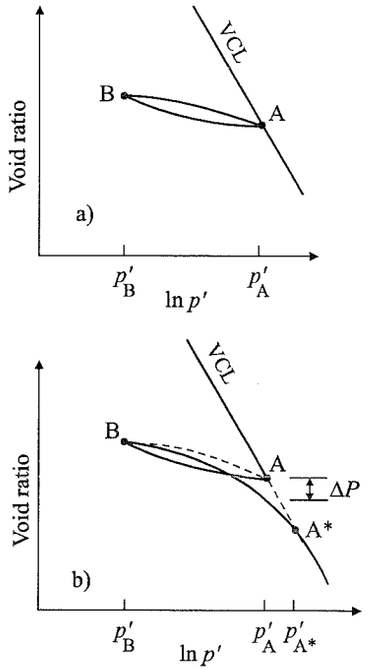

Figure 8.9: Conceptual isotropic unload-reload response used by MIT-E3

where $\eta_i = s_i/p'$ and $\eta_i^{\text{rev}} = s_i^{\text{rev}}/p'^{\text{rev}}$.

A constant Poisson's ratio (K/G constant) is used to describe the elastic shear modulus, G. Thus there is no coupled volumetric/shear behaviour in the hysteretic formulation. Another important feature of this formulation is that the hysteretic behaviour is only a function of the last load reversal point and maintains no memory of any previous loading history. As only two independent elastic parameters K and G are used, the elastic part of the model is isotropic. It is the plastic component of the model which simulates anisotropic behaviour.

It is important to emphasise, from the above formulation, that in the MIT-E3 model κ is a variable and should be distinguished from the material property κ_0:

$$\kappa = \kappa_0(1+\delta) \tag{8.41}$$

where δ depends on the last reversal point.

Whittle (1987) identified the load reversal point using a scalar strain amplitude parameter, χ, which is a measure of the strain history relative to the most recent load reversal point. There are two definitions for χ, depending on whether the sample is in a drained or undrained condition:

$$\chi = \begin{cases} \left|\varepsilon_v - \varepsilon_v^{\text{rev}}\right| & \text{if} \quad \varepsilon_v \neq 0 \\ \sqrt{\sum_{i=1}^{5}\left(E_i - E_i^{\text{rev}}\right)^2} & \text{if} \quad \varepsilon_v = 0 \end{cases} \tag{8.42}$$

where ε_v is volumetric strain and $\boldsymbol{E}=\{E_i\}$, i=1, ..., 5, is a deviatoric strain vector (see Table 8.1). A load reversal point then occurs when the magnitude of χ reduces, i.e. $\Delta\chi < 0$.

The above definition of χ lays great emphasis on the volumetric behaviour of the soil for determining the stress reversal point. However, if the model is implemented in finite element analysis, it is difficult to check the zero volumetric strain criterion for undrained behaviour. This is because the two standard methods of incorporating undrained behaviour, using a bulk fluid compressibility or using coupled consolidation, always result in a small amount of volumetric strain. Therefore, Ganendra (1993) decided to implement a more robust expression for χ:

$$\chi = \sqrt{\left(\varepsilon_v - \varepsilon_v^{\text{rev}}\right)^2 + \sum_{i=1}^{5}\left(E_i - E_i^{\text{rev}}\right)^2} \tag{8.43}$$

Although this expression does not have the same emphasis on volumetric strain as Whittle's, the consequences of this discrepancy are thought to be small.

8.7.4 Behaviour on the bounding surface

The bounding surface for the MIT-E3 model is an anisotropic form of the elliptical modified Cam clay yield surface and is defined in generalised stress space using transformed variables (see Figure 8.10):

$$F = \sum_{i=1}^{5}(s_i - p'b_i)^2 - c^2 p'(2\alpha - p') = 0 \tag{8.44}$$

where:

c is the ratio of semi-axes of the ellipsoid and is a material property;

α is a scalar variable which defines the size of the bounding surface;

$\boldsymbol{b} = \{b_i\}$, i=1, ..., 5, is a vector which describes the orientation of the bounding surface and is variable, see Table 8.1;

$\boldsymbol{s} = \{s_i\}$, i=1, ..., 5, is the deviatoric stress vector expressed using transformed variables, see Table 8.1.

The bounding surface is a distorted ellipsoid in six dimensional stress space, with its longer axis along the direction $\boldsymbol{\beta}$, see Figure 8.10. $\boldsymbol{\beta}$ is a vector which indicates the principal direction of anisotropy and $\boldsymbol{\beta} = \boldsymbol{b} + \boldsymbol{I}$, where $\{\boldsymbol{I}\}^{\mathrm{T}} = \{1\ 0\ 0\ 0\ 0\ 0\}$. $\boldsymbol{\beta}$ is initially orientated in the direction of consolidation and rotates as a function of any subsequent loading, in a manner defined by the model's hardening laws.

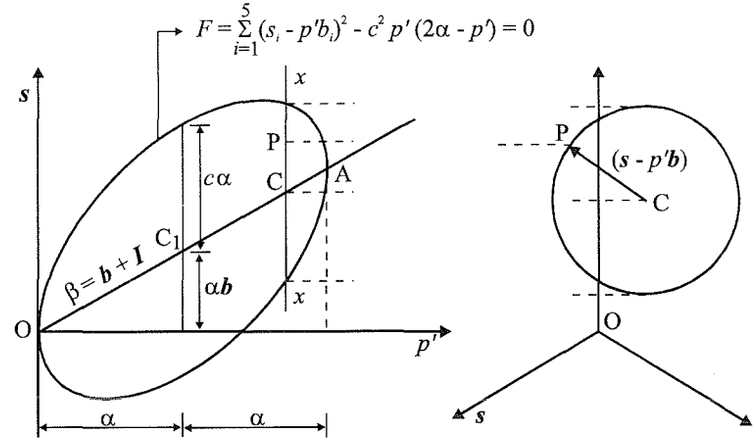

P = current stress state
C = intersection of bounding surface axis and current π plane
A = tip of the bounding surface
C_1 = Centre of bounding surface ellipsoid

Figure 8.10: Geometry of the bounding surface for MIT-E3

A virgin normally consolidated soil element lies at the tip of the bounding surface, at a stress state:

$$p' = 2\alpha$$
$$s_i = 2\alpha\, b_i$$

The gradient of the bounding surface function is defined by Q and $\boldsymbol{Q} = \{Q_i\}$, i=1, ..., 5 (the spherical and deviatoric component respectively), such that:

$$\frac{\partial F(\{\sigma'\},\{k\})}{\partial p'} = Q = 2c^2(p' - \alpha) - 2\sum_{i=1}^{5}(s_i - p'b_i)b_i \tag{8.45a}$$

$$\frac{\partial F(\{\sigma'\},\{k\})}{\partial s_i} = Q_i = 2(s_i - p'b_i) \tag{8.45b}$$

The criterion for loading and unloading then becomes:

$$K\,Q\,\Delta\varepsilon_v + 2G\sum_{i=1}^{5}Q_i\,\Delta E_i \begin{cases} \geq 0 & \text{for loading} \\ < 0 & \text{for unloading} \end{cases} \tag{8.46}$$

Failure criterion

The failure criterion, at which critical state behaviour is exhibited, is defined in generalised stress space by an anisotropic conical surface with its apex at the origin and with its axis along the direction $(\boldsymbol{I} + \boldsymbol{\xi})$. This surface is labelled the critical state cone and is illustrated in Figure 8.11. $\boldsymbol{\xi} = \{\xi_i\}$, i = 1, ..., 5 is a vector which defines

the anisotropic nature of the failure criterion and is a material property. The critical state cone is described by the equation:

$$h = \sum_{i=1}^{5}(s_i - p'\xi_i)^2 - k^2 p'^2 = 0 \qquad (8.47)$$

where k is a scalar material property which defines the size of the cone.

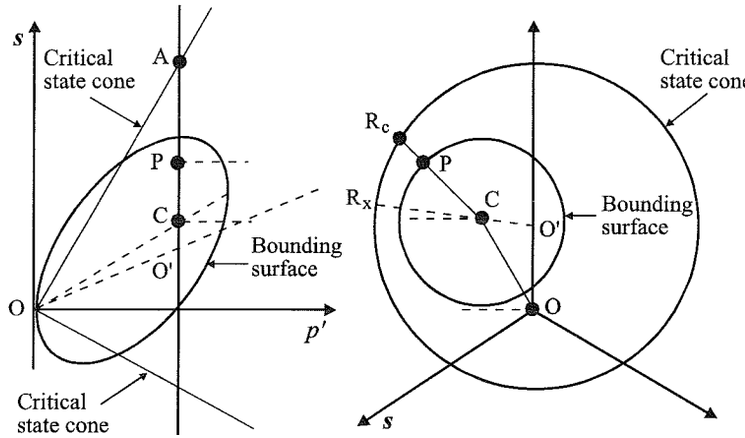

O' = intersection of axis of critical state cone and current π plane
R_c = the projection of vector CP onto the critical state cone
R_x = the projection of vector O'C onto the critical state cone

Figure 8.11: Geometry of the bounding surface and the critical state cone

Due to the restricted stress paths of most soil tests and in particular triaxial tests, it is difficult to ascertain the location and size of the critical state cone in general stress space for any particular soil. Whittle (1987) suggests that the axis of the cone should lie in triaxial stress space ($\sigma_z - \sigma_x = \sigma_{xy} = \sigma_{yz} = \sigma_{zx} = 0$), accordingly $\xi_i = 0$ for $i \neq 1$. The critical state cone is now described by the following expression:

$$h = \sum_{i=1}^{5} s_i^2 - 2s_1 p'\xi_1 + p'^2(\xi_1^2 - k^2) = 0 \qquad (8.48)$$

Parameters ξ_1 and k can now be evaluated from the critical state values of the angle of shearing resistance in triaxial compression, φ_{TC}', and triaxial extension, φ_{TE}', using the equations:

$$\xi_1 = \tfrac{1}{2}(C_c - C_e)$$
$$k = \tfrac{1}{2}(C_c + C_e)$$

where:

$$C_c = \sqrt{\frac{2}{3}}\,\frac{6\sin\varphi_{TC}'}{3-\sin\varphi_{TC}'}$$

$$C_e = \sqrt{\frac{2}{3}}\,\frac{6\sin\varphi_{TE}'}{3+\sin\varphi_{TE}'}$$

There are two important properties of the critical state cone:

- If the critical state angles of shearing resistance in triaxial extension and compression are the same, i.e. $\varphi_{TC}' = \varphi_{TE}'$, an isotropic Drucker-Prager failure surface is described.
- The direction of anisotropy of the bounding surface, $\boldsymbol{b}$, does not generally coincide with the direction of anisotropy of the critical state cone, $\boldsymbol{\xi}$. This is true even if the critical state condition is reached.

Flow rule

The flow rule satisfies two important criteria:

- The model reaches a critical state at the critical state cone, i.e. it has plastic deviatoric strains, but neither any plastic volumetric strains nor any strain hardening/softening.
- If initially virgin consolidated under K_o conditions such that the stress state is at the tip of the bounding surface, any subsequent loading under K_o conditions does not change the normally consolidated value of K_o (i.e. K_o^{NC}). Kavvadas (1982) showed that to satisfy this criterion in general, a non-associated flow rule is required.

The flow rule is expressed directly in terms of the spherical, P, and deviatoric, $\boldsymbol{P} = \{P_i\}$, i=1, ..., 5, components of the flow direction (the derivatives of the plastic potential). No equation for the plastic potential, $P(\{\boldsymbol{\sigma}'\},\{\boldsymbol{m}\})$, is presented:

$$P = \frac{\partial P(\{\boldsymbol{\sigma}'\},\{\boldsymbol{m}\})}{\partial p'} = 2c^2\alpha\, r_c \qquad (8.49a)$$

$$P_i = \frac{\partial P(\{\boldsymbol{\sigma}'\},\{\boldsymbol{m}\})}{\partial s_i} = c^2 x\left(Q_i + |r_c| s_i\right) \qquad (8.49b)$$

where:

- the parameter x is a scalar used to satisfy the above K_o criterion and is given by:

$$x = \frac{\lambda}{\lambda-\kappa}\left(\frac{1+2K_o^{NC}}{3(1-K_o^{NC})} - \frac{K}{2G}\frac{\kappa}{\lambda}\right) \qquad (8.50)$$

and:
K_o^{NC} is a material property;
λ is the slope of the virgin consolidation line and is a material property;
κ is the slope of the swelling line, but is a variable (see Equation (8.41));

- r_c is a scalar variable which is a measure of the proximity of the current stress state to the critical state cone and is graphically illustrated in Figure 8.11. $|r_c|$ denotes the absolute value of r_c, which is defined as:

$$r_c = \frac{\overline{PR_c}}{\overline{CR_c}} = \frac{A + B - D}{B - D}$$

where:

$\overline{PR_c}$ is the vector between P and R_c

$\overline{CR_c}$ is the vector between C and R_c

$A = c^2(2\alpha - p')$

$B = \sum_{i=1}^{5}(b_i - \xi_i)(s_i - p'b_i)$

$C = p'[k^2 - \sum_{i=1}^{5}(b_i - \xi_i)(b_i - \xi_i)]$

$D = (B^2 + AC)^{1/2}$

$r_c = 1$ implies that the current stress state is on the axis of the bounding surface;
$0 < r_c < 1$ implies that the current stress state lies inside the critical state cone;
$r_c = 0$ implies that the current stress state is on the critical state cone;
$r_c < 0$ implies that the current stress state is outside the critical state cone.

The incremental plastic volumetric and deviatoric strains ($\Delta\varepsilon_v^p$ and ΔE_i^p respectively) are then obtained from the equations:

$$\begin{aligned} \Delta\varepsilon_v^p &= \Lambda P \\ \Delta E_i^p &= \Lambda P_i \end{aligned} \tag{8.51}$$

where Λ is the plastic scalar multiplier obtained from the standard plasticity equation (see Equation (6.13)). In this case:

$$\Lambda = \frac{K\,Q\,\Delta\varepsilon_v + 2G\sum_{i=1}^{5} Q_i\,\Delta E_i}{A + K\,Q\,P + 2G\sum_{i=1}^{5} Q_i\,P_i} \tag{8.52}$$

A in Equation (8.52) is the elasto-plastic modulus which is specified as:

$$A = 2c^2\frac{\kappa}{\lambda - \kappa}K\left(\alpha P - S_l 2c^2\alpha\langle r_c\rangle x\sum_{i=1}^{5} Q_i b_i\right) \tag{8.53}$$

where S_l is a material property which strongly influences the model's strain softening behaviour. $\langle r_c\rangle = r_c$ if $r_c > 0$; $= 0$ if $r_c < 0$.

Hardening laws

The hardening laws consist of two equations: one controlling the change of the size of the bounding surface, $\Delta\alpha$, and another controlling the change of its orientation, Δb_i:

$$\Delta\alpha = \alpha\,\zeta\,\Delta\varepsilon_v^p \tag{8.54a}$$

$$\Delta b_i = \psi_0\langle r_x\rangle\frac{1}{\alpha}(s_i - p'b_i)\,\Delta\varepsilon_v^p \tag{8.54b}$$

where:

ζ is a variable which affects the rate at which the size of the yield surface changes;

ψ_0 is a dimensionless material property which controls the rate of rotation of the yield surface;

r_x is a scalar variable which is a measure of the relative orientation of the yield surface to the critical state cone; $\langle r_x\rangle = r_x$ if $r_x > 0$; $= 0$ if $r_x \le 0$.

The equation for ζ is derived from the consistency condition, see Ganendra (1993), and is given as:

$$\zeta = \frac{1}{\alpha}\left(\frac{1}{2c^2p'}\frac{A}{P} - \psi_0\langle r_x\rangle\frac{p'}{\alpha}(2\alpha - p')\right) \tag{8.55}$$

The scalar r_x is graphically illustrated in Figure 8.11 and is defined as:

$$r_x = \frac{\overline{CR_x}}{\overline{O'R_x}} = \frac{k - \sqrt{\sum_{i=1}^{5}(b_i - \xi_i)^2}}{k} \tag{8.56}$$

The values of r_x imply the following:

$r_x = 1$ the axis of the bounding surface coincides with the axis of the critical state cone ($\xi_i = b_i$);
$0 < r_x < 1$ the axis of the bounding surface lies inside the critical state cone;
$r_x = 0$ the axis of the bounding surface is on the critical state cone;
$r_x < 0$ the axis of the bounding surface is outside the critical state cone.

There are three important properties of Equation (8.54b), which controls the rate of rotation of the yield surface:

- When the principal axes of stress, $\boldsymbol{s}$, and anisotropy, $\boldsymbol{b}$, coincide, there is no rotation of the yield surface;
- In general, as plastic deformation occurs, the principal axes of anisotropy rotate towards the principal stress axes;
- The principal axes of anisotropy do not rotate outside the critical state cone.

8.7.5 Behaviour within the bounding surface

A stress state within the bounding surface represents overconsolidation. The plastic behaviour at any overconsolidated point R, inside the bounding surface, is linked to its image point I, on the bounding surface (see Figure 8.12). This image point is described using a radial mapping rule. The loading condition for plastic strains, Equation (8.46), is now rewritten as:

$$K\,Q^{\mathrm{I}}\,\Delta\varepsilon_v + 2G\sum_{i=1}^{5} Q_i^{\mathrm{I}}\,\Delta E_i \begin{cases} \ge 0 & \text{for loading} \\ < 0 & \text{for unloading} \end{cases} \tag{8.57}$$

where:

Q^{I} is the spherical component of the bounding surface gradient at the image point;

$\boldsymbol{Q}^{\mathrm{I}} = \{Q_i^{\mathrm{I}}\}$, $i = 1,..., 5$, is the deviatoric component of the bounding surface gradient at the image point.

During purely elastic behaviour, the size of the bounding surface (dictated by the parameter α) changes as a function of the volumetric strain, ε_v:

$$\Delta\alpha = \frac{(1+e)\alpha}{\lambda}\Delta\varepsilon_v \qquad (8.58)$$

This equation can be integrated such that if the change in volumetric strain is $\Delta\varepsilon_v$, over time increment Δt, and the values of α at times t and $t+\Delta t$ are α^t and $\alpha^{t+\Delta t}$, then:

$$\alpha^{t+\Delta t} = \alpha^t \, \mathrm{e}^{\left(\frac{v}{\lambda}\Delta\varepsilon_v\right)} \qquad (8.59)$$

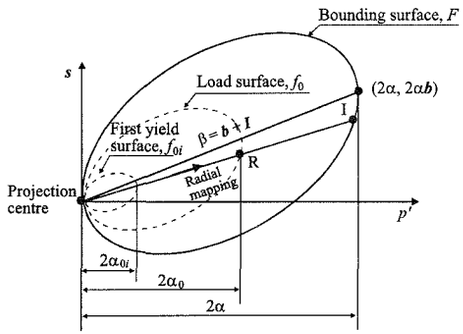

Figure 8.12: Geometry of the bounding surface, load surface and first yield surface for MIT-E3

The point at which the stress path first invokes plastic yielding, as designated by Equation (8.57), is called 'the first yield point'. The surface similar in shape to the bounding surface that passes through this point is called 'the first yield surface' and its size is given by α_{0i}. This surface does not change for any subsequent stress paths which have continuous plastic straining. To evaluate the behaviour of a yielding sample, a surface, similar in shape to the bounding surface, is fitted through the current stress state. This surface is called 'the load surface' and its size is α_0, see Figure 8.12. The elasto-plastic modulus, A, and flow directions, P and $\boldsymbol{P}$, are defined using equations:

$$\begin{aligned} P &= P^{\mathrm{I}} + g_1 P^0 \\ \boldsymbol{P} &= \boldsymbol{P}^{\mathrm{I}} \\ A &= A^{\mathrm{I}} + g_2 A^0 \end{aligned} \qquad (8.60)$$

where:

P^{I} and $\boldsymbol{P}^{\mathrm{I}} = \{P_i^{\mathrm{I}}\}$, $i = 1, ..., 5$, are the spherical and deviatoric components of the flow direction at the image point respectively;

A^{I} is the value of the elasto-plastic modulus at the image point;

P^0 and A^0 are variables which are a function of the current stress state and the image point and are defined below;

g_1 and g_2 are defined below and are scalar mapping functions which describe the relative position of the first yield surface, the load surface and the bounding surface.

$$P^0 = -\left(2c^2\alpha r_c + \sum_{i=1}^{5} \eta_i^{\mathrm{I}} Q_i^{\mathrm{I}}\right) \qquad (8.61)$$

$$A^0 = \frac{1+e}{\kappa_0}(\alpha - \alpha_0)\, h \left\|\boldsymbol{Q}^{\mathrm{I}}\right\| \left\|\boldsymbol{P}^{\mathrm{I}}\right\| \qquad (8.62)$$

$$g_1 = \left(\frac{\alpha - \alpha_0}{\alpha}\right)^{\gamma} \qquad (8.63)$$

$$g_2 = \frac{\alpha - \alpha_{0i}}{\alpha_0 - \alpha_{0i}} \qquad (8.64)$$

where:

h and γ are material properties;

$$\left\|\boldsymbol{Q}^{\mathrm{I}}\right\| = \sqrt{\sum_{i=1}^{5} Q_i^{\mathrm{I}} Q_i^{\mathrm{I}}}$$

$$\left\|\boldsymbol{P}^{\mathrm{I}}\right\| = \sqrt{\sum_{i=1}^{5} P_i^{\mathrm{I}} P_i^{\mathrm{I}}}$$

These values of A, P and $\boldsymbol{P}$, Q and $\boldsymbol{Q}$, and the current elastic moduli (K and G) are used in Equations (8.52) and (8.51) to evaluate the plastic scalar multiplier and the plastic strains respectively. These are then used to calculate the associated stress change.

When plastic strains occur within the bounding surface, there is some hardening of the bounding surface. To evaluate the amount of hardening that occurs, a second set of plastic strains, labelled as pseudo plastic strains, are calculated. These strains are calculated from the stress state at the image point, i.e. A^{I}, P^{I} and $\boldsymbol{P}^{\mathrm{I}}$, and Q^{I} and $\boldsymbol{Q}^{\mathrm{I}}$, and are substituted into Equations (8.52) and (8.51) to calculate the pseudo plastic scalar multiplier and pseudo plastic strains respectively. The elastic moduli used in these calculations are the moduli consistent with the image point, which means that in Equation (8.38) the value of p' should be the image point value (δ is unchanged). These pseudo strains are used in Equations (8.54) to evaluate the changes in the hardening parameters α and $\boldsymbol{b}$. It should be noted that all the terms in Equations (8.54) should also be calculated from the stress state at the image point.

Two important features of this formulation are that:

- At first yield α_0 is equal to α_{0i}, thus A tends to ∞ and there are no plastic strains;
- As the stress state reaches the bounding surface, α_0 becomes equal to α, the extra terms associated with bounding plasticity tend towards zero and the plastic behaviour reverts to the normally consolidated formulation, i.e. behaviour on the bounding surface.

Thus the bounding plasticity formulation gives a smooth transition from perfectly hysteretic elastic behaviour at first yield, to normally consolidated behaviour when the stress state reaches the bounding surface.

8.7.6 Comments

The 15 material parameters required to define the MIT-E3 model are summarised in Table 8.2. Unfortunately, it is not easy to determine the values of all of these parameters from conventional laboratory tests. Therefore, this model is currently used mainly in research. However, other constitutive models of this type are likely to be developed in the future, to enable more realistic simulation of observed soil behaviour. Finite element analyses of boundary value problems with the MIT-E3 model are presented in Volume 2 of this book.

Table 8.2: MIT-E3 material parameters

Parameter	Description
v_{100}	Specific volume for a K_o normally consolidated sample at p'=100 kPa
K_o^{NC}	Normally consolidate coefficient of earth pressure at rest
φ_{TC}'	Critical state angle of shearing resistance in triaxial compression
φ_{TE}'	Critical state angle of shearing resistance in triaxial extension
c	Ratio of the semi-axes of the bounding surface ellipsoid
ψ	Parameter affecting rotation of bounding surface
λ	Slope of the VCL in v - lnp' space
κ_0	Initial slope of the swelling line in v - lnp' space
μ	Poisson's ratio
S_t	Parameter affecting the degree of strain softening
C	Parameter affecting the hysteretic elasticity
n	Parameter affecting the hysteretic elasticity
ω	Parameter affecting the hysteretic elasticity
γ	Parameter affecting the bounding surface plasticity
h	Parameter affecting the bounding surface plasticity

8.8 Bubble models

8.8.1 Introduction

As noted in Section 8.6, conventional elasto-plastic models, which assume elastic behaviour within the yield surface, have difficulties in simulating the behaviour of some soils when subjected to cycles of unloading and reloading. To improve the modelling the concept of bounding surface plasticity was introduced and an example of such a constitutive model (i.e. MIT-E3) was described in Section 8.7. While such models are an improvement over conventional elasto-plastic models, they still have some deficiencies. For example, during unloading soil behaviour is assumed to be elastic and this restricts the degree of coupling between volumetric and deviatoric component of behaviour.

A way of improving the framework further is to introduce a small *kinematic yield surface* (bubble), which moves within the outer bounding surface. Within the bubble behaviour is elastic, whereas outside the bubble it is elasto-plastic. As the stresses change within the outer bounding surface, the bubble moves and hence the term 'kinematic yield surface'. Al-Tabbaa (1987) and Al-Tabbaa and Wood (1989) developed a model with a single kinematic yield surface, with the conventional modified Cam clay yield surface acting as a bounding surface. Stallebrass and Taylor (1997) extended this model, incorporating two nested kinematic yield surfaces. The additional surface in their model is called a 'history' surface and was added so that the model could simulate both yield at small strains and the effect of recent stress history.

8.8.2 Behaviour of a kinematic yield surface

In this section the conceptual framework of bubble models is presented by considering the behaviour of a model with a single kinematic yield surface. These concepts are, however, easily extended to deal with models which have multiple kinematic yield surfaces.

The main components of the model are an outer bounding surface and a kinematic yield surface (bubble), which moves within the outer surface, see Figure 8.13a. The bubble acts in the same way as a conventional yield surface in the sense that purely elastic behaviour occurs for stress states which remain within the bubble. However, if the stress state attempts to cross the perimeter of the bubble, elasto-plastic behaviour is initiated and the bubble is dragged along the stress path. This elasto-plastic behaviour is controlled by the bubble acting as yield surface, in combination with a plastic potential and plastic hardening/softening law associated with the bubble. Although the bubble moves within the outer bounding surface, it never crosses it. When the stress state reaches the bounding surface the bubble is orientated such that it lies completely within the surface. In such a condition the bounding surface essentially acts as the yield surface and behaviour is controlled by this surface and its associated plastic potential and plastic hardening/softening law. In essence, if the stress state is on the bounding surface, the elasto-plastic behaviour is exactly the same as would be obtained with a conventional elasto-

plastic model, in which the bounding surface acts as the yield surface.

The behaviour of the model is best understood by considering the example shown in Figure 8.13b. In this example, a soil element is assumed to be initially K_o normally consolidated to a stress state represented by point 'a' in Figure 8.13b. Since the soil element has been subjected to normal consolidation, its behaviour has been controlled by the bounding surface, and the relative positions of the bonding surface and bubble at the end of consolidation are shown in Figure 8.13b. If the soil element is now unloaded such that it follows the stress path 'abcd', the sequence of events is as follows. On first unloading from point 'a' the stress path moves inside the bubble and behaviour is elastic, with both the bubble and the bounding surface remaining stationary in stress space. As the unloading continues, the stress path traverses the inside of the bubble, promoting further elastic behaviour, until it reaches the other side of the bubble at point 'b'. With further unloading the behaviour of the soil element becomes elasto-plastic. The bubble is now dragged along the stress path and, because plastic strains are developed, both the bubble and the bounding surface can change size (not shown in Figure 8.13) if their hardening/softening laws are related to plastic strains and/or plastic work. After unloading to point 'd' the relative positions of the bubble and bounding surface to the stress state are as indicated in Figure 8.13b. If the soil element is now reloaded such that its stress state travels along the stress path 'def', it initially behaves elastically because the stress path moves inside the bubble. Again, during this period of elastic behaviour the bubble and bounding surface remain stationary. With sufficient loading the stress state reaches the other side of the bubble, i.e. point 'e' on Figure 8.13b, and elasto-plastic behaviour is initiated. Further loading takes the stress state to point 'f', where the bubble meets the bounding surface. Any subsequent loading causes the bubble and bounding surface to move together.

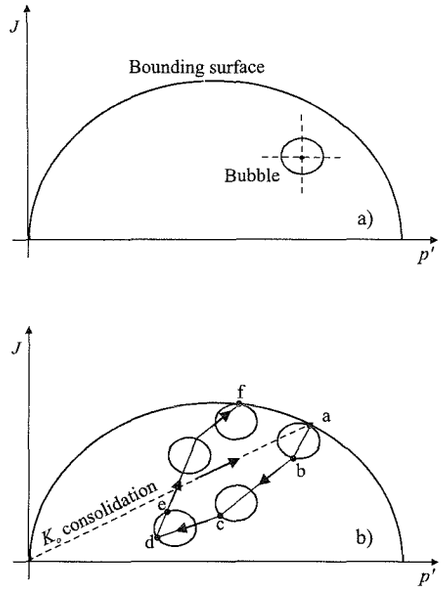

Figure 8.13: Conceptual behaviour of bubble model

To fully define the model, information must be provided for the shape of the bounding surface and its associated plastic potential and hardening/softening law. Similar information must also be provided for the bubble. A translation rule, controlling the movement and relative orientation of the bubble, is also required. This rule must be carefully defined to ensure that the bubble becomes tangential

and completely within the bounding surface when the stress state approaches the bounding surface. It is also necessary to provide mapping functions which control how the plastic modulus changes as the bubble moves. In this respect, it is important to ensure that as the bubble approaches the bounding surface, this modulus approaches that associated with the bounding surface.

To clarify the above qualitative description, the single bubble model proposed by Al-Tabbaa and Wood (1989) is briefly described below.

8.9 Al-Tabbaa and Wood model

This model is fully described by Al-Tabbaa (1987) and Al-Tabbaa and Wood (1989) and is a simple example of a single bubble model.

8.9.1 Bounding surface and bubble

The modified Cam clay model has been described in Chapter 7. In the present model the elliptical yield surface of the modified Cam clay model is used to represent the bounding surface. The equation of this surface is written in a slightly different form to that presented in Chapter 7:

$$F(\{\sigma'\},\{k\}) = \left(p' - \frac{p'_o}{2}\right)^2 + \frac{J^2}{M_J^2} - \frac{p'^2_o}{4} = 0 \qquad (8.65)$$

The inner kinematic yield surface (i.e. bubble) is assumed to have the same shape as the bounding surface, but to be of a smaller size. The equation for this surface is:

$$F_1(\{\sigma'\},\{k\}) = \left(p' - p'_\alpha\right)^2 + \left(\frac{J - J_\alpha}{M_J}\right)^2 - R^2\frac{p'^2_o}{4} = 0 \qquad (8.66)$$

where p_α' and J_α represent the stress state associated with the centre of the bubble and R represents the ratio of the size of the bubble to that of the bounding surface, see Figure 8.14.

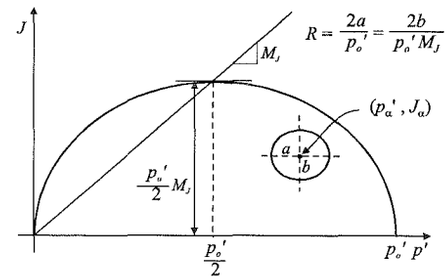

Figure 8.14: Single bubble model

When the soil is yielding, the consistency condition (i.e. $dF_1 = 0$) requires that:

$$(p' - p'_\alpha)(dp' - dp'_\alpha) + \frac{J - J_\alpha}{M_J^2}(dJ - dJ_\alpha) - \frac{R^2}{4}p'_o\, dp'_o = 0 \qquad (8.67)$$

If the stress state is within the bubble, behaviour is governed by the isotropic elastic constitutive equations, see Chapter 5, with a constant Poisson's ratio, μ, and a variable bulk stiffness given by:

$$K = \frac{p'}{\kappa^*} \tag{8.68}$$

Otherwise, behaviour is elasto-plastic, with the plastic potential assumed to be the same as the yield function, given by Equation (8.66) (i.e. associated plasticity), and the following hardening/softening law:

$$\frac{\mathrm{d}p'_o}{p'_o} = \frac{\mathrm{d}\varepsilon_v^p}{\lambda^* - \kappa^*} \tag{8.69}$$

Equations (8.68) and (8.69) differ slightly from the equivalent equations given in Chapter 7 (i.e. equations 7.40 and 7.38) because Al-Tabbaa and Wood assume that the virgin consolidation and swelling lines are straight in $\ln v$-$\ln p'$, whereas in the conventional formulation of modified Cam clay these lines are assumed to be straight in v-$\ln p'$ space. Hence, λ^* and κ^* are different to λ and κ.

8.9.2 Movement of bubble

The bubble moves such that it translates within the outer modified Cam clay bounding surface, following a rule that guarantees that the bubble and bounding surface can touch at a common tangent, but never intersect. This rule is illustrated graphically in Figure 8.15 and it states that the centre of the bubble should always move along a vector $\vec{r}$, which joins the current stress state, C, to its conjugate point on the bounding surface, D.

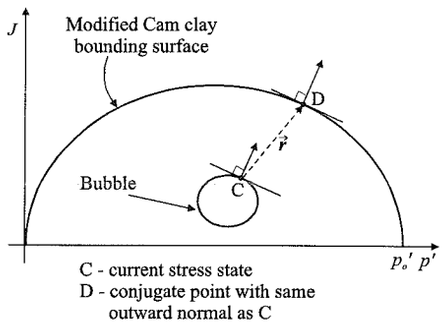

Figure 8.15: Translation of bubble

The change in position of the bubble, when plastic straining occurs, has two components: one is associated with the translation of the bubble along the vector $\vec{r}$, while the other is associated with the change in size of the bubble due to isotropic hardening/softening. This implies that when the bubble and bounding surface are in contact at the current stress state, the vector $\vec{r} = 0$ and the change in the position of the bubble is entirely due to expansion/contraction. Thus the general expression for the change of position of the bubble is:

$$\begin{Bmatrix} \mathrm{d}p'_\alpha \\ \mathrm{d}J_\alpha \end{Bmatrix} = \frac{\mathrm{d}p'_o}{p'_o}\begin{Bmatrix} p'_\alpha \\ J_\alpha \end{Bmatrix} + T\begin{Bmatrix} \dfrac{p'-p'_\alpha}{R} - \left(p' - \dfrac{p'_o}{2}\right) \\ \dfrac{J-J_\alpha}{R} - J \end{Bmatrix} \tag{8.70}$$

The first part of Equation (8.70) is the change in (p_α', J_α) due to a change in p_o', and the second part is associated with the translation along the vector $\vec{r}$. The scalar quantity T can be obtained by substituting Equation (8.70) into (8.67) and using (8.66):

$$T = \frac{(p'-p'_\alpha)\left(\mathrm{d}p' - \dfrac{\mathrm{d}p'_o}{p'_o}p'\right) + \dfrac{J-J_\alpha}{M_J^2}\left(\mathrm{d}J - \dfrac{\mathrm{d}p'_o}{p'_o}J\right)}{(p'-p'_\alpha)\left[\dfrac{p'-p'_\alpha}{R} - \left(p' - \dfrac{p'_o}{2}\right)\right] + \dfrac{J-J_\alpha}{M_J^2}\left(\dfrac{J-J_\alpha}{R} - J\right)} \tag{8.71}$$

8.9.3 Elasto-plastic behaviour

When the bubble and bounding surface are in contact, the expression for the plastic strain increments can be obtained using Equation (6.9):

$$\begin{Bmatrix} \mathrm{d}\varepsilon_v^p \\ \mathrm{d}E_d^p \end{Bmatrix} = \frac{\lambda^* - \kappa^*}{(p'-p'_\alpha)\left[p'(p'-p'_\alpha) + \dfrac{J(J-J_\alpha)}{M_J^2}\right]} \cdot \begin{bmatrix} (p'-p'_\alpha)^2 & (p'-p'_\alpha)\dfrac{J-J_\alpha}{M_J^2} \\ (p'-p'_\alpha)\dfrac{J-J_\alpha}{M_J^2} & \left(\dfrac{J-J_\alpha}{M_J^2}\right)^2 \end{bmatrix} \begin{Bmatrix} \mathrm{d}p' \\ \mathrm{d}J \end{Bmatrix} \tag{8.72}$$

This expression is then generalised for the calculation of plastic strains whenever they occur, i.e. whether or not the bubble and bounding surface are in contact:

$$\begin{Bmatrix} \mathrm{d}\varepsilon_v^p \\ \mathrm{d}E_d^p \end{Bmatrix} = \frac{1}{h}\begin{bmatrix} (p'-p'_\alpha)^2 & (p'-p'_\alpha)\dfrac{J-J_\alpha}{M_J^2} \\ (p'-p'_\alpha)\dfrac{J-J_\alpha}{M_J^2} & \left(\dfrac{J-J_\alpha}{M_J^2}\right)^2 \end{bmatrix} \begin{Bmatrix} \mathrm{d}p' \\ \mathrm{d}J \end{Bmatrix} \tag{8.73}$$

where h is a scalar hardening parameter and, from Equation (8.72), when the bubble and bounding surface are in contact:

$$h = h_o = \frac{p'-p'_\alpha}{\lambda^* - \kappa^*}\left[p'(p'-p'_\alpha) + \frac{J(J-J_\alpha)}{M_J^2}\right] \tag{8.74}$$

However, the function h_o, as written in Equation (8.74), is not completely appropriate because it falls to zero at several singularity points, implying unlimited plastic strains. For example, two singularity points exist for $p' = p_\alpha'$ (e.g. at the top and bottom of the bubble), where unlimited plastic shear strains would be predicted.

To overcome this deficiency, the hardening function is rewritten as:

$$h = h_o + H \tag{8.75}$$

where H should be greater than zero.

Based on results of laboratory tests on speswhite kaolin, Al-Tabbaa and Wood (1989) suggested a function for H in the form:

$$H = \frac{1}{\lambda^* - \kappa^*}\left(\frac{B}{B_{\max}}\right)^{\psi} p_o'^3 \tag{8.76}$$

where B is the component of the vector $\vec{r}$ in the direction of the normal to the bubble at the current stress state, and ψ is an experimentally determined positive exponent. It should be emphasised that the choice of the function H is not unique and depends on the type of soil that is being modelled.

8.9.4 Comments

This bubble model requires only 7 material parameters: v_1, λ^*, κ^*, M_J, R, ψ and Poisson's ratio μ. It was originally developed for triaxial stress space, but has been extended by Stallebrass and Taylor (1997) to general stress space and enhanced to include a second bubble. This model has been used in finite element analyses of boundary value problems with limited success.

8.10 Summary

1. Several constitutive models are available for dealing with the limited tensile capacity of soils. A model based on the theory of elasto-plasticity has been described in this chapter. This model is extremely flexible, allowing cracks to form and then rotate. A particular strength of this model is that it can be combined with other elasto-plastic models which concentrate on simulating behaviour in compression.
2. The theory for dealing with two yield surfaces which are simultaneously active has been described in this chapter. This theory could easily be extended to account for additional active yield surfaces if required.
3. As an example of a double yield surface model, Lade's double hardening model has been described. This model is particularly good at simulating the behaviour of granular soils. It has two yield surfaces, one controlling expansive strains and the other controlling collapse strains. Both surfaces are isotropic and involve work hardening/softening. Elastic behaviour is nonlinear, but isotropic. The model requires fourteen parameters, however, these can be obtained from conventional laboratory tests. The model has practical applications.
4. The framework for bounding surface plasticity has been presented and as an example of a state of the art constitutive model, the MIT-E3 model has been briefly described. This model is based on anisotropic elasto-plastic theory and includes both bounding surface plasticity and hysteretic elasticity. Because of its complexity and the difficulty in evaluating some of the fifteen input parameters, it has limited practical application, however, it does indicate how constitutive models might look like in the future.
5. The concept of kinematic yield surfaces has been presented as a way of simulating hysteretic soil behaviour within the main bounding surface. Bubble models, which are based on this concept, have been described and a particular example presented.

Appendix VIII.1 Derivatives for Lade's double hardening model

Equations (8.14) to (8.29) show that the derivatives of the yield and plastic potential functions, necessary to construct the elasto-plastic stiffness matrix for a model with two active yield surfaces, are:

$$\frac{\partial F_1}{\partial \sigma'}\ ,\ \frac{\partial P_1}{\partial \sigma'}\ ,\ \frac{\partial F_2}{\partial \sigma'}\ ,\ \frac{\partial P_2}{\partial \sigma'}\ ,\ \frac{\partial F_1}{\partial k_1}\ \text{and}\ \frac{\partial F_2}{\partial k_2}$$

In Lade's double hardening model the hardening parameters H_1 and H_2 depend on incremental plastic work, ΔW_{p1} and ΔW_{p2} respectively, consequently $\{k_1\} = \{\Delta W_{p1}\}$ and $\{k_2\} = \{\Delta W_{p2}\}$. The derivatives of F_1 and F_2 with respect to k_1 and k_2 can therefore be rewritten as:

$$\begin{aligned}
\left\{\frac{\partial F_1}{\partial k_1}\right\}\{\Delta k_1\} &= \left\{\frac{\partial F_1}{\partial H_1}\right\}\left\{\frac{\partial H_1}{\partial W_{p1}}\right\}\{\Delta W_{p1}\} = -\left\{\frac{\partial H_1}{\partial W_{p1}}\right\}\{\Delta W_{p1}\} \\
\left\{\frac{\partial F_2}{\partial k_2}\right\}\{\Delta k_2\} &= \left\{\frac{\partial F_2}{\partial H_2}\right\}\left\{\frac{\partial H_2}{\partial W_{p2}}\right\}\{\Delta W_{p2}\} = -\left\{\frac{\partial H_2}{\partial W_{p2}}\right\}\{\Delta W_{p2}\}
\end{aligned} \tag{VIII.1}$$

Noting that $\Delta W_{p1} = \{\sigma\}^{\mathrm{T}}\{\Delta \varepsilon^{p1}\}$ (see Equation (8.34)) and $\Delta W_{p2} = \{\sigma\}^{\mathrm{T}}\{\Delta \varepsilon^{p2}\}$ (see Equation (8.36)), and substituting Equations (VIII.1) into Equations (8.18) gives:

$$\begin{aligned}
A_1 &= \left\{\frac{\partial H_1}{\partial W_{p1}}\right\}\{\sigma'\}^{\mathrm{T}}\left\{\frac{\partial P_1}{\partial \sigma'}\right\} \\
A_2 &= \left\{\frac{\partial H_2}{\partial W_{p2}}\right\}\{\sigma'\}^{\mathrm{T}}\left\{\frac{\partial P_2}{\partial \sigma'}\right\}
\end{aligned} \tag{VIII.2}$$

Consequently, instead of requiring $\{\partial F_1/\partial k_1\}$ and $\{\partial F_2/\partial k_2\}$ as listed above, the derivatives $\{\partial H_1/\partial W_{p1}\}$, $\{\partial H_2/\partial W_{p2}\}$, $\{\partial P_1/\partial \sigma'\}$ and $\{\partial P_2/\partial \sigma'\}$ are needed.

The partial derivatives required to evaluate the elasto-plastic matrix $[D^{ep}]$ in Equation (8.29) have been derived by Lade and Nelson (1984) and are as follows:

Conical yield surface and plastic potential

$$\frac{\partial F_1}{\partial \sigma'} = \left(\frac{I_1^3}{I_3} - 27\right)\frac{m}{p_a}\left(\frac{I_1}{p_a}\right)^{m-1}\begin{Bmatrix}1\\1\\1\\0\\0\\0\end{Bmatrix} + \left(\frac{I_1}{p_a}\right)^{m}\frac{I_1^2}{I_3^2}\begin{Bmatrix}3I_3 - (\sigma_y'\sigma_z' - \tau_{yz}^2)I_1\\3I_3 - (\sigma_z'\sigma_x' - \tau_{zx}^2)I_1\\3I_3 - (\sigma_x'\sigma_y' - \tau_{xy}^2)I_1\\2(\sigma_x'\tau_{yz} - \tau_{xy}\tau_{zx})I_1\\2(\sigma_y'\tau_{zx} - \tau_{yz}\tau_{xy})I_1\\2(\sigma_z'\tau_{xy} - \tau_{zx}\tau_{yz})I_1\end{Bmatrix} \qquad \text{(VIII.3)}$$

$$\frac{\partial P_1}{\partial \sigma'} = \left[3I_1^2 + \frac{I_3}{I_1}m\eta_2\left(\frac{p_a}{I_1}\right)^{m}\right]\begin{Bmatrix}1\\1\\1\\0\\0\\0\end{Bmatrix} + \left[27 + \eta_2\left(\frac{p_a}{I_1}\right)^{m}\right]\begin{Bmatrix}-(\sigma_y'\sigma_z' - \tau_{yz}^2)\\-(\sigma_z'\sigma_x' - \tau_{zx}^2)\\-(\sigma_x'\sigma_y' - \tau_{xy}^2)\\2(\sigma_x'\tau_{yz} - \tau_{xy}\tau_{zx})\\2(\sigma_y'\tau_{zx} - \tau_{yz}\tau_{xy})\\2(\sigma_z'\tau_{xy} - \tau_{zx}\tau_{yz})\end{Bmatrix} \qquad \text{(VIII.4)}$$

$$\frac{\partial H_1}{\partial W_{p1}} = \frac{\partial H_1}{\partial \xi}\frac{\partial \xi}{\partial W_{p1}} = \frac{H_1}{q}\left(\frac{1}{\xi} - 1\right)\frac{1}{W_{p1p}} \qquad \text{(VIII.5)}$$

$$\{\sigma'\}^{\mathrm{T}}\left\{\frac{\partial P_1}{\partial \sigma'}\right\} = 3P_1 + m\eta_2\left(\frac{p_a}{I_1}\right)^{m} I_3 \qquad \text{(VIII.6)}$$

Cap yield surface and plastic potential

$$\frac{\partial F_2}{\partial \sigma'} = \frac{\partial P_2}{\partial \sigma'} = 2\left\{\sigma_x' \quad \sigma_y' \quad \sigma_z' \quad 2\tau_{yz} \quad 2\tau_{zx} \quad 2\tau_{xy}\right\}^{\mathrm{T}} \qquad \text{(VIII.7)}$$

$$\frac{\partial H_2}{\partial W_{p2}} = \frac{p_a}{C\,p}\left(\frac{H_2}{p_a^2}\right)^{1-p} \qquad \text{(VIII.8)}$$

$$\{\sigma'\}^{\mathrm{T}}\left\{\frac{\partial P_2}{\partial \sigma'}\right\} = 2P_2 \qquad \text{(VIII.9)}$$

However, Kovačević (1994) found that the above differentials failed to satisfy the consistency condition, i.e. $\Delta F_1 = \Delta F_2 = 0$. This occurred when the conical yield surface, F_1, was active. Inspection of Equation (8.34), defining the work hardening law for the conical yield surface, indicates that the hardening parameter is not only dependent on the plastic work, but also on the stresses. Namely, the parameter q is dependent on the minimum principal stress, σ_3'.

Correction for $\{\partial F_1/\partial \sigma'\}$

For the above reasons, the derivative of the conical yield function should be written in the following form:

$$\left\{\frac{\partial F_1}{\partial \sigma'}\right\} = \text{Equation (VIII.3)} - \left\{\frac{\partial H_1}{\partial q}\right\}\left\{\frac{\partial q}{\partial \sigma'}\right\} \qquad \text{(VIII.10)}$$

Using the chain rule, it can be shown that:

$$-\left\{\frac{\partial H_1}{\partial q}\right\}\left\{\frac{\partial q}{\partial \sigma'}\right\} = \frac{H_1}{q^2}\frac{\beta}{p_a}\ln\left[\xi\,\mathrm{e}^{(1-\xi)}\right]\left\{\frac{\partial \sigma_3'}{\partial \sigma'}\right\} \qquad \text{(VIII.11)}$$

If σ_3' is expressed in terms of stress invariants, see Equation (5.4):

$$\sigma_3' = p' + \frac{2}{\sqrt{3}}J\sin\left(\theta - \frac{2\pi}{3}\right)$$

then:

$$\left\{\frac{\partial \sigma_3'}{\partial \sigma'}\right\} = \left\{\frac{\partial \sigma_3'}{\partial p'}\right\}\left\{\frac{\partial p'}{\partial \sigma'}\right\} + \left\{\frac{\partial \sigma_3'}{\partial J}\right\}\left\{\frac{\partial J}{\partial \sigma'}\right\} + \left\{\frac{\partial \sigma_3'}{\partial \theta}\right\}\left\{\frac{\partial \theta}{\partial \sigma'}\right\} \qquad \text{(VIII.12)}$$

Derivatives of the stress invariants p', J and θ are given in Appendix VII.1, while:

$$\begin{aligned}\frac{\partial \sigma_3'}{\partial p'} &= 1\\ \frac{\partial \sigma_3'}{\partial J} &= \frac{2}{\sqrt{3}}\sin\left(\theta - \frac{2\pi}{3}\right)\\ \frac{\partial \sigma_3'}{\partial \theta} &= \frac{2}{\sqrt{3}}J\cos\left(\theta - \frac{2\pi}{3}\right)\end{aligned} \qquad \text{(VIII.13)}$$

Correction for $\{\partial P_1/\partial \sigma'\}$

Similarly, in deriving the derivatives of the plastic potential P_1, Lade and Nelson (1984) assume that the parameter η_2 is a constant. However, according to Equation (8.33), it also depends on σ_3', so that:

$$\left\{\frac{\partial P_1}{\partial \sigma'}\right\} = \text{Equation (VIII.4)} + \left\{\frac{\partial P_1}{\partial \eta_2}\right\}\left\{\frac{\partial \eta_2}{\partial \sigma'}\right\} \qquad \text{(VIII.14)}$$

where:

$$\left\{\frac{\partial P_1}{\partial \eta_2}\right\}\left\{\frac{\partial \eta_2}{\partial \sigma'}\right\} = \left\{\frac{\partial P_1}{\partial \eta_2}\right\}\left[\left\{\frac{\partial \eta_2}{\partial H_1}\right\}\left\{\frac{\partial H_1}{\partial q}\right\}\left\{\frac{\partial q}{\partial \sigma_3'}\right\} + \left\{\frac{\partial \eta_2}{\partial \sigma_3'}\right\}\right]\left\{\frac{\partial \sigma_3'}{\partial \sigma'}\right\} \qquad \text{(VIII.15)}$$

$$
\begin{Bmatrix} \frac{\partial P_1}{\partial \eta_2} \end{Bmatrix} = -\left(\frac{p_a}{3p'}\right)^m I_3
$$
$$
\begin{Bmatrix} \frac{\partial \eta_2}{\partial H_1} \end{Bmatrix} = \rho
$$
$$
\begin{Bmatrix} \frac{\partial H_1}{\partial q} \end{Bmatrix} = -\frac{H_1}{q^2} \ln\left[\xi e^{(1-\xi)}\right]
$$
$$
\begin{Bmatrix} \frac{\partial q}{\partial \sigma_3'} \end{Bmatrix} = \frac{\beta}{p_a}
$$
$$
\begin{Bmatrix} \frac{\partial \eta_2}{\partial \sigma_3'} \end{Bmatrix} = \frac{1}{2} R\left(p_a\ \sigma_3'\right)^{-\frac{1}{2}}
$$
$$
\begin{Bmatrix} \frac{\partial \sigma_3'}{\partial \sigma'} \end{Bmatrix} = \text{given above}
$$

(VIII.16)

Kovačević (1994) found that with these corrections the consistency equations were always satisfied. The only difficulty he found in implementing the model was associated with the hardening parameter ξ. For low values of ξ the model response to shearing is essentially elastic, but the conical yield surface expands rapidly. To eliminate numerical difficulties, McCarron and Chen (1988) suggested that the minimum initial value of ξ should be 0.001. For the majority of applications Kovačević (1994) found this value to be appropriate. However, in some problems he had to increase this minimum value.

9. Finite element theory for nonlinear materials

9.1 Synopsis

This chapter describes how the finite element method can be adapted to deal with the nonlinear constitutive models described in Chapters 5, 7 and 8. Several strategies are available to do this. All strategies involve applying the boundary conditions incrementally. In principle, if the solution increments are sufficiently small all solution strategies should give similar predictions. However, as the increment size increases, some solution schemes can result in extremely inaccurate predictions. Three popular solution strategies are described. These are the tangent stiffness, the visco-plastic and the modified Newton-Raphson schemes. These schemes are then compared by analysing a range of geotechnical boundary value problems. It is shown that the tangent stiffness and the visco-plastic approaches are sensitive to increment size and can lead to inaccurate predictions, unless many small solution increments are adopted. The modified Newton-Raphson scheme is consistently shown to be both the most robust and most economical. This scheme can be used with explicit or implicit stress point algorithms. Two such algorithms are the 'substepping' and 'return' methods. The basic assumptions behind these methods are described and the associated errors compared. Sufficient information is given in the chapter to enable the basics of nonlinear finite element analysis to be understood.

9.2 Introduction

To be able to use the elasto-plastic constitutive models, described in Chapters 5, 7 and 8, to represent soil behaviour in a finite element analysis, the theory, as described in Chapter 2, must be extended. In Chapter 2 the soil was assumed to be elastic and the constitutive matrix $[\boldsymbol{D}]$ was therefore constant. If the soil is nonlinear elastic and/or elasto-plastic, the equivalent constitutive matrix is no longer constant, but varies with stress and/or strain. It therefore changes during a finite element analysis. Consequently, a solution strategy is required that can account for this changing material behaviour. This strategy is a key component of a nonlinear finite element analysis, as it can strongly influence the accuracy of the results and the computer resources required to obtain them. Several different solution strategies are described in the literature, however, there does not seem to be a comparative study to establish their merits for geotechnical analysis. After

describing three popular solution strategies, the results of such a study are presented in this chapter.

The tangent stiffness, visco-plastic, and modified Newton-Raphson (MNR) schemes are described. The latter approach initially assumes an explicit 'substepping' stress point algorithm. Subsequently, implicit 'return' type algorithms are discussed and compared with the 'substepping' scheme. The three solution strategies are then used to analyse idealised drained and undrained triaxial compression tests, a footing problem, an excavation problem, and a pile problem. Soil behaviour is represented by a form of the strain hardening/softening modified Cam clay (MCC) constitutive model described in Chapter 7. This model and its variants have been shown to provide a realistic description of clay behaviour and have been widely used to analyse geotechnical boundary value problems (Gens and Potts (1988)).

9.3 Nonlinear finite element analysis

As noted in Chapter 1, when analysing any boundary value problem four basic solution requirements need to be satisfied: equilibrium, compatibility, constitutive behaviour and boundary conditions. Nonlinearity introduced by the constitutive behaviour causes the governing finite element equations to be reduced to the following incremental form, see Equation (2.30):

$$\left[\boldsymbol{K}_G\right]^i \left\{\Delta \boldsymbol{d}\right\}^i_{nG} = \left\{\Delta \boldsymbol{R}_G\right\}^i \tag{9.1}$$

where $[\boldsymbol{K}_G]^i$ is the incremental global system stiffness matrix, $\{\Delta \boldsymbol{d}\}^i_{nG}$ is the vector of incremental nodal displacements, $\{\Delta \boldsymbol{R}_G\}^i$ is the vector of incremental nodal forces and i is the increment number. To obtain a solution to a boundary value problem, the change in boundary conditions is applied in a series of increments and for each increment Equation (9.1) must be solved. The final solution is obtained by summing the results of each increment. Due to the nonlinear constitutive behaviour, the incremental global stiffness matrix $[\boldsymbol{K}_G]^i$ is dependent on the current stress and strain levels and therefore is not constant, but varies over an increment. Unless a very large number of small increments are used this variation should be accounted for. Hence, the solution of Equation (9.1) is not straightforward and different solution strategies exist. The objective of all such strategies is the solution of Equation (9.1), ensuring satisfaction of the four basic requirements listed above. Three different categories of solution algorithm are considered next.

9.4 Tangent stiffness method

9.4.1 Introduction

The tangent stiffness method, sometimes called the variable stiffness method, is the simplest solution strategy. This is the method implemented in the computer code CRISP (Britto and Gunn (1987)), which is widely used in engineering practice.

In this approach, the incremental stiffness matrix $[\boldsymbol{K}_G]^i$ in Equation (9.1) is assumed to be constant over each increment and is calculated using the current stress state at the beginning of each increment. This is equivalent to making a piece-wise linear approximation to the nonlinear constitutive behaviour. To illustrate the application of this approach, the simple problem of a uniaxially loaded bar of nonlinear material is considered, see Figure 9.1. If this bar is loaded, the true load displacement response is shown in Figure 9.2. This might represent the behaviour of a strain hardening plastic material which has a very small initial elastic domain.

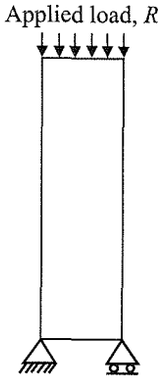

Figure 9.1: Uniaxial loading of a bar of nonlinear material

9.4.2 Finite element implementation

In the tangent stiffness approach the applied load is split into a sequence of increments. In Figure 9.2 three increments of load are shown, $\Delta \boldsymbol{R}_1$, $\Delta \boldsymbol{R}_2$ and $\Delta \boldsymbol{R}_3$. The analysis starts with the application of $\Delta \boldsymbol{R}_1$. The incremental global stiffness matrix $[\boldsymbol{K}_G]^1$ for this increment is evaluated based on the unstressed state of the bar corresponding to point 'a'. For an elasto-plastic material this might be constructed using the elastic constitutive matrix $[\boldsymbol{D}]$. Equation (9.1) is then solved to determine the nodal displacements $\{\Delta \boldsymbol{d}\}^1_{nG}$. As the material stiffness is assumed to remain constant, the load displacement curve follows the straight line 'ab'' on Figure 9.2. In reality, the stiffness of the material does not remain constant during this loading increment and the true solution is represented by the curved path 'ab'. There is therefore an error in the predicted displacement equal to the distance 'b'b', however in the tangent stiffness approach this error is neglected. The second increment of load, $\Delta \boldsymbol{R}_2$, is then applied, with the incremental global stiffness matrix $[\boldsymbol{K}_G]^2$ evaluated using the stresses and strains appropriate to the end of increment 1, i.e. point 'b'' on Figure 9.2. Solution of Equation (9.1) then gives the nodal displacements $\{\Delta \boldsymbol{d}\}^2_{nG}$. The load displacement curve follows the straight path 'b'c'' on Figure 9.2. This deviates further from the true solution, the error in the displacements now being equal to the distance 'c'c'. A similar procedure now occurs when $\Delta \boldsymbol{R}_3$ is applied. The stiffness matrix $[\boldsymbol{K}_G]^3$ is evaluated

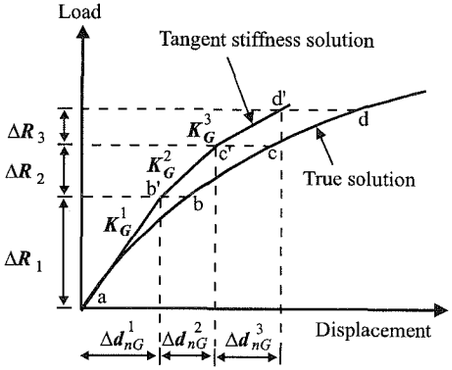

Figure 9.2: Application of the tangent stiffness algorithm to the uniaxial loading of a bar of a nonlinear material

using the stresses and strains appropriate to the end of increment 2, i.e. point 'c'' on Figure 9.2. The load displacement curve moves to point 'd'' and again drifts further from the true solution. Clearly, the accuracy of the solution depends on the size of the load increments. For example, if the increment size was reduced so that more increments were needed to reach the same accumulated load, the tangent stiffness solution would be nearer to the true solution.

From the above simple example it may be concluded that in order to obtain accurate solutions to strongly nonlinear problems many small solution increments are required. The results obtained using this method can drift from the true solution and the stresses can fail to satisfy the constitutive relations. Thus the basic solution requirements may not be fulfilled. As shown later in this chapter, the magnitude of the error is problem dependent and is affected by the degree of material nonlinearity, the geometry of the problem and the size of the solution increments used. Unfortunately, in general, it is impossible to predetermine the size of solution increment required to achieve an acceptable error.

The tangent stiffness method can give particularly inaccurate results when soil behaviour changes from elastic to plastic or vice versa. For instance, if an element is in an elastic state at the beginning of an increment, it is assumed to behave elastically over the whole increment. This is incorrect if during the increment the behaviour becomes plastic and results in an illegal stress state which violates the constitutive model. Such illegal stress states can also occur for plastic elements if the increment size used is too large, for example a tensile stress state could be predicted for a constitutive model which cannot sustain tension. This can be a major problem with critical state type models, such as modified Cam clay, which employ a v-$\log_e p'$ relationship (v = specific volume, p' = mean effective stress, see Chapter 7), since a tensile value of p' cannot be accommodated. In that case either the analysis has to be aborted or the stress state has to be modified in some arbitrary way, which would cause the solution to violate the equilibrium condition and the constitutive model.

9.4.3 Uniform compression of a Mohr-Coulomb soil

To illustrate some of the above deficiencies, drained one dimensional loading of a soil element (i.e. an ideal oedometer test) is considered. This is shown graphically in Figure 9.3. Lateral movements are restrained and the soil sample is loaded vertically by specifying vertical movements along its top surface. No side friction is assumed and therefore the soil experiences uniform stresses and strains. Consequently, to model this using finite elements, only a single

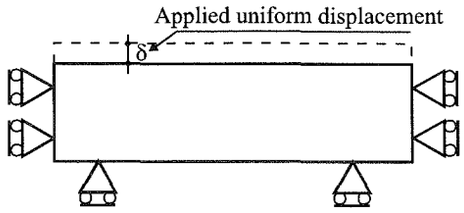

Figure 9.3: Uniform one dimensional compression of a sample

element is needed. There is no discretisation error, the finite element program is essentially used only to integrate the constitutive model over the loading path.

Firstly, it is assumed that the soil behaves according to a linear elastic perfectly plastic Mohr-Coulomb model, see Section 7.5, with properties given in Table 9.1.

Table 9.1: Properties for Mohr-Coulomb model

Youngs modulus, E'	10,000 kN/m^2
Poisson's ratio, μ	0.2
Cohesion, c'	0.0
Angle of shearing resistance, φ'	30°
Angle of dilation, v	30°

As the angles of dilation, v, and shearing resistance, φ', are the same, the model is associated (i.e. $P(\{\sigma'\},\{\boldsymbol{m}\}) = F(\{\sigma'\},\{\boldsymbol{k}\})$). For this analysis the yield function given by Equation (7.13) is written in non-dimensional form as:

$$F(\{\sigma'\},\{\boldsymbol{k}\}) = \frac{J}{\left(\dfrac{c'}{\tan\varphi'} + p'\right) g(\theta)} - 1 = 0 \tag{9.2}$$

It is also assumed that the soil sample has an initial isotropic stress $\sigma_v' = \sigma_h' = 50\text{kN/m}^2$ and that loading is always sufficiently slow to ensure drained conditions.

Figure 9.4 shows the stress path in J-p' space predicted by a tangent stiffness analysis in which equal increments of displacement were applied to the top of the sample. Each increment gave an incremental axial strain $\Delta\varepsilon_a = 3\%$. Also shown on the figure is the true solution. This was obtained by noting that initially the soil is elastic and that it only becomes elasto-plastic when it reaches the Mohr-Coulomb yield curve. In J-p' space it can be shown that the elastic stress path is given by:

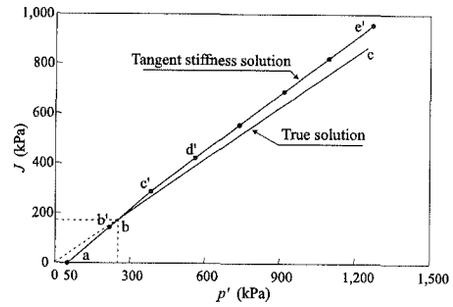

Figure 9.4: Oedometer stress path predicted by the tangent stiffness algorithm

$$J = \frac{3(1-2\mu)}{\sqrt{3}(1+\mu)}(p' - p_i) = 0.866(p' - 50) \tag{9.3}$$

The Mohr-Coulomb yield curve is given by Equation (9.2), which, with the parameters given in Table 9.1 gives:

$$J = 0.693p' \tag{9.4}$$

Equating Equations (9.3) and (9.4) gives the stress state at which the stress path reaches the yield surface. This occurs when J=173kN/m^2 and p'=250kN/m^2. Using Equation (5.8) it can be shown that this occurs when the applied axial strain ε_a=3.6%. Consequently, the true solution follows the path 'abc', where 'ab' is given by Equation (9.3) and 'bc' is given by Equation (9.4).

Inspection of Figure 9.4 indicates a discrepancy between the tangent stiffness and the true solution, with the former lying above the latter and indicating a higher angle of shearing resistance, φ'. The reason for this discrepancy can be explained as follows.

For the first increment of loading the material constitutive matrix is assumed to be elastic and the predicted stress path follows the path 'ab''. Because the applied incremental axial strain is only $\Delta\varepsilon_a$=3%, this is less than ε_a=3.6% which is required to bring the soil to yield at point 'b'. As the soil is assumed to be linear elastic, the solution for this increment is therefore correct. For the second increment of loading the incremental global stiffness matrix $[\boldsymbol{K}_G]^2$ is based on the stress state at the end of increment 1 (i.e. point 'b''). Since the soil is elastic here, the elastic constitutive matrix $[\boldsymbol{D}]$ is used again. The stress path now moves to point 'c''. As the applied strain $\varepsilon_a=(\Delta\varepsilon_a^1+\Delta\varepsilon_a^2)$=6% is greater than ε_a=3.6%, which is required to bring the soil to yield at point 'b', the stress state now lies above the Mohr-Coulomb yield surface. The tangent stiffness algorithm has *overshot* the yield surface. For increment three the algorithm realises the soil is plastic at point 'c'' and forms the incremental global stiffness matrix $[\boldsymbol{K}_G]^3$ based on the elasto-plastic matrix, $[\boldsymbol{D}^{ep}]$, consistent with the stress state at 'c''. The stress path then moves to point 'd''. For subsequent increments the algorithm uses the elasto-plastic constitutive matrix, $[\boldsymbol{D}^{ep}]$, and traces the stress path 'd'e''.

The reason why this part of the curve is straight, with an inclination greater than the correct solution, path 'bc', can be found by inspecting the elasto-plastic constitutive matrix, $[\boldsymbol{D}^{ep}]$, defined by Equation (6.16). For the current model the elastic $[\boldsymbol{D}]$ matrix is constant, and as the yield and plastic potential functions are both assumed to be given by Equation (9.2), the variation of $[\boldsymbol{D}^{ep}]$ depends on the values of the partial differentials of the yield function with respect to the stress components. In this respect, it can be shown that the gradient of the stress path in J-p' space is given by:

$$\frac{\dfrac{\partial F(\{\sigma'\},\{k\})}{\partial p'}}{\dfrac{\partial F(\{\sigma'\},\{k\})}{\partial J}} = \frac{J}{p'} \tag{9.5}$$

As this ratio is first evaluated at point 'c'', which is above the Mohr-Coulomb yield curve, the stress path sets off at the wrong gradient for increment three. This error remains for all subsequent increments.

The error in the tangent stiffness approach can therefore be associated with the overshoot at increment 2. If the increment sizes had been selected such that at the end of an increment the stress path just reached the yield surface (i.e. at point 'b'), the tangent stiffness algorithm would then give the correct solution. This is shown in Figure 9.5 where, in analysis labelled A, the first increment was selected such that $\Delta\varepsilon_a$=3.6%. After this increment the stress state was at point b, which is correct, and for increment 2 and subsequent increments the correct elasto-plastic constitutive matrix $[\boldsymbol{D}^{ep}]$ was used to obtain the incremental stiffness matrix $[\boldsymbol{K}_G]^i$. As the $[\boldsymbol{D}^{ep}]$ remains constant along the stress path 'bc', the solution is independent of the size of the increments from point 'b' onwards. In analysis labelled B in Figure 9.5, a much larger first increment, $\Delta\varepsilon_a$=10%, was applied. This causes a large overshoot on the first increment and results in a significant divergence from the true solution. As noted above, once the stress state has overshot, making subsequent increments smaller does not improve the solution.

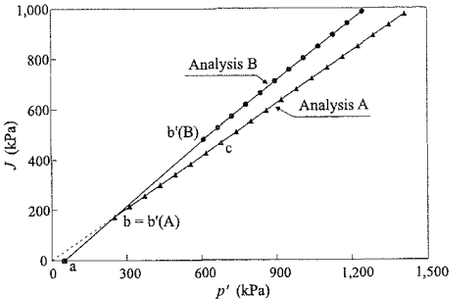

Figure 9.5: Effect of the first increment size on a tangent stiffness prediction of an oedometer stress path

It can be concluded that, for this particular problem, the tangent stiffness algorithm is always in error, unless the increment size is such that at the end of an increment the stress state happens to be at point 'b'. Because the solution to this simple one dimensional problem is known, it can be arranged for this to occur, as for analysis A in Figure 9.5. However, in general multi-axis boundary value problems, the answers to which are not known, it is impossible to choose the correct increment sizes so that overshoot never occurs. The only solution is to use a very large number of small load increments and hope for the best.

Another source of error arising from the way the tangent stiffness method works is that the answers depend on the way the yield function is implemented. While it is perfectly acceptable, from a mathematical point of view, to write the yield surface in either of the forms shown in Equations (7.13) or (9.2), the predictions from the tangent stiffness algorithm will differ if, as is usually the case, overshoot occurs. For the simple oedometer situation, this can be seen by calculating the partial differentials in Equation (9.5), for the yield function given by Equation (7.13). This gives:

$$\frac{\dfrac{\partial F(\{\sigma'\},\{k\})}{\partial p'}}{\dfrac{\partial F(\{\sigma'\},\{k\})}{\partial J}} = g(\theta) \tag{9.6}$$

As noted above, this equation gives the gradient of the resulting stress path in J-p' space. Whereas Equation (9.5) indicates that the inclination depends on the amount of overshoot, Equation (9.6) indicates that the inclination is constant and equal to the gradient of the Mohr-Coulomb yield curve. The two results are compared in Figure 9.6. The stress path based on the yield function written in the form of Equation (9.2) appears to pass through the origin of stress space, but to have an incorrect slope, indicating too higher value of φ', but the correct c'. In contrast, the stress path based on the yield function written in the form of Equation (7.13) is parallel to the true solution, but does not pass through the origin of stress space, indicating that the material has a fictitious c', but the correct φ'. Clearly, if there is no overshoot, both formulations give the same result, which for this problem agrees with the true solution. The reason for this inconsistency is that, in theory, the differentials of the yield function are only valid if the stress state is on the yield surface, i.e. $F(\{\boldsymbol{\sigma}'\},\{\boldsymbol{k}\})=0$. If it is not, it is then theoretically incorrect to use the differentials and inconsistencies will arise. The implications for practice are self evident. Two different pieces of software which purport to use the same Mohr-Coulomb condition can give very different results, depending on the finer details of their implementation. This is clearly yet another draw back with the tangent stiffness algorithm for nonlinear analysis.

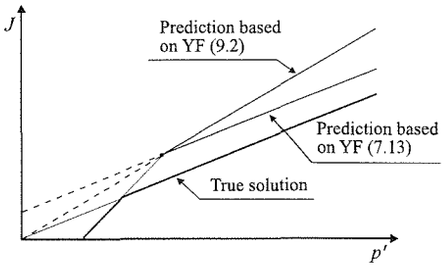

Figure 9.6: Effect of yield function implementation on errors associated with tangent stiffness algorithm

The analysis labelled A in Figure 9.5 was performed with a first increment of axial strain of $\Delta\varepsilon_a$=3.6% and subsequent increments of $\Delta\varepsilon_a$=1%. As the first increment just brought the stress path to the yield surface, the results from this analysis are in agreement with the true solution. The situation is now considered where, after being loaded to point 'c', see Figure 9.5, the soil sample is unloaded with two increments of $\Delta\varepsilon_a$=−1%. The results of this analysis are shown in Figure 9.7. The predicted stress path on unloading is given by path 'cde', which indicates that the soil remains plastic and the stress path stays on the yield surface. This is clearly incorrect as such behaviour

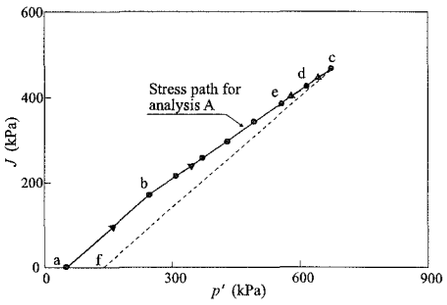

Figure 9.7: Example of an unloading stress path using the tangent stiffness algorithm

violates the basic postulates of elasto-plastic theory, see Chapter 6. When unloaded, the soil sample should become purely elastic, and the correct stress path is marked as path 'cf' on Figure 9.7. Because the soil has constant elastic parameters, this path is parallel to the initial elastic loading path 'ab'. The reason for the error in the tangent stiffness analysis arises from the fact that when the first increment of unloading occurs, the stress state is plastic, i.e. point 'c'. The algorithm does not know that unloading is going to occur, so when it forms the incremental global stiffness matrix, it uses the elasto-plastic constitutive matrix $[\boldsymbol{D}^{ep}]$. The result is that the stress path remains on the yield surface after application of the unloading increment. Since the soil is still on the yield surface, the same procedure occurs for the second increment of unloading.

9.4.4 Uniform compression of modified Cam clay soil

The above one dimensional loading problem is now repeated with the soil represented by a simplified form of the modified Cam clay model described in Chapter 7. The soil parameters are listed in Table 9.2.

Table 9.2: Properties for modified Cam clay model

Specific volume at unit pressure on virgin consolidation line, v_1	1.788
Slope of virgin consolidation line in v-$\log_e p'$ space, λ	0.066
Slope of swelling line in v-$\log_e p'$ space, κ	0.0077
Slope of critical state line in J-p' space, M_J	0.693

Because a constant value of M_J has been used, the yield (and plastic potential) surface plots as a circle in the deviatoric plane. A further simplification has been made for the present analysis. Instead of using the slope of the swelling line to calculate the elastic bulk modulus, constant elastic parameters, E'=50000 kN/m^2 and μ = 0.26, have been used. This simplification has been made to be consistent with results presented in the next section of this chapter. For the present investigation, it does not significantly affect soil behaviour and therefore any conclusions reached are valid for the full model. Again the initial stresses are $\sigma_v'=\sigma_h'$=50kN/m^2, and the soil is assumed to be normally consolidated. This later assumption implies that the initial isotropic stress state is on the yield surface.

Three tangent stiffness analyses, with displacement controlled loading increments equivalent to $\Delta\varepsilon_a$ = 0.1%, $\Delta\varepsilon_a$ = 0.4% and $\Delta\varepsilon_a$ = 1% respectively, have been performed. The predicted stress paths are shown in Figure 9.8. Also shown in this figure is the true solution. Let us first consider the analysis with the smallest increment size, $\Delta\varepsilon_a$ = 0.1%. Apart from the very first increment the results of this analysis agree with the true solution. This is not so for the other two analyses. For the analysis with $\Delta\varepsilon_a$ = 0.4% the stress path is in considerable error for the first three increments. Subsequently the stress path is parallel to the true solution,

however, there is still a substantial error. Matters are even worse for the analysis with the largest increment size, $\Delta\varepsilon_a$=1%. This has very large errors initially.

The reason for the errors in these analyses is the same as that explained above for the Mohr-Coulomb analysis. That is the yield (and plastic potential) derivatives are evaluated in illegal stress space, i.e. with stress values which do not satisfy the yield (or plastic potential) function. This is mathematically wrong and leads to incorrect elasto-plastic constitutive matrices. The reason why the errors are much greater than for the Mohr-Coulomb analyses is that the yield (and plastic potential) derivatives are not constant on the yield (or plastic potential) surface, as they are with the Mohr-Coulomb model, but vary. Matters are also not helped by the fact that the model is strain hardening/softening and, once the analysis goes wrong, incorrect plastic strains and hardening/softening parameters are calculated.

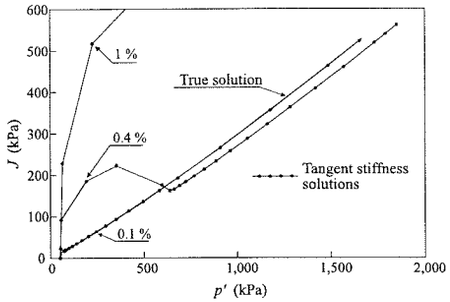

Figure 9.8: Effect of increment size on the tangent stiffness prediction of an oedometer stress path

The comments made above for the Mohr-Coulomb model on implementation of the yield function and on unloading also apply here. In fact, they apply to any constitutive model because they are caused by flaws in the tangent stiffness algorithm itself.

9.5 Visco-plastic method

9.5.1 Introduction

This method uses the equations of visco-plastic behaviour and time as an artifice to calculate the behaviour of nonlinear, elasto-plastic, time independent materials (Owen and Hinton (1980), Zienkiewicz and Cormeau (1974)).

The method was originally developed for linear elastic visco-plastic (i.e. time dependent) material behaviour. Such a material can be represented by a network of the simple rheological units shown in Figure 9.9. Each unit consists of an elastic and a visco-plastic component connected in series. The elastic component is represented by a spring and the visco-plastic component by a slider and dashpot connected in parallel. If a load is applied to the network, then one of two situations occurs in each

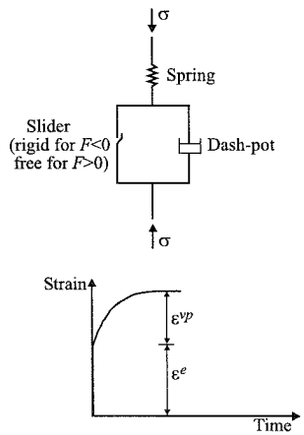

Figure 9.9: Rheological model for visco-plastic material

individual unit. If the load is such that the induced stress in the unit does not cause yielding, the slider remains rigid and all the deformation occurs in the spring. This represents elastic behaviour. Alternatively, if the induced stress causes yielding, the slider becomes free and the dashpot is activated. As the dashpot takes time to react, initially all deformation occurs in the spring. However, with time the dashpot moves. The rate of movement of the dashpot depends on the stress it supports and its fluidity. With time progressing, the dashpot moves at a decreasing rate, because some of the stress the unit is carrying is dissipated to adjacent units in the network, which as a result suffer further movements themselves. This represents visco-plastic behaviour. Eventually, a stationary condition is reached where all the dashpots in the network stop moving and are no longer sustaining stresses. This occurs when the stress in each unit drops below the yield surface and the slider becomes rigid. The external load is now supported purely by the springs within the network, but, importantly, straining of the system has occurred not only due to compression or extension of the springs, but also due to movement of the dashpots. If the load was now removed, only the displacements (strains) occurring in the springs would be recoverable, the dashpot displacements (strains) being permanent.

9.5.2 Finite element application

Application to finite element analysis of elasto-plastic materials can be summarised as follows. On application of a solution increment the system is assumed to instantaneously behave linear elastically. If the resulting stress state lies within the yield surface, the incremental behaviour is elastic and the calculated displacements are correct. If the resulting stress state violates yield, the stress state can only be sustained momentarily and visco-plastic straining occurs. The magnitude of the visco-plastic strain rate is determined by the value of the yield function, which is a measure of the degree by which the current stress state exceeds the yield condition. The visco-plastic strains increase with time, causing the material to relax with a reduction in the yield function and hence the visco-plastic strain rate. A marching technique is used to step forward in time until the visco-plastic strain rate is insignificant. At this point, the accumulated visco-plastic strain and the associated stress change are equal to the incremental plastic strain and stress change respectively. This process is illustrated for the simple problem of a uniaxially loaded bar of nonlinear material in Figure 9.10.

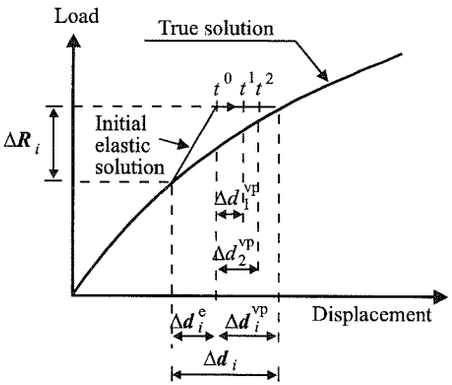

Figure 9.10: Application of the visco-plastic algorithm to the uniaxial loading of a bar of a nonlinear material

For genuine visco-plastic materials the visco-plastic strain rate is given by:

$$\frac{\partial\{\varepsilon^{vp}\}}{\partial t} = \gamma f\left(\frac{F(\{\sigma\},\{k\})}{F_o}\right)\frac{P(\{\sigma\},\{m\})}{\partial\{\sigma\}} \tag{9.7}$$

where γ is the dashpot fluidity parameter and F_o is a stress scalar to non-dimensionalise $F(\{\sigma\},\{k\})$ (Zienkiewicz and Cormeau (1974)). When the method is applied to time independent elasto-plastic materials, both γ and F_o can be assumed to be unity (Griffiths (1980)) and Equation (9.7) reduces to:

$$\frac{\partial\{\varepsilon^{vp}\}}{\partial t} = F(\{\sigma\}),\{k\})\frac{P(\{\sigma\}),\{m\})}{\partial\{\sigma\}} \tag{9.8}$$

Over a time step t to $t+\Delta t$ the visco-plastic strain is given by:

$$\{\Delta\varepsilon^{vp}\} = \int_t^{t+\Delta t}\frac{\partial\{\varepsilon^{vp}\}}{\partial t}\,dt \tag{9.9}$$

and for small time steps Equation (9.9) can be approximated to:

$$\{\Delta\varepsilon^{vp}\} = \Delta t\,\frac{\partial\{\varepsilon^{vp}\}}{\partial t} \tag{9.10}$$

The visco-plastic algorithm consists of the following steps:

1. At the beginning of a solution increment, i, formulate the boundary conditions. In particular, construct the incremental right hand side load vector $\{\Delta\boldsymbol{R}_G\}$. Assemble the incremental global stiffness matrix $[\boldsymbol{K}_G]$ using the linear elastic constitutive matrix, $[\boldsymbol{D}]$, for all elements in the mesh. Zero the visco-plastic strain increment vector, i.e. $\{\Delta\varepsilon^{vp}\} = 0$. Set $t = t_o$.
2. Solve the finite element equations to obtain a first estimate of the nodal displacements:

$$\{\Delta\boldsymbol{d}\}^t_{nG} = [\boldsymbol{K}_G]^{-1}\{\Delta\boldsymbol{R}_G\}^t \tag{9.11}$$

Loop through all integration points in the mesh and for each integration point:

3. Calculate the incremental total strains from the incremental nodal displacements:

$$\{\Delta\varepsilon\}^t = [\boldsymbol{B}]\{\Delta\boldsymbol{d}\}^t_{nG} \tag{9.12}$$

4. The elastic strains are now calculated as the difference between the total strains, from Equation (9.12), and the visco-plastic strains. Note that for the first iteration (i.e. $t = t_o$) the visco-plastic strains are zero. The elastic strains are then used with the elastic constitutive matrix $[\boldsymbol{D}]$ to evaluate the incremental stress change:

$$\{\Delta\sigma\}^t = [\boldsymbol{D}](\{\Delta\varepsilon\}^t - \{\Delta\varepsilon^{vp}\}) \tag{9.13}$$

5. This incremental stress change is added to the accumulated stress at the beginning of the solution increment, $\{\boldsymbol{\sigma}\}^{i-1}$:

$$\{\sigma\}^t = \{\sigma\}^{i-1} + \{\Delta\sigma\}^t \tag{9.14}$$

6. These stresses are then used to evaluate the yield function, $F(\{\sigma\}^t,\{k\})$.

If the yield function, $F(\{\sigma\}^t,\{k\})<0$, the current integration point is elastic. Therefore move to the next integration point (i.e. go to step 3). If the yield function $F(\{\sigma\}^t,\{k\})\geq 0$ the visco-plastic strains must be calculated:

7. Calculate the visco-plastic strain rate:

$$\left(\frac{\partial\{\varepsilon^{vp}\}}{\partial t}\right)^t = F(\{\sigma\}^t,\{k\})\frac{P(\{\sigma\}^t,\{m\})}{\partial\{\sigma\}} \tag{9.15}$$

8. Update the visco-plastic strain increment:

$$\{\Delta\varepsilon^{vp}\}^{t+\Delta t} = \{\Delta\varepsilon^{vp}\}^t + \Delta t\left(\frac{\partial\{\varepsilon^{vp}\}}{\partial t}\right)^t \tag{9.16}$$

Move to next integration point (i.e. go to step 3).
End of integration point loop.

9. Calculate nodal forces equivalent to the change in incremental visco-plastic strains and add them to the incremental global right hand side vector. The elastic stress increment associated with the change in visco-plastic strains is given by:

$$\{\Delta\sigma^{vp}\} = [\boldsymbol{D}]\,\Delta t\left(\frac{\partial\{\varepsilon^{vp}\}}{\partial t}\right)^t \tag{9.17}$$

The incremental global right hand side load vector then becomes:

$$\{\Delta\boldsymbol{R}_G\}^{t+\Delta t} = \{\Delta\boldsymbol{R}_G\}^t + \sum_{\substack{\text{All}\\ \text{elements}}}\int_{Vol}[\boldsymbol{B}]^{\mathrm{T}}[\boldsymbol{D}]\,\Delta t\left(\frac{\partial\{\varepsilon^{vp}\}}{\partial t}\right)^t dVol \tag{9.18}$$

10. Set $t = t+\Delta t$ and return to step 2. This process is repeated until convergence is obtained. When convergence is achieved, the displacements evaluated in step 2, Equation (9.11), hardly change from one time step to the next. The yield function values, step 6, and the visco-plastic strain rates, step 7, become very small and the incremental stresses, step 4, and strain increments, steps 3 and 8, become almost constant with time.
11. Once convergence is achieved the displacements, stresses and strains are updated, ready for the next load increment:

$$\{\boldsymbol{d}\}_{nG}^{i} = \{\boldsymbol{d}\}_{nG}^{i-1} + \{\Delta\boldsymbol{d}\}_{nG}^{t} \tag{9.19}$$

$$\{\varepsilon\}^{i} = \{\varepsilon\}^{i-1} + \{\Delta\varepsilon\}^{t} \tag{9.20}$$

$$\{\varepsilon^{p}\}^{i} = \{\varepsilon^{p}\}^{i-1} + \{\Delta\varepsilon^{vp}\}^{t+\Delta t} \tag{9.21}$$

$$\{\sigma\}^{i} = \{\sigma\}^{i-1} + \{\Delta\sigma\}^{t} \tag{9.22}$$

9.5.3 Choice of time step

In order to use the procedure described above, a suitable time step, Δt, must be selected. If Δt is small many iterations are required to obtain an accurate solution. However, if Δt is too large numerical instability can occur. The most economical choice for Δt is the largest value that can be tolerated without causing such instability. An estimate for this critical time step is suggested by Stolle and Higgins (1989) and is given by:

$$\Delta t_c = \frac{1}{\dfrac{\partial F(\{\sigma\},\{k\})^{\mathrm{T}}}{\partial\{\sigma\}}[\boldsymbol{D}]\dfrac{\partial P(\{\sigma\},\{m\})^{\mathrm{T}}}{\partial\{\sigma\}} + A} \tag{9.23}$$

where A is defined by Equation (6.14). For simple constitutive models, such as Tresca and Mohr-Coulomb, the yield and plastic potential functions can be written such that Equation (9.23) gives a constant value of the critical time step, which is dependent only on the elastic stiffness and strength parameters. As these parameters are constant, the critical time step has to be evaluated only once during an analysis. However, for more complex constitutive models the critical time step is also dependent on the current state of stress and strain and therefore is not constant. It must therefore be evaluated for each integration point for each iteration. It should be noted that when using the algorithm to solve elasto-plastic problems (i.e. no time dependent plastic behaviour), the time step does not have to be the same for all integration points during any particular iteration.

In order to be able to evaluate the potential of the visco-plastic algorithm, the Authors have implemented the above procedure in the Imperial College Finite Element Program (ICFEP). When dealing with elasto-plastic constitutive models the time step is calculated from the following equation:

$$\Delta t_c = \frac{\alpha}{\dfrac{\partial F(\{\sigma\},\{k\})^{\mathrm{T}}}{\partial\{\sigma\}}[\boldsymbol{D}]\dfrac{\partial P(\{\sigma\},\{m\})^{\mathrm{T}}}{\partial\{\sigma\}} + A} \tag{9.24}$$

where α is a scaling factor which is input by the user. If $\alpha = 1$ then Equation (9.24) reduces to Equation (9.23) and the critical time step is used.

9.5.4 Potential errors in the algorithm

Due to its simplicity, the visco-plastic algorithm has been widely used. However, in the Authors' opinion, the method has severe limitations for geotechnical analysis. Firstly, the algorithm relies on the fact that for each increment the elastic parameters remain constant. The simple algorithm cannot accommodate elastic parameters that vary during the increment because, for such cases, it cannot determine the true elastic stress changes associated with the incremental elastic strains, see Equation (9.13). The best that can be done is to use the elastic parameters associated with the accumulated stresses and strains at the beginning of the increment to calculate the elastic constitutive matrix, $[\boldsymbol{D}]$, and assume that this remains constant for the increment. Such a procedure only yields accurate results if the increments are small and/or the elastic nonlinearity is not great. A more complex way around this problem is described later in this chapter, but this involves the use of a separate algorithm to deal with the nonlinear elastic response.

A more severe limitation of the method arises when the algorithm is used as an artifice to solve problems involving non-viscous material (i.e. elasto-plastic materials). As noted above, the visco-plastic strains are calculated using Equations (9.15) and (9.16). In Equation (9.15) the partial differentials of the plastic potential are evaluated at an illegal stress state $\{\sigma\}^{t}$, which lies outside the yield surface, i.e. $F(\{\sigma^{t}\},\{k\})>0$. As noted for the tangent stiffness method, this is theoretically incorrect and results in failure to satisfy the constitutive equations. The magnitude of the error depends on the constitutive model and in particular on how sensitive the partial derivatives are to the stress state. This is now illustrated by applying the visco-plastic algorithm to the one dimensional loading problem (i.e. ideal oedometer test) considered above for the tangent stiffness method.

9.5.5 Uniform compression of a Mohr-Coulomb soil

As with the tangent stiffness method, the problem shown graphically in Figure 9.3, with the soil properties given in Table 9.1, is considered. Figure 9.11 shows the stress path in J-p' space predicted by a visco-plastic analysis in which equal increments of vertical displacement were applied to the top of the sample. Each increment gave an axial strain $\Delta\varepsilon_a$=3% and therefore the predictions in Figure 9.11 are directly comparable to those for the tangent stiffness method given in Figure 9.4. The results were obtained using the critical time step, α=1, in Equation (9.24)). It can be seen that the visco-plastic predictions are in

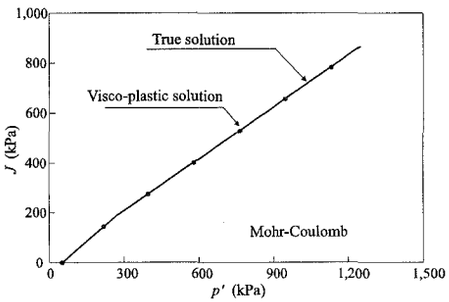

Figure 9.11: Oedometer stress path predicted by the visco-plastic algorithm

remarkably good agreement with the true solution. Even when the increment size was doubled (i.e. $\Delta\varepsilon_a$=6%), the predictions did not change significantly. Due to the problem highlighted above, concerning evaluation of the plastic potential differentials in illegal stress space, there were some small differences, but these only caused changes in the fourth significant figure for both stress and plastic strains. Predictions were also insensitive to values of the time step ($0 < \alpha \leq 1$ in Equation (9.24)).

The results were therefore not significantly dependent on either the solution increment size or the time step. The algorithm was also able to accurately deal with the change from purely elastic to elasto-plastic behaviour and vice versa. In these respects the algorithm behaved much better than the tangent stiffness method.

It can therefore be concluded that the visco-plastic algorithm works well for this one dimensional loading problem with the Mohr-Coulomb model. The Authors have also found, as have others, that it works well for other boundary value problems, involving either the Tresca or the Mohr-Coulomb model.

9.5.6 Uniform compression of modified Cam clay soil

The one dimensional loading problem was repeated with the soil represented by the simplified modified Cam clay model described in Section 9.4.4. This model has linear elastic behaviour and therefore the problem of dealing with nonlinear elasticity is not relevant. In fact, it was because of this deficiency in the visco-plastic algorithm that the model was simplified. The soil properties are given in Table 9.2 and the initial conditions are discussed in Section 9.4.4.

Results from four visco-plastic analyses, with displacement controlled loading increments equivalent to $\Delta\varepsilon_a$=0.01%, $\Delta\varepsilon_a$=0.1%, $\Delta\varepsilon_a$=0.4% and $\Delta\varepsilon_a$=1%, are compared with the true solution in Figure 9.12. The results have been obtained using the critical time step (i.e. α=1 in Equation (9.24)) and the convergence criteria was set such that the iteration process stopped when there was no change in the fourth significant figure of the incremental stresses and incremental plastic strains.

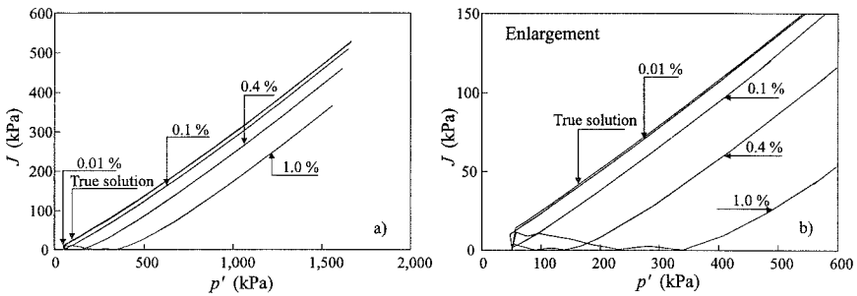

Figure 9.12: Effect of increment size on the visco-plastic prediction of an oedometer stress path

Only the solution with the smallest increment size (i.e. $\Delta\varepsilon_a$=0.01%) agrees with the true solution. It is instructive to compare these results with those given in Figure 9.8 for the tangent stiffness method. In view of the accuracy of the analysis with the Mohr-Coulomb model, it is, perhaps, surprising that the visco-plastic algorithm requires smaller increments than the tangent stiffness method to obtain an accurate solution. It is also of interest to note that when the increment size is too large, the tangent stiffness predictions lie *above* the true solution, whereas for the visco-plastic analyses the opposite occurs, with the predictions lying *below* the true solution. The visco-plastic solutions are particularly in error during the early stages of loading, see Figure 9.12b.

To explain why the visco-plastic solutions are in error, consider the results shown in Figure 9.13. The true solution is marked as a dashed line on this plot. A visco-plastic analysis consisting of a single increment, equivalent to $\Delta\varepsilon_a$ = 1%, is performed starting from point 'a', which is on the true stress path. To do this in the analysis, the initial stresses are set appropriate to point 'a': σ_v' = 535.7 kN/m^2 and σ_h' = 343.8 kN/m^2. This loading increment should move the stress path from point 'a' to point 'e'. The line 'ae' therefore represents the true solution to which the visco-plastic analysis can be compared. However, the visco-plastic analysis actually moves the stress path from point 'a' to point 'd', thus incurring a substantial error.

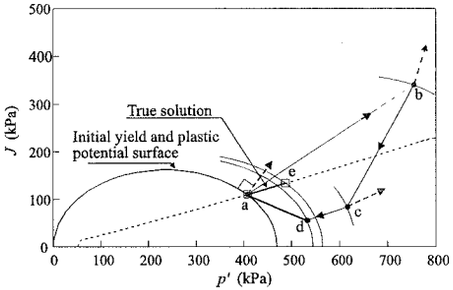

Figure 9.13: A single increment of a visco-plastic analysis

To see how such an error arises, the intermediate steps involved in the visco-plastic algorithm are plotted in Figure 9.13. These can be explained as follows. Initially, on the first iteration, the visco-plastic strains are zero and the stress change is assumed to be entirely elastic, see Equation (9.13). This is represented by the stress state at point 'b'. This stress state is used to evaluate the first contribution to the incremental visco-plastic strains, using Equations (9.15) and (9.16). These strains are therefore based on the normal to the plastic potential function at 'b'. This normal is shown on Figure 9.13 and should be compared to that shown for point 'a', which provides the correct solution. As the directions of the normals differ significantly, the resulting contribution to the visco-plastic strains is in error (note: along path 'ae' of the true solution, the normal to the plastic potential does not change significantly, being very similar to that at point 'a'). This contribution to the visco-plastic strains is used to calculate a correction vector which is added to the incremental right hand side vector, see Equations (9.17) and (9.18). They are also used to update the hardening/softening parameter for the constitutive model. A second iteration is performed which, due to the

correction vector, gives different incremental displacements (Equation (9.11)) and incremental total strains (Equation (9.12)). The incremental stresses are also now different as they depend on these new incremental total strains and the visco-plastic strains calculated for iteration 1, see Equation (9.13). The stress state is now represented by point 'c'. A second contribution to the visco-plastic strains is calculated based on the plastic potential at point 'c'. Again, this is in error because this is an illegal stress state. The error is related to the difference in direction of the normals to the plastic potential surfaces at points 'a' and 'c'. This second contribution to the incremental plastic strains is used to obtain an additional correction vector which is added to the incremental right hand side vector, Equation (9.18). A third iteration is then performed which brings the stress state to point 'd' on Figure 9.13. Subsequent iterations cause only very small changes to the visco-plastic strains and the incremental stresses and therefore the stress state remains at point 'd'. At the end of the iterative process, the incremental plastic strains are equated to the visco-plastic strains, see Equation (9.21). As the visco-plastic strains are the sum of the contributions obtained from each iteration, see Equation (9.16), and as each of these contributions has been calculated using the incorrect plastic potential differentials (i.e. wrong direction of the normal), the incremental plastic strains are in error. This is evident from Figure 9.14 which compares the predicted and true incremental plastic strains. Since the hardening parameter for the model is calculated from the plastic strains, this is also incorrect. It is therefore not surprising that the algorithm ends up giving the wrong stress state represented by point 'd' in Figure 9.13.

The reason why the stress state at point 'd' has a lower stress ratio, J/p', than the correct solution, can be explained as follows. The visco-plastic strain vector (normal to the plastic potential surface) has a steeper gradient at point 'b' than it should, compared to the true solution. This implies a greater proportion of deviatoric to volumetric visco-plastic strain. The correction vector calculated at the end of the first iteration and used for the second iteration therefore over corrects for the deviatoric stress and under corrects for the mean effective stress and, consequently, gives point 'c'. As the visco-plastic strain vector has a shallower gradient than it should have at point 'c', the reverse happens and the second correction vector tends to compensate. However, as the yield function at point 'b' is much larger than at point 'c' (i.e. the stress state is further from the yield surface) the visco-plastic strain contribution on the first iteration dominates

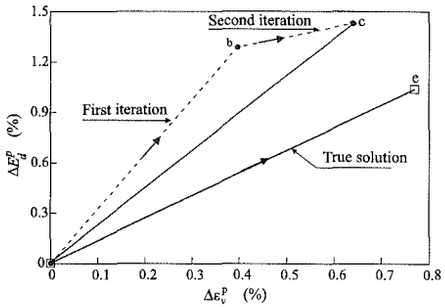

Figure 9.14: Comparison of incremental plastic strains from a single increment of a visco-plastic analysis and the true solution

the process. This is shown by the dotted lines in Figure 9.14. This occurs even when convergence is achieved. This is confirmed by Figure 9.14 which shows that only very small visco-plastic strains occur after iteration 2.

The above arguments suggest that if the dominance of the first iteration is suppressed, a better solution might be obtained. A way of doing this is to shorten the time step by reducing α in Equation (9.24). This has the effect of reducing the visco-plastic strain contribution calculated on each iteration, see Equation (9.16). The downside of this approach is that more iterations are needed to achieve convergence. To investigate this possibility and quantify its effect, the analysis discussed above was repeated with α values of 0.5, 0.2 and 0.05. The results of these analysis are presented in Figure 9.15, along with the original analysis (α = 1) and the true solution. Also noted on the figure is the number of iterations required to obtain convergence. The results show that the predictions become more accurate as α reduces, in line with the hypothesis given above, but that there is still a significant error, even if very small time steps are taken. The results also show that the number of iterations increases rapidly as the time step reduces.

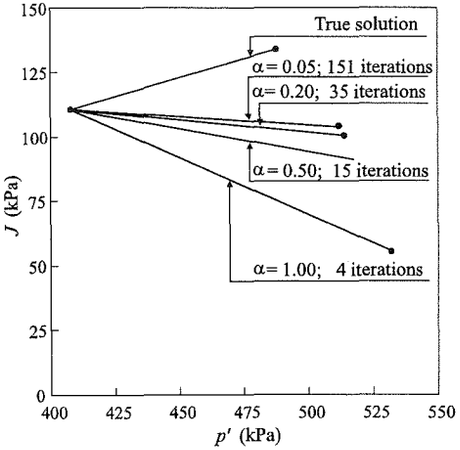

Figure 9.15: Effect of changing the time step in visco-plastic analysis

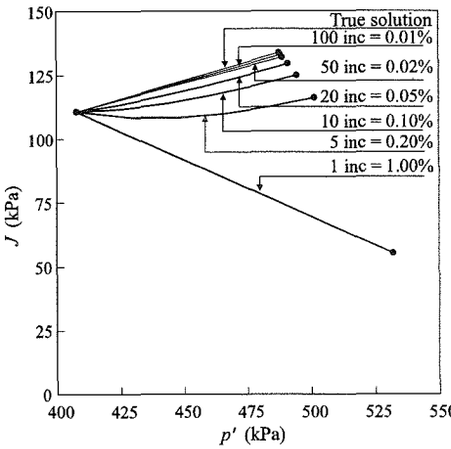

Figure 9.16: Effect of changing the increment size in visco-plastic analysis

The only way to further improve the predictions is to use smaller solution increments. As the increments become smaller, the stress states at which the visco-plastic strains are calculated lie nearer to the true solution and therefore the errors are reduced. The single increment analysis presented in Figure 9.13 was repeated, but with more increments. Five analyses, splitting the original $\Delta\varepsilon_a$=1% increment into 5, 10, 20, 50 and 100 smaller increments respectively, were performed. All analyses had α=1. The results

from these analyses are compared with the original analysis in Figure 9.16. Very small solution increments are required to obtain an accurate solution. If the soil sample is unloaded at any stage, the analysis indicates elastic behaviour and therefore behaves correctly.

It is concluded that for complex critical state constitutive models the visco-plastic algorithm can involve severe errors. The magnitude of these errors depends on the finer details of the model and, in particular, on how rapidly the plastic potential differentials vary with changes in stress state. The errors also depend on both the time step and size of solution increment used. The problems associated with the implementation of a particular constitutive model, as discussed for the tangent stiffness method, also apply here. As the plastic strains are calculated from plastic potential differentials evaluated in illegal stress space, the answers depend on the finer details of how the model is implemented in the software. Again, two pieces of software which purport to use the same equations could give different results.

The above conclusion is perhaps surprising as the visco-plastic algorithm appears to work well for simple constitutive models of the Tresca and Mohr-Coulomb types. However, as noted previously, in these simpler models the plastic potential differentials do not vary by a great amount when the stress state moves into illegal stress space.

9.6 Modified Newton-Raphson method

9.6.1 Introduction

The previous discussion of both the tangent stiffness and visco-plastic algorithms has demonstrated that errors can arise when the constitutive behaviour is based on illegal stress states. The modified Newton-Raphson (MNR) algorithm described in this section attempts to rectify this problem by only evaluating the constitutive behaviour in, or very near to, legal stress space.

The MNR method uses an iterative technique to solve Equation (9.1). The first iteration is essentially the same as the tangent stiffness method. However, it is recognised that the solution is likely to be in error and the predicted incremental displacements are used to calculate the residual load, a measure of the error in the analysis. Equation (9.1) is then solved again with this residual load, $\{\psi\}$, forming the incremental right hand side vector. Equation (9.1) can be rewritten as:

$$[\boldsymbol{K}_G]^i\left(\{\Delta \boldsymbol{d}\}^i_{nG}\right)^j = \{\psi\}^{j-1} \tag{9.25}$$

The superscript 'j' refers to the iteration number and $\{\psi\}^0 = \{\Delta \boldsymbol{R}_G\}^i$. This process is repeated until the residual load is small. The incremental displacements are equal to the sum of the iterative displacements. This approach is illustrated in Figure 9.17 for the simple problem of a uniaxially loaded bar of nonlinear material. In principle, the iterative scheme ensures that for each solution increment the analysis satisfies all solution requirements.

A key step in this calculation process is determining the residual load vector. At the end of each iteration the current estimate of the incremental displacements is calculated and used to evaluate the incremental strains at each integration point. The constitutive model is then integrated along the incremental strain paths to obtain an estimate of the stress changes. These stress changes are added to the stresses at the beginning of the increment and used to evaluate consistent equivalent nodal forces. The difference between these forces and the externally applied loads (from the boundary conditions) gives the residual load vector. A difference arises because a constant incremental global stiffness matrix $[\boldsymbol{K}_G]^i$ is assumed over the increment. Due to the nonlinear material behaviour, $[\boldsymbol{K}_G]^i$ is not constant but varies with the incremental stress and strain changes.

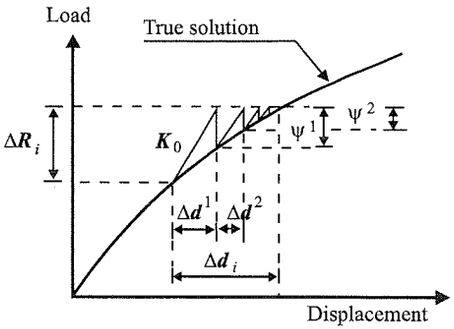

Figure 9.17: Application of the modified Newton-Raphson algorithm to the uniaxial loading of a bar of a nonlinear material

Since the constitutive behaviour changes over the increment, care must be taken when integrating the constitutive equations to obtain the stress change. Methods of performing this integration are termed *stress point algorithms* and both explicit and implicit approaches have been proposed in the literature. There are many of these algorithms in use and, as they control the accuracy of the final solution, users must verify the approach used in their software. Two of the most accurate stress point algorithms are described subsequently.

The process described above is called a Newton-Raphson scheme if the incremental global stiffness matrix $[\boldsymbol{K}_G]^i$ is recalculated and inverted for each iteration, based on the latest estimate of the stresses and strains obtained from the previous iteration. To reduce the amount of computation, the modified Newton - Raphson method only calculates and inverts the stiffness matrix at the beginning of the increment and uses it for all iterations within the increment. Sometimes the incremental global stiffness matrix is calculated using the elastic constitutive matrix, $[\boldsymbol{D}]$, rather than the elasto-plastic matrix, $[\boldsymbol{D}^{ep}]$. Clearly, there are several options here and many software packages allow the user to specify how the MNR algorithm should work. In addition, an acceleration technique is often applied during the iteration process (Thomas (1984)).

9.6.2 Stress point algorithms

9.6.2.1 Introduction

Two classes of stress point algorithms are considered. The *substepping* algorithm is essentially explicit, whereas the *return* algorithm is implicit. In both the

substepping and return algorithms, the objective is to integrate the constitutive equations along an incremental strain path. While the magnitudes of the strain increment are known, the manner in which they vary during the increment is not. It is therefore not possible to integrate the constitutive equations without making an additional assumption. Each stress point algorithm makes a different assumption and this influences the accuracy of the solution obtained.

9.6.2.2 Substepping algorithm

The schemes presented by Wissman and Hauck (1983) and Sloan (1987) are examples of substepping stress point algorithms. In this approach, the incremental strains are divided into a number of substeps. It is assumed that in each substep the strains $\{\Delta\varepsilon_{ss}\}$ are a proportion, ΔT, of the incremental strains $\{\Delta\varepsilon_{inc}\}$. This can be expressed as:

$$\{\Delta\varepsilon_{ss}\} = \Delta T \{\Delta\varepsilon_{inc}\} \tag{9.26}$$

It should be noted that in each substep, the ratio between the strain components is the same as that for the incremental strains and hence the strains are said to vary *proportionally* over the increment. The constitutive equations are then integrated numerically over each substep using either an Euler, modified Euler or Runge-Kutta scheme. The size of each substep (i.e. ΔT) can vary and, in the more sophisticated schemes, is determined by setting an error tolerance on the numerical integration. This allows control of errors resulting from the numerical integration procedure and ensures that they are negligible. Details of the substepping scheme used by the Authors are given in Appendix IX.1.

The basic assumption in these substepping approaches is therefore that the strains vary in a proportional manner over the increment. In some boundary value problems, this assumption is correct and consequently the solutions are extremely accurate. However, in general, this may not be true and an error can be introduced. The magnitude of the error is dependent on the size of the solution increment.

9.6.2.3 Return algorithm

The schemes presented by Borja and Lee (1990) and Borja (1991) are examples of one-step implicit type return algorithms. In this approach, the plastic strains over the increment are calculated from the stress conditions corresponding to the end of the increment. The problem, of course, is that these stress conditions are not known, hence the implicit nature of the scheme. Most formulations involve some form of elastic predictor to give a first estimate of the stress changes, coupled with a sophisticated iterative sub-algorithm to transfer from this stress state back to the yield surface. The objective of the iterative sub-algorithm is to ensure that, on convergence, the constitutive behaviour is satisfied, albeit with the assumption that the plastic strains over the increment are based on the plastic potential at the end of the increment. Many different iterative sub-algorithms have been proposed in the literature. In view of the Authors' previous findings, it is important that the final converged solution does not depend on quantities evaluated in illegal stress

space. In this respect some of the earlier return algorithms broke this rule and are therefore inaccurate. To simplify this procedure for modified Cam clay, Borja and Lee (1990) assumed that the elastic moduli are constant over an increment. Borja (1991) describes a more rigorous procedure that accounts for the true variation of these moduli. Analyses which make the former assumption are called *constant elasticity* return algorithms, whereas those that correctly account for changes in elastic moduli are called *variable elasticity* return algorithms. Further details of the constant elasticity return algorithm proposed by Borja and Lee (1990) are given in Appendix IX.2.

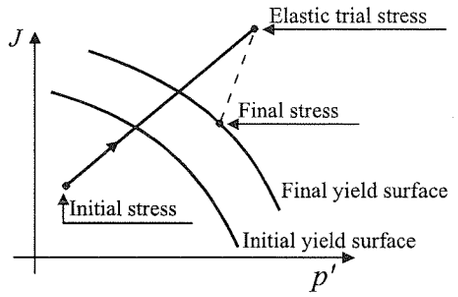

Figure 9.18: Return algorithm approach

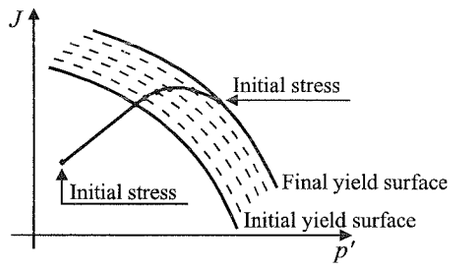

Figure 9.19: Substepping approach

The basic assumption in these approaches is therefore that the plastic strains over the increment can be calculated from the stress state at the end of the increment, as illustrated in Figure 9.18. This is theoretically incorrect as the plastic response, and in particular the plastic flow direction, is a function of the current stress state. The plastic flow direction should be consistent with the stress state at the beginning of the solution increment and should evolve as a function of the changing stress state, such that at the end of the increment it is consistent with the final stress state. This type of behaviour is exemplified by the substepping approach, as illustrated in Figure 9.19. If the plastic flow direction does not change over an increment, the return algorithm solutions are accurate. Invariably, however, this is not the case and an error is introduced. The magnitude of any error is dependent on the size of the solution increment.

9.6.2.4 Fundamental comparison

Potts and Ganendra (1994) performed a fundamental comparison of these two types of stress point algorithm and some of their results are described in Appendix IX.3. They conclude that both algorithms give accurate results, but, of the two, the substepping algorithm is better.

Another advantage of the substepping approach is that it is extremely robust and can easily deal with constitutive models in which two or more yield surfaces are active simultaneously and for which the elastic portion of the model is highly

nonlinear. In fact, most of the software required to program the algorithm is common to any constitutive model. This is not so for the return algorithm, which, although in theory can accommodate such complex constitutive models, involves some extremely complicated mathematics. The software to deal with the algorithm is also constitutive model dependent. This means considerable effort is required to include a new or modified model.

In the numerical geotechnical research group at Imperial College the tendency is, therefore, to employ the substepping approach. All examples given in both volumes of this book, that are performed using the MNR approach with ICFEP, use a modified Euler substepping algorithm, see Appendix IX.1.

9.6.3 Convergence criteria

As the MNR method involves iterations for each solution increment, convergence criteria must be set. This usually involves setting limits to the size of both the iterative displacements, $(\{\Delta \boldsymbol{d}\}^i_{nG})^j$, and the residual loads, $\{\boldsymbol{\psi}\}^j$. As both these quantities are vectors, it is normal to express their size in terms of the scalar norms:

$$\left\| \left(\{\Delta \boldsymbol{d}\}^i_{nG} \right)^j \right\| = \sqrt{\left(\left(\{\Delta \boldsymbol{d}\}^i_{nG} \right)^j \right)^{\mathrm{T}} \left(\{\Delta \boldsymbol{d}\}^i_{nG} \right)^j} \tag{9.27}$$

$$\left\| \{\boldsymbol{\psi}\}^j \right\| = \sqrt{\left(\{\boldsymbol{\psi}\}^j \right)^{\mathrm{T}} \{\boldsymbol{\psi}\}^j} \tag{9.28}$$

Often the iterative displacement norm is compared to the norms of the incremental, $\|\{\Delta \boldsymbol{d}\}^i_{nG}\|$, and accumulated, $\|\{\boldsymbol{d}\}_{nG}\|$, displacements. It should be remembered that the incremental displacements are the sum of the iterative displacements calculated for that increment so far. Likewise, the norm of the residual loads is compared to the norms of the incremental, $\|\{\Delta \boldsymbol{R}_G\}^i\|$, and accumulated, $\|\{\boldsymbol{R}_G\}\|$, global right hand side load vectors. When running the Authors' finite element code ICFEP, the convergence criteria is usually set such that the iterative displacement norm is less than 1% of both the incremental and accumulated displacement norms, and the residual load norm is less than 1-2% of both the incremental and accumulated global right hand side load vector norms. Special attention has to be given to boundary value problems which only involve displacement boundary conditions, as both the incremental and accumulated right hand side load vectors are zero.

9.6.4 Uniform compression of Mohr-Coulomb and modified Cam clay soils

The MNR method using a substepping stress point algorithm has been used to analyse the simple one dimensional oedometer problem, considered previously for both the tangent stiffness and visco-plastic approaches. Results are presented in Figures 9.20a and 9.20b for the Mohr-Coulomb and modified Cam clay soils,

respectively. To be consistent with the analyses performed with the tangent and visco-plastic algorithm, the analysis for the Mohr-Coulomb soil involved displacement increments which gave incremental strains $\Delta\varepsilon_a$=3%, whereas for the modified Cam clay analysis the increment size was equivalent to $\Delta\varepsilon_a$=1%.

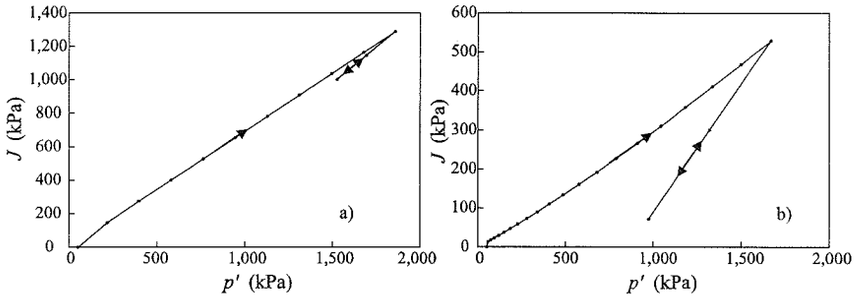

Figure 9.20: Oedometer stress paths predicted by the MNR algorithm: a) Mohr-Coulomb and b) modified Cam Clay models

The predictions are in excellent agreement with the true solution. An unload-reload loop is shown in each figure, indicating that the MNR approach can accurately deal with changes in stress path direction. For the modified Cam clay analysis it should be noted that at the beginning of the test the soil sample was normally consolidated, with an isotropic stress p' = 50kPa. The initial stress path is therefore elasto-plastic and not elastic. Consequently, it is not parallel to the unload/reload path. Additional analysis, performed with different sizes of solution increment, indicate that the predictions, for all practical purposes, are independent of increment size.

These results clearly show that, for this simple problem, the MNR approach does not suffer from the inaccuracies inherent in both the tangent stiffness and visco-plastic approaches. To investigate how the different methods perform for more complex boundary value problems, a small parametric study has been performed. The main findings of this study are presented next.

9.7 Comparison of the solution strategies

9.7.1 Introduction

A comparison of the three solution strategies presented above suggests the following. The tangent stiffness method is the simplest, but its accuracy is influenced by increment size. The accuracy of the visco-plastic approach is also influenced by increment size, if complex constitutive models are used. The MNR method is potentially the most accurate and is likely to be the least sensitive to increment size. However, considering the computer resources required for each solution increment, the MNR method is likely to be the most expensive, the tangent stiffness method the cheapest and the visco-plastic method is probably somewhere

in between. It may be possible though, to use larger and therefore fewer increments with the MNR method to obtain a similar accuracy. Thus, it is not obvious which solution strategy is the most economic for a particular solution accuracy.

All three solution algorithms have been incorporated into the single computer program, ICFEP. Consequently, much of the computer code is common to all analyses and any difference in the results can be attributed to the different solution strategies. The code has been extensively tested against available analytical solutions and with other computer codes, where applicable. The program was used to compare the relative performance of each of the three schemes in the analysis of two simple idealised laboratory tests and three more complex boundary value problems. Analyses of the laboratory tests were carried out using a single four noded isoparametric element with a single integration point, whereas eight noded isoparametric elements, with reduced integration, were employed for the analyses of the boundary value problems. These analyses were performed, some years ago, on either a Prime mini computer or a Sun workstation. The computer resources required, expressed in terms of the equivalent central processor time on a Prime 750 mini computer, are compared. It may be noted that a Sun IPX workstation is approximately 23 times faster than a Prime 750. Modern workstations are much faster than these outdated machines, however, it is the relative times that are important in the context of the present study.

As already shown, the errors in the solution algorithms are more pronounced for critical state type models than for the simpler linear elastic perfectly plastic models (i.e. Mohr-Coulomb and Tresca). Hence, in the comparative study the soil has been modelled with the modified Cam clay model. To account for the nonlinear elasticity that is present in this model, the visco-plastic algorithm was modified to incorporate an additional stress correction based on an explicit stress point algorithm, similar to that used in the MNR method, at each time step.

As both the MNR and visco-plastic algorithms involve iterations for each increment, convergence criteria must be set. This involves setting limits to the size of both the iterative displacements and out of balance loads. In the present study, convergence tolerances were set for both these quantities. However, the critical criterion turned out to be that concerning the out of balance nodal loads (i.e. the residual load vector for the MNR method and the correction vector for the visco-plastic method). In the excavation problem, which is essentially 'load controlled', a convergence criterion expressed as $\|\{\boldsymbol{\Psi}\}_{IT}\|/\|\{\Delta\boldsymbol{R}_G\}\|<1\%$ was used, where $\|\{\boldsymbol{\Psi}\}_{IT}\|$ is the norm of the out of balance iterative nodal loads and $\|\{\Delta\boldsymbol{R}_G\}\|$ is the norm of the applied incremental global right hand side load vector. For the triaxial, footing and pile problems, which are 'displacement controlled', $\|\{\Delta\boldsymbol{R}_G\}\|=0$ and therefore the magnitude of $\|\{\boldsymbol{\Psi}\}_{IT}\|$ was critical. This quantity depends on the dimensions of the problem and critical values of $0.5*10^{-3}$ and 10^{-2} were used for the footing and pile problem respectively. For the visco-plastic drained and undrained triaxial tests, 10 and 50 iterations per increment were used, whereas 10 iterations were used for the MNR drained triaxial test analyses. For the MNR undrained triaxial test analyses only one iteration was required. In all cases this resulted in $\|\{\boldsymbol{\Psi}\}_{IT}\| < 10^{-10}$. The norm of the iterative displacements was less than 1% of the norm of the incremental displacements in all analyses.

The tolerances affect both the degree of convergence and the amount of computer resources used. Parametric studies varying the number of iterations per increment were undertaken, using both the MNR and visco-plastic approaches. These studies confirmed that the values selected above were sufficient to ensure that the solution had converged, but not too severe to cause excessive use of computer resources.

9.7.2 Idealised triaxial test

Idealised drained and undrained triaxial compression tests were considered. A cylindrical sample was assumed to be isotropically normally consolidated to a mean effective stress, p', of 200kPa, with zero pore water pressure. The soil parameters used for the analyses are shown in Table 9.3.

Table 9.3: Material properties for the modified Cam clay model

Overconsolidation ratio	1.0
Specific volume at unit pressure on virgin consolidation line, v_1	1.788
Slope of virgin consolidation line in v-lnp' space, λ	0.066
Slope of swelling line in v-lnp' space, κ	0.0077
Slope of critical state line in J-p' plane, M_J	0.693
Elastic shear modulus, G / Preconsolidation pressure, p_0'	100

For drained triaxial tests, increments of compressive axial strain were applied to the sample until the axial strain reached 20%, while maintaining a constant radial stress and zero pore water pressure. The results are presented as plots of volumetric strain and deviatoric stress, q, versus axial strain. Deviatoric stress q is defined as:

$$\begin{aligned} q &= \sqrt{3}J = \sqrt{\tfrac{1}{2}[(\sigma_1'-\sigma_2')^2+(\sigma_2'-\sigma_3')^2+(\sigma_3'-\sigma_1')^2]} \\ &= \sigma_1'-\sigma_3' \quad \text{for triaxial conditions} \end{aligned} \tag{9.29}$$

For the undrained triaxial tests, increments of compressive axial strain were applied to the sample until the axial strain reached 5%, while maintaining the radial total stress constant. A high bulk compressibility of water, K_f, was introduced to ensure undrained behaviour ($=100K'_{skel}$, where K'_{skel} is the effective bulk modulus of the soil skeleton, see Section 3.4). The results are presented as plots of pore water pressure, p_f, and q versus axial strain. The label associated with each line in these plots indicates the magnitude of axial strain applied at each increment of that

analysis. The tests were deemed ideal as the end effects at the top and bottom of the sample were considered negligible and the stress and strain conditions were uniform throughout. Analytical solutions for both the drained and undrained triaxial tests are given in Appendix VII.2.

Results from the MNR drained triaxial test analyses are compared with the analytical solution in Figure 9.21. The results are not sensitive to increment size and agree well with the analytical solution. The MNR undrained triaxial test analyses matched the analytical solution and the errors were negligible, even if the analysis was carried out with just one 5% axial strain increment. Accordingly, the undrained test results are not presented graphically. In an undrained triaxial test the radial and circumferential strains are always equal to minus half of the axial strain. Consequently, all three strains vary proportionally throughout the test. Because such a variation is consistent with the main assumption of a substepping stress point algorithm (see Section 9.6.2.2), the accuracy of the MNR analysis depends only on the error tolerance controlling the number of substeps (see Appendix IX.1). In these analyses the tolerance was set low, (i.e. 0.01%), and was the same for all analyses. This explains why the MNR analyses were independent of increment size.

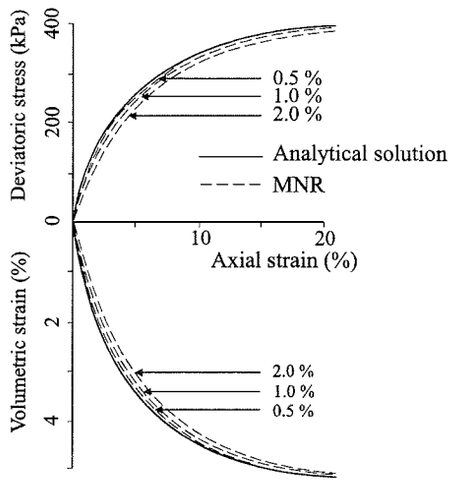

Figure 9.21: Modified Newton-Raphson: Drained triaxial test

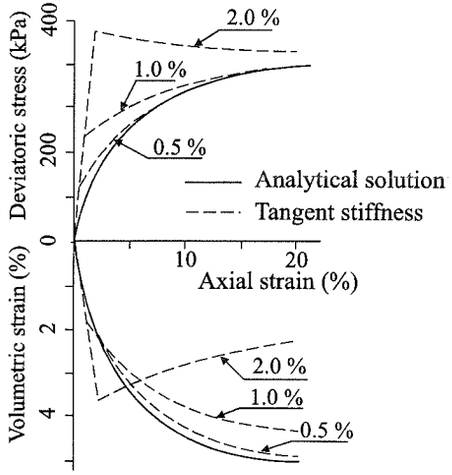

Figure 9.22: Tangent stiffness: Drained triaxial test

The tangent stiffness results are presented in Figure 9.22 for the drained test and Figure 9.23 for the undrained test. The results of both tests are sensitive to increment size, giving very large errors for the larger increment sizes. In both tests, q at failure (20% and 5% axial strain for the drained and undrained tests

respectively) is over predicted. Figure 9.24 is a plot of p' versus q for the undrained triaxial tests. The analysis with an increment size of 0.5% axial strain gave unrealistic results, predicting an increase in p' and a value of q at failure over twice as large as the analytical solution. The analyses with smaller increment sizes gave better results.

The results of the visco-plastic undrained and drained triaxial test analyses are shown in Figures 9.25 and 9.26 respectively. Inspection of these figures indicates that the solution is also sensitive to increment size. Even the results from the analyses with the smallest increment size of 0.1%, for the drained test, and 0.025%, for the undrained test, are in considerable error.

It is of interest to note that results from the tangent stiffness analyses over predict the deviatoric stress at any particular value of axial strain for both drained and undrained tests. The opposite is true for the visco-plastic analysis, where q is under predicted in all cases. This is similar to the observations made earlier for the simple oedometer test.

Values of deviatoric stress, q, volumetric strain at failure (20% axial strain), and central processor unit (CPU) times are shown in Table 9.4 for selected drained triaxial test analyses. Similarly, values of q, pore water pressure, p_f, mean effective stress, p', at failure (5% axial strain) and CPU times are given in Table 9.5 for selected undrained triaxial test analyses. The numbers in parentheses are the errors expressed as a percentage of the analytical solution.

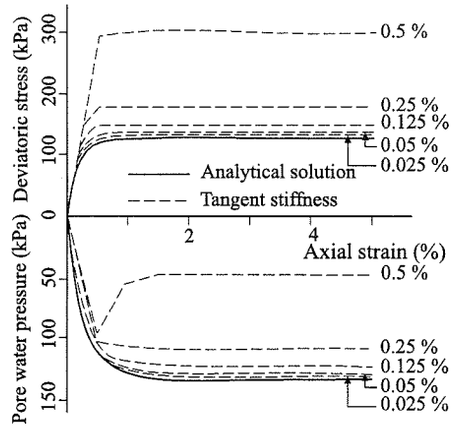

Figure 9.23: Tangent stiffness: Undrained triaxial test

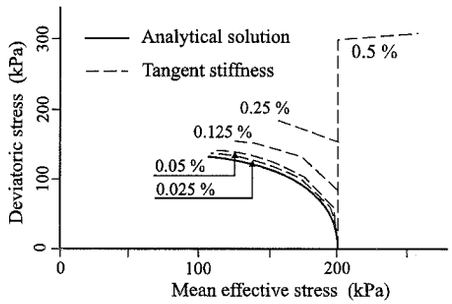

Figure 9.24: Tangent stiffness: Undrained stress paths

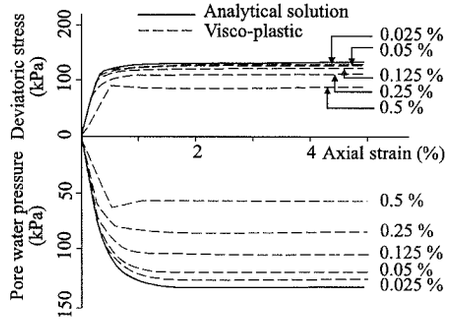

Figure 9.25: Visco-plastic: Undrained triaxial test

The size of the axial strain increment used is indicated after the analysis type.

For small increment sizes the visco-plastic analyses tend to yield results which are less accurate than the corresponding tangent stiffness analysis, even though the former method requires more computer resources than the later. Close inspection of the results indicates that the reason for the lack of accuracy of the visco-plastic method is the use of the elasto-plastic equations at illegal stress states outside the yield surface, as explained earlier in this chapter. This results in failure to satisfy the constitutive equations, see Section 9.5.6. The MNR approach is more accurate and less dependent on increment size than the other methods.

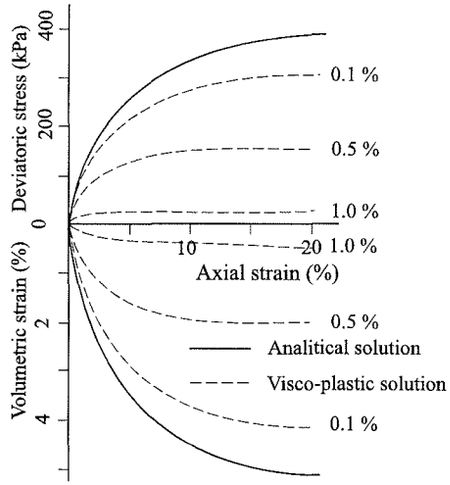

Figure 9.26: Visco-plastic: Drained triaxial test

Table 9.4: Results and CPU times for selected drained triaxial test analyses

ANALYSIS TYPE Increment size	q kPa	VOLUMETRIC STRAIN %	CPU sec
Analytical	390.1	5.18	
MNR, 2%	382.5 (-2.0%)	5.08 (-1.8%)	147
Tangent stiffness, 0.5%	387.5 (-0.6%)	5.00 (-3.4%)	88
Visco-plastic, 0.5%	156.2 (-60.0%)	2.05 (-60.4%)	204
Visco-plastic, 0.1%	275.2 (-29.4%)	3.76 (-27.4%)	701

Table 9.5: Results and CPU times for selected undrained triaxial test analyses

ANALYSIS TYPE Increment size	q kPa	p_f kPa	p' kPa	CPU sec
Analytical	130.1	134.8	108.6	
MNR, 5%	130.3 (0.1%)	134.82 (0.0%)	108.6 (0.0%)	85
Tangent stiffness, 0.025%	133.9 (2.9%)	133.08 (-1.2%)	111.5 (2.4%)	195
Visco-plastic, 0.025%	128.31 (-1.4%)	123.22 (-8.6%)	119.5 (10.0%)	774
Visco-plastic, 0.05%	127.2 (-2.2%)	113.35 (-15.9%)	128.2 (18.0%)	305

9.7.3 Footing problem

A smooth rigid strip footing subjected to vertical loading, as depicted in Figure 9.27, has been analysed. The same soil constitutive model and parameters as used for the idealised triaxial test analyses, see Table 9.3, have been employed to model the soil which, in this case, was assumed to behave undrained. The finite element mesh is shown in Figure 9.28. Note that due to symmetry about the vertical line through the centre of the footing, only half of the problem needs to be considered in the finite element analysis. Plane strain conditions are assumed. Before loading the footing, the coefficient of earth pressure at rest, K_o, was assumed to be unity and the vertical effective stress and pore water pressure were calculated using a saturated bulk unit weight of the soil of 20 kN/m^3 and a static water table at the ground surface. The footing was loaded by applying a series of equally sized increments of vertical displacement until the total displacement was 25mm.

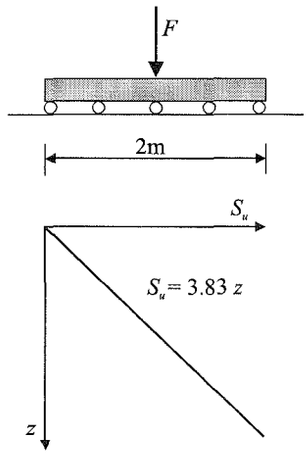

Figure 9.27: Geometry of footing

The load-displacement curves for the tangent stiffness, visco-plastic and MNR analyses are presented in Figure 9.29. For the MNR method, analyses were performed using 1, 2, 5, 10, 25, 50 and 500 increments to reach a footing settlement of 25mm. With the exception of the analysis performed with only a

single increment, all analyses gave very similar results and plot as a single curve, marked MNR on this figure. The MNR results are therefore insensitive to increment size and show a well defined collapse load of 2.8 kN/m.

For the tangent stiffness approach, analyses using 25, 50, 100, 200, 500 and 1000 increments have been carried out. Analyses with a smaller number of increments were also attempted, but illegal stresses (negative mean effective stresses, p') were predicted. As the constitutive model is not defined for such stresses, the analyses had to be aborted. Some finite element packages overcome this problem by arbitrarily resetting the offending negative p' values. There is no theoretical basis for this and it leads to violation of both the equilibrium and the constitutive conditions. Although such adjustments enable an analysis to be completed, the final solution is in error.

Results from the tangent stiffness analyses are shown in Figure 9.29. When plotted, the curve from the analysis with 1000 increments is indistinguishable from those of the MNR analyses. The tangent stiffness results are strongly influenced by increment size, with the ultimate footing load decreasing from 7.5 kN/m to 2.8 kN/m with reduction in the size of the applied displacement increment. There is also a tendency for the load-displacement curve to continue to

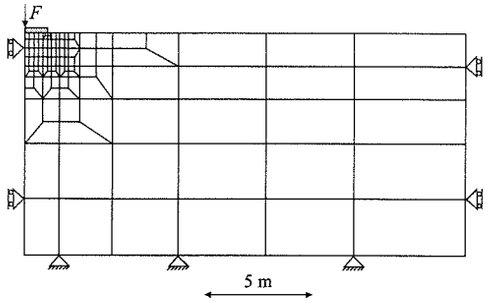

Figure 9.28: Finite element mesh for footing analyses

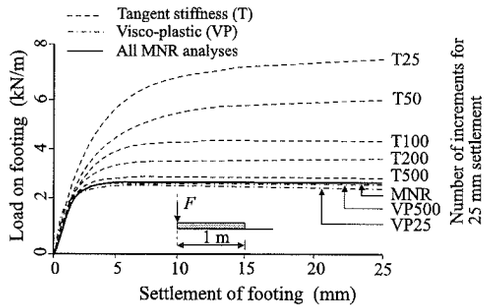

Figure 9.29: Footing load-displacement curves

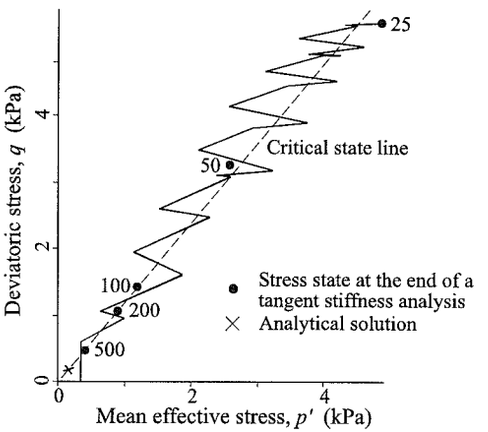

Figure 9.30: Stress paths under the edge of footing

rise and not reach a well defined ultimate failure load for the analysis with large applied displacement increments. The results are unconservative, over predicting the ultimate footing load. There is also no indication from the shape of the tangent stiffness load-displacement curves as to whether the solution is accurate, since all the curves have similar shapes.

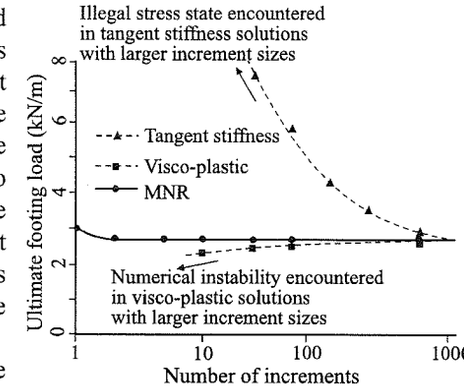

Figure 9.31: Ultimate footing load against number of increments

The plot of p' versus q for the Gauss point closest to the corner of the footing is shown in Figure 9.30. A line connecting the stress states at the end of each increment of the 25 increment tangent stiffness analysis is presented. The analytical failure point for this Gauss point is marked by an 'X'. The stress state at the end of all the MNR analyses and the 1000 increment tangent stiffness analysis match this point. The stress states at the end of the other tangent stiffness analyses are also plotted and the label associated with each point is the number of increments used in the analysis. The values of p' and q are over predicted by the tangent stiffness analyses using less than 1000 increments. For the 25 increment tangent stiffness analysis they are over predicted by more than twenty times.

Visco-plastic analyses with 10, 25, 50, 100 and 500 increments were performed. The 10 increment analysis had convergence problems in the iteration process, which would initially converge, but then diverge. Similar behaviour was encountered for analyses using still fewer increments. Results from the analyses with 25 and 500 increments are shown in Figure 9.29. The solutions are sensitive to increment size, but to a lesser degree than the tangent stiffness approach.

The load on the footing at a settlement of 25mm is plotted against number of increments, for all tangent stiffness, visco-plastic and MNR analyses, in Figure 9.31. The insensitivity of the MNR analyses to increment size is clearly shown. In these analyses the ultimate footing load only changed from 2.83 kN/m to 2.79 kN/m as the number of increments increased from 2 to 500. Even for the MNR analyses performed with a single increment, the resulting ultimate footing load of 3.13 kN/m is still reasonable and is more accurate than the value of 3.67 kN/m obtained from the tangent stiffness analysis with 200 increments. Both the tangent stiffness and visco-plastic analyses produce ultimate failure loads which approach 2.79 kN/m as the number of increments increase. However, tangent stiffness analyses approach this value from above and therefore over predict, while visco-plastic analyses approach this value from below and therefore under predict. This trend is consistent with the results from the undrained triaxial tests, where the ultimate value of q was over predicted by the tangent stiffness and under predicted

by the visco-plastic approach. The CPU times and results for selected analyses are shown in Table 9.6.

Table 9.6: CPU times and failure loads for the footing analyses

SOLUTION TYPE	NUMBER OF INCREMENTS	CPU TIME sec	COLLAPSE LOAD kN
MNR	10	15345	2.82
Tangent stiffness	500	52609	3.01
Tangent stiffness	1000	111780	2.82
Visco-plastic	25	70957	2.60
Visco-plastic	500	1404136	2.75

It can be shown that, for the material properties and initial stress conditions adopted, the undrained strength of the soil, S_u, varies linearly with depth below the ground surface (see Figure 9.27 and Appendix VII.4). Davies and Booker (1973) provide approximate solutions for the bearing capacity of footings on soils with such an undrained strength profile. For the present situation their charts give a collapse load of 1.91 kN/m and it can be seen (Figure 9.31) that all the finite element predictions exceed this value. This occurs because the analytical failure zone is very localised near the soil surface. Further analyses have been carried out using a refined mesh in which the thickness of the elements immediately below the footing has been reduced from 0.1m to 0.03m. The MNR analyses with this mesh predict an ultimate load of 2.1 kN/m. Clearly, if the mesh is further refined the Davies and Booker solution will be recovered. For this refined mesh even smaller applied displacement increment sizes were required for the tangent stiffness analyses to obtain an accurate solution. Analyses with an increment size of 0.125mm displacement (equivalent to the analysis with 200 increments described above) or greater, yielded negative values of p' in the elements below the corner of the footing and therefore these analyses could not be completed. The negative p' values occur because the amplitude of the oscillations in the stress path about the critical state line, see Figure 9.30, is further increased due to the refined mesh.

9.7.4 Excavation problem

A 3m deep undrained excavation in modified Cam clay soil has been analysed. The excavation was assumed to be very long and consequently plane strain conditions were adopted. The soil properties are shown in Table 9.7, the geometry of the problem in Figure 9.32 and the finite element mesh in Figure 9.33. The *OCR* profile was obtained by assuming the soil had undergone 25 kPa vertical effective

stress relief. The at rest earth pressure coefficient, K_o, was obtained by using the equation:

$$K_o^{OC} = K_o^{NC}\, OCR^{\sin\varphi'} \tag{9.30}$$

where φ' is the angle of shearing resistance.

Table 9.7: Material properties for the excavation problem

Specific volume at unit pressure on the VCL, v_1	2.427
Slope of virgin consolidation line in v-lnp' space, λ	0.15
Slope of swelling line in v-lnp' space, κ	0.03
Slope of critical state line in J-p' plane, M_J	0.5
Poisson's ratio, μ	0.3
Saturated bulk unit weight, γ_{sat}	17.3 kN/m^3
Vertical effective stress, σ_v' where z = the depth from original ground surface	7.5z kN/m^3
Horizontal effective stress, σ_h'	$\sigma_v'\, K_o^{OC}$
Overconsolidated coefficient of earth pressure at rest, K_o^{OC}	$K_o^{NC}\, OCR^{0.5236}$
Normally consolidated coefficient of earth pressure at rest	$K_o^{NC} = 0.63$
Overconsolidation ratio, *OCR*	$1 + 3.333/z$
Pore water pressure, p_f	9.8z kN/m^2

For all three solution methods analyses have been performed using 1, 2, 3, 6, 12, 30, 60, 120 and 600 equally sized increments to excavate to a depth of 3m. In addition, a tangent stiffness analysis with 1200 increments has been completed. An elastic stiffness matrix was used for the MNR analyses, see Section 9.6. Results from the analyses with six increments and above are presented in Figure 9.34 as plots of vertical displacement, U, at the crest of the excavation, versus depth of excavation, d. The results from the MNR and visco-plastic analyses are not sensitive to increment size and both methods produce results which plot very near to the solid curve indicated on this figure. Results from the tangent stiffness analyses with 600 and 1200

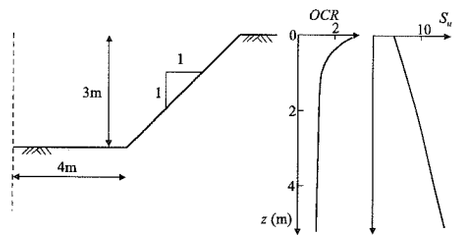

Figure 9.32: Geometry of excavation problem

increments also plot near to this curve. The tangent stiffness results are strongly influenced by the number of increments and the 120 increment analysis had displacements over 2.5 times larger than that of the 6 increment analysis.

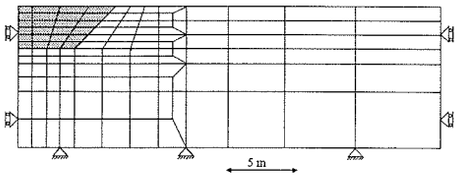

Figure 9.33: Finite element mesh for excavation problem

The final value of the vertical displacement, U, (i.e. at the end of excavation) is plotted against number of increments used in the analysis in Figure 9.35. As the number of increments increases, all methods predict a displacement, U, approaching 63.3mm and therefore this value may be taken as being 'correct'. It is evident from Figure 9.35 that for any increment size the MNR and visco-plastic analyses produce more accurate results than the tangent stiffness analysis. The latter approach requires in excess of 100 increments before acceptable results are obtained.

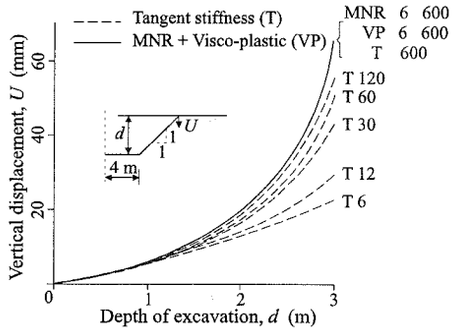

Figure 9.34: Settlement of excavation crest against the depth of excavation

The accuracy of each analysis can be expressed by the error in the prediction of the final value of the displacement, U. This error can be written as:

$$Error = \frac{\delta - \delta_{correct}}{\delta_{correct}} \qquad (9.31)$$

where δ is the predicted value of the displacement U at the end of excavation and $\delta_{correct}$ is the correct value which equals 63.3mm. Values of this error are plotted against CPU time for all analyses in Figure 9.36. As expected, the error reduces as the CPU time increases for all three solution methods. The tangent stiffness method takes substantially more CPU time for a similar solution accuracy. For example, the 120 increment tangent stiffness analysis gives results which are similar to the 6 increment MNR analysis, but takes approximately 4 times as long to perform.

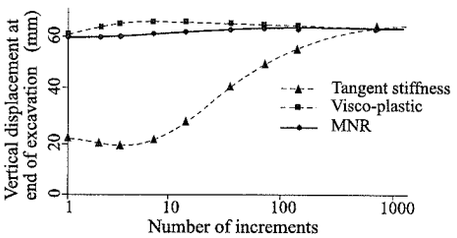

Figure 9.35: Settlement of excavation crest against number of increments

9.7.5 Pile problem

The problem of the mobilisation of the stresses in the soil immediately adjacent to a pile shaft during drained loading is considered. The behaviour of a segment of an incompressible 2m diameter pile, well away from the influence of the soil surface and pile tip, is examined (see Figure 9.37). This boundary value problem has been discussed in detail by Potts and Martins (1982) and the alternative methods of representing the problem in finite element analysis have been explored by Gens and Potts (1984). The soil is assumed to be normally consolidated, with initial stresses $\sigma_v'=\sigma_h'=200$ kPa. The parameters for the modified Cam clay model are the same as used for the triaxial test and footing problem and are given in Table 9.3. Axi-symmetric conditions are applicable to this problem and the finite element mesh is shown in Figure 9.37. Loading of the pile has been simulated in the finite element analyses by imposing a series of equal sized increments of vertical displacement to the pile shaft to give a total displacement of 100mm. The soil was assumed to behave in a drained manner throughout.

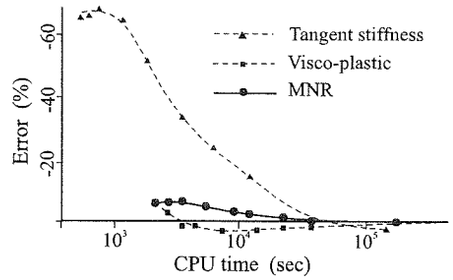

Figure 9.36: Error in excavation analysis against CPU time

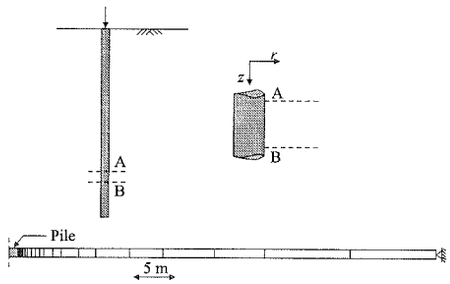

Figure 9.37: Geometry and finite element mesh for pile problem

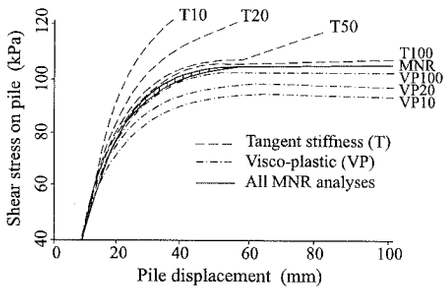

Figure 9.38: Mobilised pile shaft resistance against pile displacement

Results from analyses using all three solution strategies and with varying numbers of increments are presented in Figure 9.38, in the form of mobilised shaft resistance, τ, against vertical pile displacement. The MNR analyses with 20 increments and above plot as a single curve on this figure and are represented by the upper solid line. MNR analyses with smaller numbers of increments (i.e. with larger applied displacement increments) showed minor differences with the above results between pile displacements of 25mm and 55mm. The MNR analysis with 5 increments is shown by the lower

solid line in the figure. The spread of results between the MNR analyses with 5 and 20 increments is therefore given by the shaded band. Because this band is small it may be concluded that, as with the triaxial tests and footing and excavation problems, the MNR results are insensitive to increment size.

Results from some of the tangent stiffness and visco-plastic analyses are also shown on Figure 9.38. If small increments of applied displacement (large number of increments) are used, both these solution strategies give results which approach those of the MNR analyses. However, analyses using both these approaches are sensitive to increment size and analyses with larger increments of applied displacement are inaccurate. The tangent stiffness over predicts and the visco-plastic under predicts the mobilised shaft resistance for any given pile displacement. The visco-plastic analyses predict that the mobilised pile shaft resistance increases to a peak value and then slowly reduces with further pile displacement. This behaviour is not predicted by the MNR analyses which show that once the maximum shaft resistance is mobilised it remains constant. For the tangent stiffness analyses with less than 100 increments the mobilised pile shaft resistance continually climbs and no peak value is indicated.

Values of the mobilised pile shaft resistance, τ_f, at a pile displacement of 100mm (the end point on the curves in Figure 9.38) are plotted against number of increments used in Figure 9.39. As noted above, the MNR results are insensitive to increment size, with τ_f only increasing from 102.44 kPa to 103.57 kPa as the number of increments increases from 1 to 500. The results from the tangent stiffness and visco-plastic analyses are much more dependent on the size of the applied displacement increment and over 100 increments for the tangent stiffness and 500 increments for the visco-plastic analyses are needed to give reasonably accurate results.

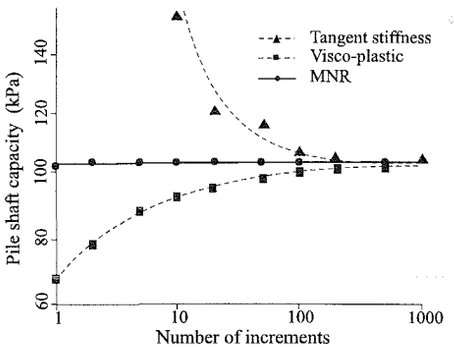

Figure 9.39: Pile shaft capacity against number of increments

As both the tangent stiffness and visco-plastic solutions approach those of the MNR when the applied displacement increment reduces, the 500 increment MNR analysis may be assumed 'correct'. The error in any analysis may therefore be expressed as:

$$Error = \frac{\tau^f - 103.6}{103.6} \qquad (9.32)$$

where τ_f for the 500 increment MNR analysis equals 103.6 kPa. This error is plotted against CPU time in Figure 9.40 for all analyses. The results clearly show that as well as being the least accurate, the visco-plastic analyses are also the most

expensive in terms of CPU time consumed. As the MNR analyses give accurate solutions with small error values, typically less than 0.2%, the results plot on the CPU time axis in this figure. These CPU times compare favourably with those of the tangent stiffness analyses.

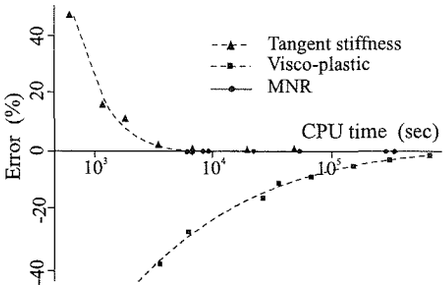

Figure 9.40: Error in pile analysis against CPU time

The relatively bad performance of the visco-plastic strategy should be noted. This contrasts to its better performance for the footing and excavation problems. However, both these problems involved undrained soil behaviour, whereas for the pile problem the soil is assumed to remain drained. The results from the triaxial tests also indicate that the relative performance of the visco-plastic strategy is worse for drained than undrained tests, see Figures 9.25 and 9.26. It may be concluded that for the analyses with the modified Cam clay model the visco-plastic approach is likely to be better behaved and less sensitive to the size of the solution increment when soil behaviour is undrained than when the soil is drained.

9.7.6 Comments

Results from the tangent stiffness analyses of both the idealised triaxial tests and the more complex boundary value problems are strongly dependent on increment size. The error associated with the tangent stiffness analyses usually results in unconservative predictions of failure loads and displacements in most geotechnical problems. For the footing problem large over predictions of failure loads are obtained, unless a very large number of increments ($\geq$1000) are employed. Inaccurate analyses based on too large an increment size produced ostensible plausible load displacement curves. Analytical solutions are not available for most problems requiring a finite element analysis. Therefore it is difficult to judge whether a tangent stiffness analysis is accurate on the basis of its results. Several analyses must be carried out using different increment sizes to establish the likely accuracy of any predictions. This could be a very costly exercise, especially if there was little experience in the problem being analysed and no indication of the optimum increment size.

Results from the visco-plastic analyses are also dependent on increment size. For boundary value problems involving undrained soil behaviour these analyses were more accurate then tangent stiffness analyses with the same increment size. However, if soil behaviour was drained, visco-plastic analyses were only accurate if many small solution increments were used. In general, the visco-plastic analyses used more computer resources than both the tangent stiffness and MNR approaches. For the triaxial tests, footing and pile problems, the visco-plastic

analyses under predicted failure loads if insufficient increments were used and were therefore conservative in this context.

For both the tangent stiffness and visco-plastic analyses the number of increments to obtain an accurate solution is problem dependent. For example, for the footing problem the tangent stiffness approach required over 1000 increments and the visco-plastic method over 500 increments, whereas for the excavation problem the former required only 100 and the later 10 increments. Close inspection of the results from the visco-plastic and tangent stiffness analyses indicated that a major reason for their poor performance was their failure to satisfy the constitutive laws. This problem is largely eliminated in the MNR approach, where a much tighter constraint on the constitutive conditions is enforced.

The results from the MNR analyses are accurate and essentially independent of increment size. For the boundary value problems considered, the tangent stiffness method required considerably more CPU time than the MNR method to obtain results of similar accuracy, e.g. over seven times more for the foundation problem and over three and a half times more for the excavation problem. Similar comparisons can be found between the MNR and visco-plastic solutions. Thus not withstanding the potentially very large computer resources required to find the optimum tangent stiffness or visco-plastic increment size, the tangent stiffness or visco-plastic method with an optimum increment size is still likely to require more computer resources than an MNR analysis of the same accuracy. Though it may be possible to obtain tangent stiffness or visco-plastic results using less computer resources than with the MNR approach, this is usually at the expense of the accuracy of the results. Alternatively, for a given amount of computing resources, a MNR analysis produces a more accurate solution than either the tangent stiffness or visco-plastic approaches.

The study has shown that the MNR method appears to be the most efficient solution strategy for obtaining an accurate solution to problems using critical state type constitutive models for soil behaviour. The large errors in the results from the tangent stiffness and visco-plastic algorithms in the present study emphasise the importance of checking the sensitivity of the results of any finite element analysis to increment size.

9.8 Summary

1. For finite element analysis involving nonlinear material behaviour, the loading history must be divided into a number of solution increments and a separate finite element solution obtained for each increment. The final solution is the sum of the incremental solutions.
2. Even though the analysis is split into increments, care must still be taken because the incremental global stiffness matrix is not constant but varies during the increment. There is no universally accepted way of dealing with this and therefore several different algorithms exist.

3. The tangent stiffness, visco-plastic and modified Newton-Raphson (MNR) algorithms have been considered in this chapter.
4. It has been shown that for all nonlinear materials the tangent stiffness approach can lead to large errors unless a large number of small solution increments are used. Particular care must be taken if there is a change between loading and unloading. Large errors occur if the constitutive model is of the critical state type.
5. The visco-plastic algorithm works well for simple linear elastic perfectly plastic models of the Tresca and Mohr-Coulomb type. However, for the more complex hardening/softening critical state type models large errors can arise. These errors are particularly severe in drained boundary value problems.
6. The errors in both the tangent stiffness and visco-plastic solutions have been shown to arise because the plastic potential derivatives are evaluated at illegal stress states. This is theoretically incorrect. It also leads to the scenario where different pieces of software, which purport to use the same basic equations for a particular constitutive model, can give very different solutions depending on the finer details of the models implementation.
7. The MNR method has been shown to be free of the errors involved in the other two methods. It produces solutions which are both accurate and reasonably insensitive to the size of the solution increments.
8. The success of the MNR method depends very much on the accuracy of the stress point algorithm. It is essential that this algorithm does not use information evaluated in illegal stress space to formulate the final solution.
9. Two classes of stress point algorithm were described, namely substepping and return algorithms. Of these two, the substepping algorithms appear to be more robust, user friendly and accurate.
10. Any finite element solutions presented in the remainder of this volume and Volume 2 of this book are based on the MNR method, with a substepping stress point algorithm.

Appendix IX.1: Substepping stress point algorithm

IX.1.1 Introduction

As noted in Section 9.6, a key step in the modified Newton-Raphson solution strategy is the determination of the residual load vector for each iteration. To calculate this load vector it is necessary to determine the accumulated stress state at the end of the previous iteration. This is done by calculating the incremental strains at each integration point from the incremental displacements determined at the end of the previous iteration, and then integrating the constitutive model along these strain paths to obtain an estimate of the stress changes. These stress changes are then added to the accumulated stresses associated with the beginning of the increment. As discussed in Section 9.6, several stress point algorithms are available for integrating the constitutive model along the incremental strain paths. In this appendix a substepping algorithm is described. For presentation purposes a linear

elastic strain hardening/softening plastic constitutive model is assumed. However, a similar procedure can be applied if the elastic behaviour is nonlinear and/or if the plasticity is work hardening/softening.

IX.1.2 Overview

Having determined the incremental strains, $\{\Delta\varepsilon\}$, for each integration point, the objective of the stress point algorithm is to evaluate the associated incremental stresses. Initially, the material is assumed to behave elastically and estimates of the incremental stresses are determined by integrating the elastic constitutive matrix $[\boldsymbol{D}]$ along the incremental strains for each integration point. As linear elasticity is assumed, the matrix $[\boldsymbol{D}]$ is constant and the stress increments are given by:

$$\{\Delta\sigma\} = [\boldsymbol{D}]\{\Delta\varepsilon\} \qquad \text{(IX.1)}$$

These stress increments are then added to the accumulated stresses at the beginning of the increment, $\{\sigma_o\}$, to obtain an estimate of the accumulated stress state, $\{\sigma\}$, at the end:

$$\{\sigma\} = \{\sigma_o\} + \{\Delta\sigma\} \qquad \text{(IX.2)}$$

The yield function is now checked to see whether or not this stress state is acceptable. If $F(\{\sigma\},\{k\})\leq 0$ behaviour is elastic and the elastic stress increment $\{\Delta\sigma\}$ is correct. The next integration point can then be considered. However, if $F(\{\sigma\},\{k\})>0$ plastic yielding is indicated and $\{\Delta\sigma\}$ is incorrect. A typical situation in which the stress state is elastic at the beginning of the increment, i.e. $F(\{\sigma_o\},\{k\})<0$, but violates yield at the end, is shown schematically in Figure IX.1. It is then necessary to determine the portion of the stress increment $\{\Delta\sigma\}$ (and therefore $\{\Delta\varepsilon\}$) that lies within the yield surface (i.e. the part AB). This can be expressed mathematically as finding the value of α that satisfies the following equation:

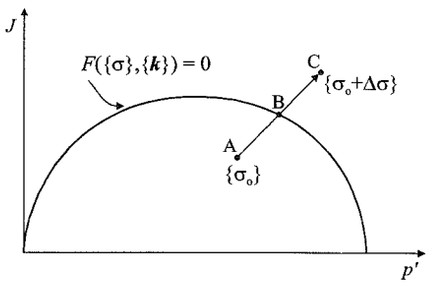

Figure IX.1: Change from elastic to elasto-plastic behaviour

$$F(\{\sigma_o + \alpha\,\Delta\sigma\},\{k\}) = 0 \qquad \text{(IX.3)}$$

where α is a scalar. A first guess for α may be obtained by a simple linear interpolation of the yield function values $F(\{\sigma\},\{k\})$, which gives:

$$\alpha = \frac{F(\{\sigma_o + \alpha\,\Delta\sigma\},\{k\})}{F(\{\sigma_o + \alpha\,\Delta\sigma\},\{k\}) - F(\{\sigma_o\},\{k\})} \qquad \text{(IX.4)}$$

This is theoretically correct if $F(\{\sigma\},\{k\})$ is a linear function of stress.

However, this is rarely the case, see Chapters 7 and 8, and consequently a more refined estimate for α is required, which involves some form of iterative scheme. This can be based on a Newton-Raphson or secant iteration approach. The latter approach can be expressed by the following equation:

$$\alpha_{i+1} = \alpha_i - \frac{F(\{\sigma_o + \alpha_i\,\Delta\sigma\},\{k\})}{F(\{\sigma_o + \alpha_i\,\Delta\sigma\},\{k\}) - F(\{\sigma_o + \alpha_{i-1}\,\Delta\sigma\},\{k\})}(\alpha_i - \alpha_{i-1}) \qquad \text{(IX.5)}$$

where $\alpha_o = 0$ and $\alpha_1 = 1$. The Authors have found such an algorithm, albeit in a slightly modified form, to be both accurate and efficient.

Ambiguity can arise if the situation exists where the stress state at the beginning of the increment is at yield, i.e. $F(\{\sigma_o\},\{k\})=0$, and at the end of the increment exceeds yield, i.e. $F(\{\sigma_o+\Delta\sigma\},\{k\})>0$. Two cases are possible and these are shown schematically in Figures IX.2 and IX.3. In the first case, Figure IX.2, behaviour is elasto-plastic over the entire stress increment and $\alpha=0$. In the second case, Figure IX.3, the stress state initially unloads, becoming elastic, i.e. moves inside the yield surface. With further straining it becomes elasto-plastic and α is therefore not zero. To distinguish between these two cases it is necessary to calculate:

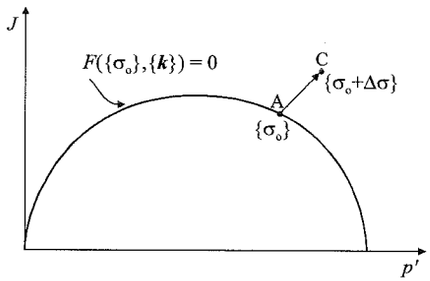

Figure IX.2: Initial stress state at yield, α = 0

$$\frac{\partial F(\{\sigma_o\},\{k\})}{\partial\sigma}\Delta\sigma$$

If this quantity is positive, the case shown in Figure IX.2 exists and $\alpha = 0$. If it is negative, the case shown in Figure IX.3 exists and care must be exercised to ensure that the correct value of α is obtained. This can be done by identifying a stress state inside the yield surface, somewhere along the elastic path AB, and using this and the stress state at the end of the increment as the initial conditions for the secant iteration algorithm, see Equation (IX.5).

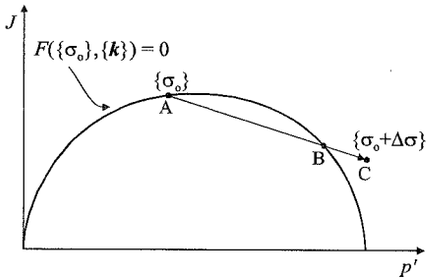

Figure IX.3: Initial stress state at yield, α ≠ 0

Having determined α, the purely elastic portions of the stress and strain increments can be evaluated as:

$$\{\Delta\sigma^e\} = \alpha\,\{\Delta\sigma\} \qquad \text{(IX.6)}$$

$$\{\Delta\varepsilon^e\} = \alpha\,\{\Delta\varepsilon\} \qquad \text{(IX.7)}$$

The portion of the strain increment that remains, i.e. $(1-\alpha)\{\Delta\varepsilon\}$, is associated with elasto-plastic behaviour and it is therefore necessary to integrate the elasto-plastic constitutive matrix $[\boldsymbol{D}^{ep}]$ over this part of the strain increment. For most constitutive models this cannot be performed analytically and some form of approximation is required. In the substepping approach the strain increment $(1-\alpha)\{\Delta\varepsilon\}$ is split into smaller substeps and various simplifications introduced. The size of the substeps can be controlled by estimating the error involved in the simplifications. Usually an Euler, modified Euler or Runge-Kutta scheme is used. As an example, a modified Euler scheme with error control is described below.

IX.1.3 Modified Euler integration scheme with error control

The objective of this approach is to integrate the elasto-plastic constitutive matrix $[\boldsymbol{D}^{ep}]$ over the elasto-plastic strain step $(1-\alpha)\{\Delta\varepsilon\}$. The scheme involves splitting the strain step $(1-\alpha)\{\Delta\varepsilon\}$ into a series of smaller substeps, $\Delta T(1-\alpha)\{\Delta\varepsilon\}$ (where $0<\Delta T\leq 1$), and using a modified Euler approximation for each such substep. The size of each substep is determined by estimating the error in the stress changes and comparing this with a user-defined tolerance, *SSTOL*. The scheme described below is based on that presented by Sloan (1987) and consists of the following essential steps.

i) Initialise parameters:

$$\{\sigma\} = \{\sigma_o\} + \{\Delta\sigma^e\} \tag{IX.8}$$

$$\{\Delta\varepsilon_s\} = (1-\alpha)\ \{\Delta\varepsilon\} \tag{IX.9}$$

$$T = 0 \tag{IX.10}$$

$$\Delta T = 1 \tag{IX.11}$$

The procedure begins by assuming that only one substep is necessary. Consequently ΔT is set to unity.

ii) Set the substep strain equal to:

$$\{\Delta\varepsilon_{ss}\} = \Delta T\ \{\Delta\varepsilon_s\} \tag{IX.12}$$

and calculate a first estimate of the associated stress and hardening/softening parameter changes using a first order Euler approximation, namely:

$$\{\Delta\sigma_1\} = [\boldsymbol{D}^{ep}(\{\sigma\},\{\boldsymbol{k}\})]\ \{\Delta\varepsilon_{ss}\} \tag{IX.13}$$

$$\{\Delta\varepsilon_1^p\} = \Lambda(\{\sigma\},\{\boldsymbol{k}\},\{\Delta\varepsilon_{ss}\})\frac{\partial P(\{\sigma\},\{\boldsymbol{m}_1\})}{\partial\sigma} \tag{IX.14}$$

$$\{\Delta\boldsymbol{k}_1\} = \{\Delta\boldsymbol{k}(\{\Delta\varepsilon_1^p\})\} \tag{IX.15}$$

iii) Using the above quantities the stresses and hardening/softening parameters at the end of the substep are $\{\sigma\}+\{\Delta\sigma_1\}$ and $\{\boldsymbol{k}\}+\{\Delta\boldsymbol{k}_1\}$ respectively. These are then used to calculate a second estimate for the changes in stress and hardening/softening parameters over the substep, namely:

$$\{\Delta\sigma_2\} = [\boldsymbol{D}^{ep}(\{\sigma+\Delta\sigma_1\},\{\boldsymbol{k}+\Delta\boldsymbol{k}_1\})]\ \{\Delta\varepsilon_{ss}\} \tag{IX.16}$$

$$\{\Delta\varepsilon_2^p\} = \Lambda(\{\sigma+\Delta\sigma_1\},\{\boldsymbol{k}+\Delta\boldsymbol{k}_1\},\{\Delta\varepsilon_{ss}\})\frac{\partial P(\{\sigma+\Delta\sigma_1\},\{\boldsymbol{m}_2\})}{\partial\sigma} \tag{IX.17}$$

$$\{\Delta\boldsymbol{k}_2\} = \{\Delta\boldsymbol{k}(\{\Delta\varepsilon_2^p\})\} \tag{IX.18}$$

iv) It is now possible to obtain a more accurate modified Euler estimate of the changes in stress, plastic strain and hardening/softening parameters as:

$$\{\Delta\sigma\} = \tfrac{1}{2}(\{\Delta\sigma_1\}+\{\Delta\sigma_2\}) \tag{IX.19}$$

$$\{\Delta\varepsilon^p\} = \tfrac{1}{2}(\{\Delta\varepsilon_1^p\}+\{\Delta\varepsilon_2^p\}) \tag{IX.20}$$

$$\{\Delta\boldsymbol{k}\} = \tfrac{1}{2}(\{\Delta\boldsymbol{k}_1\}+\{\Delta\boldsymbol{k}_2\}) \tag{IX.21}$$

v) For a given substep strain increment $\{\Delta\boldsymbol{\varepsilon}_{ss}\}$, the Euler estimates (i.e. Equations (IX.13) to (IX.15)) have a local truncation error of order $O(\Delta T^2)$, whereas the local error in the modified Euler estimates (i.e. Equations (IX.19) to (IX.21)) is of the order $O(\Delta T^3)$. Thus subtracting Equation (IX.13) from Equation (IX.19) gives an estimate of the local error in stress as:

$$E \approx \tfrac{1}{2}(\{\Delta\sigma_2\}-\{\Delta\sigma_1\}) \tag{IX.22}$$

The relative error in stress for the substep can then be expressed as:

$$R = \frac{\|E\|}{\|\{\sigma+\Delta\sigma\}\|} \tag{IX.23}$$

and this can be checked against a user defined tolerance *SSTOL*, which is typically in the range of 10^{-2} to 10^{-5}. If $R > SSTOL$ then the error in stress is unacceptable and the substep size given by ΔT must be reduced. If the new substep size is expressed as:

$$\Delta T_{\text{new}} = \beta\,\Delta T \tag{IX.24}$$

where β is a scalar and the local error estimate is $O(\Delta T^2)$, then the error estimate E_{new}, associated with ΔT_{new}, can be approximated as:

$$\|E_{\text{new}}\| = \beta^2\ \|E\| \tag{IX.25}$$

Because it is required that:

$$\frac{\|E_{\text{new}}\|}{\|\{\sigma+\Delta\sigma_{\text{new}}\}\|} \leq SSTOL \tag{IX.26}$$

an estimate for β can then be found, by assuming $\{\Delta\sigma_{\text{new}}\}\approx\{\Delta\sigma\}$, as:

$$\beta = \left[\frac{SSTOL}{R}\right]^{1/2} \tag{IX.27}$$

As this procedure is approximate, a conservative choice for β is:

$$\beta = 0.8\left[\frac{SSTOL}{R}\right]^{1/2} \tag{IX.28}$$

Adopting the factor of 0.8 reduces the number of substeps that are rejected during the course of the integration process. In addition, it is also wise to limit the range of extrapolation implied by the above procedure by restricting β to be greater than 0.1. Having defined β, a new estimate of the substep size ΔT_{new} can be calculated from Equation (IX.24) and the process from step (ii) onward repeated with $\Delta T = \Delta T_{new}$. If $R \leq SSTOL$, the substep is acceptable and the process moves to the next step.

vi) The accumulated stresses, plastic strains and hardening/softening parameters are now updated.

$$\{\sigma\} = \{\sigma\} + \{\Delta\sigma\} \tag{IX.29}$$

$$\{\varepsilon^p\} = \{\varepsilon^p\} + \{\Delta\varepsilon^p\} \tag{IX.30}$$

$$\{k\} = \{k\} + \{\Delta k\} \tag{IX.31}$$

vii) Because of the approximations made in the above procedure, it is possible that the stress state, given by Equation (IX.29), combined with the hardening/softening parameters, given by Equation (IX.31), violates the yield condition $|F(\{\sigma\},\{k\})| \leq YTOL$, where $YTOL$ is again a user defined tolerance. Whether or not this violation occurs depends on the nature of the constitutive model and the combination of the values of $SSTOL$ and $YTOL$. If it does occur, then the stresses, plastic strains and hardening/softening parameters must be adjusted to satisfy the yield condition. An accurate method for dealing with this is described in the following section of this appendix. This is the approach adopted by the Authors. Alternatively, the problem could be avoided by reducing the size of the substep even further and repeating stage (ii) onward. This procedure is then repeated until the yield criterion is satisfied.

viii) Once the yield condition is satisfied, T can be updated, i.e.

$$T = T + \Delta T \tag{IX.32}$$

and the next substep can be applied. Equation (IX.28) is again used to calculate the value of β which is then substituted in Equation (IX.24) to obtain the size of the next substep. As before, it is wise to restrict β to be greater than 0.1 and in addition to make sure it does not exceed 2.0, i.e. $0.1 \leq \beta \leq 2.0$. Also, it is important to check that $T+\Delta T_{new}$ does not exceed 1.0. If it does, then ΔT_{new} is set so that $T+\Delta T_{new} = 1.0$. ΔT is then updated as:

$$\Delta T = \Delta T_{new} \tag{IX.33}$$

and steps (ii) onwards repeated.

ix) The above procedure stops when T becomes equal to 1.0.

IX.1.4 Runge-Kutta integration scheme

In Section IX.1.3 a modified Euler scheme is described for integrating the elasto-plastic constitutive matrix. This method is based on first and second order formulae and varies the size of each substep in an effort to control the error in the integration process. Higher order schemes can be used instead of the modified Euler scheme. Sloan (1987) suggests a Runge-Kutta scheme which employs fourth and fifth order formulae. While this produces a more accurate solution for integration over a fixed sized substep as compared to the modified Euler scheme, it requires six evaluations of the $[\boldsymbol{D}^{ep}]$ matrix and hardening/softening relationships for each substep as compared to the two required by the modified Euler scheme. Consequently, for each substep it is computationally more costly than the modified Euler scheme. However, for a specific substep tolerance, $SSTOL$, the Runge-Kutta scheme allows larger, and therefore requires fewer, substeps.

The Authors have programmed both the modified Euler and Runge-Kutta schemes into their software and found that for a reasonable value of the substep tolerance, $SSTOL = 10^{-4}$, the modified Euler scheme is usually the most efficient in terms of computer resources required. However, for some boundary value problems and for highly nonlinear constitutive models the Runge-Kutta scheme is more efficient. The Runge-Kutta scheme also becomes more efficient for more stringent substep tolerances (i.e. $SSTOL < 10^{-4}$).

IX.1.5 Correcting for yield surface drift in elasto-plastic finite element analysis

As noted above in Section IX.1.3, stage (vii), if the tolerance used to control the size of the substeps ($SSTOL$) is too large compared to the yield function tolerance ($YTOL$), the combination of the stresses given by Equation (IX.29) and hardening/softening parameters given by Equation (IX.31) after each substep may not satisfy the yield condition $|F(\{\sigma\},\{k\})| \leq YTOL$. This phenomenon is often referred to as yield surface drift and, because it can lead to a cumulative error, must be corrected. Several ways of achieving this correction have been proposed in the literature and these are discussed and compared by Potts and Gens (1985). Potts and Gens show that many of these methods can lead to substantial errors and they recommend an alternative approach which is both consistent and accurate. This method is described below.

The problem under consideration is illustrated schematically in Figure IX.4. A sample of strain hardening/softening elasto-plastic material is subjected to loading which causes plastic deformation. The state of stress at an integration point is expressed by $\{\sigma\}$ and the associated hardening/softening parameters by $\{k\}$. At the beginning of a substep the stress state is represented by point A in Figure IX.4 and it lies on the yield surface given by $F(\{\sigma\},\{k\})=0$. After the substep the stress state becomes $\{\sigma+\Delta\sigma\}$ and is represented by point B in Figure IX.4. As the hardening/softening parameters also change, i.e. $\{\Delta k\}$, the yield surface moves from $F(\{\sigma\},\{k\})=0$ to $F(\{\sigma+\Delta\sigma\},\{k+\Delta k\})=0$. Owing to the tendency to drift the

predicted stress state represented by point B (i.e. $\{\sigma+\Delta\sigma\}$) does not necessarily lie on this new yield surface, as shown in Figure IX.4. The problem at hand is to decide in what manner the stresses and hardening/softening parameters at the end of the substep (i.e. point B) should be corrected so that the yield function is satisfied.

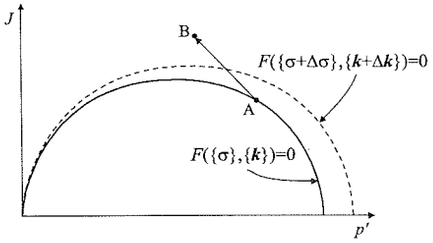

Figure IX.4: Yield surface drift

In the following, the stress states, plastic strains and hardening/softening parameters at the beginning (point A) and end (point B) of the substep are referred to as $\{\boldsymbol{\sigma}_A\}$, $\{\boldsymbol{\varepsilon}_A^p\}$, $\{\boldsymbol{k}_A\}$ and $\{\boldsymbol{\sigma}_B\}$, $\{\boldsymbol{\varepsilon}_B^p\}$, $\{\boldsymbol{k}_B\}$ respectively. In addition $\{\boldsymbol{\sigma}_C\}$, $\{\boldsymbol{\varepsilon}_C^p\}$ and $\{\boldsymbol{k}_C\}$ represent the values of the stresses, plastic strains and hardening parameters after correction.

If the stresses are corrected from $\{\boldsymbol{\sigma}_B\}$ to $\{\boldsymbol{\sigma}_C\}$, then the stress correction $\{\boldsymbol{\sigma}_B\}-\{\boldsymbol{\sigma}_C\}$ invokes an associated change in the elastic strains, given by:

$$\{\Delta\boldsymbol{\varepsilon}^e\} = [\boldsymbol{D}]^{-1}\left(\{\boldsymbol{\sigma}_C\} - \{\boldsymbol{\sigma}_B\}\right) \tag{IX.34}$$

Assuming no change in the substep total strains during the correction process implies that the elastic strain changes must be balanced by an equal and opposite change in the plastic strains. Therefore,

$$\{\Delta\boldsymbol{\varepsilon}^p\} = -\{\Delta\boldsymbol{\varepsilon}^e\} = -[\boldsymbol{D}]^{-1}\left(\{\boldsymbol{\sigma}_C\} - \{\boldsymbol{\sigma}_B\}\right) \tag{IX.35}$$

The plastic strain increments are proportional to the gradients of the plastic potential $P(\{\boldsymbol{\sigma}\},\{\boldsymbol{m}\})=0$:

$$\{\Delta\boldsymbol{\varepsilon}^p\} = \Lambda\left\{\frac{\partial P(\{\boldsymbol{\sigma}\},\{\boldsymbol{m}\})}{\partial\boldsymbol{\sigma}}\right\} \tag{IX.36}$$

where Λ is a scalar quantity. Combining Equations (IX.35) and (IX.36) gives:

$$\{\boldsymbol{\sigma}_C\} = \{\boldsymbol{\sigma}_B\} - \Lambda[\boldsymbol{D}]\left\{\frac{\partial P(\{\boldsymbol{\sigma}\},\{\boldsymbol{m}\})}{\partial\boldsymbol{\sigma}}\right\} \tag{IX.37}$$

As there are changes to the plastic strains, there are also changes to the strain hardening/softening parameters $\{\boldsymbol{k}\}$:

$$\{\boldsymbol{\varepsilon}_C^p\} = \{\boldsymbol{\varepsilon}_B^p\} + \Lambda\left\{\frac{\partial P(\{\boldsymbol{\sigma}\},\{\boldsymbol{m}\})}{\partial\boldsymbol{\sigma}}\right\} \tag{IX.38}$$

$$\{\boldsymbol{k}_C\} = \{\boldsymbol{k}_B\} + \{\Delta\boldsymbol{k}\} \tag{IX.39}$$

where:

$$\{\Delta\boldsymbol{k}\} = \{\Delta\boldsymbol{k}(\Delta\boldsymbol{\varepsilon}^p)\} = \left\{\Delta\boldsymbol{k}\left(\Lambda\frac{\partial P(\{\boldsymbol{\sigma}\},\{\boldsymbol{m}\})}{\partial\boldsymbol{\sigma}}\right)\right\} = \Lambda\left\{\Delta\boldsymbol{k}\left(\frac{\partial P(\{\boldsymbol{\sigma}\},\{\boldsymbol{m}\})}{\partial\boldsymbol{\sigma}}\right)\right\} \tag{IX.40}$$

As the corrected stress state must satisfy the yield condition:

$$F(\{\boldsymbol{\sigma}_C\},\{\boldsymbol{k}_C\}) = F\left(\left\{\boldsymbol{\sigma}_B - \Lambda[\boldsymbol{D}]\frac{\partial P(\{\boldsymbol{\sigma}\},\{\boldsymbol{m}\})}{\partial\boldsymbol{\sigma}}\right\},\left\{\boldsymbol{k}_B + \Lambda\,\Delta\boldsymbol{k}\left(\frac{\partial P(\{\boldsymbol{\sigma}\},\{\boldsymbol{m}\})}{\partial\boldsymbol{\sigma}}\right)\right\}\right) = 0 \tag{IX.41}$$

then expanding as a Taylor's series and neglecting terms in Λ^2 and above, gives, after some rearrangement:

$$\Lambda = \frac{F(\{\boldsymbol{\sigma}_B\},\{\boldsymbol{k}_B\})}{\left\{\frac{\partial F(\{\boldsymbol{\sigma}\},\{\boldsymbol{k}\})}{\partial\boldsymbol{\sigma}}\right\}^T[\boldsymbol{D}]\left\{\frac{\partial P(\{\boldsymbol{\sigma}\},\{\boldsymbol{m}\})}{\partial\boldsymbol{\sigma}}\right\} - \left\{\frac{\partial F(\{\boldsymbol{\sigma}\},\{\boldsymbol{k}\})}{\partial\boldsymbol{k}}\right\}^T\left\{\Delta\boldsymbol{k}\left(\frac{\partial P(\{\boldsymbol{\sigma}\},\{\boldsymbol{m}\})}{\partial\boldsymbol{\sigma}}\right)\right\}} \tag{IX.42}$$

To evaluate Λ, values of $\partial F(\{\boldsymbol{\sigma}\},\{\boldsymbol{k}\})/\partial\boldsymbol{\sigma}$, $\partial P(\{\boldsymbol{\sigma}\},\{\boldsymbol{m}\})/\partial\boldsymbol{\sigma}$ and $\partial F(\{\boldsymbol{\sigma}\},\{\boldsymbol{k}\})/\partial\boldsymbol{k}$ are required. Strictly speaking, these should be evaluated at the corrected stress state $\{\boldsymbol{\sigma}_C\}$, $\{\boldsymbol{k}_C\}$. However, as this is the stress state that is being pursued, it is unknown until Λ is determined. Consequently, an implicit situation arises which is similar to that associated with a return stress point algorithm, see Section 9.6.2.3 and Appendix IX.2. Although solutions to this implicit problem are available, see Appendix IX.2, it is usually sufficient to evaluate $\partial F(\{\boldsymbol{\sigma}\},\{\boldsymbol{k}\})/\partial\boldsymbol{\sigma}$, $\partial P(\{\boldsymbol{\sigma}\},\{\boldsymbol{m}\})/\partial\boldsymbol{\sigma}$ and $\partial F(\{\boldsymbol{\sigma}\},\{\boldsymbol{k}\})/\partial\boldsymbol{k}$ either at the beginning (point A) or at the end (point B) of the substep, or to use some weighted average of these values. In most finite element analyses the substepping tolerance (*SSTOL*) is usually set sufficiently small to prevent yield surface drift for the majority of the substeps for most integration points. If drift does occur, the deviation from the yield surface (i.e. point B) is usually small and the Authors' experience indicates that it makes little difference which of the above options is chosen. However, it should be noted that if an inadequate substep tolerance (*SSTOL*) is set, the deviation from the yield surface at the end of the substep could be large and the stress state could be well into illegal stress space. If this occurs and the option of evaluating $\partial F(\{\boldsymbol{\sigma}\},\{\boldsymbol{k}\})/\partial\boldsymbol{\sigma}$, $\partial P(\{\boldsymbol{\sigma}\},\{\boldsymbol{m}\})/\partial\boldsymbol{\sigma}$ and $\partial F(\{\boldsymbol{\sigma}\},\{\boldsymbol{k}\})/\partial\boldsymbol{k}$ at the end of the substep (i.e. point B) is used, then substantial errors could occur and all of the problems identified in Sections 9.4, 9.5 and 9.7 are relevant. It is therefore advisable to evaluate the above quantities at the beginning of the substep (i.e. point A).

Having evaluated Λ, the corrected stresses $\{\boldsymbol{\sigma}_C\}$, plastic strains $\{\boldsymbol{\varepsilon}_C^p\}$ and hardening/softening parameters $\{\boldsymbol{k}_C\}$ may be evaluated from Equations (IX.37) to (IX.39). It should be noted that the value of Λ is determined by neglecting the Λ^2 and higher terms in a Taylor's expansion. If the corrections are small, this procedure may be of sufficient accuracy. However, in general it is necessary to check that the combination of the corrected stress state $\{\boldsymbol{\sigma}_C\}$, and hardening/softening parameters $\{\boldsymbol{k}_C\}$ does in fact satisfies the yield condition

$F(\{\sigma_C\},\{k_C\})=0$ to some close tolerance ($YTOL$). If this is not so, the correction procedure must be repeated using an improved estimate of Λ. This improved estimate can often be based on a simple linear scaling rule using the values of $F(\{\sigma_A\},\{k_A\})$, $F(\{\sigma_B\},\{k_B\})$ and $F(\{\sigma_C\},\{k_C\})$. An iterative procedure is then involved in which Λ is continually updated until the corrected conditions $\{\sigma_C\}$, $\{\varepsilon_C^p\}$ and $\{k_C\}$ satisfy the yield condition $|F(\{\sigma_C\},\{k_C\})| \leq YTOL$.

IX.1.6 Nonlinear elastic behaviour

In the above discussion it is assumed that purely elastic behaviour is linear and that the elastic constitutive matrix $[\boldsymbol{D}]$ is constant. If this is not the case and the elasticity is nonlinear, perhaps following one of the models described in Chapters 5, 7 and 8, the procedure described in Section IX.1.2 must be modified. In particular the initial stage of the calculation process, in which the elastic constitutive matrix is integrated along the incremental strains, must be changed to account for the nonlinear $[\boldsymbol{D}]$ matrix. This can be done by adopting the modified Euler substepping algorithm described in Section IX.1.3, using the nonlinear elastic $[\boldsymbol{D}]$ matrix rather than the elasto-plastic matrix $[\boldsymbol{D}^{ep}]$. A check for yielding can then be made after each substep and, if yield occurs, the secant algorithm (or its equivalent) given by Equation (IX.5) can be used to evaluate the portion of the substep which is purely elastic. This, with the number and size of the previous substeps, allows α to be evaluated. The remaining part of the incremental strains, $(1-\alpha)\{\Delta\varepsilon\}$, which involves elasto-plastic behaviour, can then be dealt with in a similar fashion to that described in Section IX.1.3. However, when evaluating $[\boldsymbol{D}^{ep}]$ the correct nonlinear elastic matrix $[\boldsymbol{D}]$ must be accounted for.

Appendix IX.2: Return stress point algorithm

IX.2.1 Introduction

As noted in Section 9.6 and Appendix IX.1, a key step in the modified Newton-Raphson solution procedure is the integration of the constitutive model along the incremental strains to obtain the associated incremental stresses. As discussed in Section 9.6, several stress point algorithms are available for performing this task and two of the most accurate are the substepping and return algorithms. The substepping approach is described in Appendix IX.1 and the return algorithm approach is described in this appendix.

IX.2.2 Overview

In this approach, the plastic strains over the increment are calculated from the stress conditions corresponding to the end of the increment, see Section 9.6. The complication is that these stress conditions are not known, hence the implicit nature of the scheme. Most formulations involve some form of elastic predictor to give a first estimate of the stress changes, coupled with a sophisticated iterative sub-

algorithm to transfer from this stress state back to the yield surface. The basic steps in a return algorithm are as follows.

i) Obtain an elastic predictor, $\{\Delta\sigma\}^{tr}$, for the incremental stresses associated with the incremental strains, $\{\Delta\varepsilon\}$, assuming purely elastic behaviour:

$$\{\sigma_1\}^{tr} = \{\sigma_o\} + [\boldsymbol{D}]\{\Delta\varepsilon\} \qquad \text{(IX.43)}$$

where $[\boldsymbol{D}]$ is the elastic constitutive matrix and $\{\sigma_o\}$ are the accumulated stresses at the beginning of the increment. As the superscript 'tr' implies, $\{\sigma_1\}^{tr}$ refers to a trial solution.

ii) If the trial solution does not exceed yield (i.e. $F(\{\sigma_1\}^{tr},\{k\})\leq 0$), this stress state is accepted and there are neither any incremental plastic strains ($\{\Delta\varepsilon^p\}=0$) nor any incremental changes in the hardening parameters ($\{\Delta k\}=0$).

iii) If yield is exceeded (i.e. $F(\{\sigma_1\}^{tr},\{k\})>0$), plastic straining occurs. Plastic strains ($\{\Delta\varepsilon^p\}$) are evaluated such that the resulting stresses, $\{\sigma_f\}=\{\sigma_o\}+\{\Delta\sigma_f\}$, and hardening parameters, $\{k_f\}=\{k_o\}+\{\Delta k_f\}$, satisfy the yield criterion $F(\{\sigma_f\},\{k_f\})=0$. These stresses and hardening parameters are calculated from:

$$\{\sigma_f\} = \{\sigma_o\} + [\boldsymbol{D}]\left(\{\Delta\varepsilon\} - \{\Delta\varepsilon^p\}\right) \qquad \text{(IX.44)}$$

$$\{k_f\} = \{k_o\} + \{\Delta k\}\left(\{\sigma_f\},\{\Delta\varepsilon^p\}\right) \qquad \text{(IX.45)}$$

The important criterion in step (iii) is that the plastic strains, $\{\Delta\varepsilon^p\}$, are based on the stress conditions corresponding to $\{\sigma_f\}$. Clearly, as $\{\sigma_f\}$ depends on $\{\Delta\varepsilon^p\}$, see Equation (IX.45), an iterative procedure is required. The objective of the iterative sub-algorithm is to ensure that, on convergence, the constitutive behaviour is satisfied, albeit with the assumption that the plastic strains over the increment are based on the gradients of the plastic potential at the end of the increment. Many different iterative sub-algorithms have been proposed in the literature. In view of the Authors' previous findings, see Sections 9.4, 9.5, and 9.7, it is important that the final converged solution does not depend on quantities evaluated in illegal stress space. In this respect some of the earlier return algorithms break this rule and are therefore inaccurate. An example of such an algorithm is that presented by Ortiz and Simo (1986) and this is described in the next section of this appendix, in order to demonstrate the likely magnitude of the errors involved. The algorithm proposed by Borja and Lee (1990) for integrating a simple form of modified Cam clay is then presented. This algorithm does not suffer from errors related to evaluation of quantities in illegal stress space.

IX.2.3 Return algorithm proposed by Ortiz and Simo (1986)

The technique used by Ortiz and Simo (1986), to obtain the amount of plastic straining and stress relaxation required to satisfy the yield condition, linearises the plastic potential, $P(\{\sigma\},\{m\})$, and yield function, $F(\{\sigma\},\{k\})$, gradients at any stress predictor ($\{\sigma_i\}^{tr}$ for the i^{th} prediction) that exceeds yield, to obtain the

changes in plastic strains, $\{\Delta\varepsilon_{i+1}^{p}\}$ and stresses $\{\Delta\sigma_{i+1}\}^{tr}$, associated with the next prediction. Successive predictions are made until the stress state drifts back onto the yield surface, as shown schematically in Figure IX.5.

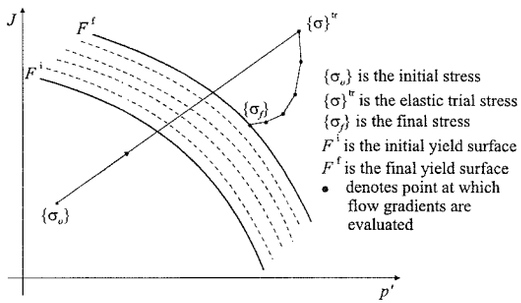

Figure IX.5: Return algorithm of Ortiz and Simo (1986)

To evaluate the plastic strains a scalar plastic multiplier, Λ, is defined such that:

$$\{\Delta\varepsilon_{i+1}^{p}\} = \{\varepsilon_{i+1}^{p}\} - \{\varepsilon_{i}^{p}\} = \Lambda\left\{\frac{\partial P_i(\{\sigma_i\}^{tr},\{\boldsymbol{m}_i\})}{\partial\sigma}\right\} \qquad \text{(IX.46)}$$

From Equation (IX.44) the associated stress changes are:

$$\{\Delta\sigma_{i+1}\}^{tr} = \{\sigma_{i+1}\}^{tr} - \{\sigma_i\}^{tr} = -[\boldsymbol{D}]\{\Delta\varepsilon_{i+1}^{p}\} = -[\boldsymbol{D}]\Lambda\left\{\frac{\partial P_i(\{\sigma_i\}^{tr},\{\boldsymbol{m}_i\})}{\partial\sigma}\right\} \qquad \text{(IX.47)}$$

The resulting changes to the hardening/softening parameters are obtained by differentiation of the hardening/softening laws with respect to Λ, at the stress/strain state consistent with the i^{th} prediction:

$$\{\Delta\boldsymbol{k}_{i+1}\} = \{\boldsymbol{k}_{i+1}\} - \{\boldsymbol{k}_i\} = \Lambda\left\{\frac{\partial\boldsymbol{k}(\{\sigma_i\}^{tr},\{\varepsilon_i^{p}\})}{\partial\Lambda}\right\} \qquad \text{(IX.48)}$$

An estimate of the yield function for the $(i+1)^{th}$ state, $F(\{\sigma_{i+1}\}^{tr},\{\boldsymbol{k}_{i+1}\})$, is obtained using Equations (IX.47) and (IX.48):

$$\begin{aligned} F(\{\sigma_{i+1}\}^{tr},\{\boldsymbol{k}_{i+1}\}) &= F(\{\sigma_i\}^{tr},\{\boldsymbol{k}_i\}) + \frac{\partial F(\{\sigma_i\}^{tr},\{\boldsymbol{k}_i\})}{\partial\sigma}\{\Delta\sigma_{i+1}\} \\ &\quad + \frac{\partial F(\{\sigma_i\}^{tr},\{\boldsymbol{k}_i\})}{\partial\boldsymbol{k}}\{\Delta\boldsymbol{k}_{i+1}\} \\ &= F(\{\sigma_i\}^{tr},\{\boldsymbol{k}_i\}) - \frac{\partial F(\{\sigma_i\}^{tr},\{\boldsymbol{k}_i\})}{\partial\sigma}[\boldsymbol{D}]\Lambda\frac{\partial P(\{\sigma_i\}^{tr},\{\boldsymbol{k}_i\})}{\partial\sigma} \\ &\quad + \frac{\partial F(\{\sigma_i\}^{tr},\{\boldsymbol{k}_i\})}{\partial\boldsymbol{k}}\Lambda\frac{\partial\boldsymbol{k}(\{\sigma_i\}^{tr},\{\varepsilon_i^{p}\})}{\partial\Lambda} \end{aligned} \qquad \text{(IX.49)}$$

To satisfy the yield criterion $F(\{\sigma_{i+1}\}^{tr},\{\boldsymbol{k}_{i+1}\})=0$, Equation (IX.49) can therefore be equated to zero and rearranged to give:

$$\Lambda = \frac{F(\{\sigma_i\}^{tr},\{\boldsymbol{k}_i\})}{\dfrac{\partial F(\{\sigma_i\}^{tr},\{\boldsymbol{k}_i\})}{\partial\sigma}[\boldsymbol{D}]\dfrac{\partial P(\{\sigma_i\}^{tr},\{\boldsymbol{k}_i\})}{\partial\sigma} - \dfrac{\partial F(\{\sigma_i\}^{tr},\{\boldsymbol{k}_i\})}{\partial\boldsymbol{k}}\dfrac{\partial\boldsymbol{k}(\{\sigma_i\}^{tr},\{\varepsilon_i^{p}\})}{\partial\Lambda}} \qquad \text{(IX.50)}$$

Using Equations (IX.47), (IX.48) and (IX.50) the next predictions $(i+1)^{th}$ for stresses, $\{\sigma_{i+1}\}^{tr}$, and hardening parameters, $\{\boldsymbol{k}_{i+1}\}$, can be calculated. These are then used to evaluate the new value of the yield function $F(\{\sigma_{i+1}\}^{tr},\{\boldsymbol{k}_{i+1}\})$. Due to the nonlinear nature of the constitutive model, the value of $F(\{\sigma_{i+1}\}^{tr},\{\boldsymbol{k}_{i+1}\})$ need not, in general, equal zero. If $F(\{\sigma_{i+1}\}^{tr},\{\boldsymbol{k}_{i+1}\})$ is equal to zero (within a specified tolerance) the prediction is accepted. If it is not, this prediction is used to obtain the next prediction using the above procedure, which is repeated until the predicted stress state satisfies the yield condition.

It should be noted that with this algorithm the final result involves a series of evaluations for the yield and plastic potential derivatives in illegal stress space. To indicate the errors that can result from such a procedure, the undrained and drained triaxial tests described in Section 9.7.2 are analysed with the modified Newton-Raphson solution strategy, using the above return algorithm. The results of the drained tests are presented as plots of volumetric strain and deviatoric stress versus axial strain, in Figure IX.6. The label associated with each line in these plots indicates the magnitude of axial strain applied in each increment of that analysis. Also shown in the figure for comparison purposes are the analytical solutions.

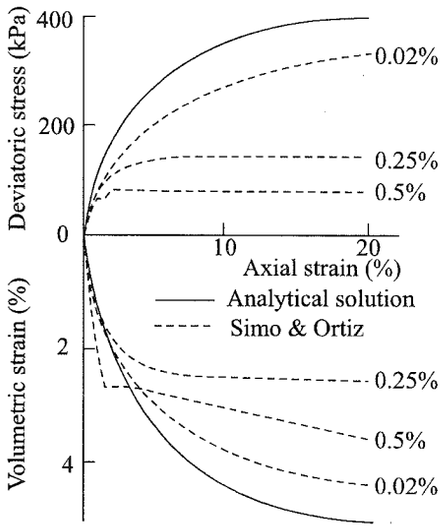

Figure IX.6: Predictions for a drained triaxial test

Values of deviatoric stress, q, and volumetric strain at failure (20% axial strain) and central processor unit times (CPU) are shown in Table IX.1 for selected analyses. The numbers in parentheses are the errors expressed as a percentage of the analytical solution. The size of the axial strain increment used is indicated after the analysis type. The results from these analyses may be compared with those given in Figures 9.21, 9.22 and 9.26 for analyses performed with the MNR (with a substepping algorithm), tangent stiffness and visco-plastic solution strategies respectively. Such a comparison reveals that the present results are similar to those from the visco-plastic analyses and large under predictions of both volumetric strain and deviatoric stress occur if large increment sizes are used. The predictions are also less accurate than the tangent stiffness analyses of the same increment size. The present method is also inefficient when comparing the CPU times required with the accuracy achieved. The magnitudes of the errors shown here are similar to those presented in Ortiz and Simo (1986) where errors of over 34% were presented for some of the problems they considered.

Table IX.1: Results and CPU times for drained triaxial test analyses using Ortiz and Simo (1986)

ANALYSIS TYPE Increment size	q (kPa)	Volumetric strain (%)	CPU sec
Analytical	390.1	5.18	
MNR (Ortiz and Simo (1986)) 0.25%	141.6 (-67.3%)	2.67 (-48.3%)	317
MNR (Ortiz and Simo (1986)) 0.02%	339.8 (-12.9%)	4.69 (-9.5%)	2697

The results for the undrained triaxial tests are presented as plots of pore water pressure and deviatoric stress versus axial strain in Figure IX.7. These results also illustrate the strong influence of increment size on the accuracy of the results. They can be compared with the predictions given in Figures 9.23 and 9.25 for the tangent stiffness and visco-plastic solution strategies.

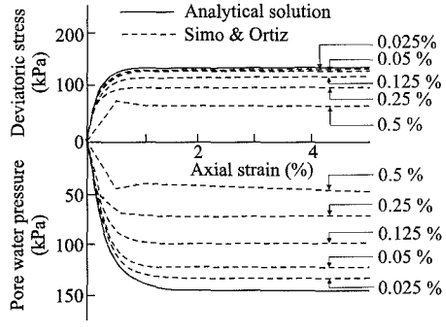

Figure IX.7: Predictions for an undrained triaxial test

The reason for the errors in the results based on this return algorithm are related to the evaluation of the yield and plastic potential gradients in illegal stress space. It can be concluded that such a return algorithm should not be used to perform analysis with complex soil models like modified Cam clay.

IX.2.4 Return algorithm proposed by Borja and Lee (1990)

The algorithm proposed by Borja and Lee (1990) is an iterative procedure to evaluate a stress state $\{\sigma_f\}$ such that the plastic strains evaluated from the flow directions at this stress state result in sufficient stress relaxation and strain hardening/softening to satisfy the yield criterion. This is illustrated in Figure 9.18 and expressed in the equation below.

$$\{\Delta\varepsilon^p\} = \Lambda\left\{\frac{\partial P(\{\sigma_f\},\{k_f\})}{\partial\sigma}\right\} \qquad \text{(IX.51)}$$

where $P(\{\sigma_f\},\{k_f\})$ is the plastic potential at the stress state $\{\sigma_f\}$. Values of $\{\sigma_f\}$ and $\{k_f\}$ can be evaluated from Equations (IX.44) and (IX.45) respectively, using these values of plastic strains. The value of $\{\sigma_f\}$ should be the same as the value used in

Equation (IX.51) and these values of $\{\sigma_f\}$ and $\{k_f\}$ should also satisfy the yield condition:

$$F(\{\sigma_f\},\{k_f\}) = 0 \qquad \text{(IX.52)}$$

Obtaining values of $\{\sigma_f\}$ and $\{k_f\}$ which satisfy Equations (IX.44), (IX.45) and (IX.51) simultaneously is not straightforward for complex models. In particular, the use of this type of return algorithm for a double yield surface model is difficult (Borja *et al.* (1990)). Borja and Lee (1990) devised an iterative procedure for obtaining such a solution for an associative form of modified Cam clay, where the slope of the critical state line in J-p' space (M_J) is constant. This procedure formulates $\{\sigma_f\}$ and $\{k_f\}$ in terms of the scalar plastic multiplier, Λ, and iterates on the value of Λ to satisfy yield.

The yield and plastic potential function is written as:

$$F(\{\sigma'\},\{k\}) = P(\{\sigma'\},\{m\}) = \frac{J^2}{M_J^2} + p'(p' - p'_o) = 0 \qquad \text{(IX.53)}$$

The yield function gradients and plastic flow directions are written as:

$$\begin{aligned}
\frac{\partial F(\{\sigma\},\{k\})}{\partial p'} &= \frac{\partial P(\{\sigma\},\{m\})}{\partial p'} = 2p' - p'_o \\
\frac{\partial F(\{\sigma\},\{k\})}{\partial J} &= \frac{\partial P(\{\sigma\},\{m\})}{\partial J} = \frac{2J}{M_J^2} \\
\frac{\partial F(\{\sigma\},\{k\})}{\partial p'_o} &= \frac{\partial P(\{\sigma\},\{m\})}{\partial p'_o} = -p'
\end{aligned} \qquad \text{(IX.54)}$$

Substituting these equations into Equation (IX.51) and dividing it into two parts consisting of volumetric plastic strains, ε_v^p, and deviatoric plastic strains, E_d^p, gives:

$$\begin{aligned}
\Delta\varepsilon_v^p &= \Lambda\frac{\partial P(\{\sigma'\},\{m\})}{\partial p'} = \Lambda(2p' - p'_o) \\
\Delta E_d^p &= \Lambda\frac{\partial P(\{\sigma'\},\{m\})}{\partial J} = \Lambda\frac{2J}{M_J^2}
\end{aligned} \qquad \text{(IX.55)}$$

Substituting Equations (IX.55) into Equation (IX.44) and dividing it into spherical and deviatoric components gives:

$$p' = p'^{\,\mathrm{tr}} - K\Delta\varepsilon_v^p = p'^{\,\mathrm{tr}} - K\Lambda(2p' - p'_o) = \frac{p'^{\,\mathrm{tr}} + K\Lambda p'_o}{1 + 2K\Lambda} \qquad \text{(IX.56)}$$

$$J = J^{\mathrm{tr}} - \sqrt{3}G\Delta E_d^p = J^{\mathrm{tr}} - \sqrt{3}G\Lambda\frac{2J}{M_J^2} = \frac{J^{\mathrm{tr}}}{1 + \dfrac{2\sqrt{3}G\Lambda}{M_J^2}} \qquad \text{(IX.57)}$$

where:

$p'^{\,\mathrm{tr}}$ and J^{tr} are the spherical and deviatoric components of the elastic predictor $\{\sigma\}^{\mathrm{tr}}$;

K and G are the elastic bulk and shear moduli respectively.

Note that in Equations (IX.56) and (IX.57) the flow directions used to obtain the values of p' and J are the flow directions evaluated at p' and J.

This procedure assumes that over any applied strain path K and G are constant. This simplifies the governing equations such that p' and J can be expressed purely as a function of Λ and the trial stresses p'^{tr} and J^{tr}. The values of K and G used are those evaluated from the initial stress:

$$K = \frac{v}{\kappa} p'^{i} \quad \text{and} \quad G = g\, p_o'^{i} \tag{IX.58}$$

where:

p'^{i} and J^{i} are the spherical and deviatoric components of the initial stress $\{\boldsymbol{\sigma}_o\}$;

$p_o'^{i}$ is the initial value of the hardening parameter.

The elastic predictors p'^{tr} and J^{tr} are also evaluated using these values of K and G. The hardening law is:

$$\Delta p_o' = \xi\, p_o'\, \Delta\varepsilon_v^p \quad \text{where} \quad \xi = \frac{v}{\lambda - \kappa} \tag{IX.59}$$

Integrating this equation and substituting in Equation (IX.55a) and (IX.56) gives:

$$p_o' = p_o'^{i}\, e^{\xi\, \Delta\varepsilon_v^p} = p_o'^{i}\, e^{\xi\, \Lambda\, (2p' - p_o')} = p_o'^{i}\, e^{\xi\, \Lambda\, \frac{2p'^{tr} - p_o'}{1 + 2\Lambda K}} \tag{IX.60}$$

Thus p', p_o' and J are expressed in terms of Λ. A Newton iterative procedure is used to obtain a value of Λ which gives values of p', p_o' and J which satisfy the yield function (IX.53), on the $(i+1)^{th}$ iteration.

$$\Lambda_{i+1} = \Lambda_i - F_i(\{\sigma'\},\{\boldsymbol{k}\}) \left\{ \frac{\partial F_i(\{\sigma'\},\{\boldsymbol{k}\})}{\partial \Lambda} \right\}^{-1} \tag{IX.61}$$

where:

Λ_i and Λ_{i+1} are the values of Λ for the i^{th} and $(i+1)^{th}$ iterations respectively;

$F_i(\{\sigma'\},\{\boldsymbol{k}\})$ is the value of the yield function on the i^{th} iteration.

The values of p', p_o' and J consistent with this value of Λ are evaluated using Equations (IX.56), (IX.60) and (IX.57) respectively. These values are substituted into Equation (IX.53) and if the yield function F_{i+1} is equal to zero (to within a prescribed tolerance, *YTOL*), these values are accepted, otherwise the above procedure is repeated until the yield criterion is met. The steps in this Newton iterative procedure are shown in Table IX.2.

The yield function gradient used in Equation (IX.61) is evaluated at the i^{th} iteration stress state and is derived from the equations below.

$$\frac{\partial F(\{\sigma'\},\{\boldsymbol{k}\})}{\partial \Lambda} = \frac{\partial F(\{\sigma'\},\{\boldsymbol{k}\})}{\partial p'} \frac{\partial p'}{\partial \Lambda} + \frac{\partial F(\{\sigma'\},\{\boldsymbol{k}\})}{\partial J} \frac{\partial J}{\partial \Lambda} + \frac{\partial F(\{\sigma'\},\{\boldsymbol{k}\})}{\partial p_o'} \frac{\partial p_o'}{\partial \Lambda} \tag{IX.62}$$

Table IX.2: Local Newton algorithm for computing the zero of F

Step	Action
1.	Initialise i=0 and $\Lambda_i = 0$;
2.	Evaluate values of p', p_o' and J consistent with Λ_i using Equations (IX.56), (IX.60) and (IX.57) respectively. Equation (IX.60) is solved using Table IX.3;
3.	Compute value of $F_i(\{\boldsymbol{\sigma}'\},\{\boldsymbol{k}\})$ using Equation (IX.53).
4.	If $\lvert F_i(\{\boldsymbol{\sigma}'\},\{\boldsymbol{k}\})\rvert$<*YTOL* then EXIT; ELSE;
5.	Evaluate Λ_{i+1} using Equation (IX.61);
6.	i=i+1 and GOTO 2.

Consider Equation (IX.56):

$$p' = p'^{tr} - K\Lambda(2p' - p_o')$$

and differentiate it with respect to Λ:

$$\frac{\partial p'}{\partial \Lambda} = -K(2p' - p_o') - 2K\Lambda \frac{\partial p'}{\partial \Lambda} + K\Lambda \frac{\partial p_o'}{\partial \Lambda} \tag{IX.63}$$

This can be rearranged as:

$$\frac{\partial p'}{\partial \Lambda}\left(\frac{1}{K} + 2\Lambda\right) - \Lambda \frac{\partial p_o'}{\partial \Lambda} = -(2p' - p_o') \tag{IX.64}$$

Consider Equation (IX.60):

$$p_o' = p_o'^{i}\, e^{\xi\, \Lambda\, (2p' - p_o')}$$

and differentiate it with respect to Λ:

$$\frac{\partial p_o'}{\partial \Lambda} = p_o' \xi \left(2p' - p_o' + 2\Lambda \frac{\partial p'}{\partial \Lambda} - \Lambda \frac{\partial p_o'}{\partial \Lambda}\right) \tag{IX.65}$$

This can be rearranged as:

$$\frac{\partial p_o'}{\partial \Lambda}\left(\frac{1}{\xi p_o'} + \Lambda\right) - 2\Lambda \frac{\partial p'}{\partial \Lambda} = 2p' - p_o' \tag{IX.66}$$

Combining Equations (IX.64) and (IX.66) gives:

$$\frac{\partial p'}{\partial \Lambda}\left(\frac{1}{K} + 2\Lambda\right) - \Lambda \frac{\partial p_o'}{\partial \Lambda} = -\frac{\partial p_o'}{\partial \Lambda}\left(\frac{1}{\xi p_o'} + \Lambda\right) + 2\Lambda \frac{\partial p'}{\partial \Lambda} \tag{IX.67}$$

which, when simplified, gives:

$$\frac{\partial p_o'}{\partial \Lambda} = -\frac{\xi p_o'}{K}\frac{\partial p'}{\partial \Lambda} \tag{IX.68}$$

Substituting Equation (IX.68) into Equation (IX.64) gives:

$$\frac{\partial p'}{\partial \Lambda} = -\frac{K(2p' - p_o')}{1 + \Lambda(2K + \xi p_o')} \tag{IX.69}$$

Substituting now this equation into Equation (IX.68) gives:

$$\frac{\partial p_o'}{\partial \Lambda} = \xi p_o' \frac{2p' - p_o'}{1 + \Lambda(2K + \xi p_o')} \tag{IX.70}$$

Consider Equation (IX.57):

$$J = \frac{J^{tr}}{1 + \dfrac{2\sqrt{3}G\Lambda}{M_J^2}}$$

Differentiating this equation with respect to Λ gives:

$$\frac{\partial J}{\partial \Lambda} = -\frac{2\sqrt{3}G}{M_J^2}\frac{J^{tr}}{\left(1 + \dfrac{2\sqrt{3}G\Lambda}{M_J^2}\right)^2} = -\frac{J}{\dfrac{M_J^2}{2\sqrt{3}G} + \Lambda} \tag{IX.71}$$

Substituting Equations (IX.54), (IX.69), (IX.70) and (IX.71) into (IX.62) gives:

$$\frac{\partial F(\{\sigma'\},\{k\})}{\partial \Lambda} = -(2p' - p_o')\frac{K(2p' - p_o') + \xi p' p_o'}{1 + (2K + \xi p_o')\Lambda} - \frac{2J^2}{M_J^2\left(\dfrac{M_J^2}{2\sqrt{3}G} + \Lambda\right)} \tag{IX.72}$$

This equation can now be used in Equation (IX.61).

The solution of Equation (IX.60) to obtain a value of p_o' is not straightforward, since p_o' appears on both sides of the equality. Borja and Lee (1990) solved this equation using a Newton iterative procedure and defined a function H such that:

$$H = p_o'^{i}\, e^{\xi \Lambda \frac{2p'^{tr} - p_o'}{1 + 2K\Lambda}} - p_o' \tag{IX.73}$$

The correct value of p_o' for any Λ gives a value of H equal to zero. Thus an iterative procedure, similar to that used to find the value of Λ which satisfies yield, can be used. This means that for the $(j+1)^{th}$ iteration:

$$p'_{o(j+1)} = p'_{o(j)} - H_j\left(\frac{\partial H_j}{\partial p_o'}\right)^{-1} \tag{IX.74}$$

where

$p_{o(j)}'$ and $p_{o(j+1)}'$ are the values of p_o' for the j^{th} and $(j+1)^{th}$ iterations respectively;
H_j is the value of H at the j^{th} iteration.

The differential in Equation (IX.74) is obtained by differentiating Equation (IX.73):

$$\frac{\partial H}{\partial p_o'} = -\frac{\xi \Lambda}{1 + 2K\Lambda} p_o'^{i}\, e^{\xi \Lambda \frac{2p'^{tr} - p_o'}{1 + 2K\Lambda}} - 1 \tag{IX.75}$$

If the value of $p_{o(j+1)}'$ calculated from Equation (IX.74) results in a value of H_{j+1} which is equal to zero (to within a prescribed tolerance, *HTOL*), this value is accepted, otherwise the above procedure is repeated until this criterion is met. This iterative procedure is a nested loop within the main loop described above for evaluating the value of Λ which gives values of p', p_o' and J which satisfy the yield equation. The procedure is depicted in the flow chart shown in Table IX.3.

Table IX.3: Sub-local Newton algorithm for computing the zero of H

Step	Action
1.	Initialise $j = 0$ and $p_{o(j)}' = p_o'^{i}$;
2.	Compute value of H_j using Equation (IX.73);
3.	If $\lvert H_j \rvert <$ *HTOL*, GOTO 6, ELSE;
4.	Evaluate $p_{o(j+1)}'$ using Equation (IX.74);
5.	$j = j+1$ and GOTO 2;
6.	Accept value of $p_{o(j)}'$ for line 2 of Table IX.2 and RETURN.

As noted above, this algorithm assumes that the elastic parameters are constant over the increment and are evaluated using the stress state at the beginning of the increment. This is an approximation as both the elastic bulk and shear stiffness can vary in a modified Cam clay model. In this respect Borja (1991) has extended the previous algorithm to deal with a limited form of nonlinear elasticity. Use of these algorithms with the MNR solution strategy leads to much more accurate predictions compared to those from the Ortiz and Simo algorithm. A comparison with the substepping algorithm described in Appendix IX.1 is given in Appendix IX.3. A limitation of the Borja and Lee (1990) and Borja (1991) algorithms is that they assume that the yield and plastic potential surfaces have a constant value of M_J and therefore form a surface of revolution about the mean effective stress axis. As noted in Section 7.9.2, this severely limits the application of the model. While in principal a return algorithm could be devised for a modified Cam clay model with a Lode's angle θ dependency, it is likely to involve major modifications to the algorithms. In fact, one of the major disadvantages of accurate return algorithms is that each constitutive model must be dealt with individually. It is not possible to set up a general algorithm which can deal with all forms of nonlinear constitutive models. Models with multiple yield surfaces, nonlinear elasticity and bounding

surface plasticity are difficult, but not impossible, to accommodate within the return algorithm framework. Research is currently underway on this subject and new advances are expected in the future. It should be noted that the substepping approach does not suffer from the above shortcomings.

Appendix IX.3: Comparison of substepping and return algorithms

IX.3.1 Introduction

A key step in the modified Newton-Raphson nonlinear solution strategy is the integration of the constitutive model over a finite strain step. Algorithms for performing such an integration are called 'stress point algorithms' and two such algorithms, namely the substepping and return algorithms, are described in Appendices IX.1 and IX.2 respectively. In this appendix a comparison between these two approaches is presented. This is done by considering results from analyses of undrained and drained ideal triaxial tests (see Section 9.7.2) and from analyses of the pile problem described in Section 9.7.5.

IX.3.2 Fundamental comparison

To investigate the accuracy of the substepping and constant and variable elasticity return algorithms the behaviour of ideal (i.e. no end effects) undrained and drained triaxial tests are considered. These triaxial tests are described in detail in Section 9.7.2. The form of the modified Cam clay model used for these analyses, the input parameters and the initial stress conditions are also given in Section 9.7.2.

IX.3.2.1 Undrained triaxial test

The correct analytical solution for an undrained triaxial test is given in Appendix VII.2. The relevant equations are Equation (VII.29), (VII.30), (VII.31), (VII.33) and (VII.39). It is also possible to obtain analytical solutions consistent with the assumptions of the constant and variable elasticity return algorithms.

Constant elasticity return algorithm

Solutions are derived by evaluating the values of E_d^p, J^f and $p_o'^f$ associated with any prescribed value of p'^f, where the superscript 'f' refers to conditions at the end of an increment. The elastic moduli K and G are calculated from the following expressions:

$$K = \frac{\nu}{\kappa} p'^i \quad \text{and} \quad G = g\, p_o'^i \tag{IX.76}$$

where the superscript 'i' refers to conditions at the beginning of an increment.

The elastic volumetric strain, ε_v^e, is equal in magnitude but opposite in sign to the plastic volumetric strain, ε_v^p, during an increment of undrained loading. They can be calculated using K:

$$\varepsilon_v^e = \frac{p'^f - p'^i}{K} = -\varepsilon_v^p \tag{IX.77}$$

Thus $p_o'^f$ can be evaluated as follows:

$$p_o'^f = p_o'^i \, e^{\varepsilon_v^p \frac{\nu}{\lambda - \kappa}} \tag{IX.78}$$

By rearranging Equation (VII.9) J^f can be expressed as:

$$J^f = M_J \sqrt{p'^f (p_o'^f - p'^f)} \tag{IX.79}$$

Using Equation (VII.10) the plastic deviatoric strain, E_d^p, can be defined as:

$$E_d^p = \frac{\partial P(\{\sigma'\},\{m\})}{\partial J} \left(\frac{\partial P(\{\sigma'\},\{m\})}{\partial p'} \right)^{-1} \varepsilon_v^p = \frac{2J^f}{M_J^2 (p_o'^f - 2p'^f)} \varepsilon_v^p \tag{IX.80}$$

The elastic deviatoric strain, E_d^e, can be evaluated from G:

$$E_d^p = \frac{J^f - J^i}{\sqrt{3}G} \tag{IX.81}$$

Thus the total deviatoric strain can be written as:

$$E_d = E_d^e + E_d^p = \frac{J^f - J^i}{\sqrt{3}G} + \frac{2J^f}{M_J^2 (p_o'^f - 2p'^f)} \varepsilon_v^p \tag{IX.82}$$

Variable elasticity return algorithm

The solutions consistent with varying elastic moduli are obtained using the equations shown above, except for Equations (IX.77) and (IX.81) which must be replaced. These equations are used to evaluate the elastic strains ε_v^e and E_d^e and are explicit linear approximations of the nonlinear elastic stiffness. The equations consistent with varying elastic moduli can be analytically derived and are as follows.

Equation (IX.77) is replaced by (see Equation (VII.16)):

$$\varepsilon_v^e = \frac{\kappa}{\lambda} \ln \frac{p'^f}{p'^i} = -\varepsilon_v^p \tag{IX.83}$$

Equation (IX.81) is replaced by Equation (VII.33).

Results from the analyses using the different stress point algorithms are compared with the correct solution in Figures IX.8a and IX.9a, which show the variation of pore water pressure and deviatoric stress, q, with axial strain. For each of the stress point algorithms a series of analyses have been performed. In each analysis a single axial strain increment was applied, the magnitude of which varied between analyses.

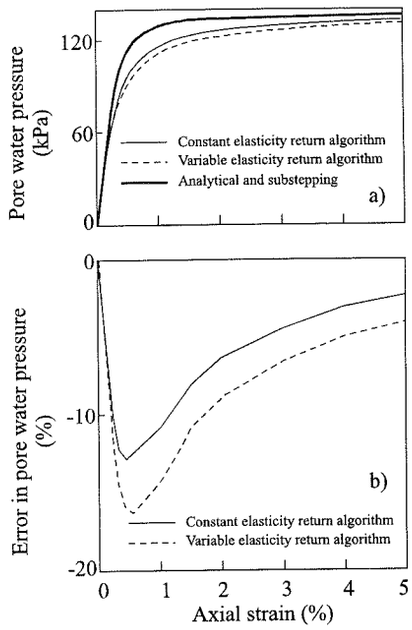

Figure IX.8: Undrained triaxial test: a) pore water pressure versus axial strain; b) error in pore water pressure

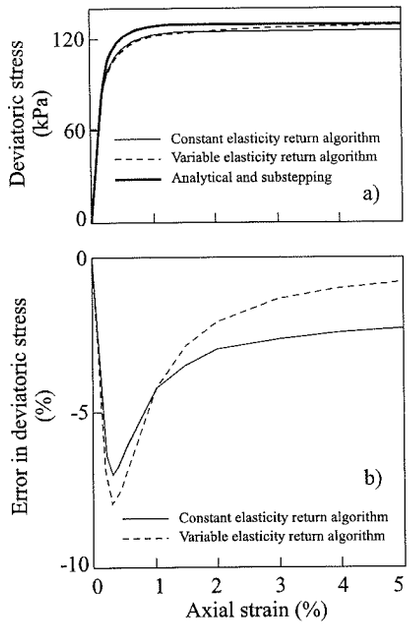

Figure IX.9: Undrained triaxial test: a) deviatoric stress versus axial strain; b) error in deviatoric stress

The undrained (no volume change) nature of the problem results in a constant ratio between radial and axial strain components. The strains are therefore varying in a 'proportional' manner and consequently the substepping algorithm is correct and independent of the size of the strain increment applied. This can be seen from Figures IX.8a and IX.9a where the results from the substepping algorithm are indistinguishable from the correct analytical solution and plot as a single curve.

Results from the analytical expressions given above, which incorporate the assumptions consistent with the constant and variable elasticity return algorithms, are also shown on Figures IX.8a and IX.9a. There is a significant difference between these results and the correct analytical solutions, with both pore pressure and deviatoric stress being under predicted. This error increases and then decreases with the size of the strain increment, as illustrated in Figures IX.8b and IX.9b, where the error in pore water pressure and deviatoric stress respectively, expressed as a percentage of the correct solution, is plotted against axial strain. Both sets of results indicate significant departures from the correct solution. The errors in the constant elasticity analyses reach a peak value of 13% for pore pressure and 7% for deviatoric stress. The errors in the variable elasticity analyses are generally worse and reach a peak value of over 16% for pore pressure and 8% for deviatoric stress.

At first, it may seem strange that the errors reduce for large strain increments. However, a review of the situation indicates that for such large strain increments a large proportion of the plastic strains occur at the end of the increment where the stress state tends to a constant condition consistent with the critical state. The implicit nature of the assumptions in the return algorithm approach therefore becomes more reasonable and the error reduces.

Another anomaly is that the less rigorous constant elasticity analyses produce more accurate predictions. Closer inspection of the results indicates that this arises due to compensating errors. The use of constant elastic moduli based on conditions at the beginning of the increment results in a stiffer elastic contribution to the incremental material stiffness. This to some extent compensates for the softer plastic contribution resulting from the implicit assumption in the return algorithm.

IX.3.2.2 Drained triaxial test

The correct analytical solution for a drained triaxial test is derived in Appendix VII.2. The relevant equations are Equations (VII.14), (VII.15), (VII.16), (VII.19), (VII.24) and (VII.29). It is also possible to obtain analytical solutions consistent with the assumptions of the constant and variable elasticity return algorithms.

Constant elasticity return algorithm

These solutions are derived by evaluating the values of E_d, J^f and $p_o'^f$ associated with any prescribed value of p'^f. J^f can be determined from Equation (VII.14). The hardening parameter can be evaluated from Equation (VII.9):

$$p_o'^f = \frac{(J^f)^2}{M_J^2 p'^f} + p'^f \qquad \text{(IX.84)}$$

The elastic moduli K and G are calculated from the values of stress at the beginning of the increment, using Equation (IX.76). The elastic volumetric strain, ε_v^e, can be calculated using Equation (IX.77). The plastic volumetric strain can be obtained from:

$$\varepsilon_v^p = \frac{v}{\lambda - \kappa} \ln\left(\frac{p_o'^f}{p_o'^i}\right) \qquad \text{(IX.85)}$$

The plastic deviatoric strains can be evaluated from the flow directions Equations (VII.10):

$$E_d^p = \frac{\partial P(\{\sigma'\},\{m\})}{\partial J}\left(\frac{\partial P(\{\sigma'\},\{m\})}{\partial p'}\right)^{-1} \varepsilon_v^p = \frac{2J^f}{M_J^2(p_o'^f - 2p'^f)}\varepsilon_v^p \qquad \text{(IX.86)}$$

The elastic deviatoric strain, E_d^e, can be evaluated using Equation (IX.81).

Variable elasticity return algorithm

The solutions consistent with varying elastic moduli are obtained using the equations shown above, except for Equations (IX.77) and (IX.81) which must be replaced. These equations are used to evaluate the elastic strains ε_v^e and E_d^e respectively, and are explicit linear approximations of the nonlinear elastic stiffness. The equations consistent with varying elastic moduli can be analytically derived and are as follows:

Equation (IX.77) is replaced by Equation (IX.83);
Equation (IX.81) is replaced by Equation (VII.19).

Results from both stress point algorithms are compared with the correct solution in Figures (IX.10) and (IX.11), which show the variation of deviatoric stress and volumetric strain with axial strain. For each of the stress point algorithms a series of analyses have been performed. In each analysis a single axial strain increment was applied, the magnitude of which varied between analyses. In all cases the radial total stress and pore water pressure were maintained constant.

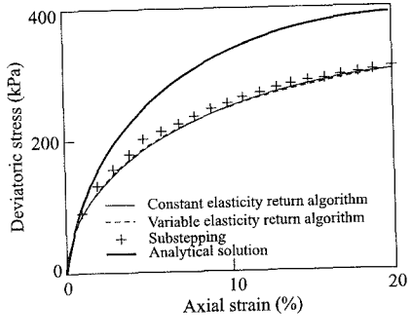

Figure IX.10: Drained triaxial test: deviatoric stress versus axial strain

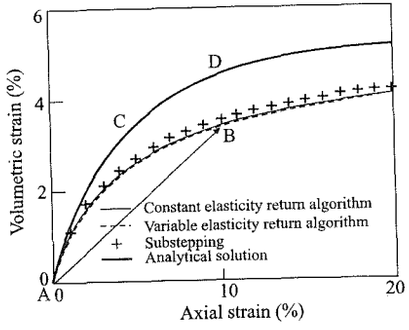

Figure IX.11: Drained triaxial test: volumetric strain versus axial strain

Results based on the substepping approach were obtained using a finite element analysis with a single four noded element and one integration point. Each symbol in Figures (IX.10) and (IX.11) represents the results from a single increment finite element analysis. In contrast to the analyses of the undrained triaxial test, these substepping results differ from the correct analytical solution. This arises because the axial and radial strains do not vary 'proportionally' throughout the test, as can be seen from the correct analytical solution shown in Figure (IX.11). For example, for the analysis with an axial strain increment of 10% the substepping algorithm assumes the 'proportional strain' path labelled AB in Figure (IX.11). This differs substantially from the correct path given by the curved response ACD. The errors associated with integrating the constitutive equations along the 'proportional' strain path AB, as opposed to the correct path ACD, are illustrated in Figure (IX.12)

which shows the variation of the total radial stress with axial strain. This indicates that although the radial stress is consistent with the applied boundary conditions of 200 kPa at the beginning and end of the strain increment, there is a significant deviation during the course of the increment. Integration of the constitutive equations along the curved strain path ACD results in a constant radial stress of 200 kPa.

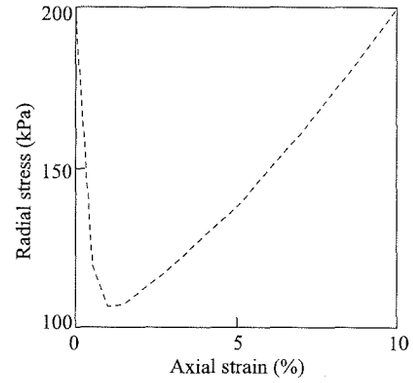

Figure IX.12: Radial stress versus axial strain

Results of the analytical expressions, which incorporate the assumptions associated with constant and variable elasticity return algorithms, are also presented in Figures (IX.10) and (IX.11) and are similar to those obtained using the substepping approach, but give slightly greater differences when compared with the correct analytical solution.

IX.3.3 Pile problem

The problem of the mobilisation of the stresses in the soil immediately adjacent to a pile shaft during drained loading is considered. The behaviour of a segment of an incompressible 7.5 mm diameter model pile, well away from the influence of the soil surface and pile tip, is examined. A similar problem is described in detail in Section 9.7.5. A modified Cam clay model, similar to that used for the triaxial test, is used to represent the soil and the material parameters and initial conditions are given in Table IX.4.

Table IX.4: Material properties for the pile problem

Specific volume at unit pressure on the VCL, v_1	3.765
Slope of VCL in v - lnp' space, λ	0.25
Slope of swelling line in v - lnp' space, κ	0.05
Slope of critical state line in J - p' space, M_J	0.52
Elastic shear modulus, G	18000 kPa
Initial overconsolidation ratio defined by p_o'/p'	1.1136
Initial radial and hoop effective stresses, σ_r' and σ_θ'	200 kPa
Initial vertical effective stress, σ_a'	286 kPa

To analyse this boundary value problem, finite element analyses were performed using the Authors' finite element program ICFEP. This program has options to use different stress point algorithms and for the work presented here analyses were either performed using a substepping algorithm based on that described in Appendix IX.1, or the constant elasticity return algorithm of Borja and Lee (1990) described in Appendix IX.2. A variable elasticity return algorithm for modified Cam clay is not implemented in the software, but its behaviour can be assessed by qualitative comparison with the results from the constant elasticity algorithm.

For each of the stress point algorithms a series of analyses were performed. In each analysis the pile was loaded by imposing a single increment of vertical displacement to the pile shaft, the magnitude of which varied between analyses. The results from these analyses are compared with the correct solution which was obtained by performing an analysis with a large number of small solution increments. Analyses based on either stress point algorithm, using the small solution increments, gave similar results.

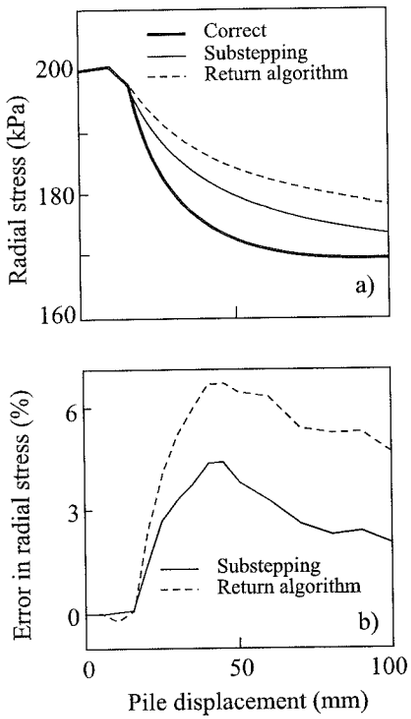

Figure IX.13: a) Radial stress versus pile displacement; b) error in radial stress

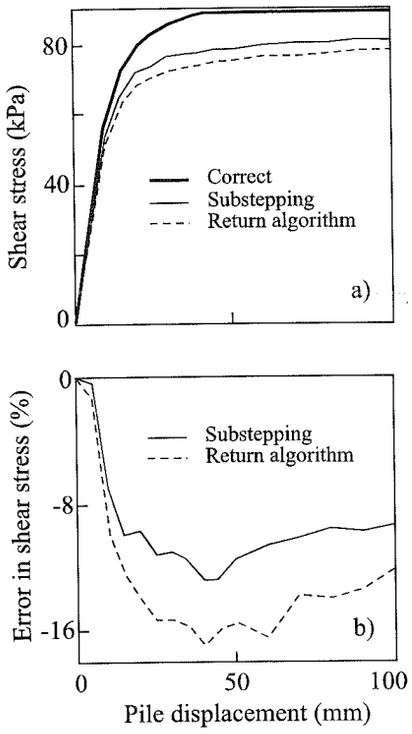

Figure IX.14: a) Shear stress versus pile displacement; b) error in shear stress

Results from the analyses are presented in Figures IX.13a and IX.14a, in the form of radial effective stress, σ_r', and shear stress, τ, at the pile, plotted against pile shaft displacement. When compared to the correct solution, the analyses based on the different stress point algorithms show errors. These errors increase and then decrease with the size of the solution increment, as illustrated in Figures IX.13b and IX.14b, where the error in σ_r' and τ respectively, expressed as a percentage of the correct solution, is plotted against pile displacement. The errors are larger for the return algorithm analyses than they are for the substepping approach. This is particularly so for the shear stress shown in Figure IX.14, where errors as high as 17% are recorded for the return algorithm analyses. Since the mean effective stress reduces as the pile is loaded, analyses using a variable elasticity return algorithm would give a softer response to that presented above and therefore result in larger errors.

An important feature of both these results and those of the undrained triaxial test is that the errors from both stress point algorithms do not increase monotonically with increasing solution increment size. This property means that extreme vigilance should be exercised when investigating the effect of solution increment size and a wide range of increment sizes should be examined.

IX.3.4 Consistent tangent operators

Borja and Lee (199)) and Borja (1991) suggest the use of a consistent tangent operator, $[\boldsymbol{D}]^{con}$, which results in a quadratic rate of convergence in the Newton-Raphson method. This involves formulating a stiffness matrix, at each iteration of an increment in a Newton-Raphson analysis, based on $[\boldsymbol{D}]^{con}$ where the $[\boldsymbol{D}]^{con}$, to be used for the $(j+1)^{th}$ iteration of the i^{th} increment, is:

$$[\boldsymbol{D}]^{con} = \frac{\delta \sigma_i^j}{\delta \varepsilon_i^j} \qquad \text{(IX.87)}$$

where:

$\boldsymbol{\sigma}_i^j$ is the stress state obtained using the return algorithm at the end of j^{th} iteration of the i^{th} increment;

$\boldsymbol{\varepsilon}_i^j$ is the applied increment of strain at the j^{th} iteration of the i^{th} increment.

$[\boldsymbol{D}]^{con}$ is a function of the return algorithm used and is in general asymmetric. However, at the beginning of the increment (when $j = 0$ and $\boldsymbol{\varepsilon}_i^0$ is the null vector), $[\boldsymbol{D}]^{con}$ is equal to the continuum elasto-plastic compliance matrix of the material, $[\boldsymbol{D}^{ep}]$. The elasto-plastic matrix is symmetric if the constitutive laws are associative. There is considerable confusion as to why $[\boldsymbol{D}]^{con}$ should be different to $[\boldsymbol{D}^{ep}]$ and why $[\boldsymbol{D}]^{con}$ should not be symmetrical in general for an associative material. Zienkiewicz and Taylor (1991) state that this difference is puzzling and is undecided as to whether $[\boldsymbol{D}]^{con}$ or $[\boldsymbol{D}^{ep}]$ should be used.

The difference between $[\boldsymbol{D}]^{con}$ and $[\boldsymbol{D}^{ep}]$ can be attributed to the error resulting from the assumptions used by the return algorithm associated with $[\boldsymbol{D}]^{con}$. This is illustrated in Figures IX.8a and IX.9a where $[\boldsymbol{D}]^{con}$ is related to the tangential

gradients of the return algorithm analyses in these stress-strain plots. $[\boldsymbol{D}^{ep}]$ is related to the tangential gradients of the correct analytical solution in these plots. Clearly, if the return algorithm was able to integrate the material constitutive laws accurately and give the correct analytical solution, there would be no difference between $[\boldsymbol{D}]^{con}$ and $[\boldsymbol{D}^{ep}]$.

IX.3.5 Conclusions

Both substepping and return algorithms attempt to integrate the constitutive equations over the strain increment derived from the modified Newton-Raphson (MNR) procedure. To do this correctly the manner in which the strain components vary during the increment must be known. Unfortunately, this information is not provided by the MNR approach and consequently, a further assumption must be made. The stress point algorithms differ in the nature of this assumption.

In the substepping approach the strains are assumed to vary 'proportionally' (i.e. the ratio between the strain components remains constant) over the increment and the constitutive equations are integrated along this strain path. If this assumption is true, then this approach results in accurate predictions. However, if this is not so, errors are introduced.

For the return algorithms the plastic strains for the increment are calculated from the plastic potential and stress conditions associated with conditions at the end of the increment. This approximation is only strictly valid if the plastic flow directions do not vary over the increment. This criterion is more stringent than the substepping criterion of 'proportional' strain variation.

Two return algorithm approaches, one assuming constant and the other assuming variable, elastic moduli over the increment have been considered in this appendix. Both approaches result in similar errors, but often the former less rigorous approach gives more accurate predictions. This arises as a result of compensating errors.

Comparisons presented in this appendix have been made using analytical solutions for simple idealised triaxial tests and by using results from finite element analyses of the pile problem. For these problems it is concluded that for the same solution increment size, analyses based on the substepping approach are more accurate than those based on the return algorithm approach. As the solution increment size is reduced, the results from both methods become similar and agree with the analytical or correct solutions.

10. Seepage and consolidation

10.1 Synopsis

In the previous chapters, analysis has been restricted to either drained or undrained soil conditions. While many problems can be solved making one, or a combination, of these two extreme conditions, real soil behaviour is often time related, with the pore water pressure response dependent on soil permeability, the rate of loading and the hydraulic boundary conditions. To account for this behaviour, the seepage equations must be combined with the equilibrium and constitutive equations. This chapter briefly describes the basis behind such a coupled approach and presents the finite element equations. It is then shown how the steady state seepage equations can be obtained from these general consolidation equations. The hydraulic boundary conditions relevant to geotechnical engineering are discussed afterwards. Some nonlinear permeability models are presented, followed by a short discussion on the numerical problems associated with unconfined seepage. The chapter finishes by presenting an example of coupled finite element analysis.

10.2 Introduction

The theory presented so far in this book has been restricted to dealing with either fully drained or undrained soil behaviour. While many geotechnical problems can be solved by adopting such extreme soil conditions, real soil behaviour is usually time related, with the pore water pressure response dependent on soil permeability, the rate of loading and the hydraulic boundary conditions. To account for such behaviour it is necessary to combine the equations governing the flow of pore fluid through the soil skeleton, with the equations governing the deformation of the soil due to loading. Such theory is called *coupled*, as it essentially couples pore fluid flow and stress strain behaviour together.

The chapter begins by presenting the theory behind the coupled finite element approach. This results in both displacement and pore fluid pressure degrees of freedom at element nodes. If the soil skeleton is rigid, the soil cannot deform and the coupled equations reduce to the steady state seepage equations. It is therefore a simple matter to establish the governing finite element equations for this situation from the more general coupled equations. Only pore fluid degrees of freedom at each node are relevant for seepage analyses.

As the flow of water within the soil skeleton is now being considered, the

hydraulic boundary conditions which control it must be accounted for. These boundary conditions consist of either prescribed flows or changes in pore fluid pressure. Some of the boundary conditions relevant to geotechnical engineering are described in this chapter. In particular sources, sinks, infiltration and precipitation boundary conditions are covered. The latter option accounts for the finite capacity of soil to accommodate the entry of pore fluids from a boundary.

Although it is often assumed that the permeability of soil is constant, laboratory and field tests show that this is not so. Fundamentally, one would expect the permeability to depend on the size of the void space between the solid soil grains and therefore depend on void ratio (or specific volume). Three nonlinear permeability models are presented in this chapter. In one of these the permeability varies with void ratio, whereas in the other two it varies with the mean effective stress.

Two different types of pore fluid flow can be identified: those which do not involve a phreatic surface (confined flow) and those which do (unconfined flow), as shown in Figure 10.1. Problems which involve unconfined flow require special attention in numerical analysis, as it is necessary to determine the position of the phreatic surface. This is not straight forward and a brief discussion of how this may be achieved is given.

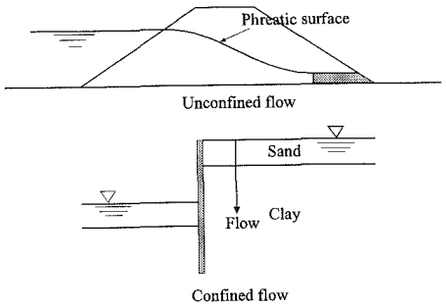

Figure 10.1: Examples of confined and unconfined flow

The chapter ends by presenting an example of a coupled analysis.

10.3 Finite element formulation for coupled problems

When deriving the finite element equations in Chapter 2, it was assumed, when evaluating the incremental strain energy in Equation (2.19), that the constitutive behaviour could be written in terms of a relationship between increments of total stress and strain:

$$\{\Delta\sigma\} = [\boldsymbol{D}]\{\Delta\varepsilon\} \tag{10.1}$$

If the material behaviour is defined in terms of total stress, as for example in the Tresca model, obtaining the constitutive matrix $[\boldsymbol{D}]$ is relatively straight forward. However, if the material behaviour is defined in terms of effective stress, which is the preferred method in soil mechanics and follows from the principle of effective stress, additional complications can arise. It has been shown in Chapter 3 how the $[\boldsymbol{D}]$ matrix can be obtained from the effective matrix $[\boldsymbol{D}']$ in the special cases of fully drained and undrained soil behaviour. If soil behaviour is somewhere between these two extreme conditions, account must be taken of the time dependency of the

changes in pore fluid pressure and effective stress. A procedure for achieving this is described below.

Using the principle of effective stress Equation (10.1) becomes:

$$\{\Delta\sigma\} = [\boldsymbol{D}']\{\Delta\varepsilon\} + \{\Delta\sigma_f\} \tag{10.2}$$

where $\{\Delta\boldsymbol{\sigma}_f\}^T=\{\Delta p_f, \Delta p_f, \Delta p_f, 0, 0, 0\}$ and Δp_f is the change in pore fluid pressure.

In the finite element approach it is assumed that the nodal displacements and the nodal pore fluid pressures are the primary unknowns. As before the incremental displacements can be expressed in terms of nodal values using Equation (2.9). In addition, it is assumed that the incremental pore fluid pressure, Δp_f, can be expressed in terms of nodal values using an equation similar to Equation (2.9):

$$\{\Delta\boldsymbol{p}_f\} = [\boldsymbol{N}_p]\{\Delta\boldsymbol{p}_f\}_n \tag{10.3}$$

where $[\boldsymbol{N}_p]$ is the matrix of pore fluid pressure interpolation functions, similar to $[\boldsymbol{N}]$. The choice of $[\boldsymbol{N}_p]$ will be discussed subsequently. However, $[\boldsymbol{N}_p]$ is often assumed to be equivalent to $[\boldsymbol{N}]$.

The analysis of time dependent consolidation requires the solution of Biot's (Biot (1941)) consolidation equations, coupled with the material constitutive model and the equilibrium equations. The following basic equations have to be satisfied for a soil saturated with an incompressible pore fluid:

- The equations of equilibrium:

$$\begin{aligned}
\frac{\partial\sigma'_x}{\partial x} + \frac{\partial p_f}{\partial x} + \frac{\partial\tau_{xy}}{\partial y} + \frac{\partial\tau_{xz}}{\partial z} + \gamma_x &= 0\\
\frac{\partial\sigma'_y}{\partial y} + \frac{\partial p_f}{\partial y} + \frac{\partial\tau_{xy}}{\partial x} + \frac{\partial\tau_{yz}}{\partial z} + \gamma_y &= 0\\
\frac{\partial\sigma'_z}{\partial z} + \frac{\partial p_f}{\partial z} + \frac{\partial\tau_{xz}}{\partial x} + \frac{\partial\tau_{yz}}{\partial y} + \gamma_z &= 0
\end{aligned} \tag{10.4}$$

  where γ_x, γ_y and γ_z are the components of the bulk unit weight of the soil acting in the x, y and z directions respectively.
- The constitutive behaviour, expressed in terms of effective stresses:

$$\{\Delta\sigma'\} = [\boldsymbol{D}']\{\Delta\varepsilon\} \tag{10.5}$$

- The equation of continuity, see Figure 10.2:

$$\frac{\partial v_x}{\partial x} + \frac{\partial v_y}{\partial y} + \frac{\partial v_z}{\partial z} - Q = \frac{\partial\varepsilon_v}{\partial t} \tag{10.6}$$

  where v_x, v_y and v_z are the components of the superficial velocity of the pore fluid in the coordinate directions, and Q represents any sources and/or sinks.

- Generalised Darcy's law:

$$\begin{Bmatrix} v_x \\ v_y \\ v_z \end{Bmatrix} = -\begin{bmatrix} k_{xx} & k_{xy} & k_{xz} \\ k_{xy} & k_{yy} & k_{yz} \\ k_{xz} & k_{yz} & k_{zz} \end{bmatrix} \begin{Bmatrix} \dfrac{\partial h}{\partial x} \\ \dfrac{\partial h}{\partial y} \\ \dfrac{\partial h}{\partial z} \end{Bmatrix} \tag{10.7}$$

or:

$$\{v\} = -[k]\{\nabla h\}$$

where h is the hydraulic head defined as:

$$h = \frac{p_f}{\gamma_f} + \left(x i_{Gx} + y i_{Gy} + z i_{Gz}\right) \tag{10.8}$$

Vector $\{i_G\}=\{i_{Gx}\ ,\ i_{Gy}\ ,\ i_{Gz}\}^T$ is the unit vector parallel, but in the opposite direction, to gravity; k_{ij} are the coefficients of the permeability matrix, $[k]$, of the soil. If the soil is isotropic with a permeability k, then $k_{xx}= k_{yy}= k_{zz}= k$ and $k_{xy}= k_{xz}= k_{yz}= 0$.

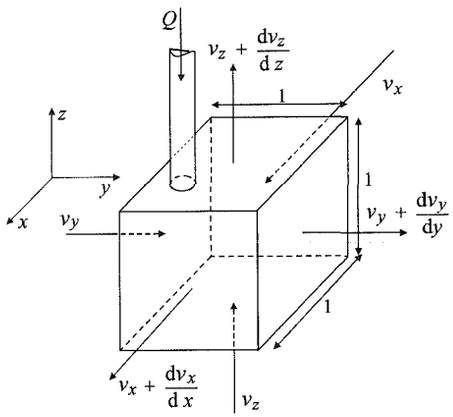

Figure 10.2: Continuity conditions

As noted in Chapter 2 a more convenient form of the equations of equilibrium expressed by Equation (10.4) can be found by considering the principle of minimum potential energy which states that (see Equation (2.18)):

$$\delta\Delta E = \delta\Delta W - \delta\Delta L = 0 \tag{10.9}$$

where ΔE is the incremental total potential energy, ΔW is the incremental strain energy and ΔL is the incremental work done by applied loads. The incremental strain energy term, ΔW, is defined as:

$$\Delta W = \tfrac{1}{2}\int_{Vol} \{\Delta\varepsilon\}^T\{\Delta\sigma\}\, dVol \tag{10.10}$$

Using Equation (10.2) this can be written in the following form:

$$\Delta W = \tfrac{1}{2}\int_{Vol} [\{\Delta\varepsilon\}^T[\boldsymbol{D'}]\{\Delta\varepsilon\} + \{\Delta\sigma_f\}\{\Delta\varepsilon\}]\, dVol \tag{10.11}$$

Noting that the second term in this equation is equivalent to $\Delta p_f \cdot \Delta\varepsilon_v$, gives:

$$\Delta W = \tfrac{1}{2}\int_{Vol} [\{\Delta\varepsilon\}^T[\boldsymbol{D'}]\{\Delta\varepsilon\} + \Delta p_f \Delta\varepsilon_v]\, dVol \tag{10.12}$$

The work done by the incremental applied loads ΔL can be divided into contributions from body forces and surface tractions, and can therefore be expressed as (see Equation (2.20)):

$$\Delta L = \int_{Vol} \{\Delta\boldsymbol{d}\}^T\{\Delta\boldsymbol{F}\}\, dVol + \int_{Srf} \{\Delta\boldsymbol{d}\}^T\{\Delta\boldsymbol{T}\}\, dSrf \tag{10.13}$$

Substituting Equations (10.12) and (10.13) into Equation (10.9) and following a similar procedure to that outlined in Chapter 2 (i.e. Equations (2.21) to (2.25)), gives the following finite element equations associated with equilibrium:

$$[\boldsymbol{K_G}]\{\Delta\boldsymbol{d}\}_{nG} + [\boldsymbol{L_G}]\{\Delta\boldsymbol{p}_f\}_{nG} = \{\Delta\boldsymbol{R_G}\} \tag{10.14}$$

where:

$$[\boldsymbol{K_G}] = \sum_{i=1}^{N} [\boldsymbol{K_E}]_i = \sum_{i=1}^{N} \left(\int_{Vol} [\boldsymbol{B}]^T[\boldsymbol{D'}][\boldsymbol{B}]\, dVol\right)_i \tag{10.15}$$

$$[\boldsymbol{L_G}] = \sum_{i=1}^{N} [\boldsymbol{L_E}]_i = \sum_{i=1}^{N} \left(\int_{Vol} \{\boldsymbol{m}\}[\boldsymbol{B}]^T[\boldsymbol{N}_p]\, dVol\right)_i \tag{10.16}$$

$$\{\Delta\boldsymbol{R_G}\} = \sum_{i=1}^{N} \{\Delta\boldsymbol{R_E}\}_i = \sum_{i=1}^{N} \left[\left(\int_{Vol} [\boldsymbol{N}]^T\{\Delta\boldsymbol{F}\}\, dVol\right)_i + \left(\int_{Srf} [\boldsymbol{N}]^T\{\Delta\boldsymbol{T}\}\, dSrf\right)_i\right] \tag{10.17}$$

$$\{\boldsymbol{m}\}^T = \{1\ \ 1\ \ 1\ \ 0\ \ 0\ \ 0\} \tag{10.18}$$

Using the principle of virtual work, the continuity Equation (10.6) can be written as:

$$\int_{Vol} [\{\boldsymbol{v}\}^T\{\nabla(\Delta p_f)\} + \frac{\partial\varepsilon_v}{\partial t}\Delta p_f]\, dVol - Q\,\Delta p_f = 0 \tag{10.19}$$

Substituting for $\{\boldsymbol{v}\}$ using Darcy's law given by Equation (10.7) gives:

$$\int_{Vol} [-\{\nabla h\}^T[\boldsymbol{k}]\{\nabla(\Delta p_f)\} + \frac{\partial\varepsilon_v}{\partial t}\Delta p_f]\, dVol = Q\,\Delta p_f \tag{10.20}$$

Noting that $\{\nabla h\} = (1/\gamma_f)\nabla\boldsymbol{p}_f + \{\boldsymbol{i_G}\}$, and approximating $\partial\varepsilon_v/\partial t$ as $\Delta\varepsilon_v/\Delta t$, Equation (10.20) can be written in finite element form as:

$$[\boldsymbol{L_G}]^T\left(\frac{\{\Delta\boldsymbol{d}\}_{nG}}{\Delta t}\right) - [\boldsymbol{\Phi_G}]\{\boldsymbol{p}_f\}_{nG} = [\boldsymbol{n_G}] + Q \tag{10.21}$$

where:

$$[\Phi_G] = \sum_{i=1}^{N} [\Phi_E]_i = \sum_{i=1}^{N} \left(\int_{Vol} \frac{[E]^T[k][E]}{\gamma_f} \, dVol \right)_i \tag{10.22}$$

$$[n_G] = \sum_{i=1}^{N} [n_E]_i = \sum_{i=1}^{N} \left(\int_{Vol} [E]^T[k]\{i_G\} \, dVol \right)_i \tag{10.23}$$

$$[E] = \left[\frac{\partial N_p}{\partial x} , \frac{\partial N_p}{\partial y} , \frac{\partial N_p}{\partial z} \right]^T \tag{10.24}$$

To solve Equations (10.14) and (10.21) a time marching process is adopted. If the solution $(\{\Delta d\}_{nG}$, $\{p_f\}_{nG})_1$ is known at time t_1, then the solution $(\{\Delta d\}_{nG}$, $\{p_f\}_{nG})_2$ at time $t_2=t_1+\Delta t$ is sought. To proceed it is necessary to assume:

$$\int_{t1}^{t2} [\Phi_G]\{p_f\}_{nG} \, dt = [\Phi_G]\left[\beta(\{p_f\}_{nG})_2 + (1-\beta)(\{p_f\}_{nG})_1\right]\Delta t \tag{10.25}$$

This approximation is shown graphically in Figure 10.3. As $\{p_f\}_{nG}$ varies over the time step Δt, the integral on the left hand side of Equation (10.25) represents the area under the curve in Figure 10.3 between t_1 and t_2. However, the manner in which $\{p_f\}_{nG}$ varies (i.e the shape of the curve) is unknown, but the value of $(\{p_f\}_{nG})_1$ is known while the value of $(\{p_f\}_{nG})_2$ is being sought. Equation (10.25) is therefore an approximation of the area under the curve. For example, if β=1 the area is essentially assumed to be $(\{p_f\}_{nG})_2\Delta t$. Alternatively, if $\beta = 0.5$ the area is approximated by $0.5\Delta t\,[(\{p_f\}_{nG})_1 + (\{p_f\}_{nG})_2]$. In order to ensure stability of the marching process, it is necessary to choose $\beta \geq 0.5$ (Booker and Small (1975)). Substituting Equation (10.25) into (10.21) gives:

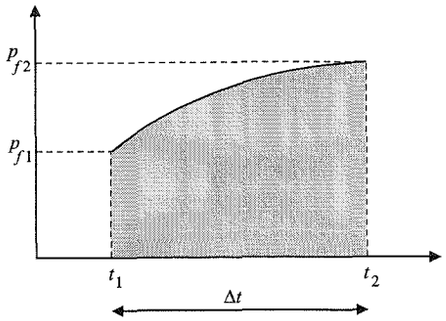

Figure 10.3: Approximation of pore fluid integral

$$[L_G]^T\{\Delta d\}_{nG} - \beta\Delta t\,[\Phi_G]\{\Delta p_f\}_{nG} = [n_G]\Delta t + Q\,\Delta t + [\Phi_G](\{p_f\}_{nG})_1\,\Delta t \tag{10.26}$$

Equations (10.14) and (10.26) may now be written in the following incremental matrix form:

$$\begin{bmatrix} [K_G] & [L_G] \\ [L_G]^T & -\beta\Delta t\,[\Phi_G] \end{bmatrix} \begin{Bmatrix} \{\Delta d\}_{nG} \\ \{\Delta p_f\}_{nG} \end{Bmatrix} = \begin{Bmatrix} \{\Delta R_G\} \\ \left([n_G] + Q + [\Phi_G](\{p_f\}_{nG})_1\right)\Delta t \end{Bmatrix} \tag{10.27}$$

10.4 Finite element implementation

Equation (10.27) provides a set of simultaneous equations in terms of the incremental nodal displacements $\{\Delta d\}_{nG}$ and incremental nodal pore fluid pressures $\{\Delta p_f\}_{nG}$. Once the stiffness matrix and right hand side vector have been assembled, the equations can be solved using the procedures described in Section 2.9.

As a marching procedure is necessary to solve for the time dependent behaviour, the analysis must be performed incrementally. This is necessary even if the constitutive behaviour is linear elastic and the permeabilities are constant. If the constitutive behaviour is nonlinear, the time steps can be combined with changes in the loading conditions so that the complete time history of construction can be simulated. The solution algorithms described in Chapter 9 can therefore be used.

In the above formulation the permeabilities have been expressed by the matrix $[k]$. If these permeabilities are not constant, but vary with stress or strain, the matrix $[k]$ (and therefore $[\Phi_G]$ and $[n_G]$) are not constant over an increment of an analysis (and/or a time step). Care must therefore be taken when solving Equation (10.27). This problem is similar to that associated with nonlinear stress-strain behaviour where $[K_G]$ is not constant over an increment. As noted in Chapter 9, there are several numerical procedures available for dealing with a nonlinear $[K_G]$, and, as demonstrated, some of these are more efficient than others. All the procedures described in Chapter 9 (e.g. tangent stiffness, visco-plastic and Newton-Raphson) can be modified to accommodate nonlinear permeability. However, the Authors' experience is that the modified Newton-Raphson scheme, with a substepping stress point algorithm, is the most accurate.

In Equation (10.3) the incremental pore fluid pressure within an element has been related to the values at the nodes using the matrix of pore fluid shape functions $[N_p]$. If an incremental pore fluid pressure degree of freedom is assumed at each node of every consolidating element, $[N_p]$ is the same as the matrix of displacement shape functions $[N]$. Consequently, pore fluid pressures vary across the element in the same fashion as the displacement components. For example, for an eight noded quadrilateral element, both the displacements and pore fluid pressures vary quadratically across the element. However, if the displacements vary quadratically, the strains, and therefore the effective stresses (at least for a linear material), vary linearly. There is therefore an inconsistency between the variation of effective stresses and pore water pressures across the element. While this is theoretically acceptable, some users prefer to have the same order of variation of both effective stresses and pore water pressure. For an eight

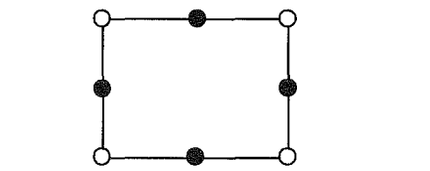

Figure 10.4: Degrees of freedom for an eight noded element

noded element this can be achieved by only having pore fluid pressure degrees of freedom at the four corner nodes, see Figure 10.4. This will result in the $[N_p]$ matrix only having contributions from the corner nodes and therefore differing from $[N]$. Similar behaviour can be achieved by only having pore fluid pressure degrees of freedom at the three apex nodes of a six noded triangle, or at the eight corner nodes of a twenty noded hexahedron. Some software programs allow the user to decide which of these two approaches to use.

It is possible to have some elements within a finite element mesh which are consolidating and some which are not. For example, if a situation where sand overlies clay is being modelled, consolidating elements (i.e. elements with pore pressure degrees of freedom at their nodes) might be used for the clay, whereas ordinary elements (i.e. no pore fluid pressure degrees of freedom at the nodes) might be used for the sand, see Figure 10.5. The sand is then assumed to behave in a drained manner by specifying a zero value for the bulk compressibility of the pore fluid, see Section 3.4. Clearly, care has to be taken to ensure the correct hydraulic boundary condition is applied to the nodes at the interface between clay and sand. Some software programs insist that the user decides which elements are to consolidate and which are not at the mesh generation stage. Others are more flexible and allow the decision to be made during the analysis stage.

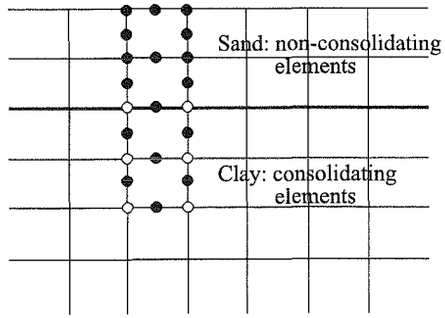

Figure 10.5: Choice of elements for consolidating and non-consolidating layers

In the theory developed above, the finite element equations have been formulated in terms of pore fluid pressure. It is also possible to formulate the equations in terms of hydraulic head, or in terms of excess pore fluid pressure. In such cases the hydraulic head or excess pore fluid pressure at the nodes will become degrees of freedom. It is important that the user is familiar with the approach adopted by the software being used, as this will affect the manner in which the hydraulic boundary conditions are specified.

10.5 Steady state seepage

If the soil skeleton is assumed to be rigid, there can be no soil deformation and only flow of pore fluid through the soil exists. Equation (10.14) is therefore not applicable and Equation (10.21) reduces to:

$$-[\Phi_G]\{p_f\}_{nG} = [n_G] + Q \qquad (10.28)$$

This is the finite element equation for steady state seepage. The only degrees of freedom are the nodal pore fluid pressures. If the permeabilties are constant and the flow is confined, Equation (10.28) can be solved by a single inversion of the matrix $[\Phi_G]$. As only pore fluid pressures are calculated, it is only possible to have permeabilities varying with pore fluid pressure. If this is the case and/or if the flow is unconfined, an iterative approach must be used to solve Equation (10.28).

If a particular piece of finite element software can deal with the coupled formulation given by Equation (10.27), but not the steady state formulation given by Equation (10.28), it is still possible to use it to obtain a steady state seepage solution. This is achieved by giving the soil fictitious linear elastic properties and applying sufficient displacement constraints to prevent rigid body motion. An analysis is then performed applying the correct hydraulic boundary conditions and sufficient time steps for steady state conditions to be achieved. Once steady state conditions have been reached, soil deformations are zero and the solution is therefore equivalent to that given by Equation (10.28).

10.6 Hydraulic boundary conditions

10.6.1 Introduction

With either coupled or steady state seepage analysis there are pore fluid pressure degrees of freedom at the nodes, and for each node on the boundary of the mesh (or of that part of the mesh consisting of consolidating elements) it is necessary to specify either a prescribed pore fluid pressure or a prescribed nodal flow. If a condition is not specified by the user, for one or several of the boundary nodes, most software packages will assume a default condition. This usually takes the form of zero nodal flow. Clearly, the user must be fully aware of the default condition that the software assumes, and account for this when specifying the boundary conditions for an analysis. Boundary conditions can also be prescribed at internal nodes of the finite element mesh.

Prescribed values of incremental nodal pore fluid pressure affect only the left-hand side (i.e. $\{\Delta p_f\}_{nG}$) of the system equations. They are dealt with in a similar fashion to prescribed displacements. Prescribed nodal flow values affect the right hand side vector (i.e. Q) of the system equations. They are treated in a similar way to prescribed nodal forces. They can be specified in the form of *sources*, *sinks*, *infiltration* and *precipitation* boundary conditions. It is also possible to *tie* nodal pore fluid pressures in a similar manner to that described for displacements in Chapter 3. Such boundary conditions will affect the whole structure of the system equations. The various hydraulic boundary condition options that are useful for geotechnical engineering are discussed below.

10.6.2 Prescribed pore fluid pressures

This option allows the user to specify a prescribed incremental change in nodal pore fluid pressure, $\{\Delta p_f\}_{nG}$. As pore fluid pressure is a scalar quantity, local axes are irrelevant. Prescribed changes in pore fluid pressures are dealt with in a similar way to prescribed displacements, as described in Section 3.7.3.

Although it is the incremental change in pore fluid pressure that is the required quantity when solving Equation (10.27), it is often more convenient for the user to specify the accumulated value at the end of a particular increment. It is then left to the software to work out the incremental change from the prescribed value, given by the user for the end of the increment, and the value stored internally in the computer, for the beginning of the increment. It is noted that not all software packages have this facility. It should also be noted that some software packages may use change in head or excess pore fluid pressure instead of pore fluid pressure, as the nodal degree of freedom. Consequently, the boundary conditions will have to be consistent.

As an example of the use of prescribed pore fluid pressures, consider the excavation problem shown in Figure 10.6. Throughout the analysis it is assumed that on the right hand side of the mesh the pore fluid pressures remain unchanged from their initial values. Consequently, for all the nodes along the boundary AB, a zero incremental pore fluid pressure (i.e. $\Delta p_f = 0$) is specified for every increment of the analysis. The first increments of the analysis simulate excavation in front of the wall and it is assumed that the excavated surface is impermeable. Consequently, no pore fluid pressure boundary condition is prescribed along this surface and a default condition of zero nodal flow is imposed. However, once excavation is completed, as shown in Figure 10.6, the excavated soil surface is assumed to be permeable, with a zero pore fluid pressure. Therefore, for the increment after excavation has been completed, the final accumulated value (i.e. $p_f = 0$) is specified along CD. As the program knows the accumulated pore fluid pressure at the nodes along this boundary at the end of excavation, it can evaluate Δp_f. For subsequent increments the pore fluid pressure remains at zero along CD and consequently $\Delta p_f = 0$ is applied.

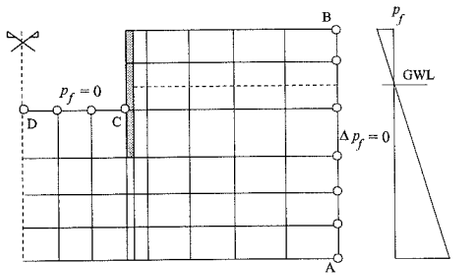

Figure 10.6: Prescribed pore fluid boundary conditions

10.6.3 Tied degrees of freedom

This boundary condition option allows a condition of equal incremental nodal pore fluid pressure to be imposed at two or more nodes, whilst the magnitude of the incremental nodal pore fluid pressure remains unknown. This concept is explained in detail for displacements in Section 3.7.4 and therefore is not repeated here. Because pore fluid pressure is a scalar quantity, there is only one tying option, compared to the several that are available for displacement which is a vector, see Figure 3.20.

As an example of the use of tied pore fluid pressure, consider the example of two consolidating layers of soil, separated by interface elements shown in Figure 10.7. Because interface elements have zero thickness, they are not usually formulated to account for consolidation. In the situation shown in Figure 10.7, there is a set of nodes along the underside of soil layer 1 and another set on the upper surface of soil layer 2, corresponding to the upper and lower side of the row of interface elements respectively. Because the interface elements do not account for consolidation, there is no seepage link between these two rows of nodes and, unless a boundary condition is specified for these nodes, most software programs will treat each row as an impermeable boundary (i.e. zero incremental nodal flow). If the interface is to be treated as a permeable boundary, the solution is to tie the incremental pore fluid pressures of adjacent nodes across the interface elements. For example, tie the incremental pore fluid pressures for nodes AB, CD, ..., etc.

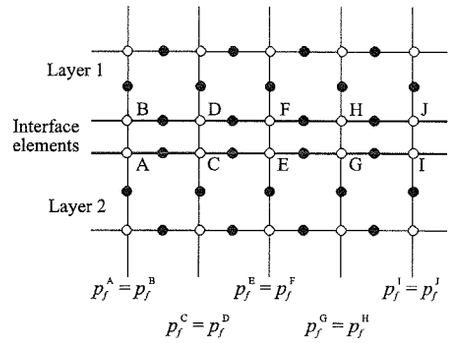

Figure 10.7: Tied pore fluid pressures

10.6.4 Infiltration

When it is necessary to prescribe pore fluid flows across a boundary of the finite element mesh for a particular increment of the analysis, infiltration boundary conditions are used. These flows are treated in a similar fashion to boundary stresses as described in Section 3.7.6.

An example of an infiltration boundary condition is shown in Figure 10.8, where it is assumed that rainfall provides a flow rate q_n on the soil surface adjacent to the excavation. In general, the flow rate may vary along the boundary over which it is active. To apply such a boundary condition in finite element analysis, the flow over the boundary must be converted into equivalent nodal flows. Many finite element programs will do this automatically for generally distributed boundary flows and for arbitrary shaped boundaries.

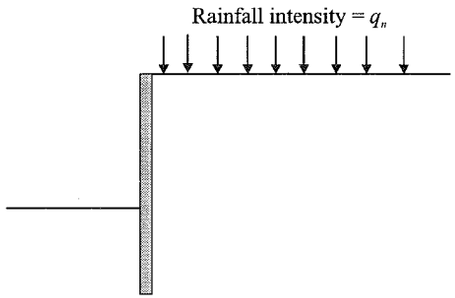

Figure 10.8: Example of infiltration boundary conditions

The nodal flows equivalent to the infiltration boundary condition are determined from the following equation:

$$\left\{\boldsymbol{Q}_{infil}\right\} = \int_{Srf} \left[\boldsymbol{N}_p\right]^{\mathrm{T}} q_n \, \mathrm{d}Srf \qquad (10.29)$$

where *Srf* is the element side over which the infiltration flow is prescribed. As with boundary stresses, this integral can be evaluated numerically for each element side on the specified boundary range, see Section 3.7.6.

10.6.5 Sources and sinks

A further option for applying flow boundary conditions is to apply sources (inflow) or sinks (outflow) at discrete nodes, in the form of prescribed nodal flows. For plane strain and axi-symmetric analyses these are essentially line flows acting perpendicularly to the plane of the finite element mesh.

An example of a source and sink boundary condition is shown in Figure 10.9 in the form of a simple dewatering scheme, involving a row of extraction wells (sinks) within an excavation and, to limit excessive settlements behind the retaining wall, a row of injection wells (sources). The effect of the extraction wells could be modelled by applying a flow rate equivalent to the pumping rate at node A, and the effect of the injection wells could be modelled by applying a flow rate equivalent to the injection rate at node B.

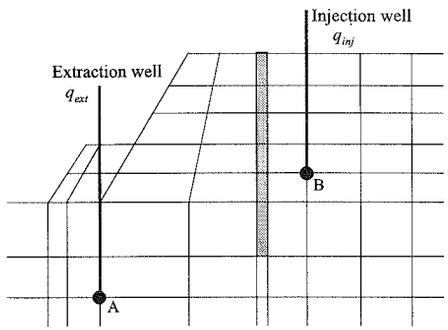

Figure 10.9: Example of sources and sinks boundary conditions

10.6.6 Precipitation

This boundary condition option allows the user to essentially prescribe a dual boundary condition to part of the mesh boundary. Both an infiltration flow rate, q_n, and a pore fluid pressure, p_{fb}, are specified. At the start of an increment, each node on the boundary is checked to see if the pore fluid pressure is more compressive than p_{fb}. If it is, the boundary condition for that node is taken as a prescribed incremental pore fluid pressure Δp_f, the magnitude of which gives an accumulated pore fluid pressure equal to p_{fb} at the end of the increment. Alternatively, if the pore fluid pressure is more tensile than p_{fb}, or if the current flow rate at the node exceeds the value equivalent to q_n, the boundary condition is taken as a prescribed infiltration with the nodal flow rate determined from q_n. The following two examples show how this boundary condition may be used.

Tunnel problem

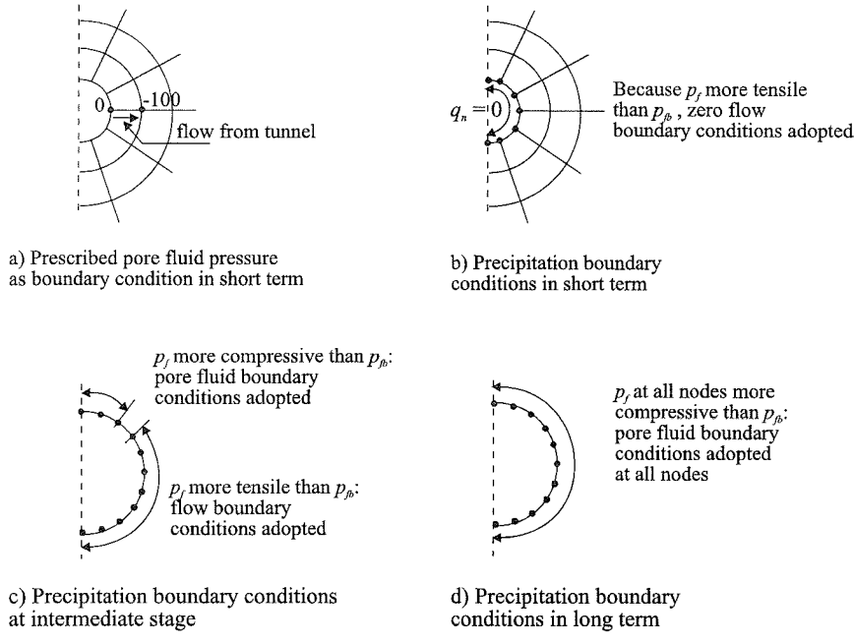

Figure 10.10: Precipitation boundary conditions in tunnel problem

After excavation for a tunnel, assuming the tunnel boundary to be impermeable, the pore fluid pressure in the soil adjacent to the tunnel could be tensile, see Volume 2 of this book. If for subsequent increments of the analysis (tunnel boundary now permeable) a prescribed zero accumulated pore fluid pressure boundary condition is applied to the nodes on the tunnel boundary, flow of water from the tunnel into the soil would result, see Figure 10.10a. This is unrealistic, because there is unlikely to be a sufficient supply of water in the tunnel. This problem can be dealt with using the precipitation boundary option with $q_n = 0$ and $p_{fb} = 0$. Initially (after excavation), the pore fluid pressures at the nodes on the tunnel boundary are more tensile than p_{fb}, consequently a flow boundary condition with $q_n = 0$ (i.e. no flow) is adopted, see Figure 10.10b. With time the tensile pore fluid pressures reduce due to swelling and eventually become more compressive than p_{fb}. When this occurs, the pore fluid stress boundary condition is applied, with a magnitude set to give an accumulated pore fluid pressure at the end of the increment equal to p_{fb}, see Figure 10.10d. The pore fluid pressure checks are made on a nodal basis for all nodes on the tunnel boundary for each increment. This implies that the boundary condition can change at individual nodes at different increments of the analysis. At any one increment some nodes can have a prescribed pore fluid stress boundary condition, while others can have a flow condition, see Figure 10.10c.

Rainfall infiltration

In this case the problem relates to a boundary which is subject to rainfall of a set intensity. If the soil is of sufficient permeability and/or the rainfall intensity is small, the soil can absorb the water and a flow boundary condition is appropriate, see Figure 10.11a. However, if the soil is less permeable and/or the rainfall intensity is high, the soil will not be able to absorb the water, which will pond on the surface, see Figure 10.11b. There is a finite depth to such ponding, which is problem specific, and consequently a pore fluid pressure boundary condition would be applicable. However, it is not always possible to decide which boundary condition is relevant before an analysis is undertaken, because the behaviour will depend on soil stratification, permeability and geometry. The dilemma can be overcome by using the precipitation boundary condition, with q_n set equal to the rainfall intensity and p_{fb} set to have a value more compressive (i.e. equivalent to the ponding level) than p_{fi}, the initial value of the pore fluid stress at the soil boundary. Because p_{fi} is more tensile than p_{fb}, a flow boundary condition will be assumed initially. If during the analysis the pore fluid pressure becomes more compressive than p_{fb}, the boundary condition will switch to that of a prescribed pore fluid pressure.

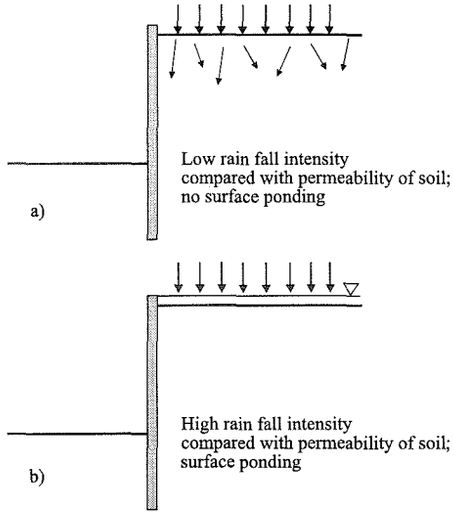

Figure 10.11: Rainfall infiltration boundary conditions

10.7 Permeability models

10.7.1 Introduction

When performing coupled (or steady seepage) analysis it is necessary to input permeability values for the soils undergoing seepage. For coupled analysis it is also necessary to input the constitutive behaviour. Several options exist for specifying permeabilities. For example, the soil can be assumed to be isotropic or anisotropic, the permeabilities can vary spatially, or they can vary nonlinearly as a function of void ratio or mean effective stress. Some of the models that the Authors find useful are briefly described below.

10.7.2 Linear isotropic permeability

This model assumes permeability to be isotropic and, at any point, defined by a single value of k. However, in most soils the permeability varies with void ratio and therefore mean effective stress, or depth. It is therefore convenient to have the option to vary k spatially. For example, options are often available for varying k in a piece wise linear fashion across a finite element mesh. This option can be used to simulate a permeability varying with depth, see Figure 10.12 (note: coefficient of permeability is plotted on a log scale). With this model, the permeability at an integration point remains constant throughout an analysis.

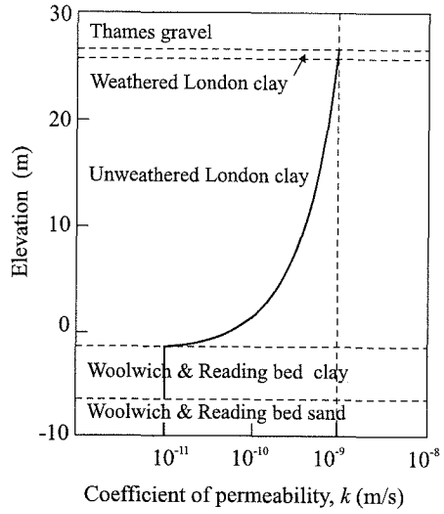

Figure 10.12: Permeability profile for London clay

10.7.3 Linear anisotropic permeability

In this model the permeability is assumed to be direction dependent. A set of permeability axes are defined (x_m , y_m , z_m) and values for the coefficient of permeability in each direction specified (k_{xm}, k_{ym}, k_{zm}). This enables the permeability matrix in Equation (10.7) to be obtained. It should be noted that this matrix is associated with the global coordinate axes and therefore, if the material and global axes differ, the permeability coefficients must be transformed. This is usually performed automatically by the software. Again, it is useful to have the option of varying the permeability values spatially.

10.7.4 Nonlinear permeability related to void ratio

In this model the permeability is assumed to be isotropic, but to vary as a function of the void ratio. The following relationship between the coefficient of permeability, k, and void ratio, e, is assumed:

$$\ln k = a + be \;\; ; \;\; k = e^{(a+be)} \qquad (10.30)$$

where a and b are material parameters. With this model it is necessary to know the void ratio at any stage of the analysis. This implies that the initial value, at the beginning of the analysis, must be input into the finite element program.

From a fundamental point of view, allowing the permeability to vary with void ratio makes sense. However, there is often little laboratory or field data available to determine the parameters a and b. Consequently, it is often convenient to adopt an expression in which k varies with mean effective stress. Two such models are presented below.

10.7.5 Nonlinear permeability related to mean effective stress using a logarithmic relationship

Again the permeability is assumed to be isotropic, but to vary as a function of mean effective stress, p', according to the following relationship:

$$\ln\left(\frac{k}{k_o}\right) = -ap' \;\; ; \;\; k = k_o e^{(-ap')} \tag{10.31}$$

where k_o is the coefficient of permeability at zero mean effective stress and a is a constant, incorporating the initial void ratio at zero mean effective stress and the coefficient of volume compressibility, m_v. The derivation of the logarithmic law therefore incorporates the assumption that m_v is constant (Vaughan (1989)).

10.7.6 Nonlinear permeability related to mean effective stress using a power law relationship

This model has been derived assuming that the compression index, C_c, remains constant (Vaughan (1989)). The relationship between permeability and mean effective stress takes the form:

$$\frac{k}{k_o} = (p')^{-a} \tag{10.32}$$

where again k_o and a are material parameters.

10.8 Unconfined seepage flow

Situations which involve unconfined flow, where it is necessary for the software to determine a phreatic surface, can be problematic, because there does not appear to be a robust algorithm for finding and accommodating the phreatic surface. There are several different algorithms available. Some of these involve adjustments to the finite element mesh so that the phreatic surface follows a mesh boundary. Such methods are not applicable to coupled consolidation analysis.

A more general approach is to reduce the permeability when the soil sustains a tensile pore fluid pressure associated with a position above the phreatic surface. A typical variation of permeability with pore fluid pressure is shown in Figure 10.13. If the accumulated pore fluid pressure is more compressive than p_{f1}, the soil's normal permeability (e.g. given by one of the models described above) is adopted. However, if the accumulated pore fluid pressure becomes more tensile than p_{f2}, the soil is assumed to be above the phreatic surface and the normal permeability is reduced by a large factor, R. Usually R takes a value somewhere between 100 and 1000. If the accumulated pore fluid pressure is between p_{f1} and p_{f2}, the permeability is found using a linear interpolation between the two extreme values. Clearly, this approach requires an iterative algorithm. It is therefore well suited to a nonlinear solution strategy of the modified Newton-Raphson type.

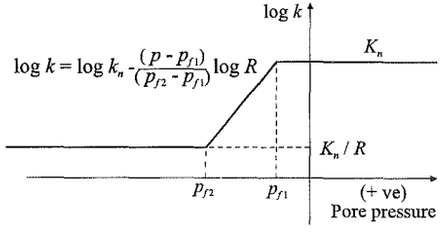

Figure 10.13: Variation of permeability with pore fluid pressure

Analysis involving a phreatic surface also require the use of the precipitation boundary option, so that boundary nodes can automatically switch from a prescribed pore fluid pressure to a prescribed flow.

The Authors' experience is that numerical instability can sometimes arise with this approach and that more research is required to obtain a robust algorithm.

10.9 Validation example

Closed form solutions for consolidation problems are not easy to obtain. This is especially true when dealing with elasto-plastic materials. Exact solutions have been found only to problems involving linear elastic materials, with simple geometry and subjected to simple boundary conditions.

One such problem is that of a porous elastic half-space, subjected to a load of intensity q over a width $2a$, under conditions of plane strain. This problem was used by the Authors as one of a series of validation exercises when coupled analysis was first coded into ICFEP. Some of the results from these analyses are now presented.

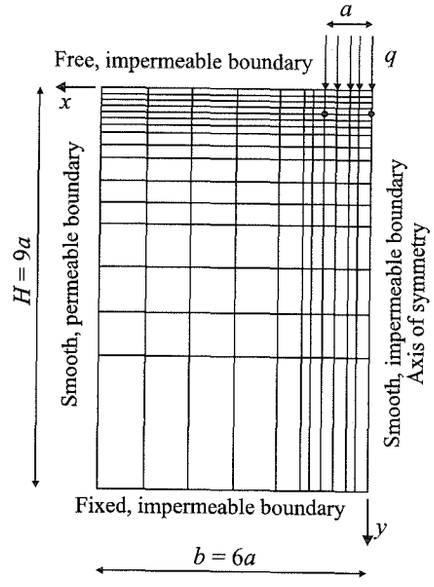

Figure 10.14: F.E. mesh for consolidation problem - I

Originally, the finite element mesh shown in Figure 10.14 was used. The boundary conditions employed are noted on this figure. The water table was assumed to be at the ground surface. The results are expressed in terms of the *adjusted time factor*, T:

$$T = \frac{\bar{c}t}{a^2} \tag{10.33}$$

and the *adjusted coefficient of consolidation*, $\bar{c}$:

$$\bar{c} = \frac{2Gk}{\gamma_f} \tag{10.34}$$

where G is the elastic shear modulus, k is the coefficient of permeability, γ_f is the bulk unit weight of the pore fluid, and t denotes time.

The load intensity q was applied in a very small time step (expressed in terms of the adjusted time factor, ΔT, it was 1.15×10^{-5}), resulting in an undrained response. Logarithmic time increments, typically five per 'log' cycle, were used thereafter. The response during the first 'log' cycle was essentially undrained, and the results for this 'log' cycle are not presented.

The variation of normalised excess pore fluid pressure, p_{excess}/q, beneath the centre of the loaded area is given in Figure 10.15 for the specific case of $T = 0.1$ and Poisson's ratio $\mu = 0$. It can be seen that the finite element prediction (open squares) over predicts the excess pore fluid pressure, particularly at greater depths beneath the loaded area. Because the closed form solution, presented by the full line in Figure 10.15 (Schiffman *et al.* (1969)), was derived for an infinite half-space, it was suspected that this discrepancy was due to the close proximity of the bottom and/or lateral boundaries in the finite element mesh. The effect of the position of both boundaries on the predictions was investigated and, surprisingly, it was found that the position of the lateral boundary has the greatest influence. Results from the mesh shown in Figure 10.16, which has a similar depth to that given in Figure 10.14, but three times the width, are shown in Figure 10.15 as solid squares. These results are in excellent agreement with the closed form solution, except for a slight discrepancy at the base of the mesh.

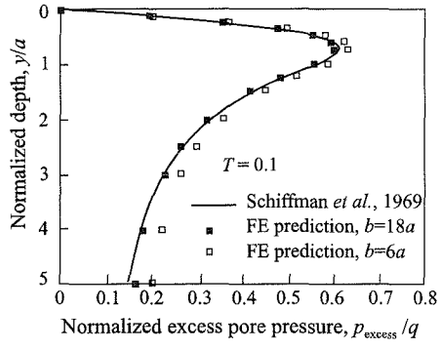

Figure 10.15: Variation of normalised excess pore pressure

In Figure 10.17 the variation of normalised excess pore fluid pressure, p_{excess}/q, with adjusted time factor, T, is given for two specific points in the half-space, see Figure 10.16. Two predictions were made, both using the mesh shown in Figure 10.16, with different forms of the element pore fluid pressure interpolation matrix, $[N_p]$. Eight noded isoparametric elements were employed and in one analysis, labelled as *code 8*, all eight nodes had a pore fluid pressure degree of freedom. In the other analysis, labelled *code 4*, only the four corner nodes had pore fluid pressure degrees of freedom. Consequently, in the *code 8* analysis there was a quadratic variation of pore fluid pressure across each finite element, whereas in the *code 4* analysis the distribution was linear. Also shown in Figure 10.17 is the closed form solution. It can be seen that the predictions from both finite element analyses are in excellent agreement with the closed form solution. In addition, there is very little difference between the predictions from the two finite element analysis.

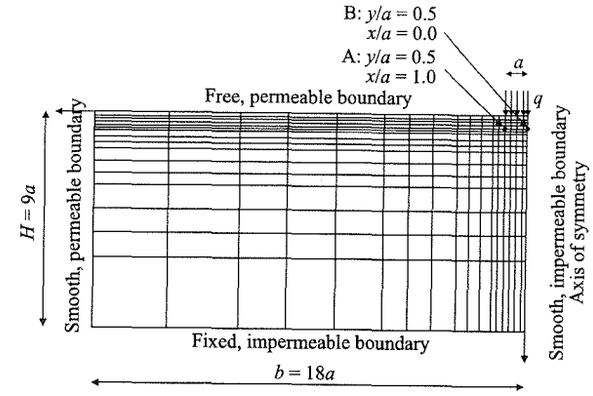

Figure 10.16: F.E. mesh for consolidation problem - II

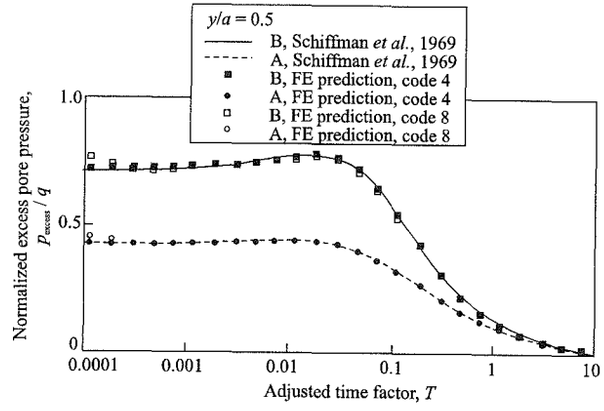

Figure 10.17: Variation of normalised excess pore pressure

10.10 Summary

1. This chapter has considered the modifications to the finite element theory that are necessary to enable time dependent soil behaviour to be simulated. This involves combining the equations governing the flow of pore fluid through the soil skeleton, with the equations governing the deformation of the soil due to loading.
2. The resulting finite element equations involve both displacement and pore fluid pressure degrees of freedom at element nodes. In addition, to enable a solution to be obtained, a time marching algorithm is necessary. This involves

an assumption of the magnitude of the average pore fluid pressures over each time step. It is assumed that, at each node, the average pore fluid pressure during the time step is linearly related to the values at the beginning and end of the time step. This involves the parameter β. For numerical stability $\beta \geq 0.5$.

3. Even for linear material behaviour analysis must be performed incrementally, to accommodate the time marching process.
4. It is possible to have some elements within a finite element mesh which are consolidating and some which are not.
5. If the soil skeleton is rigid, there can be no deformation and only flow of pore fluid through the soil occurs. This results in a considerable reduction in the complexity of the governing finite element equations. Only pore fluid pressure degrees of freedom need to be considered.
6. In coupled analysis hydraulic boundary conditions must be considered. These consist of prescribed nodal pore fluid pressures, tied pore fluid freedoms, infiltration, sinks and sources and precipitation.
7. For all nodes on the boundary of the finite element mesh either a prescribed pore fluid pressure or a flow boundary condition must be specified. If a boundary condition is not set for a boundary node, most software packages will implicitly assume that the node represents an impermeable boundary (i.e a zero nodal flow condition).
8. It is also necessary to input the coefficients of soil permeability. The permeability can take several different forms: it can be isotropic or anisotropic, it can vary spatially, or it can vary as a function of void ratio or mean effective stress. In the latter case the permeability at each integration point will vary during the analysis and the software must have the appropriate algorithms to cope with this.
9. Problems involving unconfined seepage, in which the analysis has to determine the position of a phreatic surface, can be accommodated. However, at present the algorithms that are available are not robust, which can lead to numerical instability. Further research is required.
10. The coupled theory presented in this chapter assumes the soil to be fully saturated. Further complications arise if the soil is partly saturated.

11. 3D finite element analysis

11.1 Synopsis

Although there are many geotechnical problems that can be approximated to either plane strain or axi-symmetric conditions, some remain which are very three dimensional. Such problems will therefore require full three dimensional numerical analysis. This chapter describes how the theory already presented can be extended to account for such behaviour. However, as it will be shown, the computer resources required for such analysis are considerable. Two ways can be used to reduce these resources. One way is to use iterative techniques to invert the global stiffness matrix, as opposed to the direct methods used so far. While such methods are recommended in the literature, it will be shown that, although they can lead to economies for linear elastic analysis, they are unlikely to be helpful for nonlinear analysis. The second way is to capitalise on any geometric symmetries that exist. In particular, if the geometry is axi-symmetric, but the loading or material behaviour is not, then the Fourier series aided finite element method can be used. A brief outline of this method and quantification of the savings in computer resources that can be achieved are described in Chapter 12.

11.2 Introduction

In the presentation of the finite element theory given in previous chapters, attention has been restricted to either plane strain or axi-symmetric conditions. In both these cases symmetry implies that displacements in one particular direction are zero. By choosing global axes such that one of the axes coincides with the direction of zero displacement, results in considerable simplifications. In finite element analysis it means that it is only necessary to account for two displacement degrees of freedom at each node, but more importantly, analysis can be performed over a representative two dimensional slice of the problem.

However, in reality most geotechnical problems are three dimensional, and, although in many, plane strain or axi-symmetric approximations are not unreasonable, there are some which must be treated as three dimensional. This implies that three components of displacement must be accounted for and that the complete three dimensional geometry must be considered. While theoretically this does not pose any insurmountable problems, in fact the basic theory presented in the previous chapters still holds, the quantity of data and the size of the various

vectors and matrices increases enormously. This has severe implications for computer resources. For example, while an elasto-plastic finite element analysis of a strip footing (plane strain) may take a matter of a few minutes on a fast workstation, a similar analysis of a square footing (three dimensional) may take many hours. Most of this extra time is involved in inverting the global stiffness matrix. Consequently, mathematicians have investigated ways of improving the inversion process. One way of doing this is to use iterative techniques to solve the stiffness matrix equations, rather than direct methods. In this chapter we consider one of these iterative approaches and make comparisons with the direct approach described in Chapter 2.

Another way of simplifying the analysis is to capitalise on any geometric symmetries that exist. One approach that does this is the Fourier series aided finite element method. A brief description of this approach is given in Chapter 12 and the economies that can be obtained, quantified by comparing predictions with those obtained from conventional three dimensional analysis.

This chapter begins by describing the basis of conventional three dimensional finite element analysis.

11.3 Conventional 3D finite element analysis

Conventional three dimensional finite element analysis follows exactly the same procedures as described in Chapters 2, 9 and 10. The only difference is that instead of analysing a two dimensional slice of the original boundary value problem, the whole domain must be considered. This involves discretising the geometry of the problem into an assemblage of three dimensional finite elements. The most popular elements are tetrahedra and hexahedra, see Figure 11.1. Their geometry is specified in terms of the coordinates of the element nodes. For elements with plane faces these nodes are usually located at the element corners. If the elements have curved faces, extra nodes, usually at the midpoint of each edge, must be introduced.

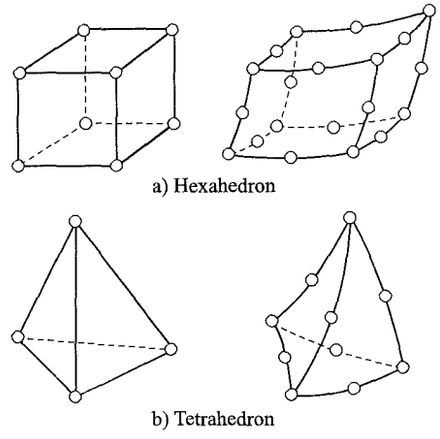

Figure 11.1: 3D finite elements

If the elements are isoparametric, see Section 2.5.1, global elements are derived from a parent element which has the same number of nodes, but is defined with respect to a natural coordinate system. Figure 11.2 shows the configuration of the parent element for a 20 noded hexahedron. For a global element derived from this parent element, the global coordinates of a point in the element can be expressed

by coordinate interpolations of the form:

$$x = \sum_{i=1}^{20} N_i x_i$$
$$y = \sum_{i=1}^{20} N_i y_i \qquad (11.1)$$
$$z = \sum_{i=1}^{20} N_i z_i$$

where x_i, y_i and z_i are the global coordinates of the 20 nodes in the element and N_i, $i = 1, ..., 20$, are the interpolation functions. These interpolation functions are expressed in terms of the natural coordinates S, T and U which vary from -1 to +1. They take the following form:

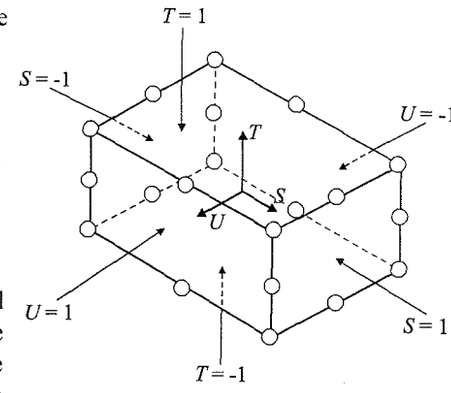

Figure 11.2: Parent element for a 20 noded hexahedron

Mid - side nodes:

$$\begin{aligned}
N_9 &= 1/4(1-S^2)(1-T)(1-U)\\
N_{10} &= 1/4(1-T^2)(1+S)(1-U)\\
N_{11} &= 1/4(1-S^2)(1+T)(1-U)\\
N_{12} &= 1/4(1-T^2)(1-S)(1-U)\\
N_{13} &= 1/4(1-U^2)(1-S)(1-T)\\
N_{14} &= 1/4(1-U^2)(1+S)(1-T)\\
N_{15} &= 1/4(1-U^2)(1+S)(1+T)\\
N_{16} &= 1/4(1-U^2)(1-S)(1+T)\\
N_{17} &= 1/4(1-S^2)(1-T)(1+U)\\
N_{18} &= 1/4(1-T^2)(1+S)(1+U)\\
N_{19} &= 1/4(1-S^2)(1+T)(1+U)\\
N_{20} &= 1/4(1-T^2)(1-S)(1+U)
\end{aligned} \qquad (11.2a)$$

Corner nodes:

$$\begin{aligned}
N_1 &= 1/8(1-S)(1-T)(1-U) - 1/2(N_9 + N_{12} + N_{13})\\
N_2 &= 1/8(1+S)(1-T)(1-U) - 1/2(N_9 + N_{10} + N_{14})\\
N_3 &= 1/8(1+S)(1+T)(1-U) - 1/2(N_{10} + N_{11} + N_{15})\\
N_4 &= 1/8(1-S)(1+T)(1-U) - 1/2(N_{11} + N_{12} + N_{16})\\
N_5 &= 1/8(1-S)(1-T)(1+U) - 1/2(N_{13} + N_{17} + N_{20})\\
N_6 &= 1/8(1+S)(1-T)(1+U) - 1/2(N_{14} + N_{17} + N_{18})\\
N_7 &= 1/8(1+S)(1+T)(1+U) - 1/2(N_{15} + N_{18} + N_{19})\\
N_8 &= 1/8(1-S)(1+T)(1+U) - 1/2(N_{16} + N_{19} + N_{20})
\end{aligned} \qquad (11.2b)$$

Since the element is isoparametric, the displacements within the element are interpolated in the same way as the geometry. Therefore, the above interpolation functions N_1, N_2, ..., N_{20}, are used as the shape functions which express the incremental displacements at any point within the element in terms of the values at the nodes:

$$\begin{Bmatrix} \Delta u \\ \Delta v \\ \Delta w \end{Bmatrix} = [N] \begin{Bmatrix} \Delta u \\ \Delta v \\ \Delta w \end{Bmatrix}_{nodes} \tag{11.3}$$

where u, v and w are the displacements in the x, y and z directions respectively. For 4 noded tetrahedron and 8 noded hexahedron the displacements vary linearly, whereas for 10 noded tetrahedron and 20 noded hexahedron the displacements vary quadratically.

The development of the finite element equations then follows the same process as described in Section 2.6, except that there are now six non-zero components of stress and strain. When performing numerical integrations to evaluate the element stiffness matrix (see Section 2.6.1), account must be taken of all three dimensions and therefore more integration points are required. For example, for the 20 noded hexahedron either 2x2x2 (reduced) or 3x3x3 (full) integration orders are used.

From the above discussion it is clear that 3D analysis involves considerably more elements, and therefore nodes and integration points, than comparable two dimensional plane strain or axi-symmetric analysis. It is therefore not surprising that they require more computer resources. As an example, let us consider the analysis of strip, circular and square smooth rigid surface footings subjected to vertical loading. As the strip and circular footings are plane strain and axi-symmetric respectively, they can be analysed using a two dimensional finite element mesh. Such a mesh is shown in Figure 11.3 and consists of 145 eight noded elements, giving a total of 482 nodes and therefore 964 degrees of freedom (note: there are two degrees of freedom per node). Because of the line of symmetry acting vertically through the centre line of the footing, the finite element mesh only considers half the problem. The square footing cannot be approximated to two dimensions and therefore a full three dimensional analysis is required. There are, however, two vertical planes of symmetry acting through the footing and, consequently, only one quarter of the problem needs to be discretised into finite elements. A mesh, which is coarser than the two dimensional mesh shown in Figure 11.3, is shown in Figure 11.4. This mesh has 416 twenty noded hexahedron elements, giving a total of 2201 nodes and therefore 6603 degrees of freedom (note: there are three degrees of freedom per node).

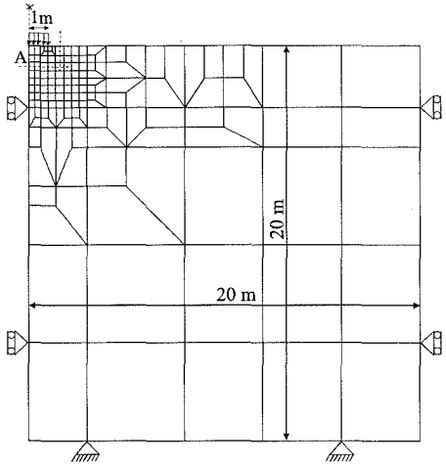

Figure 11.3: Finite element mesh for strip and circular footing

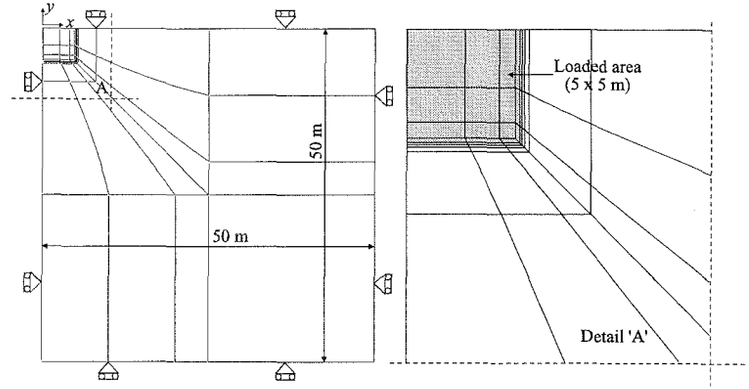

Figure 11.4a: Plan view of 3D mesh for square footing (20 noded elements)

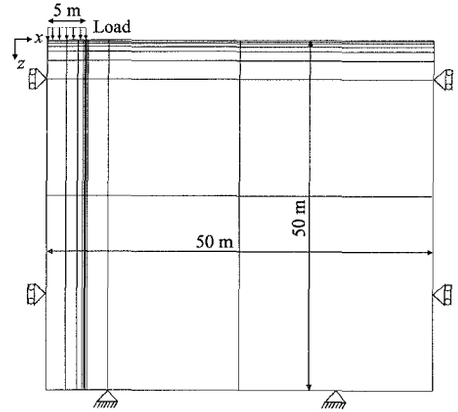

Figure 11.4b: Vertical cross-section of 3D mesh for square footing (20 noded elements)

Analyses have been performed to obtain the undrained load displacement curves for the three shapes of footing. In all cases the soil was assumed to be elasto-plastic, with a Tresca yield surface. The soil properties were: E=10000 kPa, μ=0.45 and S_u=100 kPa. For the strip and circular footings the mesh shown in

Figure 11.3 was used, whereas for the square footing the mesh shown in Figure 11.4 was used. Reduced, 2x2 for the strip and circular footing analyses and 2x2x2 for the square footing analysis, integration was used. Loading was simulated by applying increments of vertical displacement to the footings.

The resulting load-displacement curves are shown in Figure 11.5. These will be discussed in more detail in Volume 2 of this book. For the present discussion we are interested in the computer resources required for each analysis. In this respect, it should be noted that all analyses were run on the same work station. The run times were 10 min, 60 min and 18 hours for the strip, circular and square footings respectively. The memory required for the strip and circular footing analyses was the same, 0.5 Mbytes. For the square footing a much larger requirement of 38 Mbytes was needed. Although this is substantially larger than that required for the strip and square footings, the workstation had sufficient memory and it was able to run the analysis without having to resort to time consuming *swapping* between memory and disc.

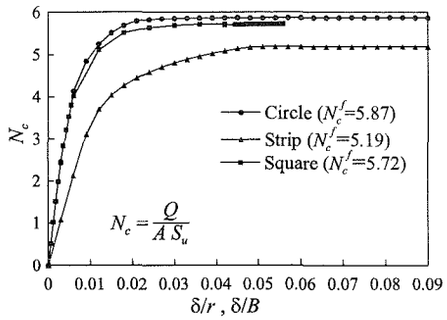

Figure 11.5: Load-displacement curves for square, circular and strip footings

These results clearly show the massive increase in computer resources that are required for three dimensional analyses. Comparing the strip and square footing analyses, the latter required a 76 fold increase in memory and an 108 fold increase in time. As most practical three dimensional geotechnical problems involve a more complex geometry and soil stratigraphy than the simple footing problems analysed above, they would require considerably more finite elements. The demand on computer resources would be such that it would not be possible to perform analyses unless a super computer is used, which would be so costly that analyses could only be justified for a minority of practical problems.

One way of reducing the computer resources is to use 8 noded instead of 20 noded hexahedron elements. A mesh of such elements for the square footing problem is shown in Figure 11.6. This consists of 1740 elements giving a total of 2236 nodes and 6708 degrees of freedom. The number of degrees of freedom is therefore slightly higher than that of the analysis described above, using the mesh shown in Figure 11.4. The analysis required 28 Mbytes of memory and a run time of 14.5 hours. The reason for the reduction in memory, compared to the analysis using 20 noded elements, is due to the reduction in band width of the global stiffness matrix that arises by using 8 noded elements. This is evident from Figure 11.7, which compares the connectivities of the centre node of a block of eight 8 noded with a block of eight 20 noded elements. For the 8 noded elements the

centre node is connected, via its eight surrounding elements, to 26 other nodes, whereas for the 20 noded elements the centre node is connected to 80 other nodes.

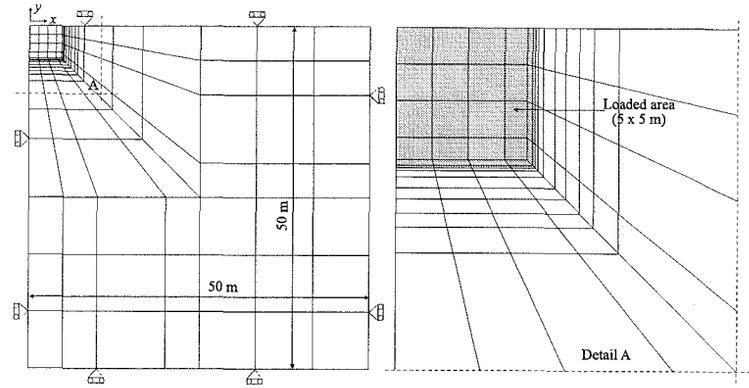

Figure 11.6a: Plan view of 3D mesh for square footing (8 noded elements)

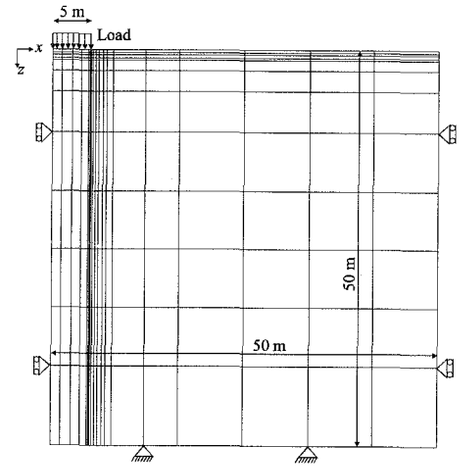

Figure 11.6b: Vertical cross-section of 3D mesh for square footing (8 noded elements)

The load displacement curves obtained from the two square footing analyses are shown in Figure 11.8. While the analysis with the 20 noded hexahedron elements gives a limit load, the analysis with 8 noded hexahedron elements continues to show increasing load with displacement. Therefore, although the latter analysis uses less computer resources, it fails to provide an accurate prediction. Similar behaviour is observed in plane strain analysis when analyses performed

with 4 and 8 noded quadrilateral elements are compared. The analysis with 4 noded elements fails to give an accurate prediction of the collapse load. The stiff behaviour of the linear elements (4 noded for 2D and 8 noded for 3D analysis) is well recognised in the literature and it is therefore recommended that the higher order quadratic elements are used.

Alternative ways of reducing the computer resources are therefore required. Two such methods are described in this book: iterative techniques for the solution of the global equations are presented in the next section, while the pseudo 3D analysis, in the form of the Fourier series aided finite element method, is the subject of Chapter 12.

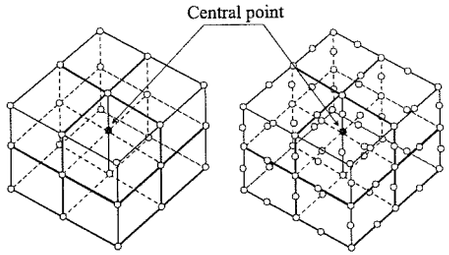

Figure 11.7: Node connectivities

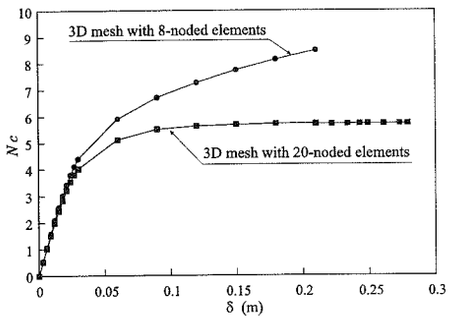

Figure 11.8: Load-displacement curves for a square footing

11.4 Iterative solutions

11.4.1 Introduction

Close examination of 3D finite element analyses reveals that most of the computer resources are used in inverting the global stiffness matrix. Therefore considerable effort has been made in trying to find ways to streamline this process. One approach that has recently been recommended in the literature is to use an iterative solution technique, as opposed to the Gaussian elimination approach outlined in Chapter 2.

In this section, the general process by which iterative solutions invert the stiffness matrix is outlined. The conjugate gradient method, which is one of the most popular iterative methods in current use, is then described. Finally, a comparison of the performance of this method with that of Gaussian elimination is given.

11.4.2 General iterative solution

The formulation of a set of global stiffness equations in the form of Equation (11.4) was presented in Chapter 2:

$$\left[\boldsymbol{K}_G\right]\left\{\Delta \boldsymbol{d}\right\}_{nG} = \left\{\Delta \boldsymbol{R}_G\right\} \tag{11.4}$$

where $[\boldsymbol{K}_G]$ is the global stiffness matrix, $\{\Delta \boldsymbol{d}\}_{nG}$ is the vector containing the incremental nodal displacements and $\{\Delta \boldsymbol{R}_G\}$ is the global right hand side vector containing equivalent incremental nodal forces. In finite element analysis it is necessary to solve this equation for the unknown incremental nodal displacements. Efficient direct solution techiques, described in Chapter 2, require elements of the stiffness matrix to form a narrow band along the main diagonal, see Figure 2.19. This narrow band entraps some zero terms, which must not be ignored because they can become non-zero during the process of elimination. As the number of elements increases, particularly in 3D problems (because of nodal connectivities, see Figure 11.7), a large number of zeros have to be stored within the band, which automatically increases the requirements for computer memory. The advantage of iterative methods is that they use only the non-zero terms in a solution process and therefore none of the zero terms need to be stored.

Writing Equation (11.4) in an open form gives a system of simultaneous Equations (11.5):

$$\begin{aligned}
K_G^{11}\Delta d_{nG}^1 &+ K_G^{12}\Delta d_{nG}^2 &+ \ldots &+ K_G^{1n}\Delta d_{nG}^n &= \Delta R_G^1 \\
K_G^{21}\Delta d_{nG}^1 &+ K_G^{22}\Delta d_{nG}^2 &+ \ldots &+ K_G^{2n}\Delta d_{nG}^n &= \Delta R_G^2 \\
\ldots &+ \ldots &+ \ldots &+ \ldots &= \ldots \\
K_G^{n1}\Delta d_{nG}^1 &+ K_G^{n2}\Delta d_{nG}^2 &+ \ldots &+ K_G^{nn}\Delta d_{nG}^n &= \Delta R_G^n
\end{aligned} \tag{11.5}$$

from which the unknown displacements can be expressed as:

$$\begin{aligned}
\Delta d_{nG}^1 &= -\frac{K_G^{12}}{K_G^{11}}\Delta d_{nG}^2 - \ldots - \frac{K_G^{1n}}{K_G^{11}}\Delta d_{nG}^n + \frac{\Delta R_G^1}{K_G^{11}} \\
\Delta d_{nG}^2 &= -\frac{K_G^{21}}{K_G^{22}}\Delta d_{nG}^1 - \ldots - \frac{K_G^{2n}}{K_G^{22}}\Delta d_{nG}^n + \frac{\Delta R_G^2}{K_G^{22}} \\
\ldots &= \ldots - \ldots - \ldots + \ldots \\
\Delta d_{nG}^n &= -\frac{K_G^{n1}}{K_G^{nn}}\Delta d_{nG}^1 - \frac{K_G^{n2}}{K_G^{nn}}\Delta d_{nG}^2 - \ldots + \frac{\Delta R_G^n}{K_G^{nn}}
\end{aligned} \tag{11.6}$$

Iterative solution methods arrive at a solution to Equations (11.6) by essentially making an initial guess at the answer:

$$\left\{\Delta \boldsymbol{d}\right\}_{nG}^{0} = \left\{\Delta d_{nG}^1(0)\ \ \Delta d_{nG}^2(0)\ \ldots\ \Delta d_{nG}^n(0)\right\} \tag{11.7}$$

and then iterating until the correct solution is obtained:

$$\Delta d_{nG}^i(k+1) = \frac{-\sum_{\substack{j=1 \\ i\neq j}}^{n} K_G^{ij}\Delta d_{nG}^j(k) + \Delta R_G^i}{K_G^{ii}}, \quad i = 1,\ldots n \tag{11.8}$$

where: $\Delta d^i{}_{nG}$ - unknown incremental displacement
k - number of iteration

Clearly, the success of such an approach depends on the initial guess and on how this is modified on successive iterations. Equation (11.8) is usually known as a

Jacobi iteration, or the 'method of simultaneous displacements', because every element of the solution vector is changed before any of the new elements are used in the iteration. It is the simplest procedure, but very often diverges and consequently there are several different manipulations which can be applied to ensure and accelerate convergence.

Adding and subtracting $\Delta d^i_{nG}(k)$ to the right hand side of Equation (11.8) gives:

$$\Delta d^i_{nG}(k+1) = \Delta d^i_{nG}(k) + \frac{-\sum_{j=1}^{n} K^{ij}_G \Delta d^j_{nG}(k) + \Delta R^i_G}{K^{ii}_G} \tag{11.9}$$

From here, the usual iterative form of Equation (11.9), for the total vector $\{\Delta \boldsymbol{d}\}_{nG}$, can be written as:

$$\left\{\Delta \boldsymbol{d}\right\}^{k+1}_{nG} = \left\{\Delta \boldsymbol{d}\right\}^{k}_{nG} - \left[\boldsymbol{K}^{ii}_G\right]^{-1}\left\{\boldsymbol{g}\right\}^{k} \tag{11.10}$$

where $\{\boldsymbol{g}\}^k$ is a residual, or out of balance, vector generated at each iteration:

$$\left\{\boldsymbol{g}\right\}^{k} = \left[\boldsymbol{K}_G\right]\left\{\Delta \boldsymbol{d}\right\}^{k}_{nG} - \left\{\Delta \boldsymbol{R}_G\right\} \tag{11.11}$$

For equilibrium, i.e. the correct solution, $\{\boldsymbol{g}\}^k$ should equal zero.

The second part of the right hand side of Equation (11.10) is generally written as an iterative vector, $\{\boldsymbol{\delta}\}^k$, and Equation (11.10) becomes:

$$\left\{\Delta \boldsymbol{d}\right\}^{k+1}_{nG} = \left\{\Delta \boldsymbol{d}\right\}^{k}_{nG} + \left\{\boldsymbol{\delta}\right\}^{k} \tag{11.12}$$

where, generally:

$$\left\{\boldsymbol{\delta}\right\}^{k} = -\left[\boldsymbol{K}_a\right]^{-1}\left\{\boldsymbol{g}\right\}^{k} \tag{11.13}$$

The matrix $[\boldsymbol{K}_a]$ in the iterative vector $\{\boldsymbol{\delta}\}^k$ should be easily invertible in order to speed up the iterative process. Equation (11.10) indicates that $[\boldsymbol{K}_a]$ should equal the matrix of diagonal stiffness terms. However, sometimes an alternative matrix is used to accelerate convergence. The simplest form of iteration is obtained for $[\boldsymbol{K}_a] = [\boldsymbol{I}]$ (i.e. the identity matrix). If $[\boldsymbol{K}_a] \neq [\boldsymbol{I}]$ the process is known as *scaled* or *pre-conditioned*.

11.4.3 The gradient method

This group of iterative methods is based on the minimisation of the following quadratic form (Ralston (1965)):

$$Q(\{\Delta \boldsymbol{d}\}^k_{nG}) = \tfrac{1}{2}(\{\Delta \boldsymbol{d}\}^k_{nG})^{\mathrm{T}}[\boldsymbol{K}_G]\{\Delta \boldsymbol{d}\}^k_{nG} - (\{\Delta \boldsymbol{d}\}^k_{nG})^{\mathrm{T}}\{\Delta \boldsymbol{R}_G\} \tag{11.14}$$

Minimising this expression with respect to $\{\Delta \boldsymbol{d}\}_{nG}$ gives:

$$\frac{\partial Q}{\partial \{\Delta \boldsymbol{d}\}^k_{nG}} = \left[\boldsymbol{K}_G\right]\left\{\Delta \boldsymbol{d}\right\}^{k}_{nG} - \left\{\Delta \boldsymbol{R}_G\right\} = \left\{\boldsymbol{g}\right\}^{k} = 0 \tag{11.15}$$

Equation (11.15) shows that the minimum of Q is the solution of Equation (11.4).

The general technique to minimise Q is to choose an initial vector $\{\Delta \boldsymbol{d}\}^0_{nG}$, a direction of minimisation v^0 and a step size η^0 to get to $\{\Delta \boldsymbol{d}\}^1_{nG}$. Further iterations can be written as:

$$\left\{\Delta \boldsymbol{d}\right\}^{k+1}_{nG} = \left\{\Delta \boldsymbol{d}\right\}^{k}_{nG} + \eta^k\left\{\boldsymbol{v}\right\}^{k} \tag{11.16}$$

The basis of the method is to choose $\{\boldsymbol{v}\}^k$ to be in the direction of the greatest rate of change of Q, namely in the direction of the gradient. However, because the gradient reflects the direction in which the system grows, and here the opposite is required (i.e. minimisation of Q), $\{\boldsymbol{v}\}^k$ should be set in the direction opposite to the direction of the gradient. Since Equation (11.15) shows that the gradient of Q is the residual vector $\{\boldsymbol{g}\}^k$, then $\{\boldsymbol{v}\}^k = -\{\boldsymbol{g}\}^k$. Generally:

$$\begin{aligned} &\left\{\Delta \boldsymbol{d}\right\}^{k+1}_{nG} = \left\{\Delta \boldsymbol{d}\right\}^{k}_{nG} + \eta^k\left\{\boldsymbol{\delta}\right\}^{k} \\ &\text{where:} \quad \left\{\boldsymbol{\delta}\right\}^{k} = -\left\{\boldsymbol{g}\right\}^{k} \end{aligned} \tag{11.17}$$

To find η^k it is necessary to rewrite Q in terms of η^k:

$$\begin{aligned} Q(\{\Delta \boldsymbol{d}\}^{k+1}_{nG}) &= Q(\{\Delta \boldsymbol{d}\}^{k}_{nG} + \eta^k\{\boldsymbol{\delta}\}^k) \\ &= \tfrac{1}{2}(\{\Delta \boldsymbol{d}\}^{k}_{nG} + \eta^k\{\boldsymbol{\delta}\}^k)^{\mathrm{T}}\,[\boldsymbol{K}_G]\,(\{\Delta \boldsymbol{d}\}^{k}_{nG} + \eta^k\{\boldsymbol{\delta}\}^k) \\ &\quad - (\{\Delta \boldsymbol{d}\}^{k}_{nG} + \eta^k\{\boldsymbol{\delta}\}^k)^{\mathrm{T}}\,\{\Delta \boldsymbol{R}_G\}^k \\ &= \tfrac{1}{2}(\{\Delta \boldsymbol{d}\}^{k}_{nG})^{\mathrm{T}}\{\boldsymbol{g}\}^k - \tfrac{1}{2}(\{\Delta \boldsymbol{d}\}^{k}_{nG})^{\mathrm{T}}\{\Delta \boldsymbol{R}_G\}^k \\ &\quad + \eta^k(\{\boldsymbol{\delta}\}^k)^{\mathrm{T}}\{\boldsymbol{g}\}^k + \tfrac{1}{2}(\eta^k)^2(\{\boldsymbol{\delta}\}^k)^{\mathrm{T}}[\boldsymbol{K}_G]\{\boldsymbol{\delta}\}^k \end{aligned} \tag{11.18}$$

If $\{\Delta \boldsymbol{d}\}^k_{nG}$ and $\{\boldsymbol{\delta}\}^k$ are fixed from the previous iteration, Q has a minimum dependent on η^k:

$$\frac{\partial Q}{\partial \eta^k} = \left(\left\{\boldsymbol{\delta}\right\}^{k}\right)^{\mathrm{T}}\left\{\boldsymbol{g}\right\}^{k} + \eta^k\left(\left\{\boldsymbol{\delta}\right\}^{k}\right)^{\mathrm{T}}\left[\boldsymbol{K}_G\right]\left\{\boldsymbol{\delta}\right\}^{k} = 0 \tag{11.19}$$

wherefrom:

$$\eta^k = -\frac{(\{\boldsymbol{\delta}\}^k)^{\mathrm{T}}\{\boldsymbol{g}\}^k}{(\{\boldsymbol{\delta}\}^k)^{\mathrm{T}}[\boldsymbol{K}_G]\{\boldsymbol{\delta}\}^k} \tag{11.20}$$

It is sometimes useful to express Equation (11.20) in an alternative form: suppose that the out of balance forces $\{\boldsymbol{g}\}^{k+1}$ are computed from the first 'trial' expression $\{\Delta \boldsymbol{d}\}^{k+1}_{nG}$ which has the step $\eta = 1$. Then:

$$\left\{\boldsymbol{g}\right\}^{k+1}_{(\eta=1)} = \left[\boldsymbol{K}_G\right]\left(\left\{\Delta \boldsymbol{d}\right\}^{k}_{nG} + \left\{\boldsymbol{\delta}\right\}^{k}\right) - \left\{\Delta \boldsymbol{R}_G\right\} \tag{11.21}$$

Subtracting Equation (11.11) from (11.21) gives:

$$\{g\}^{k+1}_{(\eta=1)} - \{g\}^{k} = [K_G]\{\delta\}^{k} \tag{11.22}$$

so that the new expression for η^k becomes:

$$\eta^k = -\frac{(\{\delta\}^k)^T\{g\}^k}{(\{\delta\}^k)^T(\{g\}^{k+1}_{(\eta=1)} - \{g\}^k)} \tag{11.23}$$

To modify $\{g\}^{k+1}(\eta = 1)$ to the new $\{g\}^{k+1}(\eta^k)$ a linear relationship is used, such that:

$$\{g\}^{k+1}_{(\eta^k)} = \eta^k \{g\}^{k+1}_{(\eta=1)} + (1-\eta^k)\{g\}^k \tag{11.24}$$

without having to resort to the computationally more expensive Equation (11.11).

The gradient method described here is based on an iterative vector, $\{\delta\}$, being equal to the residual vector, $-\{g\}$, see Equation (11.17). However, it can also be applied to the scaled, or pre-conditioned, gradient direction so that:

$$\{\delta\}^k = -[K_a]^{-1}\{g\}^k \tag{11.25}$$

11.4.4 The conjugate gradient method

This is a two parameter extension of the gradient method, which involves an iterative vector, $\{\delta\}$, of the form:

$$\{\delta\}^k = -[K_a]^{-1}\{g\}^k + \beta^k\{\delta\}^{k-1} \tag{11.26}$$

or

$$\{\delta\}^k = \{\delta\}^{k*} + \beta^k\{\delta\}^{k-1} \tag{12.27}$$

The parameter β^k is found from the condition that:

$$(\{\delta\}^k)^T[K_G]\{\delta\}^l = 0 \quad , \text{ when } l < k \tag{11.28}$$

which essentially means that the process involves generating a set of $[K_G]$-orthogonal (i.e. $[K_G]$-conjugate) vectors and then minimising successively in the direction of each of them, until reaching the final solution. It can be shown (see Crisfield (1986)) that the condition (11.28) leads to the orthogonality of the residual vectors, such that:

$$(\{g\}^{k+1})^T\{g\}^m = 0 \quad , \quad m = 0, \ldots, k \tag{11.29}$$

which is the main 'conjugate gradient' condition. From here, multiplying Equation (11.27) by $[K_G]\{\delta\}^{k-1}$ gives:

$$(\{\delta\}^k)^T[K_G]\{\delta\}^{k-1} = (\{\delta\}^{k*})^T[K_G]\{\delta\}^{k-1} + \beta^k(\{\delta\}^{k-1})^T[K_G]\{\delta\}^{k-1} \tag{11.30}$$

and bearing in mind condition (11.28) leads to:

$$\beta^k = -\frac{(\{\delta\}^{k*})^T[K_G]\{\delta\}^{k-1}}{(\{\delta\}^{k-1})^T[K_G]\{\delta\}^{k-1}} \tag{11.31}$$

As for the parameter η^k, the above expression can be simplified, in order to avoid costly calculations with the $[K_G]$ matrix, to give the following expression for β^k:

$$\beta^k = \frac{(\{\delta\}^{k*})^T(\{g\}^k - \{g\}^{k-1})}{(\{\delta\}^{k-1*})^T\{g\}^{k-1}} \tag{11.32}$$

The flow chart for the conjugate gradient method is given in Figure 11.9. As before, if $[K_a]=[I]$ the method is called 'basic', otherwise it is 'scaled' or 'pre-conditioned'.

The iteration procedure normally terminates when a convergence criterion, ρ, reaches a pre-set limit, *tol*. This convergence criterion is usually calculated as the ratio of the norm of the residual vector and the norm of the right hand side load vector:

$$\rho = \frac{\|\{g\}^k\|}{\|\{\Delta R_G\}\|} \le tol \tag{11.33}$$

11.4.5 Comparison of the conjugate gradient and banded solution techniques

This section compares the performance of the conjugate gradient (CG) and banded (BD) solution techniques. As explained in Section 11.4.2, the advantage of the CG approach is that it is only necessary to store the non-zero terms of the global stiffness matrix, while for the banded solution some of the zero terms within the band width must be stored. However, the drawback of the CG method is that the inverted global stiffness matrix is never calculated. While this is not a disadvantage in linear problems, it is for nonlinear problems, where the solution strategy involves several solutions with the same global stiffness matrix, but different right hand side load vectors (i.e. in the modified Newton-Raphson approach (MNR), see Section 9.6).

First of all, the requirements for computer memory are investigated, by considering blocks of elements with an equal number of elements on each face. These are classified as n x n x n 3D meshes, where n is the number of elements in each coordinate direction. Figure 11.10 shows how the memory requirement increases with the 'number of degrees of freedom' (NDF), based on 3D meshes of 1x1x1, 2x2x2, 5x5x5, 8x8x8, 10x10x10 and 12x12x12 twenty noded hexahedron elements. Memory is plotted against the NDF, which varies from 60 (1x1x1) to 24,843 (12x12x12). It can be seen that the CG solver is more beneficial once the NDF exceeds approximately 1000.

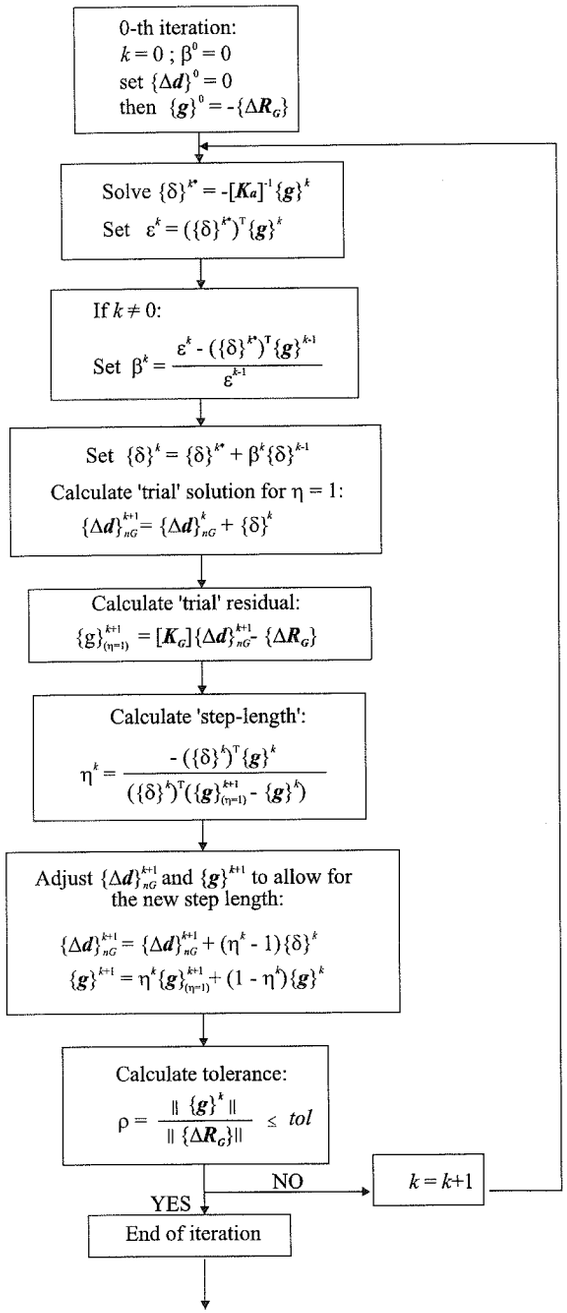

Figure 11.9: Flow chart for the conjugate gradient algorithm

For lower numbers of degrees of freedom the memory requirement for the CG method exceeds that for the BD method. This occurs because two storage vectors are required for the CG method: one containing the non-zero terms of the stiffness matrix and the other containing the positions of the terms in the stiffness matrix.

Solution times for a single inversion of the global stiffness matrix are considered next. This is done by applying a point load to the corner of the n x n x n meshes, see Figure 11.11. The soil is assumed to be isotropic linear elastic (Young's modulus, E=1000 kPa) and therefore the analyses are all linear. Two sets of analysis were performed, one set drained, with a Poisson's ratio μ=0.3, and the other set undrained, with μ=0.4998. For the CG solutions pre-conditioning was performed, with matrix $[K_a]$ equal to the diagonal matrix, $[DM]$, of the global stiffness matrix, $[K_G]$. The convergence tolerance was set to 0.001%. The results are presented in Figure 11.12 for both the CG and BD analyses. It should be noted that the solution times for the BD analysis are not dependent on the Poisson's ratio, whereas for the CG analysis the number of iterations, and hence the computer time, is. Inspection of Figure 11.12 indicates that for undrained analysis, the CG solver is beneficial only for the very large number of degrees of freedom (over 10,000), i.e. for over 1000 twenty noded 3D elements. However, for the drained analysis (μ=0.3) the CG solver is always superior to the BD solver.

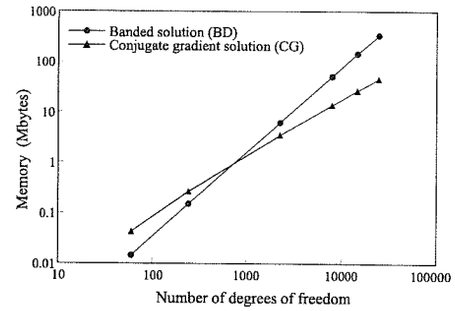

Figure 11.10: Memory requirements for CG and BD solvers

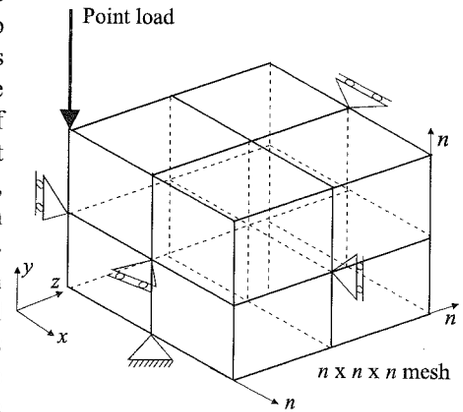

Figure 11.11: Boundary conditions for n x n x n meshes

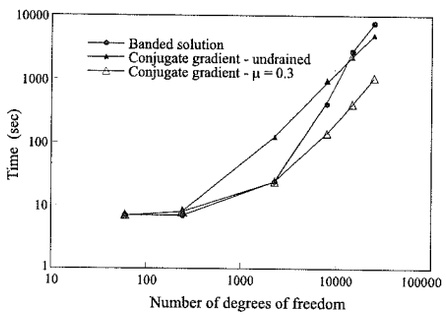

Figure 11.12: Times for a single inversion of the stiffness matrix

The number of iterations required for the drained (μ=0.3) analyses are plotted against NDF in Figure 11.13. Also shown on this Figure are equivalent results obtained using $[\boldsymbol{K}_a] = [\boldsymbol{I}]$. Comparison shows that pre-conditioning with $[\boldsymbol{DM}]$ reduces the number of iterations by about 20%.

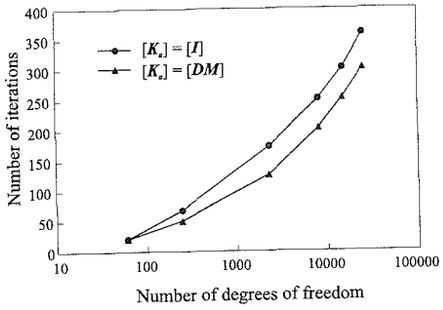

Figure 11.13: Influence of pre-conditioning on the number of iterations for the CG solver

From the results presented in Figure 11.12 it is clear that the CG solver is highly dependent on the compressibility of the soil (i.e. the value of Poisson's ratio). To investigate this further, a series of analyses using the 8x8x8 mesh, but with different Poisson's ratios (e.g. μ of 0.3, 0.4, 0.45, 0.48, 0.49, 0.495 and 0.499) have been performed. The results are presented in Figure 11.14. While the BD solver is insensitive to the value of μ, the number of iterations, and therefore computer time, for the CG solver, both with $[\boldsymbol{DM}]$ and $[\boldsymbol{I}]$ matrices, and with a 0.001% convergence tolerance, increases rapidly once $\mu > 0.48$.

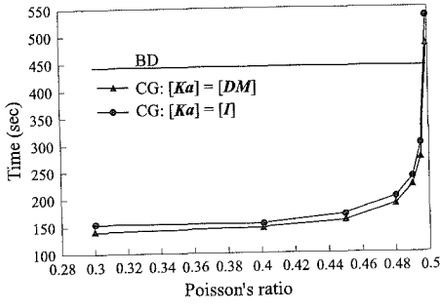

Figure 11.14: Sensitivity of a solution to the value of Poisson's ratio

As noted above, the drawback with the CG (or any iterative) method is that the global stiffness matrix is never actually inverted. While this is not a disadvantage for linear analyses, where only one solution of the stiffness matrix is required, it can be a serious drawback for nonlinear analyses in which the same global stiffness matrix needs to be solved for several different right hand side load vectors. Such a situation occurs if the visco-plastic or modified Newton-Raphson solution algorithms are used. In these methods the same stiffness matrix is used for all iterations of a particular increment of the analysis (see Sections 9.5 and 9.6). If a BD solver is used, the global stiffness matrix can be inverted on the first iteration and stored to be re-used on subsequent iterations. If the CG solver is used, the same procedure for solving the global stiffness matrix must be repeated for each new right hand side load vector and therefore for each iteration. This can be very uneconomical and can result in the situation that although the CG solver can solve the equations quicker, the BD solver wins because it does not have to resolve the equations for each iteration of an increment. As an example, the undrained bearing capacity of a smooth rigid square footing is calculated using both solvers. The mesh is given in Figure 11.4 and consists of 416 twenty noded elements with 6603 degrees of freedom. The soil is modelled as a Tresca type material, with properties as given in Section 11.3 (i.e. E=10000 kPa, μ=0.45, S_u=100 kPa). For the CG analysis the convergence tolerance for the CG algorithm was set at 0.01%. Both analyses gave the same results, but the CG analysis required 7 days of computer time, whereas the BD analysis only required 18 hours, for the same number of load increments in each analysis. Clearly, the BD analyses was far more economical for this particular situation.

11.4.6 Normalisation of the stiffness matrix

Another problem when using iterative procedures arises when terms within the stiffness matrix differ by several orders of magnitude. The iterative process then finds it difficult to converge to a very tight tolerance. Such a situation arises if a consolidation analysis is performed, because part of the stiffness matrix consists of the structural stiffness, $[\boldsymbol{K}_G]$, (which are large numbers), while the other part has terms defined from the permeability coefficients, $[\boldsymbol{\Phi}_G]$ (which are small numbers), see Equation (10.27). One possible way of overcoming this problem is to normalise the stiffness matrix in some way, so that it brings all terms within the matrix to a similar order of magnitude. Naylor (1997) suggested a very elegant form of normalisation which retains the symmetry of the stiffness matrix, but does not require large computing resources. It consists of the following steps:

- The assembled stiffness equations of the form (11.5) are:

$$\sum_{j=1}^{n} K_G^{ij}\,\Delta d_{nG}^{j} = \Delta R_G^{i} \quad , \quad i = 1,\ldots n \tag{11.34}$$

- The normalisation involves the following substitutions:

$$\begin{aligned} K_G^{ij} \quad &\text{by} \quad \overline{\overline{K}}_G^{ij} = \frac{K_G^{ij}}{\sqrt{K_G^{ii} K_G^{jj}}} \\ \Delta d_{nG}^{j} \quad &\text{by} \quad \overline{\Delta d}_{nG}^{j} = \Delta d_{nG}^{j} \sqrt{K_G^{jj}} \\ \Delta R_G^{i} \quad &\text{by} \quad \overline{\Delta R}_G^{i} = \frac{\Delta R_G^{i}}{\sqrt{K_G^{ii}}} \end{aligned} \tag{11.35}$$

which gives a new system of equations:

$$\sum_{j=1}^{n} \overline{\overline{K}}_G^{ij}\,\overline{\Delta d}_{nG}^{j} = \overline{\Delta R}_G^{i} \quad , \quad i = 1,\ldots n \tag{11.36}$$

This type of normalisation has been implemented, with pre-conditioning using the diagonal terms of the normalised stiffness matrix to obtain $[\boldsymbol{K}_a]$. As the normalised diagonal terms are equal to unity, this is equivalent to $[\boldsymbol{K}_a]$=$[\boldsymbol{I}]$. Analyses have been performed for the simple example of n x n x n 3D meshes presented above. The number of iterations for a single inversion of the stiffness

matrix in drained analyses is presented in Figure 11.15. Also shown in Figure 11.15 are results from Figure 11.13, which are based on the original (un-normalised) stiffness matrix. Comparison of these results indicates that the normalisation procedure reduces the number of iterations and is therefore more efficient. However, its effect is only marginal compared to the analyses with the original stiffness matrix and pre-conditioning with $[K_a]$=$[DM]$. A similar conclusion arises for undrained analyses of the same problem.

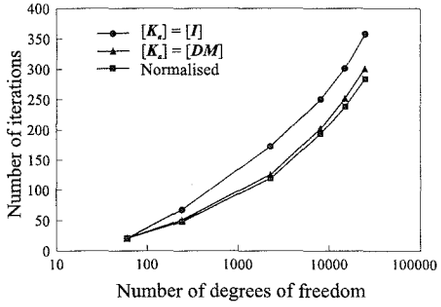

Figure 11.15: Influence of normalisation on the number of iterations for the CG solver

The Authors experience with the normalisation procedure when applied to other boundary value problems is not conclusive. In some cases it is more beneficial than the un-normalised approach, whereas in others it is not. In particular, it does not always overcome the problems involved in coupled consolidation analysis highlighted above.

11.4.7 Comments

It can be concluded from the above comparisons that the CG method becomes more economical than the BD method at solving the global stiffness equations as the number of degrees of freedom increases and/or the soil is compressible. However, because the global stiffness matrix is never actually inverted, the CG method is not ideally suited to nonlinear finite element analysis. The Authors' experience is that for nonlinear problems that are solvable in a realistic time (i.e. with a run time less than a week), the BD solver is always more economical than the CG solver. Of course, the situation may well change as computer resources improve and it is possible to analyse larger 3D meshes, in which case the CG approach may then become more effective.

11.5 Summary

1. Full 3D finite element analysis does not involve any major developments to the theory presented for 2D plane strain and axi-symmetric analyses. The main differences are that the full 3D geometry must be discretised and that there are now three, as opposed to two, displacement degrees of freedom at each node.
2. Full 3D finite element analyses require large amounts of computer resources, both memory and time. With present day computers only very simple nonlinear 3D problems can be analysed.

3. It is not advisable to use linear displacement elements in order to reduce the computer resources required, because these elements are not able to accurately reproduce limit loads. For geotechnical problems higher order (at least quadratic) displacement elements should be used.
4. In the literature it is claimed that, by using an iterative method to solve the global stiffness matrix equations, the computer resources required for full 3D analysis can be reduced. This is certainly true if the analysis is linear, there is a large number of degrees of freedom and the material is compressible. If this is not the case, it is questionable whether there is any advantage in using such a technique. For nonlinear problems, which can be solved in a reasonable time, it appears that direct solution techniques are faster than the iterative methods. This arises because the iterative techniques do not actually evaluate the inverse of the global stiffness matrix and therefore a full solution is required even if only the right hand side load vector changes.

12. Fourier series aided finite element method (FSAFEM)

12.1 Synopsis

As described in Chapter 11, a conventional three dimensional (3D) finite element analysis of a typical nonlinear geotechnical problem is complex and requires a large amount of computer resources. The Fourier series aided finite element method (FSAFEM) is a means of increasing the computational efficiency of the conventional finite element method, for a special class of 3D problems which have a geometry that does not vary in one of the coordinate directions (out of plane direction), but whose material properties and/or boundary conditions do. This efficiency is gained by assuming that the displacements in the geometrical out of plane direction can be represented using a Fourier series and exploiting its orthogonal properties. Two types of FSAFEM exist, the continuous FSAFEM (i.e. CFSAFEM) and the discrete FSAFEM (i.e. DFSAFEM) and they are described in this chapter.

12.2 Introduction

Conventional 3D analyses of nonlinear geotecnical boundary value problems require large amounts of computer resources (Brown and Shie (1990)). A large proportion of these resources are involved in inverting the global stiffness matrix. Consequently, one way of economising on computer resources is to use an efficient method of inverting this matrix. In this respect the use of iterative solution techniques was described in Chapter 11, where it was shown that, for current computer hardware technology, such techniques can result in economies for linear problems, but are unlikely to result in savings for nonlinear problems. However, the situation may improve with future developments in computer hardware.

Another way of simplifying 3D analyses is to exploit any geometrical symmetries that exist. One approach that capitalises on such symmetries is the Fourier series aided finite element method (FSAFEM). The theory behind this method and its implementation is the subject of this chapter. Conventionally, the FSAFEM has been applied to problems with an axi-symmetric geometry (but non axi-symmetric loading and/or variation of material properties) and it is the application of the method to such problems that is considered here. However, the method can also be implemented for problems expressed in terms of Cartesian geometries.

All existing formulations of the FSAFEM have been based on linear elastic material behaviour. Nonlinear problems have been analysed with some success (Winnicki and Zienkiewicz (1979), Griffiths and Lane (1990)). In these analyses the nonlinear behaviour was dealt with using a finite element algorithm in which the global stiffness matrix was based on the linear elastic material properties and the nonlinearity was dealt with by modifying the right hand side of the governing finite element equations. In addition, most of the past implementations of the FSAFEM have assumed that the system forces and displacements have a symmetry about the $\theta = 0°$ direction, where θ is the angular coordinate. This assumption results in a large saving of computer resources required for an analysis and also considerably simplifies the formulation. However, these assumptions are restrictive. Recently a new nonlinear formulation has been developed (Ganendra (1993), Ganendra and Potts (1995)), which allows the stiffness matrix to be updated during an analysis using the nonlinear material properties. It also places no symmetry constraints on the variation of system forces and displacements. However, options can be included to capitalise on any such symmetry if it exists. The chapter begins by presenting the basic theory behind the FSAFEM, and then describes its implementation.

12.3 The continuous Fourier series aided finite element method

12.3.1 Formulation for linear behaviour

The axi-symmetric geometry of the problem domain allows a cylindrical coordinate system to be defined (r-z-θ, see Figure 12.1) such that the r-z plane can be discretised using a 2D finite element mesh. Thus the distribution of variables in the r-z plane can be described using nodal values and conventional 2D finite element shape functions. The distribution of variables in the θ direction can be described using a Fourier series, e.g.. the incremental radial displacement, Δu, can be written as:

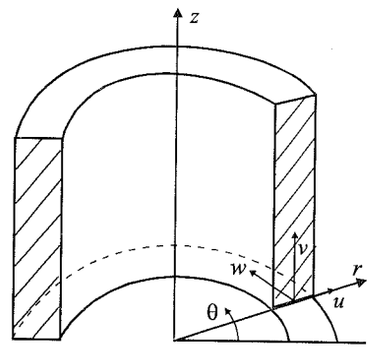

Figure 12.1:Cylindrical coordinate system

$$\Delta u = \Delta u^0 + \Delta \overline{u}^1 \cos\theta + \Delta \overline{\overline{u}}^1 \sin\theta + \Delta \overline{u}^2 \cos 2\theta + \Delta \overline{\overline{u}}^2 \sin 2\theta + \ \ldots \ + \Delta \overline{u}^l \cos l\theta + \Delta \overline{\overline{u}}^l \sin l\theta + \ \ldots \tag{12.1}$$

where Δu^0, $\Delta \overline{u}^l$ and $\Delta \overline{\overline{u}}^l$ are the 0^{th}, l^{th} order cosine and l^{th} order sine harmonic coefficients of variable Δu respectively.

Consider the displacements at a point, $\Delta \boldsymbol{u}$, with components Δu, Δv, and Δw in the r, z, and θ directions respectively. Displacements $\Delta \boldsymbol{u}$ can be expressed in vector

form in terms of the shape functions of the appropriate element in the 2D finite element mesh, and the Fourier series of the nodal displacements of the element:

$$\{\Delta \boldsymbol{u}\} = \begin{Bmatrix} \Delta u \\ \Delta v \\ \Delta w \end{Bmatrix} = \sum_{i=1}^{n} \begin{Bmatrix} \cdots \\ N_i \left(\sum_{l=0}^{L} \overline{U_i^l} \cos l\theta + \overline{\overline{U_i^l}} \sin l\theta \right) \\ N_i \left(\sum_{l=0}^{L} \overline{V_i^l} \cos l\theta + \overline{\overline{V_i^l}} \sin l\theta \right) \\ N_i \left(\sum_{l=0}^{L} \overline{W_i^l} \cos l\theta + \overline{\overline{W_i^l}} \sin l\theta \right) \\ \cdots \end{Bmatrix} \tag{12.2}$$

where:

N_i is the shape function of the i^{th} node defined in the element;

$\overline{U_i^l}$, $\overline{V_i^l}$ and $\overline{W_i^l}$ are respectively the l^{th} cosine harmonic coefficient of radial, vertical and circumferential incremental displacement at the i^{th} node;

$\overline{\overline{U_i^l}}$, $\overline{\overline{V_i^l}}$ and $\overline{\overline{W_i^l}}$ are respectively the l^{th} sine harmonic coefficient of radial, vertical and circumferential incremental displacement at the i^{th} node;

n is the number of nodes in the element;

L is the order of the harmonic series used to represent displacement and is equal to the highest order harmonic used.

The ensuing procedure for formulating the stiffness matrix for the CFSAFEM is undertaken in a manner similar to that for a full 3D analysis. However, as will become evident, the CFSAFEM uncouples the full 3D stiffness matrix, which has a form shown in Equation (12.3), into a series of smaller independent stiffness matrices of the form shown in Equation (12.4). The variables that are solved for in the CFSAFEM are the harmonic coefficients of incremental displacement at each node in the 2D mesh, i.e. $\overline{U_i^l}$, $\overline{V_i^l}$, $\overline{W_i^l}$, $\overline{\overline{U_i^l}}$, $\overline{\overline{V_i^l}}$, $\overline{\overline{W_i^l}}$.

$$\begin{bmatrix} & & & \\ & \boldsymbol{K}_G & & \\ & & & \end{bmatrix} \begin{Bmatrix} \Delta \boldsymbol{d}_0 \\ \Delta \boldsymbol{d}_1 \\ .. \\ .. \\ \Delta \boldsymbol{d}_i \\ .. \\ .. \\ \Delta \boldsymbol{d}_{N-2} \\ \Delta \boldsymbol{d}_{N-1} \end{Bmatrix} = \begin{Bmatrix} \Delta \boldsymbol{R}_0 \\ \Delta \boldsymbol{R}_1 \\ .. \\ .. \\ \Delta \boldsymbol{R}_i \\ .. \\ .. \\ \Delta \boldsymbol{R}_{N-2} \\ \Delta \boldsymbol{R}_{N-1} \end{Bmatrix} \tag{12.3}$$

$$\begin{bmatrix} [\boldsymbol{K}^0] & 0 & 0\,0 & 0 & 0\,0 & 0 & 0 \\ 0 & [\boldsymbol{K}^1] & 0\,0 & 0 & 0\,0 & 0 & 0 \\ 0 & 0 & ..\,0 & 0 & 0\,0 & 0 & 0 \\ 0 & 0 & 0\,.. & 0 & 0\,0 & 0 & 0 \\ 0 & 0 & 0\,0\,[\boldsymbol{K}^l] & 0\,0 & 0 & 0 & 0 \\ 0 & 0 & 0\,0 & 0 & ..\,0 & 0 & 0 \\ 0 & 0 & 0\,0 & 0 & 0\,.. & 0 & 0 \\ 0 & 0 & 0\,0 & 0 & 0\,0 & [\boldsymbol{K}^{L-1}] & 0 \\ 0 & 0 & 0\,0 & 0 & 0\,0 & 0 & [\boldsymbol{K}^L] \end{bmatrix} \begin{Bmatrix} \Delta \boldsymbol{d}^0 \\ \Delta \boldsymbol{d}^{1*}, \Delta \boldsymbol{d}^{1**} \\ .. \\ .. \\ \Delta \boldsymbol{d}^{l*}, \Delta \boldsymbol{d}^{l**} \\ .. \\ .. \\ \Delta \boldsymbol{d}^{L-1*}, \Delta \boldsymbol{d}^{L-1**} \\ \Delta \boldsymbol{d}^{L*}, \Delta \boldsymbol{d}^{L**} \end{Bmatrix} = \begin{Bmatrix} \Delta \boldsymbol{R}^0 \\ \Delta \boldsymbol{R}^{1*}, \Delta \boldsymbol{R}^{1**} \\ .. \\ .. \\ \Delta \boldsymbol{R}^{l*}, \Delta \boldsymbol{R}^{l**} \\ .. \\ .. \\ \Delta \boldsymbol{R}^{L-1*}, \Delta \boldsymbol{R}^{L-1**} \\ \Delta \boldsymbol{R}^{L*}, \Delta \boldsymbol{R}^{L**} \end{Bmatrix} \tag{12.4}$$

The incremental strains at a point, assuming a compression positive sign convention, are defined in cylindrical coordinates as:

$$\{\Delta \varepsilon\} = \begin{Bmatrix} \Delta\varepsilon_r \\ \Delta\varepsilon_z \\ \Delta\varepsilon_\theta \\ \Delta\varepsilon_{rz} \\ \Delta\varepsilon_{r\theta} \\ \Delta\varepsilon_{z\theta} \end{Bmatrix} = -\begin{Bmatrix} \dfrac{\partial(\Delta u)}{\partial r} \\ \dfrac{\partial(\Delta v)}{\partial z} \\ \dfrac{\Delta u}{r} + \dfrac{1}{r}\dfrac{\partial(\Delta w)}{\partial \theta} \\ \dfrac{\partial(\Delta u)}{\partial z} + \dfrac{\partial(\Delta v)}{\partial r} \\ \dfrac{1}{r}\dfrac{\partial(\Delta u)}{\partial \theta} + \dfrac{\partial(\Delta w)}{\partial r} - \dfrac{\Delta w}{r} \\ \dfrac{1}{r}\dfrac{\partial(\Delta v)}{\partial \theta} + \dfrac{\partial(\Delta w)}{\partial z} \end{Bmatrix} \tag{12.5}$$

Thus in the problem domain defined above, the incremental strains at a point can be expressed in terms of Fourier series harmonic coefficients of incremental nodal displacements and element shape functions:

$$\{\Delta \varepsilon\} = \sum_{i=1}^{n} \sum_{l=0}^{L} \begin{bmatrix} \dfrac{\partial N_i}{\partial r}\left(\overline{U_i^l}\cos l\theta + \overline{\overline{U_i^l}}\sin l\theta\right) & 0 & 0 \\ 0 & \dfrac{\partial N_i}{\partial z}\left(\overline{V_i^l}\cos l\theta + \overline{\overline{V_i^l}}\sin l\theta\right) & 0 \\ \dfrac{N_i}{r}\left(\overline{U_i^l}\cos l\theta + \overline{\overline{U_i^l}}\sin l\theta\right) & 0 & \dfrac{lN_i}{r}\left(-\overline{W_i^l}\sin l\theta + \overline{\overline{W_i^l}}\cos l\theta\right) \\ \dfrac{\partial N_i}{\partial z}\left(\overline{U_i^l}\cos l\theta + \overline{\overline{U_i^l}}\sin l\theta\right) & \dfrac{\partial N_i}{\partial r}\left(\overline{V_i^l}\cos l\theta + \overline{\overline{V_i^l}}\sin l\theta\right) & 0 \\ \dfrac{lN_i}{r}\left(-\overline{U_i^l}\sin l\theta + \overline{\overline{U_i^l}}\cos l\theta\right) & 0 & \left(\dfrac{\partial N_i}{\partial r} - \dfrac{N_i}{r}\right)\left(\overline{W_i^l}\cos l\theta + \overline{\overline{W_i^l}}\sin l\theta\right) \\ 0 & \dfrac{lN_i}{r}\left(-\overline{V_i^l}\sin l\theta + \overline{\overline{V_i^l}}\cos l\theta\right) & \dfrac{\partial N_i}{\partial z}\left(\overline{W_i^l}\cos l\theta + \overline{\overline{W_i^l}}\sin l\theta\right) \end{bmatrix} \tag{12.6}$$

These incremental strains can be rewritten as the sum of the product of a series of strain matrices, $[\boldsymbol{B}]$, and vectors of harmonic coefficients of incremental displacements. The resulting expressions can then be divided into two parts, parallel symmetry terms and orthogonal symmetry terms. Parallel symmetry terms consist of cosine harmonic coefficients of radial and vertical incremental displacements and sine harmonic coefficients of circumferential incremental displacements. Conversely, orthogonal symmetry terms consist of sine harmonic coefficients of radial and vertical incremental displacements and cosine harmonic coefficients of circumferential incremental displacements. Rearranging Equation (12.6) in this manner gives:

$$\{\Delta\varepsilon\} = \begin{Bmatrix} \Delta\varepsilon_r \\ \Delta\varepsilon_z \\ \Delta\varepsilon_\theta \\ \Delta\varepsilon_{rz} \\ \text{--} \\ \Delta\varepsilon_{r\theta} \\ \Delta\varepsilon_{z\theta} \end{Bmatrix} = -\sum_{i=1}^{n}\sum_{l=0}^{L} \begin{bmatrix} \frac{\partial N_i}{\partial r}\cos l\theta & 0 & 0 \\ 0 & \frac{\partial N_i}{\partial z}\cos l\theta & 0 \\ \frac{N_i}{r}\cos l\theta & 0 & \frac{lN_i}{r}\cos l\theta \\ \frac{\partial N_i}{\partial z}\cos l\theta & \frac{\partial N_i}{\partial r}\cos l\theta & 0 \\ \text{-------} & \text{-------} & \text{-------} \\ -\frac{lN_i}{r}\sin l\theta & 0 & \left(\frac{\partial N_i}{\partial r} - \frac{N_i}{r}\right)\sin l\theta \\ 0 & -\frac{lN_i}{r}\sin l\theta & \frac{\partial N_i}{\partial z}\sin l\theta \end{bmatrix} \begin{Bmatrix} \overline{U_i^l} \\ \overline{V_i^l} \\ \overline{\overline{W_i^l}} \end{Bmatrix}$$

$$-\sum_{i=1}^{n}\sum_{l=0}^{L} \begin{bmatrix} \frac{\partial N_i}{\partial r}\sin l\theta & 0 & 0 \\ 0 & \frac{\partial N_i}{\partial z}\sin l\theta & 0 \\ \frac{N_i}{r}\sin l\theta & 0 & \frac{lN_i}{r}\sin l\theta \\ \frac{\partial N_i}{\partial z}\sin l\theta & \frac{\partial N_i}{\partial r}\sin l\theta & 0 \\ \text{-------} & \text{-------} & \text{-------} \\ \frac{lN_i}{r}\cos l\theta & 0 & -\left(\frac{\partial N_i}{\partial r} - \frac{N_i}{r}\right)\cos l\theta \\ 0 & \frac{lN_i}{r}\cos l\theta & -\frac{\partial N_i}{\partial z}\cos l\theta \end{bmatrix} \begin{Bmatrix} \overline{\overline{U_i^l}} \\ \overline{V_i^l} \\ -\overline{W_i^l} \end{Bmatrix} \tag{12.7}$$

Splitting the equation into two parts in this manner results in the $[\boldsymbol{B}]$ matrices for each part having a similar form. The dashed lines in the matrices separate the sine and cosine terms and split the $[\boldsymbol{B}]$ matrix into a top and bottom section. Note that the cosine coefficient of circumferential incremental displacement is expressed with a sign change. Thus the strains can be written as:

$$\{\Delta\varepsilon\} = \sum_{i=1}^{n}\sum_{l=0}^{L} \begin{bmatrix} [\boldsymbol{B}1_i^l]\cos l\theta \\ [\boldsymbol{B}2_i^l]\sin l\theta \end{bmatrix} \{\Delta\boldsymbol{d}_i^{l*}\} + \begin{bmatrix} [\boldsymbol{B}1_i^l]\sin l\theta \\ -[\boldsymbol{B}2_i^l]\cos l\theta \end{bmatrix} \{\Delta\boldsymbol{d}_i^{l**}\} \tag{12.8}$$

where:

$$[\boldsymbol{B}1_i^l] = -\begin{bmatrix} \frac{\partial N_i}{\partial r} & 0 & 0 \\ 0 & \frac{\partial N_i}{\partial z} & 0 \\ \frac{N_i}{r} & 0 & \frac{lN_i}{r} \\ \frac{\partial N_i}{\partial z} & \frac{\partial N_i}{\partial r} & 0 \end{bmatrix} \quad \text{and} \quad \{\Delta\boldsymbol{d}_i^{l*}\} = \begin{Bmatrix} \overline{U_i^l} \\ \overline{V_i^l} \\ \overline{\overline{W_i^l}} \end{Bmatrix} \tag{12.9}$$

$$[\boldsymbol{B}2_i^l] = -\begin{bmatrix} -\frac{lN_i}{r} & 0 & \left(\frac{\partial N_i}{\partial r} - \frac{N_i}{r}\right) \\ 0 & -\frac{lN_i}{r} & \frac{\partial N_i}{\partial z} \end{bmatrix} \quad \text{and} \quad \{\Delta\boldsymbol{d}_i^{l**}\} = \begin{Bmatrix} \overline{\overline{U_i^l}} \\ \overline{V_i^l} \\ -\overline{W_i^l} \end{Bmatrix}$$

Note:

$\{\Delta\boldsymbol{d}_i^{l*}\}$ and $\{\Delta\boldsymbol{d}_i^{l**}\}$ are the parallel and orthogonal l^{th} order harmonic coefficients of incremental displacement for the i^{th} node respectively, and $[\boldsymbol{B}1_i^l]$ and $[\boldsymbol{B}2_i^l]$ are the top and bottom sections of the l^{th} order harmonic $[\boldsymbol{B}]$ matrix for the i^{th} node respectively.

The incremental internal work done can now be written as:

$$\begin{aligned} \Delta W &= \int_{-\pi}^{\pi}\int \{\Delta\varepsilon\}^{\mathrm{T}}\{\Delta\sigma\}\,\mathrm{d}\theta\, r\, \mathrm{d}area \\ &= \int_{-\pi}^{\pi}\int \{\Delta\boldsymbol{u}\}^{\mathrm{T}}[\boldsymbol{B}]^{\mathrm{T}}[\boldsymbol{D}][\boldsymbol{B}]\,\{\Delta\boldsymbol{u}\}\,\mathrm{d}\theta\, r\, \mathrm{d}area \\ &= \int_{-\pi}^{\pi}\int \sum_{i=1}^{n}\left\{\sum_{k=0}^{L}\begin{bmatrix}[\boldsymbol{B}1_i^k]\cos k\theta \\ [\boldsymbol{B}2_i^k]\sin k\theta\end{bmatrix}\{\Delta\boldsymbol{d}_i^{k*}\} + \begin{bmatrix}[\boldsymbol{B}1_i^k]\sin k\theta \\ -[\boldsymbol{B}2_i^k]\cos k\theta\end{bmatrix}\{\Delta\boldsymbol{d}_i^{k**}\}\right\}^{\mathrm{T}}\cdot[\boldsymbol{D}]\cdot \\ &\quad \sum_{j=1}^{n}\left\{\sum_{l=0}^{L}\begin{bmatrix}[\boldsymbol{B}1_j^l]\cos l\theta \\ [\boldsymbol{B}2_j^l]\sin l\theta\end{bmatrix}\{\Delta\boldsymbol{d}_j^{l*}\} + \begin{bmatrix}[\boldsymbol{B}1_j^l]\sin l\theta \\ -[\boldsymbol{B}2_j^l]\cos l\theta\end{bmatrix}\{\Delta\boldsymbol{d}_j^{l**}\}\right\} r\,\mathrm{d}\theta\,\mathrm{d}area \end{aligned} \tag{12.10}$$

The $[\boldsymbol{D}]$ matrix for a material relates the incremental stress vector $\{\Delta\boldsymbol{\sigma}\}$ to the incremental strain vector $\{\Delta\varepsilon\}$, i.e:

$$\{\Delta\boldsymbol{\sigma}\} = [\boldsymbol{D}]\,\{\Delta\varepsilon\} \tag{12.11}$$

It can be divided into four submatrices, $[\boldsymbol{D}_{11}]$, $[\boldsymbol{D}_{12}]$, $[\boldsymbol{D}_{21}]$, and $[\boldsymbol{D}_{22}]$, in accordance with the subdivision of the $[\boldsymbol{B}]$ matrix into two submatrices $[\boldsymbol{B}1]$ and $[\boldsymbol{B}2]$. This can be written in matrix form as:

$$\begin{Bmatrix} \Delta\sigma_r \\ \Delta\sigma_z \\ \Delta\sigma_\theta \\ \Delta\sigma_{rz} \\ -- \\ \Delta\sigma_{r\theta} \\ \Delta\sigma_{z\theta} \end{Bmatrix} = \left[\begin{array}{c|c} [\boldsymbol{D}_{11}] & [\boldsymbol{D}_{12}] \\ \hline [\boldsymbol{D}_{21}] & [\boldsymbol{D}_{22}] \end{array}\right] \begin{Bmatrix} \Delta\varepsilon_r \\ \Delta\varepsilon_z \\ \Delta\varepsilon_\theta \\ \Delta\varepsilon_{rz} \\ -- \\ \Delta\varepsilon_{r\theta} \\ \Delta\varepsilon_{z\theta} \end{Bmatrix} \tag{12.12}$$

Thus the equation for incremental internal work can be rewritten as:

$$\begin{aligned} \Delta W = \int_{-\pi}^{\pi} \sum_{i=1}^{n}\sum_{j=1}^{n} & \sum_{k=0}^{L} \{\Delta \boldsymbol{d}_i^{k*}\}^{\mathrm{T}} \begin{bmatrix} [\boldsymbol{B}1_i^k]\cos k\theta \\ [\boldsymbol{B}2_i^k]\sin k\theta \end{bmatrix}^{\mathrm{T}} \begin{bmatrix} [\boldsymbol{D}_{11}] & [\boldsymbol{D}_{12}] \\ [\boldsymbol{D}_{21}] & [\boldsymbol{D}_{22}] \end{bmatrix} \sum_{l=0}^{L} \begin{bmatrix} [\boldsymbol{B}1_j^l]\cos l\theta \\ [\boldsymbol{B}2_j^l]\sin l\theta \end{bmatrix} \{\Delta \boldsymbol{d}_j^{l*}\} \\ + & \sum_{k=0}^{L} \{\Delta \boldsymbol{d}_i^{k**}\}^{\mathrm{T}} \begin{bmatrix} [\boldsymbol{B}1_i^k]\sin k\theta \\ -[\boldsymbol{B}2_i^k]\cos k\theta \end{bmatrix}^{\mathrm{T}} \begin{bmatrix} [\boldsymbol{D}_{11}] & [\boldsymbol{D}_{12}] \\ [\boldsymbol{D}_{21}] & [\boldsymbol{D}_{22}] \end{bmatrix} \sum_{l=0}^{L} \begin{bmatrix} [\boldsymbol{B}1_j^l]\cos l\theta \\ [\boldsymbol{B}2_j^l]\sin l\theta \end{bmatrix} \{\Delta \boldsymbol{d}_j^{l*}\} \\ + & \sum_{k=0}^{L} \{\Delta \boldsymbol{d}_i^{k*}\}^{\mathrm{T}} \begin{bmatrix} [\boldsymbol{B}1_i^k]\cos k\theta \\ [\boldsymbol{B}2_i^k]\sin k\theta \end{bmatrix}^{\mathrm{T}} \begin{bmatrix} [\boldsymbol{D}_{11}] & [\boldsymbol{D}_{12}] \\ [\boldsymbol{D}_{21}] & [\boldsymbol{D}_{22}] \end{bmatrix} \sum_{l=0}^{L} \begin{bmatrix} [\boldsymbol{B}1_j^l]\sin l\theta \\ -[\boldsymbol{B}2_j^l]\cos l\theta \end{bmatrix} \{\Delta \boldsymbol{d}_j^{l**}\} \\ + & \sum_{k=0}^{L} \{\Delta \boldsymbol{d}_i^{k**}\}^{\mathrm{T}} \begin{bmatrix} [\boldsymbol{B}1_i^k]\sin k\theta \\ -[\boldsymbol{B}2_i^k]\cos k\theta \end{bmatrix}^{\mathrm{T}} \begin{bmatrix} [\boldsymbol{D}_{11}] & [\boldsymbol{D}_{12}] \\ [\boldsymbol{D}_{21}] & [\boldsymbol{D}_{22}] \end{bmatrix} \sum_{l=0}^{L} \begin{bmatrix} [\boldsymbol{B}1_j^l]\sin l\theta \\ -[\boldsymbol{B}2_j^l]\cos l\theta \end{bmatrix} \{\Delta \boldsymbol{d}_j^{l**}\} \\ & r\,\mathrm{d}\theta\,\mathrm{d}area \end{aligned} \tag{12.13}$$

When integrating with respect to θ, a large number of terms in the stiffness matrix become zero due to the orthogonal properties of the Fourier series:

$$\begin{aligned} &\int_{-\pi}^{\pi} \sin k\theta\, \cos l\theta\, \mathrm{d}\theta = 0 \quad \text{for all } k \text{ and } l\,; \\ &\int_{-\pi}^{\pi} \sin k\theta\, \sin l\theta\, \mathrm{d}\theta = 0 \quad \text{if } k \neq l,\ = \pi \text{ if } k=l \neq 0,\ = 0 \text{ if } k = l = 0\,; \\ &\int_{-\pi}^{\pi} \cos k\theta\, \cos l\theta\, \mathrm{d}\theta = 0 \quad \text{if } k \neq l,\ = \pi \text{ if } k = l \neq 0,\ = 2\pi \text{ if } k = l = 0\,. \end{aligned} \tag{12.14}$$

Thus the incremental internal work done can now be simplified to:

$$\begin{aligned} \Delta W = & \\ \pi \int \sum_{i=1}^{n}\sum_{j=1}^{n} & 2\{\Delta \boldsymbol{d}_i^{0*}\}^{\mathrm{T}}[\boldsymbol{B}1_i^0]^{\mathrm{T}}[\boldsymbol{D}_{11}][\boldsymbol{B}1_j^0]\{\Delta \boldsymbol{d}_j^{0*}\} + 2\{\Delta \boldsymbol{d}_i^{0**}\}^{\mathrm{T}}[\boldsymbol{B}2_i^0]^{\mathrm{T}}[\boldsymbol{D}_{22}][\boldsymbol{B}2_j^0]\{\Delta \boldsymbol{d}_j^{0**}\} + \\ \sum_{l=1}^{L} & \{\Delta \boldsymbol{d}_i^{l*}\}^{\mathrm{T}}[\boldsymbol{B}1_i^l]^{\mathrm{T}}[\boldsymbol{D}_{11}][\boldsymbol{B}1_j^l]\{\Delta \boldsymbol{d}_j^{l*}\} + \{\Delta \boldsymbol{d}_i^{l*}\}^{\mathrm{T}}[\boldsymbol{B}2_i^l]^{\mathrm{T}}[\boldsymbol{D}_{22}][\boldsymbol{B}2_j^l]\{\Delta \boldsymbol{d}_j^{l*}\} + \\ & \{\Delta \boldsymbol{d}_i^{l**}\}^{\mathrm{T}}[\boldsymbol{B}1_i^l]^{\mathrm{T}}[\boldsymbol{D}_{11}][\boldsymbol{B}1_j^l]\{\Delta \boldsymbol{d}_j^{l**}\} + \{\Delta \boldsymbol{d}_i^{l**}\}^{\mathrm{T}}[\boldsymbol{B}2_i^l]^{\mathrm{T}}[\boldsymbol{D}_{22}][\boldsymbol{B}2_j^l]\{\Delta \boldsymbol{d}_j^{l**}\}\ r\,\mathrm{d}area \\ + \pi \int \sum_{i=1}^{n}\sum_{j=1}^{n} & -2\{\Delta \boldsymbol{d}_i^{0*}\}^{\mathrm{T}}[\boldsymbol{B}1_i^0]^{\mathrm{T}}[\boldsymbol{D}_{12}][\boldsymbol{B}2_j^0]\{\Delta \boldsymbol{d}_j^{0**}\} - 2\{\Delta \boldsymbol{d}_i^{0**}\}^{\mathrm{T}}[\boldsymbol{B}2_i^0]^{\mathrm{T}}[\boldsymbol{D}_{21}][\boldsymbol{B}1_j^0]\{\Delta \boldsymbol{d}_j^{0*}\} + \\ \sum_{l=1}^{L} & -\{\Delta \boldsymbol{d}_i^{l*}\}^{\mathrm{T}}[\boldsymbol{B}1_i^l]^{\mathrm{T}}[\boldsymbol{D}_{12}][\boldsymbol{B}2_j^l]\{\Delta \boldsymbol{d}_j^{l**}\} + \{\Delta \boldsymbol{d}_i^{l*}\}^{\mathrm{T}}[\boldsymbol{B}2_i^l]^{\mathrm{T}}[\boldsymbol{D}_{21}][\boldsymbol{B}1_j^l]\{\Delta \boldsymbol{d}_j^{l**}\} + \\ & \{\Delta \boldsymbol{d}_i^{l**}\}^{\mathrm{T}}[\boldsymbol{B}1_i^l]^{\mathrm{T}}[\boldsymbol{D}_{12}][\boldsymbol{B}2_j^l]\{\Delta \boldsymbol{d}_j^{l*}\} - \{\Delta \boldsymbol{d}_i^{l**}\}^{\mathrm{T}}[\boldsymbol{B}2_i^l]^{\mathrm{T}}[\boldsymbol{D}_{21}][\boldsymbol{B}1_j^l]\{\Delta \boldsymbol{d}_j^{l*}\}\ r\,\mathrm{d}area \end{aligned} \tag{12.15}$$

The stiffness matrix has been uncoupled into L+1 smaller stiffness matrices of the form shown in Equation (12.4), with one independent set of equations for each harmonic order. This form of uncoupling is called *harmonic uncoupling*. However, for each set of equations associated with a particular harmonic order the parallel symmetry displacements, $\{\Delta \boldsymbol{d}_i^{l*}\}$, and orthogonal symmetry displacements, $\{\Delta \boldsymbol{d}_i^{l**}\}$, are coupled in the manner shown below:

$$\begin{Bmatrix} \{\Delta \boldsymbol{R}^{l*}\} \\ \{\Delta \boldsymbol{R}^{l**}\} \end{Bmatrix} = \begin{bmatrix} [\boldsymbol{K}^l]^p & [\boldsymbol{K}^l]^{po} \\ [\boldsymbol{K}^l]^{op} & [\boldsymbol{K}^l]^o \end{bmatrix} \begin{Bmatrix} \{\Delta \boldsymbol{d}^{l*}\} \\ \{\Delta \boldsymbol{d}^{l**}\} \end{Bmatrix} \tag{12.16}$$

The terms above the dashed line in Equation (12.15) give the independent diagonal terms $[\boldsymbol{K}^l]^p$ and $[\boldsymbol{K}^l]^o$, and those below give the cross coupling terms $[\boldsymbol{K}^l]^{op}$ and $[\boldsymbol{K}^l]^{po}$. It is noted that for materials with a $[\boldsymbol{D}]$ matrix which has zero off diagonal submatrices, $[\boldsymbol{D}_{12}]$ and $[\boldsymbol{D}_{21}]$, the cross coupling terms disappear and the stiffness matrix reduces to the following form:

$$\begin{Bmatrix} \{\Delta \boldsymbol{R}^{l*}\} \\ \{\Delta \boldsymbol{R}^{l**}\} \end{Bmatrix} = \begin{bmatrix} [\boldsymbol{K}^l]^p & 0 \\ 0 & [\boldsymbol{K}^l]^o \end{bmatrix} \begin{Bmatrix} \{\Delta \boldsymbol{d}^{l*}\} \\ \{\Delta \boldsymbol{d}^{l**}\} \end{Bmatrix} \tag{12.17}$$

In addition, it may be noted that $[\boldsymbol{K}^l]^p = [\boldsymbol{K}^l]^o$. In this case the $\{\Delta \boldsymbol{d}_i^{l*}\}$ and $\{\Delta \boldsymbol{d}_i^{l**}\}$ terms for each harmonic order can be solved independently, using the same stiffness matrix. This form of uncoupling is called *symmetric uncoupling*. The symmetrically uncoupled stiffness matrix for the l^{th} order harmonic is:

$$[\boldsymbol{K}_{ij}^l]^o = [\boldsymbol{K}_{ij}^l]^p = \Delta\pi \sum_{i=1}^{n}\sum_{j=1}^{n} \int [\boldsymbol{B}1_i^l]^{\mathrm{T}}[\boldsymbol{D}_{11}][\boldsymbol{B}1_j^l] + [\boldsymbol{B}2_i^l]^{\mathrm{T}}[\boldsymbol{D}_{22}][\boldsymbol{B}2_j^l]\ r\,\mathrm{d}area \tag{12.18}$$

where: $\Delta = 2$ if $l = 0$;
$\Delta = 1$ if $l \neq 0$.

The applied incremental loads are formulated as harmonic coefficients of incremental nodal force using the equations in Appendices XII.1 to XII.4. These harmonic coefficients of nodal force are expressed as vectors $\{\Delta \boldsymbol{R}^{l*}\}$ and $\{\Delta \boldsymbol{R}^{l**}\}$:

$\{\Delta \boldsymbol{R}^{l*}\} = \left\{\overline{R_r^l}\ \overline{R_z^l}\ \overline{\overline{R_\theta^l}}\right\}^T$ is the vector of parallel l^{th} order harmonic coefficients of incremental force;

$\{\Delta \boldsymbol{R}^{l**}\} = \left\{\overline{\overline{R_r^l}}\ \overline{\overline{R_z^l}}\ -\overline{R_\theta^l}\right\}^T$ is the vector of orthogonal l^{th} order harmonic coefficients of incremental force;

where:

$\overline{R_r^l}$, $\overline{R_z^l}$ and $\overline{R_\theta^l}$ are the l^{th} cosine harmonic coefficient of radial, vertical and circumferential incremental force respectively;

$\overline{\overline{R_r^l}}$, $\overline{\overline{R_z^l}}$ and $\overline{\overline{R_\theta^l}}$ are the l^{th} sine harmonic coefficient of radial, vertical and circumferential incremental force respectively.

Thus for each harmonic order two sets of system equations can be written:

$$\begin{aligned} \{\Delta \boldsymbol{R}^{l*}\} &= [\boldsymbol{K}^l]^p \{\Delta \boldsymbol{d}^{l*}\} \\ \{\Delta \boldsymbol{R}^{l**}\} &= [\boldsymbol{K}^l]^o \{\Delta \boldsymbol{d}^{l**}\} \end{aligned} \tag{12.19}$$

The displacements can be solved for by inverting the stiffness matrix in a similar manner to the conventional finite element method. An important feature of this linear elastic formulation is the harmonic uncoupling. A consequence of this uncoupling is that for any harmonic order the solution coefficients of displacements are only non-zero if the applied coefficients of load for the same order are non-zero. Thus the number of harmonics required for an analysis is equal to the number of harmonics required to represent the boundary conditions.

12.3.2 Symmetrical loading conditions

A symmetrical function of θ, $f_s(\theta)$, has the property that:

$$f_s(\theta) = f_s(-\theta) \tag{12.20}$$

and the Fourier series representation of such a function would only consist of the zeroth (i.e. 0^{th}) and cosine harmonic terms. An asymmetrical function of θ, $f_{ns}(\theta)$, has the property that:

$$f_{ns}(\theta) = -f_{ns}(-\theta) \tag{12.21}$$

and the Fourier series representation of such a function would only consist of sine harmonic terms.

The linear CFSAFEM formulation has divided the solution displacements, $\{\Delta \boldsymbol{d}\}$, into two parts, parallel symmetry displacements, $\{\Delta \boldsymbol{d}^*\}$, and orthogonal symmetry displacements, $\{\Delta \boldsymbol{d}^{**}\}$. The parallel symmetry displacements consist of symmetrical displacements in the r and z coordinate directions and asymmetrical displacements in the θ direction. Conversely, orthogonal symmetry displacements consist of asymmetrical displacements in the r and z coordinate directions and

symmetrical displacements in the θ direction. The applied loads, $\{\Delta \boldsymbol{R}\}$, are separated in a similar manner into parallel loads, $\{\Delta \boldsymbol{R}^*\}$, and orthogonal loads, $\{\Delta \boldsymbol{R}^{**}\}$.

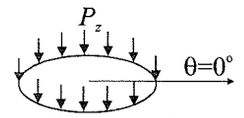

P_z is the applied vertical force/unit length

F_z is axial force applied to the pile = $2\pi r P_z$

r is the radial coordinate of the node

a) Axial load on pile

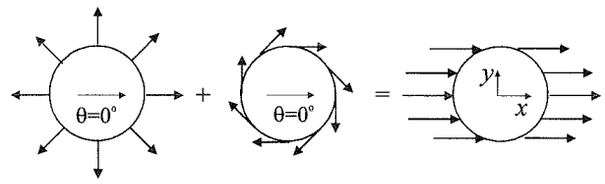

$P_r = P\cos\theta$ $P_\theta = -P\sin\theta$ $P_x = P$; $P_y = 0$

F_x is lateral force applied to the pile = $2\pi r P$

b) Lateral load on pile

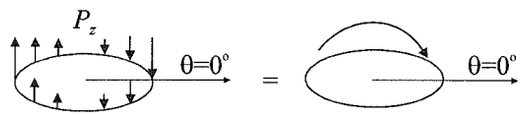

$P_z = P'\cos\theta$ $M_y = \pi r P'$

P_z is the applied vertical force/unit length

M_y is the applied turning moment

c) Moment load on pile

Figure 12.2: Load components on pile

Many boundary value problems have a symmetry about the $\theta = 0°$ direction, such that the imposed boundary conditions consist of purely parallel symmetry or orthogonal symmetry terms. For instance, the loading conditions applied to a pile may consist of a combination of axial loading, lateral loading and turning moment about an axis perpendicular to the direction of lateral loading. These boundary conditions can be represented using parallel symmetry, if the direction of lateral loading is parallel with the $\theta = 0°$ direction, see Figure 12.2a-c. Hence, all previous implementations of the CFSAFEM have been constrained to analyse either parallel symmetry conditions (Winnicki and Zienkiewicz (1979)), or orthogonal symmetry problems (Griffiths and Lane (1990)). If the applied loads in a problem do not satisfy any symmetry about the $\theta = 0°$ direction, then a non-symmetrical

formulation is required, consisting of both parallel and orthogonal symmetry terms. Analyses using only parallel or orthogonal symmetry terms benefit from the reduced number of solution coefficients of displacements that have to be solved for. This results in large savings in computer resources required for an analysis and significantly simplifies the solution algorithms.

The previous implementations of the CFSAFEM have assumed that if the applied loading conditions can be represented using either parallel or orthogonal symmetry, then the resulting solution displacements will also satisfy parallel or orthogonal symmetry, respectively. Though this may have been valid for the particular cases analysed, it is not true in general. In the linear elastic formulation presented above, this assumption has been shown to be true only for materials with a $[\boldsymbol{D}]$ matrix which has zero off diagonal terms $[\boldsymbol{D}_{12}]$ and $[\boldsymbol{D}_{21}]$, i.e an isotropic linear elastic material. Due to the coupling of parallel and orthogonal terms, the analysis of an anisotropic elastic material, with non-zero $[\boldsymbol{D}_{12}]$ and $[\boldsymbol{D}_{21}]$, would require the full non-symmetrical formulation, irrespective of any symmetry in the imposed loads.

The term parallel symmetry stems from the fact that it can be used to represent a load in a direction parallel to the $\theta = 0°$ direction, see Figure 12.2b. Similarly, orthogonal symmetry can represent loads in a direction perpendicular to the $\theta = 0°$ direction.

12.3.3 Existing formulations for nonlinear behaviour

All past implementations of the CFSAFEM have used the above formulation for linear elastic behaviour with a constant material stiffness, $[\boldsymbol{D}]$ matrix, in the θ direction. No formulation has been developed for nonlinear material behaviour with a variable $[\boldsymbol{D}]$ matrix in the θ direction. However, nonlinear analyses have been undertaken using the linear elastic formulation, in combination with a solution strategy which continually adjusts the right hand side of the governing finite element equations to cater for material nonlinearity. This is akin to using an elastic stiffness matrix to solve an elasto-plastic problem. Considering the three solution strategies described and compared in Chapter 9, only the visco-plastic and MNR approaches can be used in this way. The tangent stiffness approach cannot be employed because it involves the use of the elasto-plastic stiffness. The visco-plastic approach was used by Winnicki and Zienkiewicz (1979) and Griffiths and Lane (1990). However, as noted in Chapter 9, this method can be problematic for highly nonlinear constitutive models. A better alternative is the use of the MNR approach, with the stiffness matrix calculated using only the elastic part of the constitutive matrix.

There is some scepticism about the validity of the above approach for nonlinear problems. It is argued that, since the formulation of the CFSAFEM assumes that the $[\boldsymbol{D}]$ matrix is constant in the θ direction, its use for a material which does not satisfy this criterion is not valid. The popular practice of using purely parallel or purely orthogonal symmetry terms in an analysis requires that the system stiffness

matrix is symmetrically uncoupled. The criterion for this is that the off diagonal terms in the $[\boldsymbol{D}]$ matrix are zero, as discussed in Section 12.3.1. This criterion is not satisfied in general for elasto-plastic materials and thus questions the validity of the above practice for nonlinear analyses.

An important feature of nonlinear CFSAFEM analyses is that harmonic uncoupling no longer exists. The number of harmonics required to represent the solution displacements is not just a function of the number of harmonics required to represent the boundary conditions, but is also dependent on the material nonlinearity. This feature cannot be reproduced with the linear elastic formulation which, as noted above, only yields non-zero harmonics of displacement if a load of the same harmonic order is applied. The anomaly is overcome by allowing the corrective loads, applied by the procedure for nonlinear finite element analysis, to have harmonics other than those associated with the applied boundary conditions. Past practice has been to allow a greater number of harmonics of solution displacement than is required to represent the boundary conditions. Though this has given reasonable results, there has never been a rational for it. Increasing the number of harmonics used in an analysis increases both the amount of computer resources used and the solution accuracy. Thus the number of harmonics used in an analysis is an important parameter which is based on a trade off between solution accuracy and computer resources.

12.3.4 New formulation for nonlinear behaviour

The linear formulation for the CFSAFEM assumes that the $[\boldsymbol{D}]$ matrix is constant in the θ direction. In general, this assumption is not valid for nonlinear material behaviour, since the $[\boldsymbol{D}]$ matrix is now stress history dependent and the stresses vary in the θ direction. A new nonlinear formulation is proposed for the CFSAFEM which incorporates a variation of $[\boldsymbol{D}]$ in the θ direction.

The linear elastic CFSAFEM formulation of strain, in terms of a series of products of harmonic coefficients of displacement and harmonic $[\boldsymbol{B}]$ matrices, is used to formulate a system stiffness matrix as described by Equation (12.13). However, the $[\boldsymbol{D}]$ matrix is no longer a constant, but varies with θ. This variation can be represented with a Fourier series for each component of the $[\boldsymbol{D}]$ matrix:

$$[\boldsymbol{D}] = [\boldsymbol{D}^0] + \overline{[\boldsymbol{D}^1]}\cos\theta + \overline{\overline{[\boldsymbol{D}^1]}}\sin\theta + \overline{[\boldsymbol{D}^2]}\cos 2\theta + \overline{\overline{[\boldsymbol{D}^2]}}\sin 2\theta + \ldots \\ \overline{[\boldsymbol{D}^l]}\cos l\theta + \overline{\overline{[\boldsymbol{D}^l]}}\sin l\theta + \ldots \qquad (12.22)$$

where $[\boldsymbol{D}^0]$, $\overline{[\boldsymbol{D}^l]}$ and $\overline{\overline{[\boldsymbol{D}^l]}}$ are matrices containing the 0^{th}, l^{th} order cosine and l^{th} order sine harmonic coefficients of the components of the $[\boldsymbol{D}]$ matrix respectively. The number of harmonics used to represent the $[\boldsymbol{D}]$ matrix, M, need not be the same as the number used to represent displacements, L. These harmonic $[\boldsymbol{D}]$ matrices can also be split into 4 parts representing $[\boldsymbol{D}_{11}]$, $[\boldsymbol{D}_{12}]$, $[\boldsymbol{D}_{21}]$ and $[\boldsymbol{D}_{22}]$ terms. Separating the cosine and sine harmonics of the $[\boldsymbol{D}]$ matrix allows Equation (12.13) to be rewritten as:

$$\int_{-\pi}^{\pi}\sum_{i=1}^{n}\sum_{j=1}^{n}\sum_{k=0}^{L_c}\{\Delta d_i^{k*}\}^{\mathrm{T}}\begin{bmatrix}[B1_i^k]\cos k\theta\\ [B2_i^k]\sin k\theta\end{bmatrix}\sum_{m=0}^{M}\begin{bmatrix}\overline{[D_{11}^m]}\cos m\theta & \overline{[D_{12}^m]}\cos m\theta\\ \overline{[D_{21}^m]}\cos m\theta & \overline{[D_{22}^m]}\cos m\theta\end{bmatrix}\sum_{l=0}^{L_c}\begin{bmatrix}[B1_j^l]\cos l\theta\\ [B2_j^l]\sin l\theta\end{bmatrix}\{\Delta d_j^{l*}\}$$

$$+\sum_{k=0}^{L_c}\{\Delta d_i^{k**}\}^{\mathrm{T}}\begin{bmatrix}[B1_i^k]\sin k\theta\\ -[B2_i^k]\cos k\theta\end{bmatrix}\sum_{m=0}^{M}\begin{bmatrix}\overline{[D_{11}^m]}\cos m\theta & \overline{[D_{12}^m]}\cos m\theta\\ \overline{[D_{21}^m]}\cos m\theta & \overline{[D_{22}^m]}\cos m\theta\end{bmatrix}\sum_{l=0}^{L_c}\begin{bmatrix}[B1_j^l]\cos l\theta\\ [B2_j^l]\sin l\theta\end{bmatrix}\{\Delta d_j^{l*}\}$$

$$+\sum_{k=0}^{L_c}\{\Delta d_i^{k*}\}^{\mathrm{T}}\begin{bmatrix}[B1_i^k]\cos k\theta\\ [B2_i^k]\sin k\theta\end{bmatrix}\sum_{m=0}^{M}\begin{bmatrix}\overline{[D_{11}^m]}\cos m\theta & \overline{[D_{12}^m]}\cos m\theta\\ \overline{[D_{21}^m]}\cos m\theta & \overline{[D_{22}^m]}\cos m\theta\end{bmatrix}\sum_{l=0}^{L_c}\begin{bmatrix}[B1_j^l]\sin l\theta\\ -[B2_j^l]\cos l\theta\end{bmatrix}\{\Delta d_j^{l**}\}$$

$$+\sum_{k=0}^{L_c}\{\Delta d_i^{k**}\}^{\mathrm{T}}\begin{bmatrix}[B1_i^k]\sin k\theta\\ -[B2_i^k]\cos k\theta\end{bmatrix}\sum_{m=0}^{M}\begin{bmatrix}\overline{[D_{11}^m]}\cos m\theta & \overline{[D_{12}^m]}\cos m\theta\\ \overline{[D_{21}^m]}\cos m\theta & \overline{[D_{22}^m]}\cos m\theta\end{bmatrix}\sum_{l=0}^{L_c}\begin{bmatrix}[B1_j^l]\sin l\theta\\ -[B2_j^l]\cos l\theta\end{bmatrix}\{\Delta d_j^{l**}\}$$

$$+\sum_{k=0}^{L_c}\{\Delta d_i^{k*}\}^{\mathrm{T}}\begin{bmatrix}[B1_i^k]\cos k\theta\\ [B2_i^k]\sin k\theta\end{bmatrix}\sum_{m=0}^{M}\begin{bmatrix}\overline{\overline{[D_{11}^m]}}\sin m\theta & \overline{\overline{[D_{12}^m]}}\sin m\theta\\ \overline{\overline{[D_{21}^m]}}\sin m\theta & \overline{\overline{[D_{22}^m]}}\sin m\theta\end{bmatrix}\sum_{l=0}^{L_c}\begin{bmatrix}[B1_j^l]\cos l\theta\\ [B2_j^l]\sin l\theta\end{bmatrix}\{\Delta d_j^{l*}\}$$

$$+\sum_{k=0}^{L_c}\{\Delta d_i^{k**}\}^{\mathrm{T}}\begin{bmatrix}[B1_i^k]\sin k\theta\\ -[B2_i^k]\cos k\theta\end{bmatrix}\sum_{m=0}^{M}\begin{bmatrix}\overline{\overline{[D_{11}^m]}}\sin m\theta & \overline{\overline{[D_{12}^m]}}\sin m\theta\\ \overline{\overline{[D_{21}^m]}}\sin m\theta & \overline{\overline{[D_{22}^m]}}\sin m\theta\end{bmatrix}\sum_{l=0}^{L_c}\begin{bmatrix}[B1_j^l]\cos l\theta\\ [B2_j^l]\sin l\theta\end{bmatrix}\{\Delta d_j^{l*}\}$$

$$+\sum_{k=0}^{L_c}\{\Delta d_i^{k*}\}^{\mathrm{T}}\begin{bmatrix}[B1_i^k]\cos k\theta\\ [B2_i^k]\sin k\theta\end{bmatrix}\sum_{m=0}^{M}\begin{bmatrix}\overline{\overline{[D_{11}^m]}}\sin m\theta & \overline{\overline{[D_{12}^m]}}\sin m\theta\\ \overline{\overline{[D_{21}^m]}}\sin m\theta & \overline{\overline{[D_{22}^m]}}\sin m\theta\end{bmatrix}\sum_{l=0}^{L_c}\begin{bmatrix}[B1_j^l]\sin l\theta\\ -[B2_j^l]\cos l\theta\end{bmatrix}\{\Delta d_j^{l**}\}$$

$$+\sum_{k=0}^{L_c}\{\Delta d_i^{k**}\}^{\mathrm{T}}\begin{bmatrix}[B1_i^k]\sin k\theta\\ -[B2_i^k]\cos k\theta\end{bmatrix}\sum_{m=0}^{M}\begin{bmatrix}\overline{\overline{[D_{11}^m]}}\sin m\theta & \overline{\overline{[D_{12}^m]}}\sin m\theta\\ \overline{\overline{[D_{21}^m]}}\sin m\theta & \overline{\overline{[D_{22}^m]}}\sin m\theta\end{bmatrix}\sum_{l=0}^{L_c}\begin{bmatrix}[B1_j^l]\sin l\theta\\ -[B2_j^l]\cos l\theta\end{bmatrix}\{\Delta d_j^{l**}\}$$

$r\ \mathrm{d}\theta\,\mathrm{d}area$

(12.32)

As with the linear formulation, the $\mathrm{d}\theta$ integral is performed and a large number of terms in the stiffness matrix are zero due to the orthogonal properties of the Fourier series. For the linear formulation this integration was solved using the standard solutions for the integration of the product of two Fourier series. However, for the nonlinear formulation the corresponding integration is of the product of three Fourier series and a new set of solutions has to be derived, see Appendix XII.5. Thus the incremental internal work done can be written as:

$$\Delta W = \pi\int\sum_{i=1}^{n}\sum_{j=1}^{n}\sum_{k=0}^{L_c}\{\Delta d_i^{k*}\}^{\mathrm{T}}\begin{bmatrix}[B1_i^k]\\ [B2_i^k]\end{bmatrix}^{\mathrm{T}}\sum_{l=0}^{L_c}\begin{bmatrix}[D_{11}^{k,l}]^p & [D_{12}^{k,l}]^p\\ [D_{21}^{k,l}]^p & [D_{22}^{k,l}]^p\end{bmatrix}\begin{bmatrix}[B1_j^l]\\ [B2_j^l]\end{bmatrix}\{\Delta d_j^{l*}\}$$

$$+\sum_{k=0}^{L_c}\{\Delta d_i^{k**}\}^{\mathrm{T}}\begin{bmatrix}[B1_i^k]\\ [B2_i^k]\end{bmatrix}^{\mathrm{T}}\sum_{l=0}^{L_c}\begin{bmatrix}[D_{11}^{k,l}]^{op} & [D_{12}^{k,l}]^{op}\\ [D_{21}^{k,l}]^{op} & [D_{22}^{k,l}]^{op}\end{bmatrix}\begin{bmatrix}[B1_j^l]\\ [B2_j^l]\end{bmatrix}\{\Delta d_j^{l*}\}$$

$$+\sum_{k=0}^{L_c}\{\Delta d_i^{k*}\}^{\mathrm{T}}\begin{bmatrix}[B1_i^k]\\ [B2_i^k]\end{bmatrix}^{\mathrm{T}}\sum_{l=0}^{L_c}\begin{bmatrix}[D_{11}^{k,l}]^{po} & [D_{12}^{k,l}]^{po}\\ [D_{21}^{k,l}]^{po} & [D_{22}^{k,l}]^{po}\end{bmatrix}\begin{bmatrix}[B1_j^l]\\ [B2_j^l]\end{bmatrix}\{\Delta d_j^{l**}\}$$

$$+\sum_{k=0}^{L_c}\{\Delta d_i^{k**}\}^{\mathrm{T}}\begin{bmatrix}[B1_i^k]\\ [B2_i^k]\end{bmatrix}^{\mathrm{T}}\sum_{l=0}^{L_c}\begin{bmatrix}[D_{11}^{k,l}]^{o} & [D_{12}^{k,l}]^{o}\\ [D_{21}^{k,l}]^{o} & [D_{22}^{k,l}]^{o}\end{bmatrix}\begin{bmatrix}[B1_j^l]\\ [B2_j^l]\end{bmatrix}\{\Delta d_j^{l**}\}\ r\,\mathrm{d}area$$

(12.24)

where:

$[D^{k,l}]^p$, $[D^{k,l}]^{op}$, $[D^{k,l}]^{po}$ and $[D^{k,l}]^o$ are the $[D]$ matrices resulting from the $\mathrm{d}\theta$ integration that should be used to form the stiffness matrix relating the k^{th} harmonic coefficients of load with the l^{th} harmonic coefficients of displacement;

$[D^{k,l}]^p$ is the $[D]$ matrix that relates parallel loads to parallel displacements;

$[D^{k,l}]^{op}$ is the $[D]$ matrix that relates orthogonal loads to parallel displacements;

$[D^{k,l}]^{po}$ is the $[D]$ matrix that relates parallel loads to orthogonal displacements;

$[D^{k,l}]^o$ is the $[D]$ matrix that relates orthogonal loads to orthogonal displacements.

These $[D]$ matrices have been split into four parts representing $[D_{11}]$, $[D_{12}]$, $[D_{21}]$ and $[D_{22}]$ terms. The components of these matrices can be evaluated from the following equations:

$$[D^{k,l}]^p = \begin{bmatrix}[D_{11}^{k,l}]^p & [D_{12}^{k,l}]^p\\ [D_{21}^{k,l}]^p & [D_{22}^{k,l}]^p\end{bmatrix} = \begin{bmatrix}\alpha[\overline{\overline{D_{11}^{k-l}}}]+\beta[\overline{\overline{D_{11}^{k+l}}}] & \mp\alpha[\overline{\overline{D_{12}^{k-l}}}]+\beta[\overline{\overline{D_{12}^{k+l}}}]\\ \pm\alpha[\overline{\overline{D_{21}^{k-l}}}]+\beta[\overline{\overline{D_{21}^{k+l}}}] & \alpha[\overline{\overline{D_{22}^{k-l}}}]-\beta[\overline{\overline{D_{22}^{k+l}}}]\end{bmatrix}$$

$$[D^{k,l}]^o = \begin{bmatrix}[D_{11}^{k,l}]^o & [D_{12}^{k,l}]^o\\ [D_{21}^{k,l}]^o & [D_{22}^{k,l}]^o\end{bmatrix} = \begin{bmatrix}\alpha[\overline{\overline{D_{11}^{k-l}}}]-\beta[\overline{\overline{D_{11}^{k+l}}}] & \mp\alpha[\overline{\overline{D_{12}^{k-l}}}]-\beta[\overline{\overline{D_{12}^{k+l}}}]\\ \pm\alpha[\overline{\overline{D_{21}^{k-l}}}]-\beta[\overline{\overline{D_{21}^{k+l}}}] & \alpha[\overline{\overline{D_{22}^{k-l}}}]+\beta[\overline{\overline{D_{22}^{k+l}}}]\end{bmatrix}$$

$$[D^{k,l}]^{op} = \begin{bmatrix}[D_{11}^{k,l}]^{op} & [D_{12}^{k,l}]^{op}\\ [D_{21}^{k,l}]^{op} & [D_{22}^{k,l}]^{op}\end{bmatrix} = \begin{bmatrix}\pm\alpha[\overline{\overline{D_{11}^{k-l}}}]+\beta[\overline{\overline{D_{11}^{k+l}}}] & \alpha[\overline{\overline{D_{12}^{k-l}}}]-\beta[\overline{\overline{D_{12}^{k+l}}}]\\ -\alpha[\overline{\overline{D_{21}^{k-l}}}]-\beta[\overline{\overline{D_{21}^{k+l}}}] & \pm\alpha[\overline{\overline{D_{22}^{k-l}}}]-\beta[\overline{\overline{D_{22}^{k+l}}}]\end{bmatrix}$$

$$[D^{k,l}]^{po} = \begin{bmatrix}[D_{11}^{k,l}]^{po} & [D_{12}^{k,l}]^{po}\\ [D_{21}^{k,l}]^{po} & [D_{22}^{k,l}]^{po}\end{bmatrix} = \begin{bmatrix}\mp\alpha[\overline{\overline{D_{11}^{k-l}}}]+\beta[\overline{\overline{D_{11}^{k+l}}}] & -\alpha[\overline{\overline{D_{12}^{k-l}}}]-\beta[\overline{\overline{D_{12}^{k+l}}}]\\ \alpha[\overline{\overline{D_{21}^{k-l}}}]-\beta[\overline{\overline{D_{21}^{k+l}}}] & \mp\alpha[\overline{\overline{D_{22}^{k-l}}}]-\beta[\overline{\overline{D_{22}^{k+l}}}]\end{bmatrix}$$

(12.25)

where:

$\alpha = 1$ if $k = l$, $= \frac{1}{2}$ otherwise;

$\beta = 1$ if $k = l = 0$, $= \frac{1}{2}$ otherwise;

$\pm$ is $+$ if $k - l \geq 0$, is $-$ if $k - l < 1$;

$\mp$ is $-$ if $k - l \geq 0$, is $+$ if $k - l < 1$.

The nonlinear CFSAFEM stiffness matrix does not exhibit harmonic uncoupling, i.e. the zero terms in Equation (12.4) are now non-zero. This explains the important feature observed in nonlinear problems that solution displacements have harmonic terms with orders different from that of the applied loads. The harmonically coupled stiffness matrix from this formulation is very large and a large amount of computer resources, similar to that for a full 3D analysis, is

required to invert it. The use of the linear CFSAFEM formulation to solve strongly nonlinear problems also requires a large amount of computer resources, since the elastic $[\boldsymbol{D}]$ matrix used in the formulation is very different from the true $[\boldsymbol{D}^{ep}]$ matrix for the material, and a large amount of resources is required for the iterative correction process to account for this error. A compromise is to use the nonlinear formulation and omit the harmonically coupled terms, i.e. the $k \neq l$ terms in Equation (12.24), thus allowing the system equations for each harmonic order to be solved individually. The error associated with this omission is corrected using the nonlinear solution strategy in a similar manner to the error associated with the linear formulation. Since the correct elasto-plastic stiffness matrix is used to solve each set of harmonic system equations, the proposed partial nonlinear formulation is expected to require less computer resources for its correction process than the simple linear elastic formulation.

The nonlinear formulation is now able to yield a more rational criterion for the symmetrical uncoupling of the system equations. For symmetrical uncoupling to be valid the $[\boldsymbol{D}]^{ap}$ and $[\boldsymbol{D}]^{po}$ matrices must be zero. The four submatrices associated with each of these two matrices contain either only the 0th and cosine harmonics, or only sine harmonics. Thus the criterion the $[\boldsymbol{D}]$ matrix must satisfy for symmetrical uncoupling is that the $[\boldsymbol{D}_{11}]$ and $[\boldsymbol{D}_{22}]$ parts of the $[\boldsymbol{D}]$ matrix are symmetric functions of θ, and the $[\boldsymbol{D}_{12}]$ and $[\boldsymbol{D}_{21}]$ parts are asymmetric functions of θ. The resulting $[\boldsymbol{D}]^{ap}$ and $[\boldsymbol{D}]^{po}$ would then be zero. In a parallel symmetry analysis the stresses associated with the top part of the $[\boldsymbol{B}]$ matrix, $[\boldsymbol{B}1]$ (σ_r, σ_z, σ_θ and σ_{rz}), are symmetrical functions of θ, while the stresses associated with the bottom part, $[\boldsymbol{B}2]$ ($\sigma_{r\theta}$, $\sigma_{z\theta}$), are asymmetrical functions of θ. The strains satisfy the same symmetrical conditions. Thus a material can only be legitimately analysed using purely parallel symmetry terms if it satisfies the $[\boldsymbol{D}]$ matrix criterion while subjected to a stress and strain state associated with parallel symmetry. Similarly, for a purely orthogonal symmetry analysis the $[\boldsymbol{D}]$ matrix criterion must be satisfied for an orthogonal symmetry stress and strain state. An orthogonal symmetry stress and strain state exists when the stresses and strains associated with $[\boldsymbol{B}1]$ are asymmetrical functions and those associated with $[\boldsymbol{B}2]$ are symmetrical functions of θ.

The tangent stiffness solution strategy could be implemented using the full nonlinear CFSAFEM formulation, but the accuracy of the solution would be strongly influenced by both the size of the solution increment, as discussed in Chapter 9, and the number of harmonics used to represent the applied loads, the solution displacements and the $[\boldsymbol{D}]$ matrices.

It should be noted that the linear CFSAFEM formulation is a particular case of the nonlinear CFSAFEM where the $[\boldsymbol{D}]$ matrix does not vary with θ, i.e. only the 0th harmonic $[\boldsymbol{D}]$ matrix exists.

12.3.5 Formulation for interface elements

A formulation for zero thickness isoparametric interface elements for the CFSAFEM has been developed based on the 2D formulation of Day and Potts (1994), see Section 3.6. The coordinate system for the isoparametric six and four noded element is presented in Figure 12.3. The global displacements are defined in the same manner as for the solid elements, using u, v, and w displacement components. Local displacements for the interface elements have to be defined such that:

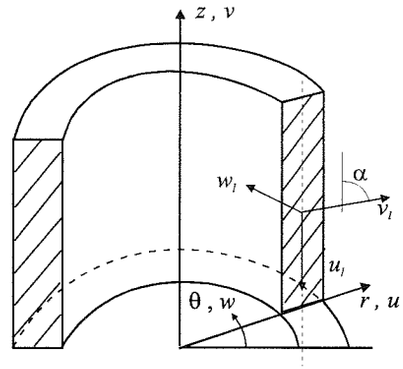

Figure 12.3: Coordinate system for interface elements

Δu_l is the incremental local tangential displacement in plane r-z;
Δv_l is the incremental local normal displacement in plane r-z;
Δw_l is the incremental local circumferential tangential displacement.

The relationship between incremental global and local displacements can be expressed in matrix form as:

$$\begin{Bmatrix} \Delta u_l \\ \Delta v_l \\ \Delta w_l \end{Bmatrix} = \begin{bmatrix} \cos\alpha & \sin\alpha & 0 \\ -\sin\alpha & \cos\alpha & 0 \\ 0 & 0 & 1 \end{bmatrix} \begin{Bmatrix} \Delta u \\ \Delta v \\ \Delta w \end{Bmatrix} \tag{12.26}$$

For any point on the interface there are 2 sets of displacements, top and bottom displacements, each set describing the displacement on one side of the interface, see Section 3.6. The incremental global displacements on each side of an interface element can be represented using isoparametric shape functions and a Fourier series in the θ direction, in a similar manner to the solid element formulation:

$$\Delta u = \sum_{i=1}^{n} N_i \left[\sum_{l=0}^{L} \left(\overline{U_i^l} \cos l\theta + \overline{\overline{U_i^l}} \sin l\theta \right) \right] \tag{12.27}$$

where:

N_i is the shape function of the i^{th} node defined in the element;
$\overline{U_i^l}$ is the l^{th} cosine harmonic coefficient of radial displacement at the i^{th} node;
$\overline{\overline{U_i^l}}$ is the l^{th} sine harmonic coefficient of radial displacement at the i^{th} node;
n is the number of nodes on each side of the interface;
L is the order of the harmonic series used to represent displacement.

The interface elements have three components of incremental strain:

$\Delta\gamma_p$ is the in plane shear strain;
$\Delta\varepsilon$ is the in plane normal strain;
$\Delta\gamma_\theta$ is the circumferential shear strain.

These can be related to the incremental global and local displacements as:

$$\begin{Bmatrix} \Delta\gamma_p \\ \Delta\varepsilon \\ \Delta\gamma_\theta \end{Bmatrix} = \begin{Bmatrix} \Delta u_l^{bot} - \Delta u_l^{top} \\ \Delta v_l^{bot} - \Delta v_l^{top} \\ \Delta w_l^{bot} - \Delta w_l^{top} \end{Bmatrix} = \begin{bmatrix} \cos\alpha & \sin\alpha & 0 \\ -\sin\alpha & \cos\alpha & 0 \\ 0 & 0 & 1 \end{bmatrix} \begin{Bmatrix} \Delta u^{bot} - \Delta u^{top} \\ \Delta v^{bot} - \Delta v^{top} \\ \Delta w^{bot} - \Delta w^{top} \end{Bmatrix} \tag{12.28}$$

Using Equation (12.27) for the incremental global displacements gives:

$$\begin{Bmatrix} \Delta\gamma_p \\ \Delta\varepsilon \\ \Delta\gamma_\theta \end{Bmatrix} = \sum_{i=1}^{2n} \begin{bmatrix} \mp\cos\alpha & \mp\sin\alpha & 0 \\ \pm\sin\alpha & \mp\cos\alpha & 0 \\ 0 & 0 & \mp 1 \end{bmatrix} \sum_{l=0}^{L} N_i \begin{Bmatrix} \overline{U_i^l}\cos l\theta + \overline{\overline{U_i^l}}\sin l\theta \\ \overline{V_i^l}\cos l\theta + \overline{\overline{V_i^l}}\sin l\theta \\ \overline{W_i^l}\cos l\theta + \overline{\overline{W_i^l}}\sin l\theta \end{Bmatrix} \tag{12.29}$$

where:

$\mp$ is $-$ for a top node and is $+$ for a bottom node;

$\pm$ is $+$ for a top node and is $-$ for a bottom node.

This can be written as:

$$\{\Delta\varepsilon\} = \sum_{i=1}^{2n} \sum_{l=0}^{L} \begin{bmatrix} [\boldsymbol{B}1_i]\cos l\theta \\ [\boldsymbol{B}2_i]\sin l\theta \end{bmatrix} \{\Delta \boldsymbol{d}_i^{l*}\} + \begin{bmatrix} [\boldsymbol{B}1_i]\sin l\theta \\ -[\boldsymbol{B}2_i]\cos l\theta \end{bmatrix} \{\Delta \boldsymbol{d}_i^{l**}\} \tag{12.30}$$

where:

$\{\Delta \boldsymbol{d}_i^{l*}\}$ and $\{\Delta \boldsymbol{d}_i^{l**}\}$ are respectively the parallel and orthogonal l^{th} order harmonic coefficients of incremental displacement for the i^{th} node;

$[\boldsymbol{B}1_i]$ is the top part of the strain matrix for the i^{th} node;

$[\boldsymbol{B}2_i]$ is the bottom part of the strain matrix for the i^{th} node, so that:

$$[\boldsymbol{B}1_i] = N_i \begin{bmatrix} \mp\cos\alpha & \mp\sin\alpha & 0 \\ \pm\sin\alpha & \mp\cos\alpha & 0 \end{bmatrix} \qquad [\boldsymbol{B}2_i] = N_i \begin{bmatrix} 0 & 0 & \mp 1 \end{bmatrix} \tag{12.31}$$

Similar to solid elements, the elasticity matrix $[\boldsymbol{D}]$ for the interface element can be split into four parts:

$$\begin{Bmatrix} \Delta\tau_p \\ \Delta\sigma \\ -- \\ \Delta\tau_\theta \end{Bmatrix} = \begin{bmatrix} [\boldsymbol{D}_{11}] & \| & [\boldsymbol{D}_{12}] \\ -- & -- & -- \\ [\boldsymbol{D}_{21}] & \| & [\boldsymbol{D}_{22}] \end{bmatrix} \begin{Bmatrix} \Delta\gamma_p \\ \Delta\varepsilon \\ -- \\ \Delta\gamma_\theta \end{Bmatrix} \tag{12.32}$$

where:

$\Delta\tau_p$ is the incremental in plane shear stress;

$\Delta\sigma$ is the incremental in plane normal stress;

$\Delta\tau_\theta$ is the incremental circumferential shear stress.

The interface element stresses and strains have been formulated in such a manner that the resulting equation for the internal incremental work has the same form as that for the solid element:

$$\Delta W = \int_{-\pi}^{\pi} \sum_{i=1}^{2n} \left[\sum_{k=0}^{L} \begin{bmatrix} [\boldsymbol{B}1_i]\cos k\theta \\ [\boldsymbol{B}2_i]\sin k\theta \end{bmatrix} \{\Delta \boldsymbol{d}_i^{k*}\} + \begin{bmatrix} [\boldsymbol{B}1_i]\sin k\theta \\ -[\boldsymbol{B}2_i]\cos k\theta \end{bmatrix} \{\Delta \boldsymbol{d}_i^{k**}\} \right]^T [\boldsymbol{D}] \sum_{j=1}^{2n} \left[\sum_{l=0}^{L} \begin{bmatrix} [\boldsymbol{B}1_j]\cos l\theta \\ [\boldsymbol{B}2_j]\sin l\theta \end{bmatrix} \{\Delta \boldsymbol{d}_j^{l*}\} + \begin{bmatrix} [\boldsymbol{B}1_j]\sin l\theta \\ -[\boldsymbol{B}2_j]\cos l\theta \end{bmatrix} \{\Delta \boldsymbol{d}_j^{l**}\} \right] r\,d\theta\,d\text{area} \tag{12.33}$$

This can be simplified to give:

$$\begin{aligned} \Delta W = \; & \pi \int \sum_{i=1,j=1}^{n} \sum^{n} \; 2\{\Delta \boldsymbol{d}_i^{0*}\}^T [\boldsymbol{B}1_i]^T [\boldsymbol{D}_{11}] [\boldsymbol{B}1_j] \{\Delta \boldsymbol{d}_j^{0*}\} + 2\{\Delta \boldsymbol{d}_i^{0**}\}^T [\boldsymbol{B}2_i]^T [\boldsymbol{D}_{22}] [\boldsymbol{B}2_j] \{\Delta \boldsymbol{d}_j^{0**}\} + \\ & \sum_{l=1}^{L} \{\Delta \boldsymbol{d}_i^{l*}\}^T [\boldsymbol{B}1_i]^T [\boldsymbol{D}_{11}] [\boldsymbol{B}1_j] \{\Delta \boldsymbol{d}_j^{l*}\} + \{\Delta \boldsymbol{d}_i^{l*}\}^T [\boldsymbol{B}2_i]^T [\boldsymbol{D}_{22}] [\boldsymbol{B}2_j] \{\Delta \boldsymbol{d}_j^{l*}\} + \\ & \{\Delta \boldsymbol{d}_i^{l**}\}^T [\boldsymbol{B}1_i]^T [\boldsymbol{D}_{11}] [\boldsymbol{B}1_j] \{\Delta \boldsymbol{d}_j^{l**}\} + \{\Delta \boldsymbol{d}_i^{l**}\}^T [\boldsymbol{B}2_i]^T [\boldsymbol{D}_{22}] [\boldsymbol{B}2_j] \{\Delta \boldsymbol{d}_j^{l**}\} \; r\,d\text{area} \\ & + \\ & \pi \int \sum_{i=1,j=1}^{n} \sum^{n} -2\{\Delta \boldsymbol{d}_i^{0*}\}^T [\boldsymbol{B}1_i]^T [\boldsymbol{D}_{12}] [\boldsymbol{B}2_j] \{\Delta \boldsymbol{d}_j^{0**}\} - 2\{\Delta \boldsymbol{d}_i^{0**}\}^T [\boldsymbol{B}2_i]^T [\boldsymbol{D}_{21}] [\boldsymbol{B}1_j] \{\Delta \boldsymbol{d}_j^{0*}\} + \\ & \sum_{l=1}^{L} -\{\Delta \boldsymbol{d}_i^{l*}\}^T [\boldsymbol{B}1_i]^T [\boldsymbol{D}_{12}] [\boldsymbol{B}2_j] \{\Delta \boldsymbol{d}_j^{l**}\} + \{\Delta \boldsymbol{d}_i^{l**}\}^T [\boldsymbol{B}2_i]^T [\boldsymbol{D}_{21}] [\boldsymbol{B}1_j] \{\Delta \boldsymbol{d}_j^{l**}\} + \\ & \{\Delta \boldsymbol{d}_i^{l**}\}^T [\boldsymbol{B}1_i]^T [\boldsymbol{D}_{12}] [\boldsymbol{B}2_j] \{\Delta \boldsymbol{d}_j^{l*}\} - \{\Delta \boldsymbol{d}_i^{l**}\}^T [\boldsymbol{B}2_i]^T [\boldsymbol{D}_{21}] [\boldsymbol{B}1_j] \{\Delta \boldsymbol{d}_j^{l*}\} \; r\,d\text{area} \end{aligned} \tag{12.34}$$

Since both interface and solid element equations are harmonically uncoupled, the system equations for each harmonic of a problem domain can be solved independently, even if it consists of both types of elements. Similarly, if the $[\boldsymbol{D}_{12}]$ and $[\boldsymbol{D}_{21}]$ terms in both solid and interface elements are zero, symmetrical uncoupling is also valid.

The linear elastic interface element formulation can be extended for nonlinear behaviour using the same approach as for the solid element. The $[\boldsymbol{D}]$ matrix is represented using a Fourier series and the equation for virtual work now yields a harmonically coupled set of system equations. The $[\boldsymbol{D}]$ matrix pertinent for each harmonic combination of equations is the same as those presented in Section 12.3.4 for the solid elements.

12.3.6 Bulk pore fluid compressibility

Saturated clays are two phase materials consisting of a compressible solid phase, the soil skeleton, and a highly incompressible fluid phase - the pore water. Undrained behaviour is assumed if these clays are loaded quickly, such that there is little dissipation of excess pore water pressure. This type of behaviour can be modelled in a conventional finite element analysis by specifying a bulk pore fluid compressibility, see Section 3.4. This formulation is now extended for use in CFSAFEM analyses.

For linear elastic material behaviour the principle of effective stress gives, see Equations (3.2) and (3.5):

$$\{\Delta\sigma\} = [\boldsymbol{D}]\{\Delta\varepsilon\} + [\boldsymbol{D}_f]\{\Delta\varepsilon\} \tag{12.35}$$

Noting Equation (3.6), the second term in the above equation can be written as:

$$[\boldsymbol{D}_f]\{\Delta\varepsilon\} = \{\eta\}\ K_e\ \Delta\varepsilon_v \tag{12.36}$$

where $\{\eta\}^{\mathrm{T}}=\{1\ 1\ 1\ 0\ 0\ 0\}$, K_e is the equivalent bulk modulus of the pore fluid and $\Delta\varepsilon_v$ is the incremental volumetric strain. Combining Equations (12.35) and (12.36) gives:

$$\{\Delta\sigma\} = [\boldsymbol{D}]\{\Delta\varepsilon\} + \{\eta\}\ K_e\ \Delta\varepsilon_v \tag{12.37}$$

Accordingly, the incremental internal work done, ΔW, can be expressed as:

$$\Delta W = \int \{\Delta\varepsilon\}^{\mathrm{T}}\{\Delta\sigma\}\ dVol = \int \{\Delta\varepsilon\}^{\mathrm{T}}[\boldsymbol{D}]\{\varepsilon\}\ dVol + \int \{\Delta\varepsilon\}^{\mathrm{T}}\{\eta\}K_e\ \Delta\varepsilon_v\ dVol \tag{12.38}$$

The first integral is the work done by the soil skeleton, which was calculated in Sections 12.3.1 and 12.3.4. Therefore only the second integral, the work done by the pore fluid, ΔW_f, has to be evaluated.

Using Equation (12.8), $\Delta\varepsilon_v$ can be expressed as:

$$\Delta\varepsilon_v = \sum_{i=1}^{n}\sum_{l=0}^{L} \{\eta 1\}^{\mathrm{T}}\ [\boldsymbol{B}1_i^l](\cos l\theta\ \{\Delta\boldsymbol{d}_i^{l*}\} + \sin l\theta\ \{\Delta\boldsymbol{d}_i^{l**}\}) \tag{12.39}$$

where $\{\eta 1\}^{\mathrm{T}} = (1, 1, 1, 0)$. From here ΔW_f can be written as:

$$\begin{aligned}\Delta W_f = \int_{-\pi}^{\pi}\sum_{i=1}^{n}\sum_{l=0}^{L} (\cos l\theta\ \{\Delta\boldsymbol{d}_i^{l*}\} + \sin l\theta\ \{\Delta\boldsymbol{d}_i^{l**}\})^{\mathrm{T}}[\boldsymbol{B}1_i^l]^{\mathrm{T}}\{\eta 1\}\ K_e \cdot \\ \sum_{j=1}^{n}\sum_{k=0}^{L} \{\eta 1\}^{\mathrm{T}}[\boldsymbol{B}1_j^k]\ (\cos k\theta\ \{\Delta\boldsymbol{d}_j^{k*}\} + \sin k\theta\ \{\Delta\boldsymbol{d}_j^{k**}\})\ r\ \mathrm{d}\theta\ darea\end{aligned} \tag{12.40}$$

Carrying out the $\mathrm{d}\theta$ integral gives:

$$\begin{aligned}\Delta W_f = \sum_{i=1}^{n}\sum_{j=1}^{n} \int 2\pi\{\Delta\boldsymbol{d}_i^{0*}\}^{\mathrm{T}}[\boldsymbol{B}1_i^0]^{\mathrm{T}}\{\eta 1\}\ K_e\ \{\eta 1\}^{\mathrm{T}}[\boldsymbol{B}1_j^0]\{\Delta\boldsymbol{d}_j^{0*}\} + \\ \pi\sum_{l=1}^{L} \Big(\{\Delta\boldsymbol{d}_i^{l*}\}^{\mathrm{T}}[\boldsymbol{B}1_i^l]^{\mathrm{T}}\{\eta 1\}\ K_e\ \{\eta 1\}^{\mathrm{T}}[\boldsymbol{B}1_j^l]\{\Delta\boldsymbol{d}_j^{l*}\} + \\ \{\Delta\boldsymbol{d}_i^{l**}\}^{\mathrm{T}}[\boldsymbol{B}1_i^l]^{\mathrm{T}}\{\eta 1\}\ K_e\ \{\eta 1\}^{\mathrm{T}}[\boldsymbol{B}1_j^l]\{\Delta\boldsymbol{d}_j^{l**}\}\Big)\ r\ darea\end{aligned} \tag{12.41}$$

This equation gives the contributions to the global stiffness matrix associated with the pore fluid compressibility. The system equations are obtained by adding these fluid compressibility terms to the terms associated with the soil skeleton stiffness calculated in Sections 12.3.1 and 12.3.4. The fluid compressibility terms are both harmonically and symmetrically uncoupled and their contributions to the parallel and orthogonal symmetry stiffness matrices are the same. For the l^{th} harmonic it is:

$$\sum_{i=1}^{n}\sum_{j=1}^{n} \int [\boldsymbol{B}1_i^l]^{\mathrm{T}}\{\eta 1\}\ K_e\ \{\eta 1\}^{\mathrm{T}}[\boldsymbol{B}1_j^l]\ r\ darea \tag{12.42}$$

In the above constant K_e formulation, the pore fluid pressure is a symmetrical function in a parallel analysis and an asymmetrical function in an orthogonal analysis.

In an undrained material K_e is prescribed a very large value, such that the volumetric strains are inhibited, see Section 3.4. There are two options for defining K_e: to assign it a constant value, or to define it as a multiple of the bulk stiffness of the soil skeleton. In the former option care must be taken in assigning the value of K_e. It must be large enough to inhibit volumetric strains, but small enough to avoid ill conditioning problems associated with a very large number in the stiffness matrix. Finding a suitable value for K_e is particularly difficult when the bulk modulus of the soil skeleton changes significantly during the course of an analysis. Accordingly, the option for defining K_e as a multiple of the bulk modulus of the soil skeleton is preferred, because these difficulties are avoided. A typical value for K_e is one hundred to one thousand times the bulk stiffness of the soil skeleton.

However, considering the Fourier series formulation, K_e could now vary in the θ direction and would have to be expressed as a Fourier series:

$$K_e = K_e^0 + \sum_{l=1}^{M} \overline{K_e^l}\cos l\theta + \overline{\overline{K_e^l}}\sin l\theta \tag{12.43}$$

where:

K_e^0, $\overline{K_e^l}$ and $\overline{\overline{K_e^l}}$ are the 0^{th}, l^{th} order cosine and l^{th} order sine harmonic coefficients of K_e;

M is the number of harmonics used to represent K_e and need not be the same as the number used to represent displacements, L.

Substituting this into the equation for ΔW_f gives:

$$\begin{aligned}\Delta W_f = \int_{-\pi}^{\pi}\sum_{i=1}^{n}\sum_{l=0}^{L} (\cos l\theta\ \{\Delta\boldsymbol{d}_i^{l*}\} + \sin l\theta\ \{\Delta\boldsymbol{d}_i^{l**}\})[\boldsymbol{B}1_i^l]^{\mathrm{T}}\{\eta 1\} \cdot \\ (K_e^0 + \sum_{l=1}^{M} \overline{K_e^l}\cos l\theta + \overline{\overline{K_e^l}}\sin l\theta) \cdot \\ \sum_{j=1}^{n}\sum_{k=0}^{L} \{\eta 1\}^{\mathrm{T}}[\boldsymbol{B}1_j^k]\ (\cos k\theta\ \{\Delta\boldsymbol{d}_j^{k*}\} + \sin k\theta\ \{\Delta\boldsymbol{d}_j^{k**}\})\ r\ \mathrm{d}\theta\ darea\end{aligned} \tag{12.44}$$

The $\mathrm{d}\theta$ integral is carried using the solutions for a triple Fourier series, as shown in Appendix XII.5. From there:

$$\begin{aligned}\Delta W_f = \sum_{i=1}^{n}\sum_{j=1}^{n} \int \sum_{l=0}^{L} \{\Delta\boldsymbol{d}_i^{l*}\}^{\mathrm{T}}[\boldsymbol{B}1_i^l]^{\mathrm{T}}\{\eta 1\} \sum_{k=0}^{L} (\alpha\overline{K_e^{l-k}} + \beta\overline{K_e^{l+k}})\ \{\eta 1\}^{\mathrm{T}}[\boldsymbol{B}1_j^k]\ \{\boldsymbol{d}_j^{k*}\} \\ + \sum_{l=0}^{L} \{\Delta\boldsymbol{d}_i^{l**}\}^{\mathrm{T}}[\boldsymbol{B}1_i^l]^{\mathrm{T}}\{\eta 1\} \sum_{k=0}^{L} (\alpha\overline{K_e^{l-k}} - \beta\overline{K_e^{l+k}})\ \{\eta 1\}^{\mathrm{T}}[\boldsymbol{B}1_j^k]\ \{\boldsymbol{d}_j^{k**}\} \\ + \sum_{l=0}^{L} \{\Delta\boldsymbol{d}_i^{l**}\}^{\mathrm{T}}[\boldsymbol{B}1_i^l]^{\mathrm{T}}\{\eta 1\} \sum_{k=0}^{L} (\pm\alpha\overline{\overline{K_e^{l-k}}} + \beta\overline{\overline{K_e^{l+k}}})\ \{\eta 1\}^{\mathrm{T}}[\boldsymbol{B}1_j^k]\ \{\boldsymbol{d}_j^{k*}\} \\ + \sum_{l=0}^{L} \{\Delta\boldsymbol{d}_i^{l*}\}^{\mathrm{T}}[\boldsymbol{B}1_i^l]^{\mathrm{T}}\{\eta 1\} \sum_{k=0}^{L} (\mp\alpha\overline{\overline{K_e^{l-k}}} + \beta\overline{\overline{K_e^{l+k}}})\ \{\eta 1\}^{\mathrm{T}}[\boldsymbol{B}1_j^k]\ \{\boldsymbol{d}_j^{k**}\}\ r\ darea\end{aligned} \tag{12.45}$$

where:

$\alpha = 1$ if $k = l$, $= \frac{1}{2}$ otherwise;
$\beta = 1$ if $k = l = 0$, $= \frac{1}{2}$ otherwise;
$\pm$ is + if $l - k \geq 0$, is − if $l - k < 1$;
$\mp$ is − if $l - k \geq 0$, is + if $l - k < 1$.

In general, there is neither harmonic nor symmetric uncoupling. The criterion for symmetric uncoupling is that K_e is a symmetrical function.

12.3.7 Formulation for coupled consolidation

The behaviour of saturated soils under any loading condition is strongly influenced by the rate at which the generated pore pressures are able to dissipate within the soil mass. As noted in Chapter 3, the conventional finite element theory, described in Chapter 2, can deal with either drained soil behaviour, where full pore fluid pressure dissipation occurs, or undrained behaviour where no dissipation occurs. The latter behaviour is achieved by introducing the effective bulk compressibility of the pore fluid, as described in Section 3.4. Accounting for such behaviour in the CFSAFEM was described in the previous section (i.e. Section 12.3.6). Often soil behaviour cannot be simplified to being either fully drained or undrained, for example when partial drainage occurs during a loading stage, followed by long term consolidation. To account for such behaviour the equations governing the flow of pore fluid and the mechanical behaviour of the soil must be combined. The finite element theory behind such a coupled approach was presented in Chapter 10. In this section this theory is extended for use with the CFSAFEM. Initially, only soil with a constant permeability is considered, but subsequently the theory is extended to account for soils which have variable permeability.

The pore fluid pressures in the problem domain are described by the element pore fluid shape functions and the Fourier series of the nodal pore fluid pressures of the element:

$$p_f = \sum_{i=1}^{m} N_{pi} \left(\sum_{l=0}^{L_c} \overline{p_{fi}^l} \cos l\theta + \overline{\overline{p_{fi}^l}} \sin l\theta \right) \tag{12.46}$$

where:

N_{pi} is the element pore fluid shape function for the i^{th} node;

$\overline{p_{fi}^l}$ and $\overline{\overline{p_{fi}^l}}$ are respectively the l^{th} cosine and sine coefficients of pore fluid pressure for the i^{th} node;

m is the number of pore fluid pressure nodes in the element which is not necessarily equal to the number of displacement nodes in the element, n.

The hydraulic gradient, $\{\nabla \boldsymbol{h}\}$, can be defined as:

$$\{\nabla \boldsymbol{h}\} = \frac{1}{\gamma_f}\{\nabla \boldsymbol{p}_f\} + \{\boldsymbol{i}_G\} = \frac{1}{\gamma_f}\begin{Bmatrix} \frac{\partial p_f}{\partial r} \\ \frac{\partial p_f}{\partial z} \\ \frac{\partial p_f}{r\partial \theta} \end{Bmatrix} + \{\boldsymbol{i}_G\} = \frac{1}{\gamma_f}\sum_{i=1}^{m}\sum_{l=0}^{L_c} \begin{Bmatrix} \frac{\partial N_{pi}}{\partial r}\cos l\theta \\ \frac{\partial N_{pi}}{\partial z}\cos l\theta \\ \frac{-lN_{pi}}{r}\sin l\theta \end{Bmatrix} \overline{p_{fi}^l} + \begin{Bmatrix} \frac{\partial N_{pi}}{\partial r}\sin l\theta \\ \frac{\partial N_{pi}}{\partial z}\sin l\theta \\ \frac{lN_{pi}}{r}\cos l\theta \end{Bmatrix} \overline{\overline{p_{fi}^l}} + \{\boldsymbol{i}_G\}$$

$$= \frac{1}{\gamma_f}\sum_{i=1}^{m}\sum_{l=0}^{L_c} \begin{bmatrix} [\boldsymbol{E}1_i^l]\cos l\theta \\ -[\boldsymbol{E}2_i^l]\sin l\theta \end{bmatrix} \overline{p_{fi}^l} + \begin{bmatrix} [\boldsymbol{E}1_i^l]\sin l\theta \\ [\boldsymbol{E}2_i^l]\cos l\theta \end{bmatrix} \overline{\overline{p_{fi}^l}} + \{\boldsymbol{i}_G\} \tag{12.47}$$

where:

γ_f is the bulk unit weight of the pore fluid;

$\{\boldsymbol{i}_G\}$ is the vector parallel to gravity, where

$$\{\boldsymbol{i}_G\} = \begin{Bmatrix} \frac{\partial h}{\partial r} \\ \frac{\partial h}{\partial z} \\ \frac{\partial h}{\partial \theta} \end{Bmatrix} = \begin{Bmatrix} \{\boldsymbol{i}_{G1}\} \\ \{\boldsymbol{i}_{G2}\} \end{Bmatrix}, \quad \{\boldsymbol{i}_{G1}\} = \begin{Bmatrix} \frac{\partial h}{\partial r} \\ \frac{\partial h}{\partial z} \end{Bmatrix} \text{ and } \{\boldsymbol{i}_{G2}\} = \begin{Bmatrix} \frac{\partial h}{\partial \theta} \end{Bmatrix}$$

$$[\boldsymbol{E}1_i^l] = \begin{Bmatrix} \frac{\partial N_{pi}}{\partial r} & \frac{\partial N_{pi}}{\partial z} \end{Bmatrix}^{\mathrm{T}} \text{ and } [\boldsymbol{E}2_i^l] = \begin{bmatrix} \frac{lN_{pi}}{r} \end{bmatrix}$$

The incremental volumetric strain at any point is defined as:

$$\Delta\varepsilon_v = \{\boldsymbol{\eta}\}^{\mathrm{T}}\{\Delta\boldsymbol{\varepsilon}\} \tag{12.48}$$

The incremental strain vector $\{\Delta\boldsymbol{\varepsilon}\}$ can be expressed in terms of the Fourier series coefficients of incremental displacement as in Equation (12.8):

$$\{\Delta\boldsymbol{\varepsilon}\} = \sum_{i=1}^{n}\sum_{l=0}^{L_c} \begin{bmatrix} [\boldsymbol{B}1_i^l]\cos l\theta \\ [\boldsymbol{B}2_i^l]\sin l\theta \end{bmatrix} \{\Delta\boldsymbol{d}_i^{l*}\} + \begin{bmatrix} [\boldsymbol{B}1_i^l]\sin l\theta \\ -[\boldsymbol{B}2_i^l]\cos l\theta \end{bmatrix} \{\Delta\boldsymbol{d}_i^{l**}\} \tag{12.49}$$

Thus the incremental volumetric strain can be expressed as:

$$\Delta\varepsilon_v = \sum_{i=1}^{n}\sum_{l=0}^{L_c} \{\boldsymbol{\eta}1\}^{\mathrm{T}}[\boldsymbol{B}1_i^l]\left(\cos l\theta\ \{\Delta\boldsymbol{d}_i^{l*}\} + \sin l\theta\ \{\Delta\boldsymbol{d}_i^{l**}\}\right) \tag{12.50}$$

The two governing equations are the equilibrium equation:

$$\int \{\Delta\boldsymbol{\varepsilon}\}^{\mathrm{T}}\{\Delta\boldsymbol{\sigma}\}\, \mathrm{d}Vol + \int \Delta\varepsilon_v\ \Delta p_f\, \mathrm{d}Vol = \textit{external work done} \tag{12.51}$$

and the continuity equation:

$$\int \Delta p_f \frac{\partial(\Delta\varepsilon_v)}{\partial t}\mathrm{d}Vol - \int \nabla(\Delta p_f)^{\mathrm{T}}\,[\boldsymbol{k}]\,\{\nabla\boldsymbol{h}\}\,\mathrm{d}Vol = Q\,(\Delta p_f) \tag{12.52}$$

where $[\boldsymbol{k}]$ is the matrix of permeabilities and Q represents any sources and/or sinks, see Chapter 10. Q is expressed as a Fourier series and the parallel and orthogonal components are $Q^{l*} = \overline{Q^l}$ and $Q^{l**} = \overline{\overline{Q^l}}$ respectively.

The first integral in Equation (12.51) is the same as that for the incremental internal work done by a solid element without consolidation, see Equation (12.38). The second integral can be expressed in terms of the incremental nodal pore fluid pressure and displacement Fourier series:

$$\int \Delta\varepsilon_v\ \Delta p_f\, \mathrm{d}Vol = \int_{-\pi}^{\pi}\sum_{i=1}^{n}\sum_{l=0}^{L_c} \left(\cos l\theta\ \{\Delta\boldsymbol{d}_i^{l*}\} + \sin l\theta\ \{\Delta\boldsymbol{d}_i^{l**}\}\right)^{\mathrm{T}}[\boldsymbol{B}1_i^l]^{\mathrm{T}}\{\boldsymbol{\eta}1\} \cdot \sum_{j=1}^{m} N_{pj}\left(\sum_{k=0}^{L_c} \Delta\overline{p_{fj}^k}\cos k\theta + \Delta\overline{\overline{p_{fj}^k}}\sin k\theta\right) r\,\mathrm{d}\theta\,\mathrm{d}area \tag{12.53}$$

where:

$$\Delta p_f = \sum_{i=1}^{m} N_{pi} \left(\sum_{l=0}^{L} \Delta \overline{p_{fi}^{l}} \cos l\theta + \Delta \overline{\overline{p_{fi}^{l}}} \sin l\theta \right)$$

and $\Delta \overline{p_{fi}^{l}}$ and $\Delta \overline{\overline{p_{fi}^{l}}}$ are respectively the l^{th} cosine and sine coefficients of incremental pore fluid pressures for the i^{th} node.

Carrying out the $d\theta$ integral and using the orthogonal properties of Fourier series gives:

$$\begin{aligned}
&\int \Delta\varepsilon_v \, \Delta p_f \, dVol \\
&= \pi \int \sum_{i=1}^{n} \sum_{j=1}^{m} 2\{\Delta \boldsymbol{d}_i^{0*}\}^{\mathrm{T}} [\boldsymbol{B}1_i^0]^{\mathrm{T}} \{\boldsymbol{\eta}1\} \, N_{pj} \, \Delta p_{fj}^{0} + \sum_{l=1}^{L} \{\Delta \boldsymbol{d}_i^{l*}\}^{\mathrm{T}} [\boldsymbol{B}1_i^l]^{\mathrm{T}} \{\boldsymbol{\eta}1\} \, N_{pj} \, \Delta \overline{p_{fi}^{l}} \\
&+ \{\Delta \boldsymbol{d}_i^{l**}\}^{\mathrm{T}} [\boldsymbol{B}1_i^l]^{\mathrm{T}} \{\boldsymbol{\eta}1\} \, N_{pj} \, \Delta \overline{\overline{p_{fi}^{l}}} \; r \, darea \\
&= \sum_{i=1}^{n} \sum_{j=1}^{m} \{\Delta \boldsymbol{d}_i^{0*}\}^{\mathrm{T}} [\boldsymbol{L}_{ij}^0]^{\mathrm{T}} \Delta p_{fj}^{0} + \sum_{l=1}^{L} \{\Delta \boldsymbol{d}_i^{l*}\}^{\mathrm{T}} [\boldsymbol{L}_{ij}^l]^{\mathrm{T}} \Delta \overline{p_{fj}^{l}} + \{\Delta \boldsymbol{d}_i^{l**}\}^{\mathrm{T}} [\boldsymbol{L}_{ij}^l]^{\mathrm{T}} \Delta \overline{\overline{p_{fj}^{l}}}
\end{aligned} \tag{12.54}$$

where $[\boldsymbol{L}_{ij}^l]^{\mathrm{T}} = 2\pi \int r \, [\boldsymbol{B}1_i^l]^{\mathrm{T}} \{\boldsymbol{\eta}1\} \, N_{pj} \, darea$ if $l = 0$; $= \pi \int r \, [\boldsymbol{B}1_i^l]^{\mathrm{T}} \{\boldsymbol{\eta}1\} \, N_{pj} \, darea$ otherwise.

This equation gives the terms that relate the applied incremental loads to the incremental pore fluid pressures. These equations are both symmetrically and harmonically uncoupled. The cosine harmonic coefficients of incremental pore fluid pressure are only associated with the parallel loads, hence they are called the parallel components of incremental pore fluid pressure. Similarly, the sine coefficients are the orthogonal components of incremental pore fluid pressure:

$$\Delta \overline{p_f^l} = \Delta p_f^{l*} \text{ and } \Delta \overline{\overline{p_f^l}} = \Delta p_f^{l**} \tag{12.55}$$

The first integral in Equation (12.52) can be treated in a similar manner to obtain the equation:

$$\begin{aligned}
\int \Delta p_f \, \Delta\varepsilon_v \, dVol = &\sum_{i=1}^{n} \sum_{j=1}^{m} (\Delta p_{fj}^{0*})^{\mathrm{T}} [\boldsymbol{L}_{ij}^0] \{\Delta \boldsymbol{d}_i^{0*}\} + \\
&\sum_{l=1}^{L} (\Delta p_{fj}^{l*})^{\mathrm{T}} [\boldsymbol{L}_{ij}^l] \{\Delta \boldsymbol{d}_i^{l*}\} + (\Delta p_{fj}^{l**})^{\mathrm{T}} [\boldsymbol{L}_{ij}^l] \{\Delta \boldsymbol{d}_i^{l**}\}
\end{aligned} \tag{12.56}$$

The second integral in Equation (12.52) can be rewritten as:

$$\begin{aligned}
&\int \nabla(\Delta p_f)^{\mathrm{T}} \, [\boldsymbol{k}] \, \{\nabla \boldsymbol{h}\} \, dVol = \\
&\int_{-\pi}^{\pi} \left\{ \sum_{i=1}^{m} \sum_{l=0}^{L} (\Delta p_{fi}^{l*})^{\mathrm{T}} \begin{bmatrix} [\boldsymbol{E}1_i^l] \cos l\theta \\ -[\boldsymbol{E}2_i^l] \sin l\theta \end{bmatrix}^{\mathrm{T}} + (\Delta p_{fi}^{l**})^{\mathrm{T}} \begin{bmatrix} [\boldsymbol{E}1_i^l] \sin l\theta \\ [\boldsymbol{E}2_i^l] \cos l\theta \end{bmatrix}^{\mathrm{T}} \right\} \cdot [\boldsymbol{k}] \cdot \\
&\left\{ \frac{1}{\gamma_f} \sum_{j=1}^{m} \sum_{k=0}^{L} \begin{bmatrix} [\boldsymbol{E}1_j^k] \cos k\theta \\ -[\boldsymbol{E}2_j^k] \sin k\theta \end{bmatrix} \Delta p_{fj}^{k*} + \begin{bmatrix} [\boldsymbol{E}1_j^k] \sin k\theta \\ [\boldsymbol{E}2_j^k] \cos k\theta \end{bmatrix} \Delta p_{fj}^{k**} + \{\boldsymbol{i}_G\} \right\} r \, d\theta \, darea
\end{aligned} \tag{12.57}$$

The $[\boldsymbol{k}]$ matrix is split into four parts in accordance with the two parts of the $[\boldsymbol{E}]$ matrix and the $d\theta$ integral is carried out. The hydraulic gradient has been divided into to two parts, consisting of the pore fluid pressure and gravity components. Accordingly, Equation (12.57) can be written in two parts:

$$\begin{aligned}
\int \nabla(\Delta p_f)^{\mathrm{T}} \, [\boldsymbol{k}] \, \nabla \boldsymbol{p}_f \, dVol \quad &= \frac{\pi}{\gamma_f} \int \sum_{i=1}^{m} \sum_{j=1}^{m} 2(\Delta p_{fi}^{0*})^{\mathrm{T}} [\boldsymbol{E}1_i^0]^{\mathrm{T}} [\boldsymbol{k}_{11}] [\boldsymbol{E}1_j^0] p_{fj}^{0*} + \\
\sum_{l=1}^{L} (\Delta p_{fi}^{l*})^{\mathrm{T}} [\boldsymbol{E}1_i^l]^{\mathrm{T}} [\boldsymbol{k}_{11}] [\boldsymbol{E}1_j^l] p_{fj}^{l*} \quad &+ \quad (\Delta p_{fi}^{l*})^{\mathrm{T}} [\boldsymbol{E}2_i^l]^{\mathrm{T}} [\boldsymbol{k}_{22}] [\boldsymbol{E}2_j^l] p_{fj}^{l*} + \\
(\Delta p_{fi}^{l**})^{\mathrm{T}} [\boldsymbol{E}1_i^l]^{\mathrm{T}} [\boldsymbol{k}_{11}] [\boldsymbol{E}1_j^l] p_{fj}^{l**} \quad &+ \quad (\Delta p_{fi}^{l**})^{\mathrm{T}} [\boldsymbol{E}2_i^l]^{\mathrm{T}} [\boldsymbol{k}_{22}] [\boldsymbol{E}2_j^l] p_{fj}^{l**} \; r \, darea \\
\text{----------} \quad &+ \quad \text{----------} \\
\frac{\pi}{\gamma_f} \int \sum_{i=1}^{m} \sum_{j=1}^{m} \sum_{l=1}^{L} (\Delta p_{fi}^{l*})^{\mathrm{T}} [\boldsymbol{E}1_i^l]^{\mathrm{T}} [\boldsymbol{k}_{12}] [\boldsymbol{E}2_j^l] p_{fj}^{l**} \quad &- \quad (\Delta p_{fi}^{l*})^{\mathrm{T}} [\boldsymbol{E}2_i^l]^{\mathrm{T}} [\boldsymbol{k}_{21}] [\boldsymbol{E}1_j^l] p_{fj}^{l**} - \\
(\Delta p_{fi}^{l**})^{\mathrm{T}} [\boldsymbol{E}1_i^l]^{\mathrm{T}} [\boldsymbol{k}_{12}] [\boldsymbol{E}2_j^l] p_{fj}^{l*} \quad &+ \quad (\Delta p_{fi}^{l**})^{\mathrm{T}} [\boldsymbol{E}2_i^l]^{\mathrm{T}} [\boldsymbol{k}_{21}] [\boldsymbol{E}1_j^l] p_{fj}^{l*} \; r \, darea
\end{aligned} \tag{12.58}$$

and

$$\begin{aligned}
\int \nabla(\Delta p_f)^{\mathrm{T}} [\boldsymbol{k}] \{\boldsymbol{i}_G\} \, dVol &= 2\pi \int \sum_{i=1}^{m} (\Delta p_{fi}^{0*})^{\mathrm{T}} [\boldsymbol{E}1_i^0]^{\mathrm{T}} \left([\boldsymbol{k}_{11}] \{\boldsymbol{i}_{G1}\} + [\boldsymbol{k}_{12}] \{\boldsymbol{i}_{G2}\} \right) r \, darea \\
&= \sum_{i=1}^{m} (\Delta p_{fi}^{0*})^{\mathrm{T}} \{\boldsymbol{n}_i\}
\end{aligned} \tag{12.59}$$

where $\{\boldsymbol{n}_i\} = 2\pi \int [\boldsymbol{E}1_i^0]^{\mathrm{T}} ([\boldsymbol{k}_{11}] \{\boldsymbol{i}_{G1}\} + [\boldsymbol{k}_{12}] \{\boldsymbol{i}_{G2}\}) \, r \, darea$.

Both equations are harmonically uncoupled, with the gravity term only affecting the 0^{th} harmonic. This is correct if gravity acts in a fixed direction in the r-z plane (i.e. z direction). If the direction of gravity acts out of this plane and is dependent on r and θ, the equations became more complex. The dashed line in Equation (12.58) separates the components that are symmetrically uncoupled from those that are coupled. Inspection of these terms reveals that the condition for symmetric uncoupling is that the $[\boldsymbol{k}_{12}]$ and $[\boldsymbol{k}_{21}]$ components of the $[\boldsymbol{k}]$ matrix are zero. Equation (12.58) can be written as:

$$\begin{aligned}
&\int \nabla(\Delta p_f)^{\mathrm{T}} [\boldsymbol{k}] \, \nabla \boldsymbol{p}_f \, dVol = \sum_{i=1}^{m} \sum_{j=1}^{m} (\Delta p_{fi}^{0})^{\mathrm{T}} [\boldsymbol{\Phi}_{ij}^0] p_{fj}^{0} + \\
&\sum_{l=1}^{L} (\Delta p_{fi}^{l*})^{\mathrm{T}} [\boldsymbol{\Phi}_{ij}^l]^{p} \, p_{fj}^{l*} + (\Delta p_{fi}^{l**})^{\mathrm{T}} [\boldsymbol{\Phi}_{ij}^l]^{o} \, p_{fj}^{l**} + (\Delta p_{fi}^{l*})^{\mathrm{T}} [\boldsymbol{\Phi}_{ij}^l]^{po} \, p_{fj}^{l**} + (\Delta p_{fi}^{l**})^{\mathrm{T}} [\boldsymbol{\Phi}_{ij}^l]^{op} \, p_{fj}^{l*}
\end{aligned} \tag{12.60}$$

where:

$$[\boldsymbol{\Phi}_{ij}^0] = 2\frac{\pi}{\gamma_f} \int [\boldsymbol{E}1_i^0]^{\mathrm{T}} [\boldsymbol{k}_{11}] [\boldsymbol{E}1_j^0] \, r \, darea$$

$$[\boldsymbol{\Phi}_{ij}^l]^{p} = [\boldsymbol{\Phi}_{ij}^l]^{o} = \frac{\pi}{\gamma_f} \int \begin{Bmatrix} [\boldsymbol{E}1_i^l] \\ [\boldsymbol{E}2_i^l] \end{Bmatrix}^{\mathrm{T}} \begin{bmatrix} [\boldsymbol{k}_{11}] & 0 \\ 0 & [\boldsymbol{k}_{22}] \end{bmatrix} \begin{Bmatrix} [\boldsymbol{E}1_j^l] \\ [\boldsymbol{E}2_j^l] \end{Bmatrix} r \, darea$$

$$[\boldsymbol{\Phi}_{ij}^l]^{po} = \frac{\pi}{\gamma_f} \int \begin{Bmatrix} [\boldsymbol{E}1_i^l] \\ [\boldsymbol{E}2_i^l] \end{Bmatrix}^{\mathrm{T}} \begin{bmatrix} 0 & [\boldsymbol{k}_{12}] \\ -[\boldsymbol{k}_{21}] & 0 \end{bmatrix} \begin{Bmatrix} [\boldsymbol{E}1_j^l] \\ [\boldsymbol{E}2_j^l] \end{Bmatrix} r \, darea$$

$$[\boldsymbol{\Phi}_{ij}^l]^{op} = \frac{\pi}{\gamma_f} \int \begin{Bmatrix} [\boldsymbol{E}1_i^l] \\ [\boldsymbol{E}2_i^l] \end{Bmatrix}^{\mathrm{T}} \begin{bmatrix} 0 & -[\boldsymbol{k}_{12}] \\ [\boldsymbol{k}_{21}] & 0 \end{bmatrix} \begin{Bmatrix} [\boldsymbol{E}1_j^l] \\ [\boldsymbol{E}2_j^l] \end{Bmatrix} r \, darea$$

A simple time stepping approach is used to carry out the integral from time t_0 to $t = t_0+\Delta t$, see Chapter 10:

$$\int_{t_0}^{t} [\boldsymbol{\Phi}]\, p_f \, \mathrm{d}t = [\boldsymbol{\Phi}](p_{f0} + \beta \Delta p_f)\, \Delta t \tag{12.61}$$

where:

p_{f0} is p_f at time $t = t_0$;

Δp_f is the change in p_f over Δt;

β is the parameter that defines the average pore water pressure over the time step, i.e. $p_f^{\mathrm{av}} = p_{f0} + \beta\, \Delta p_f$.

For the simple constant $[\boldsymbol{D}]$ and constant $[\boldsymbol{k}]$ case, all the components of Equations (12.51)and (12.52) are harmonically uncoupled. If the criterion for symmetric uncoupling is satisfied by both the $[\boldsymbol{D}]$ and the $[\boldsymbol{k}]$ matrices, the resulting equations are also symmetrically uncoupled, with the orthogonal and parallel equations having the same stiffness contributions. Thus for any harmonic order we can combine Equations (12.51) and (12.52) and write them in matrix form. For the parallel l^{th} harmonic we get:

$$\begin{bmatrix} [\boldsymbol{K}_G^l]^p & [\boldsymbol{L}_G^l]^{\mathrm{T}} \\ [\boldsymbol{L}_G^l] & -\beta\Delta t[\boldsymbol{\Phi}_G^l]^p \end{bmatrix} \begin{Bmatrix} \{\Delta \boldsymbol{d}^{l*}\}_{nG} \\ \{\Delta \boldsymbol{p}_f^{l*}\}_{nG} \end{Bmatrix} = \begin{Bmatrix} \{\Delta \boldsymbol{R}_G^{l*}\} \\ \left(\langle\langle \{\boldsymbol{n}_G\}\rangle\rangle + [\boldsymbol{\Phi}_G^l]^p \{\boldsymbol{p}_{f0}^{l*}\}_{nG} + Q\right)\Delta t \end{Bmatrix} \tag{12.62}$$

where $\langle\langle \boldsymbol{n}_G \rangle\rangle = \boldsymbol{n}_G$ if $l = 0$; $= 0$ otherwise.

The same equation can be used for the orthogonal l^{th} harmonic. However, if either the $[\boldsymbol{D}]$ matrix or the $[\boldsymbol{k}]$ matrix do not satisfy the symmetry criterion, both orthogonal and parallel coefficients have to be solved simultaneously:

$$\begin{bmatrix} [\boldsymbol{K}_G^l]^p & [\boldsymbol{L}_G^l]^{\mathrm{T}} & [\boldsymbol{K}_G^l]^{op} & 0 \\ [\boldsymbol{L}_G^l] & -\beta\Delta t[\boldsymbol{\Phi}_G^l]^p & 0 & -\beta\Delta t[\boldsymbol{\Phi}_G^l]^{op} \\ [\boldsymbol{K}_G^l]^{po} & 0 & [\boldsymbol{K}_G^l]^o & [\boldsymbol{L}_G^l]^{\mathrm{T}} \\ 0 & -\beta\Delta t[\boldsymbol{\Phi}_G^l]^{po} & [\boldsymbol{L}_G^l] & -\beta\Delta t[\boldsymbol{\Phi}_G^l]^o \end{bmatrix} \begin{Bmatrix} \{\Delta \boldsymbol{d}^{l*}\}_{nG} \\ \{\Delta \boldsymbol{p}_f^{l*}\}_{nG} \\ \{\Delta \boldsymbol{d}^{l**}\}_{nG} \\ \{\Delta \boldsymbol{p}_f^{l**}\}_{nG} \end{Bmatrix} =$$

$$\begin{Bmatrix} \{\Delta \boldsymbol{R}_G^{l*}\} \\ \left(\langle\langle \{\boldsymbol{n}_G\}\rangle\rangle + [\boldsymbol{\Phi}_G^l]^p\, \boldsymbol{p}_{f0}^{l*} + [\boldsymbol{\Phi}_G^l]^{op}\, \boldsymbol{p}_{f0}^{l**} + Q^{l*}\right)\Delta t \\ \{\Delta \boldsymbol{R}_G^{l**}\} \\ \left([\boldsymbol{\Phi}_G^l]^{po}\, \boldsymbol{p}_{f0}^{l*} + [\boldsymbol{\Phi}_G^l]^o\, \boldsymbol{p}_{f0}^{l**} + Q^{l**}\right)\Delta t \end{Bmatrix} \tag{12.63}$$

The material permeability may not be a constant and could vary with stress/strain level. Accordingly, $[\boldsymbol{k}]$ could vary in the circumferential direction. In this case $[\boldsymbol{k}]$ can be written as a Fourier series:

$$[\boldsymbol{k}] = [\boldsymbol{k}^0] + \overline{[\boldsymbol{k}^1]}\cos\theta + \overline{\overline{[\boldsymbol{k}^1]}}\sin\theta + \overline{[\boldsymbol{k}^2]}\cos 2\theta + \overline{\overline{[\boldsymbol{k}^2]}}\sin 2\theta + \ \ldots\ + \overline{[\boldsymbol{k}^l]}\cos l\theta + \overline{\overline{[\boldsymbol{k}^l]}}\sin l\theta + \ \ldots \tag{12.64}$$

where $[\boldsymbol{k}^0]$, $\overline{[\boldsymbol{k}^l]}$ and $\overline{\overline{[\boldsymbol{k}^l]}}$ are matrices containing the 0th, l^{th} order cosine and l^{th} order sine harmonic coefficients of the components of the $[\boldsymbol{k}]$ matrix respectively.

The solution to Equation (12.52) now involves the integral of the product of three Fourier series. The solution is harmonically coupled and is similar to that for a variable $[\boldsymbol{D}]$ matrix:

$$\int \nabla(\Delta p_f)^{\mathrm{T}}[\boldsymbol{k}]\, \nabla \boldsymbol{p}_f \, \mathrm{d}Vol =$$

$$\sum_{i=1}^{m}\sum_{j=1}^{m} \begin{pmatrix} \sum_{l=0}^{L} (\Delta p_{fi}^{l*})^{\mathrm{T}} \sum_{k=0}^{L} [\boldsymbol{\Phi}_{ij}^{lk}]^p (p_{fj}^{k*}) + \sum_{l=1}^{L} (\Delta p_{fi}^{l**})^{\mathrm{T}} \sum_{k=1}^{L} [\boldsymbol{\Phi}_{ij}^{lk}]^o (p_{fj}^{k**}) + \\ \sum_{l=0}^{L} (\Delta p_{fi}^{l*})^{\mathrm{T}} \sum_{k=1}^{L} [\boldsymbol{\Phi}_{ij}^{lk}]^{po} (p_{fj}^{k**}) + \sum_{l=1}^{L} (\Delta p_{fi}^{l**})^{\mathrm{T}} \sum_{k=0}^{L} [\boldsymbol{\Phi}_{ij}^{lk}]^{op} (p_{fj}^{k*}) \end{pmatrix} \tag{12.65}$$

where:

$$[\boldsymbol{\Phi}_{ij}^{lk}]^p = \frac{\pi}{\gamma_f}\int \begin{Bmatrix} [\boldsymbol{E}1_i^l] \\ [\boldsymbol{E}2_i^l] \end{Bmatrix}^{\mathrm{T}} \begin{bmatrix} \alpha\overline{[\boldsymbol{k}_{11}^{k-l}]} + \beta\overline{[\boldsymbol{k}_{11}^{k+l}]} & \pm\alpha\overline{\overline{[\boldsymbol{k}_{12}^{k-l}]}} - \beta\overline{\overline{[\boldsymbol{k}_{12}^{k+l}]}} \\ \mp\alpha\overline{\overline{[\boldsymbol{k}_{21}^{k-l}]}} - \beta\overline{\overline{[\boldsymbol{k}_{21}^{k+l}]}} & \alpha\overline{[\boldsymbol{k}_{22}^{k-l}]} - \beta\overline{[\boldsymbol{k}_{22}^{k+l}]} \end{bmatrix} \begin{Bmatrix} [\boldsymbol{E}1_j^k] \\ [\boldsymbol{E}2_j^k] \end{Bmatrix} r\, darea$$

$$[\boldsymbol{\Phi}_{ij}^{lk}]^o = \frac{\pi}{\gamma_f}\int \begin{Bmatrix} [\boldsymbol{E}1_i^l] \\ [\boldsymbol{E}2_i^l] \end{Bmatrix}^{\mathrm{T}} \begin{bmatrix} \alpha\overline{[\boldsymbol{k}_{11}^{k-l}]} - \beta\overline{[\boldsymbol{k}_{11}^{k+l}]} & \pm\alpha\overline{\overline{[\boldsymbol{k}_{12}^{k-l}]}} + \beta\overline{\overline{[\boldsymbol{k}_{12}^{k+l}]}} \\ \mp\alpha\overline{\overline{[\boldsymbol{k}_{21}^{k-l}]}} + \beta\overline{\overline{[\boldsymbol{k}_{21}^{k+l}]}} & \alpha\overline{[\boldsymbol{k}_{22}^{k-l}]} + \beta\overline{[\boldsymbol{k}_{22}^{k+l}]} \end{bmatrix} \begin{Bmatrix} [\boldsymbol{E}1_j^k] \\ [\boldsymbol{E}2_j^k] \end{Bmatrix} r\, darea$$

$$[\boldsymbol{\Phi}_{ij}^{lk}]^{op} = \frac{\pi}{\gamma_f}\int \begin{Bmatrix} [\boldsymbol{E}1_i^l] \\ [\boldsymbol{E}2_i^l] \end{Bmatrix}^{\mathrm{T}} \begin{bmatrix} \pm\alpha\overline{\overline{[\boldsymbol{k}_{11}^{k-l}]}} + \beta\overline{\overline{[\boldsymbol{k}_{11}^{k+l}]}} & -\alpha\overline{[\boldsymbol{k}_{12}^{k-l}]} + \beta\overline{[\boldsymbol{k}_{12}^{k+l}]} \\ \alpha\overline{[\boldsymbol{k}_{21}^{k-l}]} + \beta\overline{[\boldsymbol{k}_{21}^{k+l}]} & \pm\alpha\overline{\overline{[\boldsymbol{k}_{22}^{k-l}]}} - \beta\overline{\overline{[\boldsymbol{k}_{22}^{k+l}]}} \end{bmatrix} \begin{Bmatrix} [\boldsymbol{E}1_j^k] \\ [\boldsymbol{E}2_j^k] \end{Bmatrix} r\, darea$$

$$[\boldsymbol{\Phi}_{ij}^{lk}]^{po} = \frac{\pi}{\gamma_f}\int \begin{Bmatrix} [\boldsymbol{E}1_i^l] \\ [\boldsymbol{E}2_i^l] \end{Bmatrix}^{\mathrm{T}} \begin{bmatrix} \mp\alpha\overline{\overline{[\boldsymbol{k}_{11}^{k-l}]}} + \beta\overline{\overline{[\boldsymbol{k}_{11}^{k+l}]}} & \alpha\overline{[\boldsymbol{k}_{12}^{k-l}]} + \beta\overline{[\boldsymbol{k}_{12}^{k+l}]} \\ -\alpha\overline{[\boldsymbol{k}_{21}^{k-l}]} + \beta\overline{[\boldsymbol{k}_{21}^{k+l}]} & \mp\alpha\overline{\overline{[\boldsymbol{k}_{22}^{k-l}]}} - \beta\overline{\overline{[\boldsymbol{k}_{22}^{k+l}]}} \end{bmatrix} \begin{Bmatrix} [\boldsymbol{E}1_j^k] \\ [\boldsymbol{E}2_j^k] \end{Bmatrix} r\, darea$$

In the above equations:

$\alpha = 1$ if $k = l$,	$= \frac{1}{2}$ otherwise;
$\beta = 1$ if $k = l = 0$,	$= \frac{1}{2}$ otherwise;
$\pm$ is + if $k - l \geq 0$,	is − if $k - l < 1$;
$\mp$ is − if $k - l \geq 0$,	is + if $k - l < 1$.

Similarly, the solution for Equation (12.59) now involves the integral of the product of two Fourier series, thus the gravity term affects all the harmonics:

$$\int \nabla(\Delta p_f)^{\mathrm{T}}[\boldsymbol{k}]\, \{i_G\}\, \mathrm{d}Vol = \pi\sum_{i=1}^{m}\int 2(\Delta p_{fi}^0)^{\mathrm{T}}[\boldsymbol{E}1_i^0]^{\mathrm{T}}\left([\boldsymbol{k}_{11}^0]\{i_{G1}\} + [\boldsymbol{k}_{12}^0]\{i_{G2}\}\right) +$$

$$\sum_{l=1}^{L} (\Delta p_{fi}^{l*})^{\mathrm{T}}\left(\left([\boldsymbol{E}1_i^l]^{\mathrm{T}}\overline{[\boldsymbol{k}_{11}^l]} - [\boldsymbol{E}2_i^l]^{\mathrm{T}}\overline{\overline{[\boldsymbol{k}_{21}^l]}}\right)\{i_{G1}\} + \left([\boldsymbol{E}1_i^l]^{\mathrm{T}}\overline{[\boldsymbol{k}_{12}^l]} - [\boldsymbol{E}2_i^l]^{\mathrm{T}}\overline{\overline{[\boldsymbol{k}_{22}^l]}}\right)\{i_{G2}\}\right) +$$

$$(\Delta p_{fi}^{l**})^{\mathrm{T}}\left(\left([\boldsymbol{E}1_i^l]^{\mathrm{T}}\overline{\overline{[\boldsymbol{k}_{11}^l]}} + [\boldsymbol{E}2_i^l]^{\mathrm{T}}\overline{[\boldsymbol{k}_{21}^l]}\right)\{i_{G1}\} + \left([\boldsymbol{E}1_i^l]^{\mathrm{T}}\overline{\overline{[\boldsymbol{k}_{12}^l]}} + [\boldsymbol{E}2_i^l]^{\mathrm{T}}\overline{[\boldsymbol{k}_{22}^l]}\right)\{i_{G2}\}\right) r\, darea$$

$$= \sum_{i=1}^{m} (\Delta p_{fi}^0)^{\mathrm{T}}\{\boldsymbol{n}_i^0\} + \sum_{l=1}^{L} (\Delta p_{fi}^{l*})^{\mathrm{T}}\{\boldsymbol{n}_i^{l*}\} + (\Delta p_{fi}^{l**})^{\mathrm{T}}\{\boldsymbol{n}_i^{l**}\} \tag{12.66}$$

The $[\boldsymbol{L}_G]$ terms in Equation (12.63) are unchanged since they are not affected by $[\boldsymbol{k}]$ or $[\boldsymbol{D}]$. However, the $\boldsymbol{p}_{f0}$ terms now have to be multiplied with all the harmonically coupled $[\boldsymbol{\Phi}_G]$ matrices. Since the equations are now harmonically coupled, an equation with a form similar to that of Equation (12.63) can be written to relate any l^{th} harmonic right hand side with any k^{th} harmonic left hand side:

$$\begin{bmatrix} [\boldsymbol{K}_G^{lk}]^{p} & \langle\langle\langle[\boldsymbol{L}_G^{l}]^{\mathrm{T}}\rangle\rangle\rangle & [\boldsymbol{K}_G^{lk}]^{qp} & 0 \\ \langle\langle\langle[\boldsymbol{L}_G^{l}]\rangle\rangle\rangle & -\beta\Delta t[\boldsymbol{\Phi}_G^{lk}]^{p} & 0 & -\beta\Delta t[\boldsymbol{\Phi}_G^{lk}]^{qp} \\ [\boldsymbol{K}_G^{lk}]^{po} & 0 & [\boldsymbol{K}_G^{lk}]^{o} & \langle\langle\langle[\boldsymbol{L}_G^{l}]^{\mathrm{T}}\rangle\rangle\rangle \\ 0 & -\beta\Delta t[\boldsymbol{\Phi}_G^{lk}]^{po} & \langle\langle\langle[\boldsymbol{L}_G^{l}]\rangle\rangle\rangle & -\beta\Delta t[\boldsymbol{\Phi}_G^{lk}]^{o} \end{bmatrix} \begin{Bmatrix} \{\Delta\boldsymbol{d}^{k*}\}_{nG} \\ \{\Delta\boldsymbol{p}_f^{k*}\}_{nG} \\ \{\Delta\boldsymbol{d}^{k**}\}_{nG} \\ \{\Delta\boldsymbol{p}_f^{k**}\}_{nG} \end{Bmatrix} =$$

$$\begin{Bmatrix} \{\Delta\boldsymbol{R}_G^{l*}\} \\ \left(\{\boldsymbol{n}_G^{l*}\} + \sum_{j=0}^{L_c} [\boldsymbol{\Phi}_G^{lk}]^{p}\Delta p_{f0}^{j*} + [\boldsymbol{\Phi}_G^{lk}]^{qp}\Delta p_{f0}^{j**} + Q^{l*}\right)\Delta t \\ \{\Delta\boldsymbol{R}_G^{l**}\} \\ \left(\{\boldsymbol{n}_G^{l**}\} + \sum_{j=0}^{L_c} [\boldsymbol{\Phi}_G^{lk}]^{po}\Delta p_{f0}^{j*} + [\boldsymbol{\Phi}_G^{lk}]^{o}\Delta p_{f0}^{j**} + Q^{l**}\right)\Delta t \end{Bmatrix} \tag{12.67}$$

where $\langle\langle\langle[\boldsymbol{L}_G^{l}]\rangle\rangle\rangle = [\boldsymbol{L}_G^{l}]$ if $l = k$; $= 0$ otherwise.

The general criterion for symmetric uncoupling in this case is that the $[\boldsymbol{k}_{11}]$ and $[\boldsymbol{k}_{22}]$ parts of the $[\boldsymbol{k}]$ matrix are symmetric functions of θ, and the $[\boldsymbol{k}_{12}]$ and $[\boldsymbol{k}_{21}]$ parts are asymmetric. As discussed previously regarding the nonlinear material behaviour (i.e. elasto-plastic), CFSAFEM analysis of coupled problems can be performed either using the constant $[\boldsymbol{k}]$ formulation or a compromised variable $[\boldsymbol{k}]$ formulation, in which the harmonically coupled terms are ignored. In both cases appropriate correction to the right hand side of the finite element equations will be necessary if $[\boldsymbol{k}]$ is variable.

12.4 Implementation of the CFSAFEM

12.4.1 Introduction

From the formulation provided in the previous sections it is clear that the CFSAFEM involves many extensions and enhancements of the conventional finite element theory presented in Chapters 2, 10 and 11. In particular, the CFSAFEM formulation is expressed in terms of Fourier series coefficients, while the conventional finite element formulation is in terms of real values. This clearly has implications for the computer code, the boundary conditions and the output from an analysis.

Inclusion of the CFSAFEM into an existing finite element program involves a considerable effort. There is a large increase in data storage requirements compared to a conventional 2D finite element analysis. This is due to the additional coordinate direction, the two additional components of stress and strain and the use of a number of harmonic coefficients in a CFSAFEM analysis. However, due to the harmonic uncoupling this storage requirement is likely to be considerably smaller than that required for a comparable conventional 3D analysis.

Efficient data management routines are required to store data and to convert it between harmonic coefficient and real values. Methods of specifying input boundary conditions also have to be enhanced to provide a user friendly interface with the finite element program. Significant modifications must also be made to the nonlinear solution algorithm to enable the correct adjustment to be made to the right hand side of the finite element equations. In the following subsections some of these topics are considered in more detail. The material presented is based on the Authors' experiences with implementing the CFSAFEM into the computer code ICFEP.

12.4.2 Evaluating Fourier series harmonic coefficients

All the variables used in a CFSAFEM analysis have to be expressed as Fourier series, because the CFSAFEM is formulated entirely in terms of Fourier series harmonic coefficients. This is a key component of the MNR solution strategy for nonlinear CFSAFEM, since it is used to evaluate the right hand side corrective loads, as described in Section 12.4.3. It is also used to interpret complex boundary conditions and to formulate the partial nonlinear stiffness matrix, see Section 12.3.4. Thus a general approach has to be devised for expressing the distribution of variables in the θ direction as a Fourier series.

Consider a variable x which is a function of θ. The harmonic coefficients have to be evaluated such that x can be expressed as:

$$x = X^0 + \overline{X^1}\cos\theta + \overline{\overline{X^1}}\sin\theta + \overline{X^2}\cos 2\theta + \overline{\overline{X^2}}\sin 2\theta + \ \ldots\ + \overline{X^l}\cos l\theta + \overline{\overline{X^l}}\sin l\theta + \ \ldots \tag{12.68}$$

If there is an explicit expression for x, i.e. $x = f(\theta)$, then harmonic coefficients can be evaluated from the equations:

$$\begin{aligned} X^0 &= \frac{1}{2\pi}\int_{-\pi}^{\pi} f(\theta)\,\mathrm{d}\theta \\ \overline{X^l} &= \frac{1}{\pi}\int_{-\pi}^{\pi} f(\theta)\cos l\theta\,\mathrm{d}\theta \\ \overline{\overline{X^l}} &= \frac{1}{\pi}\int_{-\pi}^{\pi} f(\theta)\sin l\theta\,\mathrm{d}\theta \end{aligned} \tag{12.69}$$

Often there is no explicit expression for x, instead values of x at specific θ values are known, e.g. x_1 at θ_1, x_2 at θ_2, x_3 at θ_3, ... , x_i at θ_i, ... , x_n at θ_n, where n is the number of known values of x. There is no unique solution to this type of problem, since an assumption has to be made regarding the value of x between any two specified values. Two methods are suggested: (i) the stepwise linear method and (ii) the fitted method.

12.4.2.1 The stepwise linear method

This method is based on an approach suggested by Winnicki and Zienkiewicz (1979). Using the known values of x they assume a stepwise linear distribution with θ, see Figure 12.4. Thus the value of x at any value of θ is:

$$x = x_i + \frac{(x_{i+1} - x_i)(\theta - \theta_i)}{\theta_{i+1} - \theta_i} \quad ; \quad \theta_i < \theta < \theta_{i+1} \tag{12.70}$$

Equations (12.69) are then integrated numerically to obtain the harmonic coefficients and Bode's integration rule is suggested. There is a trade off between the error associated with this numerical integration and the amount of computer resources required to evaluate it.

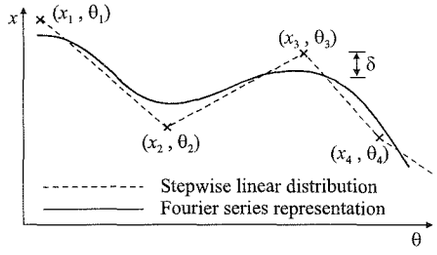

Figure 12.4: Stepwise linear method

This method is improved upon by carrying out the integration analytically. This has the advantage of both eliminating any integration errors and reducing the computer resources required. The integration is performed in Appendix XII.6 and the solutions are presented below:

$$X^0 = \sum_{i=1}^{n} \frac{(x_{i+1} + x_i)(\theta_{i+1} - \theta_i)}{4\pi}$$

$$\overline{X^k} = \sum_{i=1}^{n} \frac{(x_{i+1} - x_i)(\cos k\theta_{i+1} - \cos k\theta_i)}{k^2 \pi(\theta_{i+1} - \theta_i)} \tag{12.71}$$

$$\overline{\overline{X^k}} = \sum_{i=1}^{n} \frac{(x_{i+1} - x_i)(\sin k\theta_{i+1} - \sin k\theta_i)}{k^2 \pi(\theta_{i+1} - \theta_i)}$$

where:

$x_{n+1} = x_1$

$\theta_{n+1} = \theta_1 + 2\pi$

The harmonic coefficients obtained from Equation (12.69) would fit any continuous function exactly, if an infinite number of harmonic terms were used in expression (12.68). This is impractical in any numerical algorithm and invariably a finite number of terms is used. Usually a truncated Fourier series is used where the higher order terms are ignored and sufficient terms are considered such that the error associated with ignoring these higher order terms is small. Additionally, even though the resulting Fourier series does not fit the stepwise linear distribution exactly, it will still give a good representation of x, which may even be better than the stepwise distribution.

12.4.2.2 The fitted method

In this method it is assumed that x can be represented by a Fourier series that passes through all known values of x, see Figure 12.5. The number of harmonic terms used in the Fourier series representation is an important parameter. If there are more harmonic terms than known values of x, a number of possible solutions exist. If there are less harmonic terms, a solution does not exist in general. A unique solution exists if the number of harmonic coefficients is equal to the number of known values. This condition is achieved by using a truncated Fourier series. The harmonic coefficients for the unique solution can be obtained by substituting each known value of x and θ into Equation (12.68). This yields n equations with n unknowns, where n is the number of unknown values specified, and can be expressed in matrix form as:

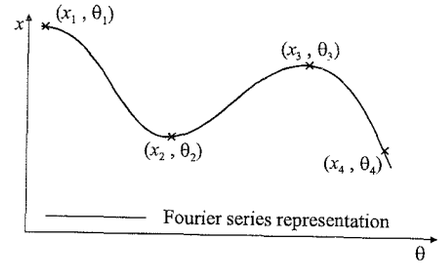

Figure 12.5: Fitted method

$$\begin{Bmatrix} x_1 \\ x_2 \\ x_3 \\ .. \\ .. \\ x_{n-1} \\ x_n \end{Bmatrix} = \begin{bmatrix} 1 & \cos\theta_1 & \sin\theta_1 & .. & .. & \cos L\theta_1 & \sin L\theta_1 \\ 1 & \cos\theta_2 & \sin\theta_2 & .. & .. & \cos L\theta_2 & \sin L\theta_2 \\ 1 & \cos\theta_3 & \sin\theta_3 & .. & .. & \cos L\theta_3 & \sin L\theta_3 \\ .. & .. & .. & .. & .. & .. & .. \\ .. & .. & .. & .. & .. & .. & .. \\ 1 & \cos\theta_{n-1} & \sin\theta_{n-1} & .. & .. & \cos L\theta_{n-1} & \sin L\theta_{n-1} \\ 1 & \cos\theta_n & \sin\theta_n & .. & .. & \cos L\theta_n & \sin L\theta_n \end{bmatrix} \begin{Bmatrix} X^0 \\ \overline{X^1} \\ \overline{\overline{X^1}} \\ .. \\ .. \\ \overline{X^{\frac{n-1}{2}}} \\ \overline{\overline{X^{\frac{n-1}{2}}}} \end{Bmatrix} \tag{12.72}$$

where L is the order of the truncated Fourier series used (equal to ½(n-1)) and can be rewritten as:

$$\boldsymbol{x} = [\boldsymbol{H}]\boldsymbol{X} \tag{12.73}$$

where

$\boldsymbol{x}$ is the vector of known values x_i;

$\boldsymbol{X}$ is the vector of unknown harmonic coefficients;

$[\boldsymbol{H}]$ is the harmonic transformation matrix that is a function of the θ values at which x is known.

The harmonic coefficients, $\boldsymbol{X}$, can now be solved for by inverting $[\boldsymbol{H}]$ and premultiplying $\boldsymbol{x}$ by $[\boldsymbol{H}]^{-1}$. If the θ values at which x is known are unchanged, then $[\boldsymbol{H}]$ is unchanged. Thus a number of $\boldsymbol{X}$ corresponding to a number of $\boldsymbol{x}$ can be obtained very easily by premultiplying the various $\boldsymbol{x}$ by the same $[\boldsymbol{H}]^{-1}$.

Solutions have been derived for the special case of having known x values at equispaced θ values, see Appendix XII.7. The number of known values, n, is assumed to be odd such that the resulting truncated Fourier series has the same

number of sine and cosine harmonic terms. If the first x value, x_1, is at $\theta = 0°$, the subsequent known x values, x_i, will occur at $\theta = (i\text{-}1)\alpha$, see Figure 12.6.

The harmonic coefficients can then be evaluated using equations:

$$X^0 = \frac{1}{n}\sum_{i=1}^{n} x_i$$

$$\overline{X^k} = \frac{2}{n}\sum_{i=1}^{n} x_i \cos k(i-1)\alpha \qquad (12.74)$$

$$\overline{\overline{X^k}} = \frac{2}{n}\sum_{i=1}^{n} x_i \sin k(i-1)\alpha$$

This equispaced fitted approach is the most efficient method for obtaining harmonic coefficients. It is, however, only applicable for the special case when the x values are equispaced and the number of harmonic terms $(2L+1)$ is equal to n. If these criteria are not satisfied, the robust stepwise linear approach is recommended, since this approach places no limitation on either the number of harmonic terms used, or the location of the x values. In the remainder of this chapter these methods will simply be referred to as the fitted and stepwise approach.

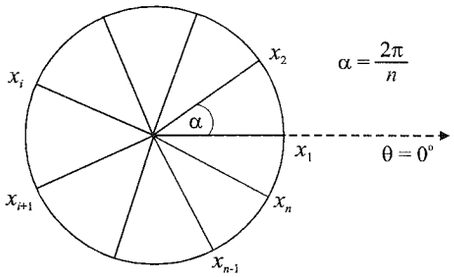

Figure 12.6: Location of x values for equispaced fitted method

12.4.3 The modified Newton-Raphson solution strategy

12.4.3.1 Introduction

The MNR solution strategy for nonlinear CFSAFEM is an iterative procedure. For any imposed boundary condition a trial solution is obtained by solving the system equations associated with the current global stiffness matrix, as described earlier in this chapter. It is acknowledged that there is possibly an error associated with this trial solution and a corrective right hand side load is evaluated. This corrective load is then used to obtain the next trial solution. The process is repeated until the corrective loads are small. This procedure is very similar to the MNR procedure for conventional nonlinear finite elements, see Chapter 9. However, the CFSAFEM formulation is in terms of Fourier series coefficients. Thus the corrective right hand side loads have to be expressed as Fourier series and are evaluated from the trial solutions which are also expressed as Fourier series. The material constitutive laws are used in the process of calculating these corrective loads. These laws are expressed in terms of real values rather than harmonic coefficients. Thus a procedure has to be developed which enables a harmonic correction load to be evaluated from the harmonic trial solution, using the material constitutive laws.

12.4.3.2 Right hand side correction

The corrective right hand side load is expressed as Fourier series coefficients of nodal load. They are evaluated by comparing the coefficients of nodal load, obtained from the imposed boundary conditions, with the coefficients of nodal load consistent with the trial solution displacements. The latter loads are obtained by calculating, at a number of sampling points within the problem domain, the stress changes associated with the solution displacements. This is performed by substituting the harmonic solution displacement into Equation (12.8) to calculate the real incremental strains at the sampling points. A stress point algorithm is used to integrate the material constitutive laws along these strain paths to obtain the incremental stresses, see Section 9.6.2. A volume integral has to be carried out to obtain the harmonic coefficients of nodal load consistent with the stress state in the problem domain. The stresses at the sampling points are used to evaluate this integral, the solution of which is presented in Appendix XII.3. The integral is divided into two parts, a $d\theta$ integral and a d*area* integral, where '*area*' is the area on the r-z plane.

The d*area* integral is carried out using a Gaussian integration technique and, accordingly, the sampling points are located at Gaussian integration points in the r-z plane. To perform the $d\theta$ integral it is necessary to know the θ coordinates of the sampling points. It is therefore convenient to situate the sampling points on a number of constant θ planes (slices). Their locations within each slice is determined by the Gaussian integration order used and the finite element mesh. The $d\theta$ integral is carried out analytically, but requires the stresses to be expressed as a Fourier series in the θ direction. There is no definitive method of obtaining the Fourier series representation of stress from the stresses at the sampling points. Similarly, there are no guidelines for the number and location of the slices in the θ direction. A rational approach is suggested below.

The number of slices used in an analysis should be influenced by the order of the Fourier series required to represent stresses. If there were the same number of slices as harmonic coefficients of stress in an analysis, a Fourier series representation of stress could be obtained, which gives the appropriate stresses on each slice. Theoretically, increasing the number of harmonics would not increase the Fourier series accuracy since the stresses on the slices could already be represented exactly. Conversely, increasing the number of slices means that the Fourier series would not be able to represent the stresses on all the slices exactly and the benefit of these additional slices cannot be fully realised. The Fourier series used to represent stresses in a CFSAFEM analysis should have the same order as the Fourier series used to represent forces and displacements. Harmonic coefficients of stress of a higher order would not influence the CFSAFEM analysis, as shown in Appendix XII.3. Thus it is proposed that the number of slices should be the same as the number of harmonic coefficients used to represent forces and displacements in a CFSAFEM analysis. It is also suggested that the slices are equispaced around the circumference, in which case the efficient fitted method, see Section 12.4.2.2, for obtaining harmonics can be used.

12.4.4 Data storage

The data storage required for CFSAFEM analysis differs from that of conventional finite element analysis in two important aspects. Firstly, for each nodal variable, e.g. nodal displacement, it is necessary to store a number of harmonic coefficients, as opposed to a single quantity. Likewise, for each variable at an integration point, e.g. stress component, it is necessary to store a number of quantities, either in the form of harmonic coefficients, or as real values one for each slice. At different stages during the analysis each variable (e.g. nodal displacement or force, stress or strain component) is needed either in harmonic form or as real value. However, it is both very inefficient and cumbersome to store data in two different forms. Consequently, efficient data management routines are required to store the data in one form and to convert between harmonic coefficients and real values and vice versa, see Section 12.4.2. The only decision then is in which form (real values or harmonic coefficients) should each variable be stored. As the nodal variables in a CFSAFEM analyses are expressed purely in terms of Fourier series harmonic coefficients, it seems sensible that these values are stored as harmonic coefficients and converted to real values when required for output purposes. The decision is more difficult for the state variables stored at integration points, e.g. stresses, strains and hardening parameters. The stress point algorithm requires these variables to be expressed as real values, however the calculation of the harmonic coefficients of nodal force, consistent with the stresses at the sampling points, requires that the stresses are expressed as Fourier series. The data output algorithms are also likely to require that these variables are expressed as Fourier series, so that their values at any θ value can be exactly calculated. For these reasons, and to be consistent with the storage of nodal variables, it seems appropriate to store the harmonic coefficients.

An important property of any coefficients obtained using the fitted method is that real values calculated from these coefficients are exactly equal to the real values the coefficients were derived from, see Figure 12.5. This interchangeability between the harmonic coefficients and real values dispenses of the need to store both harmonic coefficients and real values of any variable. Coefficients obtained using the stepwise method do not exhibit this property and there is a slight error, δ, when they are used to evaluate the real values that they were derived from, see Figure 12.4. The magnitude of this transformation error reduces as the number of harmonics used increases and, in practice, should be small.

A situation where the transformation error would be important is in the storage of the soil state variables at sampling points on the predefined slices. The stress point algorithm, and in practice the projecting back subalgorithm, in the nonlinear solution strategy ensure that the state variables are consistent with the prescribed strain path, see Chapter 9 and Appendix IX.1. These real values of the state variables are then expressed and stored as harmonic coefficients, ready for use by the CFSAFEM algorithms and the data output algorithms. When the stress point algorithms next require these variables, it is critical that the exact real values are evaluated, since even a small error could result in an illegal stress state, e.g. stresses exceeding yield. In this case the stress point and other associated algorithms would not be valid and some arbitrary form of correction is required, which could result in large errors. It is for this reason that the fitted method is recommended in preference to the stepwise method when calculating the load vector for the right hand side correction to the finite element equations.

12.4.5 Boundary conditions

As the CFSAFEM is formulated in terms of Fourier series coefficients, all boundary conditions must be specified in this manner. However, for most practical boundary value problems the boundary conditions are likely to be in terms of real values (e.g. a displacement or force in a certain direction). Consequently, before any analysis can be undertaken, these real values must be converted to an equivalent Fourier series representation. Three options for specifying boundary conditions are evident:

- The user determines the Fourier series that is equivalent (or a good approximation) to the real boundary condition, and inputs the harmonic coefficients directly.
- The user inputs a set of numbers representing the value of the boundary condition at equispaced values of θ. The number of values must be equal to the number of Fourier coefficients required. The computer program can then use the fitted method (see Section 12.4.2.2) to obtain the required harmonic coefficients.
- The user inputs two sets of numbers. The first set contains values of the boundary condition at a series of θ values. The second set contains the magnitudes of these θ values. The computer program then uses the stepwise method (see Section 12.4.2.1) to obtain the harmonic coefficients.

In the Authors' experience all three of the above options should be available to the user of a computer program. Examples of their use are given in Volume 2 of this book.

12.4.6 Stiffness matrices

The partial nonlinear formulation, as described in Sections 12.3.4 and 12.3.7, requires that the constitutive matrix $[\boldsymbol{D}]$ and permeability matrix $[\boldsymbol{K}]$ are expressed as a Fourier series. These harmonic matrices are required for every integration point located in the r-z plane. To achieve this, for each integration point the real $[\boldsymbol{D}]$ and $[\boldsymbol{K}]$ matrices are calculated at the associated circumferential series of sampling points, i.e. on each slice. The harmonic coefficients for these matrices can then be obtained using the fitted method.

The partial nonlinear no symmetry CFSAFEM formulation results in a non-symmetric stiffness matrix when the stiffness contribution for a parallel symmetry load on an orthogonal symmetry displacement is not the same as that for the corresponding orthogonal symmetry load on the corresponding parallel symmetry

displacement. As this situation is generally applicable, the global stiffness matrix must be inverted using a non-symmetric solver.

In all other situations, using the partial nonlinear CFSAFEM, the symmetry of the global stiffness matrix depends on the nature of the constitutive matrix $[\boldsymbol{D}]$ and permeability matrix $[\boldsymbol{K}]$. For example, if a non-associated elasto-plastic constitutive model is employed, the global stiffness matrix is non-symmetric.

12.4.7 Simplifications due to symmetrical boundary conditions

12.4.7.1 Introduction

As noted in Section 12.3.2, many boundary value problems have a symmetry about the $\theta = 0°$ direction, such that the imposed boundary conditions consist of purely parallel or orthogonal symmetry terms. In the parallel symmetry case all components of the boundary conditions in the r and z coordinate directions have a symmetric variation with θ, whereas the components in the θ direction have an asymmetric variation. Consequently, for all the r and z components of the boundary conditions the sine terms in their Fourier series have zero coefficients, and for the θ components the zeroth and cosine terms have zero coefficients. Conversely, for orthogonal symmetry the components of the boundary conditions in the r and z direction have an asymmetric variation and those in θ direction have a symmetric variation with θ. This results in zero values for the coefficients of the zeroth and cosine terms associated with the r and z components of the boundary conditions, and for sine terms associated with the components in the θ direction.

Consequently, for either a parallel or orthogonal symmetry problem, almost half of the harmonic coefficients are zero. The majority of previous implementations of the CFSAFEM have capitalised on the above consequences and have been coded to deal only with either parallel symmetry (e.g. Winnicki and Zienkiewicz (1979)), or orthogonal symmetry (e.g. Griffiths and Lane (1990)), by ignoring the harmonics associated with the zero coefficients. While such approaches restrict the type of boundary value problem that can be analysed, they lead to a large saving in computer resources required for an analysis and significantly simplify the solution algorithms. This saving arises due to the fact that only half of the Fourier series terms are considered. However, as noted in Section 12.3.2, 12.3.4 and 12.3.7, this approach of considering only parallel or orthogonal terms is theoretically valid only if two requirements are met. The first requirement is that the boundary conditions satisfy the appropriate symmetries, and the second requirement is that the system equations are symmetrically uncoupled. The criterion for this second requirement concerns the nature of the constitutive matrix $[\boldsymbol{D}]$ and the permeability matrix $[\boldsymbol{k}]$, see Sections 12.3.2, 12.3.4 and 12.37. If the second condition is not satisfied, it is then incorrect to perform an analysis with only parallel or orthogonal symmetry terms, even if the boundary conditions satisfy the symmetry requirements. In such a situation a full non-symmetric analysis, accounting for all terms in the Fourier series, must be performed. An example highlighting this problem is presented in the next section.

Initial stresses can also present potential problems for parallel and orthogonal symmetry analysis. Consider the situation in which the initial stresses in the soil do not vary in the θ direction. Here all the stress components can be represented by a Fourier series when all the harmonic coefficients, except the zeroth harmonic, are zero. However, from Appendix XII.3, zeroth harmonic components of $\{\Delta\boldsymbol{\sigma}1\}$ (i.e. $\Delta\sigma_r$, $\Delta\sigma_z$, $\Delta\tau_{rz}$ and $\Delta\sigma_\theta$) yield parallel loads and zeroth harmonic components of $\{\Delta\boldsymbol{\sigma}2\}$ (i.e. $\Delta\tau_{r\theta}$ and $\Delta\tau_{z\theta}$) yield orthogonal loads. This questions the validity of $\{\boldsymbol{\sigma}1\}$ initial stresses in an orthogonal analysis and $\{\boldsymbol{\sigma}2\}$ initial stresses in a parallel analysis. This problem is partly overcome if an incremental form of the CFSAFEM is implemented, which is likely to be the case for analysing nonlinear problems. At the beginning of an analysis, the initial stresses are assumed to be in equilibrium with themselves and with the initial boundary stresses. The incremental form of CFSAFEM then evaluates the stress changes, which should be consistent with the applied nodal loads. Thus, irrespective of the actual values of stress, a parallel analysis is valid if the stress changes do not yield an orthogonal load. Similarly an orthogonal analysis is valid if there are no stress changes giving parallel loads. If these conditions are not satisfied, a no symmetry analysis should be used. A no symmetry analysis is also required if on first loading from the initial stress state the constitutive matrix $[\boldsymbol{D}]$ depends on the initial state of stress, see the example given below in Section 12.4.7.2.

In a linear consolidation CFSAFEM analysis the gravity vector, $\{\boldsymbol{i}_G\}$, gives rise to a zeroth harmonic flow term on the right hand side of the finite element equations, see Section 12.3.7. This is consistent with the parallel symmetry criterion for a symmetrical flow term. However, there is a conflict between the gravity zero harmonic terms and the orthogonal symmetry criterion for an asymmetrical flow term. This conflict can be resolved by specifying a hydrostatic initial pore fluid pressure regime. The flow terms resulting from this regime counterbalance the gravity flow terms such that there are no net symmetrical right hand side flow terms. More generally, a linear or nonlinear consolidation CFSAFEM requires that the initial pore fluid pressures and $\{\boldsymbol{i}_G\}$ are consistent with the symmetry of the analysis. If the symmetry criteria cannot be satisfied, a no symmetry analysis should be undertaken.

It is the Authors' experience that all three options, e.g. parallel, orthogonal and no symmetry, are useful and should be available in a general purpose finite element code. Although a no symmetry analysis is considerably more expensive in terms of computer resources than either a parallel or orthogonal analysis, many problems have to be analysed in this way because they do not satisfy all the requirements for either a parallel or orthogonal analysis. Also, due to the uncertainties involved with satisfying the requirements concerning the nature of the constitutive matrix $[\boldsymbol{D}]$, it is often useful to compare no symmetry and the relevant parallel or orthogonal symmetry analysis, to confirm that the requirements are satisfied. It should be noted that when analysing problems with parallel or orthogonal symmetry only half of the geometry (i.e. $0° \leq \theta \leq 180°$) needs to be considered, while in a no symmetry analysis the full geometry (i.e. $0° \leq \theta \leq 360°$) must be used.

12.4.7.2 Examples of problems associated with parallel and orthogonal analysis

To illustrate some of the problems associated with implementing a CFSAFEM formulation for analysing either purely parallel or orthogonal symmetry problems, and to emphasise the importance of having the option for a no symmetry analysis, two examples are presented.

The first example considers the hollow cylinder problem described by Gens and Potts (1984). This problem involves the analysis of a hollow cylinder soil sample subjected to a torsional displacement, while maintaining the inner and outer pressures equal and constant. In addition, the axial strain is kept to zero and it is assumed that there are no end effects. As a consequence of this latter assumption, stresses and strains are independent of coordinates z and θ and it is therefore possible to analyse a section of the sample as shown in Figure 12.7. Also shown in this figure is the finite element mesh used to perform this analysis. It represents a section of the hollow cylinder wall, with an inner radius of 100 mm and an outer radius of 125 mm. The wall is divided into ten eight noded isoparametric elements of equal radial size. To simulate the test conditions a circumferential displacement is applied along the boundary CD, whereas the same displacement component is held to zero along AB. No restriction is imposed on the radial movements, but the vertical movements along AB and CD are set to zero. To ensure strain compatibility, the applied displacements along CD have to be proportional to the value of the r coordinate. Since the inner and outer pressures remain unchanged, a zero normal pressure change is applied during the analysis to boundaries AD and BC.

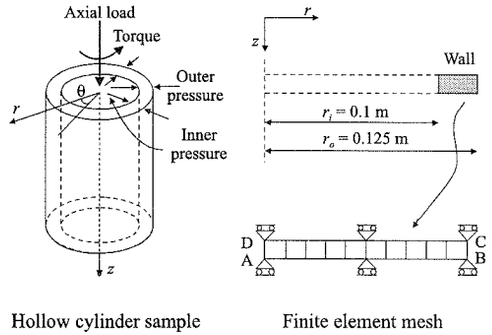

Figure 12.7: Hollow cylinder sample subjected to torsion

Gens and Potts (1984) analysed this problem using a special quasi axi-symmetric finite element formulation. However, the boundary conditions described above can be presented using orthogonal symmetry, with only the zeroth harmonic terms. Analyses are therefore performed using both an orthogonal symmetry and a no symmetry CFSAFEM formulation and the results are compared with those of Gens and Potts (1984). In these analyses the modified Cam clay model is used to represent the soil and the material parameters and initial stress conditions are given in Table 12.1. Initially, undrained analyses are performed by specifying an equivalent bulk modulus for the pore fluid, K_e, to be 100 times the bulk modulus of the soil skeleton, see Section 3.4. The results of both the CFSAFEM analyses (i.e. orthogonal and no symmetry) are identical and are in agreement with those of

Gens and Potts (1984). This can be seen in Figure 12.8, which shows the variation of the moment, applied to the top of the sample, with angular rotation (i.e. twist).

The analyses are repeated assuming drained soil conditions, i.e. all parameters and boundary conditions the same, except that the effective bulk modulus of the pore fluid, K_e, is set to zero. The result of the two CFSAFEM analyses are compared with the results from the quasi axi-symmetric analyses in Figure 12.9, again in terms of moment versus rotation.

Figure 12.1: Material properties for hollow cylinder problem

Overconsolidation ratio	1.0
Specific volume at unit pressure on virgin consolidation line, v_1	1.788
Slope of virgin consolidation line in v-lnp' space, λ	0.066
Slope of swelling line in v-lnp' space, κ	0.0077
Slope of critical state line in J-p' space, M_J	0.693
Isotropic initial stress	200kPa
Elastic shear modulus, G	18675kPa

It can be seen that the quasi axi-symmetric and no symmetry CFSAFEM results are identical. These results show a much softer response and a higher ultimate load to those from the undrained analyses presented in Figure 12.8. However, the orthogonal CFSAFEM analysis gives very different results, which are similar to those from the undrained analyses. The reason for the discrepancy is that in a drained problem the zeroth harmonic coefficients of radial displacement are non-zero. However, these are defined to be zero in an orthogonal CFSAFEM formulation. Thus, even though the boundary conditions can be specified using orthogonal symmetry, the correct drained solution cannot be obtained. The results tend towards the undrained analysis results, which, due to the incompressible material behaviour (i.e.

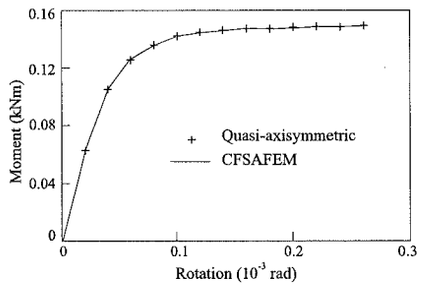

Figure 12.8: Undrained hollow cylinder test

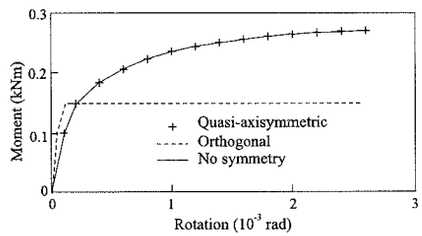

Figure 12.9: Drained hollow cylinder test

high K_c value), have no radial displacements and under predict the correct drained ultimate load by over 40%. This is an example of a problem where a no symmetry analysis is required due to the material properties, even though the boundary conditions can be specified using orthogonal symmetry.

The second example considers a rigid horizontal disk pushed laterally through a soil mass with a circular boundary. This geometry is representative of a horizontal section across a laterally loaded pile, as shown in Figure 12.10. It is assumed that there are no vertical strains, hence the problem can be analysed using both the CFSAFEM and a plane strain analysis. The boundary conditions and typical meshes used for both types of analyses are shown in Figure 12.11.

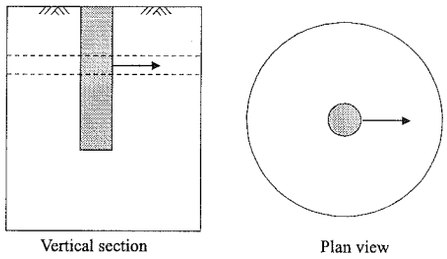

Figure 12.10: Schematic view of horizontally loaded pile section

Interface elements are located at the disk-soil boundary so that various interface conditions, e.g. rough, smooth, rough with breakway, smooth with breakway, can be investigated.

The disk diameter, D, is 2m and the boundary diameter is 40m. Only the first Fourier harmonic coefficient is required to represent the boundary conditions for the CFSAFEM analysis. However, in a nonlinear analysis the solution displacements have to be represented using more harmonics, see Section 12.3.4. For the present example ten harmonics are used. If the direction of loading is in the θ=0° direction, the boundary conditions imposed have parallel symmetry, if it is in the θ=π/2 direction they have orthogonal symmetry, and if it is in any other direction they have no symmetry. For the present example the problem is displacement controlled, with a uniform displacement in the θ=0° direction imposed on the rigid disk. A displacement δ is specified by prescribing the nodal displacements at the disk-soil interface to be:

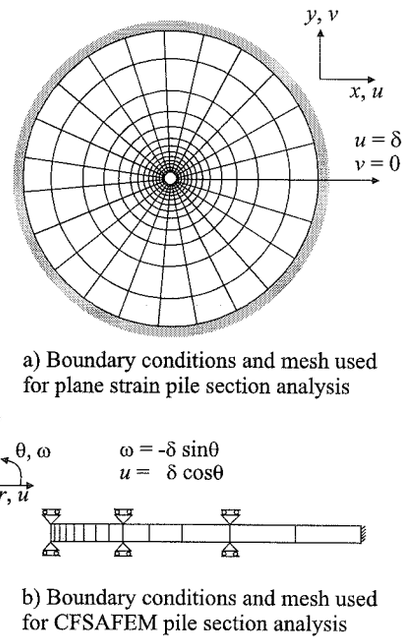

Figure 12.11: Boundary conditions and meshes for pile section analyses

Radial displacement, $u = \delta\cos\theta$;
Circumferential displacement, $\omega = -\delta\sin\theta$.

The reaction force on the disk due to the imposed displacement can be evaluated. The net reaction force in the θ=0° direction can be obtained by adding the first cosine harmonic coefficients of radial nodal reactions and subtracting the first sine harmonic coefficients of circumferential nodal reactions, see Appendix XII.4.

For case 1, the soil is modelled as modified Cam clay, using the soil properties given in Table 9.3 and has an initial isotropic stress state with $\sigma_r'=\sigma_z'=\sigma_\theta'$=200 kPa. It is assumed to behave undrained during loading and this is simulated by specifying a high bulk modulus of the pore fluid, K_c, as for the first example. The soil fails under plane strain conditions and, since an associated flow rule is used, the Lode's angle at failure is 0°, see Section 7.12. For these conditions, i.e. the soil properties given in Table 9.3 and an initial isotropic stress state of 200 kPa, the undrained shear strength for the soil is 75.12 kPa, see Appendix VII.4. The shear strength of the interface elements is also assigned a value of 75.12 kPa. The analytical limit load for this problem is $11.94S_uD$ (Randolph and Houlsby (1984)), giving a value of 1794.07 kN. The results show that both parallel symmetry and no symmetry CFSAFEM analyses are identical and are within half a percent of the plane strain analysis, as shown in Figure 12.12. The limit load achieved is within one percent of the analytical solution.

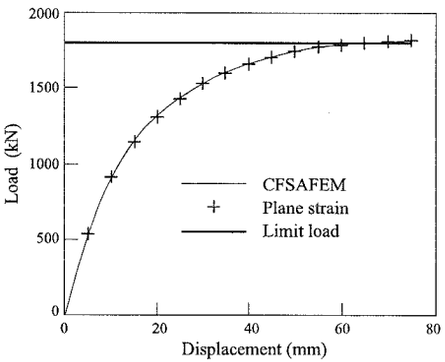

Figure 12.12: Load-displacement curves for pile section, case1

To illustrate the problems associated with the past implementations of the CFSAFEM, wherein only the parallel symmetry terms in the formulation are implemented, a further analysis, case 2, was performed. In case 2 the soil properties are the same as case 1, but there is a different initial stress regime: $\sigma_r'=\sigma_v'=\sigma_\theta'$ = 138.22 kPa and $\tau_{r\theta}$ = −69.0/r kPa, where r is the radial coordinate and an anticlockwise positive convention for θ is used.

The plane strain analyses required the initial stresses to be expressed in the global x_G and y_G directions, thus at any point the stresses defined above had to be rotated in accordance with their location. To keep the undrained shear strength and thus the limit load the same as in case 1, the pre-consolidation pressure, p_o', was set to 210 kPa. This also results in the soil adjacent to the pile being normally consolidated. The CFSAFEM analyses were carried out using the parallel symmetry and no symmetry options and the load displacement curves are shown in Figure 12.13. The no symmetry option agreed with the plane strain analysis, but

there was a significant error in the parallel symmetry analysis, which gave a stiffer response initially and reached a higher limit load. The limit loads from the no symmetry and plane strain analyses agreed with the analytical solution.

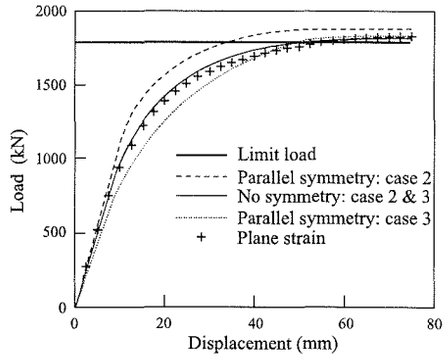

Figure 12.13: Load-displacement curves for pile section, case 2 and 3

Case 3 is similar to case 2, except that the shear stress is now applied in the opposite direction, i.e. $\tau_{r\theta}$ =69.0/r kPa. The load-displacement curve for the no symmetry analysis is the same as for case 2. There is still an error in the parallel symmetry analysis, however, the load deflection curve is now softer than for the no symmetry analyses and the same limit load is reached, see Figure 12.13. The errors in both case 2 and case 3 parallel symmetry analyses can be attributed to the symmetrically coupled nature of the soil. This is an example of a problem where a no symmetry analysis is required due to the material properties, even though the boundary conditions could be specified using parallel symmetry. These results emphasise the importance of the implementation of the no symmetry CFSAFEM formulation, which was able to analyse both case 2 and case 3 accurately.

A no symmetry analysis should be undertaken if there is any doubt about the validity of the symmetry criterion, discussed in Section 12.3.4, for the problem considered. The symmetry criterion is that the material elasto-plastic $[\boldsymbol{D}^{ep}]$ matrix has $[\boldsymbol{D}_{11}{}^{ep}]$ and $[\boldsymbol{D}_{22}{}^{ep}]$ terms that are symmetric functions of θ, and $[\boldsymbol{D}_{12}{}^{ep}]$ and $[\boldsymbol{D}_{21}{}^{ep}]$ terms that are asymmetric functions of θ, see Section 12.3.1 for the definition of $[\boldsymbol{D}^{ep}]$. Consider, for example, the $[\boldsymbol{D}^{ep}]$ matrix for case 2 of the normally consolidated material adjacent to the pile, at the beginning of the analysis:

$$[\boldsymbol{D}^{ep}]=[\boldsymbol{D}^{ep}]^0=\left[\begin{array}{cccc:cc} 48990 & 11640 & 11640 & 0 & -5402 & 0 \\ 11640 & 48990 & 11640 & 0 & -5402 & 0 \\ 11640 & 11640 & 48990 & 0 & -5402 & 0 \\ 0 & 0 & 0 & 18680 & -5402 & 0 \\ \hdashline -5402 & -5402 & -5402 & 0 & 1770 & 0 \\ 0 & 0 & 0 & 0 & 0 & 18680 \end{array}\right]=\left[\begin{array}{c:c} \boldsymbol{D}_{11} & \boldsymbol{D}_{12} \\ \hdashline \boldsymbol{D}_{21} & \boldsymbol{D}_{22} \end{array}\right]$$

This $[\boldsymbol{D}^{ep}]$ matrix is constant in the θ direction and hence is equal to the zeroth harmonic $[\boldsymbol{D}^{ep}]^0$. Thus the criterion that the $[\boldsymbol{D}_{12}{}^{ep}]$ and $[\boldsymbol{D}_{21}{}^{ep}]$ terms are asymmetrical functions of θ is not satisfied and a no symmetry CFSAFEM analysis is required. Similarly, for case 3 the $[\boldsymbol{D}^{ep}]$ matrix for the material adjacent to the pile is:

$$[\boldsymbol{D}^{ep}]=[\boldsymbol{D}^{ep}]^0=\left[\begin{array}{cccc:cc} 48990 & 11640 & 11640 & 0 & 5402 & 0 \\ 11640 & 48990 & 11640 & 0 & 5402 & 0 \\ 11640 & 11640 & 48990 & 0 & 5402 & 0 \\ 0 & 0 & 0 & 18680 & 5402 & 0 \\ \hdashline 5402 & 5402 & 5402 & 0 & 1770 & 0 \\ 0 & 0 & 0 & 0 & 0 & 18680 \end{array}\right]$$

Thus the criterion that the $[\boldsymbol{D}_{12}{}^{ep}]$ and $[\boldsymbol{D}_{21}{}^{ep}]$ terms are asymmetrical functions of θ is also not satisfied and a no symmetry CFSAFEM analysis is again required.

The $[\boldsymbol{D}^{ep}]$ matrix at the beginning of the case 1 analysis is:

$$[\boldsymbol{D}^{ep}]=[\boldsymbol{D}^{ep}]^0=\left[\begin{array}{cccc:cc} 29260 & -8091 & -8091 & 0 & 0 & 0 \\ -8091 & 29260 & -8091 & 0 & 0 & 0 \\ -8091 & -8091 & 29260 & 0 & 0 & 0 \\ 0 & 0 & 0 & 18670 & 0 & 0 \\ \hdashline 0 & 0 & 0 & 0 & 18670 & 0 \\ 0 & 0 & 0 & 0 & 0 & 18670 \end{array}\right]$$

Thus before loading the criterion for symmetrical uncoupling is satisfied and a parallel symmetry analysis can be used. The $[\boldsymbol{D}^{ep}]$ matrices for case 2 and case 3 also suggest that, during loading of case 1, the symmetry criterion is still satisfied. If the loading in case 1 causes a stress change at a point (r, θ), such that its stress state was equal to the normally consolidated stress state described in case 2, the stress state at point (r, $-\theta$) would be the normally consolidated stress state described in case 3. In this instance, the criteria for symmetrical uncoupling are still valid, since the $[\boldsymbol{D}_{11}{}^{ep}]$ and $[\boldsymbol{D}_{22}{}^{ep}]$ terms would be symmetric functions of θ and the $[\boldsymbol{D}_{12}{}^{ep}]$ and $[\boldsymbol{D}_{21}{}^{ep}]$ terms would be asymmetric functions of θ. Note that though the $[\boldsymbol{D}_{12}{}^{ep}]$ and $[\boldsymbol{D}_{21}{}^{ep}]$ terms may be non-zero at any particular θ coordinate, the zeroth and cosine harmonic coefficients of $[\boldsymbol{D}_{12}{}^{ep}]$ and $[\boldsymbol{D}_{21}{}^{ep}]$ are zero, and the symmetry criterion is satisfied.

12.5 The discrete Fourier series aided finite element method

12.5.1 Introduction

The discrete FSAFEM is similar to the continuous FSAFEM and reduces a large 3D global stiffness matrix into a series of smaller uncoupled submatrices. However, the discrete method considers a full 3D finite element mesh and employs a discrete Fourier series to represent the nodal values of force and displacement for the succession of nodes on each circumference, corresponding to each 2D axi-symmetric node. In contrast, the continuous method considers a 2D axi-symmetric mesh and employs a continuous Fourier series to represent the variation of force and displacement in the circumferential direction, for each 2D axi-symmetric node.

The first application of the discrete FSAFEM approach in geotechnical engineering was by Moore and Booker (1982) to develop a boundary element for use in deep tunnel problems. Subsequently, Lai and Booker (1991) used the method to study the behaviour of laterally loaded caissons and Runesson and Booker (1982 and 1983) used it in the study of the effects of consolidation and soil layering on soil behaviour.

12.5.2 Description of the discrete FSAFEM method

The discrete FSAFEM described in this section is for an analysis consisting of eight node constant strain brick elements. The method can be expanded to consider twenty node linear strain brick elements, and such an extension is presented in Lai and Booker (1991). The usual practice of using complex numbers in the formulation is avoided, in order to simplify the description.

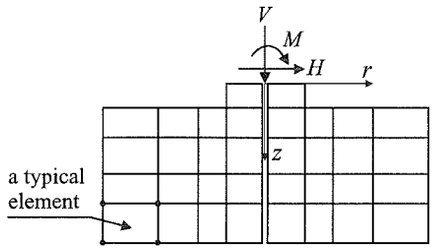

a) Elevation view of a typical vertical section

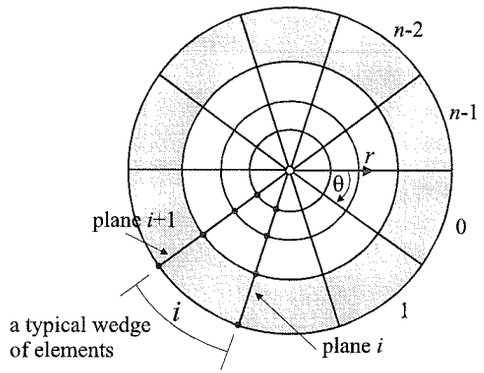

b) Plan view of a typical horizontal section

Figure 12.14: Finite element discretisation for discrete FSAFEM

The problem domain is discretised using a mesh of hexahedral finite elements consisting of n evenly spaced wedges around the circular boundary in the θ direction, as shown in Figure 12.14. This is similar to a finite element mesh for a

full 3D analysis. Consider the shaded annular ring of n elements. Let these elements be numbered from 0 to $n-1$ anticlockwise and let the vertical planes be numbered from 0 to $n-1$, such that the two vertical planes enclosing element i are plane i and $i+1$, see Figure 12.14. Thus the incremental displacements in element i are defined by the element shape functions and the incremental displacements on plane i (i.e. $\{\Delta \boldsymbol{u}_i\}$) and on plane $i+1$ (i.e. $\{\Delta \boldsymbol{u}_{i+1}\}$). The standard finite element formulation for linear elastic behaviour, see Chapter 2, expresses the incremental internal work, ΔW_i , done by element i, in terms of the incremental nodal displacements of the element, $\{\Delta \boldsymbol{u}_i\}$ and $\{\Delta \boldsymbol{u}_{i+1}\}$, and the stiffness matrix of the element $[\boldsymbol{K}_i]$ such that:

$$\Delta W_i = \left\{ \{\Delta \boldsymbol{u}_i\}^{\mathrm{T}} \quad \{\Delta \boldsymbol{u}_{i+1}\}^{\mathrm{T}} \right\} \left[\boldsymbol{K}_i \right] \begin{Bmatrix} \{\Delta \boldsymbol{u}_i\} \\ \{\Delta \boldsymbol{u}_{i+1}\} \end{Bmatrix} \tag{12.75}$$

Since the material properties are assumed not to vary in the θ direction, the stiffness matrices for each element are identical, i.e. $[\boldsymbol{K}_i] = [\boldsymbol{K}_{i+1}]$. Thus the internal incremental work done in the whole annular ring is:

$$\Delta W = \sum_{i=0}^{n-1} \left\{ \{\Delta \boldsymbol{u}_i\}^{\mathrm{T}} \quad \{\Delta \boldsymbol{u}_{i+1}\}^{\mathrm{T}} \right\} \left[\boldsymbol{K} \right] \begin{Bmatrix} \{\Delta \boldsymbol{u}_i\} \\ \{\Delta \boldsymbol{u}_{i+1}\} \end{Bmatrix} \tag{12.76}$$

The stiffness matrix, $[\boldsymbol{K}]$, can be partitioned into four submatrices $[\boldsymbol{X}]$, $[\boldsymbol{Y}]$, $[\boldsymbol{Y}]^{\mathrm{T}}$ and $[\boldsymbol{Z}]$, in accordance with the two parts of the element displacements $\{\Delta \boldsymbol{u}_i\}$ and $\{\Delta \boldsymbol{u}_{i+1}\}$. Hence, Equation (12.76) can be rewritten as:

$$\Delta W = \sum_{i=0}^{n-1} \left\{ \{\Delta \boldsymbol{u}_i\}^{\mathrm{T}} \quad \{\Delta \boldsymbol{u}_{i+1}\}^{\mathrm{T}} \right\} \begin{bmatrix} [\boldsymbol{X}] & [\boldsymbol{Y}] \\ [\boldsymbol{Y}]^{\mathrm{T}} & [\boldsymbol{Z}] \end{bmatrix} \begin{Bmatrix} \{\Delta \boldsymbol{u}_i\} \\ \{\Delta \boldsymbol{u}_{i+1}\} \end{Bmatrix} \tag{12.77}$$

Expanding Equation (12.77) and using the periodicity of the axi-symmetric geometry, where $\{\Delta \boldsymbol{u}_i\} = \{\Delta \boldsymbol{u}_{n+i}\}$, gives:

$$\Delta W = \sum_{i=0}^{n-1} \{\Delta \boldsymbol{u}_i\}^{\mathrm{T}} [\boldsymbol{X}] \{\Delta \boldsymbol{u}_i\} + \{\Delta \boldsymbol{u}_{i-1}\}^{\mathrm{T}} [\boldsymbol{Y}] \{\Delta \boldsymbol{u}_i\} + \{\Delta \boldsymbol{u}_{i+1}\}^{\mathrm{T}} [\boldsymbol{Y}]^{\mathrm{T}} \{\Delta \boldsymbol{u}_i\} + \{\Delta \boldsymbol{u}_i\}^{\mathrm{T}} [\boldsymbol{Z}] \{\Delta \boldsymbol{u}_i\} \tag{12.78}$$

Equation (12.78) is the equation solved directly in a full 3D analysis. This form of the finite element formulation yields a single large global stiffness matrix, $[\boldsymbol{K}_G]$, which relates the vector of all the incremental nodal loads, $\{\Delta \boldsymbol{R}\}$, to the vector of all the incremental nodal displacements, $\{\Delta \boldsymbol{d}\}$, as in Equation (12.3).

In the discrete Fourier series aided finite element method it is assumed that the incremental nodal displacement $\{\Delta \boldsymbol{u}_i\}$ on plane i can be evaluated from the discrete Fourier series which represents the nodal displacement for that pseudo 2D node:

$$\{\Delta \boldsymbol{u}_i\} = \frac{1}{\sqrt{n}} \sum_{k=0}^{n-1} \{\overline{U_k}\} \cos ik\alpha + \{\overline{\overline{U_k}}\} \sin ik\alpha \tag{12.79}$$

where:

$\{\overline{U_k}\}$ and $\{\overline{\overline{U_k}}\}$ are respectively vectors of the k^{th} cosine and sine harmonic coefficients of $\{\Delta \boldsymbol{u}\}$ expressed as a discrete Fourier series function;
$\alpha = 2\pi/n$.

Equation (12.79) only describes incremental nodal displacements and cannot be used to evaluate incremental displacements at intermediate values of θ, i.e. it is only valid for integer values of i. It is for this reason that the method is referred to as the 'discrete' FSAFEM.

Introducing expression (12.79) into Equation (12.78) transforms the problem from determining the unknown incremental nodal displacements to that of finding the Fourier coefficients:

$$\begin{aligned}
\Delta W = \sum_{i=0}^{n-1} & \left(\frac{1}{\sqrt{n}} \sum_{k=0}^{n-1} \{\overline{U_k}\} \cos ik\alpha + \{\overline{\overline{U_k}}\} \sin ik\alpha \right)^{\mathrm{T}} [X] \left(\frac{1}{\sqrt{n}} \sum_{l=0}^{n-1} \{\overline{U_l}\} \cos il\alpha + \{\overline{\overline{U_l}}\} \sin il\alpha \right) \\
+ & \left(\frac{1}{\sqrt{n}} \sum_{k=0}^{n-1} \{\overline{U_k}\} \cos(i-1)k\alpha + \{\overline{\overline{U_k}}\} \sin(i-1)k\alpha \right)^{\mathrm{T}} [Y] \left(\frac{1}{\sqrt{n}} \sum_{l=0}^{n-1} \{\overline{U_l}\} \cos il\alpha + \{\overline{\overline{U_l}}\} \sin il\alpha \right) \\
+ & \left(\frac{1}{\sqrt{n}} \sum_{k=0}^{n-1} \{\overline{U_k}\} \cos(i+1)k\alpha + \{\overline{\overline{U_k}}\} \sin(i+1)k\alpha \right)^{\mathrm{T}} [Y]^{\mathrm{T}} \left(\frac{1}{\sqrt{n}} \sum_{l=0}^{n-1} \{\overline{U_l}\} \cos il\alpha + \{\overline{\overline{U_l}}\} \sin il\alpha \right) \\
+ & \left(\frac{1}{\sqrt{n}} \sum_{k=0}^{n-1} \{\overline{U_k}\} \cos ik\alpha + \{\overline{\overline{U_k}}\} \sin ik\alpha \right)^{\mathrm{T}} [Z] \left(\frac{1}{\sqrt{n}} \sum_{l=0}^{n-1} \{\overline{U_l}\} \cos il\alpha + \{\overline{\overline{U_l}}\} \sin il\alpha \right)
\end{aligned} \tag{12.80}$$

The orthogonal properties of a discrete Fourier series are:

$$\begin{aligned}
\sum_{i=0}^{n-1} \cos ik\alpha \sin il\alpha &= 0 \\
\sum_{i=0}^{n-1} \cos ik\alpha \cos il\alpha &= 0 \text{ for } l \neq k\,, \; = n \text{ for } l = k \\
\sum_{i=0}^{n-1} \sin ik\alpha \sin il\alpha &= 0 \text{ for } l \neq k\,, \; = n \text{ for } l = k
\end{aligned} \tag{12.81}$$

Equations (12.81) are used to simplify Equation (12.80) such that:

$$\begin{aligned}
\Delta W = \sum_{l=0}^{n-1} & \{\overline{U_l}\}^{\mathrm{T}}[X]\{\overline{U_l}\} + \{\overline{\overline{U_l}}\}^{\mathrm{T}}[X]\{\overline{\overline{U_l}}\} \\
+ & \{\overline{U_l}\}^{\mathrm{T}}[Y]\{\overline{U_l}\}\cos l\alpha + \{\overline{\overline{U_l}}\}^{\mathrm{T}}[Y]\{\overline{\overline{U_l}}\}\cos l\alpha - \{\overline{U_l}\}^{\mathrm{T}}[Y]\{\overline{\overline{U_l}}\}\sin l\alpha + \{\overline{\overline{U_l}}\}^{\mathrm{T}}[Y]\{\overline{U_l}\}\sin l\alpha \\
+ & \{\overline{U_l}\}^{\mathrm{T}}[Y]^{\mathrm{T}}\{\overline{U_l}\}\cos l\alpha + \{\overline{\overline{U_l}}\}^{\mathrm{T}}[Y]^{\mathrm{T}}\{\overline{\overline{U_l}}\}\cos l\alpha + \{\overline{U_l}\}^{\mathrm{T}}[Y]^{\mathrm{T}}\{\overline{\overline{U_l}}\}\sin l\alpha - \{\overline{\overline{U_l}}\}^{\mathrm{T}}[Y]^{\mathrm{T}}\{\overline{U_l}\}\sin l\alpha \\
+ & \{\overline{U_l}\}^{\mathrm{T}}[Z]\{\overline{U_l}\} + \{\overline{\overline{U_l}}\}^{\mathrm{T}}[Z]\{\overline{\overline{U_l}}\}
\end{aligned} \tag{12.82}$$

The internal incremental work equation has been divided into n independent expressions, one expression for each harmonic order, thus the large global stiffness matrix has been uncoupled into n submatrices, as in Equation (12.4), i.e. the equations are harmonically uncoupled. The stiffness matrix $[\boldsymbol{K}_i]$ for any harmonic

order, i, can be obtained by substituting $l = i$ in Equation (12.82). However, for each harmonic order, both the sine and cosine coefficients of load and displacement have to be solved simultaneously. This is similar to the symmetrically coupled continuous FSAFEM, as shown in Equation (12.16).

Symmetric uncoupling is possible with the discrete method for an isotropic linear elastic material. This is achieved by first regrouping the terms in Equation (12.82) as:

$$\begin{aligned}
\Delta W = \sum_{l=0}^{n-1} & \{\overline{U_l}\}^{\mathrm{T}} ([X] + [Y]\cos l\alpha + [Y]^{\mathrm{T}}\cos l\alpha + [Z])\{\overline{U_l}\} \\
+ & \{\overline{\overline{U_l}}\}^{\mathrm{T}} ([X] + [Y]\cos l\alpha + [Y]^{\mathrm{T}}\cos l\alpha + [Z])\{\overline{\overline{U_l}}\} \\
- & \{\overline{U_l}\}^{\mathrm{T}} ([Y]\sin l\alpha - [Y]^{\mathrm{T}}\sin l\alpha)\{\overline{\overline{U_l}}\} \\
+ & \{\overline{\overline{U_l}}\}^{\mathrm{T}} ([Y]\sin l\alpha - [Y]^{\mathrm{T}}\sin l\alpha)\{\overline{U_l}\}
\end{aligned} \tag{12.83}$$

The incremental nodal displacements, and accordingly the harmonic coefficients of incremental displacement, have three components, a radial, a circumferential and a vertical component. Thus the two vectors of nodal harmonic displacements, $\{\overline{U_k}\}$ and $\{\overline{\overline{U_k}}\}$, can each be divided into two sub-vectors, a radial and vertical component sub vector, and a circumferential component sub-vector:

$$\{\overline{U_k}\} = \begin{Bmatrix} \{\overline{U_k^{rz}}\} \\ \{\overline{U_k^{\theta}}\} \end{Bmatrix} \text{ and } \{\overline{\overline{U_k}}\} = \begin{Bmatrix} \{\overline{\overline{U_k^{rz}}}\} \\ \{\overline{\overline{U_k^{\theta}}}\} \end{Bmatrix} \tag{12.84}$$

Expanding matrices $[X]$, $[Y]$, and $[Z]$ accordingly, Equation (12.83) can be written in the following form:

$$\begin{aligned}
\Delta W = \sum_{l=0}^{n-1} & \begin{Bmatrix} \{\overline{U_l^{rz}}\} \\ \{\overline{U_l^{\theta}}\} \end{Bmatrix}^{\mathrm{T}} \left(\begin{bmatrix} [X_{11}][X_{12}] \\ [X_{21}][X_{22}] \end{bmatrix} + \begin{bmatrix} [Y_{11}][Y_{12}] \\ [Y_{21}][Y_{22}] \end{bmatrix} \cos l\alpha + \begin{bmatrix} [Y_{11}][Y_{12}] \\ [Y_{21}][Y_{22}] \end{bmatrix}^{\mathrm{T}} \cos l\alpha + \begin{bmatrix} [Z_{11}][Z_{12}] \\ [Z_{21}][Z_{22}] \end{bmatrix} \right) \begin{Bmatrix} \{\overline{U_l^{rz}}\} \\ \{\overline{U_l^{\theta}}\} \end{Bmatrix} \\
+ & \begin{Bmatrix} \{\overline{\overline{U_l^{rz}}}\} \\ \{\overline{\overline{U_l^{\theta}}}\} \end{Bmatrix}^{\mathrm{T}} \left(\begin{bmatrix} [X_{11}][X_{12}] \\ [X_{21}][X_{22}] \end{bmatrix} + \begin{bmatrix} [Y_{11}][Y_{12}] \\ [Y_{21}][Y_{22}] \end{bmatrix} \cos l\alpha + \begin{bmatrix} [Y_{11}][Y_{12}] \\ [Y_{21}][Y_{22}] \end{bmatrix}^{\mathrm{T}} \cos l\alpha + \begin{bmatrix} [Z_{11}][Z_{12}] \\ [Z_{21}][Z_{22}] \end{bmatrix} \right) \begin{Bmatrix} \{\overline{\overline{U_l^{rz}}}\} \\ \{\overline{\overline{U_l^{\theta}}}\} \end{Bmatrix} \\
- & \begin{Bmatrix} \{\overline{U_l^{rz}}\} \\ \{\overline{U_l^{\theta}}\} \end{Bmatrix}^{\mathrm{T}} \left(\begin{bmatrix} [Y_{11}][Y_{12}] \\ [Y_{21}][Y_{22}] \end{bmatrix} \sin l\alpha - \begin{bmatrix} [Y_{11}][Y_{12}] \\ [Y_{21}][Y_{22}] \end{bmatrix}^{\mathrm{T}} \sin l\alpha \right) \begin{Bmatrix} \{\overline{\overline{U_l^{rz}}}\} \\ \{\overline{\overline{U_l^{\theta}}}\} \end{Bmatrix} \\
+ & \begin{Bmatrix} \{\overline{\overline{U_l^{rz}}}\} \\ \{\overline{\overline{U_l^{\theta}}}\} \end{Bmatrix}^{\mathrm{T}} \left(\begin{bmatrix} [Y_{11}][Y_{12}] \\ [Y_{21}][Y_{22}] \end{bmatrix} \sin l\alpha - \begin{bmatrix} [Y_{11}][Y_{12}] \\ [Y_{21}][Y_{22}] \end{bmatrix}^{\mathrm{T}} \sin l\alpha \right) \begin{Bmatrix} \{\overline{U_l^{rz}}\} \\ \{\overline{U_l^{\theta}}\} \end{Bmatrix}
\end{aligned} \tag{12.85}$$

Each set of wedge shaped elements defined in the mesh is geometrically symmetrical about a constant θ plane through the middle of it. For an isotropic

elastic material this implies that the element stiffness matrix has a symmetry such that:

$$[X] + [Z] = 2\begin{bmatrix} [X_{11}] & 0 \\ 0 & [X_{22}] \end{bmatrix}$$

$$[Y] + [Y]^{\mathrm{T}} = 2\begin{bmatrix} [Y_{11}] & 0 \\ 0 & [Y_{22}] \end{bmatrix} \qquad (12.86)$$

$$[Y] - [Y]^{\mathrm{T}} = 2\begin{bmatrix} 0 & -[Y_{21}]^{\mathrm{T}} \\ [Y_{21}] & 0 \end{bmatrix}$$

Equations (12.86) are used to simplify Equation (12.85):

$$\begin{aligned} \Delta W = 2\sum_{l=0}^{n-1} & \begin{Bmatrix} \{\overline{U_l^{rz}}\} \\ \{\overline{U_l^{\theta}}\} \end{Bmatrix}^{\mathrm{T}} \left(\begin{bmatrix} [X_{11}] & 0 \\ 0 & [X_{22}] \end{bmatrix} + \begin{bmatrix} [Y_{11}] & 0 \\ 0 & [Y_{22}] \end{bmatrix} \cos l\alpha \right) \begin{Bmatrix} \{\overline{U_l^{rz}}\} \\ \{\overline{U_l^{\theta}}\} \end{Bmatrix} \\ + & \begin{Bmatrix} \{\overline{\overline{U_l^{rz}}}\} \\ \{\overline{\overline{U_l^{\theta}}}\} \end{Bmatrix}^{\mathrm{T}} \left(\begin{bmatrix} [X_{11}] & 0 \\ 0 & [X_{22}] \end{bmatrix} + \begin{bmatrix} [Y_{11}] & 0 \\ 0 & [Y_{22}] \end{bmatrix} \cos l\alpha \right) \begin{Bmatrix} \{\overline{\overline{U_l^{rz}}}\} \\ \{\overline{\overline{U_l^{\theta}}}\} \end{Bmatrix} \\ + & \begin{Bmatrix} \{\overline{U_l^{rz}}\} \\ \{\overline{U_l^{\theta}}\} \end{Bmatrix}^{\mathrm{T}} \left(\begin{bmatrix} 0 & [Y_{21}]^{\mathrm{T}} \\ -[Y_{21}] & 0 \end{bmatrix} \sin l\theta \right) \begin{Bmatrix} \{\overline{\overline{U_l^{rz}}}\} \\ \{\overline{\overline{U_l^{\theta}}}\} \end{Bmatrix} \\ + & \begin{Bmatrix} \{\overline{\overline{U_l^{rz}}}\} \\ \{\overline{\overline{U_l^{\theta}}}\} \end{Bmatrix}^{\mathrm{T}} \left(\begin{bmatrix} 0 & -[Y_{21}]^{\mathrm{T}} \\ [Y_{21}] & 0 \end{bmatrix} \sin l\theta \right) \begin{Bmatrix} \{\overline{U_l^{rz}}\} \\ \{\overline{U_l^{\theta}}\} \end{Bmatrix} \end{aligned} \qquad (12.87)$$

Parallel displacement terms can be obtained by mixing cosine coefficients of radial and vertical displacement with sine coefficients of circumferential displacement. Similarly, orthogonal displacements are sine coefficients of radial and vertical displacement and cosine coefficients of circumferential displacement. Using these terms Equation (12.87) can be rearranged such that:

$$\begin{aligned} \Delta W = 2\sum_{l=0}^{n-1} & \begin{Bmatrix} \{\overline{U_l^{rz}}\} \\ \{\overline{\overline{U_l^{\theta}}}\} \end{Bmatrix}^{\mathrm{T}} \begin{bmatrix} [X_{11}]+[Y_{11}]\cos l\alpha & [Y_{21}]^{\mathrm{T}}\sin l\alpha \\ [Y_{21}]\sin l\alpha & [X_{22}]+[Y_{22}]\cos l\alpha \end{bmatrix} \begin{Bmatrix} \{\overline{U_l^{rz}}\} \\ \{\overline{\overline{U_l^{\theta}}}\} \end{Bmatrix} \\ + & \begin{Bmatrix} \{\overline{\overline{U_l^{rz}}}\} \\ -\{\overline{U_l^{\theta}}\} \end{Bmatrix}^{\mathrm{T}} \begin{bmatrix} [X_{11}]+[Y_{11}]\cos l\alpha & [Y_{21}]^{\mathrm{T}}\sin l\alpha \\ [Y_{21}]\sin l\alpha & [X_{22}]+[Y_{22}]\cos l\alpha \end{bmatrix} \begin{Bmatrix} \{\overline{\overline{U_l^{rz}}}\} \\ -\{\overline{U_l^{\theta}}\} \end{Bmatrix} \end{aligned} \qquad (12.88)$$

The parallel displacement terms have been uncoupled from the orthogonal displacement terms and the stiffness matrix for both set of terms is the same. This

is similar to the symmetrically uncoupled continuous FSAFEM stiffness matrix shown in Equation (12.17). Thus the internal incremental work equation now consists of $2n$ uncoupled vectors of harmonic incremental displacement coefficients and n stiffness matrices. There are two vectors and one stiffness matrix for each harmonic order. The stiffness matrix for the i^{th} harmonic order is obtained by substituting i for l in Equation (12.88).

The externally applied incremental loads can also be expressed as a discrete Fourier series. Parallel loads can be obtained by mixing cosine coefficients of radial and vertical loads with sine coefficients of circumferential load. Similarly, orthogonal loads can be obtained, for example for the k^{th} harmonic:

$$\begin{Bmatrix} \{\Delta\overline{R_k^{rz}}\} \\ \{\Delta\overline{\overline{R_k^{\theta}}}\} \end{Bmatrix} \text{ and } \begin{Bmatrix} \{\Delta\overline{\overline{R_k^{rz}}}\} \\ -\{\Delta\overline{R_k^{\theta}}\} \end{Bmatrix}$$

The principle of virtual work is then used to obtain the system equations which consists of $2n$ separate equations (two equations for each harmonic order), for example for the k^{th} harmonic:

$$\begin{Bmatrix} \{\Delta\overline{R_k^{rz}}\} \\ \{\Delta\overline{\overline{R_k^{\theta}}}\} \end{Bmatrix} = 2\begin{bmatrix} [X_{11}]+[Y_{11}]\cos k\alpha & [Y_{21}]^{\mathrm{T}}\sin k\alpha \\ [Y_{21}]\sin k\alpha & [X_{22}]+[Y_{22}]\cos k\alpha \end{bmatrix} \begin{Bmatrix} \{\overline{U_k^{rz}}\} \\ \{\overline{\overline{U_k^{\theta}}}\} \end{Bmatrix}$$

and

$$\begin{Bmatrix} \{\Delta\overline{\overline{R_k^{rz}}}\} \\ -\{\Delta\overline{R_k^{\theta}}\} \end{Bmatrix} = 2\begin{bmatrix} [X_{11}]+[Y_{11}]\cos k\alpha & [Y_{21}]^{\mathrm{T}}\sin k\alpha \\ [Y_{21}]\sin k\alpha & [X_{22}]+[Y_{22}]\cos k\alpha \end{bmatrix} \begin{Bmatrix} \{\overline{\overline{U_k^{rz}}}\} \\ -\{\overline{U_k^{\theta}}\} \end{Bmatrix} \qquad (12.89)$$

Thus the large global stiffness matrix has been harmonically and symmetrically uncoupled. The procedure outlined above is for a linear elastic analysis. The procedure can be extended to consider nonlinear behaviour by combining the linear elastic formulation with a solution strategy which continually adjusts the right hand side of the governing finite element equations, e.g. visco-plastic or MNR methods.

12.6 Comparison between the discrete and the continuous FSAFEM

A key difference between the discrete and the continuous FSAFEM method is the manner in which the variations in forces and displacements in the circumferential direction are described.

The discrete method notionally considers a full three dimensional finite element mesh defined in a cylindrical coordinate system. Thus the force and displacement distribution in the circumferential direction is described using the standard finite element approximation, i.e. the shape function of the pertinent element. Lai and Booker (1991) state that 'the discrete method gives an exact representation (of displacements) after a finite number of terms'. This statement is misleading since it wrongly implies that the correct displacement field can be represented after a

finite number of Fourier series terms. The discrete method uses a discrete Fourier series to represent nodal displacements and is able to exactly represent any variation of nodal displacements in the circumferential direction. However, in general these displacements would not represent the correct displacement field exactly, due to the finite element approximation, and the solution accuracy would increase with the number of nodes used.

The continuous FSAFEM uses a 2D axi-symmetric mesh and represents the variation of nodal displacements and loads in the circumferential direction as a continuous Fourier series. The accuracy of this representation depends on the number of harmonic coefficients used in an analysis. For the special case of a linear elastic continuous FSAFEM, the number of harmonics required in an analysis is equal to the number of harmonics required to represent the boundary conditions. In a discrete FSAFEM the distribution of nodal variables in the θ direction is represented using the nodal values and shape functions of the appropriate annular ring of 3D brick elements. These nodal values are expressed as a Fourier series which has the same number of coefficients as there are nodes. Increasing the number of coefficients in a nonlinear discrete FSAFEM analysis increases the number of nodes in the θ direction and increases the solution accuracy. Thus for both the continuous and discrete nonlinear FSAFEM the choice regarding the number of harmonics used in an analysis is based on a trade off between the solution accuracy desired and the computer resources required.

To assess the accuracy of the two FSAFEM, their ability to represent the distribution of radial stress around a pile is considered. In particular, the relationship between the number of harmonics or brick elements used and the accuracy with which the resulting stress distribution can represent the chosen distribution is examined.

The stress distribution around a laterally loaded pile was presented by Williams and Parry (1984), using measurements from a model pile test. Only the variation of radial stress around the pile (θ direction) is studied and the variation in the radial or vertical direction is not considered, thus the problem is one dimensional. The study compared the continuous FSAFEM, the discrete FSAFEM with eight noded constant strain brick elements and the discrete FSAFEM with twenty noded linear strain brick elements.

As noted in Section 12.4.3 for the continuous FSAFEM, the number of sampling points in the θ direction is equal to the number of harmonic coefficients used in the FSAFEM analysis, and the harmonic coefficients are obtained from the sampling point stresses using the fitted method. The sampling points are equispaced in the θ direction and are located at θ coordinates $i\alpha$, where:

$\alpha = 2\pi/n_s$;
i is an integer and $0 \le i \le n_s - 1$;
n_s is equal to the number of sampling points.

It is assumed that the stresses at the sampling points are correct, i.e. they are equal to the measured stresses shown in Figure 12.15. Thus the Fourier series

representation for radial stress is correct at the sampling points, but could be in error between sampling points.

In a discrete FSAFEM analysis with constant strain elements, the elements have a constant width in the θ direction. If the number of coefficients is equal to n, the number of nodes is also equal to n and they are located at θ coordinates $i\alpha$. Due to the linear nature of the displacements, the stresses and strains within an element are constant. It is assumed that these stresses represent the stress state at the centre of the element. This is similar to the assumption made regarding the sampling point stresses for a continuous FSAFEM analysis.

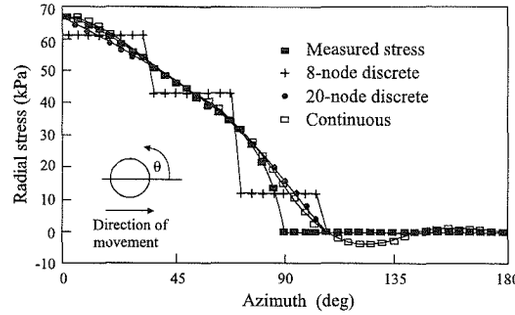

Figure 12.15: Postulated and measured stress distribution, $n = 10$

In a discrete FSAFEM analysis with linear strain elements, the elements still have a constant width and the nodes are still equispaced in the θ direction. Similarly, if the number of coefficients in a discrete FSAFEM analysis is equal to n, the number of elements is also equal to n. However, there would now be $2n$ nodes, since these elements have mid-side nodes. Due to the quadratic nature of the displacements, the stresses and strains within an element are linear. It is assumed that the stresses at the end nodes are correct and there is a linear stress distribution between them. The stresses at the mid-side node depend only on the stresses at the end nodes.

The stress distribution from each of the three types of analyses are presented in Figure 12.15, for n equal to ten. The difference between the desired stress and the stress from these analyses is a measure of the error associated with these analyses. This error, Err, is quantified using the equation:

$$Err = \frac{\int_{-\pi}^{\pi} \sqrt{\left(F(\theta) - f(\theta)\right)^2}\, d\theta}{\int_{-\pi}^{\pi} f(\theta)\, d\theta} \cdot 100\% \qquad (12.90)$$

where:

$f(\theta)$ = the measured stress distribution;
$F(\theta)$ = the postulated stress distribution.

The value of Err associated with each type of analysis is presented in Table 12.2. For any value of n the continuous method and linear strain discrete method have similar accuracies and the constant strain discrete method is substantially less accurate. However, there are n unknown harmonic coefficients in the continuous method and $2n$ unknown nodal values in the linear strain discrete method. Hence,

the stiffness matrix associated with the linear strain discrete method is larger than for the corresponding continuous method. This would result in increased computer resources required for an analysis. Thus it is concluded that the continuous FSAFEM is probably the most efficient method.

Table 12.2: Summary of errors in the representation of radial stress around pile

Number of harmonic terms	Discrete Fourier series using 8 node elements	Discrete Fourier series using 20 node elements	Continuous Fourier series
2	100.0 %	48.5 %	47.7 %
5	30.9 %	21.9 %	19.4 %
8	14.5 %	10.2 %	17.8 %
10	17.5 %	6.8 %	7.8 %

Some authors (e.g. Lai and Booker (1991)) have stated that the continuous FSAFEM could suffer from 'difficulties associated with summing a large number of Fourier terms, e.g. the Gibb's phenomenon'. However, statements like this are ambiguous since the Gibb's phenomenon does not suggest such a problem. The Gibb's phenomenon states that if a Fourier series is used to represent a function which has a discontinuity, the magnitude of the maximum error, *Err*, of the Fourier series representation in the vicinity of the discontinuity is largely independent of the number of Fourier terms used. This is illustrated in Figure 12.16 for a square wave. The error *Err* is approximately equal to 0.09 times the magnitude of the discontinuity. However, while increasing the number of Fourier terms does not reduce the magnitude of *Err*, it does reduce the total error in the vicinity of the discontinuity, i.e. the area between the Fourier series and the square wave is reduced. The Gibb's phenomenon would only be relevant in a finite element analysis if a discontinuity in displacements existed in the circumferential direction, and this is not feasible in a conventional finite element analysis. It would only be possible if non axi-symmetric interface elements were present, and it is unclear how either the discrete FSAFEM or continuous FSAFEM could incorporate such behaviour. This criticism of the continuous FSAFEM is therefor not valid.

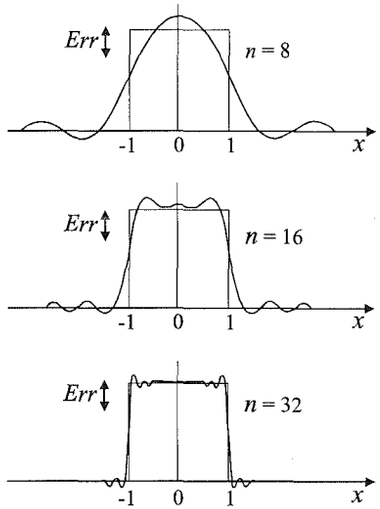

n is the number of harmonic terms used in the Fourier series

Figure 12.16: Fourier series approximation of a square wave

Lai and Booker (1991) have also stated that 'problems concerning conformity of elements is overcome' by using the discrete method rather than the continuous method. This statement is not clear: the continuous method should have no element conformity problems since the displacements at a boundary, calculated from either element sharing that same boundary, are identical, if isoparametric elements are used. However, both methods can be adapted to undertake an analysis consisting of both full 3D elements and pseudo 2D FSAFEM elements, e.g. a core consisting of full 3D elements surrounded by layers of pseudo 2D elements. In this case the displacements between nodes at the boundary, which is between the pseudo 2D discrete Fourier elements and the 3D elements, are described by both types of elements using the finite element approximation, and thus they match. The displacements in the θ direction for a continuous FSAFEM analysis are described by a continuous Fourier series. Thus at the boundary between the pseudo 2D continuous Fourier elements and the 3D elements, the displacements are equal at the nodal points of the 3D mesh, but do not match at intermediate values of θ.

A further comparison between the continuous and discrete FSAFEM, and of the influence of the number of Fourier coefficients employed in each method, can be made using results for the horizontal disk problem described in Section 12.4.7.2. Ganendra (1993) performed continuous FSAFEM analyses of this problem using the Authors' finite element code (ICFEP). He used the same boundary conditions as described in Section 12.4.7.2, but modelled the soil as a Tresca material, with a shear modulus, G, of 3000 kPa, a Poisson's ratio, μ, equal 0.49 and an undrained shear strength, S_u, of 30 kPa. Two sets of analyses were performed, one assuming a smooth, the other a rough, interface between rigid disk and soil. Each set of analyses consisted of a number of separate analyses performed with a different number of Fourier harmonics. The results are presented in Figure 12.17 in the form of normalised ultimate load, $P_u / S_u D$ (where P_u is the ultimate load and D is the diameter of the disk), against number of harmonics used in the analysis. Lai (1989) also analysed this same problem, but used the discrete FSAFEM. His results are also shown in Figure 12.17. The

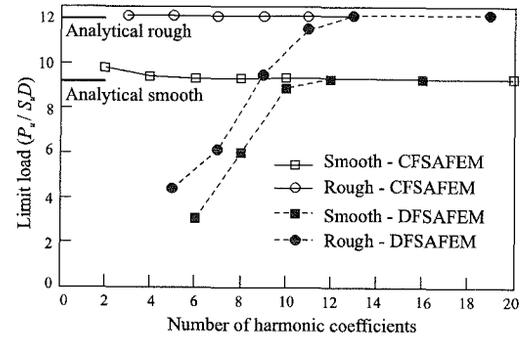

Figure 12.17: Limit load vs. number of harmonics for a pile section

analytical solutions for the limit loads for the rough and smooth interface cases are $11.945S_uD$ and $9.14S_uD$ respectively (Randolph and Houlsby (1984)). The rough solution is exact, while the smooth solution is a lower bound. Inspection of Figure 12.17 indicates that the continuous FSAFEM is not strongly influenced by the number of harmonics used, and reasonable accuracy is obtained if five or more harmonic terms are used. The discrete method is very sensitive to the number of harmonics employed, and if less than ten harmonics are used significant errors are obtained, e.g. the error is greater than 65% if 6 harmonics are used. These results are indicative of the number of harmonics required to analyse a laterally loaded pile accurately and suggest that (i) the continuous method is more economical in terms of number of harmonics required and (ii) large errors can be obtained using the discrete method if an insufficient number of harmonics are used.

12.7 Comparison of CFSAFEM and full 3D analysis

To investigate the benefits of the CFSAFEM over full 3D analysis, a rough rigid circular footing under horizontal and inclined loading has been analysed, using both approaches, see Figure 12.18. The soil is assumed to behave according to a Tresca yield criterion, with E=10000 kPa, μ=0.45 and S_u=100 kPa. The mesh for the 3D analysis is shown in Figures 12.19a and 12.19b. As there is a vertical plane of symmetry, only one half of the problem requires analysis. To be consistent, the CFSAFEM analysis used a 2D finite element mesh which was the same as the vertical section of the 3D mesh shown in Figure 12.19b. Due to the symmetry mentioned above, the CFSAFEM was run using the parallel symmetry option.

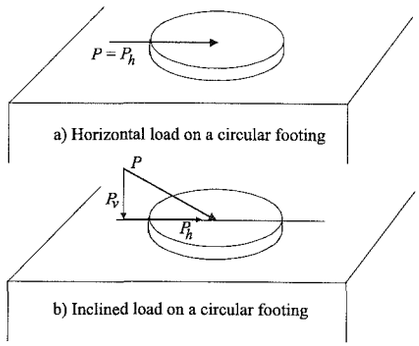

Figure 12.18: Loading schemes for circular footing

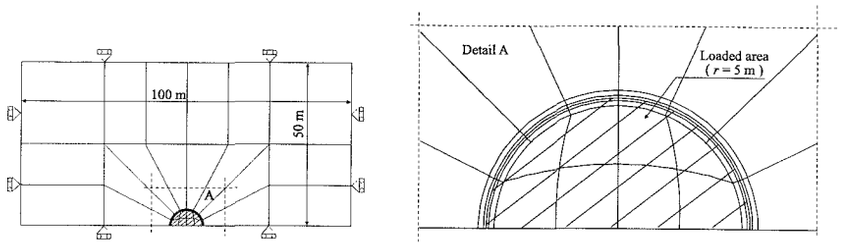

Figure 12.19a: Horizontal cross-section of a 3D mesh for a circular footing

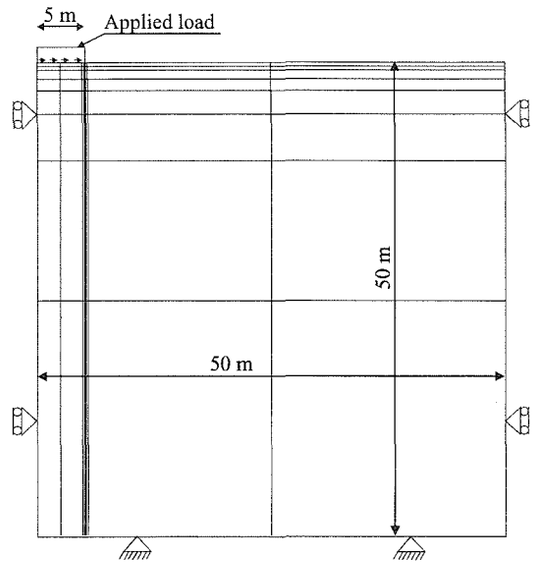

Figure 12.19b: Vertical cross-section of a 3D mesh for a circular footing; also a mesh for CFSAFEM analysis

The footing is displaced horizontally and the horizontal reaction on the foundation noted. The results from the analyses, expressed in terms of the horizontal force on the footing versus horizontal displacement, are given in Figure 12.20. Results from a full 3D analysis and three CFSAFEM analyses, each with a different number of harmonics, are given. Also noted on the figure are the run times for each analysis. It can be seen that all analyses produce very similar results, with a maximum difference of only 1%. However, the CFSAFEM have much smaller run times. For example, the CFSAFEM with five harmonics required approximately a tenth of the time of the full 3D analysis.

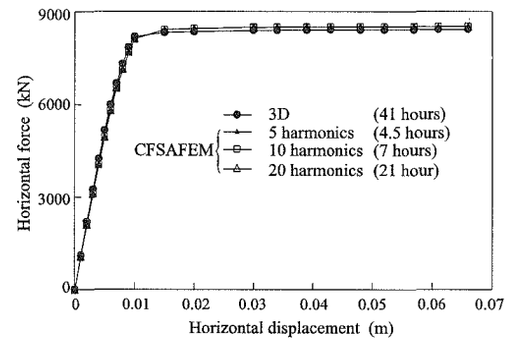

Figure 12.20: Load-displacement curves for a horizontally loaded circular footing

A second series of analyses was then performed in which the footing was displaced downwards, at an angle of 45° to the horizontal. As the displacement

increased, both the horizontal and vertical loads on the foundation were recorded. The results are shown in Figure 12.21, in the form of horizontal load plotted against horizontal displacement and vertical load plotted against vertical displacement. Results are given for a full 3D analysis and for a CFSAFEM analysis with 10 harmonics. The run times are also noted on the figure. As with the horizontal loading, both analyses give similar predictions and again the CFSAFEM is much faster. These two examples clearly show that the CFSAFEM is more economical than a full 3D analysis.

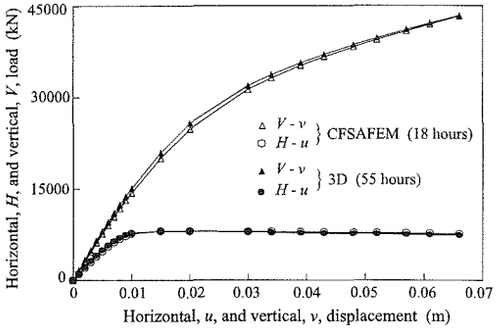

Figure 12.21: Load-displacement curves for a circular footing under inclined loading

12.8 Summary

1. The continuous Fourier series aided finite element method (CFSAFEM) has been described in detail in this chapter. This method provides a way of reducing the computer resources required to analyse certain 3D problems. In this approach a standard finite element discretisation is used in two dimensions, while displacements are assumed to vary according to a continuous Fourier series in the third dimension. In this chapter the method is applied to problems having an axi-symmetric geometry, but non axi-symmetric distribution of soil properties and/or loading conditions. A 2D finite element discretisation is used in the *r-z* plane, with displacements varying according to a Fourier series in the θ direction.
2. A new formulation for the CFSAFEM for nonlinear material behaviour has been described. A general approach has been adopted and no symmetry constraints have been imposed. The definitions of, and requirements for, *symmetrical* and *harmonic* coupling have been established and the associated computational savings identified.
3. The definitions of parallel and orthogonal symmetry have been given and the requirements for such symmetries to be valid have been discussed. One of the requirements concerns the nature of the constitutive model. It is shown how subtle changes in the constitutive behaviour can lead to violation of these requirements and hence to erroneous results. It is advised that facilities to undertake no symmetry, as opposed to parallel or orthogonal symmetry analysis, are available within the computer code being used.
4. Extension of the CFSAFEM to include interface elements, the bulk compressibility of the pore fluid and coupled consolidation has been presented.

5. An alternative to the continuous FSAFEM is the discrete FSAFEM. The theory behind this approach and the difference between the two methods have been discussed. The discrete method requires a full three dimensional finite element mesh defined in cylindrical coordinates. The distribution of nodal variables in the θ direction is represented using the nodal values and shape functions of the appropriate annular ring of 3D brick elements. These nodal values are expressed as a discrete Fourier series which has the same number of coefficients as there are nodes.
6. Comparison of the continuous and discrete FSAFEM indicates that the former method is likely to be more economical. However, each method has its advantages.
7. Comparison of CFSAFEM and full 3D analysis shows that the former requires considerably less computer resources to obtain answers of the same accuracy. For the examples considered, savings in computer time are up to an order of magnitude.

Appendix XII.1: Harmonic coefficients of force from harmonic point loads

The applied incremental load, ΔF (component of force per unit circumference), at any angle θ is written in the form of a Fourier series:

$$\Delta F = \Delta F^0 + \sum_{k=1}^{L_c} \Delta \overline{F^k} \cos k\theta + \Delta \overline{\overline{F^k}} \sin k\theta \qquad \text{(XII.1)}$$

Let the associated component of incremental nodal displacement, Δd, be described using a Fourier series:

$$\Delta d = \Delta d^0 + \sum_{k=1}^{L_c} \Delta \overline{d^k} \cos k\theta + \Delta \overline{\overline{d^k}} \sin k\theta \qquad \text{(XII.2)}$$

Thus the work done is:

$$\Delta W = \int_{-\pi}^{\pi} \Delta d \, \Delta F \; r \, \mathrm{d}\theta \qquad \text{(XII.3)}$$

where r is the radius of the circle described by the location of the node. Substituting the Fourier series into the work equation gives:

$$\Delta W = \int_{-\pi}^{\pi} \left(\Delta d^0 + \sum_{k=1}^{L_c} \Delta \overline{d^k} \cos k\theta + \Delta \overline{\overline{d^k}} \sin k\theta \right) \left(\Delta F^0 + \sum_{k=1}^{L_c} \Delta \overline{F^k} \cos k\theta + \Delta \overline{\overline{F^k}} \sin k\theta \right) r \, \mathrm{d}\theta \qquad \text{(XII.4)}$$

Carrying out the integral and using the orthogonal properties of the Fourier series gives:

$$\Delta W = 2\pi r \, \Delta d^0 \Delta F^0 + \pi r \sum_{k=1}^{L_c} \Delta \overline{d^k} \, \Delta \overline{F^k} + \Delta \overline{\overline{d^k}} \, \Delta \overline{\overline{F^k}} \qquad \text{(XII.5)}$$

Using the principle of virtual work, the contributions to the harmonic coefficients of incremental nodal force, ΔR, used in the right hand side of the FSAFEM equations, are:

$$\begin{aligned} \Delta R^0 &= 2\pi r\,\Delta F^0 && \text{for the } 0^{\text{th}} \text{ harmonic;} \\ \Delta \overline{R^k} &= \pi r\,\Delta \overline{F^k} && \text{for the } k^{\text{th}} \text{ cosine harmonic;} \\ \Delta \overline{\overline{R^k}} &= \pi r\,\Delta \overline{\overline{F^k}} && \text{for the } k^{\text{th}} \text{ sine harmonic.} \end{aligned} \qquad \text{(XII.6)}$$

Appendix XII.2: Obtaining the harmonics of force from harmonic boundary stresses

Boundary stresses are prescribed over an axi-symmetric surface defined by a section of the finite element mesh boundary. These stresses can be resolved into global r, z and θ directions to obtain σ_r, σ_z, σ_θ, τ_{rz}, $\tau_{r\theta}$ and $\tau_{z\theta}$ respectively. These stresses can be expressed as a Fourier series, and the variation of each harmonic coefficient along the boundary is described, for example, with a cubic spline function. Thus for any component of incremental stress, $\Delta\sigma$, at any point in the r-z plane, a Fourier series can be written such that:

$$\Delta\sigma = \Delta\sigma^0 + \sum_{k=1}^{L} \Delta\overline{\sigma^k} \cos k\theta + \Delta\overline{\overline{\sigma^k}} \sin k\theta \qquad \text{(XII.7)}$$

The displacement over the axi-symmetric surface is described using the shape functions of the appropriate finite elements and Fourier series of the nodal displacement of the element. Thus for $\Delta\sigma$ the corresponding component of incremental displacement, Δd, can be written as:

$$\Delta d = \sum_{i=1}^{n} N_i \left(\Delta d_i^0 + \sum_{k=1}^{L} \Delta\overline{d_i^k} \cos k\theta + \Delta\overline{\overline{d_i^k}} \sin k\theta \right) \qquad \text{(XII.8)}$$

where:

N_i is the shape function of the i^{th} node defined in the mesh;

Δd_i^0, $\Delta\overline{d_i^k}$ and $\Delta\overline{\overline{d_i^k}}$ are the 0^{th}, the k^{th} cosine and the k^{th} sine coefficients of incremental displacement respectively, for the i^{th} node;

n is the number of nodes in the element.

The work done can then be written as:

$$\Delta W = \int \Delta d\,\Delta\sigma \; \mathrm{d}area = \int_{-\pi}^{\pi} \Delta d\,\Delta\sigma \; r\,\mathrm{d}\theta\,\mathrm{d}l \qquad \text{(XII.9)}$$

where $\mathrm{d}l$ is the incremental length in the r-z plane along the boundary. Substituting the Fourier series representation in this equation gives:

$$\Delta W = \int_{-\pi}^{\pi} \sum_{i=1}^{N} N_i \left(\Delta d_i^0 + \sum_{k=1}^{L} \Delta\overline{d_i^k} \cos k\theta + \Delta\overline{\overline{d_i^k}} \sin k\theta \right) \left(\Delta\sigma^0 + \sum_{l=1}^{L} \Delta\overline{\sigma^l} \cos l\theta + \Delta\overline{\overline{\sigma^l}} \sin l\theta \right) r\,\mathrm{d}\theta\,\mathrm{d}l \qquad \text{(XII.10)}$$

Carrying out the $\mathrm{d}\theta$ integral gives:

$$\Delta W = \int \sum_{i=1}^{n} N_i \left(2\pi r\,\Delta d_i^0\,\Delta\sigma^0 + \pi r \sum_{k=1}^{L} \Delta\overline{d_i^k}\,\Delta\overline{\sigma^k} + \Delta\overline{\overline{d_i^k}}\,\Delta\overline{\overline{\sigma^k}} \right) \mathrm{d}l \qquad \text{(XII.11)}$$

The $\mathrm{d}l$ integral is carried out numerically, usually using a Gaussian integration rule. Thus using the principle of virtual work the contributions to the harmonic coefficients of incremental nodal force at the i^{th} node, ΔR_i, used in the right hand side of FSAFEM equations, are:

$$\begin{aligned} \Delta R_i^0 &= 2\pi r \int N_i\,\Delta\sigma^0\,\mathrm{d}l && \text{for the } 0^{\text{th}} \text{ harmonic;} \\ \Delta \overline{R_i^k} &= \pi r \int N_i\,\Delta\overline{\sigma^k}\,\mathrm{d}l && \text{for the } k^{\text{th}} \text{ cosine harmonic;} \\ \Delta \overline{\overline{R_i^k}} &= \pi r \int N_i\,\Delta\overline{\overline{\sigma^k}}\,\mathrm{d}l && \text{for the } k^{\text{th}} \text{ sine harmonic.} \end{aligned} \qquad \text{(XII.12)}$$

Appendix XII.3: Obtaining the harmonics of force from element stresses

The stress point algorithm evaluates the incremental stresses at integration points within the problem domain. These stresses are expressed as a Fourier series, i.e:

$$\{\Delta\sigma\} = \{\Delta\sigma^0\} + \sum_{k=1}^{L} \{\Delta\overline{\sigma^k}\} \cos k\theta + \{\Delta\overline{\overline{\sigma^k}}\} \sin k\theta \qquad \text{(XII.13)}$$

where:

$\{\Delta\boldsymbol{\sigma}\}$ is the vector of incremental stress components;

$\{\Delta\sigma_i^0\}$, $\{\Delta\overline{\sigma_i^k}\}$ and $\{\Delta\overline{\overline{\sigma_i^k}}\}$ are the vectors of the 0^{th}, the k^{th} cosine and the k^{th} sine coefficients of stress respectively.

Vector $\{\Delta\boldsymbol{\sigma}\}$ can be split into two sub-vectors, $\{\Delta\boldsymbol{\sigma}1\}$ and $\{\Delta\boldsymbol{\sigma}2\}$, i.e:

$$\{\Delta\sigma\} = \{\Delta\sigma_r \;\; \Delta\sigma_z \;\; \Delta\sigma_\theta \;\; \Delta\sigma_{rz} \,|\, \Delta\sigma_{r\theta} \;\; \Delta\sigma_{z\theta}\}^{\mathrm{T}} = \left\{ \{\Delta\sigma 1\} \;\; \{\Delta\sigma 2\} \right\}^{\mathrm{T}} \qquad \text{(XII.14)}$$

where:

$$\{\Delta\sigma 1\} = \{\Delta\sigma_r \;\; \Delta\sigma_z \;\; \Delta\sigma_\theta \;\; \Delta\sigma_{rz}\}^{\mathrm{T}} \quad \text{and} \quad \{\Delta\sigma 2\} = \{\Delta\sigma_{r\theta} \;\; \Delta\sigma_{z\theta}\}^{\mathrm{T}}$$

Accordingly, the Fourier series representation can be divided using these two sub-vectors, i.e:

$$\{\Delta\sigma\} = \begin{Bmatrix} \{\Delta\sigma 1^0\} \\ \{\Delta\sigma 2^0\} \end{Bmatrix} + \sum_{k=1}^{L} \begin{Bmatrix} \{\Delta\overline{\sigma 1^k}\} \cos k\theta \\ \{\Delta\overline{\sigma 2^k}\} \cos k\theta \end{Bmatrix} + \begin{Bmatrix} \{\Delta\overline{\overline{\sigma 1^k}}\} \sin k\theta \\ \{\Delta\overline{\overline{\sigma 2^k}}\} \sin k\theta \end{Bmatrix} \qquad \text{(XII.15)}$$

The incremental internal work done by these stresses is:

$$\int \{\Delta\varepsilon\}^{\mathrm{T}} \{\Delta\sigma\}\,\mathrm{d}Vol = \int_{-\pi}^{\pi} \{\Delta\boldsymbol{d}\}^{\mathrm{T}} [\boldsymbol{B}]^{\mathrm{T}} \{\Delta\sigma\}\; r\,\mathrm{d}\theta\,\mathrm{d}area \qquad \text{(XII.16)}$$

where:

$\{\Delta \boldsymbol{d}\}$ is the vector of incremental displacements;

$[\boldsymbol{B}]$ is the strain matrix.

Equation (XII.16) can be expressed in a Fourier series form as:

$$\Delta W = \int_{-\pi}^{\pi} \sum_{l=0}^{L} \left(\{\Delta \boldsymbol{d}^{l*}\}^{\mathrm{T}} \begin{bmatrix} [\boldsymbol{B}1^{l}] \cos l\theta \\ [\boldsymbol{B}2^{l}] \sin l\theta \end{bmatrix}^{\mathrm{T}} + \{\Delta \boldsymbol{d}^{l**}\}^{\mathrm{T}} \begin{bmatrix} [\boldsymbol{B}1^{l}] \sin l\theta \\ -[\boldsymbol{B}2^{l}] \cos l\theta \end{bmatrix}^{\mathrm{T}} \right) \cdot \left(\begin{Bmatrix} \{\Delta\sigma 1^{0}\} \\ \{\Delta\sigma 2^{0}\} \end{Bmatrix} + \sum_{k=1}^{L} \begin{Bmatrix} \{\Delta\overline{\sigma 1^{k}}\} \cos k\theta \\ \{\Delta\overline{\sigma 2^{k}}\} \cos k\theta \end{Bmatrix} + \begin{Bmatrix} \{\Delta\overline{\overline{\sigma 1^{k}}}\} \sin k\theta \\ \{\Delta\overline{\overline{\sigma 2^{k}}}\} \sin k\theta \end{Bmatrix} \right) r \, \mathrm{d}\theta \, darea \tag{XII.17}$$

Using the orthogonal properties of the Fourier series, the θ integral is carried out:

$$\Delta W = \int 2\pi \{\Delta \boldsymbol{d}^{0*}\}^{\mathrm{T}} [\boldsymbol{B}1^{0}]^{\mathrm{T}} \{\Delta\sigma 1^{0}\} + \pi \sum_{l=1}^{L} \{\Delta \boldsymbol{d}^{l*}\}^{\mathrm{T}} \begin{Bmatrix} [\boldsymbol{B}1^{l}] \\ [\boldsymbol{B}2^{l}] \end{Bmatrix}^{\mathrm{T}} \begin{Bmatrix} \{\Delta\overline{\sigma 1^{l}}\} \\ \{\Delta\overline{\overline{\sigma 2^{l}}}\} \end{Bmatrix}$$

$$- - - - - - - - - - - - + - - - - - - - - - - - - - - - -$$

$$-2\pi \{\Delta \boldsymbol{d}^{0**}\}^{\mathrm{T}} [\boldsymbol{B}2^{0}]^{\mathrm{T}} \{\Delta\sigma 2^{0}\} + \pi \sum_{l=1}^{L} \{\Delta \boldsymbol{d}^{l**}\}^{\mathrm{T}} \begin{Bmatrix} [\boldsymbol{B}1^{l}] \\ -[\boldsymbol{B}2^{l}] \end{Bmatrix}^{\mathrm{T}} \begin{Bmatrix} \{\Delta\overline{\overline{\sigma 1^{l}}}\} \\ \{\Delta\overline{\sigma 2^{l}}\} \end{Bmatrix} r \, darea \tag{XII.18}$$

The work done by the coefficients of incremental nodal force consistent with this stress state is:

$$\Delta W = \{\Delta \boldsymbol{d}^{0*}\}\{\Delta \boldsymbol{R}^{0*}\} + \sum_{k=1}^{L} \{\Delta \boldsymbol{d}^{k*}\}\{\Delta \boldsymbol{R}^{k*}\} + \{\Delta \boldsymbol{d}^{k**}\}\{\Delta \boldsymbol{R}^{k**}\} \tag{XII.19}$$

Thus using the principle of virtual work, the work done by both equations must be the same and in addition the terms which are pre-multiplied by the same coefficients of displacement can be equated. From here the contributions to the harmonic coefficients of incremental nodal load, $\{\Delta \boldsymbol{R}\}$, used in the right hand side of the FSAFEM equations, are:

$$\{\Delta \boldsymbol{R}^{0}\} = 2\pi \int \begin{Bmatrix} [\boldsymbol{B}1^{0}] \\ -[\boldsymbol{B}2^{0}] \end{Bmatrix}^{\mathrm{T}} \begin{Bmatrix} \{\Delta\sigma 1^{0}\} \\ \{\Delta\sigma 2^{0}\} \end{Bmatrix} r \, darea \quad \text{for the } 0^{\text{th}} \text{ harmonic;}$$

$$\{\Delta \boldsymbol{R}^{l*}\} = \pi \int \begin{Bmatrix} [\boldsymbol{B}1^{l}] \\ [\boldsymbol{B}2^{l}] \end{Bmatrix}^{\mathrm{T}} \begin{Bmatrix} \{\Delta\overline{\sigma 1^{l}}\} \\ \{\Delta\overline{\overline{\sigma 2^{l}}}\} \end{Bmatrix} r \, darea \quad \text{for the } l^{\text{th}} \text{ parallel harmonic;}$$

$$\{\Delta \boldsymbol{R}^{l**}\} = \pi \int \begin{Bmatrix} [\boldsymbol{B}1^{l}] \\ -[\boldsymbol{B}2^{l}] \end{Bmatrix}^{\mathrm{T}} \begin{Bmatrix} \{\Delta\overline{\overline{\sigma 1^{l}}}\} \\ \{\Delta\overline{\sigma 2^{l}}\} \end{Bmatrix} r \, darea \quad \text{for the } l^{\text{th}} \text{ orthogonal harmonic.} \tag{XII.20}$$

Appendix XII.4: Resolving harmonic coefficients of nodal force

Horizontal loads

Let Δf_r represent the incremental radial force per unit circumference on a node. This can be expressed as a Fourier series:

$$\Delta f_r = \Delta F_r^0 + \sum_{k=1}^{L} \Delta\overline{F_r^k} \cos k\theta + \Delta\overline{\overline{F_r^k}} \sin k\theta \tag{XII.21}$$

The resultant incremental force in the θ=0° direction, $\Delta T_r^{\theta=0}$, is given by equation:

$$\begin{aligned} \Delta T_r^{\theta=0} &= \int_{-\pi}^{\pi} \Delta f_r \, r \cos\theta \, \mathrm{d}\theta \\ &= \int_{-\pi}^{\pi} \left(\Delta F_r^0 + \sum_{k=1}^{L} \Delta\overline{F_r^k} \cos k\theta + \Delta\overline{\overline{F_r^k}} \sin k\theta \right) \cos\theta \, r \, \mathrm{d}\theta \\ &= \pi r \Delta\overline{F_r^1} = \Delta R_r^1 \end{aligned} \tag{XII.22}$$

Similarly, the resultant incremental force in the θ=½π direction, $\Delta T_r^{\theta=\frac{1}{2}\pi}$, is:

$$\begin{aligned} \Delta T_r^{\theta=\frac{1}{2}\pi} &= \int_{-\pi}^{\pi} \Delta f_r \, r \sin\theta \, \mathrm{d}\theta \\ &= \int_{-\pi}^{\pi} \left(\Delta F_r^0 + \sum_{k=1}^{L} \Delta\overline{F_r^k} \cos k\theta + \Delta\overline{\overline{F_r^k}} \sin k\theta \right) \sin\theta \, r \, \mathrm{d}\theta \\ &= \pi r \Delta\overline{\overline{F_r^1}} = \Delta\overline{\overline{R_r^1}} \end{aligned} \tag{XII.23}$$

If Δf_θ represents the incremental circumferential force per unit circumference on a node, the resultant incremental force in the θ=0° direction, $\Delta T_r^{\theta=0}$, is given by:

$$\begin{aligned} \Delta T_r^{\theta=0} &= \int_{-\pi}^{\pi} -\Delta f_\theta \, r \sin\theta \, \mathrm{d}\theta \\ &= \int_{-\pi}^{\pi} -\left(\Delta F_\theta^0 + \sum_{k=1}^{L} \Delta\overline{F_\theta^k} \cos k\theta + \Delta\overline{\overline{F_\theta^k}} \sin k\theta \right) \sin\theta \, r \, \mathrm{d}\theta \\ &= -\pi r \Delta\overline{\overline{F_\theta^1}} = -\Delta\overline{\overline{R_\theta^1}} \end{aligned} \tag{XII.24}$$

Similarly, the resultant incremental force in the θ=½π direction, $\Delta T_r^{\theta=\frac{1}{2}\pi}$, is:

$$\begin{aligned} \Delta T_r^{\theta=\frac{1}{2}\pi} &= \int_{-\pi}^{\pi} \Delta f_\theta \, r \cos\theta \, \mathrm{d}\theta \\ &= \int_{-\pi}^{\pi} \left(\Delta F_\theta^0 + \sum_{k=1}^{L} \Delta\overline{F_\theta^k} \cos k\theta + \Delta\overline{\overline{F_\theta^k}} \sin k\theta \right) \cos\theta \, r \, \mathrm{d}\theta \\ &= \pi r \Delta\overline{F_\theta^1} = \Delta R_\theta^1 \end{aligned} \tag{XII.25}$$

Thus the total incremental horizontal load in the θ=0° direction is:

$$\Delta T_r^{\theta=0} = \Delta\overline{R_r^1} - \Delta\overline{\overline{R_\theta^1}} \tag{XII.26}$$

and the total incremental horizontal load in the θ=½π direction is:

$$\Delta T_r^{\theta=\frac{1}{2}\pi} = \Delta\overline{\overline{R_r^1}} + \Delta\overline{R_\theta^1} \tag{XII.27}$$

Axial loads

Let Δf_z represent the incremental vertical force per unit circumference on a node. This can be expressed as a Fourier series:

$$\Delta f_z = \Delta F_z^0 + \sum_{k=1}^{L} \Delta \overline{F_z^k} \cos k\theta + \Delta \overline{\overline{F_z^k}} \sin k\theta \qquad \text{(XII.28)}$$

The total incremental force in the vertical direction, ΔT_z, is given by the equation:

$$\begin{aligned} \Delta T_z &= \int_{-\pi}^{\pi} \Delta f_z \, r \, \mathrm{d}\theta \\ &= \int_{-\pi}^{\pi} \left(\Delta F_z^0 + \sum_{k=1}^{L} \Delta \overline{F_z^k} \cos k\theta + \Delta \overline{\overline{F_z^k}} \sin k\theta \right) r \, \mathrm{d}\theta \\ &= 2\pi r \Delta F_z^0 = \Delta R_z^0 \end{aligned} \qquad \text{(XII.29)}$$

Turning moments

As in the previous case for axial load, let Δf_z represent the incremental vertical force per unit circumference on a node, which can be expressed as a Fourier series. The incremental turning moment about the θ=½π axis, $\Delta M^{\frac{1}{2}\pi}$, is equal to:

$$\begin{aligned} \Delta M^{\frac{1}{2}\pi} &= \int_{-\pi}^{\pi} \Delta f_z \, r \cos\theta \, r \, \mathrm{d}\theta \\ &= \int_{-\pi}^{\pi} \left(\Delta F_z^0 + \sum_{k=1}^{L} \Delta \overline{F_z^k} \cos k\theta + \Delta \overline{\overline{F_z^k}} \sin k\theta \right) \cos\theta \, r^2 \, \mathrm{d}\theta \\ &= \pi r^2 \Delta \overline{F_z^1} = r \Delta \overline{R_z^1} \end{aligned} \qquad \text{(XII.30)}$$

Similarly, for incremental turning moments about the θ=0° axis, ΔM^0 is equal to:

$$\begin{aligned} \Delta M^0 &= \int_{-\pi}^{\pi} \Delta f_z \, r \sin\theta \, r \, \mathrm{d}\theta \\ &= \int_{-\pi}^{\pi} \left(\Delta F_z^0 + \sum_{k=1}^{L} \Delta \overline{F_z^k} \cos k\theta + \Delta \overline{\overline{F_z^k}} \sin k\theta \right) \sin\theta \, r^2 \, \mathrm{d}\theta \\ &= \pi r^2 \Delta \overline{\overline{F_z^1}} = r \Delta \overline{\overline{R_z^1}} \end{aligned} \qquad \text{(XII.31)}$$

Appendix XII.5: Fourier series solutions for integrating the product of three Fourier series

Three standard integrals are used for the solution of the integral of the product of two Fourier series:

$$\begin{aligned} &\int_{-\pi}^{\pi} \sin k\theta \cos l\theta \, \mathrm{d}\theta = 0 \text{ for all } k \text{ and } l \\ &\int_{-\pi}^{\pi} \sin k\theta \sin l\theta \, \mathrm{d}\theta = 0 \text{ if } k \neq l, \ = \pi \text{ if } k = l \neq 0, \ = 0 \text{ if } k = l = 0 \\ &\int_{-\pi}^{\pi} \cos k\theta \cos l\theta \, \mathrm{d}\theta = 0 \text{ if } k \neq l, \ = \pi \text{ if } k = l \neq 0, \ = 2\pi \text{ if } k = l = 0 \end{aligned} \qquad \text{(XII.32)}$$

Using the above equations six standard integrals can be obtained for the solution of the integral of the product of three Fourier series:

$$\begin{aligned} &\int_{-\pi}^{\pi} \sin k\theta \sin l\theta \sin m\theta \, \mathrm{d}\theta = \int_{-\pi}^{\pi} \frac{1}{2}(\cos(k-l)\theta - \cos(k+l)\theta) \sin m\theta \, \mathrm{d}\theta \\ &\qquad = 0 \\ &\int_{-\pi}^{\pi} \cos k\theta \cos l\theta \sin m\theta \, \mathrm{d}\theta = \int_{-\pi}^{\pi} \frac{1}{2}(\cos(k-l)\theta + \cos(k+l)\theta) \sin m\theta \, \mathrm{d}\theta \\ &\qquad = 0 \\ &\int_{-\pi}^{\pi} \sin k\theta \cos l\theta \sin m\theta \, \mathrm{d}\theta = \int_{-\pi}^{\pi} \frac{1}{2}(\sin(k-l)\theta + \sin(k+l)\theta) \sin m\theta \, \mathrm{d}\theta \\ &\qquad = \pi \, (\pm\alpha + \beta) \\ &\int_{-\pi}^{\pi} \sin k\theta \sin l\theta \cos m\theta \, \mathrm{d}\theta = \int_{-\pi}^{\pi} \frac{1}{2}(\cos(k-l)\theta - \cos(k+l)\theta) \cos m\theta \, \mathrm{d}\theta \\ &\qquad = \pi \, (\alpha - \beta) \\ &\int_{-\pi}^{\pi} \cos k\theta \cos l\theta \cos m\theta \, \mathrm{d}\theta = \int_{-\pi}^{\pi} \frac{1}{2}(\cos(k-l)\theta + \cos(k+l)\theta) \cos m\theta \, \mathrm{d}\theta \\ &\qquad = \pi \, (\alpha + \beta) \\ &\int_{-\pi}^{\pi} \sin k\theta \cos l\theta \cos m\theta \, \mathrm{d}\theta = \int_{-\pi}^{\pi} \frac{1}{2}(\sin(k-l)\theta + \sin(k+l)\theta) \cos m\theta \, \mathrm{d}\theta \\ &\qquad = 0 \end{aligned}$$

where: (XII.33)

$\alpha = 1$ if $|k-l| = m = 0$; $= ½$ if $|k-l| = m \neq 0$; $= 0$ otherwise;
$\beta = 1$ if $|k+l| = m = 0$; $= ½$ if $|k+l| = m \neq 0$; $= 0$ otherwise;
$\pm$ is + if $k - l \geq 0$; is − if $k - l < 1$;
$|x|$ denotes absolute value of x.

Appendix XII.6: Obtaining coefficients for a stepwise linear distribution

The variable x is described by a stepwise linear distribution, see Figure 12.4, using n discrete values of x_i at locations θ_i, e.g. x_1 at θ_1, x_2 at θ_2, ... , x_i at θ_i, ... , x_n at θ_n, such that at any location θ the value of x is:

$$x = x_i + \frac{(x_{i+1} - x_i)(\theta - \theta_i)}{\theta_{i+1} - \theta_i} \quad \text{when} \quad \theta_i < \theta < \theta_{i+1} \qquad \text{(XII.34)}$$

The 0th harmonic is evaluated from:

$$\begin{aligned} X^0 &= \frac{1}{2\pi} \int_{-\pi}^{\pi} x \, \mathrm{d}\theta \\ &= \frac{1}{2\pi} \sum_{i=1}^{n} \int_{\theta_i}^{\theta_{i+1}} \left(x_i + \frac{(x_{i+1} - x_i)(\theta - \theta_i)}{\theta_{i+1} - \theta_i} \right) \mathrm{d}\theta \\ &= \frac{1}{2\pi} \sum_{i=1}^{n} \int_{\theta_i}^{\theta_{i+1}} \left(\frac{(x_{i+1} - x_i)\theta + \theta_{i+1} x_i - \theta_i x_{i+1}}{\theta_{i+1} - \theta_i} \right) \mathrm{d}\theta \end{aligned}$$

$$= \frac{1}{2\pi}\sum_{i=1}^{n} \frac{1}{\theta_{i+1}-\theta_i}\left((x_{i+1}-x_i)\frac{\theta^2}{2}+\theta(\theta_{i+1}x_i-\theta_i x_{i+1})\right)_{\theta_i}^{\theta_{i+1}}$$

$$= \frac{1}{2\pi}\sum_{i=1}^{n} \frac{x_{i+1}+x_i}{\theta_{i+1}-\theta_i}\left(\frac{\theta_{i+1}^2}{2}+\frac{\theta_i^2}{2}-\theta_{i+1}\theta_i\right)$$

$$= \frac{1}{4\pi}\sum_{i=1}^{n} (x_{i+1}+x_i)(\theta_{i+1}-\theta_i) \qquad \text{(XII.35)}$$

The k^{th} cosine harmonic is evaluated from:

$$\overline{X^k} = \frac{1}{\pi}\int_{-\pi}^{\pi} x\cos k\theta \, d\theta$$

$$= \frac{1}{\pi}\sum_{i=1}^{n}\int_{\theta_i}^{\theta_{i+1}} \left(x_i+\frac{(x_{i+1}-x_i)(\theta-\theta_i)}{\theta_{i+1}-\theta_i}\right)\cos k\theta \, d\theta$$

$$= \frac{1}{\pi}\sum_{i=1}^{n}\int_{\theta_i}^{\theta_{i+1}} \left(\frac{(x_{i+1}-x_i)\theta+\theta_{i+1}x_i-\theta_i x_{i+1})}{\theta_{i+1}-\theta_i}\right)\cos k\theta \, d\theta$$

$$= \frac{1}{\pi}\sum_{i=1}^{n} \frac{1}{\theta_{i+1}-\theta_i}\left((x_{i+1}-x_i)\left(\frac{\cos k\theta}{k^2}+\frac{\theta\sin k\theta}{k}\right)+\frac{\sin k\theta}{k}(\theta_{i+1}x_i-\theta_i x_{i+1})\right)_{\theta_i}^{\theta_{i+1}}$$

$$= \frac{1}{k\pi}\sum_{i=1}^{n} \frac{1}{\theta_{i+1}-\theta_i}\left[x_{i+1}\left(\frac{\cos k\theta_{i+1}-\cos k\theta_i}{k}+\sin k\theta_{i+1}(\theta_{i+1}-\theta_i)\right)\right.$$

$$\left.-x_i\left(\frac{\cos k\theta_{i+1}-\cos k\theta_i}{k}+\sin k\theta_i(\theta_{i+1}-\theta_i)\right)\right]$$

$$= \frac{1}{k\pi}\sum_{i=1}^{n}\left(\frac{(x_{i+1}-x_i)(\cos k\theta_{i+1}-\cos k\theta_i)}{k(\theta_{i+1}-\theta_i)}+x_{i+1}\sin k\theta_{i+1}-x_i\sin k\theta_i\right) \qquad \text{(XII.36)}$$

Since $x_{n+1}=x_1$ and $\theta_{n+1}=\theta_1$, the summation of the last two terms in the expression is zero, giving:

$$\overline{X^k} = \frac{1}{k^2\pi}\sum_{i=1}^{n}\left(\frac{(x_{i+1}-x_i)(\cos k\theta_{i+1}-\cos k\theta_i)}{k(\theta_{i+1}-\theta_i)}\right) \qquad \text{(XII.37)}$$

The k^{th} sine harmonic is evaluated from:

$$\overline{\overline{X^k}} = \frac{1}{\pi}\int_{-\pi}^{\pi} x\sin k\theta \, d\theta$$

$$= \frac{1}{\pi}\sum_{i=1}^{n}\int_{\theta_i}^{\theta_{i+1}} \left(x_i+\frac{(x_{i+1}-x_i)(\theta-\theta_i)}{\theta_{i+1}-\theta_i}\right)\sin k\theta \, d\theta$$

$$= \frac{1}{\pi}\sum_{i=1}^{n}\int_{\theta_i}^{\theta_{i+1}} \left(\frac{(x_{i+1}-x_i)\theta+\theta_{i+1}x_i-\theta_i x_{i+1})}{\theta_{i+1}-\theta_i}\right)\sin k\theta \, d\theta$$

$$= \frac{1}{\pi}\sum_{i=1}^{n} \frac{1}{\theta_{i+1}-\theta_i}\left((x_{i+1}-x_i)\left(\frac{\sin k\theta}{k^2}+\frac{\theta\cos k\theta}{k}\right)-\frac{\cos k\theta}{k}(\theta_{i+1}x_i-\theta_i x_{i+1})\right)_{\theta_i}^{\theta_{i+1}}$$

$$= \frac{1}{k\pi}\sum_{i=1}^{n} \frac{1}{\theta_{i+1}-\theta_i}\left[x_{i+1}\left(\frac{\sin k\theta_{i+1}-\sin k\theta_i}{k}-\cos k\theta_{i+1}(\theta_{i+1}-\theta_i)\right)\right.$$

$$\left.-x_i\left(\frac{\sin k\theta_{i+1}-\sin k\theta_i}{k}-\cos k\theta_i(\theta_{i+1}-\theta_i)\right)\right]$$

$$= \frac{1}{k\pi}\sum_{i=1}^{n}\left(\frac{(x_{i+1}-x_i)(\sin k\theta_{i+1}-\sin k\theta_i)}{k(\theta_{i+1}-\theta_i)}-x_{i+1}\cos k\theta_{i+1}+x_i\cos k\theta_i\right) \qquad \text{(XII.38)}$$

The summation of the last two terms in the expression is zero, giving:

$$\overline{\overline{X^k}} = \frac{1}{k^2\pi}\sum_{i=1}^{n}\left(\frac{(x_{i+1}-x_i)(\sin k\theta_{i+1}-\sin k\theta_i)}{k(\theta_{i+1}-\theta_i)}\right) \qquad \text{(XII.39)}$$

Simplifications can be made if x varies in either a symmetric or non-symmetric manner. If a symmetric function is stipulated, the specified values of x are constrained to be located in half space $0 \le \theta \le \pi$. For each value of x specified, a symmetrical value is assumed in the half space $-\pi < \theta < 0$, i.e. for each x_i at θ_i a value of x_i at $-\theta_i$ is assumed, see Figure XII.1. The above equations can then be used to obtain 0^{th} and cosine harmonic coefficients. Since the assumed distribution is symmetric, the sine coefficients are zero.

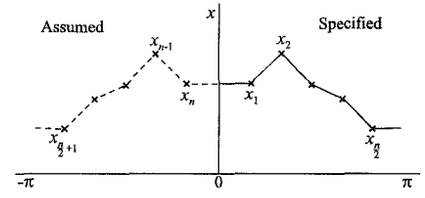

Figure XII.1: Symmetrical stepwise linear function

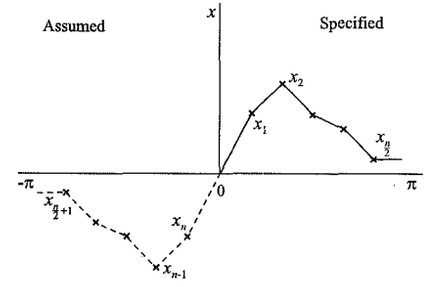

Figure XII.2: Asymmetrical stepwise linear function

Similarly, if an asymmetric function is stipulated, the specified values of x are constrained to be located in the half space $0 < \theta < \pi$. For each value of x specified, an asymmetrical value is assumed in the half space $-\pi < \theta < 0$, i.e. for each x_i at θ_i a value of $-x_i$ at $-\theta_i$ is assumed, see Figure XII.2. The above equations can then be used to obtain the sine harmonic coefficients. Since the assumed distribution is asymmetric, the 0^{th} and cosine coefficients are zero.

Appendix XII.7: Obtaining harmonic coefficients using the fitted method

A Fourier series has to be found which passes through n discrete values of x (x_1 to x_n). In order to have the same number of sine and cosine harmonics, n is

constrained to be an odd number. Thus the order of the Fourier series required, L, is equal to $\frac{1}{2}(n-1)$:

$$x = X^0 + \sum_{k=1}^{L} \overline{X^k} \cos k\theta + \overline{\overline{X^k}} \sin k\theta \qquad \text{(XII.40)}$$

The values of x are equispaced in the region $-\pi < \theta < \pi$, i.e. x_j is located at $\theta = (j-1)\alpha$, see Figure 12.6. From here Equation (XII.40) can be written such that for any integer value j:

$$x_j = X^0 + \sum_{k=1}^{L} \overline{X^k} \cos k(j-1)\alpha + \overline{\overline{X^k}} \sin k(j-1)\alpha \qquad \text{(XII.41)}$$

The harmonic coefficients for this Fourier series can then be evaluated using the equations:

$$\begin{aligned} X^0 &= \frac{1}{n} \sum_{i=1}^{n} x_i \\ \overline{X^k} &= \frac{2}{n} \sum_{i=1}^{n} x_i \cos k(i-1)\alpha \\ \overline{\overline{X^k}} &= \frac{2}{n} \sum_{i=1}^{n} x_i \sin k(i-1)\alpha \end{aligned} \qquad \text{(XII.42)}$$

This can be proved by substituting Equations (XII.42) into Equation (XII.41), which gives:

$$\begin{aligned} x_j = \frac{1}{n} \sum_{i=1}^{n} x_i + \sum_{k=1}^{L} \Bigg(& \frac{2}{n} \sum_{i=1}^{n} x_i \cos k\alpha(i-1) \cos k\alpha(j-1) \\ & + \frac{2}{n} \sum_{i=1}^{n} x_i \sin k\alpha(i-1) \sin k\alpha(j-1) \Bigg) \end{aligned} \qquad \text{(XII.43)}$$

Noting that $\cos A \cos B + \sin A \sin B = \cos(A - B)$ Equation (XII.43) can be simplified:

$$x_j = \frac{1}{n} \sum_{i=1}^{n} x_i + \frac{2}{n} \sum_{k=1}^{L} \sum_{i=1}^{n} x_i \cos k\alpha(i-j) \qquad \text{(XII.44)}$$

Equation (XII.44) can be rewritten so that the summation of k is carried out first:

$$x_j = \frac{2}{n} \sum_{i=1}^{n} x_i \left(\frac{1}{2} + \sum_{k=1}^{L} \cos k\alpha(i-j) \right) \qquad \text{(XII.45)}$$

A parameter ψ_{ij} can now be defined such that Equation (XII.45) becomes:

$$x_j = \frac{2}{n} \sum_{i=1}^{n} x_i \, \psi_{ij} \qquad \text{(XII.46)}$$

where:

$$\psi_{ij} = \frac{1}{2} + \sum_{k=1}^{L} \cos k\alpha(i-j)$$

Using the standard solution:

$$\frac{1}{2} + \sum_{k=1}^{L} \cos kx = \frac{\sin\left(L + \frac{1}{2}\right)x}{2 \sin \frac{x}{2}}$$

and if $i \neq j$ then:

$$\psi_{ij} = \frac{\sin\left(L + \frac{1}{2}\right)\alpha(j-i)}{2 \sin \frac{\alpha(j-i)}{2}} \qquad \text{(XII.47)}$$

Substituting L into the equation for α gives:

$$\alpha = \frac{2\pi}{n} = \frac{2\pi}{2L+1}$$

Substituting this into Equation (XII.47) for ψ_{ij} gives:

$$\psi_{ij} = \frac{\sin \pi(j-i)}{2 \sin \frac{\pi(j-i)}{2L+1}} = 0 \qquad \text{(XII.48)}$$

Equation (XII.48) equals zero for $i \neq j$ because $(j-i)$ is an integer, and the sine of any multiple of π is zero. If $i=j$, then $\psi_{ij} = (L+\frac{1}{2})$ since the cosine of zero is 1.

Equation (XII.46) can be written as:

$$x_j = \frac{2}{n} x_j \left(L + \frac{1}{2} \right) = x_j \qquad \text{(XII.49)}$$

Thus Equation (XII.42) yields harmonic coefficients for a Fourier series which satisfies Equation (XII.41) for all values of j.

Simplifications can again be made if x varies in either a symmetric or non-symmetric manner. If a symmetric function is stipulated, then values of x are only specified in the half space $-\pi \leq \theta \leq 0$, i.e. only x_0 to x_L is specified and x_{L+1} to x_n is obtained using the equation $x_i = x_{n-i}$. This is illustrated in Figure XII.3. Equation (XII.42) can now be used to obtain the zeroth and cosine harmonic coefficients. Since the assumed distribution is symmetric, the sine coefficients are zero.

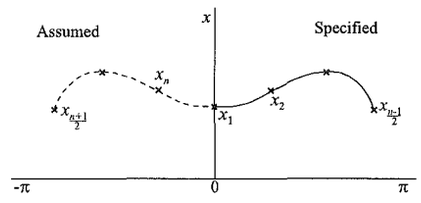

Figure XII.3: Symmetrical function

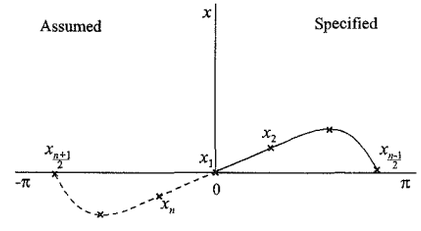

Figure XII.4: Asymmetrical function

Similarly, if an asymmetric function is stipulated, then values of x are only specified in the half space $0<\theta<\pi$ and an asymmetrical value is assumed in the half space $-\pi<\theta<0$, i.e. only x_1 to x_L is specified and x_{L+1} to x_n is obtained using the equation $x_i = -x_{n-i}$. x_0 is constrained to be zero for an asymmetric function. This is illustrated in Figure XII.4. Equation (XII.42) can now be used to obtain the sine harmonic coefficients. Since the assumed distribution is asymmetric, the zeroth and cosine coefficients are zero.

References

Addenbrooke T.I., Potts D.M. & Puzrin A.M. (1997), "The influence of pre-failure soil stiffness on numerical analysis of tunnel construction", Geotechnique, Vol. 47, No. 3, pp 693-712

Allman M.A. & Atkinson J.H. (1992), "Mechanical properties of reconstituted Bothkennar soil", Geotechnique, Vol. 42, No. 2, pp 289-301

Al-Tabbaa A. (1987), "Permeability and stress-strain response of speswhite kaolin", PhD thesis, Cambridge University

Al-Tabbaa A. & Wood D.M. (1989), "An experimentally based 'bubble' model for clay", Int. Conf. Num. Models Geomech., NUMOG III, Edt. Pietruszczak & Pande, Balkema, pp 91-99

Atkinson J.H. (1975), "Anisotropic elastic deformations in laboratory tests on undisturbed London clay", Geotechnique, Vol. 25, No. 2, pp 357-384

Atkinson J.H. & Potts D.M. (1975), "A note on associated field solutions for boundary value problems in a variable φ - variable v soil", Geotechnique, Vol. 25, No. 2, pp 379-384

Banerjee P.K., Stipho A.S. & Yousif N.B.A. (1985), "A theoretical and experimental investigation of the behaviour of anisotropically consolidated clay", Developments in soil mechanics and foundation engineering, Edt. Banerjee & Butterfield, Applied Science, Barking, pp 1-41

Bathe K.J. (1982), "Finite element procedures in engineering analysis", Prentice-Hall

Beer G. (1985), "An isoparametric joint/interface element for finite element analysis", Int. Jnl. Num. Meth. Eng., Vol. 21, pp 585-600

Biot M.A. (1941), "General theory of three-dimensional consolidation", Jnl. Appl. Phys., Vol. 12, pp 155-164

Bishop A.W., Green G.E., Garga V.K., Andersen A. & Brown J.D. (1971), "A new ring shear apparatus and its application to the measurement of residual strength", Geotechnique, Vol. 21, No. 4, pp 273-328

Bishop A.W. & Wesley L.D. (1975), "A hydraulic triaxial apparatus for controlled stress path testing", Geotechnique, Vol. 25, No. 4, pp 657-670

Booker J.R. & Small J.C. (1975), "An investigation of the stability of numerical solutions of Biot's equations of consolidation", Int. Jnl. Solids Struct., Vol. 11, pp 907-917

Borin D.L. (1989), WALLAP - computer program for the stability analysis of retaining walls; GEOSOLVE

Borja R.I. (1991), "Cam clay plasticity, part II: Implicit integration of constitutive equations based on nonlinear elastic stress prediction", Comput. Meth. Appl. Mech. Eng., Vol. 88, pp 225-240

Borja R.I. & Lee S.R. (1990), "Cam clay plasticity, part I: Implicit integration of constitutive relations", Comput. Meth. Appl. Mech. Eng., Vol. 78, pp 49-72

Bressani L.A. (1990), "Experimental properties of bonded soils", PhD thesis, Imperial College, University of London

Britto A.M. & Gunn M.J. (1987), "Critical state soil mechanics via finite elements", Ellis Horwood Ltd., Chichester, U.K.

Brown D.A. & Shie C-F. (1990), "Three dimensional finite element model of laterally loaded piles", Computers and geotechnics, Vol. 10, pp 59-79

Brown P.T. & Booker J.R. (1985), "Finite element analysis of excavation", Computers in Geotechnics, Vol. 1, pp 207-220

Calladine V.R. (1963), Correspondence, Geotechnique, Vol. 13, pp 250-255

Carol I. & Alonso E.E. (1983), "A new joint element for the analysis of fractured rock", 5th Int. Congr. Rock Mech., Melbourne, Vol. F, pp 147-151

Carter J.P., Booker J.R. & Wroth C.P. (1982), "A critical state model for cyclic loading", Soil mechanics - Transient and cyclic loads, Edt. Pande & Zinekiewicz, Wiley, Chichester, pp 219-252

Chen W.F. (1975), "Limit analysis and plasticity", Developments in geotechnical engineering, Vol. 7, Elsevier

Chen W.F. & Baladi G.Y. (1985), "Soil plasticity", Elsevier, Amsterdam

Clough G.W., Shirasuna T. & Finno R.J. (1985), "Finite element analysis of advanced shield tunnelling in soils", 5th Int. Conf. Num. Meth. Geomech., Nagoya, Vol. 2, pp 1167-1174

Clough G.W., Sweeney B.P. & Finno R.J. (1983), "Measured soil response to EPB shield tunnelling", ASCE, GT Div., Vol. 109, pp 131-149

Connolly T.M.M. (1999), "The geological and geotechnical properties of a glacial lacustrine clayey silt", PhD thesis in preparation, Imperial College, University of London

Coop M.R. (1990), "The mechanics of uncemented carbonate sands", Geotechnique, Vol. 40, No. 4, pp 607-626

Cope R.J., Rao P.V., Clark L.A. & Noris P. (1980), "Modelling of reinforced concrete behaviour for finite element analysis of bridge slabs", Num. Meth. for Nonlinear Problems, Edt. Taylor, Hinton & Owen, Pineridge Press, Swansea, Vol. 1, pp 457-470

Cornfroth D.H. (1961), "Plane strain failure characteristics of a saturated sand", PhD thesis, Imperial College, University of London

Cotecchia F. (1996), "The effects of structure on the properties of an Italian pleistocene clay", PhD thesis, Imperial College, University of London

Coulomb C.A. (1776), "Essai sur une application des regles de maxims et minims a quelques problemes de statique, relatifs a l'architecture", Mem. Acad. Royal Soc., Vol. 7, pp 343-382

Crisfield M.A. (1986), "Finite elements and solution procedures for structural analysis", Pineridge press, Swansea, UK

Cuthill E. & McKee J. (1969), "Reducing the bandwidth of sparse symmetric matrices", Proc. ACM National Conf., Association for Computing Machinery, New York, pp 157-172

Daddazio R.P., Ettourney M.M. & Sandler I.S. (1987), "Nonlinear dynamic slope stability analysis", ASCE, GT Div., Vol. 113, pp 285-298

Dafalias Y.F. (1975), "On cyclic and anisotropic plasticity: (i) A general model including material behaviour under stress reversals, (ii) Anisotropic hardening for initially orthotropic materials", PhD thesis, University of California, Berkeley

Dafalias Y.F. & Herrmann L.R. (1982), "Bounding surface formulation of soil plasticity", Soil mechanics - Transient and cyclic loads, Edt. Pande & Zienkiewicz, Wiley, Chichester, pp 253-282

Dafalias Y.F. & Popov E.P. (1976), "Plastic internal variables formalism of cyclic plasticity", Jnl. Appl. Mech., Vol. 98, No. 4, pp 645-650

Davies E.H. & Booker J.R. (1973), "The effect of increasing strength with depth on the bearing capacity of clays", Geotehcnique, Vol. 23, No. 4, pp 551-563

Day R.A. (1990), "Finite element analysis of sheet pile retaining walls", PhD thesis, Imperial College, University of London

Day R.A. & Potts D.M. (1990), "Curved Mindlin beam and axi-symmetric shell elements - A new approach", Int. Jnl. Num. Meth. Eng., Vol. 30, pp 1263-1274

Day R.A. & Potts D.M. (1994), "Zero thickness interface elements - numerical stability and application", Int. Jnl. Num. Anal. Meth. Geomech., Vol. 18, pp 689-708

De Borst T. & Nauta P. (1984), "Smeared crack analysis of reinforced concrete beams and slabs failing in shear", Int. Conf. Comp. Aided Analysis and Design of Concrete Structures, Edt. Damjanić *et al.*, Pineridge Press, Swansea, Part 1, pp 261-273

De Borst T. & Nauta P. (1985), "Non-orthogonal cracks in a smeared finite element model", Eng. Comput., Vol. 2, pp 35-46

Desai C.S. (1980), "A general basis for yield, failure and potential functions in plasticity", Int. Jnl. Num. Anal. Meth. Geomech., Vol. 4, pp 361-375

Desai C.S., Zaman M.M., Lightner J.G. and Siriwardane H.J. (1984), "Thin-layer element for interfaces and joints", Int. Jnl. Num. Anal. Meth. Gemech., Vol. 8, pp 19-43

Di Maggio F.L. & Sandler I.S. (1971), "Material model for granular soils", ASCE, EM Div., Vol. 97, pp 935-950

Drucker D.C., Gibson R.E. & Henkel D.J. (1957), "Soil mechanics and work hardening theories of plasticity", Trans. ASCE, Vol. 122, pp 338-346

Drucker D.C. & Prager W. (1952), "Soil mechanics and plastic analysis of limit design", Q. Appl. Math., Vol. 10, pp 157-164

Duncan J.M. & Chang Y.C. (1970), "Nonlinear analysis of stress and strain in soils", ASCE, SM5, Vol. 96, pp 1629-1653

Eekelen H.A.M. van (1980), "Isotropic yield surfaces in three dimensions for use in soil mechanics", Int. Jnl. Num. Anal. Meth. Geomech., Vol. 4, pp 89-101

Eekelen H.A.M. van & Potts D.M. (1978), "The behaviour of Drammen clay under cyclic loading", Geotechnique, Vol. 28, pp 173-196

Everstine G. (1979), "A comparison of three re-sequencing algorithms for the reduction of matrix profile and wavefront", Int. Jnl. Num. Meth. Eng., Vol. 14, pp 837-853

Francavilla A. & Zienkieviczs O.C. (1975), "A note on numerical computation of elastic contact problems", Int. Jnl. Num. Meth. Eng., Vol. 9, pp 913-924

Frank R., Guenot A. & Humbert P. (1982), "Numerical analysis of contacts in geomechanics", Proc. 4th Int. Conf. Num. Meth. Geomech., Rotterdam, pp 37-42

Franklin A.G. & Mattson P.A. (1972), "Directional variation of elastic wave velocities in oriented clay", Clays and clay minerals, Vol. 20, pp 285-293

Ganendra D. (1993), "Finite element analysis of laterally loaded piles", PhD thesis, Imperial College, University of London

Ganendra D. & Potts D.M. (1995), Discussion on "Evaluation of constitutive model for overconsolidated clays" by A.J. Whittle, Geotehcnique, Vol. 45, No. 1, pp 169-173

Ganendra D. & Potts D.M. (1995), "Application of the Fourier series aided finite element method to elasto-plastic problems", Computational plasticity fundamentals and applications, Edt. Owens & Onate, Pineridge press, (Proc. 4th Int. Conf. Computational Plasticity), pp 210-212

Gens A. (1982), "Stress-strain and strength of a low plasticity clay", PhD thesis, Imperial College, University of London

Gens A. & Potts D.M. (1984), "Formulation of quasi axi-symmetric boundary value problems for finite element analysis, Eng. Comput., Vol. 1, No. 2, pp 144-150

Gens A. & Potts D.M. (1988), "Critical state model in computational geomechanics", Eng. Comput., Vol. 5, pp 178-197

Georgiannou V.N. (1988), "The behaviour of clayey sands under monotonic and cyclic loading", PhD thesis, Imperial College, University of London

Ghaboussi J., Wilson E.L. & Isenberg J. (1973), "Finite element for rock joint interfaces", ASCE, SM10, Vol. 99, pp 833-848

Gibbs N.E., Poole W.G. & Stockmeyer P.K. (1976), "An algorithm for reducing the bandwidth and profile of a sparse matrix", SIAM Jnl. Num. Anal., Vol. 13, No. 2, pp 236-250

Goodman R.E., Taylor R.L. & Brekke T.L. (1968), "A model for the mechanics of jointed rock", ASCE, SM3, Vol. 94, pp 637-659

Graham J. & Houlsby G.T. (1983), "Anisotropic elasticity of a natural clay", Geotechnique, Vol. 33, No. 2, pp 165-180

Green G.E. (1971), "Strength and deformation of sand measured in an independent stress control cell", Stress-strain behaviour of soils, Proc. Roscoe Memorial Symp., Cambridge, pp 285-373

Griffiths D.V. (1980), "Finite element analyses of walls, footings and slopes", PhD thesis, University of Manchester

Griffiths D.V. (1985), "Numerical modelling of interfaces using conventional finite elements", Proc. 5th Int. Conf. Num. Meth. Geomech., Nagoya, pp 837-844

Griffiths D.V. & Lane P.A. (1990), "Finite element analysis of the shear vane test", Computers and structures, Vol. 37, No. 6, pp 1105-1116

Hambly M.A. & Roscoe K.H. (1969), "Observations and predictions of stresses and strains during plane strain of 'wet' clays", 7th ICSMFE, Mexico, Vol. 1, pp 173-181

Hashash Y.M.A. (1992), "Analysis of deep excavations in clay", PhD thesis, Massachusetts Institute of Technology

Hashigushi K. (1977), "An expression of anisotropy in a plastic constitutive equation of soils", 9th ICSMFE, Tokyo, Spec. Session 9, pp 302-305

Hata S., Ohta H., Yoshida S., Kitamura H. & Honda H.A. (1985), "Deep excavation in soft clay. Performance of an anchored diaphragm wall", 5th Int. Conf. Num. Meth. Geomech., Nagoya, Vol. 2, pp 725-730

Henkel D.J. (1960), "The relationships between the effective stresses and water content in saturated clays", Geotechnique, Vol. 10, pp 41-54

Henkel D.J. & Wade N.H. (1966), "Plane strain tests on a saturated remoulded clay", ASCE, SM Div., Vol. 92, pp 67-80

Hermann L.R. (1978), "Finite element analysis of contact problems", ASCE, EM5, Vol. 104, pp 1043-1057

Hight D.W. (1998), "Soil characterisation: the importance of structure, anisotropy and natural variability", 38th Rankine lecture, Geotechnique, in preparation

Houlsby G.T. (1982), "A derivation of the small strain theory of plasticity from thermomechanics", Int. Conf. Deform. and Flow of Granular Mat., Delft, pp 109-118

Houlsby G.T. (1985), "The use of variable shear modulus in elastic-plastic models for clays", Comput. Geotechn., Vol. 1, pp 3-13

Houlsby G.T., Wroth C.P. & Wood D.M. (1982), "Predictions of the results of laboratory tests on a clay using a critical state model", Proc. Int. Workshop on Const. Beh. of Soils, Grenoble, pp 99-121

Hueckel T. & Nova R. (1979), "Some hysteresis effects of the behaviour of geological media", Int. Jnl. Solids Struct., Vol. 15, pp 625-642

Hvorslev M.J. (1937), "Über die Festigkeitseigenschaften Gestörter", Bindiger Böden, Copenhagen

ISSMFE (1985), Subcommittee on Constitutive laws of soils, Constitutive laws

of soils, Edt. Muruyama
Jaky J. (1948), "Pressure in soils", 2nd ICSMFE, London, Vol. 1, pp 103-107
Jardine R.J. (1985), "Investigation of pile-soil behaviour, with special reference to the foundations of offshore structure", PhD thesis, Imperial College, University of London
Jardine R.J. (1992), "Some observations on the kinematic nature of soil stiffness", Soils and Foundations, Vol. 32, No. 2, pp 111-124
Jardine R.J., Potts D.M., Fourie A.B. & Burland J.B. (1986), "Studies of the influence of nonlinear stress-strain characteristics in soil-structure interaction", Geotecnique, Vol. 36, No. 3, pp 377-396
Jardine R.J. & Potts D.M. (1988), "Hutton tension leg platform foundations: An approach to the prediction of driven pile behaviour", Geotechnique, Vol. 38, No. 2, pp 231-252
Katona M.G. (1983), "A simple contact-friction interface element with application to buried culverts", Int. Jnl. Num. Anal. Meth. Geomech., Vol. 7, pp 371-384
Kavvadas M. (1982), "Nonlinear consolidation around driven piles in clays", PhD thesis, Massachusetts Institute of Technology
Kavvadas M. & Baligh M.M. (1982), "Nonlinear consolidation analyses around pile shafts", BOSS '92, Vol. 2, pp 338-347
Kirkgard M.M. & Lade P.V. (1991), "Anisotropy of normally consolidated San Francisco bay mud", Geotechnical testing journal, Vol. 14, No.3, pp 231-246
Kirkpatric W.M. & Rennie I.A. (1972), "Directional properties of consolidated kaolin", Geotechnique, Vol. 22, No. 1, pp 166-169
Kohata Y., Tatsuoka F., Wang L., Jiang G.L., Hoque E. & Kodaka T. (1997), "Modelling of nonlinear deformation properties of stiff geomaterials", Geotechnique, Vol. 47, No. 3, pp 563-580
Kondner R.L. (1963), "Hyperbolic stress-strain response: cohesive soils", ASCE, SM1, Vol. 82, pp 115-143
Kovačević N. (1994), "Numerical analyses of rockfill dams, cut slopes and road embankments", PhD thesis, Imperial College, University of London
Krieg R.D. (1975), "A practical two-surface plasticity theory", Jnl. Appl. Mech., Vol. 42, pp 641-646
Kuwano R. (1998), "The stiffness and yielding anisotropy of sand", PhD thesis, Imperial College, University of London
Lade P.V. (1977), "Elasto-plastic stress-strain theory for cohesionless soil with curved yield surfaces", Int. Jnl. Solids Struct., Vol. 13, pp 1019-1035
Lade P.V. & Duncan J.M. (1975), "Elasto-plastic stress-strain theory for cohesionless soil", ASCE, GT Div. Vol. 101, pp 1037-1053
Lade P.V. & Nelson R.B. (1984), "Incrementalisation procedure for elasto-plastic constitutive model with multiple, intersecting yield surfaces", Int. Jnl. Num. Anal. Meth. Geomech., Vol. 8, pp 311-323
Lade P.V. & Nelson R.B. (1987), "Modelling the elastic behaviour of granular

materials", Int. Jnl. Num. Anal. Meth. Geomech., Vol. 11, pp 521-542
Lagioia R. (1994), "Comportamento meccanico dei terreni cementati naturali: indagine sperimentale ed interpretazioni teoriche", PhD thesis, Politecnico di Milano
Lagioia R. & Nova R. (1995), "An experimental and theoretical study of the behaviour of a calcarenite in triaxial compression", Geotechnique, Vol. 45, No. 4, pp 633-648
Lagioia R. & Potts D.M. (1997), "Stress and strain non-uniformities in triaxial testing of structured soils", Int. Conf. Num. Models Geomech., NUMOG VI, Edt. Pietruszczak & Pande, Balkema, pp 147-152
Lagioia R., Puzrin A.M. & Potts D.M. (1996), "A new versatile expression for yield and plastic potential surfaces", Computers and Geotechnics, Vol. 19, No. 3, pp 171-191
Lai J.Y. (1989), "Stability and deformation analysis of caisson and block foundations", PhD thesis, University of Sidney
Lai J.Y. & Booker J.R. (1989), "A residual force finite element approach to soil-structure interaction analysis", Research Report No. 604, University of Sidney
Lai J.Y. & Booker J.R. (1991), "Application of discrete Fourier series to the finite element stress analysis of axi-symmetric solids", Int. Jnl. Num. Meth. Eng., Vol. 31, pp 619-647
Lo K.Y., Leonards G.A. & Yuen C. (1977), "Interpretation and significance of anisotropic deformation behaviour of soft clays", Norvegian Geotechnical Institute, Publication No. 117, Oslo
Love A.E.H (1927), "A treatise on the mathematical theory of elasticity", Dover Publications, New York
Lupini J.F., Skinner A.E. & Vaughan P.R. (1981), "The drained residual strength of cohesive soils", Geotechnique, Vol. 31, No. 2, pp 181-213
Maccarini M. (1987), "Laboratory studies of a weakly bonded artificial soil", PhD thesis, Imperial College, University of London
Magnan J.P. & Babchia M.Z. (1985), "Analyse numerique des massifs d'argiles molles", 11th ICSMFE, San Francisco, Vol. 2, pp 781-784
Magnan J.P., Belkeziz A., Humbert P. & Mouratidis A. (1982a), "Finite element analysis of soil consolidation with special reference to the case of strain hardening elasto-plastic stress-strain models", 4th Int. Conf. Num. Meth. Geomech., Edmonton, Vol. 1, pp 327-336
Magnan J.P., Humbert P. & Mouratidis A. (1982b), "Finite element analysis of soil deformations with time under an experimental embankment failure", Int. Symp. Num. Models Geomech., Zurich, pp 601-609
Matsui T. & Abe N. (1981), "Multi-dimensional elasto-plastic consolidation analysis by finite element method", Soils & Foundations, Vol. 21, pp 79-95
Matsui T. & Abe N. (1982), "Multi-dimensional consolidation analysis of soft clay", 4th Int. Conf. Num. Meth. Gemech., Edmonton, Vol. 1, pp 337-347

Matsuoka H. & Nakai T. (1974), "Stress-deformation and strength characteristics of soil under three different principal stresses", Proc. Jap. Soc. Civ. Eng., Vol. 232, pp 59-70

Mayne P.W. & Kulhawy F.H. (1982), "K_o - *OCR* relationship in soils" ASCE, GT6, Vol. 108, pp 851-872

McCarron W.F. & Chen W.F. (1988), "An elasto-plastic two surface model for non-cohesive soils", Constitutive equations for granular non-cohesive soils, Edt. Saada & Bianchini, Balkema, pp 427-445

Menkiti C.O. (1995), "Behaviour of clay and clayey sand, with particular reference to principal stress rotation", PhD thesis, Imperial College, University of London

Moore I.D. & Booker J.R. (1982), "A circular boundary element for the analysis of deep underground oppenings", 4th Int. Conf. Num. Meth. Geomech., Edmonton, Canada, pp 53-60

Mouratidis A. & Magnan J.P. (1983), "Un modele elastoplastique anisotrope avec ecrouissage pour les argilles molles naturelles: Melanie", Rev. Fr. Geotechn., Vol. 25, pp 55-62

Mroz Z., Norris V.A. & Zienkiewicz O.C. (1978), "An anisotropic hardening model for soils and its application to cyclic loading", Int. Jnl. Num. Anal. Meth. Geomech., Vol. 2, pp 203-221

Naylor D.J. (1974), "Stresses in nearly incompressible materials by finite elements with application to the calculation of excess pore water pressure", Int. Jnl. Num. Meth. Eng., Vol. 8, pp 443-460

Naylor D.J. (1975), "Nonlinear finite elements for soils", PhD thesis, University of Swansea

Naylor D.J. (1985), "A continuous plasticity version of the critical state model", Int. Jnl. Num. Meth. Eng., Vol. 21, pp 1187-1204

Naylor D.J. (1997), "How an iterative solver can affect the choice of f.e. method", Int. Conf. Num. Models Geomech., NUMOG VI, Edt. Pietruszczak & Pande, Balkema, pp 445-451

Naylor D.J., Pande G.N., Simpson B. & Tabb R. (1981), "Finite elements in geotechnical engineering", Pineridge Press, Swansea, UK

Nilson A.H. (1982), "Finite element analysis of reinforced concrete", State of the Art report prepared by the Task Committee on finite element analysis of reinforced concrete structures", Chairman Nilson A.H., published by the ASCE

Nova R. (1991), "A note on sand liquefaction and soil stability", Conf. Constitutive Laws for Eng. Materials, ASME Press, Tucson, AZ

Nova R. & Hueckel T. (1981), "A unified approach to the modelling of liquefaction and cyclic mobility of sands", Soils & Foundations, Vol. 21, pp 13-28

Nyaoro D.L. (1989), "Analysis of soil-structure interaction by finite elements", PhD thesis, Imperial College, University of London

Ochiai H. & Lade P.V. (1983), "Three-dimensional behaviour of sand with anisotropic fabric", ASCE, GT Div., Vol. 109, No. 10, pp 1313-1328

Ohta H., Kitamura H., Itoh M. & Katsumata M. (1985), "Ground movement due to advance of two shield tunnels parallel in vertical plane", 5th Int. Conf. Num. Meth. Geomech., Nagoya, Vol. 2, pp 1161-1166

Ohta H. & Wroth C.P. (1976), "Anisotropy and stress reorientation in clay under load", 2nd Int. Conf. Num. Meth. Geomech., Blacksburg, Vol. 1, pp 319-328

Ortiz M. & Simo J.C. (1986), "An analysis of a new class of integration algorithms for elasto-plastic constitutive relations", Int. Jnl. Num. Meth. Eng., Vol. 23, pp 353-366

Ovando-Shelley E. (1986), "Stress-strain behaviour of granular soils tested in the triaxial cell", PhD thesis, Imperial College, University of London

Owen D.R.J. & Hinton E. (1980), "Finite elements in plasticity: Theory and practice", Peneridge Press, Swansea, UK

Pande G.N. & Pietruszczak S. (1982), "Reflecting surface model for soils", Int. Symp. Num. Mod. Geomech., Zurich, pp 50-64

Pande G.N. & Sharma K.G. (1979), "On joint/interface elements and associated problems of numerical ill-conditioning", Int. Jnl. Num. Anal. Meth. Geomech., Vol. 3, pp 293-300

Papin J.W., Simpson B., Felton P.J. & Raison C. (1985), "Numerical analysis of flexible retaining walls", Conf. Numerical methods in engineering theory and application, Swansea, pp 789-802

Parathiras A.N. (1994), "Displacement rate effects on the residual strength of soils", PhD thesis, Imperial College, University of London

Parry R.H.G. & Nadarajah V.A. (1973), "A volumetric yield locus for lightly overconsolidated clay", Geotechnique, Vol. 23, pp 450-453

Pastor M., Zienkiewicz O.C. & Leung K.H. (1985), "Simple model for transient soil loading in earthquake analysis. II. Non-associative models for sands", Int. Jnl. Num. Anal. Meth. Geomech., Vol. 9, pp 477-498

Pestana J.M. (1994), "A unified constitutive model for clays and sands", PhD thesis, Massachusetts Institute of Technology, Cambridge, USA

Porović E. & Jardine R.J. (1994), "Some observations on the static and dynamic shear stiffness of Ham River sand", Pre-failure deformation of geomaterials, Edt. Shibuya S., Mitachi T. and Miura S., Balkema, Vol. 1, pp 25-30

Potts D.M. (1985), "Behaviour of clay during cyclic loading", Developments in soil mechanics and foundation eng., Edt. Banerjee & Butterfield, Elsevier, pp 105-138

Potts D.M. & Day R.A. (1991), "Automatic mesh generation of zero thickness interface elements", Proc. 7th Int. Conf. Int. Assoc. Comp. Meth. Advanc. Geomech., Edt. Beer, Booker & Carter, Balkema, Vol. 1, pp 101-106

Potts D.M., Dounias G.T. & Vaughan P.R. (1990), "Finite element analysis of progressive failure of Carsington embankment", Geotechnique, Vol. 40, No. 1, pp 79-101

Potts D.M. & Ganendra D. (1994), "An evaluation of substepping and implicit stress point algorithms", Comput. Meth. Appl. Mech. Eng., Vol. 119, pp 341-354

Potts D.M. & Gens A. (1984), "The effect of the plastic potential in boundary value problems involving plane strain deformation", Int. Jnl. Num. Anal. Meth. Geomech., Vol. 8, pp 259-286

Potts D.M. & Gens A. (1985), "A critical assessment of methods of correcting for drift from the yield surface in elasto-plastic finite element analysis", Int. Jnl. Num. Anal. Meth. Geomech., Vol. 9, pp 149-159

Potts D.M., Kovačević N. & Vaughan P.R. (1997), "Delayed collapse of cut slopes in stiff clay", Geotechnique, Vol. 47, No. 5, pp 953-982

Potts D.M. & Martins J.P. (1982), "The shaft resistance of axially loaded piles in clay", Geotechnique, Vol. 32, No. 4, pp 369-386

Poulos H.G. (1967), "Stresses and displacements in an elastic layer underlain by a rough rigid base", Geotechnique, Vol. 17, pp 378-410

Prevost J.H. (1978), "Plasticity theory for soil stress-strain behaviour", ASCE, EM Div., Vol. 104, pp 1177-1194

Puzrin A.M. & Burland J.B. (1996), "A logarithmic stress-strain function for rocks and soils", Geotechnique, Vol. 46, No. 1, pp 157-164

Puzrin A.M. & Burland J.B. (1998), "Nonlinear model of small strain behaviour of soils", Geotechnique, Vol. 48, No. 2, pp 217-233

Ralston A. (1965), "A first course in numerical analysis", International series in pure and applied mathematics, McGraw-Hill

Randolph M.F. & Houlsby G.T. (1984), "The limiting pressure on a circular pile loaded laterally in cohesive soil", Geotechnique, Vol. 34, No. 4, pp 613-623

Rankine W.J.M. (1857), "On the stability of loose earth", Phil. Trans. Royal Soc., Vol. 147, pp 9-27

Rendulic L. (1936), "Relation between void ratio and effective principal stress for a remoulded silty clay", 1st ICSMFE, Harvard, Vol. 3, pp 48-51

Roscoe K.H. & Burland J.B. (1968), "On the generalised stress-strain behaviour of 'wet' clay", Eng. plasticity, Cambridge Univ. Press, pp 535-609

Roscoe K.H., Schofield A.N. & Wroth C.P. (1958), "On the yielding of soils", Geotechnique, Vol. 8, pp 22-52

Roscoe K.H. & Schofield A.N. (1963), "Mechanical behaviour of an idealised 'wet' clay", 2nd ECSMFE, Wiesbaden, Vol. 1, pp 47-54

Rossato G. (1992), "Il comportamento tensioni-deformazioni nella prova di taglio semplice diretto", PhD thesis, University of Padova (in Italian)

Runesson K.R. & Booker J.R. (1982), Efficient fine element analysis of consolidation", 4th Conf. Num. Meth. Geomech., Edmonton, Canada, pp 359-364

Runesson K.R. & Booker J.R. (1983), "Finite element analysis of elasto-plastic layered soil using discrete Fourier series expansion", Int. Jnl. Num. Meth. Eng., Vol. 19, pp 473-478

Saada A.S., Bianchini G.F. & Palmer Shook L. (1978), "The dynamic response of anisotropic clay", Earthquake engineering and soil dynamics, Pasadena CA, Vol. 1, pp 777-801

Sachdeva T.D. & Ramakrishnan C.V. (1981), "A finite element solution for the two dimensional elastic contact problem", Int. Jnl. Num. Meth. Eng., Vol. 17, pp 1257-1271

Sandler I.S., Di Maggio F.L. & Baladi G.Y. (1976), "Generalised cap model for geological materials", ASCE, GT Div., Vol. 102, pp 683-697

Sandler I.S. & Rubin D. (1979), "An algorithm and a modular subroutine for the cap model", Int. Jnl. Num. Anal. Meth. Gemech., Vol. 3, pp 177-186

Schiffman R.L., Chen A.T.F. & Jordan J.C. (1969), "An analysis of consolidation theories", ASCE, SM1, Vol. 95, pp 285-312

Schofield A.N. & Wroth C.P. (1968), "Critical state soil mechanics", McGraw Hill, London

Seah T.H. (1990), "Anisotropy of normally consolidated Boston Blue clay", ScD thesis, Massachusetts Institute of Technology, Cambridge, USA

Seed H.B., Duncan J.M. & Idriss I.M. (1975), "Criteria and methods for static and dynamic analysis of earth dams", Int. Symp. Criteria and assumptions for numerical analysis of dams, Edt. Naylor, Stagg & Zienkiewicz, pp 564-588

Sekiguchi H. & Ohta H. (1977), "Induced anisotropy and time dependency in clays", 9th ICSMFE, Tokyo, Spec. Session 9, pp 163-175

Simpson B. (1973), "Finite element computations in soil mechanics", PhD thesis, University of Cambridge

Skinner A.E. (1975), "The effect of high pore water pressures on the mechanical behaviour of sediments", PhD thesis, Imperial College, University of London

Sloan S.W. (1987), "Substepping schemes for numerical integration of elasto-plastic stress-strain relations", Int. Jnl. Num. Meth. Eng., Vol. 24, pp 893-911

Small J.C., Booker J.R. & Davies E.H. (1976), "Elasto-plastic consolidation of soils", Int. Jnl. Solids Struct., Vol. 12, pp 431-448

Smith I.M. (1970), "Incremental numerical analysis of a simple deformation problem in soil mechanics", Geotechnique, Vol. 20, pp 357-372

Smith I.M. & Griffiths D.V. (1988), "Programming the finite element method", John Wiley and Sons, New York

Smith P.R. (1992), "The behaviour of natural high compressibility clay with special reference to construction on soft ground", PhD thesis, Imperial College, University of London

Soga K., Nakagawa K. & Mitchel J.K. (1995), "Measurement of stiffness degradation characteristics of clay using a torsional shear device", Earthquake geotechnical engineering, IS-Tokyo, Edt. K. Ishihara, Balkema, Vol. 1, pp 107-112

Sokolovski V.V. (1960), "Statics of soil media", Butterworth Scientific

Publications, London, UK
Sokolovski V.V. (1965), "Statics of granular media", Pergamon Press, Oxford, UK
Stallebrass S.E. & Taylor R.N. (1997), "The development and evaluation of a constitutive model for the prediction of ground movements in overconsolidated clay", Geotechnique, Vol. 47, No. 2, pp 235-254
Stolle D.F. & Higgins J.E. (1989), "Viscoplasticity and plasticity - numerical stability revisited", Int. Conf. Num. Models Gemech., NUMOG III, pp 431-438
Stroud M.A. (1971), "Sand at low stress levels in the SSA", PhD thesis, Cambridge University
Tanaka T., Yasunaka M. & Tani Y.S. (1986), "Seismic response and liquefaction of embankments - numerical solution and shaking table tests", 2nd Int. Symp. Num. Mod. in Geomech., Ghent, pp 679-686
Tanaka T., Shiomi T. & Hirose T. (1987), "Simulation of geotechnical centrifuge test by two-phase FE analysis", Proc. Int. Conf. Computational Plast., Barcelona, Vol. 2, pp 1593-1606
Tavenas F. (1981), "Some aspects of clay behaviour and their consequences on modelling techniques", ASTM STP No. 740, pp 667-677
Tavenas F. & Leroueil S. (1977), "Effects of stresses and time on yielding of clays", 9th ICSMFE, Tokyo, Vol. 1, pp 319-326
Thomas J.N. (1984), "An improved accelerated initial stress procedure for elasto-plastic finite element analysis", Int. Jnl. Num. Meth. Geomech., Vol. 8, pp 359-379
Timoshenko S & Goodier J.N. (1951), "Theory of elasticity", McGraw Hill, New York
Vaid P. & Campanella R.G. (1974), "Triaxial and plane strain behaviour of natural clay", ASCE, Jnl. Geotechnical Eng., Vol. 100, No. 3, pp 207-???
Vaughan P.R. (1989), "Nonlinearity in seepage problems - Theory and field observations", De Mello Volume, Edgard Blucher Ltd., Sao Paulo, pp 501-516
Ward W.H., Samuels S.G. & Gutler M.E. (1959), "Further studies of the properties of London clay", Geotechnique, Vol. 9, No. 2, pp 321-344
Westlake J.R. (1968), "A handbook of numerical matrix inversion and solution of linear equations", John Wiley & Sons
Whittle A.J. (1987), "A constitutive model for overconsolidated clays with application to the cyclic loading of friction piles", PhD thesis, Massachusetts Institute of Technology
Whittle A.J. (1991), "MIT-E3: A constitutive model for overconsolidated clays", Comp. Meth. and Advances Geomech., Balkema, Rotterdam
Whittle A.J. (1993), "Evaluation of a constitutive model for overconsolidated clays", Geotechnique, Vol. 43, No. 2, pp 289-313
Wilson E.L. (1977), "Finite elements for foundations, joints and fluids", Chapter 10 in Finite elements in Geomechanics, Edt. Gudehus, John Wiley & Sons

Winnicki L.A. & Zienkiewicz O.C. (1979), "Plastic (or visco-plastic) behaviour of axisymmetric bodies subjected to non-symmetric loading; semi-analytical finite element solution", Int. Jnl. Num. Meth. Eng., Vol. 14, pp 1399-1412
Wissman J.W. & Hauck C. (1983), "Efficient elasto-plastic finite element analysis with higher order stress point algorithms", Comput. Struct., Vol. 17, pp 89-95
Wroth C.P. & Houlsby G.T. (1980), "A critical state model for predicting the behaviour of clays", Proc. Workshop on Limit Eq., Plasticity and Gen. Stress-strain in Geotech. Eng., Montreal, pp 592-627
Wroth C.P. & Houlsby G.T. (1985), "Soil mechanics - property characterisation and analysis procedures", 11th ICSMFE, San Francisco, Vol. 1, pp 1-55
Yong R.N. & Silvestri V. (1979), "Anisotropic behaviour of sensitive clay", Canadian geotechnical journal, Vol. 16, No. 2, pp 335-350
Zdravković L. (1996), "The stress-strain-strength anisotropy of a granular medium under general stress conditions", PhD thesis, Imperial College, University of London
Zienkiewicz O.C., Chan A.H.C., Paul D.K., Pastor M. & Shiomi T. (1987), "Computational model for soil-pore-fluid interaction in dynamic or static environment", Symp. Centrifuge dynamic model test data and the evaluation of numerical modelling, Cambridge
Zienkiewicz O.C., Chang C.T. & Hinton E. (1978), "Nonlinear sesmic response and liquefaction", Int. Jnl. Num. Anal. Meth. Geomech., Vol. 2, pp 381-404
Zienkiewicz O.C. & Cheng Y. (1967), "Application of the finite element method to problems in rock mechanics", 1st Cong. Int. Soc. Rock. Mech., Lisbon
Zienkiewicz O.C. & Cormeau I.C. (1974), "Visco-plasticity, plasticity and creep in elastic solids - a unified numerical solution approach", Int. Jnl. Num. Meth. Eng., Vol. 8, pp 821-845
Zienkiewicz O.C., Leung K.H. & Hinton E. (1982), "Earthquake response behaviour of soils with drainage", 4th Int. Conf. Num. Meth. Geomech., Edmonton, Vol. 3, pp 982-1002
Zienkiewicz O.C., Leung K.H., Hinton E. & Chang C.T. (1981), "Earth dam analysis for earthquakes: numerical solutions and constitutive relations for nonlinear (damage) analysis", Dams and earthquakes, T. Telford, London, pp 179-194
Zienkiewicz O.C., Leung K.H. & Pastor M. (1985), "Simple model for transient soil loading in earthquake analysis. I. Basic model and its application", Int. Jnl. Num. Anal. Meth. Geomech., Vol. 9, pp 453-476
Zienkiewicz O.C. & Naylor D.J. (1973), "Finite element studies of soils and porous media", Lect. Finite elements in continuum mechanics, Edt. Oden & de Arantes, UAH press, pp 459-493
Zytinski M., Randolph M.F., Nova R. & Wroth C.P. (1978), "On modelling the unloading-reloading behaviour of soils", Int. Jnl. Num. Anal. Meth.

Geomech., Vol. 2, pp 87-93
Zienkiewicz O.C. & Taylor R.L. (1991), "The finite element method", Vol. 2, McGraw Hill, London
Zienkiewicz O.C., Valliapan S. & King I.P. (1968), "Stress analysis of rock as a no-tension material", Geotechnique, Vol. 18, pp 56-66

List of symbols

This list contains definitions of symbols and an indication of the section in the book where they first appear. Because of the large number of parameters that are used, some symbols represent more than one quantity. To minimise any confusion this may cause, all symbols are defined in the text, when they are first used.

a , b	parameters for hyperbolic model	(5.7.4)
b	relative magnitude of the intermediate principal stress	(4.4.3)
$\boldsymbol{b}$	vector which describes the orientation of the bounding surface in transformed variables	(8.7)
c	ratio of semi-axes of the bounding surface ellipsoid in MIT-E3 model	(8.7)
c'	soil cohesion	(1.9.1)
c_p'	soil cohesion at peak strength	(4.3.6)
c_r'	soil cohesion at residual strength	(4.3.6)
$\overline{c}$	adjusted coefficient of consolidation	(10.9)
$\boldsymbol{d}_E$	vector of element nodal displacements	(2.3)
$\boldsymbol{d}_{nG}$	vector of global nodal displacements	(2.3)
$\boldsymbol{d}_u$	vector of unknown displacements	(3.7.3)
$\boldsymbol{d}_p$	vector of prescribed displacements	(3.7.3)
$\boldsymbol{d}^{vp}$	visco-plastic component of displacement	(9.5.2)
$\boldsymbol{d}^{l*}$, $\boldsymbol{d}^{l**}$	vectors of parallel and orthogonal symmetry displacements respectively	(12.3.1)
e	void ratio	(4.3.1)
e_o	initial void ratio	(4.4.1)
$\vec{e}_1$, $\vec{e}_2$	unit vectors in local coordinate system	(II.1.1)
$g(\theta)$	gradient of the yield function in J-p' plane, as a function of Lode's angle	(7.5)
$g_{pp}(\theta)$	gradient of the plastic potential function in J-p' plane, as a function of Lode's angle	(7.5)
$\boldsymbol{g}$	out of balance vector in iterative solution procedures	(11.4)
h	parameter affecting bounding surface plasticity in MIT-E3 model	(8.7)

h	hydraulic head	(10.3)
$\boldsymbol{i}_G$	vector defining the direction of gravity	(10.3)
$\vec{i}, \vec{j}$	unit vectors in global coordinate system	(II.1.1)
k_s	spring stiffness	(3.7.5)
$\boldsymbol{k}$	vector of state parameters for yield function	(6.8)
$\boldsymbol{k}$	permeability matrix	(10.3)
l	length of the failure surface	(1.9.1)
l	distance along beam element	(3.5.2)
$\boldsymbol{m}$	vector of state parameters for plastic potential function	(6.8.3)
m	parameter for plastic expansive strains for Lade' model	(8.5)
n	soil porosity	(3.4)
n	parameter affecting hysteretic elasticity in MIT-E3 model	(8.7)
p	parameter for plastic collapse strains for Lade' model	(8.5)
p_a	atmospheric pressure	(8.5)
p_f	pore fluid pressure	(3.4)
p'	mean effective stress	(4.3.2)
p_c'	mean effective stress at current stress state	(7.5)
p_o'	hardening parameter for critical state models	(7.9)
$\overline{p'_{fi}}$, $\overline{\overline{p'_{fi}}}$	the l^{th} cosine and sine harmonic coefficients respectively, of pore fluid pressure at the i^{th} node	(12.3.7)
q	deviatoric stress	(9.7.2)
q_n	infiltration flow rate	(10.6.4)
$\vec{r}$	position vector	(II.1.1)
s	natural ordinate for beam element	(3.5.4)
$\boldsymbol{s}$	vector of transformed deviatoric stress components	(8.7)
t	parameter for plastic expansive strains for Lade' model	(8.5)
t_c	critical time step for visco-plastic analysis	(8.5.3)
v	specific volume	(7.9.1)
v_1	specific volume at unit mean effective stress (parameter for critical state models)	(7.9.1)
v_{100}	specific volume at p'=100 kPa (parameter for MIT-E3 model)	(8.7)
v_x , v_y , v_z	components of pore fluid velocity in Cartesian coordinate directions	(10.3)
u, v, w	displacement components in x, y, z directions respectively	(1.5.3)
u_l , w_l	displacements tangential and normal to a beam element	(3.5.2)
u_l , v_l	displacement components in local coordinate system	(3.6.2)
u_l^{top} , v_l^{top}	displacement components for the top side of an interface element	(3.6.2)
u_l^{bot} , v_l^{bot}	displacement components for the bottom side of an interface element	(3.6.2)
x, y, z	Cartesian coordinates	(1.5.3)
x_p , y_p	point loading axes	(3.7.7)
z, r, θ	cylindrical coordinates	(1.6.2)
A	cross sectional area of a beam element	(3.5.3)
A	parameter for small strain stiffness model	(5.7.5)
A	elasto-plastic modulus	(6.13)
$\boldsymbol{B}$	strain matrix	(2.6)
B	parameter for small strain stiffness model	(5.7.5)
C	parameter for small strain stiffness model	(5.7.5)
C	parameter for plastic collapse strains for Lade' model	(8.5)
C	parameter affecting hysteretic elasticity in MIT-E3 model	(8.7)
C_C	compression index, i.e. inclination of the VCL in e-$\log_{10}\sigma_v'$ plane	(4.3.1)
C_S	swelling index, i.e. inclination of a swelling line in e-$\log_{10}\sigma_v'$ plane	(4.3.1)
CSL	critical state line	(7.9.1)
$\boldsymbol{D}$	total stress constitutive matrix	(1.5.5)
$\boldsymbol{D}'$	effective stress constitutive matrix	(1.5.5)
$\boldsymbol{D}^{ep}$	elasto-plastic constitutive matrix	(6.13)
$\boldsymbol{D}_f$	pore fluid matrix	(1.5.5)
$\boldsymbol{DM}$	diagonal matrix	(2.9.2)
D	dilatancy	(7.11.1)
E'	drained Young's modulus	(1.5.5)
E_u	undrained Young's modulus	(4.3.2)
E_h'	Young's modulus in horizontal direction	(4.3.5)
E_v'	Young's modulus in vertical direction	(4.3.5)
E_S'	Young's modulus in the depositional direction	(5.6)
E_P'	Young's modulus in the plane of deposition	(5.6)
E	total potential energy	(2.6)
$\boldsymbol{F}$	vector of body forces	(2.6)
F	meridional force for beam element	(3.5.3)
F_ψ	circumferential force for beam element	(3.5.3)
$F(\{\sigma\},\{k\})$	yield function	(6.8)
G	elastic shear modulus	(5.5)

G_{sec}	secant shear modulus	(5.7.5)
G_{tan}	tangent shear modulus	(4.3.3)
G_{vh}	shear modulus in vertical plane	(4.5.1)
G_{PS}	shear modulus in the plane of the direction of deposition	(5.6)
G_{PP}	shear modulus in the plane of deposition	(5.6)
H_1 , H_2	hardening parameters for Lade's model	(8.5)
I	cross sectional moment of inertia of a beam element	(3.5.3)
I_p	plasticity index	(4.5.3)
$\boldsymbol{J}$	Jacobian matrix	(2.6)
J	deviatoric stress invariant	(5.3)
J_c	deviatoric stress invariant at current stress state	(7.5)
$\boldsymbol{K}_E$	element stiffness matrix	(2.3)
$\boldsymbol{K}_G$	global stiffness matrix	(2.3)
$\boldsymbol{K}_u$, $\boldsymbol{K}_p$	diagonal components of the global stiffness matrix, corresponding to unknown and prescribed displacements respectively	(3.7.3)
$\boldsymbol{K}_{up}$	off diagonal terms of the global stiffness matrix	(3.7.3)
$\boldsymbol{K}_a$	pre-conditioning matrix in iterative solvers	(11.4)
K_f	bulk modulus of pore fluid	(3.4)
K_s	bulk modulus of the solid soil particles	(3.4)
K_{skel}	bulk modulus of the soil skeleton	(3.4)
K_e	equivalent bulk modulus	(3.4)
K_s	elastic shear stiffness of interface element	(3.6.2)
K_n	elastic normal stiffness of interface element	(3.6.2)
K_o	coefficient of earth pressure at rest	(4.3.2)
K_o^{NC}	coefficient of earth pressure at rest for normally consolidated soil	(7.9.3)
K_o^{OC}	coefficient of earth pressure at rest for overconsolidated soil	(7.9.3)
K'	effective bulk modulus	(5.5)
K_{sec}	secant bulk modulus	(5.7.5)
K_{tan}	tangent bulk modulus	(4.3.3)
K_{F1} , K_{F2}	parameters for an alternative shape for the yield function for critical state models	(7.11)
K_{P1} , K_{P2}	parameters for an alternative shape for the plastic potential function for critical state models	(7.11)
L	load on a beam	(1.5.2)
L	work done by the applied loads	(2.6)
$\boldsymbol{L}$	lower triangular matrix	(2.9.2)

L_i	area coordinates	(II.1.1)
LER	linear elastic region in stress space	(5.7.6)
$\boldsymbol{L}_G$	off diagonal submatrix in consolidation stiffness matrix	(10.3)
M	bending moment for beam element	(3.5.3)
M_ψ	circumferential bending moment for beam element	(3.5.3)
M_J	gradient of the critical state line in J-p' plane as a constant independent of Lode's angle	(7.9.1)
M_{JP}	yield function parameter	(7.6)
M_{JJ}^{pp}	plastic potential function parameter	(7.6)
N	elastic parameter for Lade's model	(8.5)
$\boldsymbol{N}$	matrix of displacement shape or interpolation functions	(2.5)
$\bar{N}_i$	substitute shape functions	(3.5.4)
$\boldsymbol{N}_p$	matrix of pore fluid pressure interpolation functions	(10.3)
OCR	overconsolidation ratio	(4.3)
$P(\{\boldsymbol{\sigma}\},\{\boldsymbol{m}\})$	plastic potential function	(6.8)
P	parameter for plastic expansive strains for Lade' model	(8.5)
P	spherical component of the flow direction	(8.7)
P^I	spherical component of the flow direction at the image point	(8.7)
$\boldsymbol{P}$	vector of deviatoric components of flow direction, in transformed variables	(8.7)
$\boldsymbol{P}^I$	vector of deviatoric components of flow direction at the image point, in transformed variables	(8.7)
Q	spherical component of the gradient of the bounding surface	(8.7)
$\boldsymbol{Q}$	vector of deviatoric components of the gradient of the bounding surface, in transformed variables	(8.7)
$\boldsymbol{Q}^I$	vector of deviatoric components of the gradient of the bounding surface at the image point, in transformed variables	(8.7)
Q	flow through sources and sinks	(10.3)
$\boldsymbol{Q}$	rotation matrix of direction cosines	(3.7.2)
R	parameter for small strain stiffness model	(5.7.5)
R	parameter for plastic expansive strains for Lade' model	(8.5)
R	parameter for All-Tabbaa & Wood model	(8.9)
$\boldsymbol{R}_E$	vector of element nodal forces	(2.3)

$\boldsymbol{R}_G$	vector of global nodal forces	(2.3)
$\boldsymbol{R}_p$	right hand side load vector corresponding to prescribed displacements	(3.7.3)
$\boldsymbol{R}_u$	right hand side load vector corresponding to unknown displacements	(3.7.3)
$\boldsymbol{R}^{l*}$, $\boldsymbol{R}^{l**}$	parallel and orthogonal symmetry right hand side load vectors respectively	(12.3.1)
$\overline{R_r^l}$, $\overline{R_z^l}$, $\overline{R_\theta^l}$	the l^{th} cosine harmonic coefficient of radial, vertical and circumferential incremental force respectively	(12.3.1)
$\overline{\overline{R_r^l}}$, $\overline{\overline{R_z^l}}$, $\overline{\overline{R_\theta^l}}$	the l^{th} sine harmonic coefficient of radial, vertical and circumferential incremental force respectively	(12.3.1)
S	parameter for small strain stiffness model	(5.7.5)
S	shear force for beam element	(3.5.3)
S, T	natural coordinates	(2.5.1)
S_t	parameter affecting the degree of strain softening in MIT-E3 model	(8.7)
S_u	undrained shear strength	(1.9.1)
Srf	surface of integration	(2.6)
SSR	small strain region in stress space	(5.7.6)
$SSTOL$	substep tolerance in substepping stress point algorithm	(IX.1)
T	parameter for small strain stiffness model	(5.7.5)
T	length of substep in substepping stress point algorithm	(9.6.2)
T	adjusted time factor in consolidation analysis	(10.9)
$\boldsymbol{T}$	vector of surface tractions	(2.6)
T_o	tensile soil strength	(8.3)
$\overline{U_i^l}$, $\overline{V_i^l}$, $\overline{W_i^l}$	the l^{th} cosine harmonic coefficients of radial, vertical and circumferential displacement respectively, at the i^{th} node	(12.3.1)
$\overline{\overline{U_i^l}}$, $\overline{\overline{V_i^l}}$, $\overline{\overline{W_i^l}}$	the l^{th} sine harmonic coefficients of radial, vertical and circumferential displacement respectively, at the i^{th} node	(12.3.1)
Vol	volume of integration	(2.6)
VCL	virgin consolidation line	(7.9.1)
W	weight of a failing block	(1.9.1)
W	strain energy	(2.6)
W_i	weights for numerical Gaussian integration	(2.6.1)

$YTOL$	yield function tolerance for drift	(IX.1)
α	inclination of the major principal stress to the vertical	(4.3.4)
α	parameter for small strain stiffness model	(5.7.5)
α	parameter for plastic expansive strains for Lade' model	(8.5)
α	size of the bounding surface for MIT-E3 model	(8.7)
α	time step parameter in visco-plastic analysis	(9.5.3)
α	parameter for defining the elastic portion of the stress increment in the substepping stress point algorithm	(IX.1)
α_K , α_G	parameters for K-G model	(5.7.3)
α_P , α_F	parameters for an alternative shape for the yield and plastic potential functions for critical state models	(7.11)
β	inclination of failure surface to the vertical	(1.9.1)
β	parameter for plastic expansive strains for Lade' model	(8.5)
β	parameter for iterative solver	(11.4)
β_G	parameter for K-G model	(5.7.3)
β_P , β_F	parameters for an alternative shape for the yield and plastic potential functions for critical state models	(7.11)
γ	bulk unit weight	(1.5.2)
γ	shear strain for beam element	(3.5.2)
γ	parameter for small strain stiffness model	(5.7.5)
γ	parameter affecting bounding surface plasticity in MIT-E3 model	(8.7)
γ_f	bulk unit weight of pore fluid	(10.3)
γ_{xy} , γ_{xz} , γ_{yz}	shear strain components in Cartesian coordinates	(1.5.3)
γ_{rz} , $\gamma_{r\theta}$, $\gamma_{z\theta}$	shear strain components in cylindrical coordinates	(1.6.2)
δ	parameter for small strain stiffness model	(5.7.5)
$\boldsymbol{\delta}$	vector of nodal displacements and rotations for beam element	(3.5.4)
$\boldsymbol{\delta}$	iterative vector	(11.4)
$\boldsymbol{\varepsilon}$	strain vector	(1.5.5)
ε_x , ε_y , ε_z	direct strain components in Cartesian coordinates	(1.5.3)
ε_z , ε_r , ε_θ	direct strain components in cylindrical coordinates	(1.6.2)
ε_v	volumetric strain	(3.4)

ε_v^e	volumetric elastic strain	(7.9.1)
ε_v^p	volumetric plastic strain	(7.9.1)
ε_l	axial strain for beam element	(3.5.2)
ε_ψ	circumferential membrane strain for beam element	(3.5.2)
ε_s	deviatoric strain for triaxial stress space	(4.3.3)
ε^p	component of plastic strain	(6.3)
ε^e	component of elastic strain	(6.13)
$\varepsilon^{\text{crack}}$	crack strain	(8.3)
ε^{vp}	visco-plastic strain	(9.5.2)
ε_s	elasto-plastic portion of the strain increment in substepping stress point algorithm	(IX.1)
ε_{ss}	substep strains in substepping stress point algorithm	(9.6.2)
η	parameter for small strain stiffness model	(5.7.5)
η	stress ratio ($=J/p'$)	(7.11.2)
η	parameter for iterative solver	(11.4)
η_P , η_F	parameters for an alternative shape for the yield and plastic potential functions for critical state models	(7.11)
η_1	parameter for plastic expansive strains for Lade' model	(8.5)
θ	inclination of the major principal stress to the horizontal	(1.9.2)
θ	Lode's angle	(5.3)
θ_c	Lode's angle at current stress state	(7.5)
θ_f	Lode's angle at failure	(7.12)
κ	inclination of swelling line in v-lnp' plane (parameter for critical state models)	(7.9.1)
κ_0	initial slope of the swelling line in v-lnp' plane, MIT-E3 model	(8.7)
κ^*	inclination of swelling line in ln$v$-lnp' plane (parameter for All-Tabbaa & Wood model)	(8.9)
λ	inclination of VCL in v-lnp' plane (parameter for critical state models)	(7.9.1)
λ^*	inclination of VCL in ln$v$-lnp' plane (parameter for All-Tabbaa & Wood model)	(8.9)
μ'	drained Poisson's ratio	(3.3)
μ_u	undrained Poisson's ratio	(3.3)
μ_{SP}'	Poisson's ratio for straining in the plane of deposition due to a stress acting in the direction of deposition	(5.6)
μ_{PS}'	Poisson's ratio for straining in the direction of deposition due to a stress acting in the plane of deposition	(5.6)
μ_{pp}'	Poisson's ratio for straining in the plane of deposition due to a stress acting in the same plane	(5.6)
μ_P , μ_F	parameters for an alternative shape for the yield and plastic potential functions for critical state models	(7.11)
μ	elastic parameter for Lade's model	(8.5)
ν	angle of dilation	(7.5)
ξ , η	system of local coordinates coinciding with two sides of a triangle	(II.1.1)
ρ	parameter for plastic expansive strains for Lade' model	(8.5)
$\boldsymbol{\sigma}$	total stress vector	(1.5.5)
$\boldsymbol{\sigma}'$	effective stress vector	(1.5.5)
$\boldsymbol{\sigma}_f$	pore fluid stress vector	(1.5.5)
σ_x , σ_y , σ_z	direct stress components in Cartesian coordinates	(1.5.2)
σ_z , σ_r , σ_θ	direct stress components in cylindrical coordinates	(1.6.2)
σ_1 , σ_2 , σ_3	major, intermediate and minor principal stress	(1.9.2)
σ_v' , σ_h'	vertical and horizontal effective stress	(4.3.1)
σ_a , σ_r	axial and radial total stress	(4.3.2)
σ_a' , σ_r'	axial and radial effective stress	(4.3.3)
σ_{vc}'	vertical effective consolidation stress	(4.3.4)
σ_Y	yield stress	(6.4)
σ_{nf}'	normal effective stress on the failure plane	(7.5)
σ^{tr}	trial stress in return algorithm	(IX.2)
τ_{xy} , τ_{xz} , τ_{yz}	shear stress components in Cartesian coordinates	(1.5.2)
τ_{rz} , $\tau_{r\theta}$, $\tau_{z\theta}$	shear stress components in cylindrical coordinates	(1.6.2)
τ_f	shear stress on the failure plane	(7.5)
φ'	angle of shearing resistance	(1.9.1)
φ_{cs}'	critical state angle of shearing resistance	(4.3.2)
φ_p'	peak angle of shearing resistance	(4.3.6)
φ_r'	residual angle of shearing resistance	(4.3.6)
φ_{TC}'	critical state angle of shearing resistance in triaxial compression	(8.7)
φ_{TE}'	critical state angle of shearing resistance in triaxial extension	(8.7)
χ_l	bending strain for beam element	(3.5.2)
χ_ψ	circumferential bending strain for beam element	(3.5.2)

ψ	parameter affecting rotation of bounding surface in MIT-E3 model	(8.7)
ψ	parameter for All-Tabbaa & Wood model	(8.9)
ω	elastic parameter for Lade's model	(8.5)
ω	parameter affecting the hysteretic elasticity in MIT-E3 model	(8.7)
$\boldsymbol{\psi}$	vector of residual load	(9.6)
E_d	invariant deviatoric strain	(5.3)
E_d^e	elastic deviatoric strain	(VII.2)
E_d^e	plastic deviatoric strain	(VII.2)
$\boldsymbol{E}$	vector of deviatoric strains in transformed variables	(8.7)
Λ	scalar multiplier for plastic strains	(6.8.3)
$\boldsymbol{\Phi}_G$	permeability submatrix in consolidation stiffness matrix	(10.3)

Index